UNIVERSITY OF VERONA

Department of Neurosciences,
Biomedicine and Movement

Life and Health Sciences PhD School

PhD course in Molecular Biomedicine

XXXIII cycle

HUMAN AROMATIC L-AMINO ACID DECARBOXYLASE: WHEN STRUCTURE AND MOBILITY DRIVE EFFICIENT CATALYSIS. IMPLICATIONS FOR AADC DEFICIENCY

S.S.D. BIO/10

Coordinator: Prof. Massimo Donadelli

Tutor: Prof. Mariarita Bertoldi

PhD candidate: Dott. Giovanni Bisello

"HUMAN AROMATIC L-AMINO ACID DECARBOXYLASE (AADC): WHEN STRUCTURE AND MOBILITY DRIVE EFFICIENT CATALYSIS. IMPLICATIONS FOR AADC DEFICIENCY"

Giovanni Bisello

PhD thesis

Verona, July 11th, 2021

To Elisa

"My only merit is that I did not neglect the observation and that I pursued the subject as a bacteriologist"

Alexander Fleming, 1945

ABSTRACT

Aromatic L-Amino Acid Decarboxylase (AADC) is the enzyme responsible for the synthesis of two essential neurotransmitter dopamine and serotonin from L-Dopa and L-hydroxytryptophan. AADC owes its specific catalytic activity to the chemistry of its cofactor, pyrydoxal-5'-phosphate (PLP). Almost 20 years ago, the crystal structure of a mammalian holoAADC (porcine, sharing 90% of sequence identity) was solved and the availability of its 3D structure paved the way to structural studies. Moreover, 10 years later, human apoAADC structure was published, shedding light on the conformational rearrangement occurring on the apo enzyme upon addition of PLP.

Importantly, apo and holoAADC structures provided crucial insights for the comprehension of the pathogenicity of a number of AADC deficiency associated variants. AADC deficiency (OMIM#608643) is a rare autosomal recessive inborn disease due to missense mutations in the *AADC* gene. Patients bearing these mutations show mild to severe phenotypes, whose destiny is often fatal. Due to the rarity of the disease and to the heterogeneous response to the treatments, medications are not often satisfactory.

In the past years, some efforts on human recombinant AADC pathogenic variants have tried to provide support to the research on AADC deficiency by means of biochemical and biophysical approaches determining the impact of the amino acid substitutions on the enzyme features.

Here, a further contribution to the comprehension of the AADC deficiency is provided. The crystal structure of human holoAADC has been solved under different conditions, both in its native and ligand bound form. The combination of crystallographic studies, molecular dynamics simulations (MD) and site directed mutagenesis uncovered novel aspects of the AADC structure-function relationship. Moreover, the characterization of 21 novel identified pathogenic variants (spread on each AADC domain, N-terminal, Large and C-terminal Domains) led to the widening of the range of enzymatic phenotypes associated to AADC deficiency. The proposed combination of biochemical and kinetic studies permitted to determine correlations between structural and functional signals. Enzymatic phenotypes span from variants characterized by a mild phenotypes to variants

(mainly located at the NTD-CTD interface) whose dramatic structural defects lead to a catalytic incompetence. In addition, MD simulations and *in solutions* data point out a critical role for the loop3 element that contains the essential catalytic residue Tyr332. A group of variants affecting loop3 has been identified as catalytically incompetent and their structural features have been dissected thanks also to the solving of the crystal structure of pathogenic variant L353P, which constitutes the first solved structure of an AADC variant.

Altogether, this study on human AADC provides new elements for the comprehension of the structure-function relationship of AADC with a particular focus on protein dynamics and mobility. Lastly, structural details might represent the basis for both the designing of novel specific inhibitors and for a better comprehension of the molecular aspects of the variants associated with the AADC deficiency.

LIST OF ABBREVIATIONS

5-HIAA	5-hydroxyindoleacetic acid
5-HTR	L-5-hydroxytryptophan receptor
AADC	aromatic amino acids decarboxylase
AC	adenylate cyclase
ADHD	attention deficit hyperactivity disorder
ALDH	aldehyde dehydrogenase
ATP	adenosine triphosphate
BBB	blood-brain barrier
cAMP	cyclic adenosine monophosphate
CarbiDopa	L-α-methyl-α-hydrazino-3,4-2,3,4-trihydroxyphenylpropionic acid
CL	catalytic loop
CNS	central nervous system
CSAD	cysteine sulfinic acid decarboxylase
CSF	cerebrospinal fluid
CTD	C-terminal domain
DA	dopamine
DA	neurons dopaminergic neurons
DAT	dopamine active transporter
DME	L-3,4-dihydroxyphenylalanine methyl ester
DR	dopamine receptor
DTT	1,4-dithiothreitol
GAD65/67	glutamate decarboxylase
HDC	histidine decarboxylase
HME	histidine methyl ester
HVA	homovanillic acid
L-5HTP	L-5-hydroxytryptophan
L-Dopa	L-3,4-dihydroxyphenylalanine
LD	large domain
MAO	monoamine oxidase
NTD	N-terminal Domain
NT	N-terminal
PD	Parkinson's disease
PKA	cAMP-dependent protein kinase
PKC	protein kinase C
pk	pig kidney
PL	Pyridoxal
PLP	pyridoxal 5’-phosphate
PLK	pyridoxal kinase
PMP	pyridoxamine 5’-phosphate
PN	pyridoxine
PNPOx	pyridox(am)ine phosphate oxidase
PTMs	post-translational modifications
SSRIs	selective serotonin reuptake inhibitors
TH	tyrosine hydroxylase
VMAT2	vesicular monoamine transporter-2

SUMMARY

INTRODUCTION

Chapter 1. PYRIDOXAL 5'-PHOSPHATE ENZYMES AND α-DECARBOXYLASES

A. Vitamers B6

Pyridoxal 5'-phosphate (PLP) is the derivative of Pyridoxal (PL) which is a vitamer of vitamin B_6. Vitamin B_6 is a generic term which refers to three interconvertible pyridine compounds called vitamers (PL together with pyridoxamine -PM and pyridoxine -PN) which differ in the chemical group present at the 4' position and in their three phosphorylated forms (PLP, PMP and PNP respectively). While microorganisms and plants are able to perform a *de novo* synthesis of PLP, in humans this anabolic pathway does not exist. Nonetheless, vitamin B_6 can be found in many foods, including meat, milk products, potatoes, beans, nuts and several fruits and vegetables [1]. In addition, once obtained from diet and absorbed in the intestine, vitamers B_6 can be recycled through a "salvage pathway" involving phosphorylation steps (catalysed by pyridoxal kinase, PLK; EC2.7.1.35) and oxidation steps of PNP and PMP (thanks to pyridox(am)ine phosphate oxidase, PNPOx; EC1.4.3.5) and several different phosphatases that altogether yield to PLP, the catalytically active form of vitamin B_6 (**Figure 1**) [2,3].

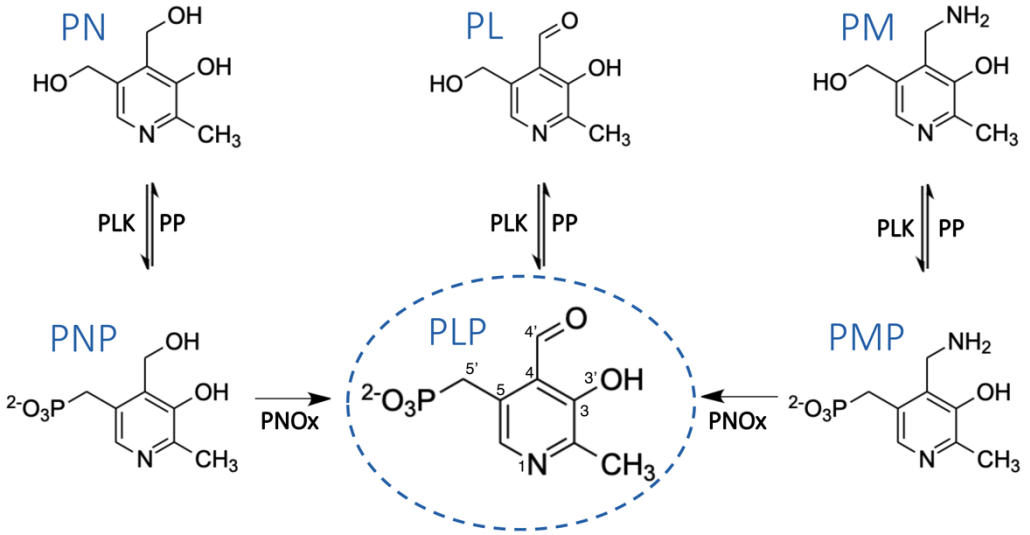

Fig. 1. The structure of free B6 vitamers and PLP salvage pathway. Adapted from [4].

PL coming from diet is cleared by the liver, phosphorylated and secreted into the circulatory blood system where is tightly bound to a lysine residue of albumin [5]. The delivery of PLP to the peripheral tissues and in particular to the blood-brain-barrier (BBB) is combined with activity of membrane associated alkaline phosphatases. Once entered into the target cell, PL is finally re-phosphorylated by PLK [6].

B. PLP-dependent enzymes

Vitamin B_6, in its biologically active form of PLP, plays a primary role acting as a cofactor for a large number of essential enzymes arguably making it the most versatile organic cofactor in all organisms [7–11]. The catalytic versatility of this cofactor is well represented by the genomic data reported by Percudani & Peracchi in [12]. **Figure 2** illustrates 145 PLP-dependent activities as set of enzyme families and superfamilies classified in accordance with the Enzyme Nomenclature Committee of the International Union of Biochemistry and Molecular Biology (EC; http://www.chem.qmul.ac.uk/iubmb/enzyme/).

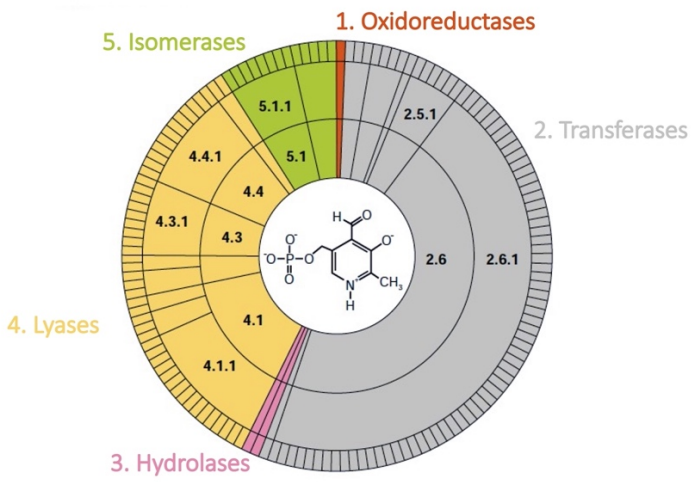

Fig. 2. Catalytic versatility of PLP-dependent enzymes. The Enzyme Commission (EC) identifies an enzyme activity using a four-digit number, where the first digit indicates the general class of the catalyzed reaction (1, oxidoreductases; 2, transferases; 3, hydrolases; 4, lyases; 5, isomerases; 6, synthetases). Of six general classes, five include pyridoxal phosphate (PLP)-dependent enzymes. The catalytic diversity within enzyme families and superfamilies can be illustrated by a set of concentric pie charts [13]. Here, we show the distribution of the 145 PLP-dependent activities that have been classified so far. Sectors are colored according to EC classes. The circles, from inner to outer, represent the first, second, third and fourth levels in the EC hierarchy. The structure of PLP is shown in the center of the graph. Adapted from [12].

The PLP-dependent enzymes belong to five (1, oxidoreductases; 2, transferases; 3, hydrolases; 4, lyases; 5, isomerases) out of seven enzyme classes, performing essential reactions in metabolism of amino acids and amines. In addition to this, despite their incredible functional variety, all these proteins have been initially grouped into five structural families [11,14]. It is a common opinion that PLP-dependent enzymes, sharing similar structure and sequence and catalysing different reactions, represent a remarkable example of divergent evolution.

C. Classification and families of PLP-dependent enzymes

The traditional classification of the PLP-dependent enzymes was initially proposed in 1995 on the basis of amino acid sequence comparisons and structural informations published therefore [14]. This classification has been updated in 1998 by Jansonius *et al.*, and by Denessiou and Schneider [8,11,15]. Subsequently it has been expanded in 2009 [16].

The actual seven structural superfamilies called 'fold type' I to VII are also associated with the name of the prototype enzyme (**Table 1**). Fold type I is the most common superfamily and includes aminotransferases (except for aminotransferase class IV), α-decarboxylases of groups II and III [14,17], and some enzymes performing α-, β- or γ-elimination [18].

Table 1. The fold type superfamily of PLP-dependent enzymes

Superfamily	**Prototype enzyme**	
Fold type I	Aspartate aminotransferase	Proposed by [8,11,14,15]
Fold type II	Tryptophan synthase	
Fold type III	Alanine racemase and eukaryotic ornithine decarboxylase	
Fold type IV	D-amino acid aminotransferase	
Fold type V	Glycogen phosphorylase family	
Fold type VI	D-lysine-5,6-aminomutase	Added by [16]
Fold type VII	Lysine 2,3-aminomutase	

Since the topic of the present thesis regards an α-decarboxylases belonging to fold type I, **table 2** lists a classification of the α-decarboxylases in different groups based on evolutionary extent of conservation of their amino-acid sequence in association to the group of folding [19].

Table 2. PLP-dependent α-decarboxylases. Adapted from [19].

Decarboxylase group	Superfamily	Enzyme members
Group I	Fold type I	Glycine decarboxylase (EC 1.4.4.2)
Group II	Fold type I	Glutamate decarboxylase (EC 4.1.1.15) Histidine decarboxylase (EC 4.1.1.22) Aromatic-L-amino-acid decarboxylase (EC 4.1.1.28) Cysteine sulfinic acid decarboxylase (EC 4.1.1.29)
Group III	Fold type I	prokaryotic Ornithine decarboxylase (EC 4.1.1.17) Lysine decarboxylase (EC 4.1.1.18) Arginine decarboxylase (EC 4.1.1.19)
Group IV	Fold type III	eukatyotic Ornithine decarboxylase (EC 4.1.1.17) Arginine decarboxylase (EC 4.1.1.19) Diaminopimelate decarboxylase (EC 4.1.1.20)

At the beginning of the new century the structural features of group II PLP-dependent α-decarboxylases have attracted particular attention starting from the first crystal structure of a member of this family, *i.e. Sus scrofa* Aromatic L-Amino Acid Decarboxylase (AADC) in 2001 [20] (among other PLP-dependent decarboxylases belonging to different evolutionary groups, only ornithine decarboxylase [21], and dialkylglycine decarboxylase [22] were solved at that time).

D. Group II α-decarboxylases overall topology

Common features of the α-decarboxylases belonging to the fold type I are those of (i) presenting a glycine-rich motif upstream from the PLP-bound lysine residue and (ii) showing a conserved aspartate residue interacting with the cofactor pyridine nitrogen [14,19]. A deep and comprehensive bioinformatics analysis of the deposited structures of the mammalian α-decarboxylases listed in **table 3** has been carried out by Paiardini *et al* [23].

Table 3. PLP-dependent α-decarboxylases belonging to group II [23].

Enzyme	Substrates	Products	Sequence[a]	Structures[b]
AADC	L-Dopa; 5-hydroxy-L-Tryprophan	Dopamine; Serotonin	P20711 (DDC_HUMAN)	1JS3[c], 1JS6[c], 3RBF, 3RBL, 3RCH
HDC	L-Histidine	Histamine	P19113 (DCHS_HUMAN)	4E1O
GAD67	L-Glutamate	GABA	Q99259 (DCE1_HUMAN)	2OKJ, 3VP6[d]
GAD65	L-Glutamate	GABA	Q05329 (DCE1_HUMAN)	2OKK
CSAD	3-sulfino-L-Alanine	Hypotaurine	Q9Y600 (CSAD_HUMAN)	2JIS

[a] *accession code on UniProtKB*
[b] *accession code on ProteinDataBank*
[c] *AADC from Sus scrofa (90% sequence identity with the human enzyme)*
[d] *GAD65/67 chimaera*

In the review, the authors provide details on the structure-function relationships of AADC, histidine decarboxylases (HDC), the two isoforms of glutamate decarboxylase (GAD65 and GAD67) and cysteine sulfinic acid decarboxylase (CSAD) highlighting, at the same time, overall common features and key differences responsible for substrate specificity. These enzymes maintained a number of structural features in common with fold type I PLP-dependent enzymes. Some of these features regard for example their conserved quaternary structure as structural and functional dimeric enzymes [8], and that they maintain all the seventeen structurally conserved regions and the positioning of key residues for the cofactor binding [23]. Moreover, a peculiar feature of human group II decarboxylases is the presence of a highly flexible loop at the active site which is crucial for the decarboxylation mechanism.

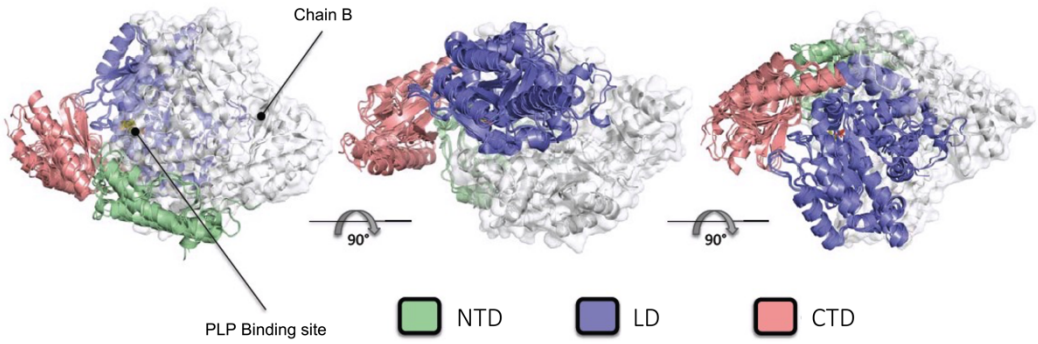

Fig. 3. Structural superposition of AADC, HDC, GAD67, GAD65 and CSAD. In the case of AADC, the *Sus scrofa* structure was used. The N-terminal, large and C-terminal domains are represented in green, cyan and pink, respectively. Chain B is represented as grey cartoons and surface. Adapted from [23].

Each dimer is composed of three distinct domains (**Figure 3**) called: N-terminal domain (NTD, residues 1-85 in AADC), large domain (LD, residues 86-360 in AADC), C-terminal domain (CTD, also called 'small domain' and comprising residues 361-486 in AADC). Moreover, among a number of unstructured loops belonging to the various domains, three have been identified to participate to the active site architecture and named loop1 (amino acids 66-84) loop2 (amino acids 100-110) and loop3 (amino acids 323-354). As firstly described by Burkhard *et al* [20], the LD contains the PLP binding site and its architecture consists in seven-stranded mixed β-sheet (β-barrel) surrounded by eight α-helices in a typical α/β fold. CTD comprises a four-stranded antiparallel β-sheets and three helices. NTD represents a distinctive tract of group II decarboxylases and is composed of two parallel helices linked by an extended strand. Moreover, the two helices of one monomer form a clamp to the neighbouring subunit with each helix aligning antiparallel with the equivalent one of the cognate monomer forming an extended four helix bundle network (**Figure 4**). The intricate organization between these helices leads to the extension of the monomer-monomer interface, and in the case of AADC and GAD65 to the formation of a functional 'hinge' [24,25].

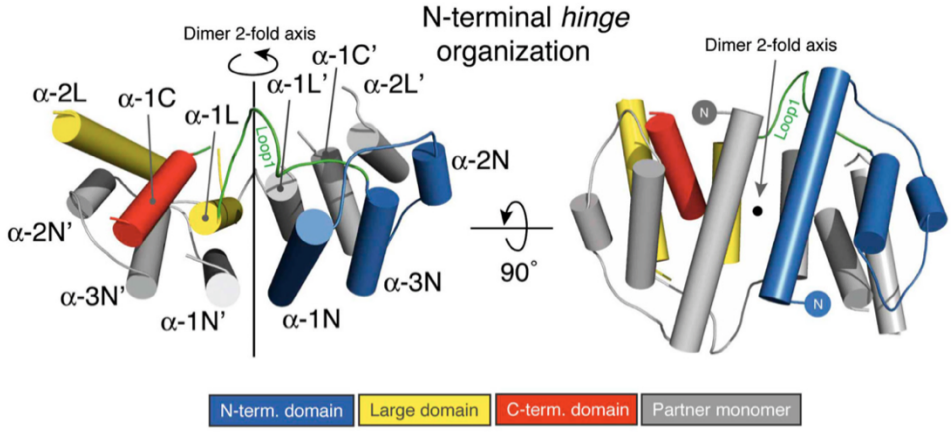

Fig. 4. Structural organization of the N-terminal domain of AADC and dimer interface [24]**.** Organization of the 12 helices cluster that arises from the domain swapping of the N-terminal domain which is peculiar of the Group II decarboxylases. These helices are organized as an extended four helix bundle network and build the dimer interface. Colour code: blue-NTD; yellow-LD; red-CTD. The capital letters used after the helix number denote the domain to which each helix belongs (i.e., α-1N-NTD, α-1L-LD, α-1C-CTD).

E. Group II α-decarboxylases active site

AADC, HDC, GAD65, GAD67 and CSAD exhibit conserved residues interacting with the cofactor (**Table 4**).

The active site of these homologous enzymes is buried in the dimer and at the monomer-monomer interface with the majority of the residues interacting with PLP belonging to one subunit. The cofactor binds to an evolutionarily invariant ε-amino group of a lysine residue through a Schiff base linkage. The protonated nitrogen of PLP is stabilized by the carboxylate group of an aspartate residue (already mentioned as conserved in fold type I enzymes), *via* an electrostatic interaction. The pyridine ring of PLP is further stabilized through a well conserved histidine or arginine forming a base-stacking on its *re* face and a hydrophobic interaction with a conserved alanine residue on its *si* face. A conserved threonine residue stabilizes the oxygen atom in position 3 of PLP *via* a hydrogen bond. Finally, the phosphate group of PLP is anchored to the protein moiety through an extended hydrogen bond network (**Figure 5A**).

Table 4. Residues of group II decarboxylases interacting with PLP and substrate [23].

Enzyme	Cofactor						Ligand	
	Schiff base	N1	O3	Re side	Si side	Phosphate	α –COOH	Side-chain
AADC[1]	K303	D271	T246	H192	A273	S147, A148, S149, N300, H302	H192	T82, I101, H302
HDC	K305	D273	T248	H194	A275	V150, S251, N302, S354	H194	Y81, L102, S354
GAd67[2]	K396	D364	T339	H282	A306	G243, A244, N393, H295, G447	R558	S183, N203, F205
GAD65[3]	K405	D373	T348	H291	A375	G252, A253, N402, H404, G456	R567	S192, N212, F214
CSAD[4]	K305	D273	T248	H191	A275	G152, S153, N302, H304, G357	R466	F94, S114, Y116

[1] *AADC structure from Sus scrofa*
[2, 3] *GAD67 and GAD65 have been solved in complex with the reaction product GABA*
[4] *CSAD have been solved solely in its internal aldimine form with PLP.*

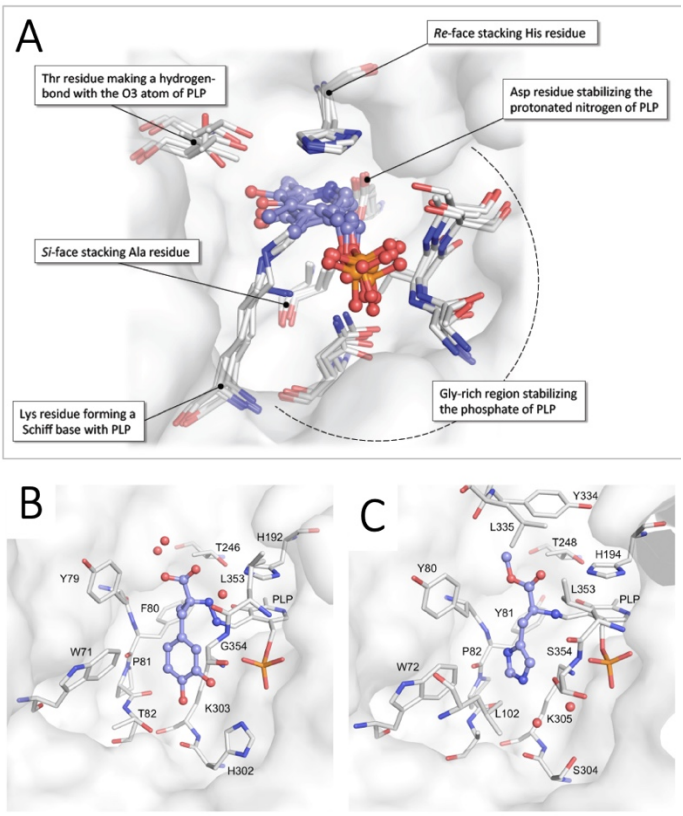

Fig. 5. Homologous residues of group II PLP-dependent α-decarboxylases interacting with cofactor and comparison of AADC and HDC active sites [23]. A) residues are represented as white sticks, PLP is represented as cyan balls and sticks. B) AADC active site, C) HDC active site in presence of carbiDopa and HME respectively. Residues are labelled according to PDB numbering and shown as white sticks. Ligands are shown as cyan ball-and-sticks.

F. AADC and HDC binding to ligands

Porcine AADC and human HDC have been crystallised both in the ligand-free form and in complex with their respective ligands carbiDopa [20] and histidine methyl ester (HME) [26]. In particular, both compounds place the α-carboxylate group approximately orthogonal to the plane of the PLP pyridine ring according with the Dunathan's hypothesis [27], thus these structures provide precious insights into the binding mode of the substrate and into the reaction specificity of these enzymes. The comparison of the crystal structure of the enzymes bound to carbiDopa and HME shows at the same time, a highly similar conformation of the respective external aldimines and key differences responsible for substrate specificity (**figure 5B, C**).

CarbiDopa binds to AADC through its hydrazine group thus forming a hydrazone linkage mimicking the external aldimine [28,29]. His192 and three structural water molecules interact with the α-carboxylate moiety of the compound and Thr82 side chain makes a hydrogen bond with one hydroxyl group of the catechol ring. The second hydroxyl group of carbiDopa interacts with the phosphate moiety of PLP and with His302. In HDC, the imidazole ring of HME points toward the *si* face of the PLP-HME complex and makes two hydrogen bonds with the main chain of Tyr81 and a structural water molecule. Interestingly, the latter and second water molecule occupies the same position of the two hydroxyl groups of the catechol ring of carbiDopa in AADC. The discriminant residue that confers substrate specificity has been suggested to be Ser354 of HDC [26]. In fact, in AADC this residue consists in a glycine residue that permits to accommodate the six-membered ring of the catechol substrate into an enlarged pocket. The S354G mutation in HDC resulted in a decreased affinity for histidine and an acquired ability to bind and catalyse the decarboxylation of L-Dopa [26].

G. Active site mobile catalytic loop of group II α-decarboxylases

As mentioned before, a distinctive structural feature of the human group II decarboxylases is the presence of a highly flexible element generally called 'catalytic loop' (CL) (**figure 6**).

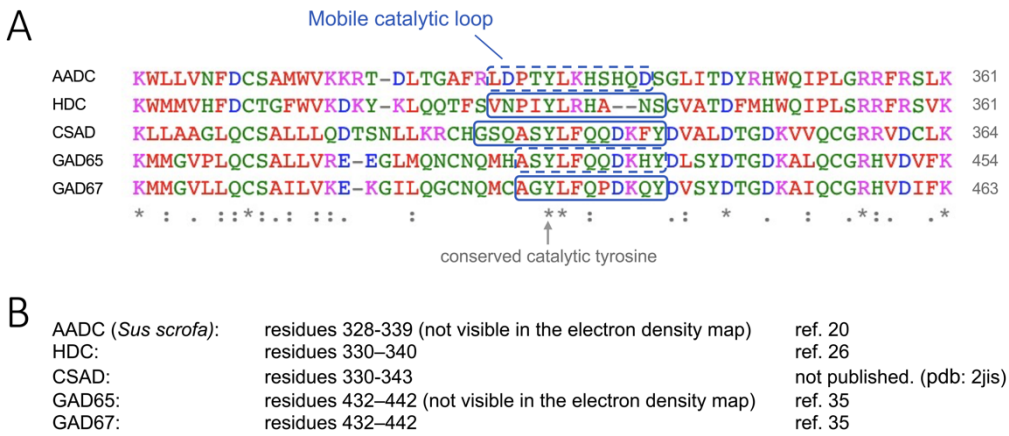

Fig. 6. Multiple sequence alignment of group II PLP-dependent α-decarboxylases. A) Sequences were taken from the NCBI website (https://www.ncbi.nlm.nih.gov/) and aligned with Clustal Omega alignment (http://www.ebi.ac.uk/Tools/msa/clustalo/). Amino acid one-letter code is used. Dashes represent insertions and deletions. Invariant positions are indicated with *. Mobile catalytic loop is circled with a dashed line when electron density map is missing. Conserved catalytic tyrosine is indicated. B) CL residues are reported for each enzyme.

Despite its highly disordered structure, it is clearly assigned in the electron density map of HDC, CSAD and GAD67 (pdb: 4e1o, 2jis and 2okj) while it lacks of the coordinates in the structures of AADC and GAD65 (pdb: 1js6 and 2okk). The solved structures show that the loop is located at the dimer interface and extends towards the active site of the other monomer 'closing' the active site. The mobility of this loop has been associated with an important catalytic role [30–32]. Several studies have shown that this loop is more prone to the cleavage of proteases in the ligand-free form of the enzyme whereas it is somehow protected from proteolysis when the substrate/ligand is bound at the active site [30,33]. Taken together, structural and mechanistic data suggest that in the native form the catalytic loop adopts an 'open' and more solvent exposed conformation that is prone to the proteolytic attack, while upon binding of the substrate/inhibitor the CL becomes more rigid, less susceptible to the cleavage and occludes the active site cleft shielding it from the solvent. The identified tryptic site is a conserved positively charged residue, identified to be Lys334 in AADC, Arg336 in HDC, Lys431 in GAD64 and Lys440 in GAD67 (even if no tryptic data are available on CSAD, according to its amino acid sequence it shows a conserved lysine residue in position 341 analogue with those of GAD56 and GAD67) [25,26,31,32,34,35]. Moreover, structural analysis together

with site direct mutagenesis (Tyr→Phe) in AADC, GAD and HDC suggest that a conserved residue of tyrosine belonging to the CL acts as proton donor to the carbanionic quinonoid intermediate (formed upon release of CO_2) (**Figure 6**) [26,31,35]. Once the substrate/inhibitor is bound, the tyrosine residue moves in close proximity to the PLP-stacking histidine residue that induces a decrease of the pK_a of the tyrosine favoring the protonation of the negatively charged Cα atom of the catalytic intermediate. AADC CL (residues 328-339 in the pk-holo enzyme) constitutes the 'X-ray invisible' part of the element called loop3 (mentioned before).

H. Open conformation of the human apo enzymes AADC and GAD65

In 2011, Giardina *et al* published the first crystal structure of an apo- form of the group II α-decarboxylases, human AADC [24]. Until that moment, *in vitro* biochemical and biophysical analysis clearly pointed out the existence of some conformational differences between holo and apo enzymes [3,36–38]. Human apoAADC, in its crystal form, appears to exist in an unexpected 'open' conformation compared with the compact and 'closed' porcine holo form. In the absence of bound PLP, the dimer subunits move up to 20 Å apart and the active sites become solvent-exposed (with a solvent accessible surface area increased of 14 % (**figure 7**) [25].

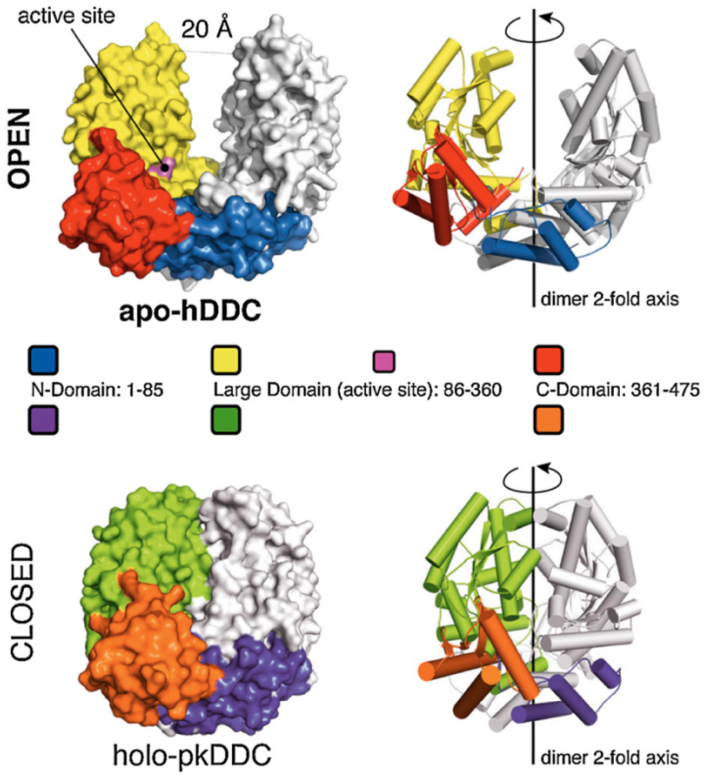

Fig. 7. Human apoAADC in its crystallographic open conformation [24]**.** Surface and cartoon representation of the human apoAADC structure in the open conformation. The domain organization of one monomer is highlighted using different colors (blue - NTD; yellow - LD; Red - CTD) while the other monomer is shown in white. The structure of the porcine holoAADC (pdb id: 1js6) in the closed conformation is shown for comparison in the same orientation; the three domains are colored differently for clarity (purple - NTD; green - LD; orange - CTD).

Globally, the fold of each domain is essentially unchanged in the holo and apoAADC meaning that the achievement of the open conformation occurs through a rigid body quaternary rearrangement of the dimer. The active site and hydrophobic regions become solvent exposed and the two interconnected N-terminal domains remain the only interfaced part of the open-dimer (**figure 7**). The dimeric enzyme has been compared with an 'open bivalve shell' that can close upon coenzyme binding and the extended four helix bundle network of NTD acts as a 'hinge'.

The mechanism of this gross conformational change and its structural determinants have been proposed. In fact, some intermediate structures were solved by soaking the crystals of the apo protein in solution with different PLP concentrations. These structures trapped the active site in different conformations with increasing PLP

occupancy (0, 0.5, 1.5) but never acquiring the catalytically competent complete holo form. Once compared with that of the already published porcine holoAADC, the authors proposed a morphing process occurring upon PLP addition to the apo enzyme [24]. In the apo-to-holo transition a crucial role has been attributed to loop1 (residues 66-84) that, once PLP has bound to Lys303 in the open structure, triggers the rearrangement to the closed conformation by transmitting the change sub sequentially to loop2 (residues 100-110) and in turn to loop3 (which contains the CL). Notably, loop2 and loop3 are not visible in the electron density of both subunits of the apoAADC, meaning that these are mobile or unstructured in absence of PLP.

More recently, another apo structure of PLP-dependent group II decarboxylases was published by Kass *et al*. [25]. In this study the authors coupled *in silico* analysis with small-angle X-ray scattering and limited proteolysis to describe the conformational opening of *holo*-GAD65. Using the origami analogy, they illustrated the mechanism of dimer opening. Their data indicate that GAD65 is more dynamic and flexible than GAD67 and much more susceptible to proteolytic cleavage (at the CL, NTD and CTD) and that a conformational change in GAD65 occurs when PLP is released. Kass *el al*. postulate that for both GAD and AADC the apo-to-holo transition 'unlikely depends solely on the CL conformation' but involves a structural crosstalk between the mobile CL and the CTD [25].

Chapter 2. AADC STRUCTURE-FUNCTION RELATIONSHIP

I. PLP chemistry in catalysis

As already mentioned in chapter 1, the ubiquitous PLP-dependent enzymes account on one hand a limited number of different scaffolds, called fold types, and on the other hand a very wide variety of catalysed reactions, in particular, reactions involved in the metabolism of amino acid and amines. The heteroaromatic pyridinium ring of the PLP carries a strong electron withdrawing capability that enables the coenzyme to stabilize and delocalize the electrons of the α- or β-carbanionic intermediate called quinonoid, facilitating the wide variety of the reactions [39,40].

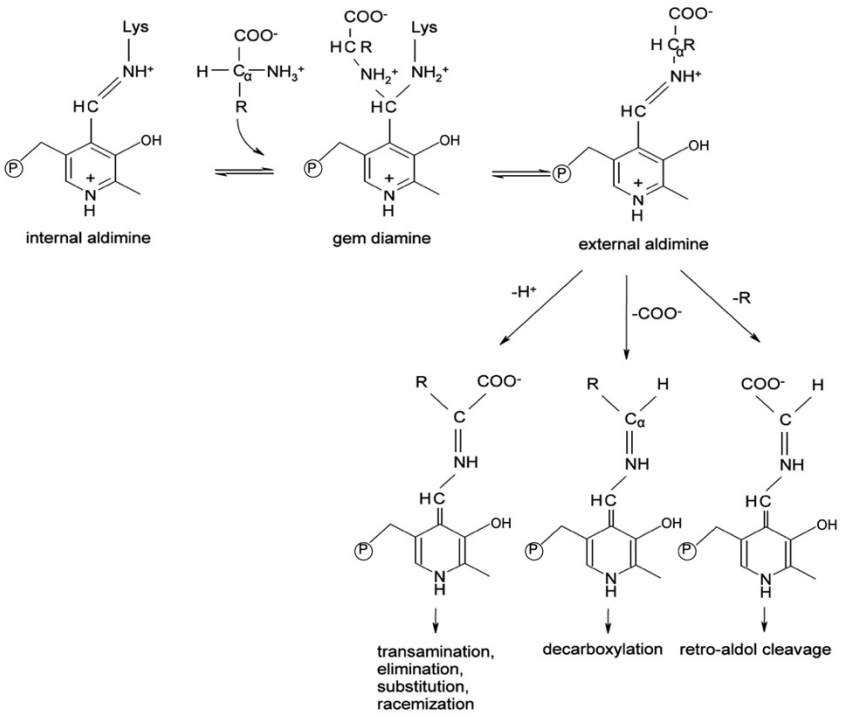

Fig. 8. Catalytic intermediates and versatility of PLP-catalyzed reactions. From [23]

Once the external aldimine is appropriately located, the protein environment confers the reaction specificity. In the PLP-dependent enzymes, the aldehyde group of the cofactor is invariably bound to the ε-amino group of a lysine residue forming a Schiff base structure commonly referred as 'internal aldimine'. The internal aldimine is converted into the 'external aldimine' when the C4' of the cofactor ads

to the α-amino group of the substrate amino acid. This multistep process is called 'transaldimination' and proceeds through a geminal diamine in which both enzyme and substrate amino groups are bound to C4' (**figure 8**). Once the external aldimine is formed, the course of the reaction depends on which of the three substituents in Cα is lost, according to the Dunathan's hypothesis [27]: (i) elimination of CO_2 (α-decarboxylation), (ii) deprotonation (transamination, racemization, β- or γ-elimination) and (iii) elimination of the side chain of the substrate amino acid (α-synthesis and aldol cleavage) (**figure 8**). Once the α-substituent has left, a coplanar structure between the substrate and the cofactor is formed, called quinonoid intermediate (with the exception of PLP-dependent phosphorylases that use PLP in an acid-base chemistry on sugar substrates [41]). The destiny of each intermediate depends on the polypeptide chain and the residues forming the active site cleft.

J. AADC α-decarboxylation and side reactions

As for all group II α-decarboxylases, in AADC the mechanism of α-decarboxylation proceeds by a re-protonation of the Cα to form the amine product (re-protonation mediated by Tyr332 of the CL, as described in chapter 1g) [31]. Finally, after a second transaldimination reaction, the aromatic amine (dopamine or serotonin) is released from the active site with the concomitant reconstitution of the internal aldimine (**figure 9A).** The comprehension of the mechanistic details of AADC catalysis have been initially undertaken on the pig [42] and rat [43] enzymes since the human recombinant form has been obtained solely in 2011 [44]. In these investigations, the use of non-natural ligands has been a useful approach to dissect the properties of the external aldimine.

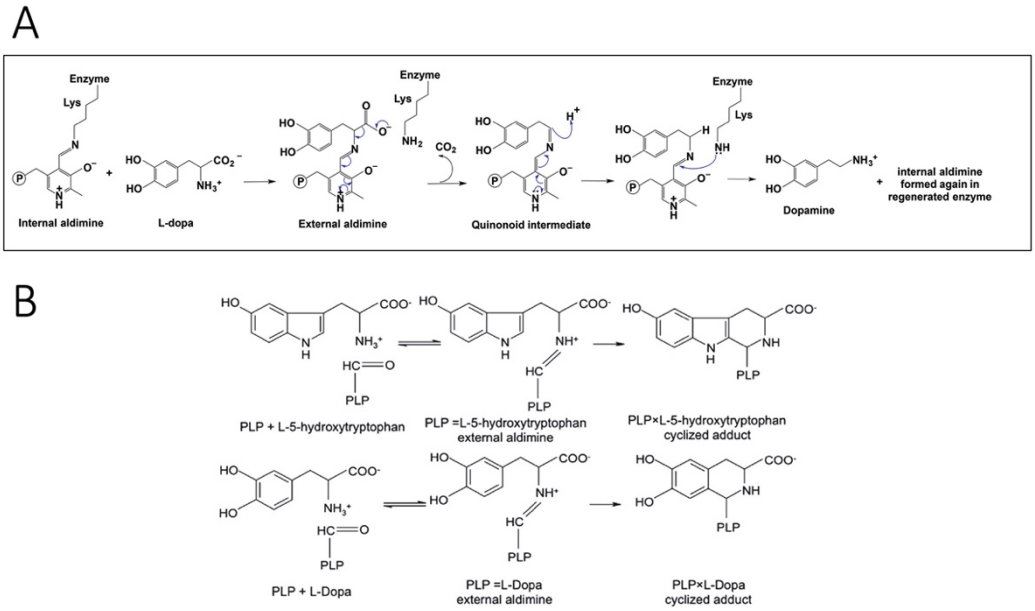

Fig. 9. A) Decarboxylation reaction od L-Dopa and B) Pictet-Spengler cyclization of PLP and L-Dopa. Adapted from [45,46].

Given the inherent high reactivity of the PLP, it is common among PLP-dependent enzymes the possibility to catalyse side-reactions that could sometimes be physiologically significant. D-aromatic amino acids are AADC substrates for a half-transamination reaction [30]. The products of this reaction, reviewed in [47], are an α-keto acid as result of the hydrolysis of the ketimine resulting from the re-protonation of the quinonoid intermediate and the PMP cofactor form that dissociates from the enzyme, leaving it inactive in the apo form.

Reactions with molecular oxygen have been reported in the past twenty years to occur in ADDC and other group II α-decarboxylases (recently reviewed by our group [48]). The unexpected AADC reactivity with molecular oxygen has been described to occur both in presence of the aminic products dopamine and serotonin [49,50] and with other substrates like L-α-methylDopa and D-tryptophan methyl ester [50] (**see figure 10**). This reaction consists in an oxidative deamination that leads to the release of the amino group as ammonia and the oxidation of the Cα forming a carbonyl compound (aldehydic/ketonic product). It has been suggested that the produced aromatic compound, (such as dihydroxyphenyl acetaldehyde, DOPAL, from dopamine [51]) represents a strong biological active signal [48].

Finally, a Pictet-Spengler condensation has been described to occur between the aromatic ring of the substrate and PLP leading to the formation of a cyclic covalent adduct that irreversibly inactivates the enzyme [30,44]. This reaction has been firstly described to occur concomitantly with AADC half transamination in presence of D-substrate (D-5-hydroxytryptophan and D-Dopa) or in the nicked AADC treated with trypsin [30]. All together these results indicate that an inefficient control of PLP reactivity due to a mispositioning of the coenzyme or to a non-natural substrate or to an unproductive 'closure' of the active site may lead to the formation of an unproductive external aldimine that is released as a cyclic substrate-PLP adduct [30].

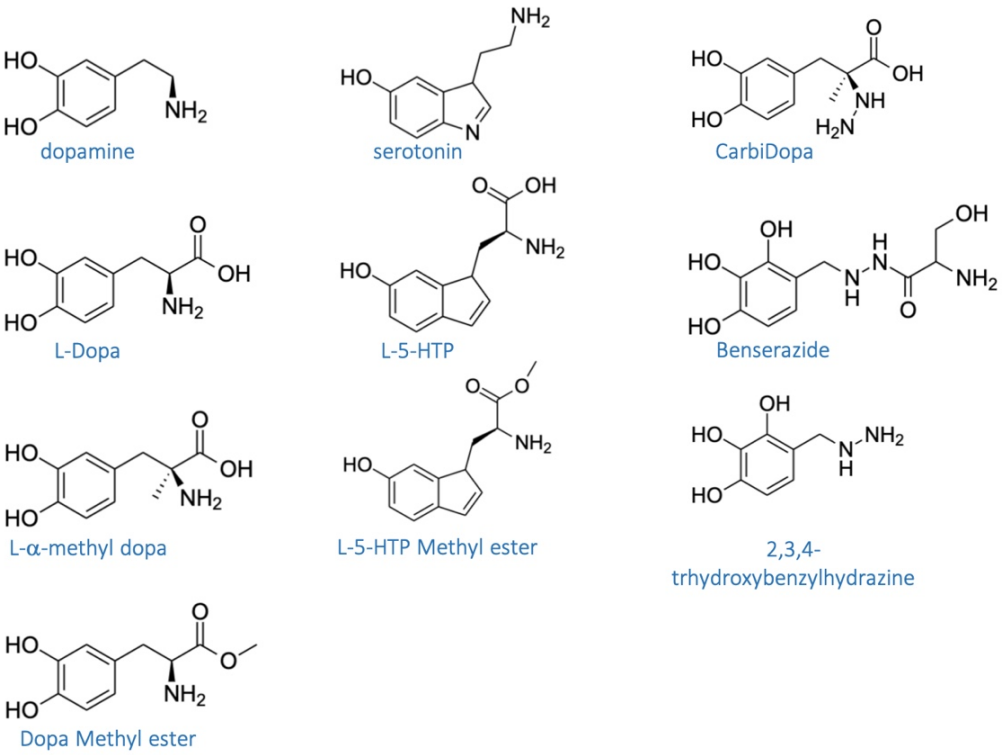

Fig. 10. AADC natural substrates, products, analogues and inhibitors. Dopamine (3,4 dihydroxyphenethylamine), L-Dopa (L-3,4-dihydroxyphenylalanine), DME (Dopa methyl ester), serotonin (5-hydroxytryptamine), L-5-HTP (L-5-hydroxytryptophan), carbiDopa (L-α-methyl-α-hydrazino-3,4-dihydroxyphenylpropionic acid, MK 485), benserazide (trihydroxybenzylhydrazine seryl derivative, Ro-4-4602).

K. Kinetic and spectroscopic features of holo and apoAADC

Human AADC is a homodimeric enzyme where each monomer is composed by 480 residues with a molecular weight of 53926 Da (no disulphide bridges are present, despite the numerous cysteine residues). The protein shows a slight acidic nature having a pI equal to 6.76.

The available functional analysis of human AADC is resumed in **table 5**, in comparison with those of the recombinant porcine enzyme [52].

Table 5. Kinetic parameters of human and porcine ADDC for the decarboxylation of L-Dopa and L-5-HTP. Human kinetic parameters have been calculated in 100 mM potassium phosphate, pH 7.4 while porcine has been analyzed in 50 mM hepes, pH 7.5.

Enzyme	L-aa	k_{cat} (s^{-1})	K_m (mM)	k_{cat}/K_m ($s^{-1}mM^{-1}$)
Human [44]	L-Dopa	7.6 ± 0.1	0.11 ± 0.01	69.1 ± 10
Porcine [52]	L-Dopa	4.3 ± 0.2	0.07 ± 0.005	61.4 ± 7
Human [a]	L-5-HTP	0.63 ± 0.02	0.029 ± 0.006	21.7 ± 4.5
Porcine [52]	L-5-HTP	1.9 ± 0.3	0.15 ± 0.01	13.3 ± 1.7

[a] *calculated during the PhD program, still not published.*

The catalytic features have been evaluated by measuring the kinetic parameters for the decarboxylation of natural substrates L-Dopa and L-5-hydroxytryptophan under steady state conditions. The catalytic efficiency of the two enzymes toward L-Dopa is similar. Notably, activity data of human AADC toward L-5HTP have been determined in this PhD thesis and can be found in **table 5**.

Moreover, the apparent equilibrium dissociation constant for PLP has been calculated to be 43 ± 12 nM for the human enzyme and 44 ± 13 mM for the porcine one, indicating a consistent high affinity for the coenzyme [44,53].

Structure/function relationships of AADC have been obtained by means of spectroscopic and structural studies originally on both the naturally occurring and the recombinant purified pig kidney and rat liver enzymes [30,43,49,51–57] and later on the recombinant purified human AADC [24,44,58–60]. ApoAADC lacks of absorbance in the visible region, while the holo enzyme is characterised by two absorbance bands peaking at 335 nm and 420 nm, associated with positive dichroic signals at

the same wavelengths (**Figure 11A**). These two visible bands have been associated with two ionization states of the internal aldimine. In fact, the Schiff base formed between PLP and Lys303 exists as a tautomeric equilibrium between an enolimine and a ketoenamine tautomer (**Figure 11B**), peaking respectively at 335 nm and 420 nm [59].

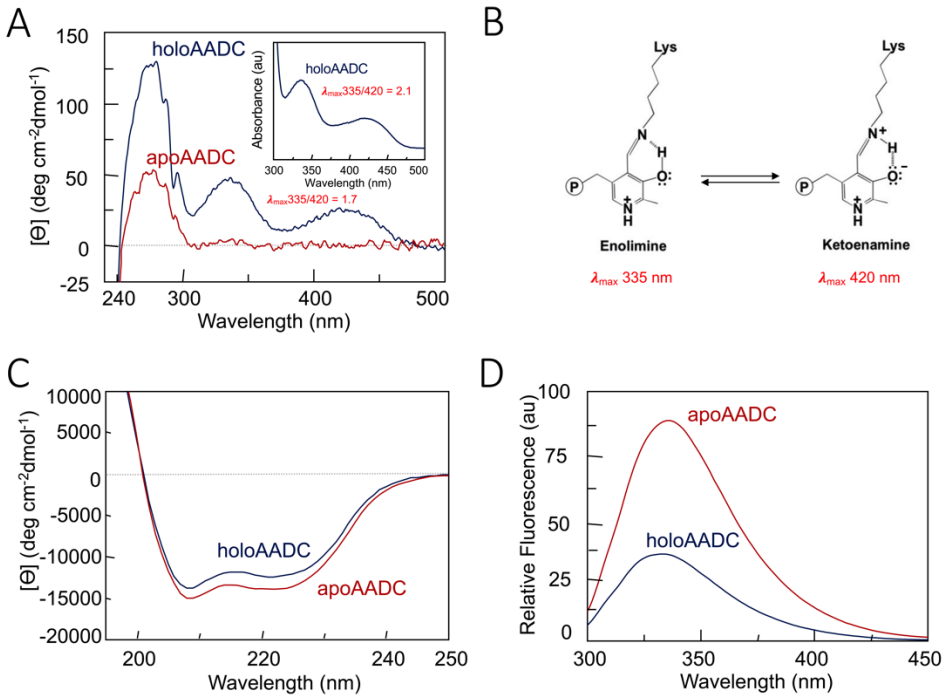

Fig. 11. Spectroscopic features of human apo and holoAADC. A) Near UV-visible circular dichroism spectra of apo and holoAADC together with holoAADC visible absorbance spectrum (inset). Tautomeric equilibrium is indicated as ratio between 335 nm and 420 nm bands, B) chemical representation of the enolimine and ketoenamine species generating the absorbance band in the visible range and peaking at 335 nm and 420 nm, respectively, C) intrinsic fluorescence spectra of apo and holoAADC obtained upon excitation at 280 nm, D) CD spectra of apo and holoAADC recorded in the far-UV region.

In the near-UV region, holoAADC presents a positive dichroic band at 280 nm while the apoAADC presents a band at the same wavelength but with a decreased magnitude, suggesting some structural changes in the microenvironment of aromatic amino acids. Secondary structure signals recorded in the far-UV region consist in intense negative dichroic signals relative in particular to the abundant α-helical content (**Figure 11D**). Upon excitation at 280 nm, the buried environment of the aromatic residues produces an emission spectrum with a λ_{max} of emission at around 330 nm, due to an energy transfer effects to the imine-pyridine system (**figure 11C**).

L. AADC inhibition and regulation

The inhibition of AADC has been object of long research, starting from the identification of carbiDopa and benserazide in 1970s, to the more recent structure based virtual screening of novel molecules [58,61]. In addition, also plant-derived and natural-derived compounds have been tested for AADC activity inhibition [61]. Most of the efforts in the finding of AADC specific inhibitors are focused on the treatment of Parkinson's disease (PD).

PD is neurodegenerative disease consisting in a motor system disorder mainly due to a progressive loss of dopamine-producing cells in the *substantia nigra* in the midbrain. The severe phenotype of PD is mainly characterized by tremor at rest, slowness of movement, and rigidity associated with other non-motor symptoms. At present while no cure exist for PD, a number of palliatives reduces the disease symptoms [62]. Drug treatments aim to replenish dopamine levels at the CNS and since dopamine is enable to cross the BBB, L-Dopa was approved by FDA for the PD treatment in 1970. The common therapy relies on the co-administration of L-Dopa - which represent the gold standard in PD treatment - with peripheral inhibitors (not crossing the BBB) of AADC that prevent L-Dopa degradation by peripheral enzyme and thus increasing its bioavailability for central nervous system (CNS) uptake.

CarbiDopa (L-α-methyl-α-hydrazino-3,4-dihydroxyphenylpropionic acid, MK 485) together with benserazide (trihydroxybenzylhydrazine seryl derivative, Ro-4-4602), are the only two AADC inhibitors actually used as drugs. While carbiDopa is a *per se* AADC powerful irreversible inhibitor [29], benserazide behaves as a poor inhibitor [29], but is rapidly bioactivated to 2,3,4-triydroxybenzylhydrazine [28] (**figure 10**). However, both inhibitors have been shown to react also with free PLP, generating hydrazone-derivatives inhibitors for PLK [63], and also for many other PLP-dependent enzymes, such as kynureninase and kynurenine aminotransferase [64].

Among the chemical compounds tested as AADC inhibitors (but still not used as drugs) there are various α-derivative substrates that act *via* suicide mechanism by alkylating the enzyme. α-chloromethyl-, α-fluoromethyl-, α-vinyl- and α-acetylenic derivative of L-Dopa are reported in [52]. Other compounds consist in the

phosphopyridoxyl aromatic amino acid Schiff base analogs [65] and substrate analogs (such as green tea polyphenols (-)-epigallocatechin-3-gallate, EGCG, and (-)-epicatechin-3-gallate, ECG) [66]. The K_D values reported for these compounds range between 10^{-2} and 10^{-6} M. A more promising AADC inhibitor, called Amb2470350, has been identified through a virtual screening approach and the *in vitro* analysis measured a K_i of 500 nM [58]. Interestingly this leading compound was predicted not to cross the BBB, not to bind free PLP (since it does not contain a hydrazinic group) and to reversibly inhibit AADC.

A putative modulator role has been associated to the paracatalytic reaction of AADC with α-methylDopa. In fact, the oxidative-deaminated product 3,4-dihydroxyphenylacetone behaves as a site direct affinity label forming a covalent adduct at the active site and irreversibly inactivating the enzyme [50]. Moreover, also the carbonyl compounds generated by the oxidative deamination of serotonin (and/or its aldehyde) act as mechanism-based inhibitor [49]. In addition to the mentioned AADC inhibition, evidence for AADC activity modulation by drugs that act on dopamine receptor and other neurotransmitter receptors suggest to consider these drugs a potent adjuvant when developing strategies for L-Dopa treatment augmentation (these aspects are widely reviewed in [67]).

M. Biology of AADC

AADC was first identified in extracts from mammalian kidney in 1938, thus 80 years ago [68]. However, despite its crucial physiological role, the knowledge on its regulation is, till now, fragmented, partial or not mechanistically detailed. For this reason, AADC has classically been regarded as a post-translational unregulated enzyme. Even if no information is found in the official online resource for the notation of protein post-translational modifications (PTMs) *i.e.* biochemically validated data and mass spectrometry data (PhosphoCitePlus®, [69]), some evidences of AADC regulations came from literature.

Until now, no PTMs sites have been identified for human AADC, even if its primary structure contains a number of recognition motifs for phosphorylation by PKA, PKC, Ca-CM PKII, and proline-directed protein kinase [70]. Moreover, its

amino acid sequence shares some conserved residues that have been identified to be ubiquitynated (Lys205, Lys207) [71] and acetylated (Gln383, Lys443) [72] in mouse and rat AADC respectively. Despite this, evidence for a regulated activity mediated by phosphorylation (in mouse AADC) comes from [73] and [74]. More recent data on the mouse enzyme have been reported *in vitro* on the recombinant and immunoprecipitated AADC [41,75]. The main finding in these works is that the enzymatic activity increases up to 70 % once phosphorylated by PKA [75], and that the V_{max} and K_m are increased of ~ 30-60 % respectively when AADC is phosphorylated by cyclic guanosine monophosphate/protein kinase G (cGMP/PKG) [41]. In neither of the cases the authors identified the phosphorylation site. The activation effect carried by phosphorylation has also been reported by Tehranian *et al.* [76]. In their work the authors described a functional direct interaction between AADC and α-synuclein in rat striatum. The effect of this interaction would be a reduction in the AADC phosphorylation level (probably by activation of a phosphatase) and a concomitant inhibition of AADC activity [76].

In addition to the proposed interaction with α-synuclein, human AADC has been suggested to take part of a functional protein complex involving dopamine synthesis and its transport into the synaptic vesicles [77]. Cartier *et al* identified an interaction between the vesicular monoamine transporter-2 (VMAT2) and both tyrosine hydroxylase (TH) and AADC indicating that dopamine synthesis occurs at the synaptic vesicle membrane [77]. Taken together these data suggest that the activation of neuronal AADC by drugs that increase phosphorylation could be a novel and promising approach to the treatment not only of PD but also of other pathological conditions where catecholamine homeostasis is impaired, such as AADC deficiency (see chapter 4). Anyway, at present, no data are available on the effects of phosphorylation and/or other PTMs on AADC activity.

Chapter 3. AADC IN HUMAN METABOLISM

AADC is the enzyme at the crossroad of two monoamine biosynthetic pathways. AADC converts L-Dopa and L-5HTP into the neurotransmitters dopamine and serotonin, respectively. Moreover, dopamine is the precursor of monoamines norepinephrine and epinephrine, also known as noradrenaline and adrenaline (**Figure 12**).

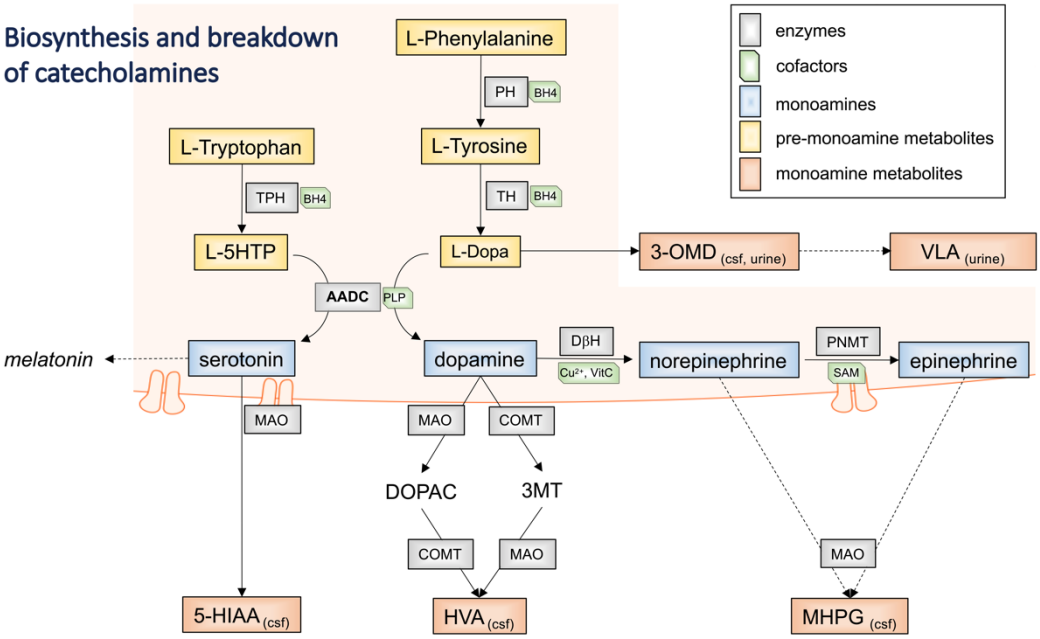

Fig. 12. Summary scheme of the biosynthesis and breakdown of serotonin and the catecholamines (dopamine, norepinephrine and epinephrine), and melatonin synthesis. Cofactors (BH4, PLP, Cu, vitamin C) and methyldonor (SAM) are positioned on the lines relative to the respective enzyme reactions. Dashed arrows do not show intermediate steps. BH4: tetrahydrobiopterin; COMT: catechol O-methyl transferase; CSF: cerebrospinal fluid; Cu: cupper; DβH: dopamine beta hydroxylase; DOPAC: dihydroxyphenylacetic acid; 5-HIAA: 5-hydroxyindoleacetic acid; L-5-HTP: L-5-hydroxytryptophan; HVA: homovanillic acid; L-Dopa: 3,4-dihydroxyphenylalanine; MAO: monoamine oxidase; MHPG: 3-methoxy 4-hydroxyphenylglycol; 3-OMD: 3-O-methyldopa (=3-methoxytyrosine); PH: phenylalanine hydroxylase; SAM: s-adenosylmethionine; TH: tyrosine hydroxylase; TPH: tryptophan hydroxylase; VLA: vanillactic acid.

This enzyme owes its name to the ability to decarboxylate, although with much less efficiency, also other aromatic L-amino acids such as tyrosine, tryptophan and phenylalanine to the corresponding amines tyramine, tryptamine and phenethylamine, known as trace amines. Biochemically, their regulation is quite

similar, with similar proteins regulating synthesis, storage, release, uptake and metabolism. Monoamines and their products are metabolised by the same set of enzymes, mainly by monoamine oxidases (MAO-A/B), aldehyde dehydrogenase (ALDH), catechol-O-methyl transferase (COMT) (**Figure 12**). Final products of their breakdown are homovanillic acid (HVA) from dopamine, and 5-hydroxyindoleacetic acid (5-HIAA) from serotonin. The levels of these metabolites are measured in clinical research, as first line of the analysis to diagnose possible pathological states.

Despite the convergence of dopamine and serotonin metabolic pathways on AADC, this enzyme is not considered rate-limiting for the neurotransmitter synthesis. The rate-limiting enzymes in dopamine and serotonin synthesis are tyrosine hydroxylases (TH) and tryptophan hydroxylase (TPH) respectively. AADC assumes a rate limiting role in those pathological conditions with aberrant dopamine production such as Parkinson's disease and the AADC deficiency [46,61]. In the following paragraphs the main aspects regarding dopamine and serotonin synthesis are discussed, as well as the pathological states in which dopamine homeostasis is involved.

N. Dopaminergic system

There are only ~ 200000 dopaminergic neurons on each side of human brain [78], and the cell bodies of these neurons are confined to a few relatively small brain areas (retrorubral field, RRF, *substantia nigra pars compacta*, ventral tegmental area, posterior hypothalamus, arcuate nucleus, *zona incerta*, and periventricular nucleus) [79,80]. However, their axons project to many other brain areas playing important roles in neuromodulation, such as roles in motor control, motivation, reward, cognitive function, maternal, and reproductive behaviours [81]. There are two main groups of dopamine-producing cells called *substantia nigra* (SN) and ventral tegmental area (VTA). SN neurons project the so-called nigrostriatal dopamine pathway to the striatum and VTA neurons project the mesolimbic and mesocortical pathways to the nucleus accumbens and to the prefrontal cortex respectively [80,82] (**Figure 13A**).

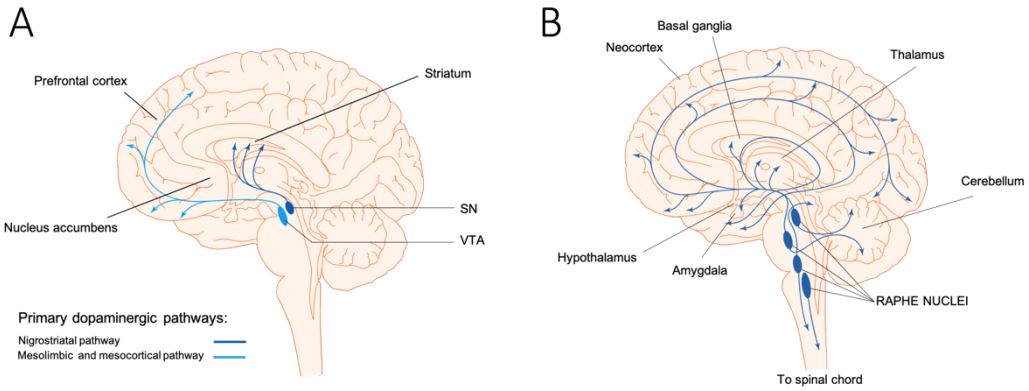

Fig. 13. Representation of midbrain dopaminergic (A) and serotonergic (B) neurons organization and projections in CNS. SN: *substantia nigra*; VTA: ventral tegmental area.

In particular:

- nigrostriatal pathway mediates motor function and learning of new motor skills. Hyperactivity of dopamine in this pathway can lead to dystonia, parkinsonian symptoms and hyperkinetic movements such as dyskinesias [83].
- mesolimbic pathway is the site of the rewards circuit and mediates pleasure. Hyperactivity of dopamine in the mesolimbic pathway mediates positive psychotic symptoms and aggression [83]
- mesocortical pathway regulate cognition, executive functioning as well as emotions. Decreased dopamine in the mesocortical pathway may lead to schizophrenia [83].

Once released from presynaptic terminals, dopamine can be removed from the synaptic cleft by the dopamine active transporter (DAT) and stored again into the vesicles through VMAT2 until a new action potential triggers its release through exocytosis. Tissue-specific response is mediated upon binding to post-synaptic specific G-coupled receptors (GPCRs), expressed in both peripheral and central nervous system, that mediate the signal transduction. Dopamine can bind to five distinct but closely related post-synaptic receptors (D_1-D_5). These receptors are divided into two major groups: D_1-like family receptor comprises D_1 and D_5 receptors, whereas the D_2, D_3 and D_4 receptors are members of the D_2-like family [84,85]. In the brain, GPCRs are expressed at a high level of density in those area where the SN and VTA neurons are projected *i.e* striatum, the nucleus accumbens, the olfactory bulb, frontal cortex among others [84].

Since dopamine does not cross the BBB, dopaminergic signalling in the brain is functionally separated from peripheral dopamine actions [86]. Peripheral dopamine secreting tissues are located in the adrenal medulla, peripheral sympathetic nerves and in those cells that actively take up L-Dopa. In the periphery, dopamine acts as autocrine/paracrine factor regulating the olfaction, retinal processes, cardiovascular functions, immune system, renal functions and is also involved in hormonal regulation and sympathetic regulation [85,87–90]. Moreover, dopamine can be absorbed from food in digestive system and interestingly, up to ~ 95 % of plasma dopamine circulates in a detoxified sulfo-conjugated form [91], while free-dopamine concentration in human plasma is normally very low, about 0.1 nmol/L [92]. Dopamine signalling is crucial for maintaining a number physiological processes and an unbalanced activity may eventually be involved in the progression of neurodegenerative diseases such as Parkinson's disease and Huntington's diseases, and in the nervous system such as schizophrenia, attention deficit hyperactivity disorder, addiction and Tourette's syndrome [81,84]. Targeting dopamine receptors with specific agonists and antagonists still is the opportunity to influence dopaminergic transmission and dopamine-dependent functions by enhancing or blocking the signal transduction.

O. Serotonergic system

Since its isolation in the 40's, serotonin was supposed to be the vasoconstrictor substance contained in platelets [93]. In 1957, Brodie & Shore proposed the role of serotonin as neurotransmitter since it was demonstrated the localization of serotonin receptors in specific areas of the vertebrate brain [94,95]. Only in 1972, Christenson *et al,* demonstrated that a single enzyme, namely AADC, is responsible for the decarboxylation of both L-Dopa and 5-hydroxytryptophan (L-5-HTP) (initially supposed to be Dopa Decarboxylase and Tryptophan Decarboxylase respectively) [96].

Serotonin acts as an important neurotransmitter in the central nervous system (CNS) and a critical hormone in the peripheral tissues [97], and since it does not cross the BBB, each pool of serotonin has distinct functions [98]. Accordingly, in

vertebrate, tryptophan hydroxylase (TPH) is encoded by two different genes generating two different enzymes: TPH1, which is expressed in the periphery, and TPH2 expressed mainly in the brain. Only 5% of the total body serotonin acts as neurotransmitter regulating however multiple physiological roles: behaviour, learning, appetite and glucose homeostasis [98–100]. Serotonin exerts its effects in target cells through at least fourteen identified specific receptors mainly belonging to the G-protein coupled superfamily [101]. The re-uptake of extracellular serotonin occurs through the serotonin transporters (SERT), member of the class of the monoamine transporter, that removes the neurotransmitter from the synaptic cleft. Within the CNS, serotonin is synthesized and stored in the presynaptic neurones (serotonergic neurons, as well as pineal gland and dopaminergic neurons). Nine groups of cell bodies, called raphe nuclei, have been isolated in the midbrain. They have both ascending and descending pathways projecting their axons to the forebrain and spinal cord respectively (**Figure 13B**).

Availability of serotonin in the peripheral tissues is determined by both local production (pancreatic b cells, adipocytes and osteoclasts [101]) and by free-serotonin in the blood. In fact, the 95 % of serotonin is produced in the peripheral organs, where it can acts locally or enter into the blood circulation and being stored by platelets. In fact, only 2 % of the blood serotonin is free and can act as hormone [102]. Decreased serotonin levels are associated with several diseases and disturbs [103]. Consequently a number of drugs are available to help bringing serotonin back to physiological levels. Serotonin homeostasis is altered in major depressive disorders such as mood disorder, anxiety disorder, schizophrenia, addiction, attention deficit hyperactivity disorder and autism [103]. The most diffused and specific class of drug is that of the selective serotonin reuptake inhibitors (SSRIs) that specifically bind to SERT increasing the availability of the neurotransmitter in the synaptic cleft for receptor binding.

Chapter 4. A GENETIC DISEASE OF AROMATIC L-AMINO ACID DECARBOXYLASE: AADC DEFICIENCY

P. AADC deficiency: an overview, from incidence to diagnosis and therapy

AADC deficiency (AADCd, OMIM #608643) is caused by mutations on the *AADC* gene (short arm of chromosome 7 between positions 12.2 and 12.1) that can be present in both homozygosis or compound heterozygosis. AADCd is inherited in an autosomal recessive manner and the age of onset is typically neonatal/infancy. AADCd is classified as very rare disorder since the estimated worldwide prevalence is $<1/10^6$ according to the Orphanet Epidemiological data (www.orpha.net/consor/cgi-bin/index). To date, ~ 130 patients have been identified worldwide, but the total number seems to be under-estimated [104–107]. A total of 82 *AADC* mutations are listed in the locus-specific database (BIOMDB available at: http://biopku.org/home/pnddb.asp). This current variant list includes 58 missense, 6 frame-shift, 9 splice-site, 1 in-frame, 3 complex and 2 nonsense variants. To date, 123 confirmed patients with AADC deficiency have been diagnosed [107]. Due to the rarity of the AADCd and to the heterogeneous phenotype and response to the treatments, to date no univocal guidelines exist. Many efforts have been made, and in 2013 the International Working Group on Neurotransmitter Relater Disorder (iNTD) has been founded and proposed new guidelines of therapy [104].

AADCd is typically detected through detailed clinical assessment and a number of diagnostic tests, starting from the most common symptoms identification. When the diagnosis is clinically suspected, cerebrospinal fluid (CSF) analysis of neurotransmitters should be undertaken, in order to detect the characteristic reduction of homovanillic acid (HVA), 5-hydroxyindoleacetic acid (5-HIAA) and 3-methoxy 4-hydroxyphenylglycol (MHPG) together with an increasing of L-Dopa, L-5-HTP, 3-O-methyldopa (3-OMD) and vanillactic acid (VLA) (see **Figure 14**).

Furthermore, AADC enzymatic activity can be measured in plasma, confirming a decreased or lost enzymatic activity, and finally, AADC genetic sequencing can be performed to definitely confirm the diagnosis [108]. AADCd was first reported by

Hyland *et al*. nearly 30 years ago in male monozygotic twins [109,110]. Their findings demonstrated that both dopamine and serotonin synthesis were affected in central and peripheral nervous systems (as well as norepinephrine and epinephrine), consistent with a deficiency of AADC. Treatment with a monoamine oxidase inhibitor, dopamine agonist and pyridoxine resulted in a striking improvement [109]. The parents were asymptomatic heterozygous. In the following decades the number of diagnosed patients increased, thanks to the growing literature about this disease, with a prevalence in certain Asian population [104], especially in Taiwan and Japan [111], due to an early emergence of a founder splice point variant mutation [111,112].
The range of AADCd symptoms and the variability in clinical manifestation are consequences of the deficiency of the four neurotransmitters dopamine, epinephrine, norepinephrine and serotonin (**Table 6**).

Table 6. Typical signs and symptoms reported in patients with AADC deficiency. Adapted from [107].

Common	**Less common**	**Non-neurologic**
Hypokinesia	Epileptic seizures	Short stature
Hypotonia (proximal)	Sleep disturbance	Diarrhea
Hypertonia (proximal)	Irritability	Constipation
Oculogyric crises	Dysphoria	Feeding difficulties
Developmental delay	Autism-like symptoms	Nasal congestion
Ptosis	Temperature instability	Gastroesophageal reflux
Excessive sweating		Hypoglycemia
Dystonia		

Generally, AADCd should be considered as an early-onset parkinsonism. Deficiencies in dopamine result in altered cognitive function, voluntary movements and can impact emotional state. Reduced levels of epinephrine and norepinephrine can affect mood, attention, normal sleep patterns, cognition and stress hormone levels [107]. Altered serotonin levels affect a number of basal functions, including mood, sleep, memory/learning and bloody temperature as well as cardiovascular and endocrine function [108]. While most patients present a severe phenotype with early onset hypotonia, oculogyric crises, ptosis, dystonia, hypokinesia, impaired development and autonomic dysfunction [108], a few patients with milder disease course are known [113]. In these cases, initial symptoms evolve to become dystonia–

parkinsonism in adulthood. Complications linked to many different aspects of this disease may lead, in some cases, to vegetative state and premature death [108].

There is currently no cure for AADCd. Current medications help the treatments of the signs and symptoms of the disease. Whether or not a treatment works, may depend on the exact nucleotide substitution and the enzymatic phenotype. First-choice medication could include any one or combination of the following [104]: (i) dopamine receptor agonists (such as bromocriptine, pramipexole, or ropinirole) to mimic the effect of dopamine by activating postsynaptic dopamine receptors, (ii) monoamine oxidase inhibitors (such as selegiline or tranylcypromine) in order to avoid dopamine, serotonin and norepinephrine further breaking down, (iii) pyridoxine (vitamin B_6) and PLP to keep AADC saturated with its coenzyme and optimize residual enzyme activity (**Figure 14**).

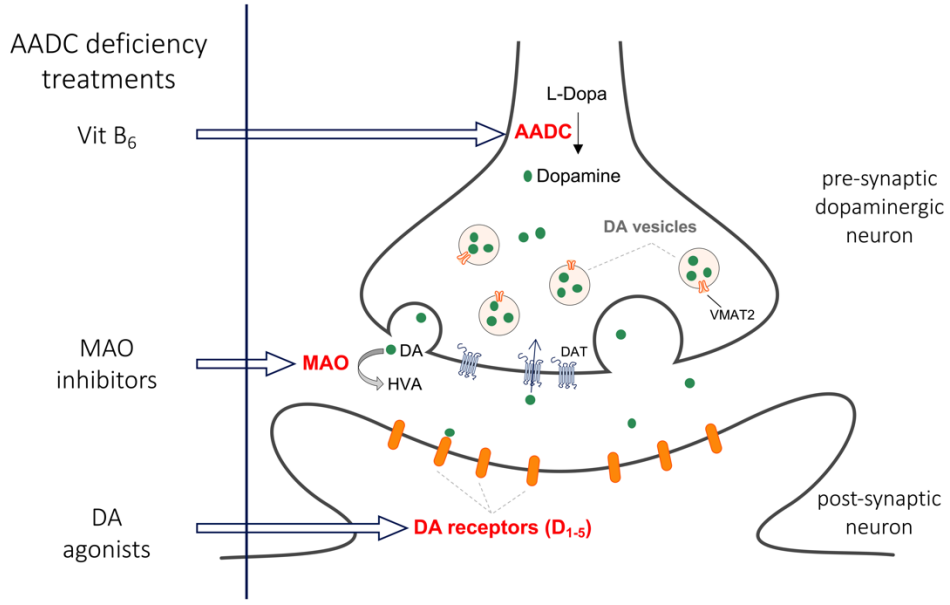

Fig. 14. Alteration of neurotransmitters level in AADC deficiency and current treatment options. Abbreviations: AADC: Aromatic L-Amino Acid Decarboxylase; DA: dopamine; DAT: dopamine transporter; VMAT2: vesicular monoamine transporter-2; MAO: monoamine oxidase.

Other treatments may depend on the symptoms of each individual patient [108]. These treatment options include: (i) anticholinergic agents to treat movement disorders, (ii) seizure medication, (iii) melatonin to treat sleep disturbances, (iv) selective serotonin reuptake inhibitors. In few cases the use of L-Dopa in combination with

pyridoxine has been reported to lead to positive effects only in those patients whose mutations has impact on the substrate binding at the enzyme active site (*i.e* G102S, R160W, R347Q [78,114]). Globally, the response to the treatment of AADCd is often disappointing, in fact, only a small subset of patients shows a good response to dopamine agonists [113], and often, patients show no or poor response [108]. Side effects have been reported for almost every drug used, and are listed in [104]. For most patients, treatment response still cannot be predicted.

Since AADCd is a genetic disease it makes sense to consider therapies that use gene addition or repair to correct and mitigate the effects of the involved genetic lesions. Promising and clinical studies in humans are currently underway [106]. Gene therapy, aimed at targeting to the brain the human *AADC* gene, was originally developed for treating PD patients [115]. Gene transfer aimed at treating AADCd has been firstly performed by Hwu *et al.* in 2012 in four patients in Taiwan with modest but promising results [116]. Gene therapy for AADCd is today under development in Taiwan, Japan and also USA and Europe [106,117,118].

The crucial step in changing the natural history of AADCd in patients still consists in the ability to identify this disorder after its initial presentation and before the onset of brain damage.

Q. AADC deficiency – A molecular investigation

In the past years, molecular investigations on the AADC protein have been undertaken with the aim to provide a better comprehension of the molecular aspects of AADCd by determining the impact of the amino acid substitutions on the enzyme structure and function. In 2011 Montioli *et al.* published the first *in vitro* biochemical investigation of four AADC pathogenic variants [44]. Until now, a number of studies on the recombinant purified homodimeric enzymes are available [44,60,119,120]. More recently, after the emergence of heterozygous genotypes, also heterodimeric enzymes have been obtained, mimicking both the homozygous and heterozygous patients respectively and expanding the spectrum of enzymatic phenotypes associated with AADCd [121,122].

Table 7 lists the kinetic parameters and coenzyme binding affinity of the homodimeric pathogenic variants characterized up to 2019. The picture, emerged in almost a decade after the publication of the human apoAADC crystal structure [24], revealed that the majority of the mutations led to amino acid substitutions of residues belonging to regions involved in the apo-to-holo transition [119]. A correlation between the structural and functional effects of these missense substitutions has been proposed and a role for loop1 region has been suggested [119]. In addition, some catalytically inactive variants showing no gross structural alteration and located close to the active site have been pointed out to play a crucial role in the catalysis [44,120]. In some cases, the biochemical characterization of the pathogenic variants permitted to propose therapeutic promptings based on the *in vitro* determined functional properties [44,60,119].

Table 7. Reported kinetic parameters for L-Dopa of all homodimeric recombinant AADC pathogenic variants from 2011 to 2019.

Enzyme	k_{cat} (s^{-1})	K_m (mM)	k_{cat}/K_m ($sec^{-1}mM^{-1}$)	$K_{D(PLP)}$ (nM)	references
WT	7.6 ± 0.1	0.11 ± 0.01	70.6 ± 8.4	43 ± 12	
G102S	1.2 ± 0.1	1.2 ± 0.1	1.0 ± 0.2	61.7 ± 9.2	
F309L	0.37 ± 0.03	3.8 ± 1.0	0.10 ± 0.03	360 ± 118	44
S147R	0.0090 ± 0.0002	0.12 ± 0.01	0.076 ± 0.008	846 ± 63	
A275T	1.4 ± 0.04	0.35 ± 0.03	4 ± 0.4	7200 ± 1200	
T79M	3.5 ± 0.2	0.46 ± 0.07	7.6 ± 1.2	100 ± 13	
H70T	0.34 ± 0.02	0.69 ± 0.09	0.49 ± 0.07	510 ± 90	
H72Y	0.20 ± 0.01	1.38 ± 0.23	0.14 ± 0.02	2145 ± 409	
Y79C	0.32 ± 0.01	3.98 ± 0.37	0.080 ± 0.007	487 ± 110	
P81L	0.50 ± 0.01	0.19 ± 0.02	2.6 ± 0.5	390 ± 63	
A110Q	0.015 ± 0.01	3.6 ± 0.4	0.004 ± 0.002	829 ± 60	
R347Q	0.087 ± 0.005	0.49 ± 0.08	0.16 ± 0.06	54 ± 10	
L38P	n.d.	n.d.	n.d.	460 ± 58	
P47H	1.70 ± 0.06	0.60 ± 0.05	2.8 ± 0.2	100 ± 24	119
L408I	0.78 ± 0.06	1.78 ± 0.26	0.44 ± 0.07	105 ± 33	
R412W	1.45 ± 0.05	0.27 ± 0.03	5.37 ± 0.61	84 ± 23	
R447H	0.38 ± 0.02	0.79 ± 0.13	0.41 ± 0.07	1010 ± 160	
R462P	0.40 ± 0.01	0.25 ± 0.03	1.60 ± 0.19	544 ± 50	
G123R	3.30 ± 0.14	0.74 ± 0.07	4.46 ± 0.45	101 ± 13	
S250F	2.1 ± 0.1	0.22 ± 0.04	9.3 ± 1.7	62 ± 24	
R285W	2.08 ± 0.08	0.16 ± 0.03	13.0 ± 2.5	335 ± 39	
F309A	0.47 ± 0.03	4.8 ± 0.6	0.097 ± 0.013	225 ± 26	
R347G	0.016 ± 0.001	0.64 ± 0.13	0.025 ± 0.05	178 ± 14	120
R358H	0.030 ± 0.001	4.9 ± 0.4	0.0061 ± 0.0005	1300 ± 100	121
R160W	1.12 0.07	1.95 ± 0.25	0.6 ± 0.08	560 ± 60	
A91V	0.0083 ± 0.0007	0.15 ± 0.01	0.055 ± 0.009	782 ± 47	122
C410G	4.4 ± 0.2	0.27 ± 0.04	16.3 ± 2.4	1070 ± 19	

[n.d] not detectable

The AADCd management still presents a number of still not addressed challenging questions: (i) is there a rational behind the heterogeneity of the medication response? (ii) what are the molecular bases of each clinic phenotype? (iii) is there an approach to get a more effective therapeutic intervention? (iv) is it possible to cluster the patients on the basis of their enzymatic phenotype?

In order to provide a contribution in addressing all these challenges, the present thesis aims at expanding the knowledge of the enzymatic phenotypes associated with the AADCd by characterizing 20 novel identified pathogenic variants (**Table 8**) in their homodimeric form.

Tabel 8. New reported AADC homozygous or hemizygous variants from 2014 to 2020.

New variant	Reference	Note
Y20del	p.c	-
E25K	p.c	-
V60A	44	Hemizygous, the other allele produces a protein that ends prematurely at 248 amino acids, with no formation of the active site
H70Y	123 119	Homozygous, reported incorrectly as H70T
H70R/W71del	p.c	-
F77L	www.bioku.org/pnd/home.asp	-
G96R	107	Hemizygous, the other allele produces a protein that ends prematurely at 248 amino acids, with no formation of the active site
W105C	p.c	-
A110E	104,122	Homozygous, reported incorrectly as A110Q
G146R		-
P210L	124	Hemizygous, the other allele has a mutation leading to a premature stop codon
L222P	124	Homozygous
F237S	113	Hemizygous, the other allele has a mutation leading to a premature stop codon
F251S	125	Hemizygous, the other allele produces a protein that ends prematurely at 248 amino acids, with no formation of the active site
W267R	R. Pons, p.c	R. Pons, personal communication
C281W	p.c	-
E283A	126	Hemizygous, the other allele produces a protein that ends prematurely at 248 amino acids, with no formation of the active site
P330L	p.c	-
L353P	126	Hemizygous, the other allele produces a protein that ends prematurely at 248 amino acids, with no formation of the active site
M362T	p.c	-
R453C	127	Homozygous, reported incorrectly as R375C

[p.c] *personal communication*

MATERIALS AND METHODS

Materials

PLP, L-Dopa, D-Dopa, dopamine, dopa methylester (DME), carbiDopa, hydroxylamine hydrochloride, isopropyl-β-D-thiogalactopyranoside (IPTG), trinitrobenzenesulfonic acid (TNB), phenylmethylsulfonyl fluoride (PMSF), trichoroacetic-acid (TCA), protease inhibitor cocktail (P8849), were purchased from Sigma. Anti AADC monoclonal antibody (8E8) and mouse IgG kappa binding protein (m-IgGk BP) conjugated with HRP were purchased from Santa Cruz Biotechnology.

Site-directed mutagenesis

AADC variants were obtained by mutating the template DNA on the pDDChis vector as previously described [44]. Each mutagenesis reaction has been performed using the Quick-Change II kit (Agilent technologies) using the appropriate oligonucleotides (summarized in the table below) and their complements. All mutations were confirmed by DNA sequence analysis of the whole ORF. S193A plasmid was kindly provided by Prof. Robert S. Phillips at the University of Georgia in Athens (USA), while K334Q by Dr. Riccardo Montioli at the University of Verona (Italy).

Mutation	Oligonucleotide sequence
Y20del	5'-GTGGCCAACATGGAAGGCATTG-3'
Y20A	5'-GTGGCCAACGCCATGGAAGGCATTG-3'
Y20S	5'-CGTGGCCAACAGCATGGAAGGCATTG-3'
E25K	5'-GGAAGGCATTAAGGGACGCCAGGTCTACCC-3'
R27A	5'-CATTGAGGGAGCCCAGGTCTACCCTG-3'
R27Q	5'-CATTGAGGGACAGCAGGTCTACCCTG-3'
V60A	5'-GACATCATCAACGACGCGGAGAAGATAATC-3'
E61A	5'- CGACGTTGCGAAGATAATCATGCCTGGGG-3'
H70Y	5'-CCTGGGGTGACGTATTGGCACAGCC-3'
H70R/W71del	5'-CTGGGGTGACGCGCCACAGC-3'
W71A	5'-CTGGGGTGACGCACGCGCACAGC-3'
F77L	5'-CAGCCCCTACTTCCTGGCCTACTTCC-3
G96R	5'-GACATGCTGTGCCGTGCCATTGGCTGCAT-3'
W105C	5'-CATCGGCTTCTCCTGTGCGGCAAGCCCAG-3'
A110E	5'-GGCAAGCCCAGAATGCACAGAGCTGGAG-3'
S193A	/
S193D	5'-CCGATCAGGCACACGACTCAGTGGAAAGAG-3'
S193E	5'-CATCCGATCAGGCACACGAGTCAGTGGAAA-3'
P210L	·GAAATTAAAAGCCATCCTGTCAGATGGCAACTTC-3'
L222P	5'-ATGCGTGCGTCTGCCCCACAGGAAGCC-3'
F237S	5'-CTGGCCTGATTCCTAGCTTTATGGTTGCCAC-3'
F251S	'-CAACATGCTGCTCCAGCGACAATCTCTTAGAAG-3'
W267R	5'-CAAGGAAGACATACGGCTGCACGTTGATGC-3'
C281W	5'-CAGTGCATTCATCTGGCCTGAGTTCCGGCA-3'
E283A	5'-CATTCATCTGCCCTGCATTCCGGCACCTTC-3'
P330L	5' CCTTTAGACTGGACCTCACTTACCTGAAGC-3'
K334Q	/
L353P	5'-CATTGGCAGATACCACCGGGCAGAAGATTT-3'
M362T	5'-GAAGATTTCGCTCTTTGAAAACGTGGTTTG-3'
R453C	5'-CTTTGCCATCTGTTCTTGCACGGTGGAATCTG-3'

Expression and purification of AADC variants

E. coli BL21 (DE3) cells were transformed by heat shock at 42 °C with the desired construct and grown in 4.5 L of Luria–Bertani (LB) broth in presence of ampicillin (100 mg/ml). The cultures were grown at 37 °C to an OD_{600nm} of 0.4–0.6, and expression was induced with 0.1 mM IPTG for 15 h at 30 °C. Cells were harvested and resuspended in 20 mM sodium phosphate buffer pH 7.4, containing 0.5 M NaCl, 20 mM imidazole, 50 µM PLP, 0.5 mM PMSF and protease inhibitor cocktail. Lysozyme was then added to a concentration of 0.2 mg/ml and the culture was incubated for 30 min at room temperature. After a freeze thaw, leupeptin and pepstatin (both at 1 µg/ml concentration) were added and the suspension was centrifuged at 16,000 g for 30 min. The crude cellular lysate was loaded on a HisPrep FF 16/10 column (GE Healthcare) equilibrated with 20 mM sodium phosphate buffer pH 7.4, containing 0.5 M NaCl and 20 mM imidazole. AADC was eluted with a linear gradient (0–100% in 200 ml) of the same buffer containing 500 mM imidazole. After addition of 100 µM PLP, the protein solution was concentrated and imidazole and unbound coenzyme were removed by extensive

washing with 100 mM potassium phosphate buffer pH 7.4, using Amicon Ultra 15 concentrators (Millipore). The enzymes concentration was determined using an εM of $1.42 \cdot 10^5$ M^{-1} cm^{-1} at 280 nm. PLP content was determined by releasing the coenzyme in 0.1 M NaOH using εM of 6600 M^{-1} cm^{-1} at 388 nm [44].

Size-exclusion liquid chromatography

Size-exclusion liquid chromatography was applied as further purification step. Samples were loaded on a Superdex 200 (10/300) (GE Healthcare) column equilibrated with 100 mM potassium phosphate buffer pH 7.4, on an Akta FPLC system (GE Healthcare). The run was performed using the same buffer at a flow rate of 0.3 ml/min with detection at 280 nm.

Crystallization

Crystallization conditions for WT h-holoAADC were screened at 21 °C by hanging drop vapor diffusion method using commercial crystallization kit (Molecular Dimension, MemGold2^{TM}). Small crystals were obtained under the preliminary conditions of 0.1 M Tris pH 8.5, 44% PEG200, by mixing 1 µl of protein solution (holoAADC 20 mg/mL in 50 mM Hepes pH 7.4) with 1 µl of reservoir. In order to obtain bigger crystals, we further optimized the conditions by changing the buffer, pH and increasing the amount of protein by mixing 1.5 µl of protein solution with 0.5 µl of reservoir. Best crystals were obtained in the four conditions 0.1 M Hepes pH 7.5, 40% PEG 200; 0.1 M Hepes pH 8.5, 40% PEG 200; 0.1 M Tris pH 8.0, 50% PEG 200; 0.1 M Tris pH 9.0, 46% PEG 200. Crystal grew in 2–6 days under all conditions.

Crystals of holoAADC with 1 equivalents of carbiDopa per monomer were obtained by mixing 1.5 µl of protein solution (holoAADC 20 mg/mL in 50 mM Hepes pH 7.4, 2mM carbiDopa) with 0.5 µl. of 0.1 M Hepes pH 7.5, 48% PEG 200; 0.1 M Tris pH 8.0, 42% PEG 200; 0.1 M Tris pH 8.5, 42% PEG 200; 0.1 M Tris pH 9.0, 42% PEG 200.

Crystals of holoL353P were grown at 21 °C by hanging drop vapor diffusion method my mixing 1.5 µl of protein solution (20 mg/mL in 50 mM Hepes pH 7.4) with 0.5 µl of reservoir (0.1 M Tris pH 8.0, 40% PEG 200).

Data Collection, Phasing and Refinement

The diffraction data were collected from crystals frozen at 100°K after a brief immersion in a mixture of 80% of the mother liquor and 20% glycerol.

The data used for refinement of all the crystal structures were collected on the XRD2 beamline of the Elettra Synchrotron in Trieste. The data were indexed, integrated, reduced and converted to structure factors using the programs MOSFLM [128] and the CCP4 software suite [129].

The high resolution structure of WT h-holoAADC at pH 8.0 in Tris buffer was solved using the molecular replacement method as implemented in the program Molrep [130]. The search probe used was the available model to 2.8 Å resolution without LLP, PLP and solvent molecules (pdb: 3rch). All the other crystal forms were modeled into difference Fourier maps phased by the refined WT h-holoAADC pH 8.0 structure.

The final refinement of the nine crystal forms of AADC was carried out initially using the program REFMAC [131] and, in a second stage, with the program Phenix.refine [132].

The models were built using the program Coot [133] and finally subjected to a final round of TLS refinement. The ligands in the co-crystals were modelled into difference Fourier maps phased by the refined, unliganded structure. Solvent molecules were added to the models in the final stages of refinement according to hydrogen-bond criteria and only if their β-factors refined to reasonable values and if they improved the R free.

The diffraction data and refinement statistics of all the models are summarized in Table 9. All solved structures have not been deposited yet.

Modelling of the loops

To obtain complete structures of the enzyme on the apo and holoAADC, we performed molecular modeling using available crystal structures as templates. ApoAADC was modeled against available crystal structure (pdb: 3rbl) using Modeller v9.21 [134]. One hundred models for the apo structure were generated and assessed through DOPE [135] and GA341 [136] scores. The best model was chosen according these scores and visual observation to avoid crossing loops. The same modelling protocol was applied to model the holo enzyme against the solved crystal

structure (structure 1 of **table 9**). However because Modeller wasn't able to correctly model the loops, we used Swissmodel [137] instead, which allowed us to obtain a better model. Once the holo state was modeled, the Lysin-Pyridoxal phosphate was manually introduced in the structure on position 303 of both chains.

Lysin-Pyridoxal phosphate parametrization

The topology parameters of the zwitterionic form of Lys303-PLP (LLP) complex were generated using antechamber package of the AMBER20 tools [134]. The atomic partial charges were computed according to the bcc scheme [135] and the AMBER atom types were assigned. Then, the residue library and parameters forcefield were prepared according to the ff99SB force field. Finally, the topology files were converted to GROMACS' compatible files using the ACPYPE tool [138].

MD Simulations

All atom MD simulations of the apo and holo states of the enzyme were carried out using the GROMACS program, version 2019 . For the holo state simulation, LLP parameters were manually included into the force-field. Water, described with the TIP3P water model [136], and ion molecules (0.154 M of Na^+/Cl^- to mimic physiological conditions) were added to complete the systems. Each system was then equilibrated through a complete workflow: steepest descents minimization of 5000 steps, NVT equilibration of 100 ps, NPT equilibration of 100 ps, and MD production under the NPT ensemble for 300 ns at room temperature.

All calculations were performed within a GPU node available by the computational platform from the "***C**entro **P**iattaforme **T**ecnologiche"* of the University of Verona.

Bioinformatic analysis and Molecular graphics

Human AADC sequence (EC: 4.1.1.28) was aligned with 75 homologues sequences retrieved from Uniref-90 database by the homolog search algorithm PSI-BLAST and aligned using Multiple Sequence Alignment software CLUSTALW on ConSurf server (http://consurf.tau.ac.il). A conservation score (9 = highly conserved, 1 = highly variable) was attributed to each residue. Structural analysis, measurements and figures of the human holoAADC structure (structure 1 in **table 9**) was carried out using Pymol 2.2.3 (The The PyMOL Molecular Graphics

System, Version 2.0 Schrödinger, LLC). Dimeric AADC has been obtained by generating the symmetric mate of the crystallographic monomer. BindProfX was used to predict changes in binding affinity upon mutations in the form of ΔΔG (change in free energy of binding) values. The algorithm combines the FoldX physics-based potential with the conservation scores from pairs of protein-protein interaction surfaces sequence profiles.

Determination of solubility level of the AADC variants

E. coli has been used as a model for the expression study of the pathogenic AADC variants. Chemical competent bacteria were transformed with the proper mutagenized plasmid as described in the expression and purification section. Cultures were grown even in the absence or in the presence of 50 μM exogenous PLP and 1 ml of each culture was processed following the same procedure described above. After lysis, samples were treated with DNase (10 U) at room temperature for 30 min. The whole cell extract was separated by centrifugation at 13,200 rpm, 10 min, 4 °C. Total protein content in the crude cellular lysate was quantified and 15 μg of total protein was run on a 12% (w/w) SDS-PAGE gel. Proteins from the gel were transferred on a nitrocellulose membrane by a Mini Trans-Blot cell (Bio-Rad). Membrane was blocked with a 5% (w/w) milk solution at 37 °C for 1 h and, after the washing steps, it was incubated with a 1:200 (v/v) diluted anti-AADC monoclonal antibody solution over night at 4 °C. Membrane was then washed and then incubated with a 1:4000 (v/v) anti-mouse secondary antibody solution for 1 h at 25 °C. Blotted proteins were detected and quantified with ECL (Millipore), using the ChemiDoc XRS Imaging System (Bio-Rad, Hercules, CA). Quantification of the band was obtained with ImageJ software (Fiji).

Apoenzyme preparation and coenzyme binding affinity measurements

Apoenzyme was obtained by incubating 5 μM holoenzyme with 10 mM hydroxylamine in 0.5 M potassium phosphate buffer pH 6.8 at 25 °C for 3 h. The solution was then loaded on a Desalting 26/10 column (GE Healthcare) pre-equilibrated with 0.5 M potassium phosphate buffer pH 6.8 and eluted at 1 mL/min. The eluted enzyme was then concentrated on an Amicon Ultra 15 concentrators

(Millipore) and washed with 100 mM potassium phosphate buffer pH 7.4. The equilibrium apparent dissociation constant for PLP, KD(PLP), was determined by measuring the quenching of the intrinsic fluorescence of 0.1 μM AADC apoenzyme incubated in the presence of PLP at concentrations ranging from 0.005 to 20 μM for 3 h at 25 °C (in the dark) in 100 mM potassium phosphate buffer pH 7.4.
The data were fitted to the following equation:

$$Y = Y\mathrm{MAX}\frac{[E]t + [PLP]t + KD(PLP) - \sqrt{([E]t + [PLP]t + KD(PLP))2 - 4[E]t[PLP]t}}{2[E]t}$$

where [E]t and [PLP]t represent the total concentrations of the enzyme and PLP, respectively, Y refers to the intrinsic quenching changes at a PLP concentration, and Y_{max} refers to the fluorescence changes when all enzyme molecules are complexed with coenzyme. Curves fitting was performed using Prism, 8.4.0, (GraphPad ®).

Enzyme activity assays

The decarboxylase activity was measured by a stopped spectrophotometric assay [140,141]. Each variant enzyme (at appropriate concentration) was incubated for 1 h under saturating PLP concentration (10 μM) and different L-Dopa concentrations in a final volume of 250 μL in 100 mM potassium phosphate buffer pH 7.4 for a time within which a linear product formation is observed. The reaction was then stopped by heating at 100 °C for 2 min. TNB (1 ml of a 4.3 mM solution) and toluene (1.5 ml) were added and the extraction of trinitrophenyl-derivative was carried out at 42 °C for 45 min with continuous shaking. The concentration of trinitrophenyl-derivative in the toluene layer was quantified using prepared calibration curve of absorbance at 340 nm as a function of trinitrophenyl-derivative concentration [141]. In the case of variants losing the PLP during the reaction with L-Dopa (Y20del, Y20A, Y20S, H70R/W71del, W105C, A110E, S193D, S193E, P330L, R347Q, L353P) kinetic parameters were determined at the HPLC. Each enzyme was incubated in presence of 100 μM PLP and different L-Dopa concentrations in a final volume of 225 μL in 100 mM potassium phosphate buffer pH 7.4 for a time within which a linear product formation is observed. The reaction

was quenched with 25 µL of a 100 % TCA solution. Proteins were precipitated in ice and removed by centrifugation. Supernatants were analyzed by HPLC as described [49,50] using a Gemini C18 column (150 Å~ 4.6 mm, Phenomenex, CA, USA) on a Jasco PU-2080 Plus HPLC system equipped with a UV-1570 detector set at 295 nm. Samples were eluted in 50 mM potassium phosphate, pH 2.35, at a flow rate of 1 mL/min. Standard curves of dopamine peak area were prepared with commercially available dopamine. The kinetic parameters were determined by fitting the data obtained with the Michaelis-Menten equation using Prism, 8.4.0, (GraphPad ®).

Spectroscopic measurements

All spectral measurements were acquired in 100 mM potassium phosphate, pH 7.4, at 25 °C. CD measurements were recorded with a Jasco J-710 spectropolarimeter at a scan speed of 50 nm/min with a bandwidth of 2 nm at a protein concentration of 1–5 µM. Thermal denaturation was performed by monitoring the CD signal at 222 nm of 4 µM enzyme on a 25–90 °C linear temperature gradient, with a temperature slope of 1 °C/min. 100 µM of exogenous PLP was added to the holoenzymes. Analysis of the external aldimine spectral modifications has been carried out on a Jasco V-550 spectrophotometer at a protein concentration of 10 µM in absence or in presence of saturating concentration (2 µM) for all variants, and 20 µM for G96R and G146R) of substrates L-Dopa, DME, carbiDopa. Pictet Spengler adduct has been obtained by incubating PLP and L-Dopa and the corresponded HPLC peak has been collect, desalted, lyophilized. PMP profile was obtained by commercially available compound.

HPLC analysis of coenzyme modification and dopamine formation

Catalytically inactive AADC variants were incubated at 10 µM protein concentration with 2 mM L-Dopa in 100 mM potassium phosphate buffer, pH 7.4 at 25 °C. Concentration-time curves were followed by withdrawing aliquots at time intervals and quenching the reaction by adding trichloroacetic acid to a final concentration of 10% (v/v). Proteins were then precipitated in ice and removed by centrifugation. Supernatants were analyzed by HPLC as described [49,50], using a

GeminiC18 column (150 Å~ 4.6 mm, Phenomenex, CA, USA) and performed on a Jasco PU-2080 Plus HPLC system equipped with a UV-1570 detector set at 295 nm. Samples were eluted in 50 mM potassium phosphate, pH 2.35, at a flow rate of 1 mL/min. Standard curves of peak area as a function of coenzyme or cyclic adducts concentration were prepared with commercially available PLP and coenzyme adducts obtained by synthesis.

NMR experiments

Before NMR analysis, the HPLC-purified compounds were exchanged in water, lyophilized and re-dissolved in D2O. All the NMR spectra were recorded at 298 K on a 600 MHz Bruker AVIII HD spectrometer equipped with a TCI cryogenic probe. For the acquisition we used a spectral width of 20 ppm, an acquisition time of 1.36 s, 32,000 data points and 128 or 256 scans. NMR data were processed with Topspin 3.2. PLP and PMP peak assignments were confirmed by comparing the chemical shifts of the 1D 1H NMR spectra with those from reference spectra deposited in the Biological Magnetic Resonance Data Bank (BMRB). The 1H NMR peak assignments to the Pictet-Spengler adduct were verified by comparing the chemical shifts with previously reported resonances [30], and supported by 2D correlation NMR experiment (TOCSY).

DLS measurements

DLS measurements were obtained on a Zetasizer Nano ZS instrument (Malvern), using disposable ZEN0112 polystyrene cuvettes. Setting used for particle size measurements was the following: solvent refractive index 1.330, viscosity 0.8872 cP, protein refractive index 1.450, protein absorption 0.001, temperature 25 °C, equilibration 2 min, measurement angle 173° backscatter, analysis model multiple narrow modes. Samples were prepared at 3-4 µM protein concentration in 100 mM potassium phosphate, pH 7.4 (with additional 100 µM PLP for the holo forms) and filtered using a 0.02 µm Anotop 10 filter (Whatman). The reported sizes are based on 20 measurements, each consisting of 12-18 runs. Particle size for each sample is indicated as mean ± standard error of means (SEM). The results were compared using Student's t-test between holoWT and holo variants and between apoWT and

apo variants *P < 0.05; **P < 0.01; ***P < 0.001; ****P < 0.0001. Aggregation study was performed with a constant 90° scattering angle and a 633 nm wavelength laser. Protein samples were prepared at 4 μM concentration under physiological conditions (58 mM potassium phosphate, pH 7.4 at 37 °C). 100 μM PLP was added to samples relative to holo forms. The buffer was filtered a 0.02 μm immediately before the use.

Limited proteolysis experiments

Limited proteolysis were performed by incubating 0.54 mg/mL AADC with trypsin at the final E/S ratio of 1:100 (*w/w*) in 100 mM potassium phosphate, pH 7.4 at 25 °C, with the addition of 100 μM PLP for the holoAADC samples. Time points were taken within 1 h of incubation and compared with AADC sample in absence of trypsin. At each time point, the reaction was boiled in SDS sample buffer to stop trypsin activity. The digestion products were separated by SDS/PAGE, and gels were stained with Coomassie blue. The gels were scanned, and peak profiles were obtained for the bands using National Institutes of Health IMAGE J software. All species were calculated as percentage of the undigested band and were graphed against time. Monomer disappearance where fitted to a one phase exponential function. N-terminal cleavage initial rate was estimated by analyzing the appearance of the nicked monomer (51.5 kDa species) with a linear fit.

Identification of the tryptic sites by LC-MS

A solution containing 0.54 mg/mL of WT and variants AADC has been digested with trypsin at 1:100 (*w/w*) in 100 mM potassium phosphate, pH 7.4 at 25 °C, with the addition of 100 μM PLP for the holoAADC samples. Digestion was quenched after 30 min by adding specific trypsin inhibitor at the ratio 1:2 (*w/w*). Reaction mixture was then analyzed and desalted by RP-HPLC (Agilent, mod. 1200, Santa Clara, Ca, USA) with a Jupiter C4 column (4.6 mm x 250 mm, 5 μm; Phenomenex, CA, USA). Peptides peaks were eluted with a gradient of water and acetonitrile, containing 0.1 % of trifluoroacetic acid: from 5 to 38 % in 5 min and from 38 to 43 % in 15 minutes at 226 nm. Peptide identity was assessed with a Xevo® G2-XS ESI-Q-TOF mass spectrometer (Waters Corporation, Milford, Massachusetts,

USA) in positive mode. The capillary potential was set at 1.5 kV. The source temperature was at 100°C. Mass values were determined at a resolution >35.000 and an accuracy <5 ppm. Mass spectra were analyzed by the Mass-Lynx 4.1 software (Waters).

Microfluidic Modulation Spectroscopy

Wilde type AADC and L353P variant were prepared in the apo and holo form at the protein concentration of 0.5 mg/mL in 100mM potassium phosphate, pH 7.4 with the addition of 100 µM PLP for the holoenzymes. Samples with matched buffers were prepared in pairs in 96-well plates. Microfluidic Modulation Spectroscopy (MMS) measurements were made using an automated AQS^{3}Pro system from RedShiftBio, collecting differential absorption spectra between sample and reference pairs. The system provides highly-sensitive and reproducible IR spectra encompassing the amide I band, used for protein secondary structure analysis (1590 - 1710 cm^{-1}). Measurements are made using a Y-shaped microfluidic cell in combination with a tunable quantum cascade laser (QCL) and a thermoelectric cooled HgCdTe (TEC-MCT) detector. Protein sample and reference are alternately flowed through the flow cell with pathlength 24.9 µm at 1 Hz, using dry compressed air at a positive pressure of 5 psi to record differential absorption spectra with a spacing of 4 cm^{-1}. Subtraction of reference from sample spectra in real time due to modulation results in cancellation of any laser output variance and prevents the influence of absorbing components in this range, such as that of water. Flow cell and needle cleaning was performed as part of the measurements, and system cleanliness was measured between samples to ensure no contamination. Differential absorption spectra were deconvoluted to provide secondary structure information automatically as part of the measurement, using inbuilt AQS^3 delta analytics software. Analysis was performed using gaussian curve fitting, based on the model described in [142].

AIMS OF THE THESIS

Many efforts have been made in the past years for elucidating the structural and functional features of human AADC. Biochemical and biophysical approaches contributed to the dissection of the mechanistic aspects of its catalysis. However, some pieces of the puzzle regarding AADC are still missing.

The first part of this thesis aims to provide additional structural details on the WT AADC. The objectives regard:

- determining the crystal structure of human holoAADC in its native and ligand bound form and as a function of pH, in order to unravel structural determinants for the achievement of the structurally competent state;
- analyzing the differences between the apo and holoAADC by means of molecular dynamics simulation highlighting region flexibility, protein mobility and domains crosstalk/communication;
- providing *in solution* data to validate structural data by means of biochemical and biophysical techniques (limited proteolysis, spectroscopy, kinetics, site directed mutagenesis).

The second part aims to expand the knowledge of the enzymatic phenotypes associated with the AADC deficiency. To this, the following objectives were pursued:

- Cloning, expressing and purifying both artificial and novel pathogenic AADC variants;
- Performing a biochemical characterization of the variants, possibly correlating different parameters and clustering the variants on the basis of their structural and/or functional defects;
- Obtaining the crystal structure of a pathogenic variant and combining *in silico* and *in solution* data.

Final aim of the present study consists in expanding the AADC structure-function relationship by correlating the new results of the WT protein with those obtained from the pathogenic and rationally designed variants possibly mapping the functional and structural effects of the mutations on the different protein regions and creating predictive models for future analysis.

This approach will lead to better understand the molecular basis of AADCd and provide useful tools for the improvement of severity prediction as well as to give suggestion for a more personalized precision therapy to counteract pathological manifestations.

RESULTS

Part 1. NOVEL INSIGHTS ON AADC STRUCTURE-FUNCTION RELATIONSHIP

1. Overall spatial structure of human holoAADC

While the apo human crystal structure of AADC has been solved in 2011 [24], the only holo structure available until now is that of pig [20]. Even if this is a good model of the human holo (89% sequence identity), the resolution of the human counterpart is desirable.

Human holoAADC (h-holoAADC) crystal structure has been obtained at pH 7.5 by Molecular Replacement (MR) method at 1.90 Å resolution in collaboration with Prof. Massimiliano Perduca at the University of Verona (**Table 9**).

While the porcine holoAADC exists as homodimer in the asymmetric unit like other group II α-decarboxylases (such as GAD67, HDC, CSAD), h-holoAADC exists as monomer in the asymmetric unit. The backbone atoms of h-holoAADC at pH 7.5 superposes to chainA of pk-holoAADC (pdb: 1js6) with a Root Mean Square Deviation (RMSD) of 0.356 Å and with chainB with a RMSD of 0.347 Å. These deviations on the Cα atoms of the backbone reflect the high similarity of the structures.

Table 9. Data collection and refinement statistics for structure 1–9.

RBP4 Data set	holoAADC pH 7.5	holoAADC pH 8.0	holoAADC pH 8.5	holoAADC pH 9.0	AADC - carbiDopa pH 8.0	AADC - carbiDopa pH 8.5	AADC - carbiDopa pH 9.0	AADC - carbiDopa pH 7.5	holoL353P pH 8.0
Space group	$P6_122$	$P6_122$	$P6_122$	$P6_122$	$P6_122$	$P6_122$	$P6_122$	$P6_122$	$P6_122$
Structure	1	2	3	4	5	6	7	8	9
a (Å)	107.17	106.98	107.14	107.23	107.39	107.12	107.40	107.39	107.25
b (Å)	107.17	106.98	107.14	107.23	107.39	107.12	107.40	107.39	107.25
c (Å)	218.98	218.49	219.14	219.14	219.11	218.92	219.17	218.97	219.19
a	90.0	90	90	90.0	90.0	90.0	90.0	90.0	90.0
b	90.0	90	90	90.0	90.0	90.0	90.0	90.0	90.0
g	120.0	120	120	120.0	120.0	120.0	120.0	120.0	120.0
Molecules in the asymmetric unit	1	1	1	1	1	1	1	1	1
Resolution range (Å)	85.45 - 1.90	85.30 – 1.86	85.44 - 1.96	73.05 – 2.10	73.04 - 2.00	92.77 - 2.44	85.62 - 2.05	93.00 - 2.84	48.17 - 2.05
Observed reflections	341,933	361,504	526,391	305,21	447,404	235,952	405,605	107,44	455,055
Independent reflections	59,247	62,715	54,173	43,448	51,277	27,751	47,724	18,359	47,57
Multiplicity	5.8 (6.0)	5.8 (5.9)	9.7 (9.9)	7.0 (7.0)	8.7 (9.0)	8.5 (8.3)	8.5 (8.1)	5.9 (5.9)	9.6 (9.7)
Rmerge (%)	10.6 (47.4)	8.2 (48.4)	11.8 (49.9)	10.7 (49.8)	11.2 (48.2)	14.8 (49.7)	12.4 (48.7)	16.3 (50.9)	6.3 (53.0)
<I/s(I)>	10.1 (3.0)	12.4 (3.0)	11.4 (3.7)	12.1 (3.5)	11.3 (3.8)	8.2 (3.3)	10.3 (3.5)	9.5 (3.4)	24.6 (4.3)
Completeness (%)	99.9 (100.0)	100.0 (100.0)	100.0 (100.0)	98.8 (99.5)	100.0 (100.0)	98.2 (97.5)	100.0 (100.0)	99.8 (100.0)	100.0 (100.0)
Reflections in refinement	59,121	62,62	54,04	43,414	51,155	27,73	47,585	18,281	47,502
Rcryst (%)	19.05	17.85	18.07	17.53	17.06	17.89	16.71	19.90	18.47
Rfree (%) (test set 5%)	21.54	20.06	19.26	19.76	19.40	20.92	20.32	23.24	20.44
Protein atoms	3,667	3,559	3,64	3,553	3,636	3,636	3,642	3,553	3,556
Ligand atoms	28	48	28	48	57	57	44	59	41
Water molecules	250	206	205	173	199	135	196	156	232
RMSD on bond lengths (Å)	0.002	0.010	0.003	0.008	0.007	0.002	0.015	0.004	0.003
RMSD on bond angles (Å)	0.527	1.173	0.618	0.850	0.869	0.578	1.196	0.874	0.654
Planar groups (Å)	0.004	0.007	0.005	0.005	0.005	0.004	0.007	0.006	0.004
Chiral volume dev. ($Å^3$)	0.041	0.068	0.044	0.053	0.051	0.042	0.076	0.048	0.042
Average B factor ($Å^2$)	24.59	30.60	28.87	31.11	29.72	40.43	31.48	33.99	34.76
Protein atoms	24.28	30.29	28.68	30.87	29.34	40.16	31.26	33.93	34.45
Ligand atoms	29.38	38.91	29.76	42.42	44.43	62.61	38.12	43.63	46.85
Solvent atoms	28.57	34.08	32.00	32.82	32.59	38.23	34.06	31.83	37.40

***** The values in parentheses refer to the highest resolution shells.
[a] Rmerge = ΣhΣi | Iih – <Ih> / ΣhΣi <Ih> where <Ih> is the mean intensity of the i observations of reflection h.
[b] Rcryst = Σ | |Fobs| - |Fcalc| | / Σ |Fobs|, where |Fobs| and |Fcalc| are the observed and calculated structure factor amplitudes, respectively. Summation includes all reflections used in the refinement.
[c] Rfree = Σ | |Fobs| - |Fcalc| | / Σ |Fobs|, evaluated for a randomly chosen subset of 5% of the diffraction data not included in the refinement.
[d] Root mean square deviation from ideal values.

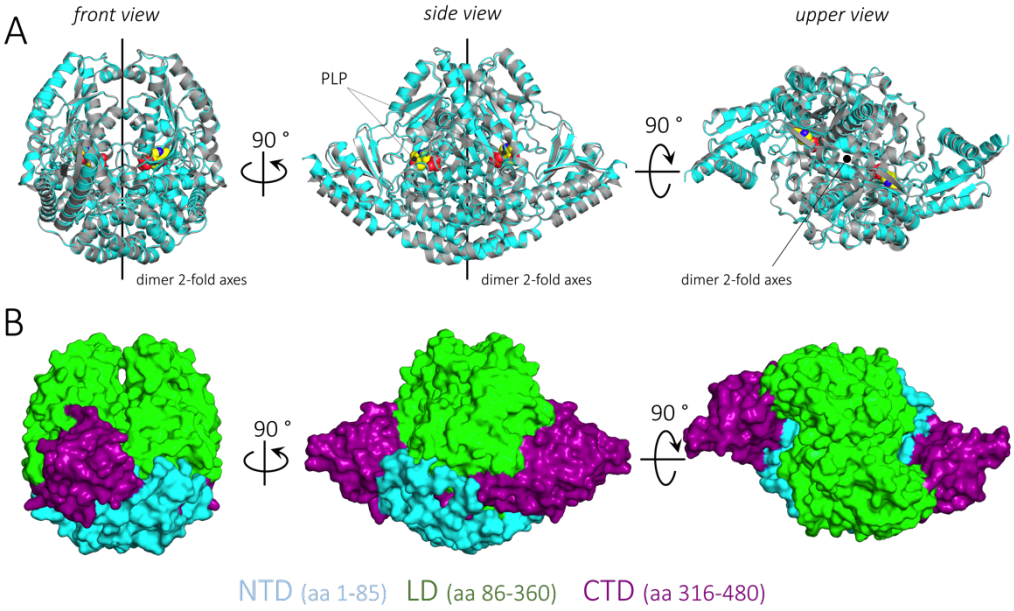

Fig. 15. Crystal structure of porcine and human holoAADC. Novel human holoAADC (represented as cartoon, colored: cyan) aligned to pk-holoAADC (cartoon, green, pdb: 1js6) shows the typical Fold type 1, group II α-decarboxylases organization. A) PLP (represented as yellow spheres) is bound to the conserved Lys303 of each LD. The two mammalian enzymes display identical overall topology in terms of high order secondary structure content as well as domain organization. B) Two LDs (green colored surface) of each monomer are faced, in a tightly closed bivalve conformation, the NTDs (cyan colored surface) are strictly intertwined forming a single stable interconnected structure. The CTDs (magenta colored surface) of each monomer are located at the opposite side of the molecule. Dimeric human enzyme has been obtained by generating symmetric mate to the crystallographic monomer using PyMol.

Once the dimeric form of human holoAADC is generated by adding the symmetric mate, the overall structures of human and porcine AADC have been superposed (**Figure 15**). The NTD, LD and CTD are recognizable with regions 1-85, 86-360 and 361-486 respectively. The N-terminal helices (helix-1 (residues 1-25), helix-2 (residues 37-41) and helix-3 (residues 56-64)) of each monomer are strictly intertwined. The H1-loop-H2 is facing the CTD, in particular helix-16 (aa 416-431), on the same monomer. On the opposite side helix-3 drives the correct positioning of loop1 (aa 66-84). Each LD forms mainly water-mediated electrostatic interactions with the juxtaposed LD of the second monomer also mediated by some residues (Ile101 and Phe103) of loop2 (aa 100-110) and the whole loop3 (aa 323-357) **(Figure 16)**. As in the porcine structure the region corresponding to the CL is here lacking (aa 327-341) in electron density, thus reflecting its high flexibility.

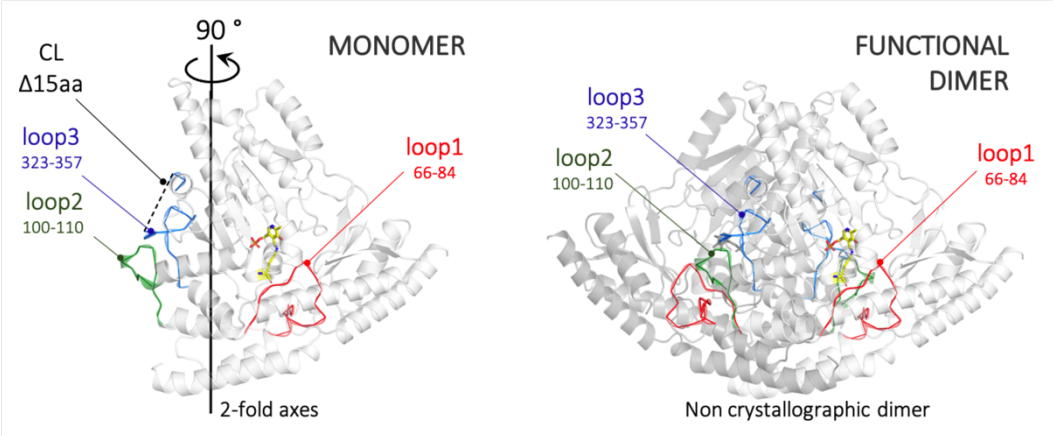

Fig. 16. Essential AADC unstructured regions called loop1, loop2 and loop3. A) Crystallographic monomer of human AADC (white) presents the characteristic functionally unstructured regions (represented as cartoon and ribbons) named loop1 (red), loop2 (green) and loop3 (blue). (B) While loop1 (residues 66-84) is sandwiched between NTD and CTD of the same monomer (white), loop2 and loop3 extend to the active site of the second monomer (gray).

The structure obtained here completes the sequence of an open asymmetric bivalve that acquires symmetry upon closure, and reaches a symmetric and final conformation (**Figure 17**).

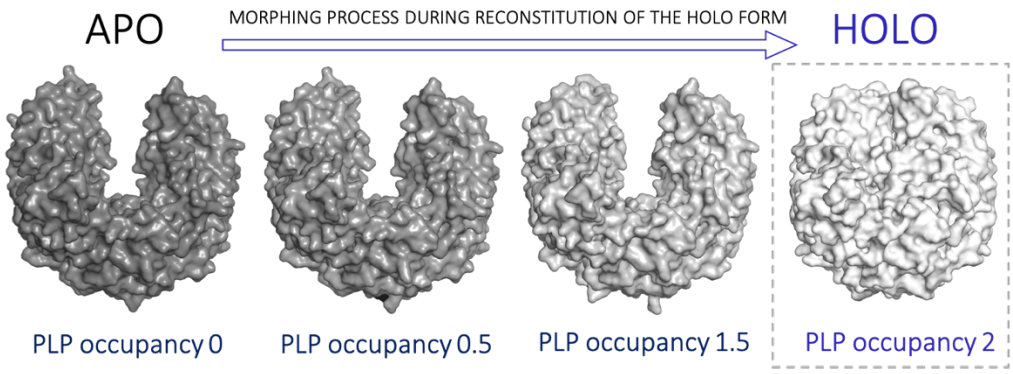

Fig. 17. Novel human holoAADC completes the last frame of the apo reconstitution movie. The transition from the open apo structure to the closed holo one has been described as a morphing process consisting in an increasing PLP occupancy that drives the bivalve closure [24]. ApoAADC structure used correspond to the following id: no PLP occupancy pdb: 3rbl; PLP occupancy 0.5 pdb: 3rbf; PLP occupancy 1.5 pdb: 3rch.

2. Active site of native and ligand bound human holoAADC

AADC active site is mainly composed by residues of one monomer, with a few residues belonging to loop2 (Ile101', Phe103' (the prime ' denotes residues coming from the neighboring subunit) and loop3 (Leu353', Gly354') of the second monomer (**Figure 18A**).

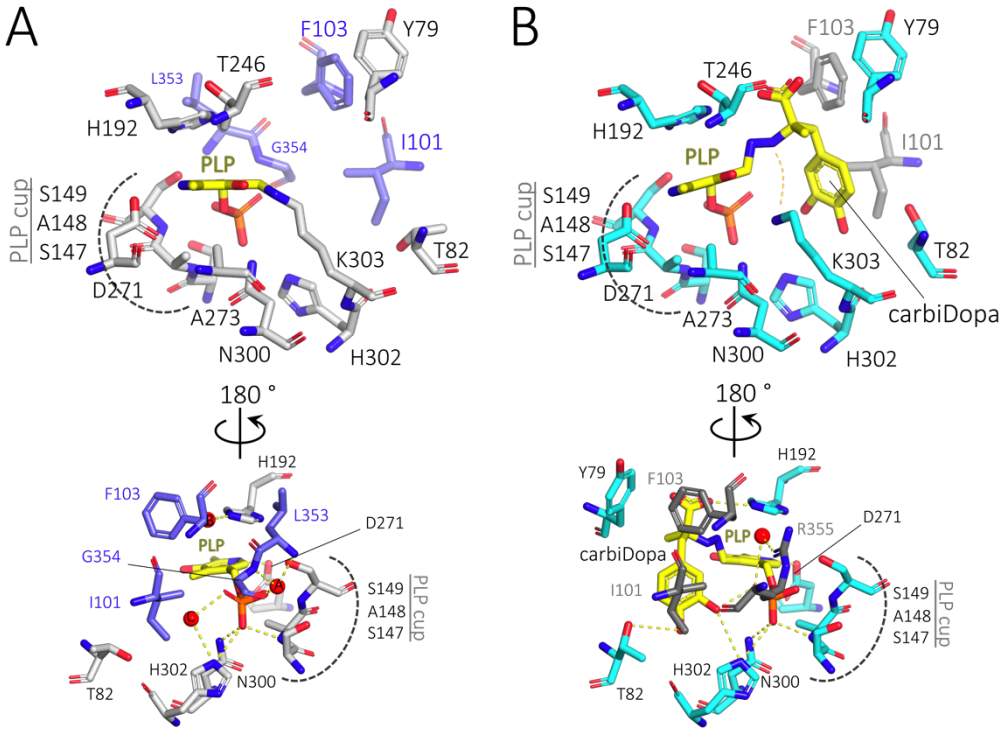

Fig. 18. View of the AADC active site in presence and in absence of Parkinson's disease associated inhibitor carbiDopa. A) Lys303-PLP monomer is shown in white, facing monomer is shown in gray. Structural water molecules are represented as spheres and colored in red. B) Lys303 monomer is colored in cyan, while facing monomer in shown in magenta. Panels C and D shows the hydrogen bond network stabilizing PLP and carbiDopa, together with structural water molecules.

As described in [20], a salt bridge between Asp271 side chain and protonated pyridine nitrogen of the cofactor stabilizes the PLP that forms a Schiff base with Lys303. PLP ring is further stabilized by His192 and Ala273 by stacking interactions. In addition, the cofactor phosphate group is anchored to the protein through an extended hydrogen bond network in which several residues (Ser147, Ala148, Ser149, Asn300, His302) and, as a novelty with respect to the pig structure [20], three water molecules are present (**Figure 18A**). While Ile101' and Phe103', involved in

hydrophobic interactions with the substrate catechol ring, do not participate in polar interactions, Leu353' and Gly354' backbones contact a water molecule A (WatA) that acts as bridge between loop3 and PLP. Water molecule B (WatB) is interacting with His192 side chain and molecule C (WatC) is shared between phosphate group of PLP and His302.

The spatial structure of human AADC solved in complex with carbiDopa at pH 7.5 at 2.84 Å shows the inhibitor forming a hydrazone linkage that mimics the external aldimine enzyme-substrate intermediate. **Figure 18B** shows the penetration of the catechol ring in the active site cleft generated by residues Thr82, Ile101', Phe103' and Tyr79. Carboxylate group of carbiDopa interacts with the imidazole ring of His192 still stacking the pyridine ring, while the 3' and 4' catechol hydroxyl groups of the inhibitor contact Thr82 and His302 respectively (**Figure 18B**).

The superposition of human holoAADC solved at pH 7.5 in the absence and presence of carbiDopa reveals new details. In the absence of carbiDopa, loop3 keeps Leu353' in proximity to the phosphate moiety contacting WatA, as mentioned, and WatB is hydrogen bonded to His192. In this conformation, Arg355' is turned in the opposite direction lying on a backward position. Once the PLP-carbiDopa complex is formed, the carboxylate group of the ligand is positioned at 2.3 Å from where WatB was placed and replaces it in interacting with His192. Loop3 undergoes a gross rearrangement, since Leu353' and Gly354' are displaced and become invisible in the electron density map. Interestingly, Arg355' undergoes a 90° rotation, moving forward in proximity to the PLP and interacting with WatA' that replaced WatA (**Figure 19**). WatC is placed in the same position in both structures. Altogether, this could represent a model of the catalytically competent conformation possibly favoring the rearrangement of CL and the positioning of Tyr332 in close proximity to the carboxylate group of the substrate.

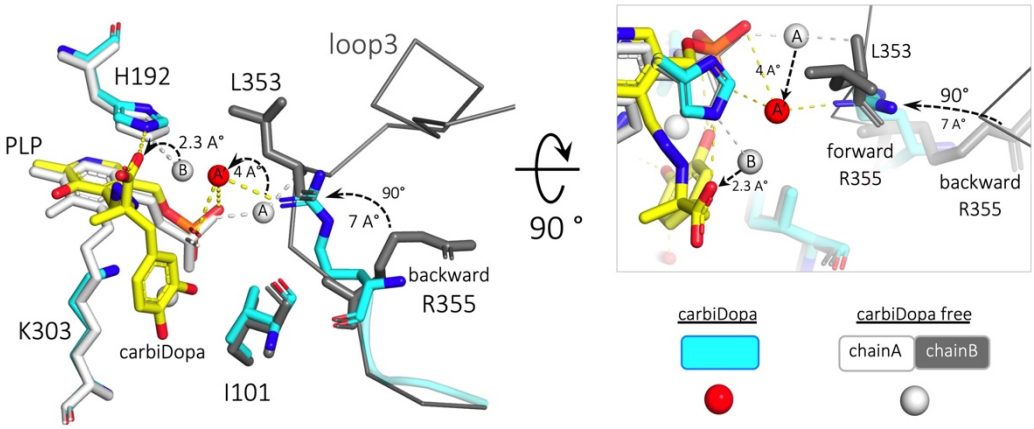

Fig. 19. Proposed conformational change occurring at the AADC active site at pH 7.5 when carbiDopa is bound. Ribbon and sticks representation of the Leu353 and Arg355 rearrangement. Ligand free monomer A is shown in white and loop3 is shown in gray. Ligand bound enzyme is shown in cyan. Water molecules are shown in red. In absence of carbiDopa, Leu353 and PLP are interacting with structural water molecule A while His192 with water molecule B. In this active site conformation Arg355 lies on a backward position. Once ligand is bound, the carboxylate group of carbiDopa substitutes molecule B in interacting with His192 and molecule A' replaces molecule A. Loop3 is rearranged, Arg355 is moved into a forward conformation interacting with molecule A'. Once displaced from the active site Leu353 electron density is missing.

Overall, the human AADC architecture of the active site solved at physiological pH confirms the known cofactor binding mode of this class of PLP α-decarboxylases [23], and reveals new structural elements possibly implicated in catalysis.

3. Effect of pH on AADC monomer-monomer interface: sensitivity of loop3

Given the modifications in terms of crystallographic water molecules as well as loop3 residues visible in the transition from the internal aldimine to PLP-carbiDopa complex, we decided to undertake an investigation of the pH effect on AADC active site at first of the native unliganded form and then in complex with carbiDopa. Human structures obtained at different pH values have been superposed to the porcine one (pdb: 1js6) obtained at pH 6.5 [20]. Although the structures share identical overall topology (**Figure 20A**), they reveal slight structural alterations at the dimer interface, *i.e* at the active site and on loop2 and loop3. $AADC_{pH7.5}$ aligns to $AADC_{pH8.0}$ with a RMSD of 0.140 Å, to $AADC_{pH8.5}$ with RMSD of 0.100 Å, to $AADC_{pH9.0}$ with RMSD of 0.143 Å indicating a global good similarity.

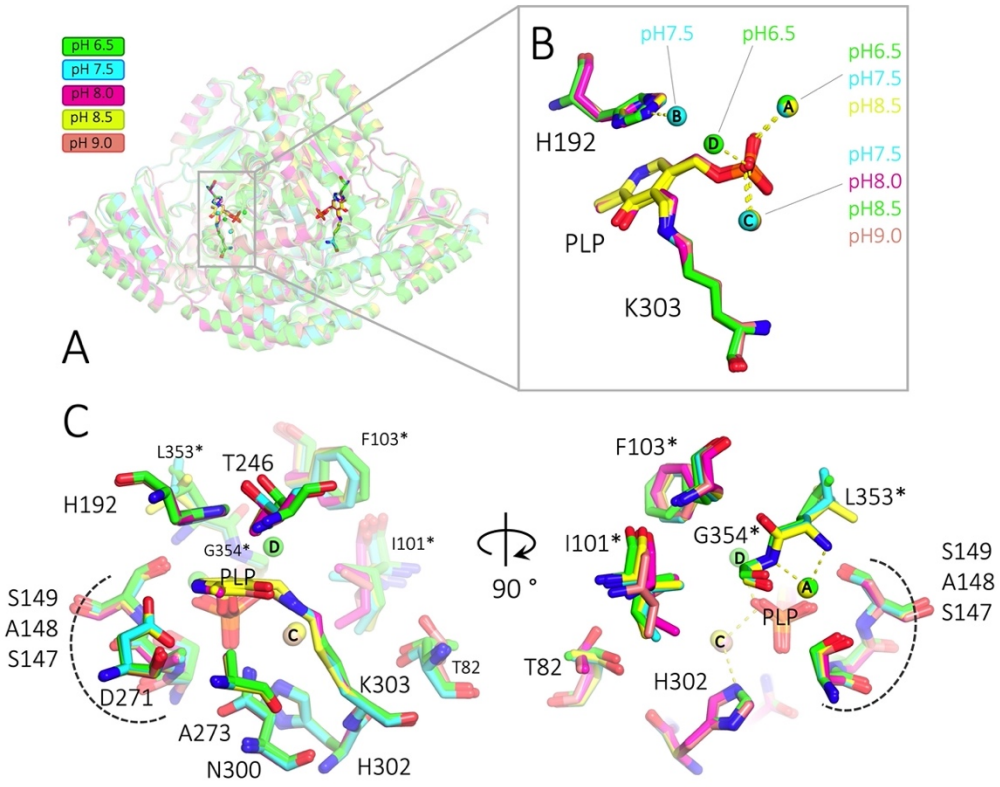

Fig. 20. View of the AADC active site under different pH values. A) Human structures solved at pH 7.5, 8.0, 8.5, 9.0 (colored cyan, purple, yellow, pink, respectively) are superposed to the porcine holoAADC solved at pH 6.5 (green, pdb: 1js6) without showing any relevant topological differences. B) While the PLP is similarly bound Lys303, active site differences come from surrounding structural water molecules. C) Major differences of the active site residues are mainly visible on those residues belonging to loop2 and loop3 (Ile101, Phe103, Lue353, Gly354) and Thr82. In particular, Leu353 and Pro352 are missing at pH 8.0 and 9.0.

An insight into the active site of the internal aldimine shows nearly identical positions of the PLP-Lys303 Schiff base with base-stacked His192 in the different structures, being the main differences, not observed in [20], mainly related to water molecules number and position as well as to displacement of interface residues and loop3 elements.

Molecule WatA, together with WatC, stabilizes the phosphate moiety at pH 6.5, 7.5 and 8.5. WatA also interacts with Leu353' and Gly354' backbone. At pH 8 and pH 9 only WatC is visible, being WatA absent. Wat B, as mentioned above, bridges His192 only at pH 7.5. Finally, WatD is present only in the published structure at pH 6.5 [20] and concurs to phosphate binding (**Figure 20B**).

In each subunit, active site residues of the same chain composing for the great part the active site exhibit subtle differences at the different pH values mainly visible on

Thr246 and Thr82 (**Figure 20C**). Residues contributing to this active site from the cognate subunit, Ile101' and Phe103' of loop2 and Leu353' and Gly354' of loop3 exhibit larger alteration of the amino acid side chains (**Figure 20D**), particularly evident at basic pH values where the electron density of the latter two loop3 amino acids is missing. Notably, the larger effects are displayed by Arg355' (immediately following the previous two amino acids stretch) and the interface residue Glu150. Interestingly, this residue immediately follows Ser147-Ala148-Ser149 triad that anchors the phosphate PLP moiety, as mentioned above. It can be observed that the glutamate side chain carboxylate is oriented towards the dimer interface at acid and neutral pH, while it is instead turned inside at the more basic pH values.

In more depth, at pH 6.5 and pH 7.5, Glu150 connects the two active sites through sequential polar interactions that cross the inter-subunit surface (top view, **Figure 21A**). In details, Glu150 side chain connects Ser147 backbone to a water molecule located at the center of the dimer interface (**Figure 21A**). This central water molecule is shared between the two monomers through the same weak interaction with the respective Glu150 residue as shown from the top view of **figure 21A**. At pH 8.5 the side chain of Glu150 rotates and contacts the backbone nitrogen of Ile351 on loop3 thus disrupting the bridge of interactions between the two subunits (**Figure 21B**) and the central water molecule is trapped into a small pocket. At pH 8 and pH 9 a deep rearrangement of the dimer interface occurs. Two water molecules are now accommodated at the monomer-monomer interface, each one interacting with the Glu150 carboxylate of each monomer. As said, at pH 8.0 and 9.0 residues Leu353' and Gly354' are invisible and Arg355' moves in close proximity to PLP and generates a new polar contact directly with the phosphate moiety creating a new inter-subunit interaction (**Figure 21C**) between loop3 and PLP. The observed Arg355 plasticity is similar but not identical to that described at pH 7.5 in presence of carbiDopa, since in the former structure, a water molecule (A') is interposed between Arg355' and PLP. Thus, being the two active sites near the interface, our structures solved at different pH values suggest that an effect at the interface is then transferred to essential elements of the active site.

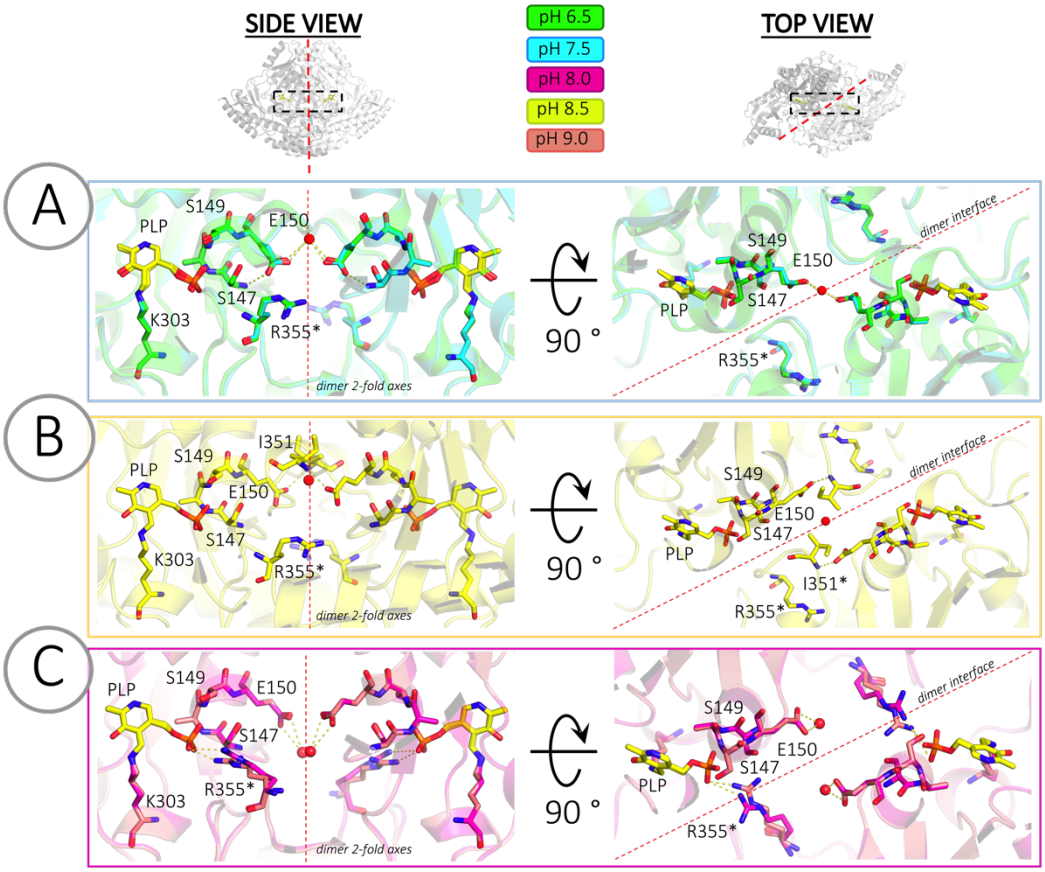

Fig. 21. Effect of pH on the monomer-monomer interface of AADC. Human holoAADC structures solved under different conditions are compared with that of pk-holoAADC. AADC structures are represented as cartoon and residues discussed in the text and PLP are shown as sticks, while water molecules as spheres. Each active is shown form both a side point of view and from a top point of view and the dimer 2-fold axes and the dimer interface are indicated with a dashed red lines for clarity. Color code is indicated, A) $AADC_{pH6.5}$ and $AADC_{pH7.5}$ are colored in green and cyan respectively, B) $AADC_{pH8.5}$ is colored in yellow and C) $AADC_{pH8.0}$ and $AADC_{pH9.0}$ are colored magenta and pink respectively.

Loop3 has been associated to catalytic functions since it includes the flexible CL (see above). At pH 6.5, 7.5 and 8.5 residues 328-339, 327-341 and 323-341 respectively, are missing. Interestingly, at pH 8.0 and 9.0 a longer segment of residues, 323-354 is missing. A comparison of the invisible stretch of the here-described new holo-structures with that of the apoAADC structure provides insights on the flexibility not only of the CL but also of the entire loop3 (the underlined residues are those that differ from the human enzyme) (**Figure 22A**).

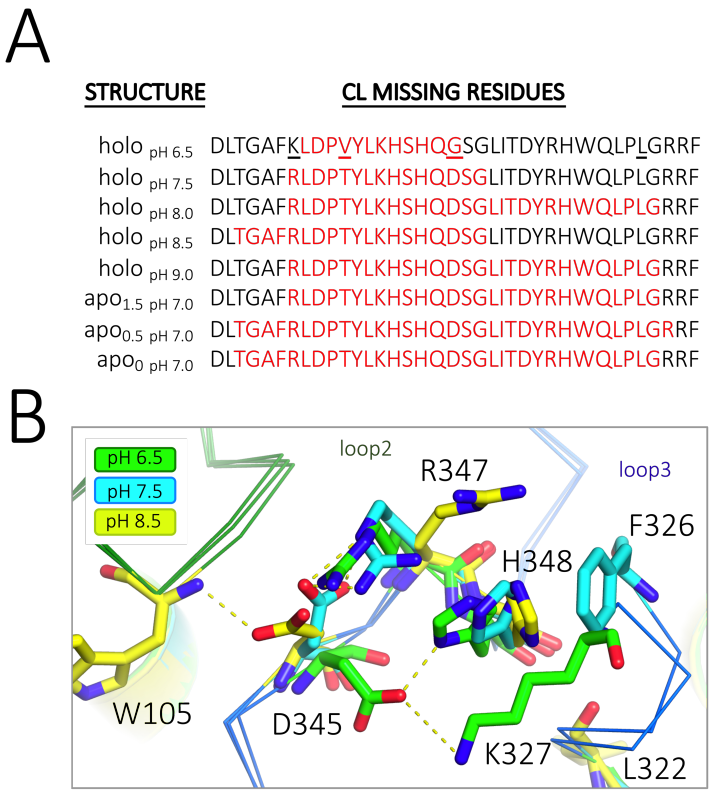

Fig. 22. Mobility of loop3 at different pH values. A) Alignment of loop3 amino acid sequence of all available mammalian AADC crystal structures. CL missing residues are highlighted in red. Residues that differ between *S. scrofa* and *H. sapiens* are underlined. Loop3 sequences available for human apo AADC are shown. Apo intermediates solved in presence of different PLP occupancy are named $apo_{1.5}$ (pdb: 3rch, one monomer showing the internal aldimine and the other with unbound PLP) and $apo_{0.5}$ (pdb: 3rbf, unbound PLP present in one monomer active site). Apo0 corresponds to the loop3 sequence of pdb: 3rbl. B) Conformational changes visible on loop3 of holoAADC at pH 6.5, 7.5 and 8.5. Residues showing pH sensitivity are represented as sticks. Structures are represented as cartoon, colored green - pH 6.5 (pdb: 1js6), cyan - pH 7.5 and yellow - pH 8.5 respectively. Loop2 and loop3 are represented in green and blue ribbons.

There is a general trend in subtle loop3 conformational changes from pH 6.5 to pH 9. Interestingly, residues of the part of loop3 following the CL (from Arg347 on) are visible at the active site and their different positions at different pH values could influence the mobility and thus the catalytic competence of the CL. In particular, Asp345 undergoes a substantial rearrangement from pH 6.5 (**Figure 22B**), where it contacts Lys327 upstream CL and His348 downstream the CL, to pH 7.5 where it is tilted and interacts with Arg347, to finally pH 8.5 where it is rotated on the opposite side bridging Phe103 of loop2. These displacements could relapse in altered flexibility of loop3 reflecting on CL mobility.

4. Effect of the pH on the active site in presence of carbiDopa

In an effort to understand the role of loop3 elements, so essential for enzymatic activities, we solved the AADC-carbiDopa complex at different pH values. According to the Dunathan's hypothesis [27], the carboxylate group of the inhibitor places the Cα–CO_2 bond in an orthogonal orientation to the plane of the coenzyme ring under each pH condition (**Figure 23A**).

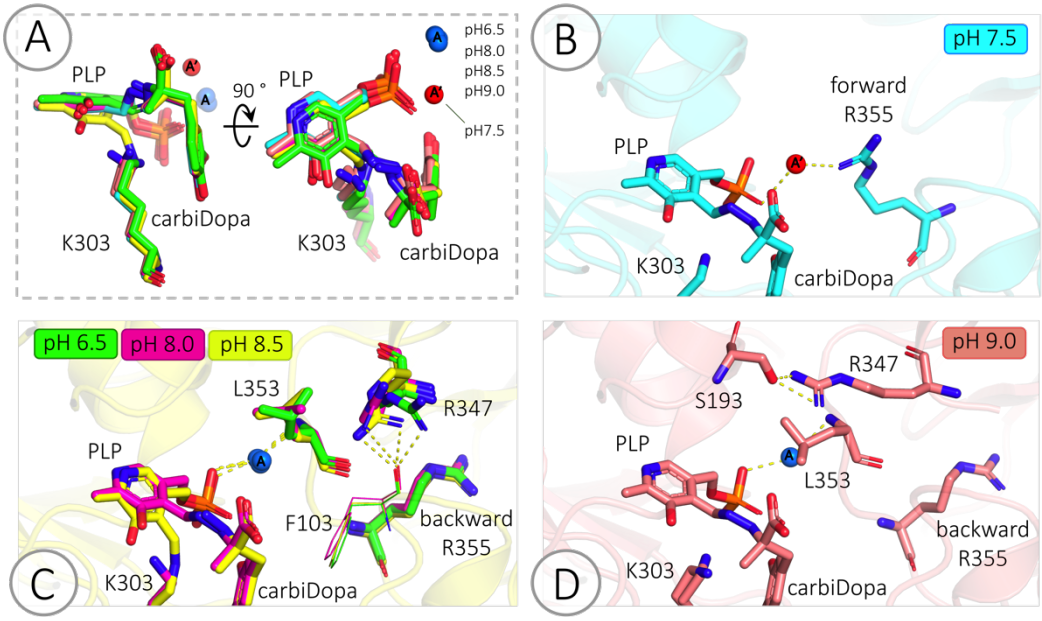

Fig. 23. Effect of the pH on AADC active site in presence of carbiDopa. Proteins scaffold is represented as cartoon, PLP, carbiDopa and residues as sticks. Colored code: green (pk AADC, pH 6.5), cyan (pH 7.5), magenta (pH 8.0), yellow (pH 8.5), pink (pH 9.0). A) PLP-carbiDopa complex together with water molecules WatA and WatA' solved at different pH are superposed showing slight differences. B) Active site of $AADC_{pH7.5}$ shows Arg355 in the forward position, interacting with WatA'. Differently, in C) Arg355 is stacked in the backward conformation and Leu353 is contacting WatA. Arg347 shows a new contact with Phe103 on loop2 (represented as lines for clarity). Similarly, at pH 9.0 (D) loop3 shows a conformation where Leu353 is facing PLP and Arg347 interacts with Ser193.

CarbiDopa is present as bound with the formyl group of PLP in all structures but at pH 8.5 since under this condition the Lys303-PLP Schiff-base is still present even if the carbiDopa molecule is properly positioned in a sort of Michaelis complex structure. Despite this difference, under all conditions, no alterations of the PLP anchoring residues are notable. Again, and interestingly, the relevant differences among the solved structures consist in the position of the structural water molecules and in the orientation of some loop3 residues (**Figure 23A**).

If in the ligand-free structures Arg355' is positioned in the backward conformation at pH values 6.5, 7.5 and 8.5 and it is rotated inside at pH 8 and 9, in the carbidopa complexes it rotates forward at pH 7.5, as mentioned above, while it is located in the backward position at all other pH values.

Interestingly, at pH 6.5, 8 and 8.5 loop3 seems to be more "locked" due to a new interaction between Arg347' side chain and Phe103' backbone. This is corroborated by the fact that Leu353' and Gly354' are still visible in the electron density map and in these structures WatA is indeed positioned in the same place as in the ligand-free structures. At pH 9, a further difference is present in addition to WatA, Leu353' and Arg355' stacked in the backward position, and regards Arg347' interacting with Ser193 of the opposite subunit (**Figure 23C**).

Altogether, the observed alterations at different pH values of the structural water molecules and the conformational plasticity of Leu353 and Arg355, highlight the role of loop3 in AADC. Interestingly, k_{cat} of the decarboxylase reaction of AADC exhibits an optimum at pH 7.5 with a reduced activity at lower or higher pH that could be related to slightly differences in the interface and in the interconnection between the active sites [59].

5. MD simulations show the different flexibility of the apo and holoAADC, the asymmetric movements of the monomer chains and domain communication

The availability of the solved crystal structure of human apoAADC (pdb: 3rbl) together with the novel holoAADC structure gave us the unprecedent opportunity to investigate the dynamics of the apo and holo human enzymes by means of molecular dynamics (MD) simulations. Since both structures lack of some regions, we started our analysis with the kind support of Dr. Rui Ribeiro from the lab of Prof. Alejandro Giorgetti at the University of Verona by modeling loop2 (in the apo) and loop3 (in the apo and holo). For the holo system, Lys-PLP complex was separately parametrized as described (see materials and methods). All-atom MD simulations were then carried out following the protocol described in the material and methods section.

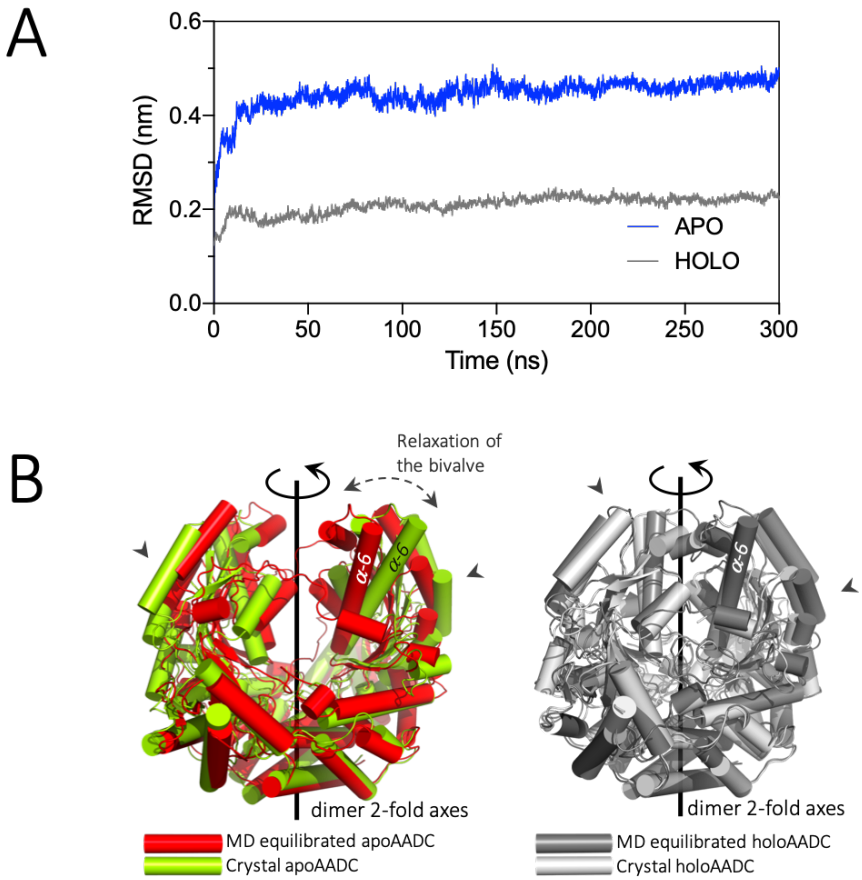

Fig. 24. Representative backbone RMSD and overviews on the structural rearrangement of apo and holo AADC during simulations. A) Backbone RMSD as function of time for representative trajectories of dimeric apoAADC (blue) and holoAADC (gray). After an initial structural rearrangement during the initial 50 ns of simulation, the average backbone RMSDs were found to reach a plateau at 0.457 ± 0.001 nm (apo), 0.2268 ± 0.002 nm (holo). B) Comparison between the crystallographic apo (pdb: 3rbl) and holo (structure 1) structures and the structures equilibrated after 300 ns and representative of the last MD snapshot. Arrows indicates the regions where relaxation is more evident.

Afterwards a 300 ns long simulation was performed. Inspection of the RMSD values of the backbone throughout the simulation, indicates that both systems reach equilibrium in 50 ns of simulations, during which time an initial structural rearrangement is seen (**Figure 24A**). Calculated values of backbone RMSD for the production stage show that the apo system reaches a plateau at 0.457 ± 0.001 nm, while the holo system at 0.2268 ± 0.002 nm. These data indicate that both systems reach stability during the simulations and that apoAADC is overall more dynamic than holoAADC. In fact, once the equilibrated apoAADC structure (structure relative to the last snapshot of the MD) is superimposed to the crystallographic one,

larger differences emerge with respect to the holo enzyme. As shown in **figure 24B**, relaxed apoAADC results in a partially closed bivalve. It has been reported that the two LDs of the crystal apoAADC are distant up to ~ 20 Å [24]. Here, we observe that the equilibrated apo structure moves the two LDs closer to each other, in a reduced open conformation of ~ 15 Å. Moreover, the relaxation of the structure seems to occur symmetrically only in one monomer, and in particular in the very apical part of the protein in proximity of helix-6 (residues 147-171), being the top of the helix moved apart by ~ 10 Å in the MD structure with respect to the crystal one. This helix has been already seen to constitute a highly flexible region in homologous human HDC and GAD [25,143]. As for the holo, the equilibrated structure does not show gross relaxation in comparison to the crystal form even if some asymmetric motions are visible in the proximity of helix-6 (**Figure 24B**).

In order to highlight the structural/dynamical features underlying the different mobility between the two monomers, we compared the root mean square fluctuation (RMSF) of the apo chainA and chainB together with those of the holo form. The apo form (**Figure 25A**) presents overall more flexibility along the polypeptide chain with respect to the holo form. In general, the LD is the domain showing the highest flexibility in the chains of both apo and holo enzymes, being loop3, in particular the CL, that displays the highest mobility.

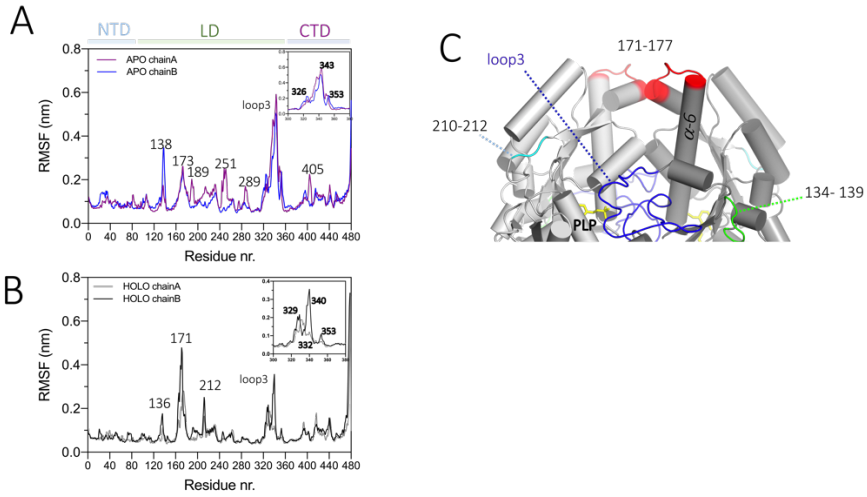

Fig. 25. Flexibility profile (RMSF) provided by MD of modelled apoAADC and holoAADC. A) RMSF profile along chainA (magenta) and chainB (blue) sequence of apoAADC, B) RMSF relative to chainA (gray) and chainB (black) of holoAADC. Residue number are indicated in correspondence of maximum RMSF values for clarity. Domains division are highlighted in colors, Loop3 fluctuation is shown in detail in the insets. C) regions of maximum flexibility are shown on the holo form (structure 1).

Concerning the differences between the two monomers of each structure, in addition to the CL inspection, apoAADC shows a marked different backbone mobility between chainA and chainB in the 189-289 region, as evidenced by higher RMSF values in chainA. This region constitutes the external part of the open bivalve indicating that the opening of the dimer leads to a relaxation of this part of LD and is in connection again with helix-6.

On the contrary, the holoAADC backbone flexibility does not present relevant differences in terms of RMSF between the two chains, mirroring the closed and rigid bivalve-like structure, unless the CL (as observed above), thus reflecting a possible asymmetrical behavior (**Figure 25B**).

Interestingly, also human HDC shows a previously unrecognized asymmetric mobility in the oxidized forms, which interestingly constitutes the more active species [143]. Considering the oxidized HDC, one monomer results more flexible in the LD in the same regions as AADC (around residue 140, around residue 175 and in its CL region). In addition, in the holo and apo GAD65 dynamic structures [25], the CL fluctuates slightly more than the CTD, while in both HDC (reduced and oxidized) and AADC (apo and holo) the flexibility of the CL and loop3 is more relevant than small signals at the CTD and NTD.

While in the apo AADC, loop3 swings symmetrically between chainA and chainB, in the holo system, chainB shows an increased rigidity at Tyr332 level. Interestingly, this is concomitant with an increased mobility at Leu353 suggesting that the overall protein conformation (even in absence of substrate) facilitates the positioning of the catalytic Tyr332 in proximity of the active site.

This asymmetry in holo CL region led to a deeper inspection of the holo and apo structures equilibrated after 300 ns of MD simulation. Here, apoAADC maintains loop3 in a solvent exposed conformation in both monomers (**Figure 26**).

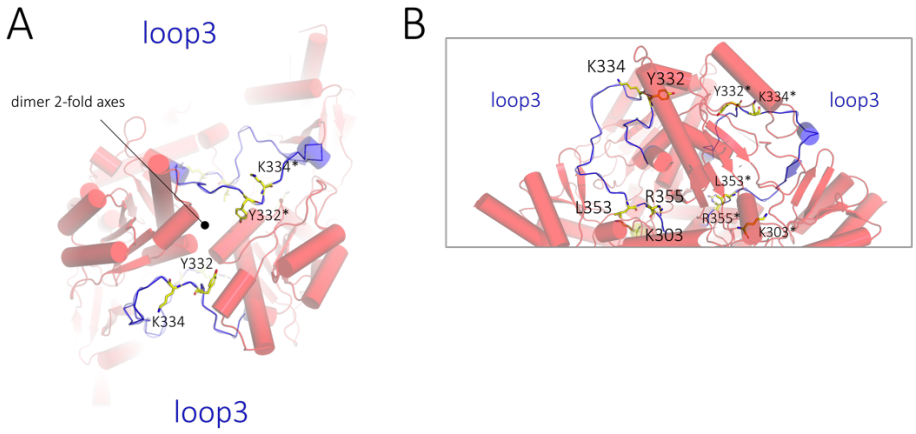

Fig. 26. ApoAADC structure after 300 ns of MD simulation. A) Upper view in cartoon representation of equilibrated apoAADC. The protein shows a partially closed conformation, with loop3 (represented as ribbon and colored in blue) showing the exposure of Lys334 and Tyr332 to the solvent. B) Side view of apoAADC. Some residues of loop3 are shown as sticks, Lys334, Tyr332, Leu353, Arg355, Lys303 on both monomer chainA and chainB*.

Lys334, that is trypsin accessible in both apo and holo enzymes, shows a similar conformation in both chains, as well as Tyr332. Moreover, in the absence of PLP, both residues Leu353 and Arg355 at the end of loop3 are rolled out. The equilibrated holoAADC shows instead an asymmetric conformation (**Figure 27**).

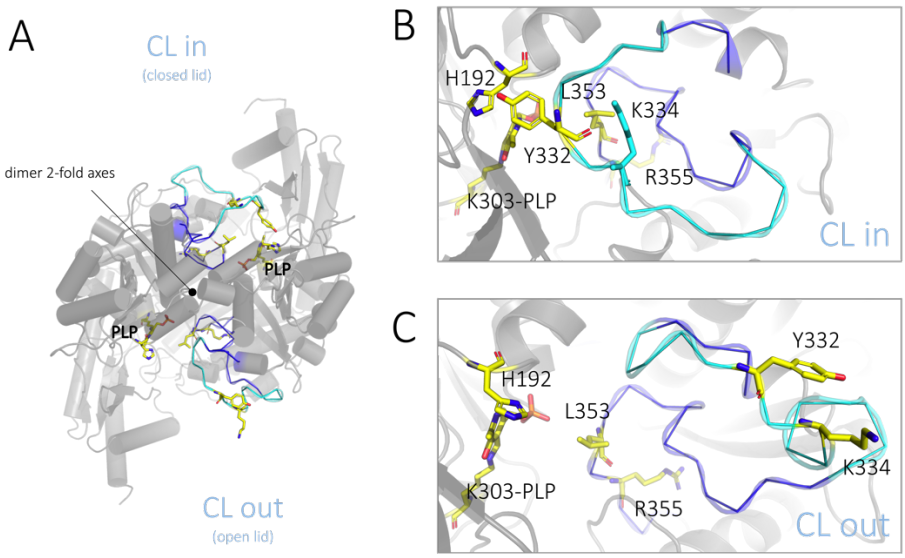

Fig. 27. HoloAADC structure after 300 ns of MD simulation. A) Upper view of holoAADC, represented as cartoon; loop3 is represented as ribbon and colored in blue, while CL is highlighted in cyan. PLP, and residues His192, Lys303, Try332, Lys334, Leu353, Arg355 are shown as sticks. CL shows two alternative conformations acting as a closed or open lid on the active site. B) When CL is in a closed conformation -CL in-, Tyr332 is placed in closed proximity of His912 and PLP and CL acts as a closed lid on the active site. C) Different possible conformation of loop3 showing Tyr332 and Lys334 exposed to the solvent -CL out-.

Monomer A shows indeed a conformation of loop3 in which the CL is twisted inward the active site (-CL in-), placing Tyr332 in proximity of His192 and PLP. In this conformation Lys334 is less solvent exposed. Monomer B shows instead a loop3 conformation in which Leu353 is still anchored to the PLP but CL is twisted outward the active site (-CL out-) and Lys334 is solvent exposed as indicated also by higher RMSF values. The found -CL in- conformation is very similar with the CL conformation found in HDC and GAD67 crystal structures, in which the catalytic tyrosine is consistently placed in proximity of the PLP (**Figure 28**).

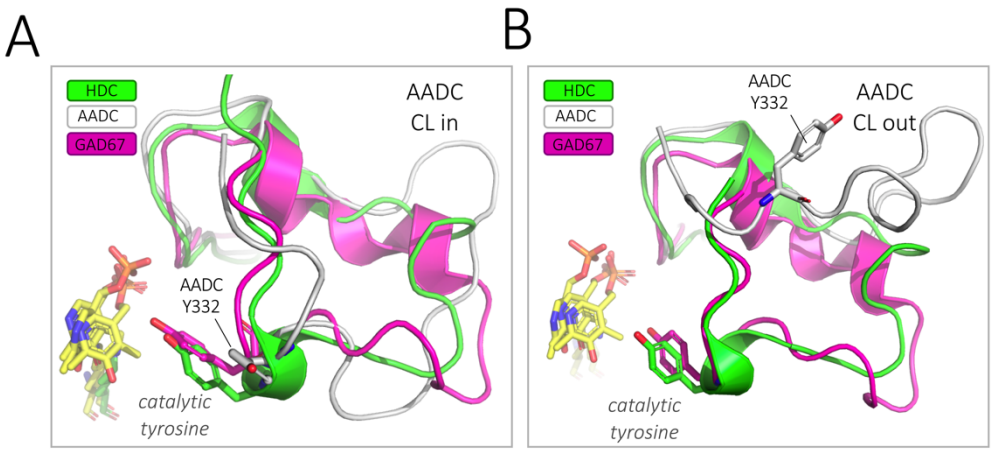

Fig. 28. Comparison between the AADC, HDC and GAD67 loop3 conformation. The AADC loop3 snapshot obtained after 300 ns of MD simulation is superposed to the crystallographic structures of human HDC (pdb: 4e1o) and GAD67 (pdb: 2okj). A) in the -CL in- conformation of AADC, catalytic Tyr332 is placed in proximity of PLP similarly to HDC and GAD67 catalytic tyrosine, while B) shows that loop3 is similarly anchored but CL of AADC is positioned as an open lid.

In order to detect differences in the global large-amplitude motions between the two proteins, we decided to apply the Principal Component Analysis (PCA) to the MD simulation trajectories. A comparison between apoAADC and holoAADC shows that the overall magnitude of the fluctuations is higher in the apoAADC while both systems do not show mobility of the region encompassing Lys303 (**Figure 29**).

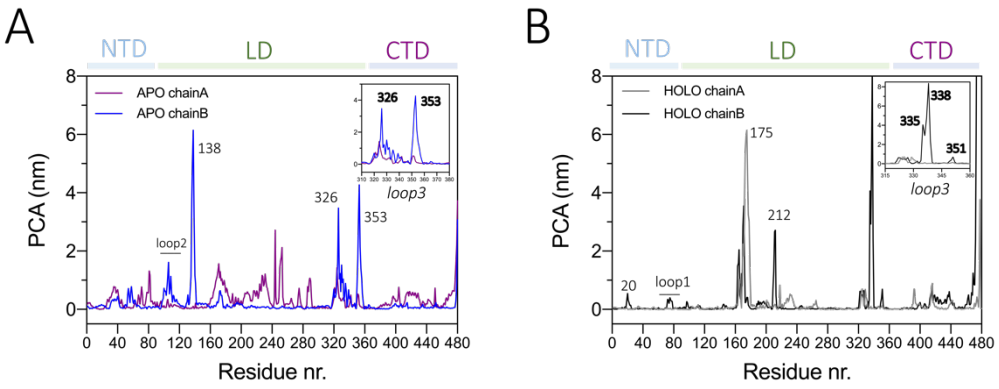

Fig. 29. Principal component analysis (PCA) on the apo and holo MD trajectories. A) PCA analysis along chainA (magenta) and chainB (blue) sequence of apoAADC, B) PCA relative to chainA (gray) and chainB (black) of holoAADC. Residue number are located in correspondence of maximum mobility for clarity. Domains division are reported, Loop3 mobility is highlighted in the insets.

ApoAADC displays an asymmetric profile of fluctuations along each domain, particularly pronounced at LD level (possibly related with the solvation properties of apoAADC that favors dimer opening [25]). In addition, in concomitance of an overall mobility of LD and a slight change in NTD (in the loop connecting helix-1 and helix-3) and CTD (on helix-16, aa416-431) on chainA, chainB exhibits high mobility on loop2, on surface loop 134-139 and loop3, particularly at Leu353 level (as shown in the inset).

The inspection of the principal components relative to holoAADC evidences a global rigidity of the protein (**Figure 29B**). HoloAADC displays an asymmetric fluctuation similar to that of the apoAADC. In fact, even if both monomers are mobile, chainA fluctuations are visible in defined regions of the LD, while chainB is more mobile in the NTD (in particular at the end of helix-1), loop1, loop3 and the CTD (helix-16). Interestingly, loop1 is located at the NTD-CTD interface of the same monomer while proximal loop3, and thus CL, comes from the other monomer (**Figure 30A, B**).

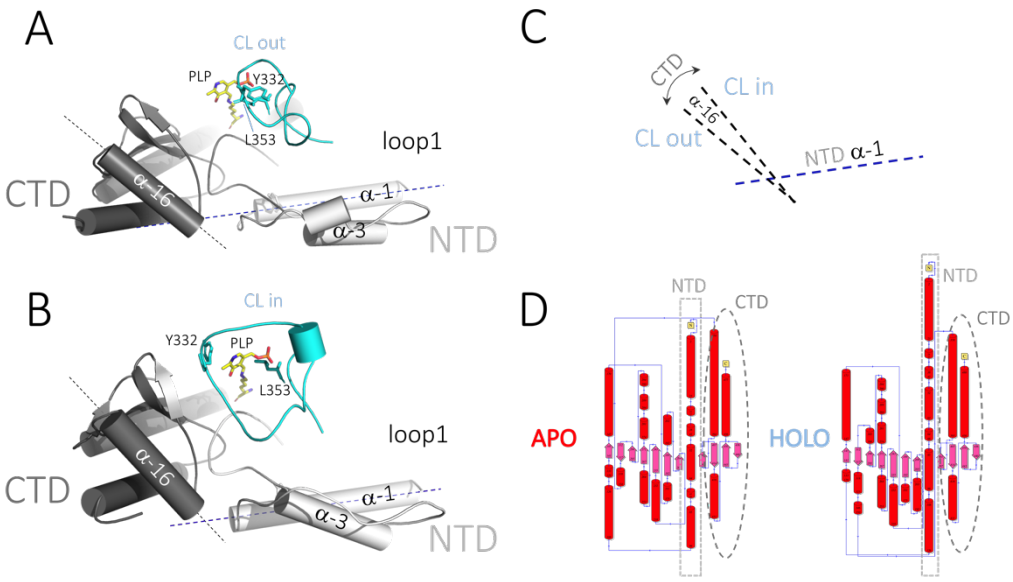

Fig. 30. Crosstalk between NTD, CTD and CL. Equilibrated structure of holoAADC shows two possible motions of NTD (white), CTD (gray) and CL (cyan) and the position of loop1 at the monomers interface. A) when Tyr332 is exposed to the solvent, CL acts as an open lid, while B) when Tyr332 is placed in proximity of PLP, CL acts as a closed lid. These two CL conformations are synchronized with the motions ("breath") of CTD in relation to NTD (C). D) Similar considerations can be done on apoAADC since NTD and CTD of the same monomer are faced in both protein forms.

CL conformations -in- and -out- could be related to CTD and NTD mobility: the -CL in- conformation is favored by high mobility of CTD while the -CL out- conformation could be related to a more rigid behavior (**Figure 30C**). A similar but not identical dependency has been observed in GAD65 where the fluctuation amplitude of CTD complemented by the CL, influences the opening/closing the active site [25].

Here, in holoAADC for the first time we add more information connecting NTD to both CTD and LD, mainly reflected in CL movements.

6. Limited proteolysis provides additional insights on the different mobility of the apo and holoAADC

We decided to follow the flexibility of apo and holoAADC by means of limited proteolysis with trypsin for identifying critical exposed regions. As previously described, in presence of trypsin holoAADC is nicked in the CL, in correspondence to Lys334. The nicked pig enzyme is digested into two species of 36 kDa and 18

kDa, remains folded but loses its decarboxylase activity [30]. We subjected holo and apo human AADC to tryptic digestion and monitored the products during time on an SDS-page (as described in material and methods).

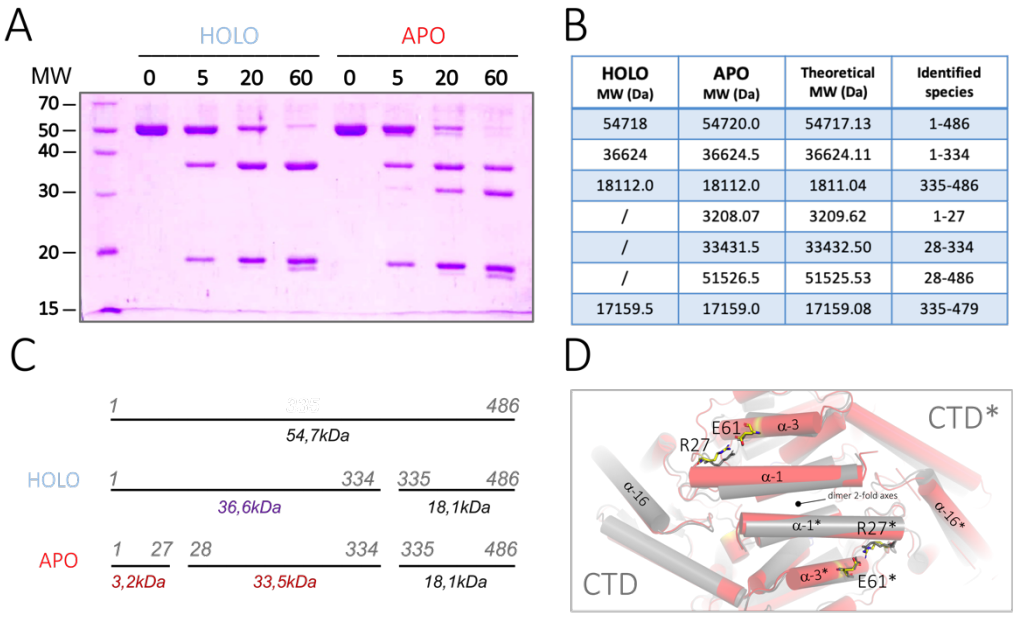

HOLO MW (Da)	APO MW (Da)	Theoretical MW (Da)	Identified species
54718	54720.0	54717.13	1-486
36624	36624.5	36624.11	1-334
18112.0	18112.0	1811.04	335-486
/	3208.07	3209.62	1-27
/	33431.5	33432.50	28-334
/	51526.5	51525.53	28-486
17159.5	17159.0	17159.08	335-479

Fig. 31. Differential N-terminal susceptibility of apo and holoAADC to trypsin. A) limited proteolysis of apo and holoAADC in presence of trypsin at E:S ratio of 1:100 (by weight) in 100 mM potassium phosphate pH 7.4 at 25 °C with the addition of 100 µM PLP for holoAADC. At indicated times aliquots of the reaction mixture were boiled in SDS sample buffer and the reactions were resolved by SDS-page. B) Same reaction mixture were stopped after 30 min of digestion with specific trypsin inhibitor, and analyzed by RP-HPLC and MS (see materials and methods). Experimental masses are listed in B) and compared with the expected theoretical masses of the identified peptide species. C) Proposed pattern of proteolysis for holo and apoAADC in accordance to the identified tryptic sites. D) Comparison of equilibrated holo (gray) and apoAADC (orange) showing Arg27 on helix-1 (α-1) being involved is a salt bridge with Glu61 of helix-3 (α-3) is a similar way between the two forms, suggesting that the N-terminal susceptibility of apoAADC to trypsin unlikely depends on Arg27 conformation.

Surprisingly, while the human holoAADC exhibits the formation of two bands at ~36 kDa and ~18 kDa resulting from the cleavage of the monomer (54.7 kDa) in position 334-335, as the porcine enzyme, the apo protein shows a different tryptic pattern, characterized by the presence of novel bands. At 5 minutes, one species, close to that of the monomer, appears, suggesting the presence of an N- or C-terminal novel tryptic site (**Figure 31A**) in addition to the 36 kDa and 18 kDa species of the holo. From 5 to 60 minutes, a second novel band accumulates referred to a species of around 30 kDa. In both apo and holo enzymes with time, further species are visible at molecular weight smaller that 18 kDa, possibly attributed to

subsequent proteolytic events. The proteolytic mixture has been analyzed by MS and the identified fragments are reported in **figure 31B**. These data confirmed the main tryptic site in correspondence to Lys334 in both apo and holo forms, and a second never observed site only in apoAADC corresponding to the N-terminal Arg27, in a loop connecting helix-1 and helix-3. Complementary N-terminal peptide 1-27 (running out of the gel) has been identified with a mass of 3208.07 Da. Lastly, the identification of the lighter band of 17.1 kDa reveals that the C-terminal 335-486 fragment if further cleaved at the flexible C-terminal histidine tag forming a 17.1 kDa as reveled from the fragment 335-479. A scheme of the characteristic pattern of proteolysis of holo and apoAADC is reported in **figure 31C**.

A bioinformatic inspection of the holo and apoAADC equilibrated structures shows that Arg27 is involved in a salt bridge with Glu61 located downstream on helix-3. This contact seems a structural requirement for keeping associated helix-1 and helix-3. As shown in **figure 31D**, the NTD of holoAADC superposes to the NTD of the apoAADC. However, MD simulations demonstrate that the overall apo structure is more mobile and eventually accessible to tryptic digestion. In addition, they reveal that the region of the first 40 amino acids is certainly more mobile in the apo structure than the holo one, as indicated by both PCA and RMSF analysis, suggesting that this stretch of residues could be relevant for conformational movements. A cleavage at this level could have a double consequence: on one side it could exert some effects on helix-16 of CTD contacted by the loop following helix-1, on the other, through the disassembling of the Arg27-Glu61 interaction, it could influence loop1 that follows helix-3. It is known that loop1 has a strong effect on apo to holo conformational change [24].

Notably, also GAD65 exhibits a pattern of proteolysis [25], where apoGAD N-terminal is susceptible to trypsin attack as apoAADC. However, here, differently from GAD65, holoAADC is cleaved at CL, while apoAADC is simultaneously cleaved at Arg27 and Lys334. Instead, apoGAD65 does not present the same proteolytic sites as holoGAD65 [25]. This should not surprise since each enzyme has evolved specific structural elements and performs highly specific substrate recognition and catalysis.

A superimposition of the human group II α-decarboxylases sequences shows the same basic N-terminal residue whose susceptibility to trypsin may constitute an informative probe for the global stability of the NTD (**Figure 32**).

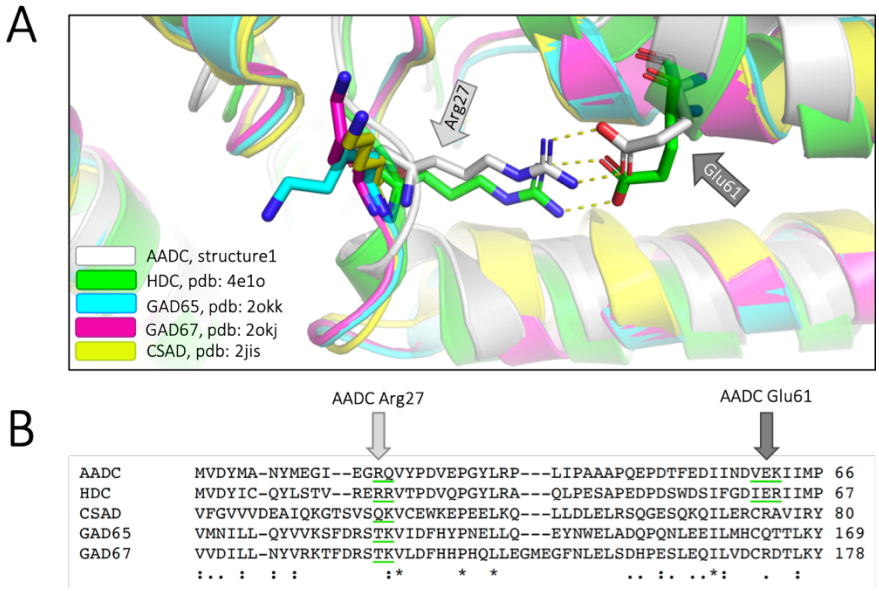

Fig. 32. N-terminal Arg27 is conserved among group II α-decarboxylases. A) Superposition of human AADC (white, structure1), HDC (green, pdb: 4e1o), GAD65 (cyan, pdb: 2okk), GAD67 (purple, pdb: 2kj) and CSAD (yellow, pdb: 2jis) shows the conservation of a basic N-terminal amino acid consisting in a lysine residue in GAD65, GAD67 and CSAD and in an arginine residue in AADC and HDC. B) AADC and HDC shows the formation of the same salt bridge between conserved arginine and glutamate.

7. Removal of tryptic sites by mutagenesis provides *in solution* evidences of the asymmetric motion of the dimer.

We then decided to make artificial variants R27Q and K334Q (the latter kindly provided by Dr. Riccardo Montioli of the University of Verona) in order to study the role of these residues on the holo and apo protein. Residual activity of the R27Q and K334Q variants resulted to be 36.2 % and 84.2 % of that of the WT respectively, indicating that, even if the substitutions are conservative, the effect of the N-terminal variant is more relevant respect to the variant of the CL region. When subjected to trypsin digestion, the variants provide interesting results. HoloR27Q shows the characteristic holo-pattern with the formation of the two bands deriving from the monomer cleavage in the CL. HoloK334Q remains instead completely resistant to proteolysis (**Figure 33A**). As for the apo variants, apoR27Q still shows the holoWT pattern and apoK334Q shows the formation of a second

high weighted species deriving from the N-terminal cleavage (the corresponding 3.2 kDa migrates out of the gel).

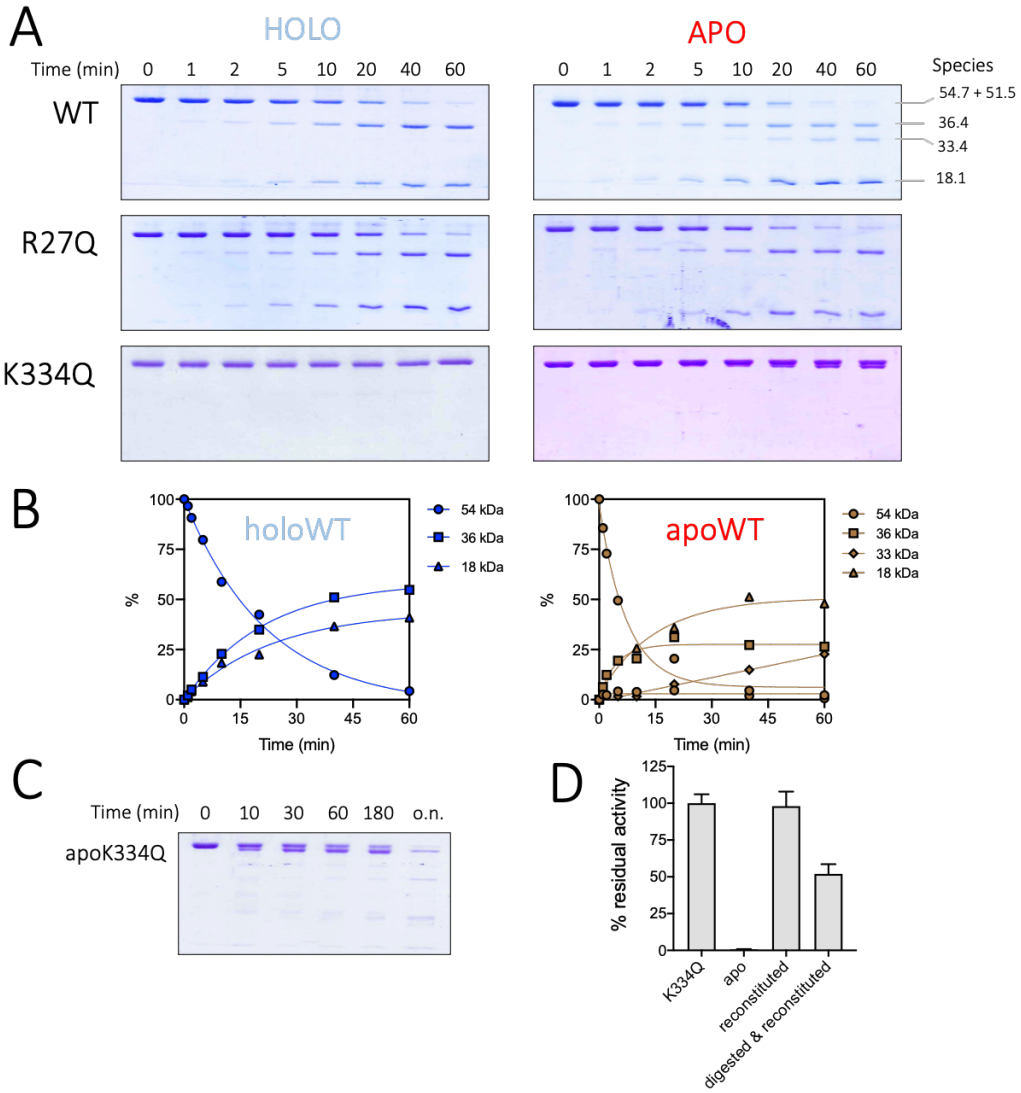

Fig. 33. Limited proteolysis of WT, R27Q and K334Q variants. Susceptibility of WT and R27Q and K334Q variants to digestion was determined by incubating 0.54 mg/mL of AADC with trypsin at the E:S ratio of 1:100 (w/w) (for WT) or 1:200 (w/w) (variants) in 100 mM potassium phosphate pH 7.4 at 25 °C with the addition of 100 µM PLP for the holo forms. Time points were taken along 1 h of incubation and compared with AADC sample in absence of trypsin. At each time point, the reaction was boiled in SDS sample buffer to stop trypsin activity. The digestion products were separated by SDS-page. B) Plot of Plot of disappearance and formation of digested holo and apoWT AADC during the limited proteolysis time course. Species are expressed as a percentage of initial undigested band. C) Digestion of apoK334Q with trypsin at the increased ratio of 1:50 (w/w). Time points are shown. D) ApoK334Q was firstly incubated 60 minutes with trypsin at the E:S ratio of 1:50 (w/w) and then PLP was added to the final concentration of 100 µM. The enzyme was then reconstituted over night at 8 °C and its residual activity was evaluated.

The initial rate of apoWT monomer disappearance (54.7 kDa species) has been calculated to be ~ 3.9 fold more rapid than in the holoWT, and the increase of apo 18.1 kDa band (resulting only from the CL cleavage) is ~ 2.1 fold more rapid than the holo. These observed rates reflect the higher extent of exposure of the apo CL, mirroring indeed the higher conformational mobility of apo loop3 highlighted with MD.

Since under these experimental conditions we could not observe a complete conversion of the undigested species into the nicked one, we decided to increase the trypsin ratio up to 1:50 for apoK334Q. Surprisingly, the undigested monomer and its nicked derived species fast reach an equilibrium at about 50 % of undigested monomer suggesting the possibility that the asymmetric conformation of apoAADC is mirrored by an asymmetric mobility of the two monomers, as revealed by half of the N-terminal being attacked (**Figure 33B**). A second slow phase is visible after some hours of incubation in which the high trypsin ration lead to a progressive disappearance of the monomer (further derived species are visible).

Thus, we assayed the activity of reconstituted apoK334Q obtained after 60 minutes of digestion (**Figure 33C**). While the reconstituted undigested apoK334Q shows to be fully reconstituted, the digested and reconstituted apo enzyme presents 50 % of the holo enzyme activity possibly meaning that 50 % of the protein population is digested and does not reactivate, while the remaining population perfectly reconstitutes. These results together with MD data strongly sustain evidence of an asymmetric mobility of AADC.

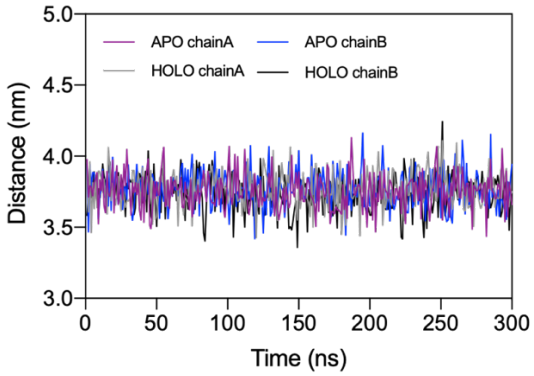

Fig. 34. Analysis of the solvent accessible surface area (SASA) of Arg27. Solvent accessible surface area of Arg27 during MD simulations is similar in all AADC chains, both in the apo and holo form, suggesting that the Arg27-Glu61 salt bridge is stable along 300 ns. The accessibility of apoArg27 to trypsin could be due to large amplitude motions instead of local conformational changes.

A further confirmation of the trypsin accessibility of Arg27 on the apo protein is given by the analysis of the solvent accessible surface area (SASA) of Arg27 (**Figure 34**). No differences are visible among the apo and holo chains during the simulation, meaning that the accessibility of the NTD for the protease is ascribable to the large-amplitude fluctuation of the CTD with respect to NTD. In fact, as evidenced by PCA analysis, residues 416-431 of helix-16 facing the NTD show the highest mobility only in one chain.

8. Characterization of the new N-terminal tryptic site by site-directed mutagenesis

In order to investigate the effect of the Arg27-Glu61 interaction on the protein features, we designed non-conservative variants R27A and E61A carrying the advantages of abolishing in both cases the salt bridge interaction and removing the tryptic site only in R27A. In addition, variant K334Q has been investigated as tryptic site probe of the CL.

The biochemical analysis carried out on R27A and E61A reveals that both of them show a loss of their thermal stability ($Tm_{222\ nm}$) and tertiary structure signals (CD at 280 nm) in both their holo and apo form. The coenzyme microenvironment generates signals (both dichroic and in absorbance) relative to an altered tautomeric equilibrium shifted to the ketoenamine tautomer **(Figure 35A**). The affinity for the PLP of R27A and E61A is reduce by ~ 4.3 fold and 3 fold respectively. Differently, K334Q exhibits unaltered spectroscopic signals, preserved thermal stability, high coenzyme affinity, superimposable to those of the WT (**Figure 35B**).

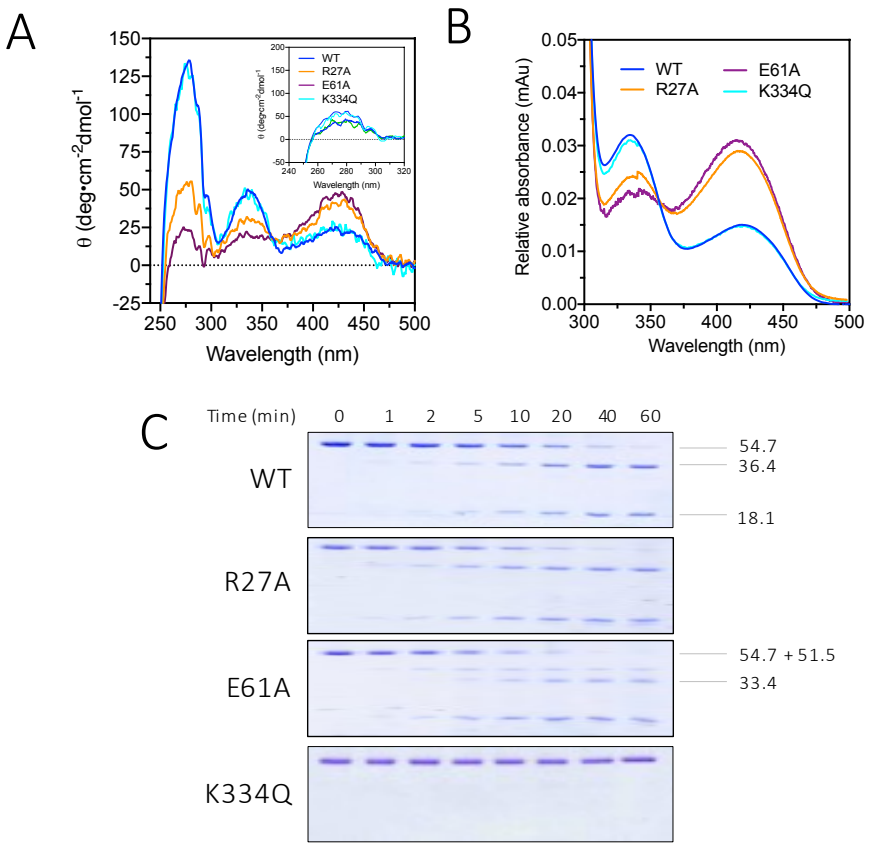

Fig. 35. Biochemical characterization of artificial R27A, E61A and K334Q variants. A) Near-UV visible CD spectra of holo variants compared with holoWT. Signals relative to the apo species are reported in the inset. CD spectra are recorded at 5 µM protein concentration, in 100 mM potassium-phosphate buffer, pH 7.4 in presence of 100 µM PLP for the holo forms. B) Internal aldimine absorbance spectra of holoWT and variants. Spectra are recorded at 10 µM protein concentration, in 100 mM potassium-phosphate buffer, pH 7.4. C) Limited proteolysis with trypsin at 1:100 $_{(w/w)}$ ratio were performed in 100 mM potassium phosphate pH 7.4 at 25 °C with the addition of 100 µM PLP.

Kinetic parameters calculated for L-Dopa (**Table 10)** show catalytic efficiency of 8.4 % for R27A (showing that the substitution to Ala is worse than Gln as reported above) and 12.1 % for E61A mainly caused by a 7 fold reduced catalytical constant in both variants. As expected, holoR27A is not cleaved at its N-terminal, holoE61A shows the typical apoWT tryptic pattern.

Table 10. Kinetic parameters for L-Dopa, apparent equilibrium dissociation constant for PLP and melting temperatures of variants R27A, E61A and K334Q.

Enzyme	k_{cat} (s-1)	K_m (mM)	k_{cat}/K_m ($s^{-1}mM^{-1}$)	$K_{D(PLP)}$ (nM)	Tm (°C)	
					holo	apo
WT[a]	7.6 ± 0.1	0.11 ± 0.01	69.1 ± 10	101 ± 10	69.42 ± 0.02	64.84 ± 0.03
R27A	1.10 ± 0.05	0.19 ± 0.03	5.8 ± 1.1	438 ± 86	64.64 ± 0.01	61.49 ± 0.02
E61A	1.02 ± 0.04	0.12 ± 0.03	8.4 ± 2.1	307 ± 44	65.41 ± 0.01	61.37 ± 0.02
K334Q	6.4 ± 0.2	0.14 ± 0.02	45 ± 0.15	165 ± 30	66.04 ± 0.02	62.99 ± 0.03

Altogether, mutation of residues of the new tryptic site determines heavy effects in terms of structure and function, evidencing that, like a domino effect, a modification in NTD could have impacts on CTD and LD, finally to CL.

CONCLUSIONS FROM PART 1

Human AADC crystal structure has been solved in its holo and catalytically competent form since only porcine holo and human apoAADC were available until now. HoloAADC has been solved in its native and carbiDopa bound form at physiological pH providing new insights on the mechanism of formation of the external aldimine. A role in the rearrangement of the active site upon binding of the ligand could be attributed to loop3 conformation (in particular to residues Leu353, Gly354, Arg355) and to some structural water molecules. When carbiDopa-PLP complex is formed, Loop3 reorganization is driven by an exchange between Leu353 and Arg355 in contacting the PLP through a water molecule, possibly favoring the catalytically competent CL position.

In order to investigate the effect of pH on AADC active site we solved the crystal structure of the native and inhibitor bound enzyme at different pH. We identified the AADC monomer-monomer interface region (including loop3) to be the most susceptible to the pH. The position of some structural water molecules together with the orientation of specific residues (Glu150 and Arg355) are found to determine conformational changes. Glu150 has been identified as crucial in putting the two active sites in communication through sub sequential hydrogen bonds. The increase leads to an increased flexibility of loop3 as revealed by a progressive lack of the electron density and to slight alterations of Ile101 on loop2. Similarly, also in presence of carbiDopa, the effect of the pH appears to be addressed to water molecules, loop3 (and possibly to CL). In fact, the increase in pH leads to the acquisition of deficient active site conformations determined by the establishment of improper interactions of loop3 (*via* Arg347, Leu353 and Arg355). Thus, pH sensitivity provides us with a tool to understand Leu353 and Arg355 movements in coordinating the positioning of loop3 inside the active site and concurring to -CL in- and -CL out- conformations.

Protein mobility has been also investigated by MD and limited proteolysis. MD analysis reveals that apoAADC is partially closed with respect to its crystallographic structure and that it shows however higher mobility than the corresponding holo form. Both apo and holoAADC show an asymmetric motion during the simulated time. In fact, chainA and chainB of each protein exhibit

differential fluctuations along each domain. While apoAADC shows, on one hand a asymmetric motion of the two monomers and on the other hand, similar loop3 fluctuations, holoAADC reveals a different conformational plasticity involving loop3 of one monomer and NTD and CTD of the second monomer. In fact, a more rigid CL conformation, in which catalytic Tyr332 is positioned closed to PLP (-CL in- conformation), is stabilized in presence of more mobile CTD and NTD (that are facing one each other). On the contrary, a -CL out- conformation is favored when CTD and NTD exhibit less mobility in the respective facing regions (H1-loop-H3), leading to the proposal of the existence of a functional coordination between these regions. Limited proteolysis highlights the differential mobility between apo and holoAADC and reiterates the existence of asymmetric motions in AADC. Thus we identified Arg27 as novel tryptic site for the apo protein that could constitute a powerful *in solution* tool for assessing protein mobility.

Our study on WT human AADC provides new elements for the comprehension of the structure-function relationship of AADC. Structural details might represent the basis for both the designing of novel specific inhibitors and for a better comprehension of the molecular aspects of the mutation of AADC associated with diseases.

Part 2. CHARACTERIZATION OF AADC DEFICIENCY ASSOCIATED VARIANTS

9. Localization, distribution and conservation of the residues involved in this study

The 28 residues involved in substitutions and deletions characterized in this study are reported in **table 11** that lists the pathogenic changes involved in AADCd and **table 12** that displays the non-pathogenic variants. 8 out of 28 of the residues belong to the NTD, 16 to the LD and 2 to the CTD. Moreover, some residues belong to the structural elements called loop1 (His70, Trp71, Leu77), loop2 (Trp105, and Ala110) and loop3 (Pro330, Lys334, Arg347, Leu353) already described to be crucial for AADC activity (see introduction and part1).

In order to have a preliminary idea on the role of these residues, we determined their conservation level by aligning the human AADC amino acid sequence with those of 75 homologous proteins by the ConSurf web server. Results are reported in **table 11** as a score where 9 means highly conserved and 1 highly variable.

About 65% of the modified residues are conserved/highly conserved (score 8 and 9 for Tyr20, His70, Phe77, Trp105, Ala110, Leu222, Phe251, Trp267, Cys281, Glu283, Pro330, Arg347, Leu353). Glu25, Gly146 and Phe237 are quite conserved (score 6/7). Glu25 could be substituted with both positively and negatively charged amino acids, Gly146 with small apolar or polar residues. Phe237 could be substituted by polar and apolar residues. The others have a low conservation score, although the chemical nature of the residues (polar or apolar) is maintained for Val60 and Arg453. Gly96 and Pro210 show to be the residues with highest variability, although a negatively charged amino acid in position 96 and a hydrophobic one in position 210 are not contemplated in the possible substitutions.

In this thesis, in addition to residues causing pathogenic effects, some artificial variants are presented. Non-pathogenic Y20A, Y20S and W71A variants will be discussed as controls together with their counterpart pathogenic deletions Y20del and H70R/W71del.

Table 11. Preliminary overview on the 21 residues involved in pathogenic substitutions. For each residue the localization is indicated. N-Terminal Domain (residues 1-85) includes loop1 (66-84), Large Domain (residues 86-360) includes loop2 (100-110), Lys303 stretch (200-310), loop3 (323-357) and the flexible Catalytic Loop (CL, 327-341). The C-Terminal Domain includes residues 361-480. Conservation score based on the alignment of 75 AADC homologues has been calculated with ConSurf server (http://consurf.tau.ac.il). The conservation score of 9 indicates a highly conserved residues while 1 is associated to highly variable residue. According to the conservation score, residue variety is also indicated. The variants characterized in this study are listed.

resi #	localizzation	Conservation score	Residue variety	mutation
20	NTD	9	Y	Y20del
25	NTD	6	E, R, D	E25K
60	NTD	5	I, V	V60A
70	NTD – loop1	9	H	H70Y H70R/W71del
77	NTD – loop1	8	H, Y, F	F77L
96	LD	4	G, S, A, D	G96R
105	LD – loop2	8	W	W105C
110	LD – loop2	8	A	A110E
146	LD	6	G, A, S	G146R
210	LD	4	E, S,P, C, Q	P210L
222	LD	8	L, C	L222P
237	LD	6	C, F, I	F237S
251	LD	9	F	F251S
267	LD	9	W	W267R
281	LD	9	C	C281W
283	LD	9	E	E283A
330	LD – loop3	9	P	P330L
347	LD – loop3	8	M, R	R347Q
353	LD – loop3	9	M, L	L353P
362	CTD	5	L, M	M362T
453	CTD	4	R, S	R453C

Table 12. Overview of the 6 residues involved in artificial substitutions. The localization, the conservation score (calculated with ConSurf server; http://consurf.tau.ac.il), the residue variety and the studied variants are listed.

resi #	localizzation	Conservation score	Residue variety	mutation
20	NTD	9	Y	Y20A Y20S
27	NTD	9	R	R27A
61	NTD	8	E, D	E61A
71	NTD – loop1	8	W	W71A
193	LD	9	S	S193A S193D S193E
334	LD – loop3	5	R, Q, K	K334Q

In addition, Ser193 variants comprise three artificial species characterized in a research project regarding post translational modifications carried out in collaboration with Prof. Robert S. Phillips at the University of Georgia (USA). Preliminary *in vitro* analysis identified Ser193 as putative phosphorylation site in AADC. Interestingly, Ser193 follows His192, that is the conserved residue involved in the stabilization of the cofactor.

Finally, the already characterized R347Q has been more deeply investigated to examine its role in loop3 [119,120].

About 50% of the studied residues are located at the large interface between the two monomers. This interface comprises 144 residues of the total 480 amino acids of each monomer and covers the 27.3% of the total solvent-accessible area (ASA) of each subunit. In comparison, the dimer interface of the prototype of Fold-Type I PLP-enzymes, aspartate aminotransferase, covers only 19.8% of the total ASA. The effect of the substitutions on the binding affinity between the monomers has been evaluated by measuring the difference of free energy between the variants and the WT protein using the BindProfX online software ($\Delta\Delta G = \Delta G_{mut}-\Delta G_{WT}$). Results obtained for each monomer are listed in **table 13**.

Table 13. Effect of the interface pathogenic variants on the monomer-monomer binding affinity. ΔΔG has been predicted using BindProfX server. The changes in free energy are displayed as ΔΔG. In the case of deletions (Y20del and double mutant (H70R/W71del) the ΔΔG was not determinable (n.d). Residues not located at the dimer interface are indicated as not an interface residue (n.i).

mutation	ΔΔG
WT	0.000
Y20del	n.d
V60A	1.271
H70Y	0.000
H70R	0.000
G96R	3.253
W105C	1.700
A110E	1.849
G146R	0.000
P330L	n.d
R347Q	0.990
L353P	1.953
M362T	0.000
R453C	1.166

n.d = not determinable

Table 14. Effect of interface artificial variants on the monomer-monomer binding affinity. ΔΔG has been predicted using BindProfX server. The changes in free energy are displayed as ΔΔG. In the case of deletions (Y20del and double mutant (H70R/W71del) the ΔΔG was not determinable (n.d). Residues not located at the dimer interface are indicated as not an interface residue (n.i).

mutation	ΔΔG
Y20A	2.377
Y20S	2.393
E61A	0.000
W71A	2.790
S193A	0.798
S193D	1.052
S193E	0.955
K334Q	n.d

n.d = not determinable

The measured ΔΔG values show that mutations H70Y, G146R, M362T even if involving interface residues do not affect the monomer-monomer affinity. Substitutions, V60A, G96R, W105C, A110E, R347Q, L353P, R453C show a positive ΔΔG indicating that the interaction networks between monomers is affected at different extent. In particular, G96R, W71A and Y20A, Y20S seem to be the most destabilizing substitutions, followed by L353P, A110E and W105C. In

order to find a structural basis for these effects, an investigation of the position and interaction network of each residue in the 3D structure of AADC has been undertaken.

10. AADC crystal structure inspection provides insights on the role of the residues involved in the pathogenic mutations.

A preliminary analysis of the position of residues undergoing substitution due to the new mutations identified in the last years (from 2014 to 2019) shows that they are dispersed in the whole ORFs of the *AADC* gene, as reported also by recent reviews [107], resulting in a protein bearing altered amino acids throughout its polypeptide chain.

Here, for the first time, we can base our observations on the human ligand-free AADC structure solved as described in part 1 of this thesis.

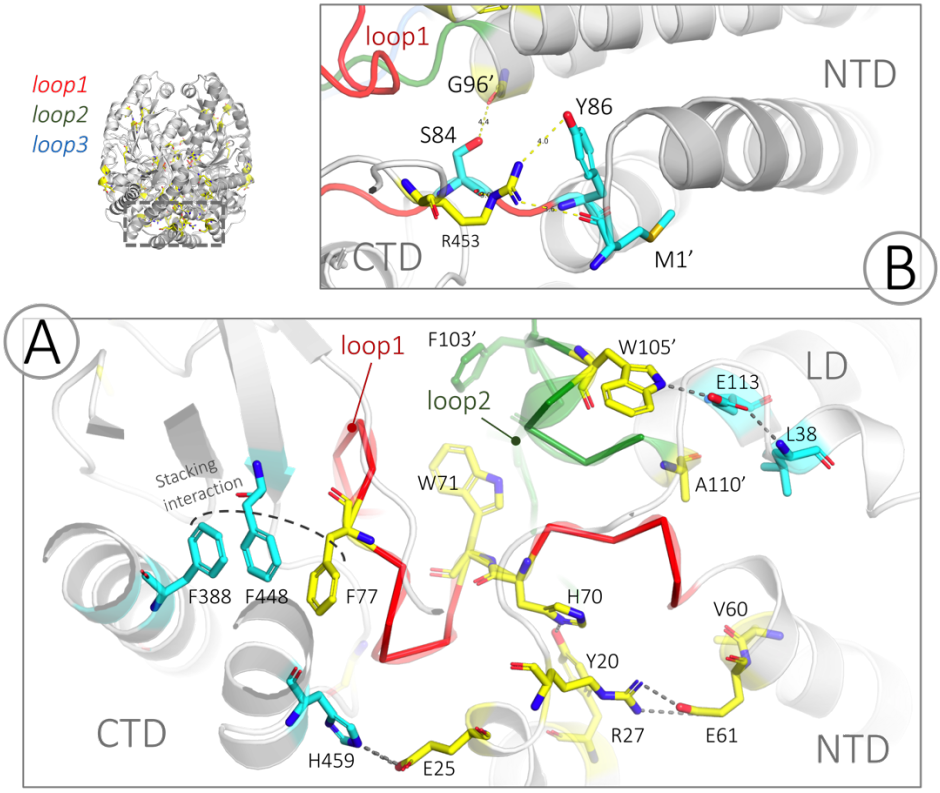

Fig. 36. *In silico* inspection of the mutation sites located at the NTD and CTD. Dimeric holoAADC has been obtained from structure1 (see part1) using Pymol 2.2.3 (The The PyMOL Molecular Graphics System, Version 2.0 Schrödinger, LLC). The two monomers are colored white and gray. Loop1, loop2 and loop3 are represented as ribbon and colored red, green and blue respectively. In each panel the mutation sites (yellow) and the interacting residues (cyan) are indicated and represented as sticks. Lys303 is colored white and PLP is colored yellow. Residues of loop2 are colored green.

Starting from the NTD, Tyr20 and Glu25 are located at the end of helix-1 and, although close to each other, interact with different structural elements. Glu25 generates the turn of the helix by interacting with His459 of the CTD, Tyr20 makes a hydrogen bond with His70, located on loop1, immediately preceding Trp71. Trp71 is a loop1 residue described to be involved in the direct interaction with loop2 of the neighboring subunit, in a hydrophobic network with residues such as Phe103 proposed to facilitate the binding of the substrate aromatic ring [24] (**Figure 36A**). Phe77 is another loop1 residue that is part of a stacking sandwich with residues Phe448 and Phe388, thus acting as a communication element with the CTD.

Val60 contributes to the monomer-monomer interface and its side chain engages the helix 85-99, that connects loop1 to loop2, of the neighboring subunit by several hydrophobic contacts (**Figure 36B**).

Gly96 belongs to helix 85-99 at the end of loop1 and just before the beginning of loop2 (**Figure 36B**). At the beginning of the same helix, Ser84 interacts with both Gly96' on the second monomer and with Arg453 of the same monomer favoring loop1 correct positioning. Moreover, Arg453 provides an additional junction between CTD and loop1, since its side chain is in proper position to interact with Met1' backbone oxygen of the neighboring subunit by a H-bond contributing to the monomer-monomer interaction (**Figure 36B**).

Trp105 and Ala110 belong to loop2, a short stretch of amino acids that protrudes towards the active site of the neighboring subunit placing Ile101 and Phe103 in strict contact with the aromatic ring of the substrate. **Figure 37A**, shows also residue Cys100 which has been object of a project in collaboration with Prof. Kurian Manju and Dr. Giada Rossignoli at the University College of London (UK) (see **paper 2**). Cys100 is placed in a small apolar pocket sandwiched between loop1 and loop3. Trp105 seems to be involved in a weak interaction relay involving Glu113 and Leu38 (whose pathogenic substitution causes a dramatic decrease of activity [119].

Ala110 is the last residue of loop2, belongs to the monomers interface and is placed into an apolar cavity at the beginning of the large domain and for this reasons it should be better considered as borderline between loop2 and LD. Its substitution with glutamate may lead to local steric hindrance between the two subunits and

could exert some effects on the position of the residues present at the active site, *i.e*. Ile101 and Phe103 (**Figure 37A**). This is corroborated by results obtained in the biochemical characterization and the molecular dynamics simulation of the recombinant A110Q protein [119].

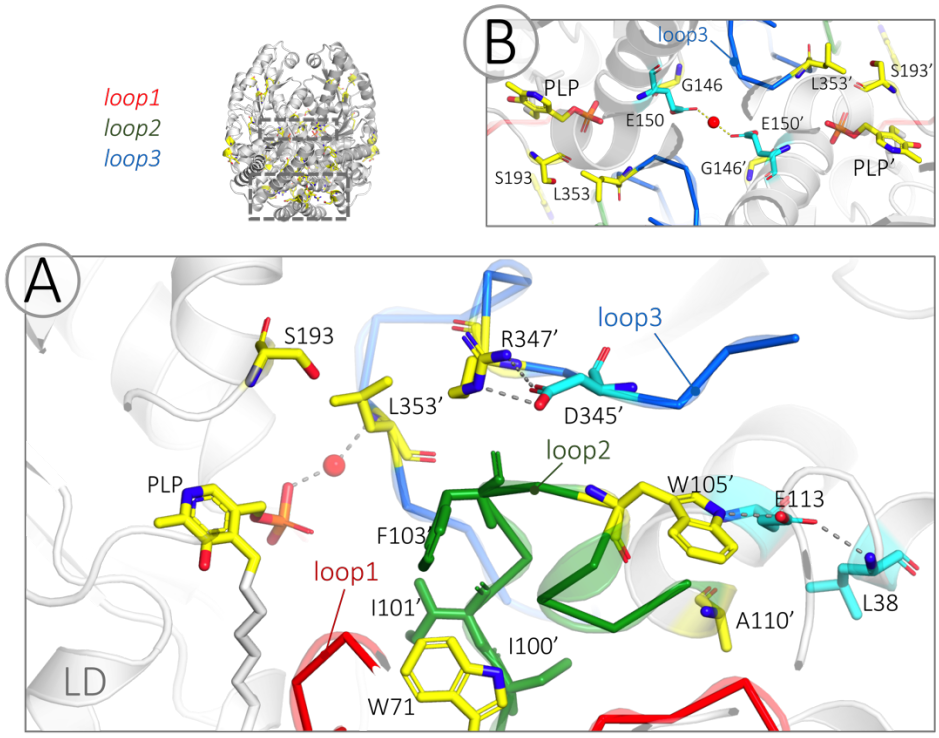

Fig. 37. *In silico* inspection of the residues located on loop2, loop3 and at the interface. Dimeric holoAADC has been obtained from structure1 (see part1) using Pymol 2.2.3 (The The PyMOL Molecular Graphics System, Version 2.0 Schrödinger, LLC). The two monomers are colored white and gray. Loop1, loop2 and loop3 are represented as ribbon and colored red, green and blue respectively. In each panel the mutation sites (yellow) and the interacting residues (cyan) are indicated and represented as sticks. Lys303 is colored white and PLP is colored yellow. Residues of loop2 are colored green.

Pro330 and Leu353 belongs to loop3, the former at the very beginning, the latter at approximately the end. Pro330 belongs to the CL and is therefore invisible in the AADC crystal structure. Pro330 is followed by Thr331 and by the essential catalytic residue Tyr332, suggesting that its substitution could affect CL. Leu353 (**Figure 37A**) is placed at the dimer interface, participates in the active site architecture, and contacts PLP through a water molecule together with Gly354 (see part 1).

Gly146 is located immediately below Glu150 (see part 1) on a turn connecting helix-6 and a β-sheet at the center of the monomer-monomer interface. In fact,

Gly146 of monomerA faces Gly146 of monomerB at the distance of 9.2 Å (**Figure 37B**).

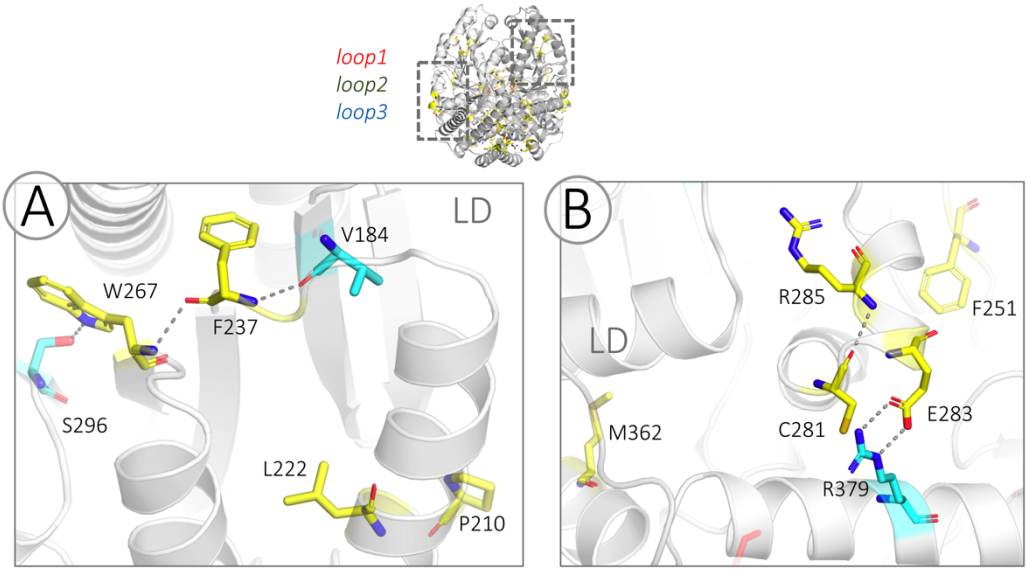

Fig. 38. Localization of residues located on the protein surface and/or in hydrophobic clusters. Dimeric holoAADC has been obtained from structure1 (see part1) using Pymol 2.2.3 (The PyMOL Molecular Graphics System, Version 2.0 Schrödinger, LLC). The two monomers are colored white and gray. Loop1, loop2 and loop3 are represented as ribbon and colored red, green and blue respectively. In each panel the mutation sites (yellow) and the interacting residues (cyan) are indicated and represented as sticks. Lys303 is colored white and PLP is colored yellow. Residues of loop2 are colored green.

Pro210, Leu222, Phe237 and Trp267 belong to a β-barrel system of the LD that surrounds the two active sites and that constitute the typical PLP-dependent enzyme architecture (**Figure 38A**). Pro210 is placed on a flexible stretch on the surface (aa 209-218). Leu222 belongs to the helix 218-232 and lies into a hydrophobic cleft. Phe237 and Trp267 lie on two adjacent β-sheets and are involved in several hydrophobic contacts contributing to the folding of the β-barrel.

Phe251 lies on the loop 234-252 in proximity of the protein surface and participates to a hydrophobic network involving residues of the LD and of the CTD (**Figure 38B**).

Cys281 and Glu283 are located on the same surface helix and together with Arg285 contribute to its stabilization [119] (**Figure 38B**). In detail, Arg285 contacts, among others, Cys281 through its backbone. Cys281 side chain is accommodated in a small apolar environment, unlikely being able to hosting residues with high steric hindrance. Glu283 is exposed on the protein surface and contacts by a salt bridge

Arg379 side chain. This interaction represents the only connection between the helix283-294 on LD and helix372-395 on the CTD (**Figure 38B**). On the basis of the local microenvironment, this interaction might prevent the exposure of hydrophobic residues to the solvent. Met362 belongs to helix358-369 that crosses the molecule from the active site to the surficial helix372-395 in contact with Glu283. Met362 side chain is located on a hydrophobic cleft and does not participate in any interaction (**Figure 38B**).

11. Some pathogenic variants exhibit low expression level in the soluble fraction.

The analysis of the relative expression of the pathogenic proteins in the soluble fraction (**Table 15**) reveals the presence of a group of variants (P210L, L222P, F237S, W267R, C281W, E283A, M362T) characterized by a poor solubility (9-30%) with respect to the WT protein. A low expression level in the soluble fraction may be related to a solubility alteration at least in the *E. coli* system, suggesting possible folding defects.

These variants, whose position in the protein has been already mapped (see above), can be divided in two clusters: those located on same structural regions, distant from the active site, and commonly characterized by lying on the surface of the protein (P210L, E283A) and those belonging to hydrophobic clusters (L222P, F237S, W267R, C281W, M362T), as already shown in **figure 38**.

The effect of decreasing solubility can be not only determined by the position but also by the identity of the substitution. As for M362T, even if methionine to threonine is a conservative substitution, a threonine residue could lead to a destabilization of the helix also affecting Glu283. In addition, C281W and E283A low solubility could be probably attributable to the loss of the surficial Glu283-Arg379 salt bridge with the consequent exposure of hydrophobic patches. L222P, F237S and W267R are alterations changing the chemical feature of the residues located on a hydrophobic region on the β-barrel system. It has been previously observed that some AADC variants affecting the same region can show low purification yields, in particular, R285W exhibited a ~20% of solubility level respect with the WT [119].

Table 15. Analysis of the relative expression level of the pathogenic variants in the soluble fraction of E. coli.

Protein	% expression
wild type	100
Y20del	73
E25K	95
V60A	74
H70Y	87
H70R/W71del	68
F77L	97
G96R	93
W105C	100
A110E	72
G146R	103
P210L	27
L222P	14
F237S	15
F251S	79
W267R	23
C281W	9
E283A	30
P330L	38
L353P	100
M362T	20
R453C	99

All the other variants are expressed and present in the soluble fraction at higher amount, ranging from 72% to 103% of the WT, with the exception of P330L that exhibit a 38 % of expression. This may be related with the type of substitution, being Pro → Leu localized on the CL that is exposed to the solvent thus may reduce protein solubility.

Considering the protein yields after purification, some variants exhibit nearly good to good yields *i.e* 30–85% with respect to the WT (Y20del, E25K, H70R/W71del, F77L, G96R, W105C, A110E, G146R, F251S, L353P, R453C). Others display low 5–10% (V60A, H70Y, P330L, M362T) and very low (less than 2% for E283A, P210L, W267R) yields. Unfortunately, it was not possible to purify L222P, F237S and C281W which were recovered in extremely low amounts (<0.3%) preventing us to carry out a complete biochemical characterization. The purified variants appear to be homogenous as indicated by a single band on SDS-page with mobility identical to that of the corresponding WT protein (**Figure 39**). Once purified, all the variants bind 2 mol of PLP per dimer.

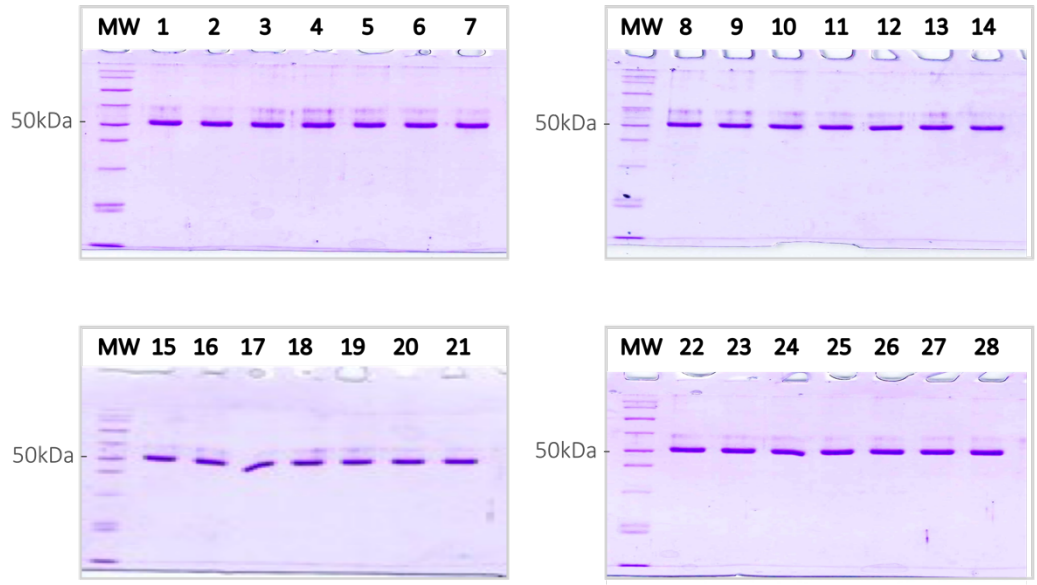

Fig. 39. Quality of all AADC variants preparations. All purified variants appear to be homogenous as indicated by a single band on SDS-page with mobility identical to that of the corresponding WT protein. Lane numbers are the following: 1-WT, 2-Y20del, 3-Y20A, 4-Y20S, 5-E25K, 6-R27A, 7-V60A, 8-E61A, 9-H70Y, 10-H70R/W71del, 11-W71A, 12-F77L, 13-G96R, 14-W105C, 15-A110E, 16-G146R, 17-S193A, 18-S193D, 19-S193E, 20-P210L, 21-F251S, 22-W267R, 23-E283A, 24-P330L, 25-R347Q, 26-L353P, 27-M362T, 28-R453C.

12. Aggregation propensity of the apo forms of the low solubility variants

Given the great variability in both solubility level and purification yield of the analysed variants (also reported in sporadic cases for other characterized AADC variants [119,122]) DLS analyses have been carried out in order to monitor the aggregation propensity of the purified enzymes under physiological conditions (58 mM potassium phosphate buffer, pH 7.4 at 37 °C). DLS measurements evaluating the increase in the mean count rate (kcps) of the holo and apo forms of the majority of AADC variants and of WT do not show aggregation under these experimental conditions. Instead, apoP210L, apoE283A and apoM362T, even if at different extent, tend to aggregate as indicated by the increase in kcps (**Figure 40**).

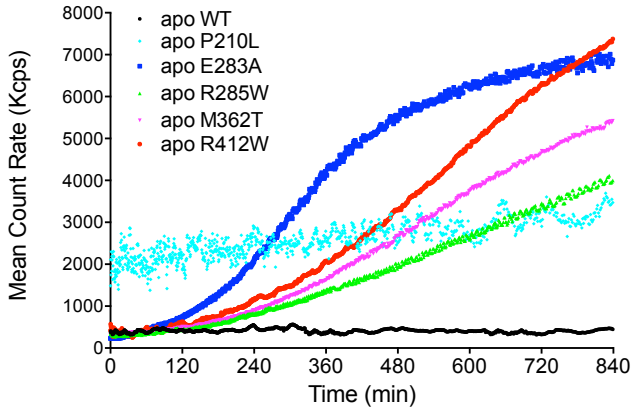

Fig. 40. Some pathogenic variants exhibits aggregation propensity in their apo form. Aggregation of apoP210L, apoE283A, apoR285W, apoM362T, apoR412W in comparison with apoWT recorded at 4 μM protein concentration in 58 mM potassium phosphate pH 7.4 at 37 °C. DLS analysis as function of time reveals an increase of the mean count rate (Kcps) proportional to protein aggregation.

Since in 2014 it was reported that R285W and R412W variants were poorly expressed in *E. coli* [119], we re-expressed and purified them to investigate their possible aggregation propensity. It is known that Arg285 belongs to the same helix of Glu283 (paragraph 3) while R412W variant has been proposed to affect global CTD folding [119]. Interestingly, their apo forms show a similar propensity to aggregate. With the exception of apoP210L that shows a scattered and almost linear aggregation curve, all other apo variants show a complete or partial sigmoidal aggregation process, constituted by a first lag phase followed by a consistent increase in the mean count rate.

This analysis provides the first evidence of *in vitro* aggregation of AADC variants. Taken together, these data underline the relevance of residues belonging to the LD and to the first part of the CTD for the global protein folding. Either if present on the surface (Pro210, Glu283, Glu285 and Arg412) or in hydrophobic clefts (Leu222, Phe237, Trp267, Cys281, Met362), they deeply affect solubility and, in some cases, show aggregation propensity of their apo forms.

13. Secondary structure content and thermal stability of new pathogenic AADC variants

In order to monitor overall protein stability, at first far-UV CD spectra of holo WT and of the new holo AADC variants have been carried out.

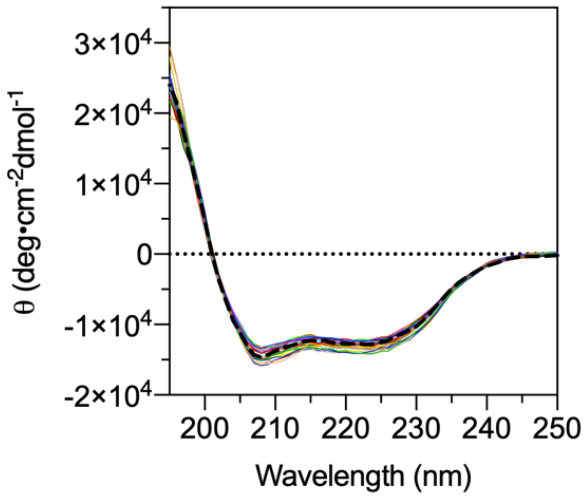

Fig. 41. Overall Integrity of all WT and AADC variants. Far-UV CD spectra of holo WT (black dashed line) and all holo AADC variants (coloured lines) recorded at 5 μM protein concentration, in 100 mM potassium-phosphate buffer, pH 7.4 with the addition of 100 μM PLP.

They overlap and display unaffected signals or slightly differences in the secondary structure content, thus indicating no gross modifications in the total percentages of secondary structure elements of the enzymatic species (**Figure 41**). The fact that the secondary structure content is maintained almost unchanged implies that, in addition to WT, the purified variants are properly folded species.

Then, melting temperature of all purified holo and apoAADC variants and WT have been measured by following the loss of the α-helical dichroic signal at 222 nm.

Table 16, lists the Tm values of the holo and apo forms in comparison to those of the WT. As for the holo forms, variants can be grouped in those faintly affecting the Tm (± 3°C), such as W105C, G146R, P210L, F251S, W267R, P330L, L353P, M362T and R453C, or deeply decreasing the Tm (-4 to -10 °C) as Y20del, E25K, V60A, H70Y, H70R/W71del, F77L, G96R, A110E, and E283A. It should be noted that the most affected variants seem to be those mapping on NTD-loop1 (**Figure 42A, B**).

Table 16. Melting Temperatures of WT AADC and pathogenic variants. Melting temperature values obtained by following the CD signal at 222 nm and varying the temperature linearly from 25 to 90 °C with a slope of 1.5 °C/min.

	Tm (°C)	
Enzyme	**holo**	**apo**
WT	69.42 ± 0.02	64.84 ± 0.03
Y20del	59.01 ± 0.03	58.04 ± 0.02
Y20A	63.20 ± 0.02	61.72 ± 0.02
Y20S	59.97 ± 0.01	57.13 ± 0.02
E25K	65.26 ± 0.02	63.64 ± 0.03
V60A	62.13 ± 0.02	59.30 ± 0.03
H70Y	65.95 ± 0.04	63.28 ± 0.05
H70R/W71del	63.71 ± 0.02	63.46 ± 0.03
W71A	71.85 ± 0.02	63.95 ± 0.02
F77L	63.58 ± 0.03	61.70 ± 0.03
G96R	65.64 ± 0.05	58.46 ± 0.04
W105C	69.45 ± 0.01	62.00 ± 0.01
A110E	63.20 ± 0.05	62.04 ± 0.04
G146R	69.77 ± 0.02	62.15 ± 0.05
P210L	66.10 ± 0.10	60.91 ± 0.05
L222P	n.p	n.p
F237S	n.p	n.p
F251S	70.49 ± 0.04	63.37 ± 0.06
W267R	70.30 ± 0.10	63.60 ± 0.03
C281W	n.p	n.p
E283A	62.89 ± 0.02	58.66 ± 0.07
P330L	68.04 ± 0.02	62.47 ± 0.02
R347Q	66.64 ± 0.02	63.60 ± 0.02
L353P	68.10 ± 0.07	60.82 ± 0.03
M362T	67.54 ± 0.02	59.89 ± 0.02
R453C	69.36 ± 0.03	66.70 ± 0.02

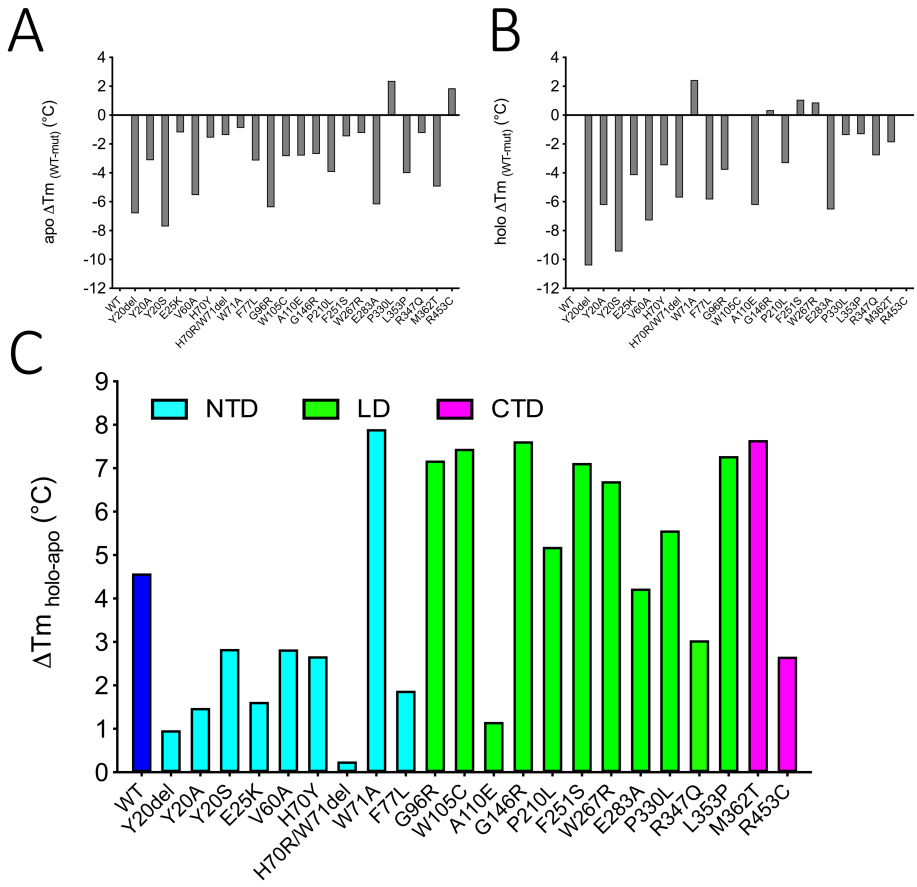

Fig. 42. Destabilization effect of the mutations along each AADC domain. Effect of the mutations on A) apo and B) holo thermal stability expressed $\Delta Tm_{(WT\text{-}mut)}$ represented along protein sequence. C) Preferential effect of the variants on the apo or on the holo form expressed as $\Delta Tm_{(holo\text{-}apo)}$.

In particular the following apo species are weakly affected in Tm values (± 3°C) E25K, H70Y, H70R/W71del, F77L, W105C, A110E, G146R, F251S, W267R, P330L and R453C. The other apo species result in Tm values decreased by 4 to 6 degrees and are Y20del, G96R, P210L, E283A, L353P and M362T. In order to better understand the differential effect of the mutation on the two protein forms, we evaluated the ΔT_m value ($Tm_{(holo\text{-}apo)}$) for each protein (**Figure 42C**). The $\Delta T_{m(holo\text{-}apo)}$ of the WT AADC is 4.6 °C and this value represents the different thermal stability of the closed and open conformations. In this view, a change of the $\Delta T_{m(holo\text{-}apo)}$ may indicate a preferential effect of the mutation on just one form. The NTD results to be the region with a clear reduction of the $\Delta T_{m(holo\text{-}apo)}$. This effect is mainly due to a destabilized holo protein that leads to a reduced difference in Tm respect to the corresponding apo form, arguing that these enzymatic species

resemble more apo than holo structures. The more prominent effect of the decreased $\Delta T_{m(holo-apo)}$ is evident in the deletion variants, Y20del and H70R/W71del. The site-directed variants Y20A and Y20S show Tm values for the holo and apo species slightly different from those of the pathogenic naturally occurring Y20del exhibiting curiously the Ala substitution a less destabilizing effect than the Ser modification. On the contrary, W71A site specific substitution demonstrates that Trp71 does not play a crucial role on protein thermal stability (**Table 16)** being its holo and apo Tm values nearly identical to those of the WT. Thus, the results collected with the H70R/W71del species should be related to His70 that is highly affected in the holo rather than in the apo form.

Even if the effect of the variants of the LD is more heterogeneous some considerations could be done. The majority of the variants showing unchanged or small changes in both holo and apo Tm values belong to this domain: W105C, G146R, F251S, and W267T. The two CTD variants M362T and R453C have the same behaviour in Tm even if apoM362T is less stable than apoWT, as evidenced by its propensity to aggregate.

Notably, some exceptions should be mentioned: A110E has a same value in holo and apo Tm due especially to holo rather than apo destabilization and the two surface variants, P210L and E283A, exhibit a pronounced destabilization effect on both the holo- and apo-protein resulting in an overall $\Delta T_{m(holo-apo)}$ similar to that of the WT but due to an overall less stable protein.

14. Aromatic amino acids microenvironment and PLP binding in AADC pathogenic variants

We characterized the structural features of pathogenic variants in their apo and holo form by near UV CD spectroscopic signals related to the asymmetric aromatic amino acids environment, with respect to protein moiety, providing insight into tertiary structure arrangement. As already mentioned in the Introduction apo and holo WT AADC display near UV signals presenting a major band at 280 nm, being that of the apo in magnitude about half that of the holo. Here, taking into consideration all pathogenic variants, a decrease is evident for both apo and holo species, however the apo enzymes signals are diminished by no more than 50%,

being Y20A, E25K, H70Y and R453C the variants with a 40-50% decrease of the apo CD signal. A much wider spectrum of alteration is visible for the dichroic signals relative to the holo forms, spanning from ~ 0 to 100 % of the WT signal (**Figure 43A**). Interestingly, mainly evident in the holo protein, the NTD variants are, above all species, those highly affected by the change in the aromatic microenvironment with a decrease more than 50%, being those of the LD less affected and the two belonging to the CTD mid affected (**Figure 43**).

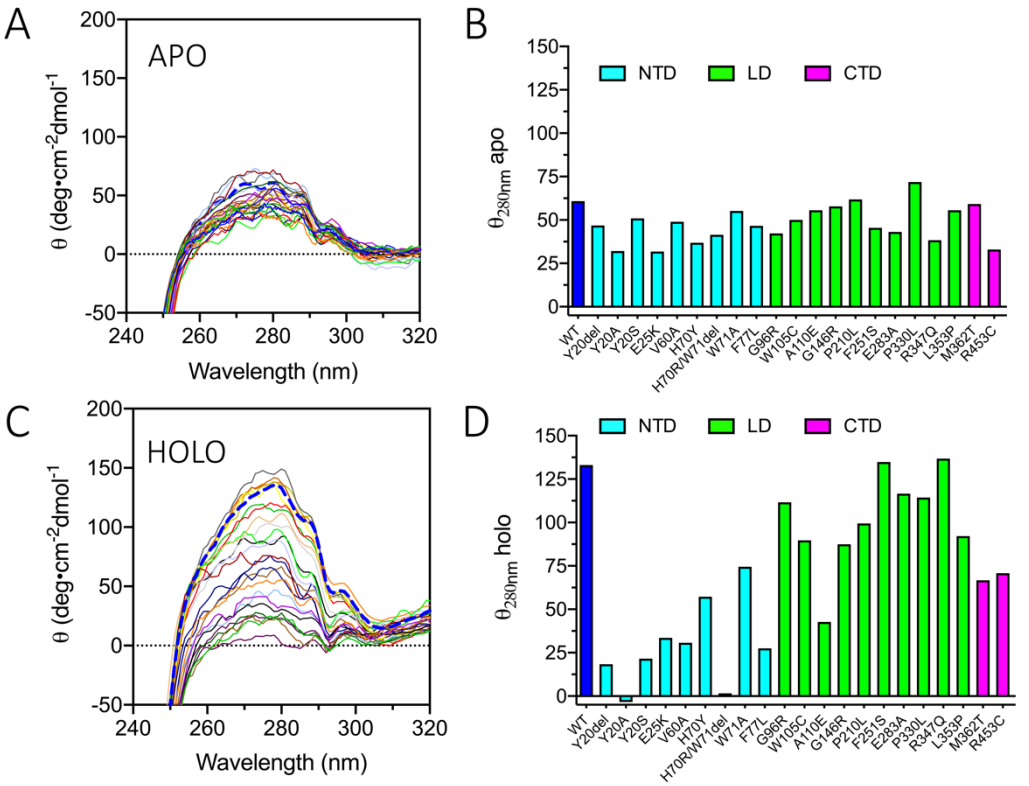

Fig. 43. Near-UV CD spectra of WT AADC and pathogenic variants in their holo and apo forms. The spectra are recorded at 5 µM protein concentration, in 100 mM potassium-phosphate buffer, pH 7.4. Spectra of the holo forms are recorded in the presence of 100 µM PLP. Spectra of all AADC apo variants (colored lines) are shown superposed to that of the apoWT (dashed blue line) (A) and along protein sequence (B). Holo variants spectra are shown in comparison to the holoWT (dashed blue line) and along each protein domain.

In order to explain the behaviour of the CTD residue Arg453 (so similar to those of the NTD) and of the two deletion mutants, it can be observed that, as reported by the bioinformatic analyses above, Arg453 is spatially close to Tyr20, Arg27 and His70. The artificial variant Y20S presents apo and holo signals similar to those of the natural occurring Y20del, while Y20A shows to affect protein structure even at a higher extent. This could be interpreted as the loss of Tyr20 has a deep impact

into tertiary structure environment. W71A exhibits increased signals in both apo and holo enzymatic species respect to the pathogenic counterpart, and the combination of the effects of natural H70Y, H70R/W71del together with artificial W71A shows that the removal of Trp71 is not detrimental by itself in tertiary structure assembly (and for protein thermal stability).

The binding of the coenzyme is associated with characteristic bands in the visible range as revealed by absorption and circular dichroism in the visible region.

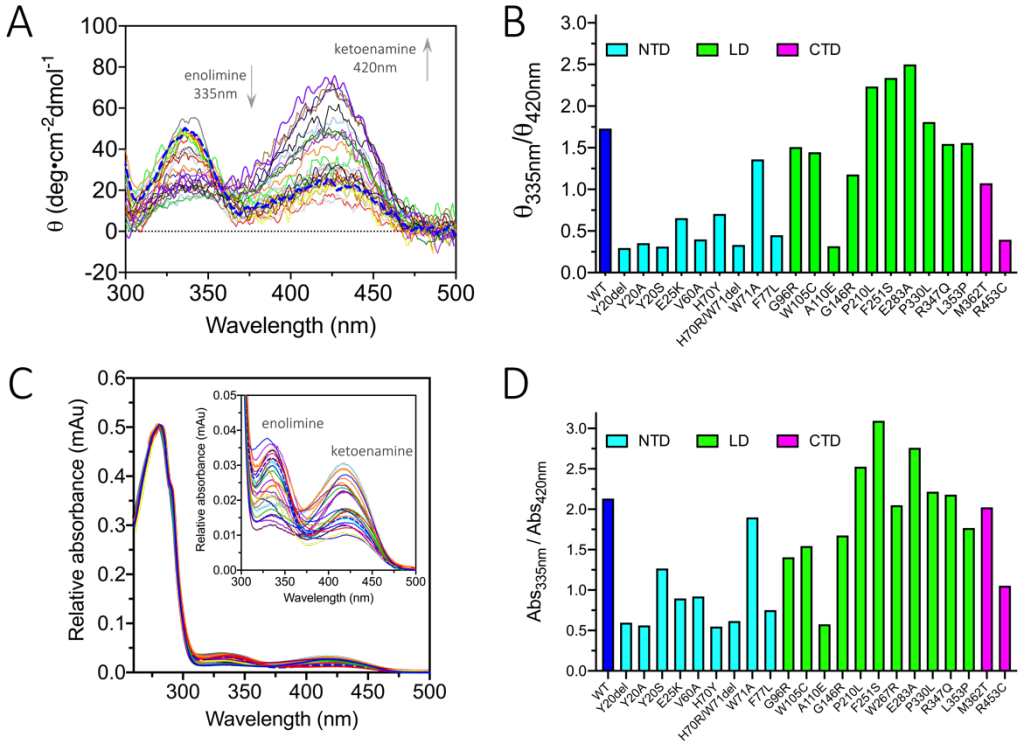

Fig. 44. Visible CD spectra and absorbance profile of WT AADC and pathogenic variants in their holo forms. A) CD spectra are recorded at 5 μM protein concentration, in 100 mM potassium-phosphate buffer, pH 7.4 in presence of 10 μM PLP. B) Representation of impact to the mutations on the tautomeric equilibrium (ratio between $\theta_{335\ nm}$ and $\theta_{420\ nm}$) along protein sequence. C) Absorbance profile of WT and holo variants recorder in the near-UV visible range. Inset represents the magnification of the internal aldimine bands. D) Tautomeric equilibrium (ratio between $Abs_{335\ nm}$ and $Abs_{420\ nm}$) along protein domains.

As shown in **figure 44**, AADC variants exhibit great variability in their visible CD and absorption spectra. These differences are consistent with an alteration of the equilibrium between the two tautomers at 335 nm and 420 nm. The WT internal aldimine presents a characteristic 335 nm/420 nm ratio in the dichroic bands of about 1.7. AADC variants show a distribution of ratios consistent to both the prevalence of the ketoenamine band over the enolimine (variant A110E, R453C

together with variants of the NTD) and the prevalence of the second one over the ketoenamine (variants of the LD - with the exception of A110E). In this picture, M362T constitute a midpoint between the two groups of variants, showing a ratio of ~1 (**Figure 44A**). Absorbance spectra for all pathogenic variants show the same behaviour highlighting a wide spectrum of alteration of the tautomeric equilibrium. The ratio Abs 335 nm/Abs 420 nm correlates with the CD 335 nm/420 nm ratio with $R^2 = 0.8652$ (**Figure 45A**).

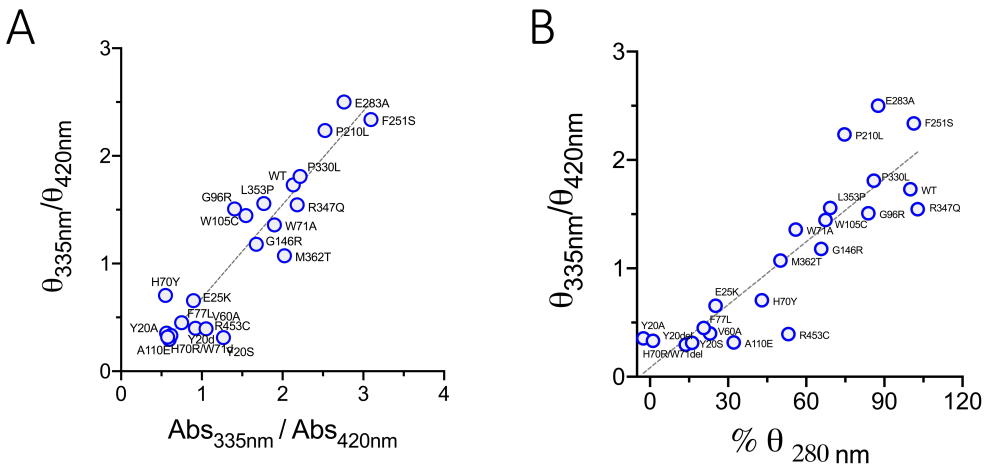

Fig. 45. Correlation between CD and absorbance signals. A) The correlation between the tautomeric equilibrium observable by dichroism or absorbance can be well described by a linear fit with $R^2 = 0.8652$. B) The % of the 280 nm dichroic band is plotted versus the tautomeric equilibrium and fitted to a linear regression with R^2 value of 0. 7776.

The tautomeric equilibrium has been generally related with the PLP microenvironment [44,53,60,119,120], with no focus on the relation with global tertiary structure of the protein. **Figure 45B** shows as the loss of CD 280nm signal is concomitant with the decrease of the 335 nm band and the increase of the 420 nm band. This tendency correlates with a linear fit with a $R^2 = 0.7776$. The artificial variants Y20A, Y20S and W71A confirm the features of their naturally occurring counterpart, being the combination of W71A and H70Y less affected than H70R/W71del.

In order to correlate the alterations in the tautomeric PLP environment to the equilibrium dissociation constant of PLP, we measured this value for all variants as described under Materials and Methods section. As shown in **table 17** the variants exhibit a great heterogeneity in the coenzyme affinity.

Table 17. $K_{D(PLP)}$ values for AADC wild-type and variants. [a] PLP affinity value for R347Q has been obtained from [119].

Enzyme	$K_{D(PLP)}$ (nM)
Wild-Type	101 ± 10
Y20del	970 ± 120
Y20A	778 ± 50
Y20S	648 ± 121
E25K	594 ± 24
V60A	252 ± 35
H70Y	70 ± 18
H70R/W71del	420 ± 60
W71A	148 ± 13
F77L	222 ± 38
G96R	132 ± 14
W105C	162 ± 17
A110E	321 ± 26
G146R	120 ± 20
P210L	47 ± 7
L222P	n.p
F237S	n.p
F251S	33 ± 9
W267R	121 ± 10
C281W	n.p
E283A	330 ± 30
P330L	123 ± 19
R347Q[a]	54 ±10
L353P	199 ± 34
M362T	271 ± 20
R453C	468 ± 36

Some variants exhibit PLP affinity very similar to that of the WT (H70Y, P210L, F251S, R347Q), others show a wide array of values ranging from only small changes (W71A, G96R, W105C) to a 6/10-folds decreased affinity (such as Y20del, Y20A, Y20S, E25K). Interestingly, most of the variants exhibiting more than 2-fold higher K_{DPLP} with respect to the WT are located on the NTD (with the exception of loop1 variants H70Y and W71A, underlining here a possible requisite of a hydrophobic environment for PLP binding) and on the CTD (**Figure 46**). Among the variants of the LD, A110E, E283A and L353P show the worst decrease in coenzyme affinity.

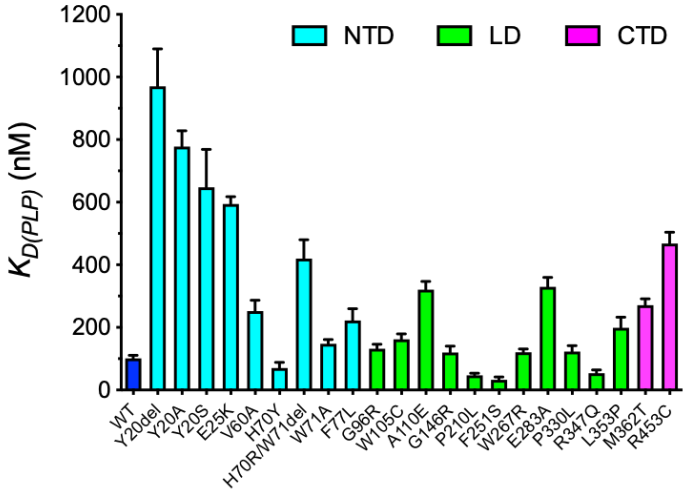

Fig. 46. Distribution of the $K_{D(PLP)}$ effect on AADC domains. Variants at the N-terminal domain are colored in cyan, at the Large domain are colored green, and those on the C-terminal domain are colored in magenta.

Overall, the K_{DPLP} values of the pathogenic variants show an inverse correlation with the CD signals at 280 nm arguing that the more the aromatic microenvironment is similar to the WT, the higher is the affinity for the PLP, tautomerized in favor of the enolimine form (**Figure 47**).

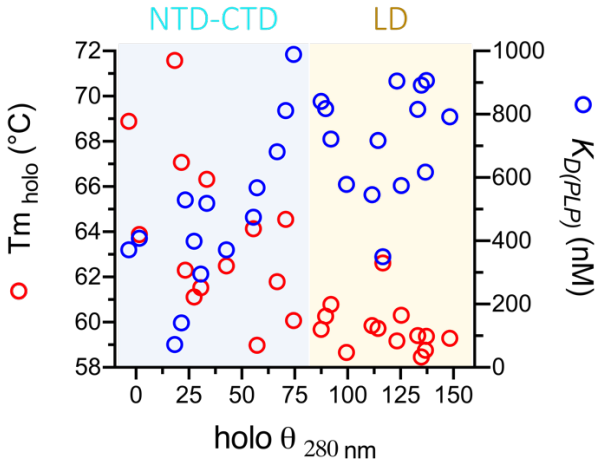

Fig. 47. Correlation between different structural signals. Thermal stability of the holo proteins and $K_{D(PLP)}$ values are plotted as function of tertiary structure integrity. The subdivision between NTD-CTD variants and LD variants is highlighted in cyan and yellow. In the plot also non-pathogenic variants are included, and will be discussed later in the text.

The addition of the Tm values to this plot exhibits a trend evocative of a preserved thermal stability with preserved tertiary structure content (CD signal at 280 nm) and low $K_{D(PLP)}$ values (**Figure 47**). Notably, NTD and CTD (with the exception of A110E) residues are found at the left part of the plot (low CD 280 nm values, low

Tm values and high K_D values), and the variants of the LD are found on the right part of the plot, suggesting that the maintenance of a correct folding ensures high coenzyme affinity and high thermal stability. In this sense, the substitution due to mutations of residues mapping on NTD and CTD seems to be detrimental to reach a structurally competent holo scaffold, while LD residues, in particular those of loop3, experience less global destabilization.

In addition, none of the variants involving residues in close proximity to the PLP moiety, or taking part to the active site architecture at different extents (*i.e* Trp71, Trp105, Pro330, Arg347 and Leu353), shows a dramatic decrease in the apparent equilibrium dissociation constant (ranging between 54% to 162% of the WT, with L353P having a 2-fold decrease PLP affinity) arguing that the $K_{D(PLP)}$ values are related to a larger folding and/or stability effects rather than subtle and localized active site changes. Since the signals related to the cofactor microenvironment (335nm/420nm ratio in both absorbance and CD measurements) is related to the 280 nm CD value (**Figure 45**), we can add that, at the extremes of the plot, the LD residues favour the enolimine tautomer of PLP, as the WT, while those of the NTD favour the ketoenamine one.

Having determined the structural determinants of the coenzyme binding and the affinity for PLP, the functional properties in terms of catalytic activity have been measured.

15. Steady-state kinetic parameters for L-Dopa of pathogenic variants

The study of the effect of AADCd variants on the decarboxylase activity has been carried out by measuring the kinetic parameters for L-Dopa under steady state conditions (**Table 18**).

Table 18. Steady-state kinetic parameters for L-Dopa of wild-type AADC and variants. [a] WT parameters has been firstly reported in [44], and those of [b] in [119].

Enzyme	k_{cat} (s^{-1})	K_m (mM)	k_{cat}/K_m ($sec^{-1}mM^{-1}$)
WT[a]	7.6 ± 0.1	0.11 ± 0.01	69.1 ± 10
Y20del	0.04 ± 0.01	0.44 ± 0.04	0.088 ± 0.024
Y20A	0.0197 ± 0.0005	0.12 ± 0.01	0.16 ± 0.01
Y20S	0.0250 ± 0.0006	0.12 ± 0.01	0.21 ± 0.01
E25K	1.4 ± 0.1	0.07 ± 0.01	20 ± 3.2
V60A	1.7 ± 0.6	0.18 ± 0.02	9.44 ± 3.34
H70Y	0.58 ± 0.09	0.26 ± 0.04	2.23 ± 0.41
H70R/W71del	0.00067 ± 0.00004	0.22 ± 0.06	0.0023 ± 0.0009
W71A	0.12 ± 0.05	0.16 ± 0.04	0.75 ± 0.36
F77L	0.35 ± 0.07	0.51 ± 0.05	0.68 ± 0.15
G96R	3.72 ± 0.7	1.81 ± 0.03	2.06 ± 0.38
W105C	0.0067 ± 0.0004	0.18 ± 0.04	0.037 ± 0.001
A110E	0.00031 ± 0.00001	0.09 ± 0.01	0.0037 ± 0.0007
G146R	0.17 ± 0.01	8.34 ± 0.94	0.020 ± 0.002
P210L	4.4 ± 0.2	0.12 ± 0.02	36.6 ± 6.3
L222P	n.p	n.p	n.p
F237S	n.p	n.p	n.p
F251S	4.1 ± 0.1	0.09 ± 0.01	45.77 ± 5.19
W267R	2.11 ± 0.04	0.194 ± 0.014	10.9 ± 0.81
C281W	n.p	n.p	n.p
E283A	6.4 ± 0.2	0.29 ± 0.05	22.0 ± 0.04
P330L	0.056 ± 0.001	0.12 ± 0.01	0.45 ± 0.04
R347Q[b]	0.087 ± 0.005	0.49 ± 0.08	0.16 ± 0.06
L353P	0.00062 ± 0.00006	0.26 ± 0.03	0.0023 ± 0.0003
M362T	4.6 ± 0.2	0.18 ± 0.06	25.5 ± 8.6
R453C	0.67 ± 0.07	0.40 ± 0.06	1.67 ± 0.31

A first consideration comes from the comparison between the effect of the mutations on k_{cat} and K_m parameters. Variants exhibit a wider range of alterations in terms of k_{cat} than of K_m since the first ones span from 1-3 orders of magnitude of difference to about $2.5 \cdot 10^5$ decrease with respect to the WT. Substrate affinity is instead less variable with an average alteration of about 2-folds respect to the WT once excluded variants G96R and G146R that show a dramatic increase in K_m of ~ 16 and ~ 83-folds respectively.

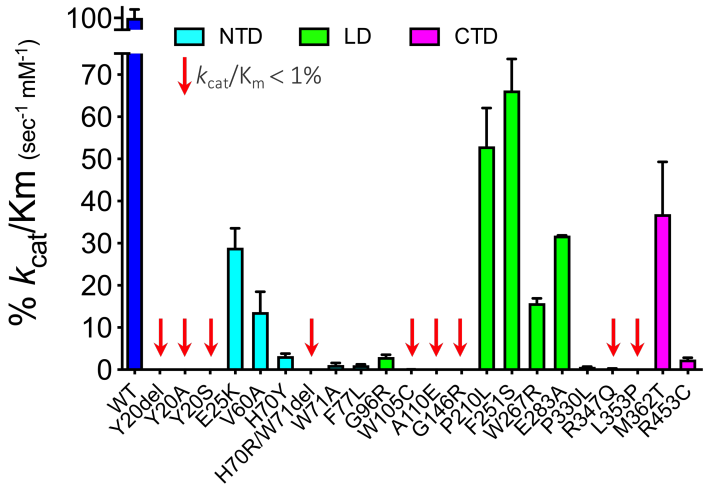

Fig. 48. Effect of the mutations on the protein catalytic efficiency along protein sequence. Catalytic efficiency is indicated as percentage of that of the WT and represented along protein sequence. The variants exhibiting a k_{cat}/Km lower than 1% with respect of the WT are highlighted with a red arrow. N-terminal domain is colored in cyan, the large domain in green, and the C-terminal domain is colored in magenta.

In order to find a possible rationale, the catalytic efficiency, k_{cat}/K_m, has been compared as percentage of that of the WT. **Figure 48** shows that there are variants exhibiting a medium-to-good catalytic efficiency (>1%). In particular, variants of the NTD (E25K, V60A and the loop1 H70Y, W71A, F77L) retain a catalytic efficiency of 1-30 % with respect to the WT, while variants of the LD present on the surface or related to the surface (P210L, F251S, W267R and E283A) retain good values of catalytic activity (from 15% to 70%) with the exception of G96R (about 3%, value highly influenced by its K_m). The two variants of the CTD show marked differences, conserving M362T an efficiency of about 40%, while R453C of about 2.5%. Since Arg453 is predicted to be a junction between CTD and NTD by bioinformatic analyses, it is not strange that its k_{cat}/K_m is similar to those of NTD variants.

A consistent different group includes those variants with a dramatic decrease in the k_{cat}/K_m below 0.6% of that of the WT. These variants, severely impaired in catalysis, are present on NTD and on loop2 and loop3 of LD and are: Y20del (and also the artificial Y20A and Y20S), double mutant H70R/W71del, W105C, A110E, G146R, P330L, and L353P. Although distributed in different protein regions, all these variants, belong to the dimer interface and the amino acid substitutions,

induced by the mutation, lead to ΔΔG (monomer-monomer) values (**Table 13**) that indicate an overall destabilization of the dimer interface.

In an attempt to correlate the structural data to the functional results we have plotted k_{cat}/K_m and k_{cat} as a function of the structural parameters and obtained interesting insights (**Figure 49**).

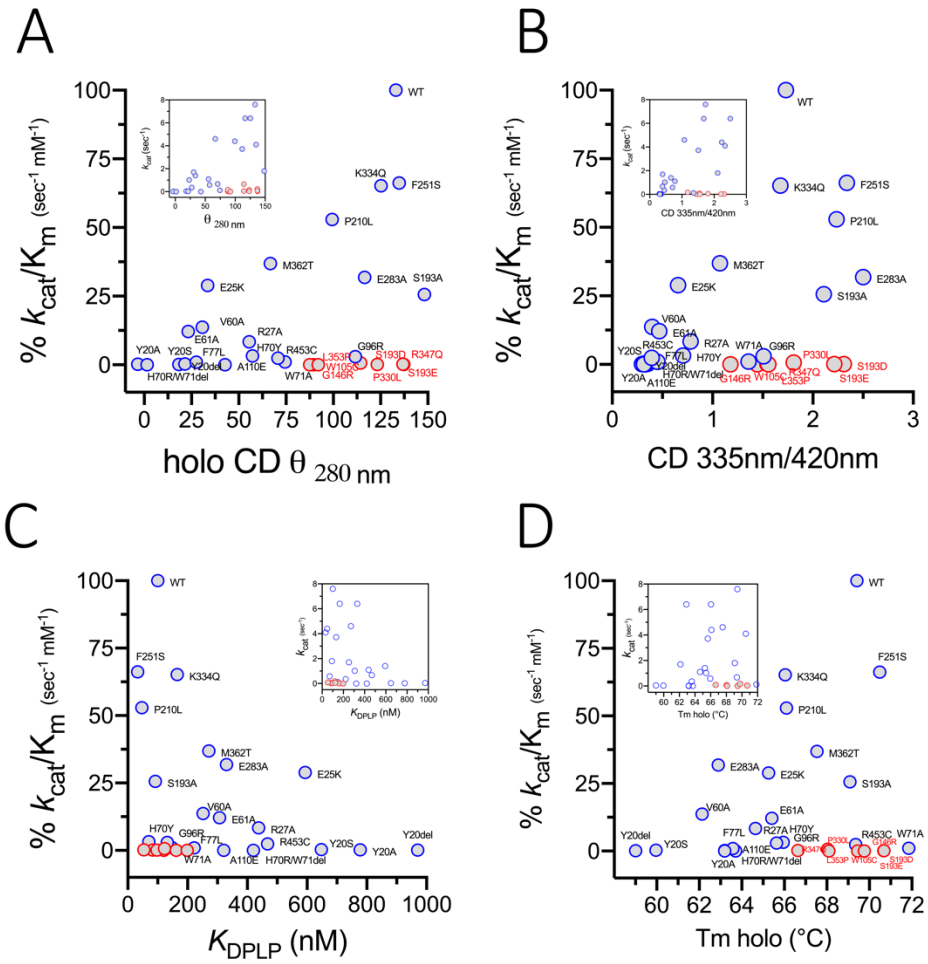

Fig. 49. Correlations between structural and functional signals. Functional parameter k_{cat}/K_m (as well as k_{cat} in the insets) has been correlated with different structural parameters, A) dichroic signal at 280nm, B) CD 335 nm/420 nm ratio, C) $K_{D(PLP)}$ and D) holo thermal stability. Catalytic incompetent variants W105C, P330L, R347Q and L353P together with G146R are shown in red. In the plot also non-pathogenic variants Y20A, Y20S, R27A, E61A, W71A, K334Q, S193D, S193E are included. S193D and S193E and will be discussed later in the text.

Data of both k_{cat}/K_m and k_{cat} as a function of the CD 280 nm signal show that there are some variants whose catalytic signals are correlated with aromatic microenvironment (E25K, V60A, H70Y, F77L, G96R, P210L, F251S, E283A, M362T and R453C), and a group of catalytically incompetent variants that can be

clustered in: those altered in dichroic signals (Y20del and the two artificial ones, H70R/W71del and A110E) and those retaining a high CD signal at 280 nm (W105C, G146R, P330L, R347Q and L353P), (**Figure 49)**. Notably, the first group is mainly composed by NTD residues while the second one by loop2 and loop3 variants. The only exception is A110E.

This behavior of k_{cat}/K_m and k_{cat} is also mirrored by the same correlation as function of the tautomeric equilibrium (**insets of Figure 49A, B**). These findings, on one side, suggest that the enolimine building up is proportional to best k_{cat} value and, on the other side, place the following variants W105C, G146R, P330L and L353P outside of the correlation. Interestingly, also the already characterized R347Q is clustered with this group [119,120].

The comparison of the k_{cat}/K_m data with the thermal stability of the holo species as well as with K_D for PLP shows the same trend in terms of different behavior of the two groups of catalytically incompetent variants (**Figure 49C, D**). If on one side it is easy to understand the catalytically inert NTD variants: lower extent of structural signals, of thermal stability and of equilibrium binding of PLP, it is difficult to find a rationale for the other group of residues belonging to loop2 and loop3 of the LD. The fact that all of them belong to the interface is not sufficient to explain the lack of correlation of the well-structured incompetent variants.

16. The external aldimine of AADC incompetent pathogenic variants with Dopa methylester (DME) and carbiDopa

In order to understand if the external aldimine microenvironment of all incompetent variants is altered as that of internal aldimine, we carried out an extensive spectral characterization in the presence of two analogs that are inhibitors of AADC: DME, unable to perform decarboxylation given the esterified carboxylate [47,120], and carbiDopa (a known drug used for Parkinson's disease to inhibit peripheral AADC) that presents a hydrazine group instead of an aminic one and forms an hydrazone with PLP.

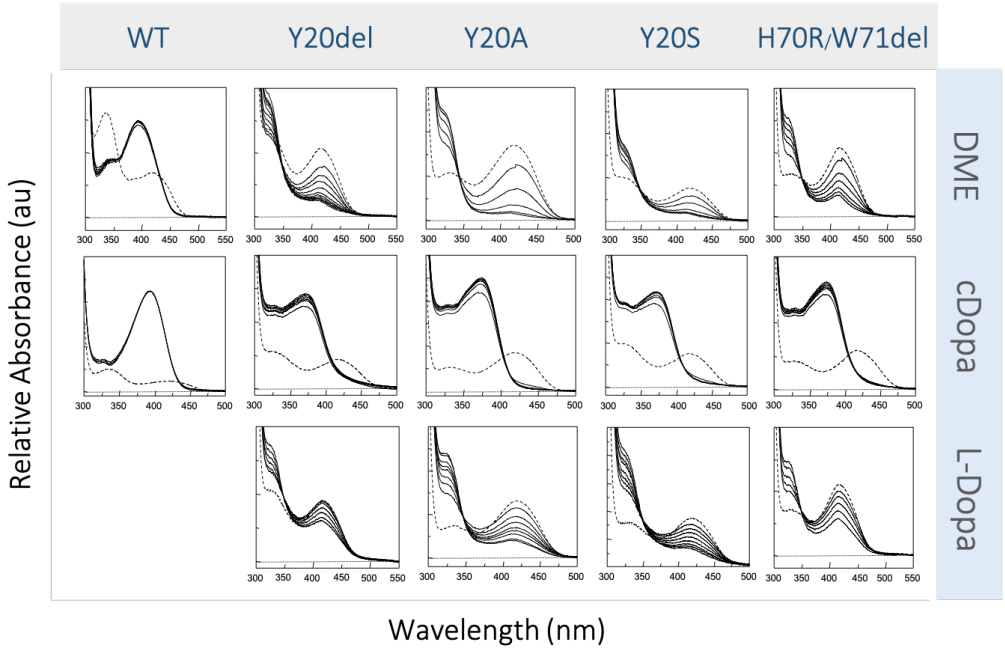

Fig. 50. Spectral modification of WT, Y20del, Y20A, Y20S, H70R/W71del incompetent variants in presence of different catechol endowed substrates. Absorbance spectra of 10 μM enzyme in presence of saturating concentrations of DME, carbiDopa (cDopa) and L-Dopa recorded in 100 mM potassium phosphate, pH 7.4 at 25 °C within 30 min. Dashed lines represent the spectra of the protein recorded in absence of substrate.

The absorbance spectrum of human WT AADC in presence of DME, shows a rapid (within 1 minute) formation of the external aldimine displaying a band with a λ_{max} at 395 nm that remains stable with time (**Figure 50**). The spectral modifications displayed by the catalytically incompetent variants permitted us to cluster them in two groups. The variants of the NTD (Y20del, Y20A, Y20S, H70R/W71del) and A110E show a major band at around 420 nm decreasing with time in concomitance with an increase at 329 nm. Variants belonging to the LD (W105C, G146R, P330L and L353P) show, in addition to a peak at 395-420 nm, the presence of a 500 nm species reminiscent of the ability of AADC to deprotonate DME at the α-carbon reaching an equilibrium between external aldimine and quinonoid species [30,47]. Small amplitude spectral changes are visible for these variants (**Figures 50, Figure 50**).

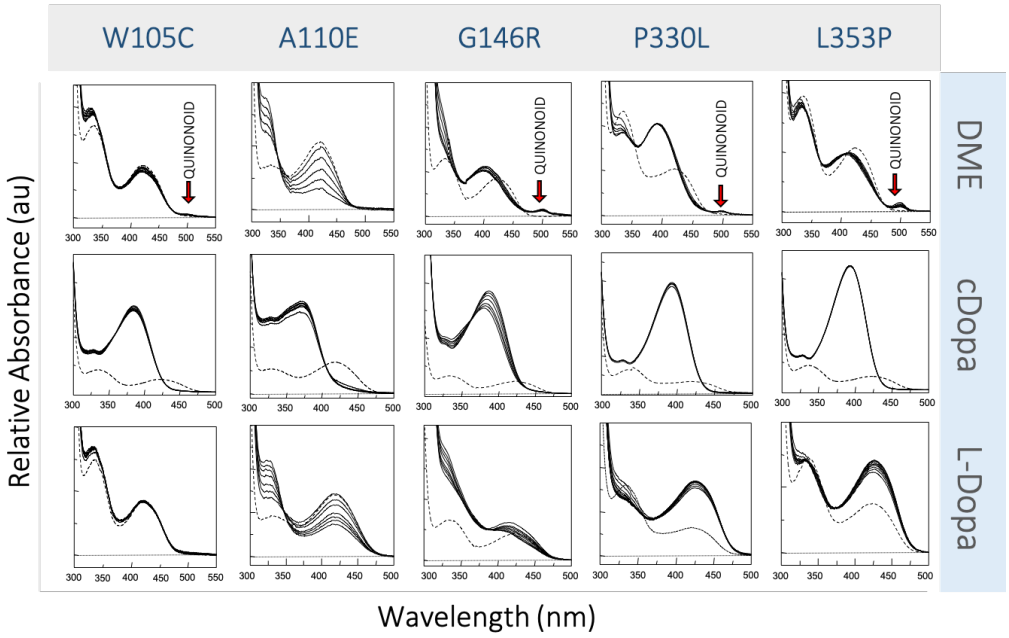

Fig. 51. Spectral modification of W105C, A110E, G146R, P330L, L353P incompetent variants in presence of different catechol endowed substrates. Absorbance spectra of 10 μM enzyme in presence of saturating concentrations of DME, carbiDopa and L-Dopa recorded in 100 mM potassium phosphate, pH 7.4 at 25 °C within 30 min. Dashed lines represent the spectra of the protein recorded in absence of substrate. The formation of the quinonoid species is highlighted with a red arrow.

The addition of carbiDopa to the WT determines the formation of a stable band absorbing at 395 nm. In presence of carbiDopa the NTD variants (Y20del, Y20A, Y20S, H70R/W71del) and A110E show a main band visible at 374 nm and second one at 329 nm both slowly increasing during the first 30 minutes. Instead, the group of variants of the LD presents the same spectral signals of WT binding carbiDopa with a band at 395 nm that remains stable during time (**Figures 50 and 51**). Only for G146R small alterations in the spectrum can be measured in the first 30 min with the ~ 390 nm band decreasing and shifting after 2 minutes to 380 nm with the concomitant formation of a 329 nm band.

These spectral results join to the above reported structural signals. We identify a difference among the incompetent variants also in terms of enzyme-ligand complex formation: those of the NTD show differences in external aldimine microenvironment with respect to the WT while those of the LD behave similarly to the WT.

We then decided to check spectral changes in the presence of the natural substrate L-Dopa (**Figures 50 and 51**). In presence of L-Dopa, NTD (and A110E) variants

show a fast decrease of the 420 nm band and a concomitant increase of a 329 nm band. The second group of incompetent variants of LD (W105C, G146R, P330L and L353P) show a fast increase of the 420 nm band concomitant with a small amplitude decrease of the 335 nm band shifted to 329 nm in the first minute of analysis (**Figures 50 and 51**). After few minutes, the 420 nm band slowly decreases and the 329 nm slowly increases.

In order to understand the consequences of the spectral modifications and thus the alteration of the requirements for productive external aldimine positioning, we decided to analyze in depth the spectral modifications for variants A110E and L353P in presence of L-Dopa since these two are the less active variants of the two emerging groups of incompetent variants.

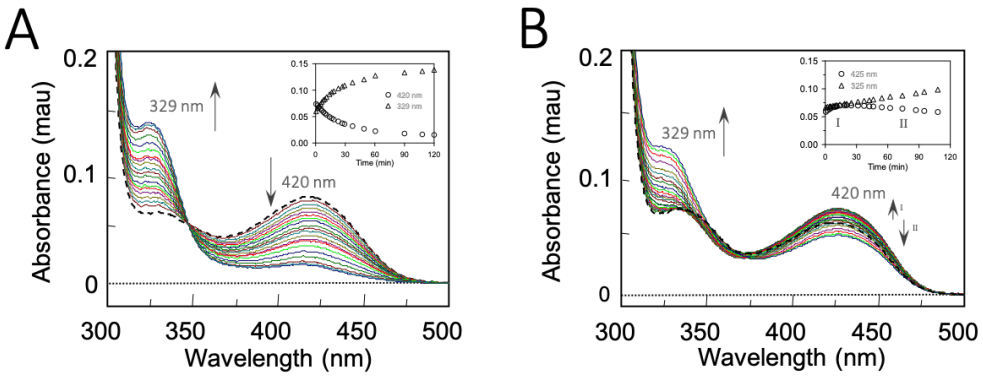

Fig. 52. Spectral modification of A110E and L353P variants in presence of L-Dopa. Panels A) and B) show the absorbance spectra of 10 µM A110E and L353P respectively in presence of 2 mM L-Dopa. Spectra were recorded in 100 mM potassium phosphate, pH 7.4 at 25 °C for 2 h. Dashed lines represent the absorbance spectra of A110E and L353P variants in absence of substrate. The arrows indicate the increase at 329 nm and the concomitant decrease at 420 nm with time. Insets: increase of the 329 nm and decrease of the 420 nm signals as a function of time.

As shown in **figure 52**, A110E exhibits a constant decrease of the 420 nm band and an increase of the band at 329 nm. These two bands generate an isosbestic point indicating that one single process is responsible for the direct conversion of one species to another. Differently, L353P shows a more complex process since the first phase (I) of increase of the 420 nm band, possibly related to the slow formation of the external aldimine (4'-N-protonated), is followed by a second phase (II) consisting in the decrease of the 420 nm. Concomitantly, a constant increase of a band peaking at 329 nm is visible (**Figure 52**).

Since under the same experimental conditions WT AADC determines the formation of a 390 nm absorbing species, interpreted as a 4'-N-unprotonated Schiff base [59], both these variants seem to be impaired in the conversion of the 4'-N-protonated external aldimine to the 4'-N-unprotonated one.

17. Coenzyme modification during the reaction of pathogenic variants with L-Dopa.

In order to identify possible coenzyme modifications during catalysis, we performed an HPLC analysis of the reaction of free PLP and AADC variants with substrate L-Dopa. A reaction mixture containing 20 µM free PLP or 10 µM enzyme with saturating concentration of L-Dopa has been treated and subjected to HPLC analysis, as reported in Materials and Methods section. It has been already demonstrated that PLP converts in the presence of the catechol ring of L-Dopa into a cyclic adduct due to a Pictet-Spengler condensation [30]. Once the adduct is eluted, collected and the pH adjusted, its absorbance spectrum shows two bands centered at 290 nm and 326 nm (**Figure 53**).

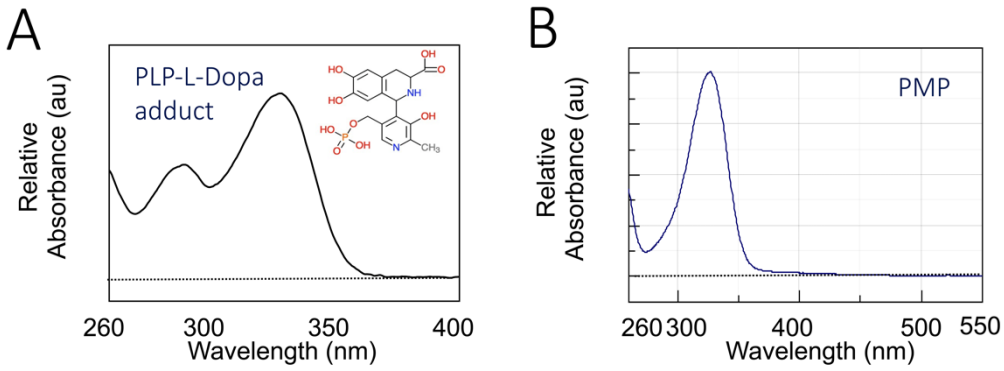

Fig. 53. Absorbance profile of PLP-L-Dopa adduct and PMP. Absorbance spectra of HPLC purified Pictet-Spengler adduct between PLP and L-Dopa. D) Absorbance spectra of commercially available PMP. Both spectra are recorded in in 100 mM potassium phosphate buffer, pH 7.4 at 25 °C

This non-enzymatic reaction does not occur with the WT AADC since the reaction rate of L-Dopa decarboxylation is faster than Pictet-Spengler condensation [30], however the formation of this adduct has been demonstrated for WT in the presence of non-natural substrates such as D-Dopa or by some previously characterized AADC pathogenic variants [44]. Free PLP in the presence of L-Dopa is completely

converted into the cyclic adduct in about 15 min (**Table 19**). All incompetent variants exhibit a gradual decrease of the initial PLP amount concomitantly with the irreversible transformation into an inactive coenzyme-derived species (**Figure 54A, B**) attributed to a Pictet-Spengler condensation.

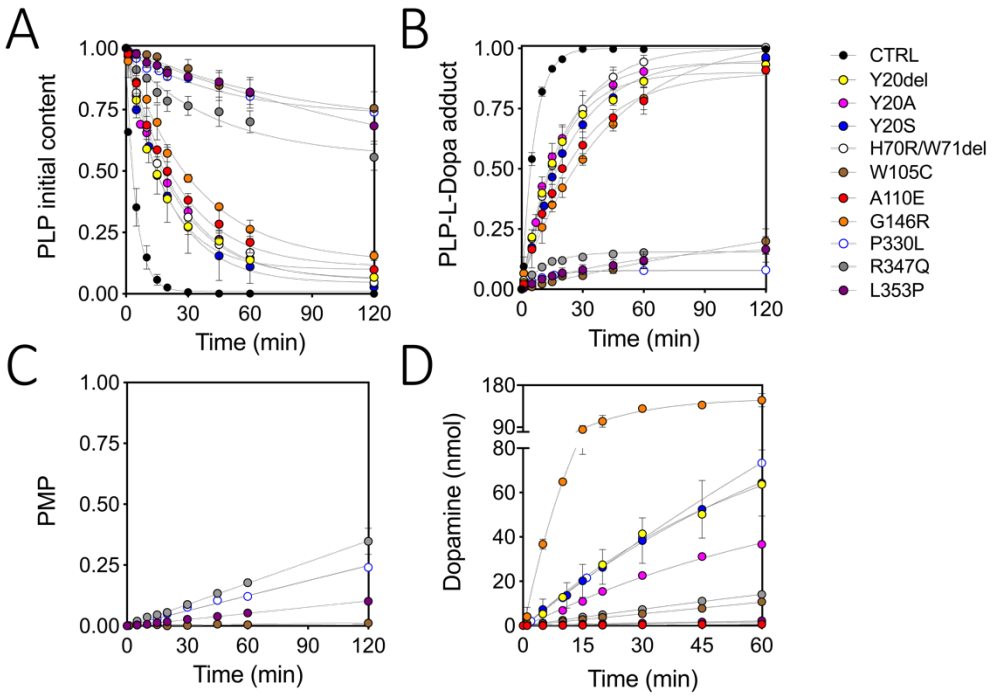

Fig. 54. Coenzyme modification during the reaction of incompetent variants with L-Dopa. HPLC analyses results of the reaction mixture of 10 µM incompetent variants in presence of saturating concentration of L-Dopa in 100 mM potassium phosphate buffer, pH 7.4 at 25 °C. PLP (A), PLP-L-Dopa adduct (B), PMP (C) and dopamine (D) are normalized for the initial amount of PLP detected in absence of substrate.

Notably, it can be observed that a group of them, comprising those of the NTD together with A110E and G146R, irreversibly convert 50% the cofactor into the Pictet-Spengler adduct in about 12-17 min and are almost completely inactivated in 90 min (**Table 19**).

A second group of variants, accounting for those of loop3 (P330L, R347Q and L353P) and W105C are much less prone to undergo Pictet-Spengler condensation. The overall decrease in the initial PLP content of this second group is about 5-folds slower respect with the first group and about 20-fold slower respect with the control. Furthermore, in addition to the Pictet-Spengler adduct, these variants also form small amounts of pyridoxamine 5′-phosphate (PMP) (whose absorbance spectrum is reported in **Figure 53**), also produced by WT AADC in the presence of

D-5-hydroxytryptophan [30] or as intermediate of the oxidative deamination reaction catalyzed by AADC on aromatic amines [47], α-methylDopa and D-tryptophan methyl ester [50] (**Figure 54C**).

Table 19. Initial velocities of PLP decrease, Pictet-Spengler and PMP increase and dopamine formation following reaction of 10 μM AADC incompetent variants with saturating concentration of L-Dopa. Free protein reaction of 20 μM PLP with 2 mM L-Dopa is also indicated .

Species	PLP Half-life (min)	PLP initial rate (min^{-1})	ADDUCT Initial rate (min^{-1})	PMP Initial rate (min^{-1})	DOPAMINE Initial rate (min^{-1})
PLP	3.3	0.200 ± 0.024	0.163 ± 0.006	/	/
Y20del	12.4	0.056 ± 0.005	0.050 ± 0.004	/	1.65 ± 0.04
Y20A	16.4	0.041 ± 0.003	0.052 ± 0.006	/	0.90 ± 0.02
Y20S	14.2	0.048 ± 0.007	0.040 ± 0.004	/	1.49 ± 0.05
H70R/W71del	17.0	0.041 ± 0.005	0.047 ± 0.003	/	0.0316 ± 0.0005
W105C	52.9	0.013 ± 0.006	0.002 ± 0.003	$10 \cdot 10^{-5} \pm 1.4 \cdot 10^{-5}$	0.176 ± 0.002
A110E	17.6	0.039 ± 0.003	0.033 ± 0.003	/	0.0133 ± 0.0002
G146R	22.8	0.030 ± 0.004	0.025 ± 0.003	/	8.70 ± 0.64
S193D	73.5	0.009 ± 0.005	0.013 ± 0.004	$9.5 \cdot 10^{-5} \pm 0.8 \cdot 10^{-5}$	1.46 ± 0.02
S193E	124.5	0.005 ± 0.004	0.005 ± 0.001	$10.2 \cdot 10^{-5} \pm 2.6 \cdot 10^{-5}$	1.04 ± 0.01
P330L	32.4	0.021 ± 0.004	0.007 ± 0.001	$207 \cdot 10^{-5} \pm 5.8 \cdot 10^{-5}$	1.42 ± 0.02
R347Q	31.3	0.014 ± 0.005	0.012 ± 0.002	$291 \cdot 10^{-5} \pm 7.5 \cdot 10^{-5}$	0.260 ± 0.002
L353P	119.1	0.006 ± 0.004	0.003 ± 0.002	$85.4 \cdot 10^{-5} \pm 1.7 \cdot 10^{-5}$	0.040 ± 0.001

The identity of Pictet-Spengler adduct and PMP, whose absorbance spectra are reported in **Figure 53**, has been confirmed by NMR analyses (**Figure 55**).

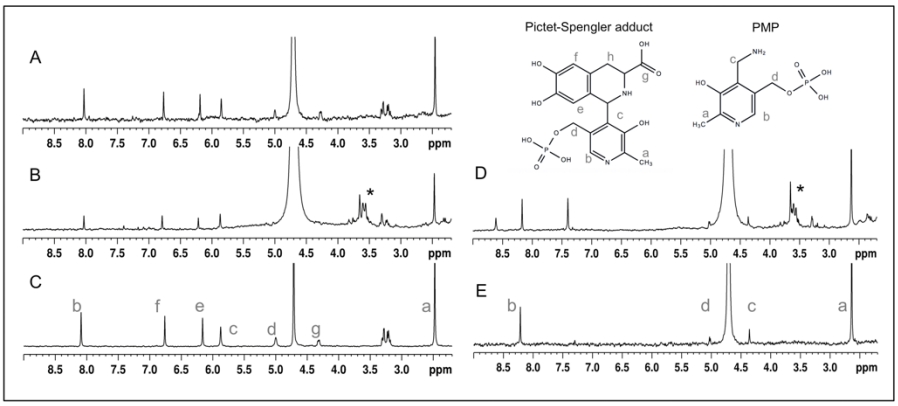

Fig. 55. NMR analysis of purified products. 1H-NMR spectrum of HPLC-isolated peak corresponding to the Pictet-Spengler adducted formed by variants A110E (A) and L353P (B) in comparison with the spectrum of the chemically synthesized cyclic adduct (C). 1H-NMR spectra of HPLC purified PMP after the enzymatic reaction of variant L353P with L-Dopa (D) in comparison with the spectrum of commercially available PMP (E). Signals arising from impurities in the buffer are indicated with an asterisk. Proton assignment is indicated with grey letters.

Formation of dopamine is also included (**Figure 54D**) and shows that all variants catalyze slow amine formation in long times. This rules out that any of the residues involved is essential for the catalytic mechanism of decarboxylation. After one hour of reaction time some variants have slowed down their reaction rate due to irreversible entrapment of the coenzyme in the cyclic adduct.

While the behavior of NTD and loop3 variants is clear and continuously validated from structural to functional results (see the correlation plots), G146R behaves in a borderline manner. Its bioinformatics localization and spectral features with substrate analogs DME and carbiDopa are similar to loop3 variants but it shows a kinetics of PLP conversion analogous to NTD enzymes. It should be remembered that this particular amino acid substitution leads to a variant with an unusually high K_m for L-Dopa (8.34 ± 0.94 mM) that could account for fast loss of coenzyme during catalysis. In addition, the loop2 variants W105C and A110E display differences among them. W105C resembles loop3 variants from a structural and kinetic point of view, while A110E is more similar to NTD variants. This behaviour can be interpreted by their specific localization on loop2, being Trp105 in close proximity to loop3 residues, while Ala110 can be found at the end of loop2.

Previous studies have tried to explain the loss of the coenzyme during the catalysis of pathogenic variants as consequence of the mispositioning of the PLP located in an altered microenvironment and/or as the inability of the protein to acquire a closed

and catalytically competent conformation [30,44]. Here, we can add more information suggesting that incompetent variants are mainly at the interface of the dimer and group in those structurally impaired (NTD and loop1) and those without structural modifications but affecting loop3, sensitive to slight alterations (as reported in part1) and connected to CL correct positioning.

18. Limited proteolysis affects NTD incompetent variants but not those of loop3.

It is already known that WT AADC is susceptible to trypsin attack on Lys334-Leu335 site of the CL and also some variants present the same accessibility [44]. Moreover, in part1 it has been shown that apoAADC undergoes a second tryptic cleavage at Arg27-Gln28 on NTD.

In order to detect possible alteration on flexible regions on the incompetents variants, we treated all incompetent variants with trypsin in a 1:100 ratio for 1 h and aliquots of the mixture were withdrawn at different incubation times and the digestion patterns analyzed on SDS-page (**Figure 56**). Surprisingly, some holoAADC variants exhibit the typical digestion pattern of the apoWT, showing the formation of the 18.1 kDa and 36.6 kDa species resulting from the CL cleavage and the additional 51.5 kDa and 33.4 kDa bands from the N-terminal cleavage.

The results show that catalytically impaired NTD variants are also cleaved at Arg27 as the apoWT, while the loop3 incompetent variants display the same tryptic pattern as the holoWT. This would suggest that the NTD variants present the H1-loop-H3 exposed and flexible in their holo proteins as the already mentioned artificial holoE61A.

In this sense, similarly to what emerged from the structural and functional analyses, limited proteolysis reveals the presence of two different groups of incompetent variants (**Figure 56**). W105C, P330L, R347Q and L353P, showing a digestion pattern identical to that of the WT protein, both in their apo and holo form, are characterized by (i) maintenance/preservation of the WT structural features (near-UV and visible region, thermal stability, $K_{D(PLP)}$), (ii) a microenvironment for external aldimine similar to that of the WT and a slow rate of Pictet-Spengler condensation.

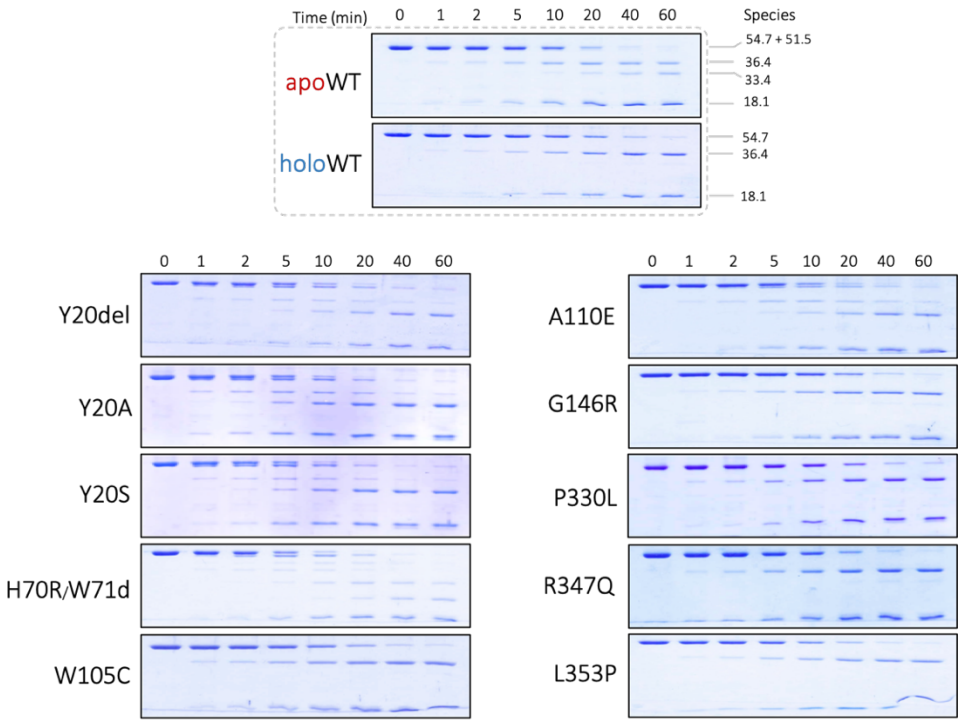

Fig. 56. Limited proteolysis of holoAADC incompetent variants in comparison with the holo and apoWT. Susceptibility of WT and incompetent variants to digestion has been determined by incubating 0.54 mg/mL of AADC with trypsin at the E:S ratio of 1:100 (by weight) in 100 mM potassium phosphate pH 7.4 at 25 °C with the addition of 100 µM PLP for the holo forms. Time points were taken within 1 h of incubation and compared with AADC sample in absence of trypsin. At each time point, the reaction was boiled in SDS sample buffer to stop trypsin activity. The digestion products were separated by SDS/PAGE.

On the contrary, variants Y20del, Y20A, Y20S, H70R/W71del and A110E show a proteolytic pattern similar to that of the apoWT both in their holo and apo form, are characterized by structural defects in terms of tertiary structure, coenzyme microenvironment, thermal stability, mispositioning of PLP during external aldimine formation, leading to a rapid coenzyme irreversible inactivation during catalysis. Altogether it could be suggested that the NTD holo variants impairment is connected to an increased mobility of the NTD, as the apoWT and holoE61A. An exception is represented by G146R since from one side it shows good structural features as the loop3 incompetent variants (in terms of stability and tertiary structure) and on the other side the dramatically decreased K_m for L-Dopa lead the enzyme to the release of the coenzyme during catalysis similarly to the NTD incompetent variants. Notably, N-terminal cleavage is visible in G146R, even if at very slow extent (**Figure 56**).

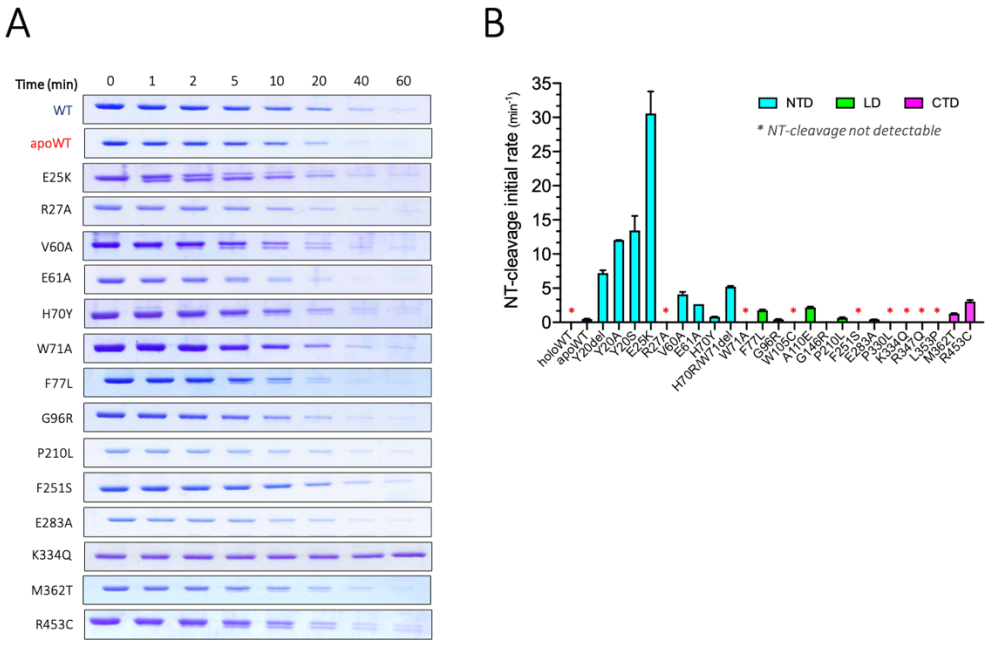

Fig. 57. Limited proteolysis of holoAADC pathogenic variants show a wide range of susceptibility to trypsin digestion. HoloAADC variants were incubated with trypsin at the E:S ratio of 1:100 (by weight) in 100 mM potassium phosphate pH 7.4 at 25 °C with the addition of 100 µM PLP. Digestion time course was analyzed on SDS-page and compared with holoWT. A) Disappearance of the monomer band and concomitant formation of the N-terminal nicked monomer resulting from the cleavage at Arg27 level. All gels were scanned and analyzed using National Institute of health IMAGE J software. B) Impact of the mutations on AADC N-terminal conformation. The susceptibility of each variants to trypsin attack at Arg27 level is represented as initial rate of formation of the N-terminal nicked monomer (51.5 kDa species) and constitutes a bar in the figure.

We have then enlarged the proteolysis analysis to all variants (not only the catalytical incompetent once) to understand if the rate of N-terminal cleavage could be correlated to former structural and functional analyses (**Figure 57**) (as samples, digestion mixture of E25K, F77L, R453C have been analyzed by MS confirming the sites, see **table 20**)).

In their holo form, the variants exhibit heterogeneity in the proteolytic pattern, spanning from variants showing gross to modest accessibility of the N-terminal site to variants with no exposure of this site under these experimental conditions (**Figure 57B**). It can be observed that NTD variants are those mainly sensitive to Arg27 cleavage as expected. In addition, a slight propensity of the CTD variants is visible, confirming the communication between NTD and CTD, as evidenced in part1. Finally, also some LD variants, (P210L, E283A) show a small extent of N-terminal cleavage.

Table 20. Identification of the tryptic sites on some AADC variants. Experimental masses are listed and compared with the expected theoretical masses of the identified peptide species. Some peptides were not found (n.f).

E25K MW (Da)	Theoretical MW (Da)	F77L MW (Da)	Theoretical MW (Da)	R453C MW (Da)	Theoretical MW (Da)	Identified species
n.f	54716.19	54681	54683.11	54763.5	54664.08	1-486
n.f	36623.17	36588	36623.17	36623.5	36624.11	1-334
18111.5	18111.04	18112	18111.04	18059	18057.99	335-486
3206.6	3208.68	3209.5	3209.62	3210	3209.62	1-27
33433	33432.50	33396	33398.49	33433	33432.50	28-334
n.f	51525.53	51499	51491.51	n.f	51472.48	28-486
17159	17159.08	n.f	17159.08	n.f	17106.03	335-479

19. Hydrodynamic radii of incompetent variants

We aimed at determine the particle size of Y20del, Y20A, Y20S, H70R/W71del, W105C, A110E, G146R, P330L, R347Q and L353P by means of dynamic light scattering as the effect of the mutations may be reflected on the hydrodynamic radius. Since the difference in particle size between holo and apoWT reflects the closed and partially open conformation of the dimer, and possibly also the difference is domain mobility and loop3 conformation, one could expect that a variant with a relaxed and somehow open conformation would result is a particle size similar or even bigger than that of the apoWT.

As shown in **figure 58**, almost all variants in both their holo and apo form show a difference in the particle size. The statistical analysis revealed that all holo proteins exhibit a significantly higher dimer size (p value <0.0001 with respect to the WT) particularly evident in Y20S and H70R/W71del (12.43 ± 0.19 nm and 10.67 ± 0.10 nm respectively while those of the holoWT is 9.32 ± 0.04 nm). As for the apo proteins, all variants show a statistically significant increase in the particle size, showing at the same time great differences (such as for Y20S and A110E) and smaller ones (P330L, L353P).

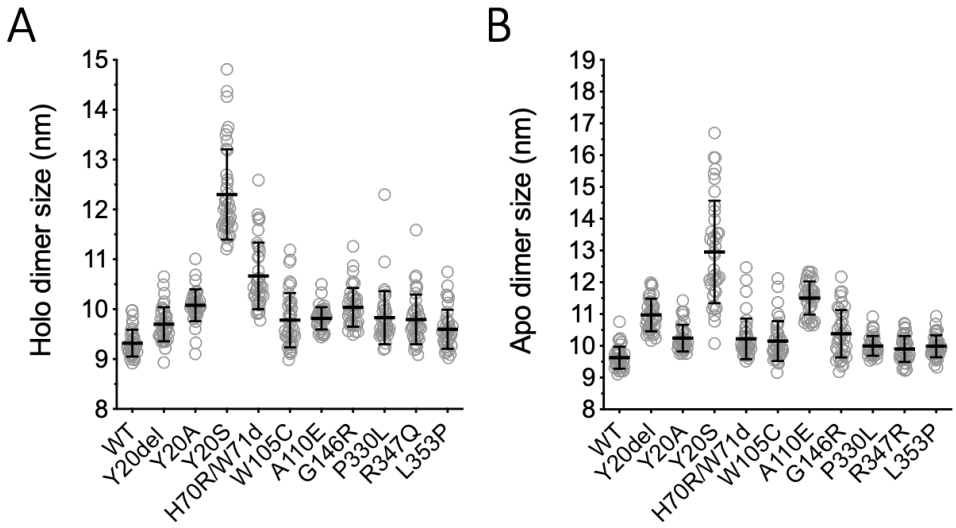

Fig. 58. In solution particle size obtained by DLS. Comparison between diameters measured at 25°C for WT and catalytically incompetent variants. A) holo, B) apo forms. Each circle represent the diameter size mean value obtained from one measurement. Each measurement was the accumulation of 12-18 runs. Mean is reported with standard deviation.

In the light of previously observed data, the increased hydrodynamic radio may be related to both an increased solvent exposure of loop3 (Pictet-Spengler cyclization may indicates a somehow more 'open' active site) and an increased protein mobility (as revealed by limited proteolysis).

Table 21. Comparison of the hydrodynamic diameter estimation of holo and apo WT and variants. DLS measurements were collected at about 4 μM protein concentration in 100 mM potassium phosphate, at pH 7.5 with the addition of 100 μM PLP for the holo forms, at 25 °C.

Enzyme	WT		Y20del		Y20A		Y20S		H70R/W71del	
form	holo	apo	holo	apo	holo	apo	holo	apo	holo	apo
mean±SEM [a]	9.32±0.04	9.63±0.05	9.70±0.05	10.97±0.08	10.08±0.05	10.25±0.07	12.43±0.19	12.96±0.25	10.67±0.10	10.22±0.10
P value summary [b]		****	****	****	****	****	****	****	****	****

Enzyme	W105C		A110E		P330L		R347Q		L353P	
form	holo	apo	holo	apo	holo	apo	holo	apo	holo	apo
mean±SEM [a]	9.78±0.08	10.15±0.10	9.82±0.03	11.50±0.08	9.83±0.08	9.99±0.05	9.79±0.08	9.90±0.6	9.60±0.06	9.99±0.05
P value summary [b]	****	****	****	****	****	****	****	**	****	****

[a] Data are reported as mean ± SEM and expressed in (nm)
*[b] Results were compared using Student's t-test between holoWT and holo variants and between apoWT and apo variants. ApoWT is compared to holoWT. *P < 0.05; **P < 0.01; ***P < 0.001; ****P < 0.0001.*

Despite this, the distinction between the two previously identified groups of incompetent variants is here not evident. It is however notable that all the variants

showing a fast release of the Pictet-Spengler adduct exhibit in their apo form a mean dimer size bigger than the other variants (**Figure 58 and table 21**) meaning that these mutations affect the overall shape of the protein also in their open conformation.

20. Crystal structure of L353P AADC variant

We have here obtained the first structure of a pathogenic variant of AADC, in particular of the catalytically incompetent L353P since the Leu353 belongs to loop3 immediately after the CL and could shed light on an important protein region. In addition, MD simulations (part 1) and the inspection of both the ligand-free and carbiDopa bound enzyme structures at different pH values have demonstrated the propensity of this Leu residue to undergo small alterations, revealing how its movements could be related to conformational changes at the active site. L353P 3D structure has been solved at 2.05 Å resolution at pH 8.0 (**table9 in part1**).

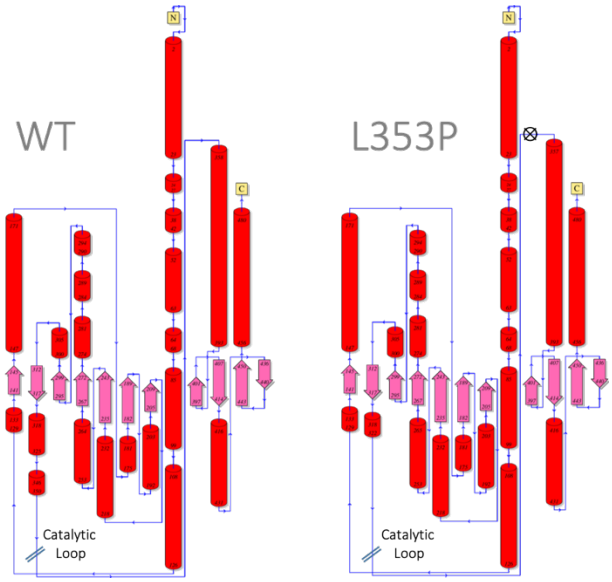

Fig. 59. Overall topology of holoWT and holoL353P crystal structure. Domain organization and secondary structure elements are obtained with PDBsum server [144]. Mutation site is indicated by the symbol ⊗.

As the WT AADC, L353P is a perfect symmetric dimer. Its backbone atoms superpose to the $WT_{pH8.0}$ structure with a RMSD of 0.089 Å and to the $WT_{pH7.5}$ with a RMSD of 0.141 Å indicating that no gross structural alterations are induced by

the mutation, thus corroborating structural results obtained in solution with this variant (**Figure 59**).

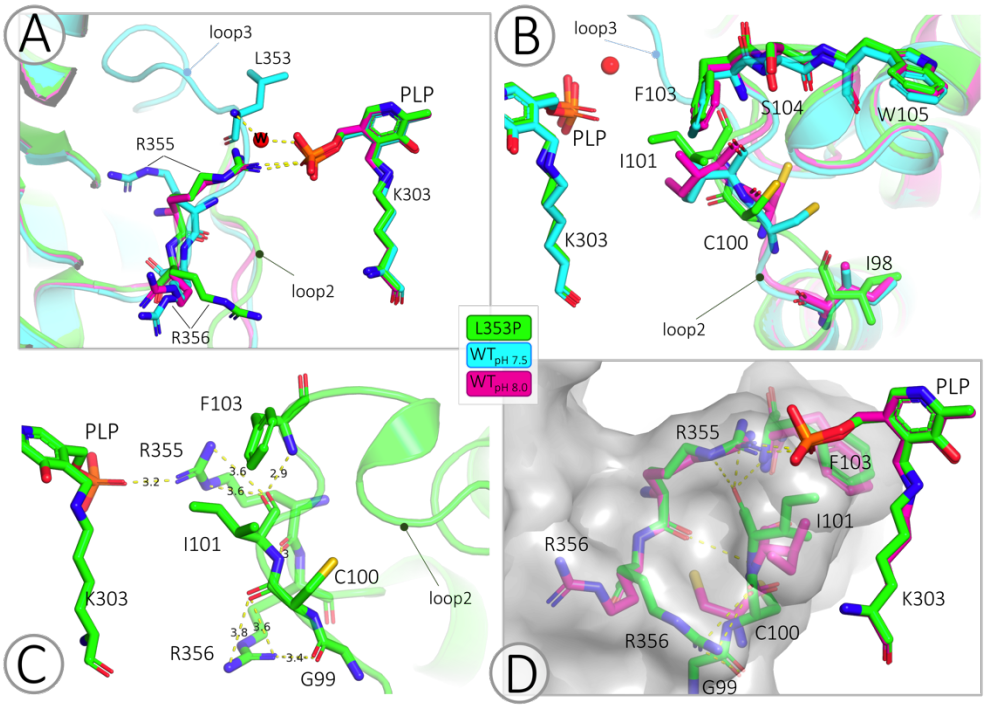

Fig. 60. Structural effects of L353P at loop2 and loop3 level. Cartoon representation of superimposed $WT_{pH\ 7.5}$ (cyan), $WT_{pH\ 8.0}$ (magenta) and $L353P_{pH\ 8.0}$ (green) crystal structures. Protein residues of monomer a are shown as sticks, while only Lys3030-PLP of facing monomer b are represented as sticks. Loop2 and loop3 are indicated. A) Effect of the pH and L353P substitution on loop3 at Atg355 and Arg356 level. At pH 8.0 (both WT and L353P) stretch 327-354, including Leu353, is missing. Structural water molecule indicated with W and represented as a red sphere is relative to $WT_{pH\ 7.5}$ structure. B) Effect of pH and L353P mutation on loop2. Main differences between the three structures are visible at Ile98, Cys100, Ile101, Phe103, Ser104 and Trp105 level. C) L353P structural effect on loop2 and loop3. Novel interactions are highlighted and measured distances are shown. D) Superimposition of $WT_{pH\ 8.0}$ and $L353P_{pH\ 8.0}$. The effect of the mutation on loop2 conformation and its steric hindrance is highlighted by showing the protein surface of monomer a, while monomer b is only represented by Ly303-PLP complex.

Unfortunately, as shown in **figure 60**, L353P loop3 misses residues 327-354 thus the Leu→Pro substitution is not visible. Notably, as for $WT_{pH8.0}$, L353P shows that Arg355 is rotated in the forward position and contacts the PLP phosphate moiety (see part1). In addition to Arg355 rotation, Arg356 displays a novel conformation distinguishing the WT and the L353P proteins (**Figure 60A, B**). In analogy to loop3, also loop2 results affected by the mutation. In fact, as shown in **figure 60B**, the backbones of residues 98-103 in $WT_{pH7.5}$ and $WT_{pH8.0}$ are almost superimposable; on the contrary, L353P shows a different conformation of the loop,

with a particular alteration on Ile98, Cys100, Ile101 and Phe103 stretch. A deeper investigation reveals that the mutation causes the formation of a network of weak electrostatic interactions (3.2-3.8 Å) between loop3 and loop2 (**Figure 60C**). In fact, the altered loop2 conformation is stabilized by novel contacts between Ile101 backbone and Arg355 side chain and Phe103 backbone together with novel contacts between Arg356 sidechain with Gly99 and Cys100 backbones. Taken together, these alterations cause (i) a change in the steric hindrance of loop2 (**Figure 60D**) with potential effect on substrate binding since Ile101 is involved in its stabilization and (ii) a dramatic change in loops conformation due to established new contacts between loop3 and the PLP (*via* Arg355) and between loop2 and loop3 (*via* Arg355 and Arg356).

These observations are mirrored by the *in solution* biochemical results, indicating that the variant as compared with the WT protein shows (i) an overall preserved tertiary structure, (ii) a reduced thermal stability only in its apo-form (probably due to an increased mobility of loop3 in the open conformation). The previously observed slight increase in the hydrodynamic diameter of holoL353P (9.60 ± 006 nm *vs* 9.32 ± 0.04 nm of the holoWT) may indeed be related with the mobility of loop3. The coenzyme microenvironment does not show relevant spectroscopic differences with the WT even if the PLP and substrate affinity shows a 2-fold reduction (**Table 18**). Moreover, the dramatically reduced dopamine synthesis is not linked to a high conversion of PLP into the cyclic adduct, thus the catalytic defect is not due to gross structural effects, as for the NTD incompetent variants. The residue Leu353 is on the same time not essential for the decarboxylation mechanism. The “local” structural alterations visible at the active site indicate that it is well constructed in each monomer. However, the residues coming from the partner monomer that complete the active site architecture in substrate binding (loop2) and functionality (loop3) are somewhat displaced and more connected by weak interactions, maybe rendering overall loop3 and its CL less prone for productive catalysis.

21. *In solution* secondary structure differences of apo and holo WT and L353P by microfluidic modulation spectroscopy (MMS)

It is well known that, in crystals, a protein is rigidly constrained in the crystal lattice and its dynamic movements are prevented. As shown for the WT AADC in part 1 of this study, during the initial 50 ns of MD simulations both holo and apoAADC show a structural rearrangement before reaching the equilibrium. Similarly, on one side L353P crystal structure provides important structural details and on the other side it does not represent the protein in its natural occurring dynamics. The combination of near-UV CD, X-ray crystallography and limited proteolysis, provides us a comprehensive picture of the Protein Higher Order Structure (HOS) of both WT protein and L353P variant in terms of secondary, tertiary structure, protein folding and spatial arrangements.

We have already measured the far-UV CD spectra of apo and holo WT and of holo variants. These spectra do not show traits of a dissimilar organization (**Figure 41**).

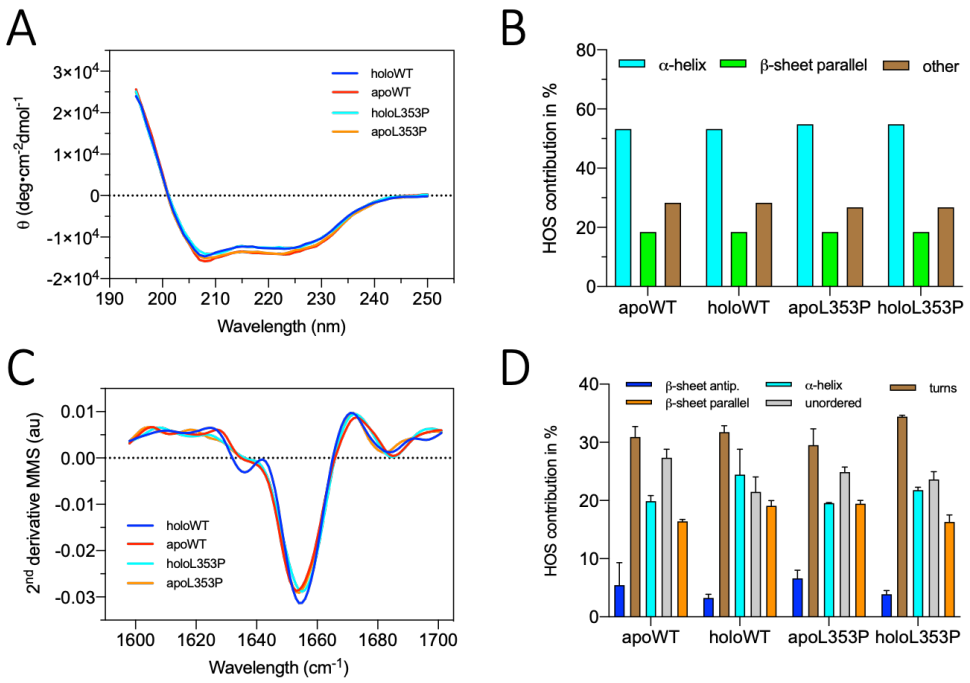

Fig. 61. Secondary structure content of WT AADC and L353P by means of CD and MMS. A) Far-UV CD spectra of holo and apo WT and L353P. B) Estimation of the structural content were obtained with the K2D3 server [145]. C) Overlaid second derivative MMS spectra of holo and apoWT and L353P variant recorded in the IR amide I band region (1590-1710 cm^{-1}). B) Percentage of secondary structure composition of holo and apoL353P compared to holo and apoWT.

However, far-UV CD does not constitute a highly sensitive approach in determining *in solution* secondary structural differences between different AADC variants since the intense α-helical signals lead to a loss in the sensitivity to the other signals. In fact, the far-UV CD spectra of holo and apo WT and L353P are superimposable (**Figure 61A**).

The predicted secondary structure content estimated with the K2D3[145] server indicates a slight increase of the helical content in L353P (from 53.2 % of the WT to 54.8 %) and an unchanged β-sheet content (18.4 %) in both apo and holo enzymes (**Figure 61B**). Since FTIR spectroscopy has long been used as powerful approach (as powerful as far-UV CD) in the study of protein secondary structure, we decided to follow the absorbance of the amide I band (1710 – 1590 cm^{-1}) for studying secondary structure element such as β-sheet, α-helix, turns and unordered [142]. In collaboration with RedSchift BioAnalytics we analyzed AADC samples with the novel automated IR spectroscopy technique called Microfluidic Modulation infrared Spectroscopy (MMS) [146,147].

Figure 61C shows the MMS absorbance spectra in the IR region of WT and L353P in their holo and apo forms. We then determined the amount of secondary structures by gaussian curve fitting as described (materials and methods, [146,147]). As reported in **figure 61D**, MMS detects small differences with high sensitivity. As expected, for the WT protein MMS data reflect the different conformation between apo and holoAADC mainly in terms of acquisition of order and rigidity. In fact, we can observe a conversion of the extended unordered content (from 27.3 % of the apo to 21.5 % of the holo) to a higher composition of α-helix and total β-sheets (increased α-helix from 19.9 % to 24.2 % and almost unchanged global β-sheets). Variant L353P shows a similar trend between its apo and holo state in terms of acquisition of helical content (from 19.5 % to 21.7 %). However, differently form the transition observed in the WT, the variant shows an overall gain in turn content (from 29.5 % in the apo to 34.4 % in the holo) with a decrease of both parallel and antiparallel β-sheets. If compared to the holoWT, holoL353P shows an increased unstructured content (from 53.2 % to 58 %) (**Figure 61D**). These results highlight the great sensitivity of MMS technology if compared to far-UV CD spectroscopy.

The reduced contribution of secondary structured elements and the increased unstructured content, together with the observed differences revealed by crystallographic analyses occurring on loop2 and loop3, corroborate more quantitatively the observed differences.

22. An investigation on Ser193 role provides further information on loop3

S193A, S193D and S193E are three non-pathogenic variants designed on the basis of preliminary data obtained in collaboration with Prof. Robert S. Phillips at the University of Georgia (USA). AADC has been extensively characterized in the recombinant purified form but little is known about its regulation, and post-translational modifications both *in vitro* and *in vivo*. We have recently found that AADC is phosphorylated by murine recombinant protein kinase A (PKA) *in vitro*. The modified residue has been identified to be Ser193 by mass spectrometry [148]. Interestingly, the solvent exposed Ser193 is located at the active site of AADC and is highly conserved among homologous proteins (**see Table 14**).

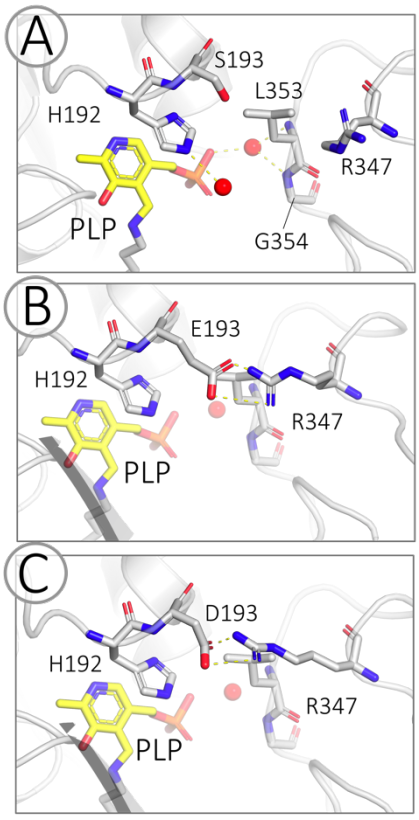

Fig. 62. Localization of Ser193 and proposed effect of S193D and S193E on loop3 mobility. A) Ser193 is located at the active site and its side chain is not involved in polar interactions. *In silico* mutagenesis suggests that aspartate (B) and glutamate (C) variants could interact with Arg347 already observed to be highly sensitive to slight alterations of the active site.

In AADC Ser193 follows His192 base stacked with the PLP ring and its side chain does not seem to be involved in any polar interaction (**Figure 62A**). Functional analysis of phosphorylated AADC revealed an influence on the kinetic parameter in increasing the catalytic efficiency toward L-Dopa mainly due to a decrease in K_m [148].

Table 22. Kinetic parameters for L-Dopa, apparent equilibrium dissociation constant for PLP and melting temperatures of variants S193A, S193D and S193E.

Enzyme	k_{cat} (s^{-1})	K_m (mM)	k_{cat}/K_m ($s^{-1}mM^{-1}$)	$K_{D(PLP)}$ (nM)	Tm (°C) holo	Tm (°C) apo
WT[a]	7.6 ± 0.1	0.11 ± 0.01	69.1 ± 10	101 ± 10	69.42 ± 0.02	64.84 ± 0.03
S193A	1.8 ± 0.1	0.096 ± 0.02	17.7 ± 4.9	92 ± 10	69.09 ± 0.02	65.08 ± 0.03
S193D	0.032 ± 0.001	0.31 ± 0.04	0.103 ± 0.004	84 ± 10	70.67 ± 0.02	67.55 ± 0.03
S193E	0.026 ± 0.001	0.25 ± 0.03	0.104 ± 0.004	98 ± 13	70.69 ± 0.02	66.85 ± 0.04

Variants S193A, S193D and S193E have been designed with the aim of determining the role of the serine residue. The functional characterization of the three Ser193 variants provide unexpected informations (**Table 22**). S193A displays the 25.6 % of catalytic efficiency of the WT AADC, mainly due to a ~ 4-fold reduced k_{cat}. S193D and S193E are found to be catalytically incompetent. In fact, their k_{cat}/K_m value is less than 0.6% of that of the WT (being both around 0.15 %). S193D and S193E exhibit a dramatic decrease in k_{cat} as well as a decreased substrate affinity. The possibility that these two variants share common features with the identified LD incompetent ones (W105C, P330L, R347Q, L353P) is confirmed by the following structural analysis. **Figure 63A and B** show the spectroscopic features of Ser variants as revealed by near-UV visible CD and absorbance.

The variants show a preserved tertiary structure in both their apo and holo form. As for the Lys303-PLP internal aldimine, the tautomeric equilibrium is similar to that of the WT, with a predominance enolimine band over the ketoenamine one. The PLP affinity measured for these variants show to be maintained, being very similar to that calculated for the WT (**Table 17**).

Limited proteolysis revealed that catalytically incompetent S193D and S193E are resistant to N-terminal cleavage while S193A is only faintly cleaved (**Figure 63C**). S193D and S193E in presence of DME show spectral modifications within 30 minutes consistent with the formation of the external aldimine, peaking at 395 nm, and the observable 500 nm band relative to an equilibrium between the external aldimine and the unprotonated quinonoid species (**Figure 64A**).

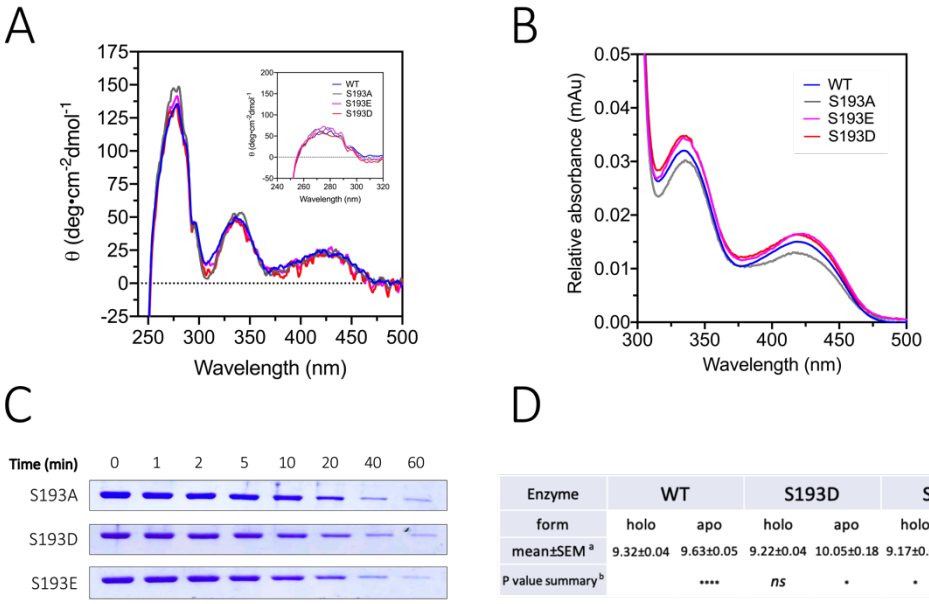

Enzyme	WT		S193D		S193E	
form	holo	apo	holo	apo	holo	apo
mean±SEM [a]	9.32±0.04	9.63±0.05	9.22±0.04	10.05±0.18	9.17±0.04	9.87±0.08
P value summary [b]		****	*ns*	*	*	*

Fig. 63. Characterization of artificial S193, S193D and S193E variants. A) Near-UV visible CD spectra of holo variants compared with holoWT. Signals relative to the apo species are reported in the inset. CD spectra are recorded at 5 μM protein concentration, in 100 mM potassium-phosphate buffer, pH 7.4 in presence of 100 μM PLP for the holo forms. B) Internal aldimine absorbance spectra of holoWT and variants. Spectra are recorded at 10 μM protein concentration, in 100 mM potassium-phosphate buffer, pH 7.4. C) Limited proteolysis with trypsin at 1:100 (w/w) ratio were performed in 100 mM potassium phosphate pH 7.4 at 25 °C with the addition of 100 μM PLP. Figure shows the disappearance of the dimer along 1 hour of incubation. D) hydrodynamic diameters calculated by DLS. [a] Data are reported as mean ± SEM and expressed in (nm) [b] Results were compared using Student's t-test between holoWT and holo variants and between apoWT and apo variants *P < 0.05; ***P < 0.001; ns not significantly different. apoWT is compared to holoWT.

When L-Dopa is added to the mutants, a first fast phase occurs within 1 min in which an increase of the 420 nm band and a shift of the 335 nm band to 329 nm are visible. A second slower phase consists in the decrease of the 420 nm species and the concomitant increase of the 329 nm band, as observed for L353P. The HPLC analysis of the coenzyme during the reaction with L-Dopa shows the trapping of the PLP into the cyclized adduct with L-Dopa and the linear formation of PMP with initial rates consistent with those observed for W105C, P330L, R347Q and L353P (**Figure 64B**).

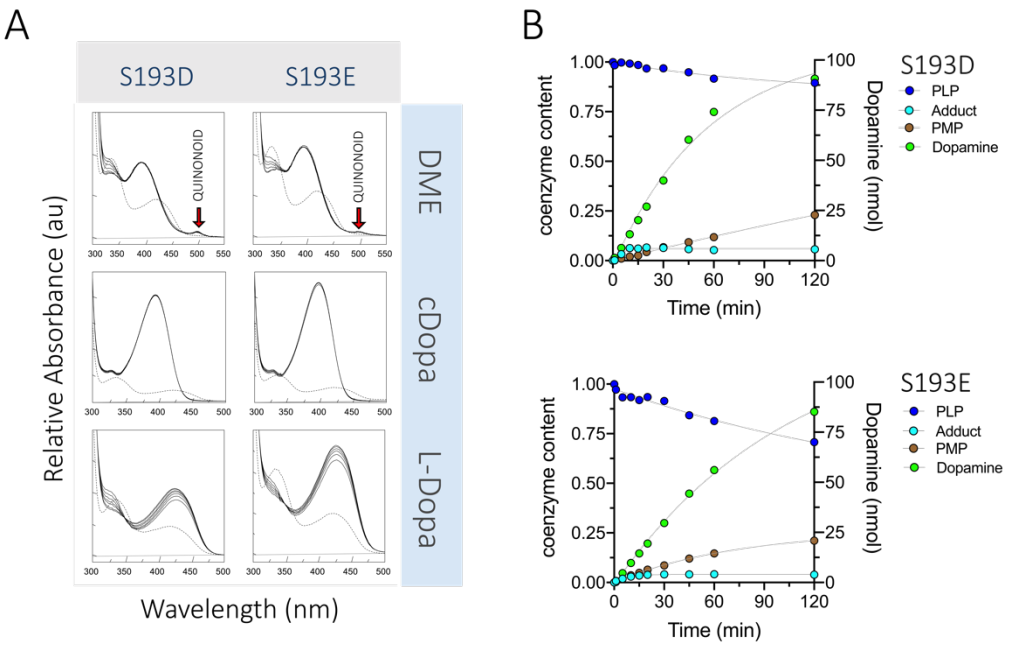

Fig. 64. External aldimine of S193D and S193E in presence of DME, carbiDopa and L-Dopa and coenzyme modifications during reaction with L-Dopa. A) Absorbance spectra of 10 μM enzyme in presence of saturating concentrations of DME, carbiDopa (cDopa) and L-Dopa recorded in 100 mM potassium phosphate, pH 7.4 at 25 °C within 30 min. Dashed lines represent the spectra of the protein recorded in absence of substrate. The formation of the quinonoid species is highlighted with a red arrow. B) Coenzyme modification was followed by HPLC during the reaction 10 μM S193D and S193E in presence of saturating concentration of L-Dopa in 100 mM potassium phosphate buffer, pH 7.4 at 25 °C. PLP (blue), PLP-L-Dopa adduct (cyan), PMP (brown) and dopamine (green) are normalized for the initial amount of PLP detected in absence of substrate.

These findings of Ser193 variants indicate that this conserved residue located at the active site does not play a crucial role in the catalysis since S193A biochemical features are only slightly affected. Our study on S193D and S193E provide on one side unsuccessfully results data on the comprehension of possible effect of the phospho-serine since we found a dramatic drop of the catalytic efficiency. On the other side, these two variants reinforce our analysis on the group of the catalytically incompetents. In fact, *in silico* mutagenesis provide suggestions for a possible novel inter-subunit interactions between Glu/Asp193 and Arg347 of loop3 thus corroborating loop3 sensitivity to slight alterations at the active site. This interaction may be related with the observed increased of thermal stability, particularly evident in the apo forms. The particle size estimated for variants S913D and S193E (**Figure 63D**) might indicate that the glutamate and aspartate substitutions do not affect neither the domains mobility nor loop3 solvent exposure.

It is however evident from functional data that loop3 conformation is impaired, and as already suggested in [120], the acquisition of an incorrect loop3 conformation is associated with functional impairment, as confirmed by the WT crystal structures solved at different pH values (see part1) and in L353P crystal structure.

Altogether, the biochemical data relative to variants S193A, S193D and S193E provide additional value to the above proposed correlations between structural and functional features of AADC pathogenic variants. In fact, the three Ser193 mutants display the characteristic features of the LD variants, exhibiting good structural features in terms of tertiary structure, thermal stability, internal and external aldimine spectroscopic signals. S193D and S193E, behaving similarly to the loop3 and W105C catalytically incompetent variants, reinforce the finding that an impact on loop3 leads to a loss of catalytic efficiency.

CONCLUSION OF PART 2 and OVERALL DISCUSSION

The present study provides a biochemical characterization of recently identified AADC variants associated to AADC deficiency. This effort was driven by the aim of providing the molecular basis for the pathogenicity of each enzymatic species leading to a better comprehension of the severity/mildness of the clinical phenotype.

While previously characterized variants were mainly localized in a 'central belt' of AADC [119], the novel pathogenic amino acid substitutions are spread over almost every region of the protein allowing us to widen the spectrum of enzymatic phenotypes related to AADC deficiency. In particular, a novel cluster of variants, mapping in the LD (P210L, L222P, F237S, W267R, C281W, E283A, M362T) is characterized by a low (or null) recovery in the soluble fraction. A deep discussion on this novel phenotype is presented in **paper 1** [33]. Here, we underline the identification of a LD region as responsible for the aggregation of these variants in their apo form. In fact, respect to [33], C281W and M362T have been newly characterized and, together with R285W and R412W, have been analyzed for their propensity to aggregate in the apo form. Since P210L, W267R, E283A, M362T variants do not exhibit gross functional impairments and structural alterations, their pathogenicity is attributable to a folding defect and possibly to an aggregation propensity.

Structural and functional signals obtained from the characterization of the total AADCd variants have been combined with those of some non-pathogenic ones (Y20A, Y20S, R27A, E61A, W71A, S193A, S193D, S193E). The range of the structural modifications was found to be wide, as well as the extent of functional alterations. We could relate different structural signals (**Figure 47**) observing that the loosening of the aromatic microenvironment is associated by a reduced thermal stability and by an impact on the cofactor binding (both in terms of affinity and tautomeric equilibrium). Moreover, the degree of the structural effects is mirrored by the extent of the catalytic effects (both in terms of catalytic efficiency and catalytical constant) (**Figure 49**). A gradient of severity of the effect of the mutations on AADC biochemical features is observable along the three protein domains. In fact, we could observe that variants located at the NTD and CTD show

a highest detrimental effect on protein structure and activity, while gradually proceeding along the LD, milder effects are reported. The observed linear structure-function relationship nicely describes the behavior of all N-terminal and C-terminal variants, and the majority of the LD ones. In fact, at one extreme the NTD variants exhibiting a dramatic loss of structural signals show to be incompetent from a catalytically point of view, while mutations of the LD at the opposite extreme (regarding both variants distant from the active site, *i.e* E283A and F251S, or close to the PLP, *i.e* S193A) maintain good catalytical competence.

Tautomeric equilibrium expressed as the ratio between the intensity of the 335 nm and 420 nm bands has been for the first time cotrelated to other structural and functional signals. The disruption of the tertiary structure and the loosing of the NTD-CTD might be related to a structural alteration at the active site that favors the ketonic tautomer of the PLP, peaking at 420 nm. It is indeed still unclear if the alteration of the tautomeric equilibrium is related with an altered binding of the PLP and/or to a chemical modification. It is however deducible that dichroic visible bands of PLP and $K_{D(PLP)}$ share common structural aspects related again with protein mobility (**Figure 49**).

In addition to the spectroscopic techniques, we have used limited proteolysis as a powerful structural tool for studying protein mobility/flexibility. It has been reported in part 1 of this thesis that N-terminal cleavage likely results from large amplitude motion of the NTD-CTD (particularly visible on H1-loop-H3 and helix-16), that makes Arg27 accessible to trypsin only in the apo and not in the holo form. Thanks to MD simulations and artificial variants (R27A, E61A and K334Q), limited proteolysis has the advantages, with respect to the spectroscopic techniques, of localizing the structural elements responsible for the observed data, thus confining the affected region.

The finding that some variants exhibit in their holo form a similar N-terminal cleavage to that of apoWT, may indicate that these proteins manifest an inadequate/altered NTD-CTD mobility. Some of them show to be somehow more mobile than apoWT, as revealed by higher rate of proteolysis, especially those variants located at the monomer-monomer interface (Y20del, Y20A, Y20S, V60A, E61A, H70Y, H70R/W71del, G96R, A110E, M362T, R453C) or in the interface

between NTD and CTD of the same monomer (E25K, F77L). Others, mainly located on the LD, distant from Arg27 and distant from the active site, show to be less prone to digestion and thus more similar to holoWT.

Since structural results were shown to be related to each other, we aimed at establishing a relationship among signals. As shown in **figure 65**, the rates of cleavage at the N-terminal domain (related to N-terminal mobility) correlate to the previously discussed structural data: 280 nm CD band, 335nm/420 nm ratio, thermal stability and $K_{D(PLP)}$. Importantly, in addition to k_{cat}, also catalytic efficiency exhibits a dependence on the protein mobility (**Figure 65, insets**). Altogether these correlations suggest that the functional effects of the mutations are related to common structural causes, leading to a wide spectrum of similar enzymatic phenotypes.

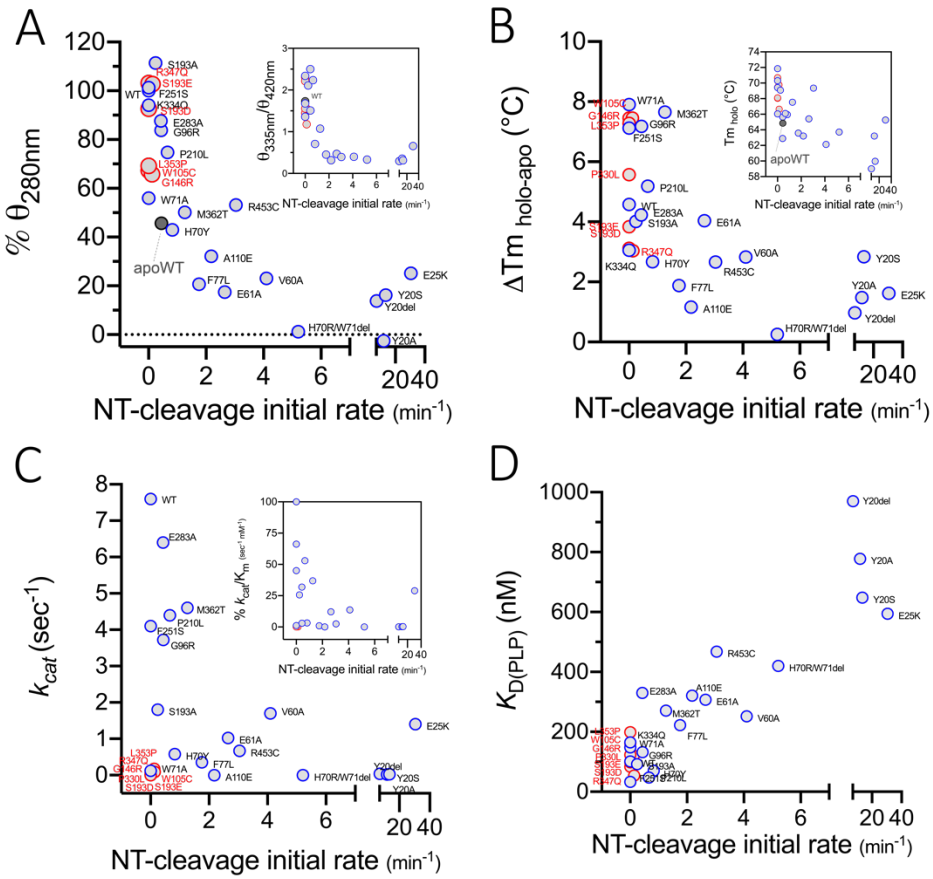

Fig. 65. Correlations of N-terminal cleavage with other structural and functional parameters. The structural effect of the mutations at NTD level has been correlated with A) tertiary structure CD signal at 280 nm and the tautomeric equilibrium (inset); B) global thermal stability ($\Delta T_{m(holo-apo)}$) and holo Tm (inset); (C) k_{cat} and (D) $K_{D(PLP)}$. ApoWT is included and represented as green circle. Catalytic incompetent variants W105C, S193D, S193E, P330L, R347Q and L353P together with G146R are shown in red.

Our data provide novel insights on the structure-function relationship of AADC. In fact, the PCA analysis discussed in part1, and proposed again here (**Figure 65A**), shows high mobility of those N-terminal residues facing the CTD, in particular on loop1 and Tyr20. This is mirrored by high mobility of the facing C-terminal residues (416-438, including helix-16) of the same monomer. This flexibility observed on one side of the protein, asymmetrically corresponds to a -CL in- conformation (low mobility) on the same side of the protein. It follows that, on the other side of the protein, NTD and CTD are more rigid and CL is found in a -CL out- conformation (showing higher mobility). The existence of a functional crosstalk between these regions has been proposed on the basis of MD simulations and limited proteolysis. The study on the AADC variants reinforce this hypothesis since we observe a progressive decrease of the activity concomitantly with the increased accessibility of the N-terminus. Affecting protein mobility would ultimately lead to alter CL conformation by disrupting domains crosstalk.

Among highly similar human enzymes involved in pathogenic states, whose structure have been solved (HDC and GAD), the motion of specific domains and the possible implication in catalytic mechanism has been proposed but not addressed.

The correlation between variants CD signals and NT-cleavage suggests that the aromatic microenvironment responsible for the 280 nm dichroic band (generally attributed to the global tertiary structure) is highly susceptible to the NTD-CTD motion. In support of this, two considerations can be done, both addressing a dependency between NTD-CTD mobility and 280 nm CD signal.

Firstly, apoWT shows ~2.2 fold decrease dichroic 280 nm band with respect of holoWT and shows an NT-cleavage consistent with that of those holo variants with a similar CD signal of about 50 % of that of the holoWT, such as H70Y (**Figure 65A**).

Secondly there is a group of previously reported variants (**figure 66B**) showing an abolished 280 nm dichroic signal in their apo and/or holo form [119]. Variants causing gross decrease (> 70%) of the CD aromatic signal (in the holo and/or apo form) are L38P, P47H, H70T, H72Y, P81L, R412W, R447H, R462P from [119] and residues

Tyr20 from this thesis (**Figure 66C**). Similarly, variants causing a modest reduction of the 280 nm CD band are E25K, R27A, V60A, E61A, A110E, R453C from this thesis and F80A from [119].

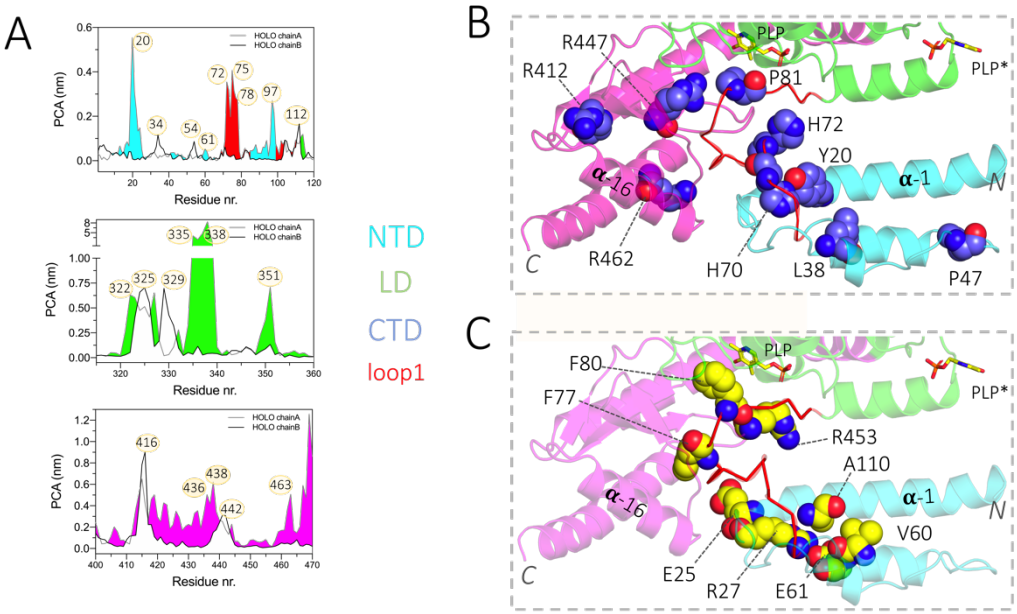

Fig. 66. Role of the interface between NTD and CTD in protein mobility. A) PCA analysis described in part1 of this study is proposed again, highlighting the different mobility of chainA (gray line, colored filled area in accordance to the different regions) and chain B (black line and white area) in specific regions: 1-120 (including the NTD, loop1 and loop2), 315-360 including loop3 and the motion of the C-terminal region encompassing residues 400-470. Panel B and C show AADC crystal structure (structure 1) represented as cartoon. All variants reported to have gross tertiary structure alterations in this study or in previous reports [44,119] are located at the NTD or CTD of AADC. NTD is colored in cyan, LD in green, CTD is colored in magenta. Loop1 is represented as ribbon and colored in red. PLP is represented as sticks and colored in yellow while all discussed residues are represented as spheres. Residues involved in substitutions with gross impact on AADC tertiary structure (near UV CD signal) are colored in blue (B) while those sites involved in substitutions leading to a ~50 % decreased CD signal are colored in yellow (C).

All these residues exhibit the common feature of being located in proximity of the interface between the NTD and CTD of the same monomer. In addition, most of them show a decreased catalytical efficiency [33,119].

These results were initially interpreted on the basis of the role attributed to loop1 [24,119]. Variants belonging to loop1, or interacting with it, were proposed to be impaired in the apo to holo transition. Here, by means of correlations between structural and functional parameters, we propose novel insights on AADC structure-function relationship. We can advance that the impact of the mutations on AADC catalytic activity can be attributed to an impairment of protein mobility or

to a direct effect on loop3. In the first case, a wide spectrum of alterations has been observed, ranging from variants exhibiting slight structural and functional alterations (F251S, K334Q, E283A) to variants that are drastically affected in their structural signals and from a catalytic point of view can be considered incompetent (Y20del, Y20A, Y20S, H70R/W71del, A110E). All these proteins (accounting for the majority of the AADCd associated variants) show an altered protein mobility that has lastly an impact on CL conformation. In the second case, we identified a group of catalytic incompetent variants (W105C, S193D, S193E, P330L, R347Q and L353P) belonging to loop3 or interacting with it that, despite exhibiting good structural features, have a dramatically reduced catalytic efficiency. These variants escape from the described correlations (structure-function). Affecting loop3 results in an extremely slowed down decarboxylation reaction and to the aberrant formation of PMP, whose origin still has to be determined. Nonetheless, the specific features of this group of variants have been furtherly dissected by solving the crystal structure of L353P and identifying the subtle alterations caused by the substitution, mainly visible on loop2 and loop3 conformation.

A specific exception to the proposed hypothesis emerged. W71A exhibits a decrease activity on one side and good structural features on the other side. Despite this, W71A cannot be considered incompetent since no cyclic PLP-L-Dopa adduct nor PMP have been detected during reaction. A possible explanation for its behavior could be related with the type of substitution, suggesting that (i) Trp71 is not involved in substrate affinity as previously proposed, (ii) aromatic microenvironment generating CD signal in the near UV region does not account on Trp71, (iii) the sensitivity of NTD-CTD to loop1 conformation is not affected by W71A mutation.

To the best of our knowledge, this is the first deep investigation of correlation between structural and functional data for a consistent number of variants causing a disease in an enzyme involved in monoamine neurotransmitter biosynthetic pathways.

REFERENCES

1. Bender, D. A. Non-nutritional uses of vitamin B6. *Br J Nutr* **81**, 7–20 (1999).
2. Albersen, M. *et al.* The intestine plays a substantial role in human vitamin B6 metabolism: a Caco-2 cell model. *PLoS One* **8**, e54113 (2013).
3. McCormick, D. B. & Chen, H. Update on interconversions of vitamin B-6 with its coenzyme. *J Nutr* **129**, 325–327 (1999).
4. Cellini, B., Montioli, R., Oppici, E., Astegno, A. & Voltattorni, C. B. The chaperone role of the pyridoxal 5'-phosphate and its implications for rare diseases involving B6-dependent enzymes. *Clin. Biochem.* **47**, 158–165 (2014).
5. Bohney, J. P., Fonda, M. L. & Feldhoff, R. C. Identification of Lys190 as the primary binding site for pyridoxal 5'-phosphate in human serum albumin. *FEBS Lett* **298**, 266–268 (1992).
6. Jang, Y. M. *et al.* Human pyridoxal phosphatase. Molecular cloning, functional expression, and tissue distribution. *J Biol Chem* **278**, 50040–50046 (2003).
7. John, R. A. Pyridoxal phosphate-dependent enzymes. *Biochim Biophys Acta* **1248**, 81–96 (1995).
8. Jansonius, J. N. Structure, evolution and action of vitamin B6-dependent enzymes. *Curr Opin Struct Biol* **8**, 759–769 (1998).
9. Christen, P. & Mehta, P. K. From cofactor to enzymes. The molecular evolution of pyridoxal-5'-phosphate-dependent enzymes. *Chem Rec* **1**, 436–447 (2001).
10. Mehta, P. K. & Christen, P. The molecular evolution of pyridoxal-5'-phosphate-dependent enzymes. *Adv Enzymol Relat Areas Mol Biol* **74**, 129–184 (2000).
11. Schneider, G., Käck, H. & Lindqvist, Y. The manifold of vitamin B6 dependent enzymes. *Structure* **8**, R1-6 (2000).
12. Percudani, R. & Peracchi, A. A genomic overview of pyridoxal-phosphate-dependent enzymes. *EMBO Rep* **4**, 850–854 (2003).
13. Bray, J. E., Todd, A. E., Pearl, F. M., Thornton, J. M. & Orengo, C. A. The CATH Dictionary of Homologous Superfamilies (DHS): a consensus approach for identifying distant structural homologues. *Protein Eng* **13**, 153–165 (2000).
14. Grishin, N. V., Phillips, M. A. & Goldsmith, E. J. Modeling of the spatial structure of eukaryotic ornithine decarboxylases. *Protein Sci* **4**, 1291–1304 (1995).
15. Denessiouk, K. A., Denesyuk, A. I., Lehtonen, J. V., Korpela, T. & Johnson, M. S. Common structural elements in the architecture of the cofactor-binding domains in unrelated families of pyridoxal phosphate-dependent enzymes. *Proteins* **35**, 250–261 (1999).
16. Percudani, R. & Peracchi, A. The B6 database: a tool for the description and classification of vitamin B6-dependent enzymatic activities and of the corresponding protein families. *BMC Bioinformatics* **10**, 273 (2009).
17. Steffen-Munsberg, F. *et al.* Bioinformatic analysis of a PLP-dependent enzyme superfamily suitable for biocatalytic applications. *Biotechnol Adv* **33**, 566–604 (2015).
18. Kappes, B., Tews, I., Binter, A. & Macheroux, P. PLP-dependent enzymes as potential drug targets for protozoan diseases. *Biochim Biophys Acta* **1814**, 1567–

1576 (2011).
19. Sandmeier, E., Hale, T. I. & Christen, P. Multiple evolutionary origin of pyridoxal-5'-phosphate-dependent amino acid decarboxylases. *Eur. J. Biochem.* **221**, 997–1002 (1994).
20. Burkhard, P., Dominici, P., Borri-Voltattorni, C., Jansonius, J. N. & Malashkevich, V. N. Structural insight into Parkinson's disease treatment from drug-inhibited DOPA decarboxylase. *Nat. Struct. Biol.* **8**, 963–967 (2001).
21. Momany, C., Ernst, S., Ghosh, R., Chang, N. L. & Hackert, M. L. Crystallographic structure of a PLP-dependent ornithine decarboxylase from Lactobacillus 30a to 3.0 A resolution. *J Mol Biol* **252**, 643–655 (1995).
22. Toney, M. D., Hohenester, E., Cowan, S. W. & Jansonius, J. N. Dialkylglycine decarboxylase structure: bifunctional active site and alkali metal sites. *Science* **261**, 756–759 (1993).
23. Paiardini, A., Giardina, G., Rossignoli, G., Voltattorni, C. B. & Bertoldi, M. New Insights Emerging from Recent Investigations on Human Group II Pyridoxal 5'-Phosphate Decarboxylases. *Curr. Med. Chem.* **24**, 226–244 (2017).
24. Giardina, G. *et al.* Open conformation of human DOPA decarboxylase reveals the mechanism of PLP addition to Group II decarboxylases. *Proc. Natl. Acad. Sci. U.S.A.* **108**, 20514–20519 (2011).
25. Kass, I. *et al.* Cofactor-dependent conformational heterogeneity of GAD65 and its role in autoimmunity and neurotransmitter homeostasis. *Proc Natl Acad Sci U S A* **111**, E2524-2529 (2014).
26. Komori, H., Nitta, Y., Ueno, H. & Higuchi, Y. Structural study reveals that Ser-354 determines substrate specificity on human histidine decarboxylase. *J Biol Chem* **287**, 29175–29183 (2012).
27. Dunathan, H. C. Conformation and reaction specificity in pyridoxal phosphate enzymes. *Proc. Natl. Acad. Sci. U.S.A.* **55**, 712–716 (1966).
28. Borri Voltattorni, C., Minelli, A. & Borri, P. The interaction of 2,3,4-trihydroxybenzylhydrazine with DOPA decarboxylase from pig kidney. *Life Sci* **28**, 103–108 (1981).
29. Borri-Voltattorni, C., Minelli, A. & Borri, P. Interaction of N-(DL-seryl)N'-(2,3,4-trihydroxybenzyl)-hydrazine with L-dopa decarboxylase from pig kidney. *Experientia* **33**, 158–160 (1977).
30. Bertoldi, M., Frigeri, P., Paci, M. & Voltattorni, C. B. Reaction specificity of native and nicked 3,4-dihydroxyphenylalanine decarboxylase. *J. Biol. Chem.* **274**, 5514–5521 (1999).
31. Bertoldi, M., Gonsalvi, M., Contestabile, R. & Voltattorni, C. B. Mutation of tyrosine 332 to phenylalanine converts dopa decarboxylase into a decarboxylation-dependent oxidative deaminase. *J Biol Chem* **277**, 36357–36362 (2002).
32. Langendorf, C. G. *et al.* Structural characterization of the mechanism through which human glutamic acid decarboxylase auto-activates. *Biosci Rep* **33**, 137–144 (2013).
33. Montioli, R. *et al.* New variants of AADC deficiency expand the knowledge of enzymatic phenotypes. *Arch Biochem Biophys* **682**, 108263 (2020).
34. Ishii, S., Hayashi, H., Okamoto, A. & Kagamiyama, H. Aromatic L-amino acid decarboxylase: conformational change in the flexible region around Arg334 is required during the transaldimination process. *Protein Sci* **7**, 1802–1810 (1998).

35. Fenalti, G. *et al.* GABA production by glutamic acid decarboxylase is regulated by a dynamic catalytic loop. *Nat Struct Mol Biol* **14**, 280–286 (2007).
36. Moya-Garcia, A. A., Medina, M. A. & Sánchez-Jiménez, F. Mammalian histidine decarboxylase: from structure to function. *Bioessays* **27**, 57–63 (2005).
37. Arreola, R. *et al.* Immunomodulatory Effects Mediated by Dopamine. *J Immunol Res* **2016**, 3160486 (2016).
38. Moore, P. S., Dominici, P. & Borri Voltattorni, C. Cloning and expression of pig kidney dopa decarboxylase: comparison of the naturally occurring and recombinant enzymes. *Biochem. J.* **315 (Pt 1)**, 249–256 (1996).
39. Metzler, D. E. & Snell, E. E. Deamination of serine. I. Catalytic deamination of serine and cysteine by pyridoxal and metal salts. *J Biol Chem* **198**, 353–361 (1952).
40. Metzler, D. E. & Snell, E. E. Deamination of serine. II. D-Serine dehydrase, a vitamin B6 enzyme from Escherichia coli. *J Biol Chem* **198**, 363–373 (1952).
41. Duchemin, A.-M., Neff, N. H. & Hadjiconstantinou, M. Aromatic L-amino acid decarboxylase phosphorylation and activation by PKGIalpha in vitro. *J Neurochem* **114**, 542–552 (2010).
42. Voltattorni, C. B., Minelli, A. & Dominici, P. Interaction of aromatic amino acids in D and L forms with 3,4-dihydroxyphenylalanine decarboxylase from pig kidney. *Biochemistry* **22**, 2249–2254 (1983).
43. Hayashi, H., Tsukiyama, F., Ishii, S., Mizuguchi, H. & Kagamiyama, H. Acid-base chemistry of the reaction of aromatic L-amino acid decarboxylase and dopa analyzed by transient and steady-state kinetics: preferential binding of the substrate with its amino group unprotonated. *Biochemistry* **38**, 15615–15622 (1999).
44. Montioli, R., Cellini, B. & Borri Voltattorni, C. Molecular insights into the pathogenicity of variants associated with the aromatic amino acid decarboxylase deficiency. *J. Inherit. Metab. Dis.* **34**, 1213–1224 (2011).
45. Liang, J., Han, Q., Tan, Y., Ding, H. & Li, J. Current Advances on Structure-Function Relationships of Pyridoxal 5′-Phosphate-Dependent Enzymes. *Front. Mol. Biosci.* **6**, 4 (2019).
46. Bertoldi, M. Mammalian Dopa decarboxylase: structure, catalytic activity and inhibition. *Arch. Biochem. Biophys.* **546**, 1–7 (2014).
47. Bertoldi, M. & Borri Voltattorni, C. Reaction and substrate specificity of recombinant pig kidney Dopa decarboxylase under aerobic and anaerobic conditions. *Biochim Biophys Acta* **1647**, 42–47 (2003).
48. Bisello, G., Longo, C., Rossignoli, G., Phillips, R. S. & Bertoldi, M. Oxygen reactivity with pyridoxal 5'-phosphate enzymes: biochemical implications and functional relevance. *Amino Acids* **52**, 1089–1105 (2020).
49. Bertoldi, M., Moore, P. S., Maras, B., Dominici, P. & Voltattorni, C. B. Mechanism-based inactivation of dopa decarboxylase by serotonin. *J Biol Chem* **271**, 23954–23959 (1996).
50. Bertoldi, M., Dominici, P., Moore, P. S., Maras, B. & Voltattorni, C. B. Reaction of dopa decarboxylase with alpha-methyldopa leads to an oxidative deamination producing 3,4-dihydroxyphenylacetone, an active site directed affinity label. *Biochemistry* **37**, 6552–6561 (1998).
51. Bertoldi, M., Cellini, B., Montioli, R. & Borri Voltattorni, C. Insights into the mechanism of oxidative deamination catalyzed by DOPA decarboxylase.

Biochemistry **47**, 7187–7195 (2008).
52. Bertoldi, M. & Borri Voltattorni, C. Reaction of dopa decarboxylase with L-aromatic amino acids under aerobic and anaerobic conditions. *Biochem J* **352 Pt 2**, 533–538 (2000).
53. Dominici, P., Moore, P. S., Castellani, S., Bertoldi, M. & Voltattorni, C. B. Mutation of cysteine 111 in Dopa decarboxylase leads to active site perturbation. *Protein Sci* **6**, 2007–2015 (1997).
54. Voltattorni, C. B., Minelli, A. & Turano, C. Spectral properties of the coenzyme bound to DOPA decarboxylase from pig kidney. *FEBS Lett* **17**, 231–235 (1971).
55. Voltattorni, C. B., Minelli, A., Vecchini, P., Fiori, A. & Turano, C. Purification and characterization of 3,4-dihydroxyphenylalanine decarboxyase from pig kidney. *Eur J Biochem* **93**, 181–188 (1979).
56. Dominici, P., Tancini, B., Barra, D. & Voltattorni, C. B. Purification and characterization of rat-liver 3,4-dihydroxyphenylalanine decarboxylase. *Eur J Biochem* **169**, 209–213 (1987).
57. Fiori, A., Turano, C., Borri-Voltattorni, C., Minelli, A. & Codini, M. Interaction of L-DOPA decarboxylase with substrates: a spectrophotometric study. *FEBS Lett* **54**, 122–125 (1975).
58. Daidone, F. *et al.* Identification by virtual screening and in vitro testing of human DOPA decarboxylase inhibitors. *PLoS ONE* **7**, e31610 (2012).
59. Montioli, R., Cellini, B., Dindo, M., Oppici, E. & Voltattorni, C. B. Interaction of human Dopa decarboxylase with L-Dopa: spectroscopic and kinetic studies as a function of pH. *Biomed Res Int* **2013**, 161456 (2013).
60. Montioli, R. *et al.* S250F variant associated with aromatic amino acid decarboxylase deficiency: molecular defects and intracellular rescue by pyridoxine. *Hum. Mol. Genet.* **22**, 1615–1624 (2013).
61. Montioli, R., Voltattorni, C. B. & Bertoldi, M. Parkinson's Disease: Recent Updates in the Identification of Human Dopa Decarboxylase Inhibitors. *Curr. Drug Metab.* **17**, 513–518 (2016).
62. Gárdián, G. & Vécsei, L. Medical treatment of Parkinson's disease: today and the future. *Int J Clin Pharmacol Ther* **48**, 633–642 (2010).
63. McCormick, D. B. & Snell, E. E. PYRIDOXAL KINASE OF HUMAN BRAIN AND ITS INHIBITION BY HYDRAZINE DERIVATIVES. *Proc Natl Acad Sci U S A* **45**, 1371–1379 (1959).
64. Bender, D. A. & Smith, W. R. Inhibition of kynurenine hydrolase by benserazide, carbidopa and other aromatic hydrazine derivatives: evidence for sub-clinical iatrogenic niacin deficiency [proceedings]. *Biochem Soc Trans* **6**, 120–122 (1978).
65. Orlacchio, A., Borri-Voltattorni, C. & Turano, C. The binding of the coenzyme pyridoxal 5'-phosphate and analogues of the substrate-coenzyme complex to tyrosine decarboxylase. *Biochem J* **185**, 41–46 (1980).
66. Bertoldi, M., Gonsalvi, M. & Voltattorni, C. B. Green tea polyphenols: novel irreversible inhibitors of dopa decarboxylase. *Biochem Biophys Res Commun* **284**, 90–93 (2001).
67. Hadjiconstantinou, M. & Neff, N. H. Enhancing aromatic L-amino acid decarboxylase activity: implications for L-DOPA treatment in Parkinson's disease. *CNS Neurosci Ther* **14**, 340–351 (2008).

68. Holtz, P., Heise, R. & Lüdtke, K. Fermentativer Abbau von l-Dioxyphenylalanin (Dopa) durch Niere. *Archiv f. experiment. Pathol. u. Pharmakol* **191**, 87–118 (1938).
69. Hornbeck, P. V. *et al.* PhosphoSitePlus, 2014: mutations, PTMs and recalibrations. *Nucleic Acids Res* **43**, D512-520 (2015).
70. Kemp, B. E. & Pearson, R. B. Protein kinase recognition sequence motifs. *Trends Biochem Sci* **15**, 342–346 (1990).
71. Wagner, S. A. *et al.* Proteomic analyses reveal divergent ubiquitylation site patterns in murine tissues. *Mol Cell Proteomics* **11**, 1578–1585 (2012).
72. Lundby, A. *et al.* Proteomic analysis of lysine acetylation sites in rat tissues reveals organ specificity and subcellular patterns. *Cell Rep* **2**, 419–431 (2012).
73. Vutskits, L., Menache, C., Manzano, S., Haenggeli, C.-A. & Habre, W. Anesthesia management in a young child with aromatic l-amino acid decarboxylase deficiency. *Paediatr Anaesth* **16**, 82–84 (2006).
74. Young, E. A., Neff, N. H. & Hadjiconstantinou, M. Phorbol ester administration transiently increases aromatic L-amino acid decarboxylase activity of the mouse striatum and midbrain. *J Neurochem* **63**, 694–697 (1994).
75. Duchemin, A. M., Berry, M. D., Neff, N. H. & Hadjiconstantinou, M. Phosphorylation and activation of brain aromatic L-amino acid decarboxylase by cyclic AMP-dependent protein kinase. *J Neurochem* **75**, 725–731 (2000).
76. Tehranian, R., Montoya, S. E., Van Laar, A. D., Hastings, T. G. & Perez, R. G. Alpha-synuclein inhibits aromatic amino acid decarboxylase activity in dopaminergic cells. *J. Neurochem.* **99**, 1188–1196 (2006).
77. Cartier, E. A. *et al.* A biochemical and functional protein complex involving dopamine synthesis and transport into synaptic vesicles. *J. Biol. Chem.* **285**, 1957–1966 (2010).
78. Stark, A. K. & Pakkenberg, B. Histological changes of the dopaminergic nigrostriatal system in aging. *Cell Tissue Res* **318**, 81–92 (2004).
79. Björklund, A. & Dunnett, S. B. Dopamine neuron systems in the brain: an update. *Trends Neurosci* **30**, 194–202 (2007).
80. Dahlstroem, A. & Fuxe, K. EVIDENCE FOR THE EXISTENCE OF MONOAMINE-CONTAINING NEURONS IN THE CENTRAL NERVOUS SYSTEM. I. DEMONSTRATION OF MONOAMINES IN THE CELL BODIES OF BRAIN STEM NEURONS. *Acta Physiol Scand Suppl* SUPPL 232:1-55 (1964).
81. Klein, M. O. *et al.* Dopamine: Functions, Signaling, and Association with Neurological Diseases. *Cell Mol Neurobiol* **39**, 31–59 (2019).
82. Anden, N. E. *et al.* DEMONSTRATION AND MAPPING OUT OF NIGRO-NEOSTRIATAL DOPAMINE NEURONS. *Life Sci (1962)* **3**, 523–530 (1964).
83. Kapur, S., Zipursky, R., Jones, C., Remington, G. & Houle, S. Relationship between dopamine D(2) occupancy, clinical response, and side effects: a double-blind PET study of first-episode schizophrenia. *Am J Psychiatry* **157**, 514–520 (2000).
84. Beaulieu, J.-M. & Gainetdinov, R. R. The physiology, signaling, and pharmacology of dopamine receptors. *Pharmacol Rev* **63**, 182–217 (2011).
85. Missale, C., Nash, S. R., Robinson, S. W., Jaber, M. & Caron, M. G. Dopamine receptors: from structure to function. *Physiol Rev* **78**, 189–225 (1998).
86. Pardridge, W. M. Blood-brain barrier delivery. *Drug Discov Today* **12**, 54–

61 (2007).
87. Snyder, S. H., Taylor, K. M., Coyle, J. T. & Meyerhoff, J. L. The role of brain dopamine in behavioral regulation and the actions of psychotropic drugs. *Am J Psychiatry* **127**, 199–207 (1970).
88. Sibley, D. R. New insights into dopaminergic receptor function using antisense and genetically altered animals. *Annu Rev Pharmacol Toxicol* **39**, 313–341 (1999).
89. Carlsson, A. *et al.* Interactions between monoamines, glutamate, and GABA in schizophrenia: new evidence. *Annu Rev Pharmacol Toxicol* **41**, 237–260 (2001).
90. Iversen, S. D. & Iversen, L. L. Dopamine: 50 years in perspective. *Trends Neurosci* **30**, 188–193 (2007).
91. Kuchel, O. G. & Kuchel, G. A. Peripheral dopamine in pathophysiology of hypertension. Interaction with aging and lifestyle. *Hypertension* **18**, 709–721 (1991).
92. Goldstein, D. S. & Holmes, C. Neuronal source of plasma dopamine. *Clin Chem* **54**, 1864–1871 (2008).
93. Mohammad-Zadeh, L. F., Moses, L. & Gwaltney-Brant, S. M. Serotonin: a review. *J Vet Pharmacol Ther* **31**, 187–199 (2008).
94. Brodie, B. B. & Shore, P. A. A concept for a role of serotonin and norepinephrine as chemical mediators in the brain. *Ann N Y Acad Sci* **66**, 631–642 (1957).
95. Twarog, B. M. & Page, I. H. Serotonin content of some mammalian tissues and urine and a method for its determination. *Am J Physiol* **175**, 157–161 (1953).
96. Christenson, J. G., Dairman, W. & Udenfriend, S. On the Identity of DOPA Decarboxylase and 5-Hydroxytryptophan Decarboxylase. *Proc. Nat. Acad. Sci. USA* 5 (1972).
97. Keszthelyi, D., Troost, F. J. & Masclee, A. a. M. Understanding the role of tryptophan and serotonin metabolism in gastrointestinal function. *Neurogastroenterol Motil* **21**, 1239–1249 (2009).
98. Marston, O. J., Garfield, A. S. & Heisler, L. K. Role of central serotonin and melanocortin systems in the control of energy balance. *Eur J Pharmacol* **660**, 70–79 (2011).
99. Lesch, K.-P., Araragi, N., Waider, J., van den Hove, D. & Gutknecht, L. Targeting brain serotonin synthesis: insights into neurodevelopmental disorders with long-term outcomes related to negative emotionality, aggression and antisocial behaviour. *Philos Trans R Soc Lond B Biol Sci* **367**, 2426–2443 (2012).
100. Oury, F. & Karsenty, G. Towards a serotonin-dependent leptin roadmap in the brain. *Trends Endocrinol Metab* **22**, 382–387 (2011).
101. El-Merahbi, R., Löffler, M., Mayer, A. & Sumara, G. The roles of peripheral serotonin in metabolic homeostasis. *FEBS Lett* **589**, 1728–1734 (2015).
102. Berger, M., Gray, J. A. & Roth, B. L. The expanded biology of serotonin. *Annu Rev Med* **60**, 355–366 (2009).
103. Lin, S.-H., Lee, L.-T. & Yang, Y. K. Serotonin and mental disorders: a concise review on molecular neuroimaging evidence. *Clin Psychopharmacol Neurosci* **12**, 196–202 (2014).
104. Wassenberg, T. *et al.* Consensus guideline for the diagnosis and treatment of aromatic l-amino acid decarboxylase (AADC) deficiency. *Orphanet J Rare Dis* **12**, 12 (2017).

105. Hyland, K. & Reott, M. Prevalence of Aromatic l-Amino Acid Decarboxylase Deficiency in At-Risk Populations. *Pediatr Neurol* **106**, 38–42 (2020).
106. Chien, Y.-H. *et al.* Efficacy and safety of AAV2 gene therapy in children with aromatic L-amino acid decarboxylase deficiency: an open-label, phase 1/2 trial. *Lancet Child Adolesc Health* **1**, 265–273 (2017).
107. Himmelreich, N. *et al.* Aromatic amino acid decarboxylase deficiency: Molecular and metabolic basis and therapeutic outlook. *Mol Genet Metab* **127**, 12–22 (2019).
108. Brun, L. *et al.* Clinical and biochemical features of aromatic L-amino acid decarboxylase deficiency. *Neurology* **75**, 64–71 (2010).
109. Hyland, K. & Clayton, P. T. Aromatic amino acid decarboxylase deficiency in twins. *J. Inherit. Metab. Dis.* **13**, 301–304 (1990).
110. Hyland, K. & Clayton, P. T. Aromatic L-amino acid decarboxylase deficiency: diagnostic methodology. *Clin Chem* **38**, 2405–2410 (1992).
111. Lee, H.-F., Tsai, C.-R., Chi, C.-S., Chang, T.-M. & Lee, H.-J. Aromatic L-amino acid decarboxylase deficiency in Taiwan. *Eur J Paediatr Neurol* **13**, 135–140 (2009).
112. Tay, S. K. H. *et al.* Unusually mild phenotype of AADC deficiency in 2 siblings. *Mol Genet Metab* **91**, 374–378 (2007).
113. Leuzzi, V. *et al.* Report of two never treated adult sisters with aromatic L-amino Acid decarboxylase deficiency: a portrait of the natural history of the disease or an expanding phenotype? *JIMD Rep* **15**, 39–45 (2015).
114. Barth, M. *et al.* Kinetic analyses guide the therapeutic decision in a novel form of moderate aromatic Acid decarboxylase deficiency. *JIMD Rep* **3**, 25–32 (2012).
115. Christine, C. W. *et al.* Safety and tolerability of putaminal AADC gene therapy for Parkinson disease. *Neurology* **73**, 1662–1669 (2009).
116. Hwu, W.-L. *et al.* Gene therapy for aromatic L-amino acid decarboxylase deficiency. *Sci Transl Med* **4**, 134ra61 (2012).
117. Kojima, K. *et al.* Gene therapy improves motor and mental function of aromatic l-amino acid decarboxylase deficiency. *Brain* **142**, 322–333 (2019).
118. National Taiwan University Hospital. *A Clinical Trial for Treatment of Aromatic L-amino Acid Decarboxylase (AADC) Deficiency Using AAV2-hAADC - An Expansion (NTUH-AADC-011)*. https://clinicaltrials.gov/ct2/show/NCT02926066 (2020).
119. Montioli, R. *et al.* A comprehensive picture of the mutations associated with aromatic amino acid decarboxylase deficiency: from molecular mechanisms to therapy implications. *Hum. Mol. Genet.* **23**, 5429–5440 (2014).
120. Montioli, R. *et al.* The novel R347g pathogenic mutation of aromatic amino acid decarboxylase provides additional molecular insights into enzyme catalysis and deficiency. *Biochim. Biophys. Acta* **1864**, 676–682 (2016).
121. Montioli, R., Janson, G., Paiardini, A., Bertoldi, M. & Borri Voltattorni, C. Heterozygosis in aromatic amino acid decarboxylase deficiency: Evidence for a positive interallelic complementation between R347Q and R358H mutations. *IUBMB Life* **70**, 215–223 (2018).
122. Montioli, R. *et al.* A novel compound heterozygous genotype associated with aromatic amino acid decarboxylase deficiency: Clinical aspects and

biochemical studies. *Mol Genet Metab* **127**, 132–137 (2019).
123. Manegold, C. *et al.* Aromatic l-amino acid decarboxylase deficiency: clinical features, drug therapy and follow-up. *Journal of Inherited Metabolic Disease* **32**, 371–380 (2009).
124. Helman, G., Pappa, M. B. & Pearl, P. L. Widening Phenotypic Spectrum of AADC Deficiency, a Disorder of Dopamine and Serotonin Synthesis. in *JIMD Reports, Volume 17* (eds. Zschocke, J., Gibson, K. M., Brown, G., Morava, E. & Peters, V.) 23–27 (Springer, 2014). doi:10.1007/8904_2014_327.
125. Chien, Y.-H. *et al.* 3-O-methyldopa levels in newborns: Result of newborn screening for aromatic l-amino-acid decarboxylase deficiency. *Mol Genet Metab* **118**, 259–263 (2016).
126. Hwu, W.-L., Chien, Y.-H., Lee, N.-C. & Li, M.-H. Natural History of Aromatic L-Amino Acid Decarboxylase Deficiency in Taiwan. *JIMD Rep* **40**, 1–6 (2018).
127. Graziano, C. *et al.* Syndromic intellectual disability: a new phenotype caused by an aromatic amino acid decarboxylase gene (DDC) variant. *Gene* **559**, 144–148 (2015).
128. Battye, T. G. G., Kontogiannis, L., Johnson, O., Powell, H. R. & Leslie, A. G. W. iMOSFLM: a new graphical interface for diffraction-image processing with MOSFLM. *Acta Crystallogr D Biol Crystallogr* **67**, 271–281 (2011).
129. Winn, M. D. *et al.* Overview of the CCP4 suite and current developments. *Acta Crystallogr D Biol Crystallogr* **67**, 235–242 (2011).
130. Vagin, A. & Teplyakov, A. Molecular replacement with MOLREP. *Acta Crystallogr D Biol Crystallogr* **66**, 22–25 (2010).
131. Murshudov, G. N. *et al.* REFMAC5 for the refinement of macromolecular crystal structures. *Acta Crystallogr D Biol Crystallogr* **67**, 355–367 (2011).
132. Adams, P. D. *et al.* PHENIX: a comprehensive Python-based system for macromolecular structure solution. *Acta Crystallogr D Biol Crystallogr* **66**, 213–221 (2010).
133. Emsley, P., Lohkamp, B., Scott, W. G. & Cowtan, K. Features and development of Coot. *Acta Crystallogr D Biol Crystallogr* **66**, 486–501 (2010).
134. Case, D. A. *et al.* Amber 2020. (2020).
135. Jakalian, A., Jack, D. B. & Bayly, C. I. Fast, efficient generation of high-quality atomic charges. AM1-BCC model: II. Parameterization and validation. *J Comput Chem* **23**, 1623–1641 (2002).
136. Jorgensen, W. L., Chandrasekhar, J., Madura, J. D., Impey, R. W. & Klein, M. L. Comparison of simple potential functions for simulating liquid water. *J. Chem. Phys.* **79**, 926–935 (1983).
137. Melo, F., Sánchez, R. & Sali, A. Statistical potentials for fold assessment. *Protein Science* **11**, 430–448 (2002).
138. Sousa da Silva, A. W. & Vranken, W. F. ACPYPE - AnteChamber PYthon Parser interfacE. *BMC Research Notes* **5**, 367 (2012).
139. Van Der Spoel, D. *et al.* GROMACS: fast, flexible, and free. *J Comput Chem* **26**, 1701–1718 (2005).
140. Sherald, A. F., Sparrow, J. C. & Wright, T. R. A spectrophotometric assay for Drosophila dopa decarboxylase. *Anal Biochem* **56**, 300–305 (1973).
141. Charteris, A. & John, R. An investigation of the assay of dopamine using trinitrobenzensulphonic acid. *Anal Biochem* **66**, 365–371 (1975).

142. Dong, A., Huang, P. & Caughey, W. S. Protein secondary structures in water from second-derivative amide I infrared spectra. *Biochemistry* **29**, 3303–3308 (1990).
143. Rossignoli, G. *et al.* Cysteine 180 Is a Redox Sensor Modulating the Activity of Human Pyridoxal 5'-Phosphate Histidine Decarboxylase. *Biochemistry* **57**, 6336–6348 (2018).
144. Laskowski, R. A., Jabłońska, J., Pravda, L., Vařeková, R. S. & Thornton, J. M. PDBsum: Structural summaries of PDB entries. *Protein Sci* **27**, 129–134 (2018).
145. Louis-Jeune, C., Andrade-Navarro, M. A. & Perez-Iratxeta, C. Prediction of protein secondary structure from circular dichroism using theoretically derived spectra. *Proteins* **80**, 374–381 (2012).
146. Wälchli, R., Vermeire, P.-J., Massant, J. & Arosio, P. Accelerated Aggregation Studies of Monoclonal Antibodies: Considerations for Storage Stability. *JPharmSci* **109**, 595–602 (2020).
147. Liu, L. L., Wang, L., Zonderman, J., Rouse, J. C. & Kim, H.-Y. Automated, High-Throughput Infrared Spectroscopy for Secondary Structure Analysis of Protein Biopharmaceuticals. *J Pharm Sci* **109**, 3223–3230 (2020).
148. Rossignoli, Giada. Aromatic amino acids decarboxylase and histidine decarboxylase: deep functional investigations give insights into pathophysiological mechanisms with possible therapeutic implications. (Universitá di Verona, 2019).

ACKNOWLEDGMENTS

I miei ringraziamenti a *Mita* (*Prof.ssa Bertoldi)*, per aver sostenuto con fiducia la libertà di ricerca, a *Rik (Dr. Montioli)* per avermi introdotto con entusiasmo a questo progetto ed alla *Prof.ssa Polverino De Laureto* per l'appoggio e la disponibilità sempre dimostratami.

A tutti i colleghi ed amici della sezione di Chimica Biologica dell'Università di Verona, per aver condiviso impegno e sudore. In particolare a *Nidula*, *Cristian, Silvia*, *Giada*, *Giuditta, Carmen*, *Samuele*.

Ai miei amici *Epa*, *Johnny*, *Bonny*, *Bejor*, con i quali ho imparato complicità e gioco di squadra.

Alle mie radici, *Pà*, *Mà* e *Joy* per la stima e fiducia infinite.

A *Elisa*, che mi accompagna ogni giorno, con pazienza e amore, in una ricerca profonda, in un laboratorio sempre nuovo.

CONTRIBUTION TO THE ATTACHED PAPERS

The main object of this thesis is the study of AADC on its wild type and its variant forms. Besides my PhD program I have also contributed to other research projects, collaborating with different groups. My contribution to the following papers is reported.

1. **New variants of AADC deficiency expand the knowledge of enzymatic phenotypes.**
   Montioli R, Bisello G*, Dindo M, Rossignoli G, Voltattorni CB, Bertoldi M.
   *co-first author
   Archives of Biochemistry and Biophysics. **2020** Mar 30;682:108263. **doi**: 10.1016/j.abb.2020.108263.
   Contribution in designing and performing the experiments, analysis of the data.

2. **Aromatic L-Amino Acid Decarboxylase deficiency: a patient-derived neuronal model for precision therapies.**
   Rossignoli G, Krämer K, Lugará E, Alrashidi H, Pope S, De La Fuente Barrigon C, Barwick K, Bisello G, Ng Counsell, Lignani G, J. R. Heales S, Bertoldi M, Barral S, A. Kurian M.
   Under second revision, submitted to *Brain* in **2020**
   Contribution in designing and performing the experiments, analysis of the data.

3. **Oxygen reactivity with pyridoxal 5'-phosphate enzymes: biochemical implications and functional relevance.**
   Bisello G, Longo C, Rossignoli G, Phillips RS, Bertoldi M.
   Amino Acids. **2020** Aug;52(8):1089-1105. **doi**: 10.1007/s00726-020-02885-6.
   Contribution in writing, review and editing the manuscript.

4. **Cysteine 180 Is a Redox Sensor Modulating the Activity of Human Pyridoxal 5'-Phosphate Histidine Decarboxylase.**
   Rossignoli G, Grottesi A, Bisello G, Montioli R, Borri Voltattorni C, Paiardini A, Bertoldi M. *Biochemistry.* **2018** Nov 6;57(44):6336-6348. **doi**: 10.1021/acs.biochem.8b00625.
   Contribution in designing and performing the experiments, analysis of the data.

5. **Oleuropein aglycone stabilizes the monomeric α-synuclein and favours the growth of non-toxic aggregates.**
   Palazzi L, Bruzzone E, Bisello G, Leri M, Stefani M, Bucciantini M, Polverino de Laureto P.
   Scientific Reports. **2018** May 29;8(1):8337. **doi**: 10.1038/s41598-018-26645-5.

Contribution in designing and performing the experiments, analysis of the data.

6. **Tyrosine Phosphorylation Modulates Peroxiredoxin-2 Activity in Normal and Diseased Red Cells.**
Mattè A, Federti E, Tibaldi E, Di Paolo ML, Bisello G, Bertoldi M, Carpentieri A, Pucci P, Iatchencko I, Wilson AB, Riccardi V, Siciliano A, Turrini F, Kim DW, Choi SY, Brunati AM, De Franceschi L.
Antioxidants (Basel). **2021** Feb 1;10(2):206. **doi**: 10.3390/antiox10020206.
Contribution in designing and performing bioinformatics analysis and enzymatic assays.

Archives of Biochemistry and Biophysics 682 (2020) 108263

Contents lists available at ScienceDirect

Archives of Biochemistry and Biophysics

journal homepage: www.elsevier.com/locate/yabbi

New variants of AADC deficiency expand the knowledge of enzymatic phenotypes

Riccardo Montioli[a,1], Giovanni Bisello[a,1], Mirco Dindo[b], Giada Rossignoli[c], Carla Borri Voltattorni[a], Mariarita Bertoldi[a,*]

[a] Department of Neuroscience, Biomedicine and Movement Sciences, Section of Biological Chemistry, University of Verona, Strada Le Grazie, 8, 37134, Verona, Italy
[b] Okinawa Institute of Science and Technology Graduate University, 1919-1 Tancha, Onna-son, Okinawa, 904-0412, Japan
[c] Molecular Neurosciences, Developmental Neurosciences Programme, UCL Great Ormond Street Institute of Child Health, 30 Guildford Street, London, WC1N 1EH, UK

ARTICLE INFO

Keywords:
Pyridoxal 5′-phosphate enzymes
Aromatic amino acid decarboxylase deficiency
AADC deficiency variants
Structure and function relationship
Protein chemistry
Enzymology

ABSTRACT

AADC deficiency is a rare genetic disease caused by mutations in the gene of aromatic amino acid decarboxylase, the pyridoxal 5′-phosphate dependent enzyme responsible for the synthesis of dopamine and serotonin. Here, following a biochemical approach together with an *in silico* bioinformatic analysis, we present a structural and functional characterization of 13 new variants of AADC. The amino acid substitutions are spread over the entire protein from the N-terminal (V60A), to its loop1 (H70Y and F77L), to the large domain (G96R) and its various motifs, i.e. loop2 (A110E), or a core β-barrel either on the surface (P210L, F251S and E283A) or in a more hydrophobic *milieu* (L222P, F237S and W267R) or loop3 (L353P), and to the C-terminal domain (R453C). Results show that the β-barrel variants exhibit a low solubility and those belonging to the surface tend to aggregate in their apo form, leading to the identification of a new enzymatic phenotype for AADC deficiency. Moreover, five variants of residues belonging to the large interface of AADC (V60A, G96R, A110E, L353P and R453C) are characterized by a decreased catalytic efficiency. The remaining ones (H70Y and F77L) present features typical of apo-to-holo impaired transition. Thus, defects in catalysis or in the acquirement of the correct holo structure are due not only to specific local domain effects but also to long-range effects at either the protein surface or the subunit interface. Altogether, the new characterized enzymatic phenotypes represent a further step in the elucidation of the molecular basis for the disease.

1. Introduction

Aromatic amino acid decarboxylase (AADC) deficiency is a rare autosomic disease first reported by Hyland et al. [1,2] nearly 30 years ago. It is caused by mutations (mainly missense but also frameshift and splicing alterations) present in homozygosis or compound heterozygosis in the gene encoding for AADC, the pyridoxal 5′-phosphate (PLP) enzyme responsible for the synthesis of dopamine and serotonin following decarboxylation of L-Dopa and 5-hydroxytryptophan [3,4]. The disease is mainly diagnosed in infancy and exhibits many different symptoms reflecting the lack or low levels of catechol and indole biogenic amines. Patients experience several altered physiological functions such as hypotonia, hypokinesia, oculogyric crises, development and behavioural problems, autonomic dysfunctions such as nasal congestion, modified circadian rhythm, pain and temperature instability [5–10]. The present pharmacological treatment foresees a combination of pyridoxine, the precursor of PLP to keep AADC saturated with its coenzyme, monoamine oxidase inhibitors, to avoid dopamine and serotonin further depletion, and dopamine agonists, to mimic the effect of dopamine. Unfortunately, in many cases, the response is generally poor and this infantile form of Parkinsonism is particularly threatening and, in the most severe forms, leads to death in the first decade of life.

Up to now, nearly 120 patients have been identified worldwide [9], but the number is continuously growing since knowledge about this defect is increasing among child neurologists. Moreover, the extent of affected people might be even higher considering i) newly reported case of a heterozygous patient that possesses one allele with a mild mutation, while the other allele has no mutations [11], ii) another heterozygous case with typical AADC deficiency symptoms (case II-2 in Ref. [12]) and iii) a milder case of AADC deficiency reported by Ref. [13].

Abbreviations: PLP, pyridoxal 5′-phosphate; AADC, aromatic amino acid decarboxylase; Dopa, 3,4-dihydroxyphenylalanine

* Corresponding author.
E-mail address: mita.bertoldi@univr.it (M. Bertoldi).

[1] Equal contribution.

https://doi.org/10.1016/j.abb.2020.108263
Received 15 November 2019; Received in revised form 5 January 2020; Accepted 8 January 2020
Available online 15 January 2020
0003-9861/

These unsuspected patients expand the spectrum of AADC deficiency with recent estimates [14,15] predicting that the number of affected people is higher than reported and many patients remain not diagnosed or misdiagnosed [15].

In order to counteract AADC deficiency, some strategies have currently been undertaken. Firstly, a gene therapy approach has been carried out in Taiwan by Dr. Hwu and co-workers [16–19] and in Japan [20] with some patients, leading to some benefits but still not decisive improvements. Secondly, mouse models with different genetic defects have been generated to simulate AADC deficiency and understand the human disease [21–24], but much has still to be done.

A biochemical research of genotype to phenotype correlation has been carried out in order to elucidate the molecular basis of an altered phenotype by characterizing the related enzymatic variant. Previously, the structural/functional correlation of the effects of mutations for 16 AADC variants were studied [25]. This approach deepened the understanding of the role played by individual amino acids on enzyme structure and function, suggesting more effective therapeutic interventions.

After five years the number of identified mutations has rapidly increased. The total number of the identified *AADC* mutations leading to the disease, including missense mutations determining homozygosis or compound heterozygosis, insertions, deletions, introns and non-coding regions modifications, has been recently updated [15]. In particular, 13 new mutations have been identified in homozygosis or hemizygosis and their protein variants are listed in Table 1. Notably, the variants of His-70 and Ala-110 have been re-characterized since they were incorrectly reported (see Table 1).

On the basis of the structure of AADC, solved both in the pig holo (~90% sequence identity with the human enzyme) [26] and in the human apo form [27], the new sites of mutation are spread overall the entire protein and not only in the central part of each monomer as previously claimed [25] (Fig. 1).

Here, by a combination of bioinformatic and physico-chemical techniques, we present a structural and functional characterization of the new homozygous and hemizygous variants of AADC. The data obtained pertain to residues that belong to: i) loop1 (aa 66–84) of the N-terminal region (H70Y and F77L), ii) the interface between monomers (V60A, G96R, A110E, L353P and R453C) and iii) different regions of the large domain (P210L, L222P, F237S, F251S, W267R and E283A). The correlation between position and functional effect represents a powerful approach for disease phenotype prediction.

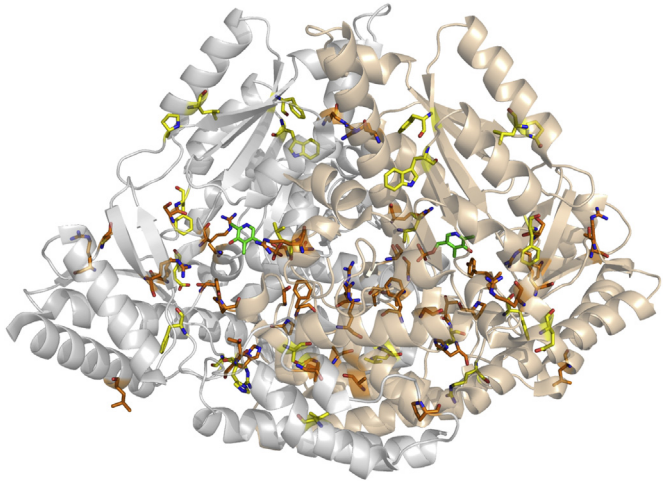

Fig. 1. New and already identified amino acid substitutions in AADC variants. Ribbons representation of the holo AADC (pdb ID 1JS6). The two monomers are white and light orange, respectively, and PLP molecules are represented as green sticks. Mutation sites of previously characterized variants and new variants are presented as orange and yellow sticks, respectively. Image was rendered by PyMol software (Schrödinger). (For interpretation of the references to colour in this figure legend, the reader is referred to the Web version of this article.)

2. Materials and Methods

2.1. Materials

PLP, L-Dopa, dopa methylester (DME), hydroxylamine hydrochloride, isopropyl-β-D-thiogalactopyranoside (IPTG), trinitrobenzenesulfonic acid (TNB), phenylmethylsulfonyl fluoride (PMSF), protease inhibitor cocktail (P8849), were purchased from Sigma. Anti AADC monoclonal antibody (8E8) and mouse IgG kappa binding protein (m-IgGk BP) conjugated with HRP were purchased from Santa Cruz Biotechnology.

2.2. Site-directed mutagenesis

AADC variants were obtained by mutating the template DNA on the pDDChis vector as previously described [25]. Each mutagenesis

Table 1
New reported AADC homozygous or hemizygous variants from 2014 to 2019.

new variant	reference	Note
V60A	Hwu et al., 2017 [13]	in hemizygosis, the other allele produces a protein that ends prematurely at 248 amino acids, with no formation of the active site
H70Y	Manegold et al., 2009 [10]; Gucuyener et al., 2014 [45] Montioli et al., 2014 [25]	homozygous, reported incorrectly as H70T
F77L	www.bioku.org/pnd/home.asp	homozygous, on line submission in database in 2012
G96R	Hwu et al., 2017 [16]	in hemizygosis, the other allele produces a protein that ends prematurely at 248 amino acids, with no formation of the active site
A110E	Ide et al., 2010 [44]; Wassenberg et al., 2010 [46]; Montioli et al., 2014 [25]	homozygous, reported incorrectly as A110Q
P210L	Helman et al., 2014 [42]	in hemizygosis, the other allele has a mutation leading to a premature stop codon
L222P	Helman et al., 2014 [42]	Homozygous
F237S	Leuzzi et al., 2015 [12]	in hemizygosis, the other allele has a mutation leading to a premature stop codon
F251S	Chien et al., 2016 [14]	in hemizygosis, the other allele produces a protein that ends prematurely at 248 amino acids, with no formation of the active site
W267R	R. Pons, personal communication	homozygous, R. Pons, personal communication
E283A	Hwu et al., 2017 [13]	in hemizygosis, the other allele produces a protein that ends prematurely at 248 amino acids, with no formation of the active site
L353P	Hwu et al., 2017 [13]	in hemizygosis, the other allele produces a protein that ends prematurely at 248 amino acids, with no formation of the active site
R453C	Graziano et al., 2015 [43]	homozygous, reported incorrectly as R375C

reaction has been performed using the Quick-Change II kit (Agilent technologies) using the appropriate oligonucleotides (summarized in Table S1) and their complements. All mutations were confirmed by DNA sequence analysis of the whole ORF.

2.3. Expression and purification of AADC variants

E. coli BL21 (DE3) cells were transformed by heat shock at 42 °C with the desired construct and grown in 4.5 L of Luria–Bertani (LB) broth in presence of ampicillin (100 mg/ml). The cultures were grown at 37 °C to an OD_{600nm} of 0.4–0.6, and expression was induced with 0.1 mM IPTG for 15 h at 30 °C. Cells were harvested and resuspended in 20 mM sodium phosphate buffer pH 7.4, containing 0.5 M NaCl, 20 mM imidazole, 50 μM PLP, 0.5 mM PMSF and protease inhibitor cocktail. Lysozyme was then added to a concentration of 0.2 mg/ml and the culture was incubated for 20 min at room temperature. After a freeze-thaw, leupeptin and pepstatin (both at 1 μg/ml concentration) were added and the suspension was centrifuged at 16,000 g for 30 min. The crude cellular lysate was loaded on a HisPrep FF 16/10 column (GE Healthcare) equilibrated with 20 mM sodium phosphate buffer pH 7.4, containing 0.5 M NaCl and 20 mM imidazole. AADC was eluted with a linear gradient (0–100% in 200 ml) of the same buffer containing 500 mM imidazole. After addition of 50 μM PLP, the protein solution was concentrated and imidazole and unbound coenzyme were removed by extensive washing with 100 mM potassium phosphate buffer pH 7.4, using Amicon Ultra 15 concentrators (Millipore). The enzymes concentration was determined using an ε_M of $1.42 \times 10^5\ M^{-1}\ cm^{-1}$ at 280 nm. PLP content was determined by releasing the coenzyme in 0.1 M NaOH using ε_M of 6600 $M^{-1}\ cm^{-1}$ at 388 nm [28].

2.4. Size-exclusion liquid chromatography

Size-exclusion liquid chromatography was applied as further purification step. Samples were loaded on a Superdex 200 (10/300) (GE Healthcare) column equilibrated with 100 mM potassium phosphate buffer pH 7.4, on an Akta FPLC system (GE Healthcare). The run was performed using the same buffer at a flow rate of 0.3 ml/min with detection at 280 nm.

2.5. Determination of solubility level of the AADC variants

E. coli has been used as a model for the expression study of the pathogenic AADC variants. Chemical competent bacteria were transformed with the proper mutagenized plasmid as described in the expression and purification section. Cultures were grown even in the absence or in the presence of 50 μM exogenous PLP and 1 ml of each culture was processed following the same procedure described above. After lysis, samples were treated with DNase (10 U) at room temperature for 30 min. The whole cell extract was separated by centrifugation at 13,200 rpm, 10 min, 4 °C. Total protein content in the crude cellular lysate was quantified and 15 μg of total protein was run on a 12% (w/w) SDS-PAGE gel. The same amount of a sample consisting of the membrane insoluble pellet of wild-type (WT), P210L, L222P, F237S, W267R and E283A variants was analyzed. Proteins from the gel were transferred on a nitrocellulose membrane by a Mini Trans-Blot cell (Bio-Rad). Membrane was blocked with a 5% (w/w) milk solution at 37 °C for 1 h and, after the washing steps, it was incubated with a 1:200 (v/v) diluted anti-AADC monoclonal antibody solution over night at 4 °C. Membrane was then washed and then incubated with a 1:4000 (v/v) anti-mouse secondary antibody solution for 1 h at 25 °C. Blotted proteins were detected and quantified with ECL (Millipore), using the ChemiDoc XRS Imaging System (Bio-Rad, Hercules, CA). Quantification of the band was obtained with ImageJ software (Fiji).

2.6. Apoenzyme preparation and coenzyme binding affinity measurements

Apoenzyme was obtained by incubating 5 μM holoenzyme with 10 mM hydroxylamine in 0.5 M potassium phosphate buffer pH 6.8 at 25 °C for 3 h. The solution was then loaded on a Desalting 26/10 column (GE Healthcare) pre-equilibrated with 0.5 M potassium phosphate buffer pH 6.8 and eluted at 1 mL/min. The eluted enzyme was then concentrated on an Amicon Ultra 15 concentrators (Millipore) and washed with 100 mM potassium phosphate buffer pH 7.4.

The equilibrium apparent dissociation constant for PLP, $K_{D(PLP)}$, was determined by measuring the quenching of the intrinsic fluorescence of 0.1 μM AADC apoenzyme incubated in the presence of PLP at concentrations ranging from 0.005 to 20 μM for 3 h at 25 °C (in the dark) in 100 mM potassium phosphate buffer pH 7.4.

The data were fitted to the following equation:

$$Y = Y_{max} \frac{[E]_t + [PLP]_t + K_{D(PLP)} - \sqrt{([E]_t + [PLP]_t + K_{D(PLP)})^2 - 4\,[E]_t\,[PLP]_t}}{2[E]_t}$$

where $[E]_t$ and $[PLP]_t$ represent the total concentrations of the enzyme and PLP, respectively, Y refers to the intrinsic quenching changes at a PLP concentration, and Y_{max} refers to the fluorescence changes when all enzyme molecules are complexed with coenzyme. Curves fitting was performed using Origin® 9.1 Pro (OriginLab).

2.7. Enzyme activity assays

The decarboxylase activity was measured by a stopped spectrophotometric assay [29,30]. Each variant enzyme (at appropriate concentration) was incubated under saturating PLP concentration (10 μM) and different L-Dopa concentrations in a final volume of 250 μL in 100 mM potassium phosphate buffer pH 7.4 for a time within which a linear product formation is observed. The reaction was then stopped by heating at 100 °C for 2 min. TNB (1 ml of a 4.3 mM solution) and toluene (1.5 ml) were added and the extraction of trinitrophenyl-derivative was carried out at 42 °C for 45 min with continuous shaking. The concentration of trinitrophenyl-derivative in the toluene layer was quantified using prepared calibration curve of absorbance at 340 nm as a function of trinitrophenyl-derivative concentration [31]. The kinetic parameters were determined by fitting the data obtained with the Michaelis-Menten equation using Origin® 8 Pro (OriginLab).

2.8. Spectroscopic measurements

All spectral measurements were acquired in 100 mM potassium phosphate, pH 7.4, at 25 °C. CD measurements were recorded with a Jasco J-710 spectropolarimeter at a scan speed of 50 nm/min with a bandwidth of 2 nm at a protein concentration of 1–5 μM and 10 μM of exogenous PLP for the holoenzymes. Thermal denaturation was performed by monitoring the CD signal at 222 nm of 4 μM enzyme on a 25–90 °C linear temperature gradient, with a temperature slope of 1 °C/min. Intrinsic fluorescence emission spectra were monitored using a FP-750 Jasco spectrofluorometer at a protein concentration of 1 μM setting at 5 nm excitation and emission bandwidths upon excitation at 280 nm.

2.9. Dynamic light scattering (DLS)

Aggregation study was performed on a Zetasizer Nano ZS instrument (Malvern) with a constant 90° scattering angle and a 633 nm wavelength laser. Protein samples were prepared at 4 μM concentration under physiological conditions (58 mM potassium phosphate, pH 7.4 at 37 °C). The buffer was filtered immediately before the use.

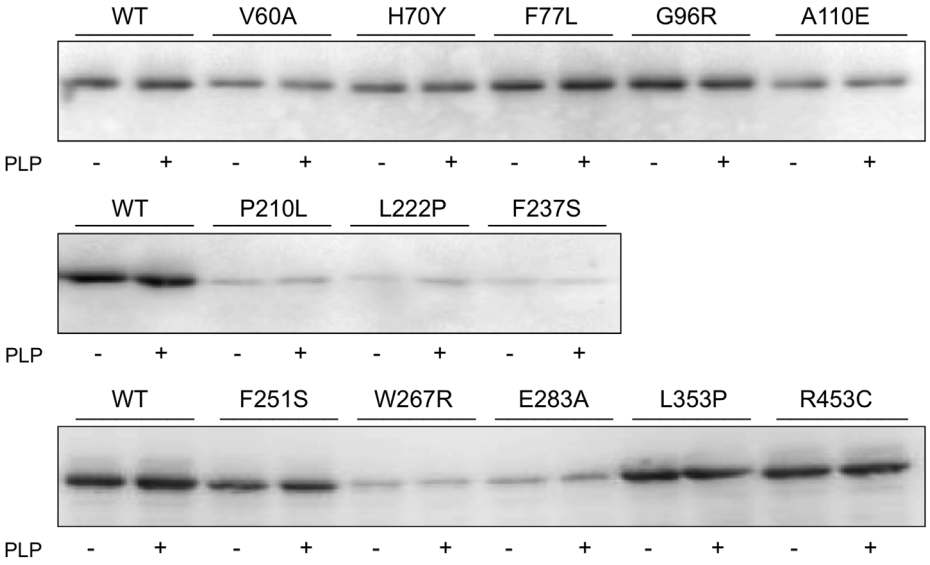

Fig. 2. Soluble fractions of WT and variants AADC. Western blot analysis is performed with 10 μg of total protein content from soluble lysates of *E. coli* loaded on 12% acrylamide gel. Each bacteria culture has been grown in absence (−) and presence (+) of exogenous PLP. Determination of the expression levels of each variant was estimated using ImageJ software (Fiji) and is reported in the text as percentage with respect to the WT.

2.10. HPLC analysis of coenzyme modification and dopamine formation

Catalytically inactive AADC variants were incubated at 10 μM protein concentration with 2 mM L-Dopa in 100 mM potassium phosphate buffer, pH 7.4 at 25 °C. Concentration-time curves were followed by withdrawing aliquots at time intervals and quenching the reaction by adding trichloroacetic acid to a final concentration of 10% (v/v). Proteins were then precipitated in ice and removed by centrifugation. Supernatants were analyzed by HPLC as described [32] using a Gemini C18 column (150 × 4.6 mm, Phenomenex, CA, USA) and performed on a Jasco PU-2080 Plus HPLC system equipped with a UV-1570 detector set at 295 nm. Samples were eluted in 50 mM potassium phosphate, pH 2.35, at a flow rate of 1 mL/min. Standard curves of peak area as a function of coenzyme or cyclic adducts concentration were prepared with commercially available PLP and coenzyme adducts obtained by synthesis.

2.11. NMR experiments

Before NMR analysis, the HPLC-purified compounds were exchanged in water, lyophilized and re-dissolved in D_2O. All the NMR spectra were recorded at 298 K on a 600 MHz Bruker AVIII HD spectrometer equipped with a TCI cryogenic probe. For the acquisition we used a spectral width of 20 ppm, an acquisition time of 1.36 s, 32,000 data points and 128 or 256 scans. NMR data were processed with Topspin 3.2. PLP and PMP peak assignments were confirmed by comparing the chemical shifts of the 1D 1H NMR spectra with those from reference spectra deposited in the Biological Magnetic Resonance Data Bank (BMRB). The 1H NMR peak assignments to the Pictet-Spengler adduct were verified by comparing the chemical shifts with previously reported resonances [33] and supported by 2D correlation NMR experiment (TOCSY).

2.12. Limited proteolysis in presence of the substrate analog DME

Protection studies against tryptic proteolysis were performed as described [32]. WT AADC and variants were incubated with the substrate analog DME at concentration of 2 mM for 30 s, 10 min and 30 min and then digested with trypsin for 10 min at the 1:50 (w/w) ratio. Proteolysis was stopped with the addition of trypsin inhibitor at the 1:10 (w/w) ratio and the reaction samples were then analyzed on a 10% (w/w) SDS-PAGE gel.

2.13. Bioinformatics analyses

Human AADC sequence was aligned with 75 homologues sequences retrieved form Uniref-90 database by the homolog search algorithm PSI-BLAST and aligned using Multiple Sequence Alignment software CLUSTALW on ConSurf server (http://consurf.tau.ac.il). A conservation score (9 = highly conserved, 1 = highly variable) was attributed to each residue. Structural analysis and *in silico* mutagenesis of the pig DDC (PDB: 1JS6; ~90% sequence identity with the human homologous) was carried out using Pymol 2.0 (The PyMOL Molecular Graphics System, Version 2.0 Schrödinger, LLC.). BindProfX was used to predict changes in binding affinity upon mutations in the form of ΔΔG (change in free energy of binding) values. The algorithm combines the FoldX physics-based potential with the conservation scores from pairs of protein-protein interaction surfaces sequence profiles. Interface residues and solvent accessible area (ASA) have been determined starting from the available crystal structure of pig DDC (PDB: 1JS6) by means of the Protein interfaces, surfaces and assemblies' service PISA at the European Bioinformatics Institute (http://www.ebi.ac.uk/pdbe/prot_int/pistart.html) [34].

3. Results

3.1. Solubility and purification yields of the new AADC variants

The 13 new AADC variants were examined for their presence in the soluble fraction. Soluble V60A, H70Y, F77L, G96R, A110E, F251S, L353P and R453C levels are similar with respect to the WT (more than 70%), while P210L, L222P, F237S, W267R and E283A are poorly expressed in the soluble fraction (10–30%) (Fig. 2). The addition of PLP did not significantly improve expression of either the WT or the variants. A low expression level might be related to a solubility alteration at least in *E. coli* system, suggesting folding defects for low expressed variants.

The insoluble fractions of the poorly expressed variants show that the amount of protein recovered in the pellet is slightly higher as compared to that of the WT (Fig. S1). However, considering the high soluble/insoluble ratio of WT AADC expressed in *E. coli* system, even subtle differences in insoluble fractions might be indicative of high differences in protein solubility.

Considering the protein yields after purification, some variants exhibit nearly good to good yields (30–85% with respect to the WT), including A110E, L353P, R453C, F251S, F77L and G96R. Others display low (5–10% for V60A and H70Y) and very low (less than 2% for E283A,

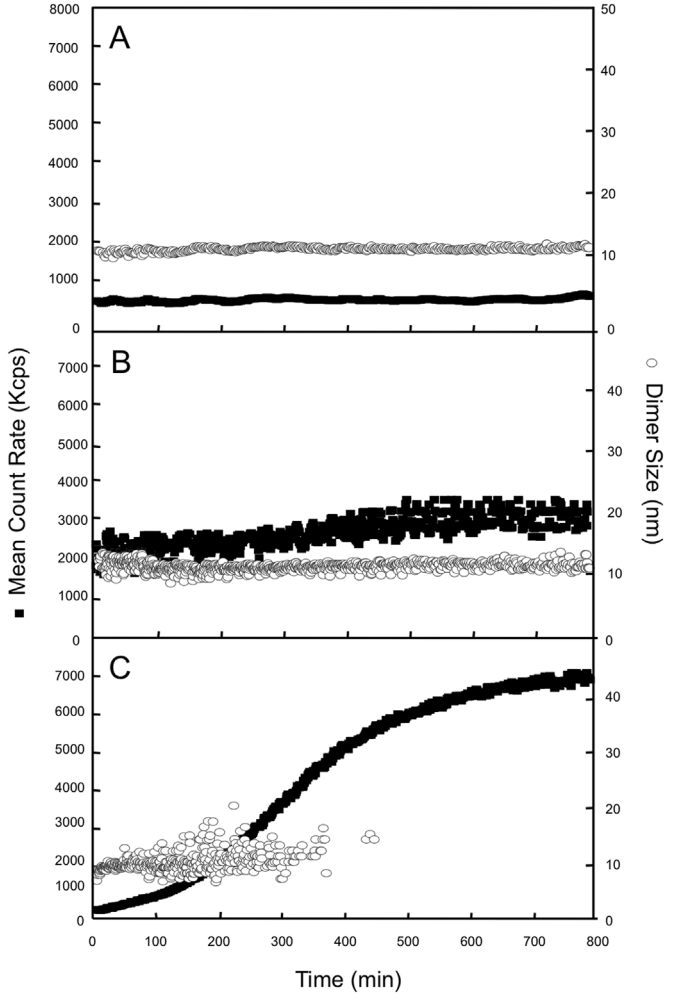

Fig. 3. DLS analyses of apo WT, apo P210L and apo E283A as a function of time. 4 μM apo WT (A), apo P210L (B) and apo E283A (C) are incubated in 58 mM potassium phosphate buffer pH 7.4 at 37 °C. Grey open symbols indicate the size of the dimer, solid squares indicate the mean count rate.

P210L and W267R) yields. Unfortunately, it was not possible to purify L222P and F237S which were recovered in extremely low amounts (0.3%) preventing us to carry out a complete biochemical characterization.

3.2. Aggregation of apoP210L and apoE283A

Given the great variability in both solubility level and purification yield of the analyzed variants (already reported in sporadic cases for other characterized AADC variants [25,35–37]), DLS analyses were carried out in order to evaluate the aggregation propensity of the purified enzymes under physiological conditions (58 mM potassium phosphate buffer, pH 7.4 at 37 °C). DLS measurements of the holo and apo forms of the majority of AADC variants and of WT (Fig. 3A) do not show signs of aggregation suggesting that the enzyme is not prone to aggregate under these experimental conditions. Instead, apoP210L and apoE283A, even if at different extent, tend to aggregate as demonstrated by both the increase in kcps and the disappearance of the dimeric species (Fig. 3B and C). While dimeric apoE283A disappears in about 300 min, apoP210L aggregation process is much slower. This led us to conclude that some AADC variants in their apo form are prone to undergo an aggregation process.

Table 2
Melting Temperatures of WT AADC and variants. Melting temperature values obtained by following the CD signal at 222 nm and varying the temperature linearly from 25 to 90 °C with a slope of 1.5 °C/min.

T_m (°C)		
Enzyme	holo	apo
WT	69.42 ± 0.02	64.84 ± 0.03
V60A	62.13 ± 0.02	59.30 ± 0.03
H70Y	65.95 ± 0.04	63.28 ± 0.05
F77L	63.58 ± 0.03	61.70 ± 0.03
G96R	65.64 ± 0.05	58.46 ± 0.04
A110E	63.20 ± 0.05	62.04 ± 0.04
P210L	66.10 ± 0.10	60.91 ± 0.05
L222P	n.d	n.d
F237S	n.d	n.d
F251S	70.49 ± 0.04	63.37 ± 0.06
W267R	70.30 ± 0.10	63.60 ± 0.03
E283A	62.89 ± 0.02	58.66 ± 0.07
L353P	68.10 ± 0.07	60.82 ± 0.03
R453C	69.36 ± 0.03	66.70 ± 0.02

3.3. Secondary structure and thermal stability of the new AADC variants

The structural integrity of all variants in terms of secondary structure has been evaluated by measuring the far-UV CD spectra of all purified variants in the 190–260 nm region. The signals are superimposable to that of the WT indicating that the substitutions do not alter the secondary structure of the protein (data not shown). In order to determine the intrinsic stability, we measured the T_m's of holo and apo forms of all variants (Table 2) by following the loss of the dichroic signal at 222 nm under physiological conditions (58 mM potassium phosphate buffer, pH 7.4).

As for the holo proteins, the value of T_m for F251S, W267R, L353P and R453C is almost identical to that of the WT. Instead, the ΔT_m value ($T_{m(variant)}$-$T_{m(WT)}$) is consistently lower for V60A, A110E and E283A followed by F77L, G96R, H70Y and, to a lesser extent, P210L.

The apo species of V60A, G96R and E283A evidence a marked decrease in T_m with respect of the WT, followed by L353P, P210L, F77L and A110E, while the others exhibit ΔT_m of ± 2 °C.

It is interesting to note that the $\Delta T_{m(holo-apo)}$ for the WT is of about 5 °C. This value, indicative of the different thermal stability of the holo and the apo form, is maintained (or even increased) for all variants but V60A, H70Y, F77L, A110E, and R453C.

3.4. Aromatic amino acids dichroic and fluorescence signals and coenzyme dichroic microenvironment features of the new AADC variants

We then measured signals, collected by near UV-CD and intrinsic fluorescence, related to aromatic amino acids environment to monitor possible folding alterations in AADC variants. The near UV-CD at 280 nm provides insight into asymmetric aromatic amino acid residues, mainly tryptophan(s), located in an appropriate position, and is linked to a proper protein tertiary structure arrangement. While the holo forms of G96R, P210L, F251S, and E283A have a 280 nm CD signal very similar to that of the WT, the other variants exhibit decreases in the intensity of the 280 nm band, although at different extent, particularly relevant in V60A, F77L and A110E (Fig. 4A and B). Since the apo form has a spatial arrangement different from the holo one [27], it is useful to compare the 280 nm CD signals of the apo variants in order to better understand how substitutions exert their effects on the entire protein structure or if the modifications are confined to the PLP binding region. An analysis of the CD near UV bands of the apo forms (insets of Fig. 4A and B) reveals that they are almost superimposable to that of the WT, unless a subtle decrease of the 280 nm band in G96R, F251S and E283A and a more evident one in V60A and R453C.

Interestingly, the signals in the near UV region of the holo forms of

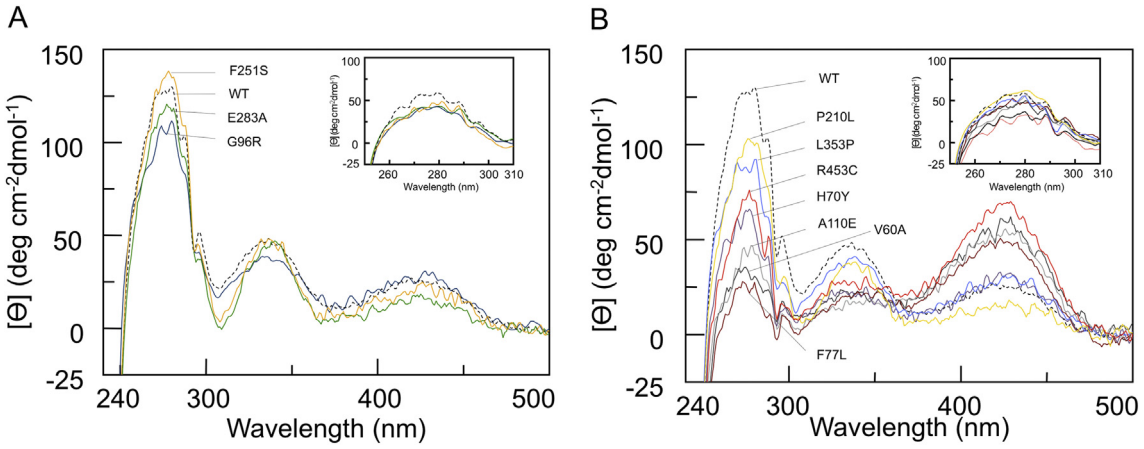

Fig. 4. Near UV and visible CD spectra of WT AADC and variants in their holo and apo forms. The spectra are recorded at 5 μM protein concentration, in 100 mM potassium-phosphate buffer, pH 7.4. Spectra of the holo forms are recorded in the presence of 10 μM PLP. (A) The holo forms of: WT, F251S, E283A, G96R. (B) The holo forms of: WT, P210L, L353P, R453C, H70Y, A110E, V60A and F77L. Spectra of the corresponding apo forms are reported in the insets.

V60A, F77L, and A110E are not so much different from the corresponding ones in the apo species.

The intrinsic fluorescence signal is measured to provide insight into the correct folding features of the enzyme. Following excitation at 280 nm, the fluorescence spectrum of holo WT is characterized by an emission spectrum with a maximum at 332 nm indicative of the buried environment of the aromatic amino acid residues (Fig. S2). Those variants displaying a decrease of the 280 nm CD band present in general an emission band higher than that of the WT, while the 332 nm fluorescence emission is similar to that of the WT for the other variants whose 280 nm CD band is identical or similar to that of the WT. Considering that consistent alterations of tertiary structure were found mainly in the holo forms, the deleterious effects of mutations are reasonably due to an impairment in the correct holo folding rather than to the achievement of the spatial structure of the apo form.

It should be remembered that the apo WT emits at nearly the same wavelength as the holo but with higher intensity values given to different position of aromatic amino acids in this structure or to the energy transfer process from aromatic side chains fluorophores to the pyridine ring of the cofactor. This suggests that some variants remain in a sort of apo structure being somewhat prevented in the apo-to-holo transition or in the acquirement of a correct holo folding, as evidenced above.

Altogether, these spectroscopic results witness slight alterations in global protein folding of the new variants.

As for possible coenzyme microenvironment modifications, we measured the visible CD spectrum of all species. WT AADC presents two bands centered at 335 nm and 420 nm indicative of a tautomeric equilibrium between the enolimine and the ketoenamine forms of the internal aldimine that PLP forms with Lys-303. The spectra of the new variants display small differences with respect to the WT. In details, the spectra of H70Y, G96R, F251S and L353P are similar to that of the WT, while P210L and E283A exhibit a 420 nm band lower than the corresponding one of the WT. On the contrary, V60A, F77L, A110E and R453C show a predominance of the ketoenamine over the enolimine tautomer (Fig. 4A and B). Since this tautomeric equilibrium is unrelated with catalytic efficiency (see below), these results only reveal subtle PLP microenvironment modifications influencing the tautomeric equilibrium of the internal aldimine.

3.5. Kinetic parameters and apparent PLP equilibrium dissociation constants, $K_{D\ PLP}$, of new AADC variants

The purified variants were functionally characterized by measuring their kinetic parameters. It could be observed (Table 3) that the catalytic efficiencies of P210L, F251S and E283A are not so much affected

Table 3
Steady-state kinetic parameters and apparent equilibrium dissociation constant, Kd, for PLP of the new AADC variants.

Enzyme	k_{cat} (s^{-1})	K_m (mM)	k_{cat}/K_m (s^{-1} mM^{-1})	$K_{D\ PLP}$ (nM)
WT	7.6 ± 0.1	0.11 ± 0.01	69.1 ± 10	43 ± 12
V60A	0.93 ± 0.02	0.16 ± 0.01	5.8 ± 0.4	252 ± 35
H70Y	0.58 ± 0.09	0.26 ± 0.04	2.2 ± 0.5	70 ± 18
F77L	0.35 ± 0.07	0.51 ± 0.05	0.7 ± 0.1	222 ± 38
G96R	5.7 ± 0.4	3.5 ± 0.4	1.6 ± 0.2	132 ± 14
A110E	n.d.	n.d.	n.d.	321 ± 26
P210L	4.4 ± 0.2	0.12 ± 0.02	37 ± 6	47 ± 7
L222P	n.p.	n.p.	n.p.	n.p.
F237S	n.p.	n.p.	n.p.	n.p.
F251S	5.7 ± 0.2	0.26 ± 0.02	22.0 ± 0.2	88 ± 16
W267R	2.11 ± 0.04	0.19 ± 0.01	11.1 ± 0.6	120 ± 10
E283A	6.4 ± 0.2	0.29 ± 0.05	22.0 ± 0.2	330 ± 30
L353P	n.d.	n.d.	n.d.	199 ± 34
R453C	0.67 ± 0.07	0.40 ± 0.06	1.7 ± 0.3	468 ± 36

n.d., not detectable under standard assay conditions; n.p., not purified.

being 52%, 31% and 31%, respectively, compared to that of the WT. These values are due to a small decrease in k_{cat} and nearly equal K_m values for P210L, while in F251S and E283A the decrease of k_{cat} is negligible with respect to that of the WT and K_m is slightly increased.

W267R exhibits a catalytic efficiency value of 15% with respect to WT caused by a decrease in k_{cat} of about 70% and an increase in K_m of about 1.7-fold.

The other variants (V60A, H70Y, F77L, G96R and R453C) are characterized by a marked decrease in catalytic efficiency. This drop is due to a concomitant strong decrease in k_{cat} (mainly for V60A and H70Y) and increase in K_m (mainly for G96R) or both (F77L and R453C). Notably, A110E and L353P are catalytically incompetent under the standard assay conditions.

As for the coenzyme binding affinity, while the $K_{D\ PLP}$ is almost invariant for H70Y and P210L, it increases by 2 up to 5-fold in F77L, G96R, F251S, W267R and L353P and by 6 up to 10-fold in V60A, A110E, E283A and R453C. Thus, the cofactor in many variants is mispositioned and its contacts with the protein moiety are somewhat altered, as also witnessed by the visible CD signals.

3.6. Some AADC variants convert PLP into cyclic Pictet-Spengler adduct in the presence of L-Dopa

Among the variants, A110E and L353P seem to be severely impaired in catalysis since the kinetic parameters could not be measured under the standard assay conditions. Noteworthy, the addition of L-Dopa to

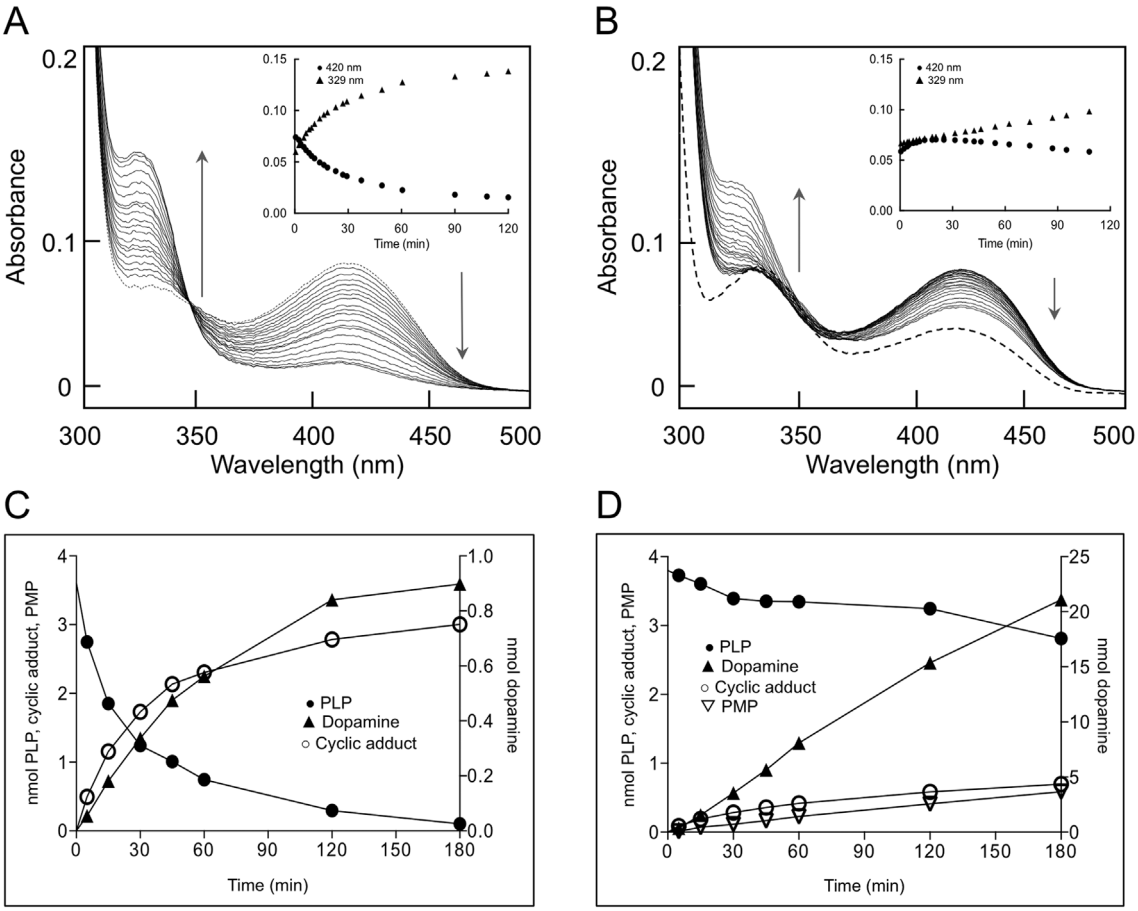

Fig. 5. Absorbance spectra of A110E and L353P in the presence of L-Dopa. To a solution of 10 μM A110E (**A**) and L353P (**B**), L-Dopa has been added and spectra are recorded with time in 100 mM potassium phosphate buffer, pH 7.4 at 25 °C. Dotted line: variant without L-Dopa. The arrows indicate the increase at 329 nm and the concomitant decrease at 420 nm with time following addition of 2 mM L-Dopa. Insets: increase of the 329 nm and decrease of the 420 nm signals as a function of time. HPLC analyses results of the reaction mixture of 10 μM A110E (**C**) and L353P (**D**) in the presence of 2 mM L-Dopa in 100 mM potassium phosphate buffer, pH 7.4 at 25 °C. PLP (●), Pictet-Spengler PLP-L-Dopa (◯), dopamine (▲) and PMP (▽).

Table 4
Initial velocities of dopamine formation, PLP decrease, Pictet-Spengler and PMP increase following reaction of 10 μM A110E or L353P or 20 μM PLP with 2 mM L-Dopa.

initial velocity (v_0) (nmol/min/nmol)	A110E	L353P	free PLP
v_0 dopamine	0.006 ± 0.001	0.067 ± 0.001	–
v_0 PLP decrease	0.040 ± 0.004	0.006 ± 0.002	0.12 ± 0.01
v_0 Pictet-Spengler	0.042 ± 0.006	0.005 ± 0.003	0.10 ± 0.04
v_0 PMP	–	0.002 ± 0.00005	–

both A110E and L353P leads to a decrease of the 420 nm absorbance band and an increase of the 335 nm band that slightly shifts to 329 nm with time. These absorbance bands are associated with the coenzyme bound at the active site. The spectral modifications are indicative of a reaction determining the conversion of the external aldimine between PLP and L-Dopa into an intermediate absorbing at ~330 nm, already observed for other AADC variants [35,38] located in proximity of the active site and attributed to the Pictet-Spengler adduct [33]. The process is faster in A110E and slower in L353P (Fig. 5A and B). A reaction mixture containing 10 μM A110E or 10 μM L353P with 2 mM L-dopa has been treated and subjected to HPLC analysis, as reported in Materials and Methods section. As shown in Fig. 5C and D, in both cases the PLP content decreases with an initial rate similar to that of the increase of the Pictet-Spengler cyclic adduct [32,33]. Table 4 shows the initial velocities, measured as slopes in the linear part of each curve (PLP decrease and Pictet-Spengler increase) for the two variants in comparison with free PLP under the same experimental conditions. It should be noted that a small amount of dopamine is also produced by both variants (Table 4). Given the fact that WT forms dopamine in the presence of saturating L-Dopa (2 mM) with an initial velocity of 7.6 nmol/s/nanomol of enzyme (Table 3), it follows that the initial velocity of A110E is approximately 7.6×10^4 times and that of L353P of 6.8×10^3 times slower than that of the WT value under the same experimental conditions. It should be noted that, in the case of L353P, a small aliquot of pyridoxamine 5′-phosphate (PMP) is formed, due to the ability of AADC to catalyze multiple side reactions in addition to the main decarboxylation one [33].

While free PLP incubated with L-Dopa forms the cyclic adduct with an initial rate faster than in the two variants (Table 4), WT AADC does not form it since the protein moiety prevents unwanted reactions of its highly reactive coenzyme. This suggests that in both A110E and L353P the altered enzyme active site structure renders PLP rather free. The identification of the Pictet-Spengler adduct between L-Dopa and PLP was confirmed by NMR analyses [33] (Fig. S3). In order to check if the active site of the two catalytic variants is somewhat open or not capable of attaining the correct closed and catalytically competent conformation, we added to WT, A110E and L353P the substrate analog DME that binds to PLP but is unable to undergo decarboxylation. At the indicated times (Fig. 6), we subjected the enzyme-analog complex to limited proteolysis to monitor the extent of protection. It has been already demonstrated that [33] a protection from proteolysis is indicative of active site correct closure and productive catalysis. While WT does

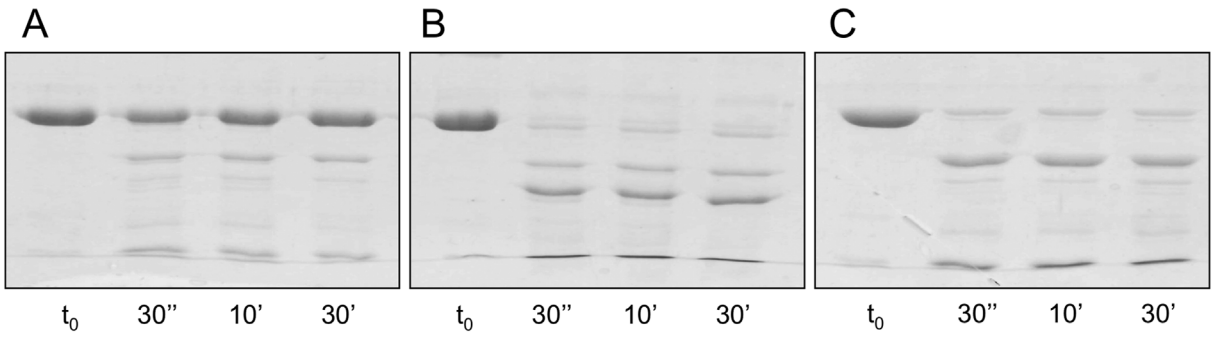

Fig. 6. Limited tryptic proteolysis of WT (A), A110E (B) and L353P (C) in the presence of DME. WT, A110E and L353P are incubated at a concentration of 10 μM protein with 2 mM DME for various times and then digested with trypsin for 10 min at the trypsin/enzyme ratio 1:50 (w:w). t_0 is the control in the absence of trypsin.

protect from proteolysis, both A110E and L353P do not protect, suggesting that some structural elements of the active site are altered and the closed catalytically competent conformation could not be attained.

3.7. Bioinformatic analyses

In order to verify the conservation level of the newly identified residues of AADC undergoing pathogenic substitution, the AADC amino acid sequence was aligned with those of 75 homologous proteins by the ConSurf web server. About 60% of the modified residues are highly conserved (His-70, Phe-77, Ala-110, Leu-222, Phe-251, Trp-267, Glu-283 and Leu-353). Phe-237 is quite conserved and substituted only by apolar residues or amino acids endowed by a π-system. The others have a low conservation score, although the chemical nature of the residues (polar or apolar) is maintained for Val-60, Gly-96 and Pro-210, while Arg-453 resulted more prone to be substituted by several amino acids in homologous enzymes (Table S2).

A bioinformatic analysis examining the arrangement of each residue undergoing substitution was then carried out to understand the *in-silico* impact of each substitution on protein structure and/or binding networks (Fig. 7A).

Each monomer of AADC is composed of three domains: the N-terminal domain (residues 1–85) which comprises the structural element loop1 (residues 66–84), the large domain (residues 86–360), which in turn includes loop2 (residues 100–110), the PLP-Lys-303 loop (residues 300–310) and loop3 (residues 323–357, containing the flexible catalytic loop 328–339), and, finally, the C-terminal domain (residues 361–480) [26,27]. In the holo dimer the two monomers are strictly intertwined leading to a large interlocked interface and, as for the active site, the flexible catalytic loop together with loop1 of each subunit directly interacts with elements of the loops 2 and 3 of the neighbouring one [27]. As for the role played by these key loops: loop1 is located in proximity to the active site and is involved in the apo-to-holo conformational change of AADC [27], loop2 hosts residues near the active site, possibly interacting with the substrate moiety [25,26], and loop3 is functionally essential for catalysis [26,27,31,39].

Starting from the N-terminal stretch, Val-60 contributes to the monomer-monomer interface and its side chain engages the helix 85–99, that connects loop1 to loop2, of the neighbouring subunit by several hydrophobic contacts (Fig. 7B). V60A modification reduces the inter-chain hydrophobic contacts within the two N-terminal regions of the AADC dimer. Moreover, the mispositioning of the helix 52–67, due to the substitution of Val-60 with Ala, affects the conformation of loop1. His-70 and Phe-77 belong to loop1. In particular, His-70 side chain interacts with Tyr-20 by an H-bond linkage, while Phe-77 is involved mainly in a base-stacking interaction with the Phe-448 side chain (Fig. 7C). Together His-70 and Phe-77 represent two anchoring points of loop1 and, of course, of the N-terminal and to the C-terminal domain influencing loop1 correct positioning.

Gly-96 belongs to helix 85–99 at the end of loop1 and just before the beginning of loop2 (Fig. 7B). Its backbone oxygen interacts with the Asn-308 side chain of the adjacent monomer in proximity of the active site. The G96R substitution could generate a consistent steric hindrance between the two antiparallel helices 85–99 probably perturbing the dimer assembly and the active site.

Ala-110 is the last residue of loop2, belongs to the monomers interface and is placed into an apolar cavity (Fig. 7D) at the beginning of the large domain. Its substitution with glutamate generates local steric hindrance between the two subunits and seems to exert some effects on the position of residues present at the active site (i. e. Phe-103 and Ile-101, that face PLP, and are part of loop2). This is corroborated by results obtained in the biochemical characterization and the molecular dynamics simulation of the recombinant A110Q protein [25].

Pro-210, Leu-222, Phe-237 and Trp-267 belong to a β-barrel-helices system of the large domain that surrounds the active site. Such complex architecture is highly conserved in the large domain of PLP-dependent enzymes. In details, Pro-210 is placed on a flexible surface stretch (aa 209–218) joining a β-strand to a surface α-helix (Fig. 7E). The P210L substitution exposes a hydrophobic residue on the protein surface probably inducing local structural rearrangement. Leu-222 belongs to the α-helix 218–232 and lies into a hydrophobic cleft (Fig. 7E). The exchange to Pro could alter, or even interrupt, the α-helix folding causing a dramatic structural effect. Phe-237 and Trp-267 lie on two adjacent β-sheet elements and are involved in several hydrophobic contacts contributing to the folding features of the β-barrel (Fig. 7F). It can be expected that the drastic changes of polarity and dimension of the residues introduced by the F237S or W267R substitutions could affect the proper folding of the β-strand/helices packaging.

Phe-251 lies on the loop 243–252 in proximity of the protein surface and takes place to a hydrophobic network involving residues of the large and C-terminal domains (Fig. 7G). The substitution F251S does not generate significant steric hindrance but it is expected to abolish most of the hydrophobic contacts.

Glu 283 is exposed on the protein surface and contacts by a salt bridge the Arg 379 side chain (Fig. 7H). This interaction represents the only connection between the helix 283–294 and the helix 372–395 and, on the basis of the local microenvironment, might prevent the exposure of hydrophobic residues to the solvent. The E283A substitution abolishes such interaction and therefore generates a local conformational change by altering the relative position of surface secondary structure elements.

Leu-353 belongs to loop3 of the large domain, and, in particular, is placed at the dimer interface, near the active site, at a proper distance to interact by hydrophobic contact with two residues: Phe-103, a residue essential for the active site conformation [26] and Arg-347, a key catalytic residue [25,31] (Fig. 7D). This network is established in a region critical for catalysis and the substitution of Leu with Pro might determine deep effects on the active site architecture.

Lastly, Arg-453, even if it belongs to the C-terminal domain, provides an additional junction between the C-terminal domain and the

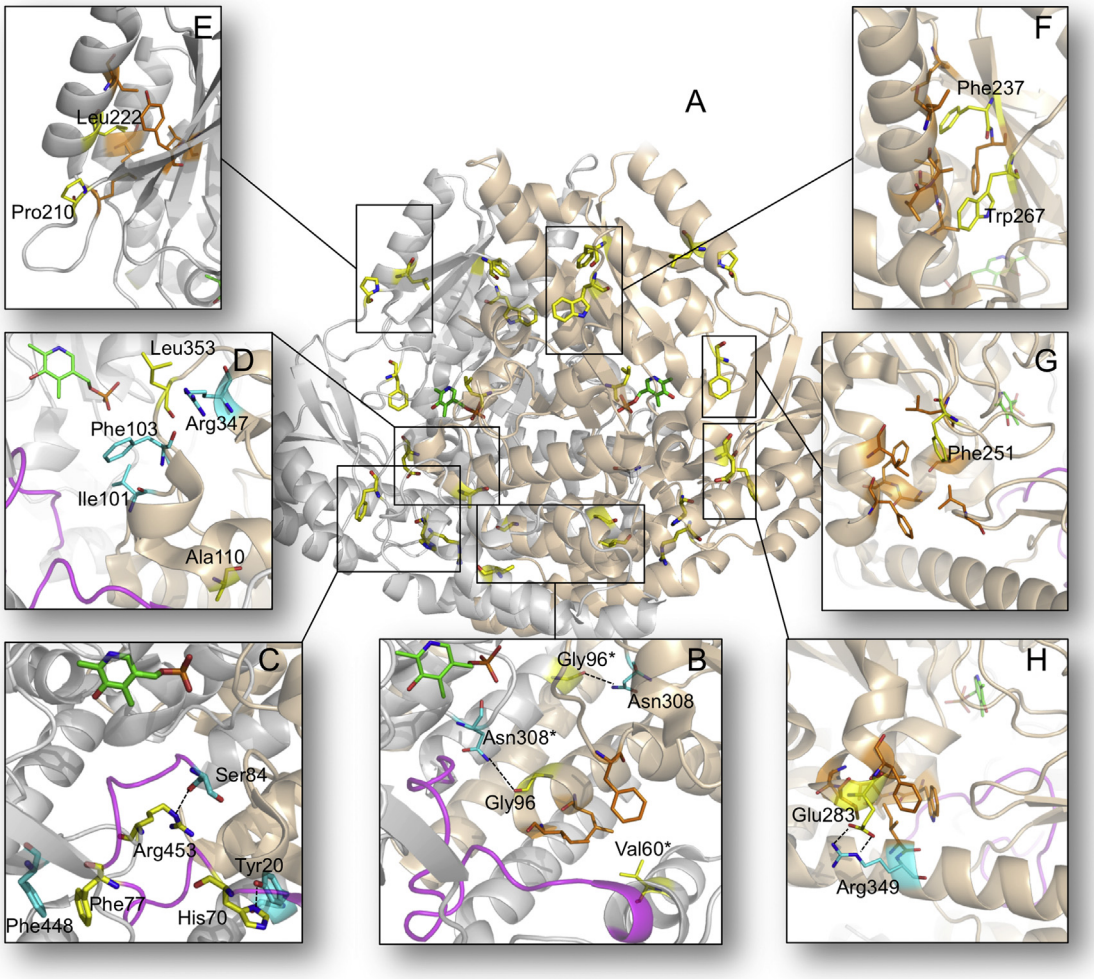

Fig. 7. ***In silico*** **inspection of the mutation sites**. Ribbons representation of the holo AADC (pdb ID 1JS6). The two monomers are white and light orange, respectively, loop1 (aa 66–84) is magenta and PLP molecules are represented as green sticks. In each panel: (i) the mutation sites are indicated and represented as yellow sticks; (ii) specific interacting residues are in cyan; (iii) clusters of hydrophobic residues are represented as orange sticks. *residues belonging to the neighbouring subunit. Image was rendered by PyMol software (Schrödinger). (For interpretation of the references to colour in this figure legend, the reader is referred to the Web version of this article.)

loop1, in fact the arginine side chain interacts with the Ser-84 backbone oxygen through an H-bond (Fig. 7C) and would favour loop1 correct conformation. Moreover, Arg-453 side chain is in proper position to interact with Met-1 backbone oxygen of the neighbouring subunit by a H-bond contributing to the monomer-monomer interaction.

Considering that a significant number of the new mutations are localized at the dimer interface (V60A, G96R, A110E, L353P and R453C), we predicted the values of ΔΔG of the monomer-monomer interaction of WT AADC and of all interface variants using BindProfX (Table S3). Results indicate that, even if at different extent, all the interface mutations significantly destabilize the AADC dimer interface.

4. Discussion

In an effort to understand the molecular bases of AADC deficiency, our biochemical approach is aimed to unravel the structure-function relationships of the so-far identified variants in order to elucidate the enzymatic phenotypes. The present study is focused on 13 new pathogenic variants of AADC reported in literature from 2014 to 2019 in homozygosis and hemizygosis. At a first glance, it can be observed that these new amino acid substitutions are spread on the entire protein and not only in the central belt as the previously characterized mutations [25]. Until now, the previously studied enzymatic phenotypes resulted in impaired apo-to-holo transition and catalysis [25,31,35,40].

Following the investigations previously published [25], the loop1 variants H70Y and F77L resemble, in terms of catalytic efficiency and of structural conformation, the already studied ones affecting loop1 [25]. They are characterized by a drop in k_{cat} and in catalytic efficiency. Less evident are the effects regarding $K_{D(PLP)}$. This behaviour is reasonably due to a stabilizing function of this region [25], whose alteration causes perturbation of both protein conformation and active site architecture. Moreover, the ΔT_m's values with respect to the WT of both holo and apo proteins are notable and the holo-to-apo T_m's difference is diminished with respect to the WT, evidencing that substitutions in loop1 are characterized by a lesser variation in terms of degrees, arguing that these enzymatic species resemble apo rather than holo structures, as also shown by their spectroscopic signals. Interestingly, the clinical phenotypes of patients carrying these mutations are severe [10,13]. Overall, these new data support the fact that loop1 is crucial for apo-holo transition as suggested by Ref. [25].

In addition to this, the remaining newly characterized variants allowed us to widen the spectrum of enzymatic phenotypes related to AADC deficiency. In particular, an interesting cluster of variants is represented by those belonging to the large domain (P210L, L222P, F237S, F251S, W267R and E283A). The bioinformatic analysis reveals that these residues are located either on the surface (P210L, F251S and

E283A) or in hydrophobic environments (L222P, F237S and W267R). Except for F251S (see below), all of them are characterized by a low (or null) recovery in the soluble fraction.

Since their apo near UV CD signals are similar to that of the apo WT and their holo near UV CD as well as intrinsic fluorescence spectra are not so much affected, it follows that these purified proteins do not present deep changes in their global structure. This can be correlated to the good catalytic efficiency as well as the quite high PLP affinity, unless for E283A, displayed by these variants. Thus, another mechanism for the pathogenicity for this class of variants should be considered in addition to the already proposed ones [25]. Indeed, the DLS analysis shows that apoE283A and apoP210L have a tendency to aggregate, while neither WT nor any of the other characterized variants has. Even if the time course of disappearance of the dimeric apoE283A and apoP210L is slow under our experimental conditions, it might represent a signal of a trend for these proteins to undergo an aggregation process in their apo form that in part explains the reason why the expression of these variants is so low. Only a small fraction is thus able to reach a competent state binding the coenzyme and performing catalysis, while the great part undergoes aggregation in the apo form. Notably, in the highly crowded cellular microenvironment the aggregation process might be reinforced and facilitated, even if we have no information regarding relative rates of aggregation with respect to apo-to-holo transition. Interestingly, these two variants present a large effect of ΔT_m of the holo and apo form with respect to holo and apo WT, suggesting that their structure is more labile. Consistently, the very low T_m value of apoE283A may be correlated with the aggregation propensity of this variant. The bioinformatic analyses support the possible protein misfolding effect caused by these variants. The affected soluble expression level of the other large domain variants suggests possible folding defects, whose process should be studied in a more appropriate cell model, as performed previously [40]. The low expression is also in line with what we have observed for R160W variant [37]. The reported clinical phenotypes of patients carrying these mutations are from mild to severe. Patients with F237S substitution have rather mild manifestations compared to others [12], reaching adulthood and for one of them a successful pregnancy has been reported [41]. The other clinical phenotypes are from intermediate to severe [13,42], suggesting that alterations in the large domain could give rise to a wide spectrum of disease outputs.

Phe-251 is an exception for this cluster of residues in the large domain since its substitution to Ser gives rise to a protein variant which behaves in a similar way to the already characterized S250F variant [40]. The bioinformatic analysis of F251S shows the modest effect exerted that is in line with the results obtained and with the mildness of the clinical phenotype of the patient [14]. This variant is only slightly affected by the substitution in catalytic parameters, in PLP affinity and in the spectroscopic signals.

Considering the remaining new variants (V60A, G96R, A110E, L353P and R453C), their common feature is the belonging to the large interface of AADC. This interface comprises 144 residues of the total 480 amino acids of each monomer and covers the 27.3% of the total solvent-accessible area (ASA) of each subunit. In comparison, the dimer interface of the prototype of Fold-Type I PLP-enzymes, aspartate aminotransferase, covers only 19.8% of the total ASA. The AADC interface goes through the contact surface of the two subunits crossing different regions from the N-terminal to the large domain and to, finally, the C-terminal. Taken together, interface variants could be distinguished in those showing modest effects on catalysis (V60A, G96R and R453C) or large catalytic drops (A110E and L353P). This is expected since they affect different protein regions and may exert long-range effects acting at the strictly tight monomer-monomer interface of AADC. Since the active sites are at the interface, a defect in this wide part of the protein might affect catalysis and/or coenzyme binding.

The interface variants V60A, G96R and R453C are characterized by a low catalytic efficiency due to low k_{cat} for V60A and R453C and high K_m for G96R. This could be also mirrored by the fact that the affinity for the coenzyme is compromised in V60A and R453C, as well as the environment of aromatic amino acids, and decreased in G96R. Their ΔT_m variations are similar to those recorded for loop1 variants, however the measured $\Delta\Delta G$ values show that the interaction networks between monomers is here affected. The bioinformatic analyses show that Val-60 and Gly-96 maintain the protein interface and are thus involved in dimer assembly, while the effect of Arg-453 on interface affects N-terminal and loop1 proper positioning. Notably, V60A and G96R display the lowest values of T_m for their apo structures, supporting the stabilizing role for this interface region. The effects for R453C are less pronounced and this might in part be related to the observation that patients with R453C substitution have a milder clinical phenotype than the others of this group [43].

A110E and L353P are interface variants with strong catalytic impairments. Both A110E and L353P exhibit a change in the aromatic amino acid environment even if at a different extent. Moreover, the lack of catalytic activity, the irreversible trapping of the coenzyme into a cyclic inactive form and the incapability of these variants to protect from proteolysis in the presence of the substrate analog DME, witness a direct effect of the substituted residues in the active site. This effect is expected since both residues are located in proximity to critical amino acids at the active site such as Ile-101, Phe-103 and Arg-347. The critical role of Arg-347 has already been discussed [31]. Other AADC variants near the active site have been previously described and were able to perform Pictet-Spengler condensation reaction [35] even if at a slower rate. The $\Delta\Delta G$ value for A110E and L353P is positive and suggests that a proper active site closure depends on a productive dimeric assembly. This alteration is also witnessed by changes in T_m values with respect to the WT of both holo and apo A110E (whose $\Delta T_{m(holo\text{-}to\text{-}apo)}$ in terms of degrees is of only 1 °C) and apo L353P. It derives that AADC residues affecting catalysis are positioned not only at the active site but also at the dimer interface affecting elements of the active site directly (such as Leu-353) or by long-range interactions (such as Ala-110). It is not strange that patients bearing these mutations are severely affected [13,44].

Altogether, the combination of bioinformatic analyses with biochemical data has been useful in defining the behaviour of enzymatic variants and deepens the knowledge on enzymatic phenotypes. We have here characterized a new enzymatic phenotype leading to aggregation of AADC variants that open the way on investigations regarding the variants with the hallmark of being low expressed. Furthermore, we have encountered new types of variants located at the protein interface able to play short-range (L353P) and long-range (V60A, G96R, A110E and R453C) effects at the active site, highlighting the importance of the large interface of AADC in protein proper functioning.

The ultimate aim of our approach is to correlate the position of each mutation occurring in a defined protein region to the severity of the enzymatic phenotype in order to contribute in the understanding of the clinical phenotype.

Funding

The contribution of Agilis Biotherapeutics-PTC and of the AADC Research Trust is gratefully acknowledged.

CRediT authorship contribution statement

Riccardo Montioli: Formal analysis, Writing - original draft. **Giovanni Bisello:** Formal analysis. **Mirco Dindo:** Formal analysis. **Giada Rossignoli:** Formal analysis. **Carla Borri Voltattorni:** Conceptualization, Supervision. **Mariarita Bertoldi:** Conceptualization, Funding acquisition, Supervision, Writing - original draft, Writing - review & editing.

Acknowledgments

We would like to acknowledge Dr. Serena Zanzoni, Centro Piattaforme Tecnologiche, Università di Verona, for the NMR analyses and Silvia Bianconi for the excellent technical support. We would like to thank Prof. Andrea Mozzarelli for critical reading of the manuscript.

Appendix A. Supplementary data

Supplementary data to this article can be found online at https://doi.org/10.1016/j.abb.2020.108263.

References

[1] K. Hyland, P.T. Clayton, J. Inherit. Metab. Dis. 13 (1990) 301–304.
[2] K. Hyland, R.A. Surtees, C. Rodeck, P.T. Clayton, Neurology 42 (1992) 1980–1988.
[3] W. Lovenberg, H. Weissbach, S. Udenfriend, J. Biol. Chem. 237 (1962) 5.
[4] M. Bertoldi, Arch. Biochem. Biophys. 546 (2014) 1–7, https://doi.org/10.1016/j.abb.2013.12.020 S0003-9861(13)00394-9 [pii].
[5] K.J. Swoboda, K. Hyland, D.S. Goldstein, K.C. Kuban, L.A. Arnold, C.S. Holmes, H.L. Levy, Neurology 53 (1999) 1205–1211.
[6] R. Pons, B. Ford, C.A. Chiriboga, P.T. Clayton, V. Hinton, K. Hyland, R. Sharma, D.C. De Vivo, Neurology 62 (2004) 1058–1065.
[7] G.F. Allen, J.M. Land, S.J. Heales, Mol. Genet. Metab. 97 (2009) 6–14, https://doi.org/10.1016/j.ymgme.2009.01.010 S1096-7192(09)00010-9 [pii].
[8] L. Brun, L.H. Ngu, W.T. Keng, G.S. Ch'ng, Y.S. Choy, W.L. Hwu, W.T. Lee, M.A. Willemsen, M.M. Verbeek, T. Wassenberg, L. Regal, S. Orcesi, D. Tonduti, P. Accorsi, H. Testard, J.E. Abdenur, S. Tay, G.F. Allen, S. Heales, I. Kern, M. Kato, A. Burlina, C. Manegold, G.F. Hoffmann, N. Blau, Neurology 75 (2010) 64–71, https://doi.org/10.1212/WNL.0b013e3181e620ae WNL.0b013e3181e620ae [pii].
[9] T. Wassenberg, M. Molero-Luis, K. Jeltsch, G.F. Hoffmann, B. Assmann, N. Blau, A. Garcia-Cazorla, R. Artuch, R. Pons, T.S. Pearson, V. Leuzzi, M. Mastrangelo, P.L. Pearl, W.T. Lee, M.A. Kurian, S. Heales, L. Flint, M. Verbeek, M. Willemsen, T. Opladen, Orphanet J. Rare Dis. 12 (2017) 12 10.1186/s13023-016-0522-z10.1186/s13023-016-0522-z [pii].
[10] C. Manegold, G.F. Hoffmann, I. Degen, H. Ikonomidou, A. Knust, M.W. Laass, M. Pritsch, E. Wilichowski, F. Horster, J. Inherit. Metab. Dis. 32 (2009) 371–380, https://doi.org/10.1007/s10545-009-1076-1.
[11] S. Portaro, A. Gugliandolo, D. Scionti, S. Cammaroto, R. Morabito, S. Leonardi, F. Fraggetta, P. Bramanti, E. Mazzon, Medicine (Baltim.) 97 (2018) e10953, , https://doi.org/10.1097/MD.0000000000010953 00005792-201806010-00069 [pii].
[12] V. Leuzzi, M. Mastrangelo, A. Polizzi, C. Artiola, A.B. van Kuilenburg, C. Carducci, M. Ruggieri, R. Barone, B. Tavazzi, N.G. Abeling, L. Zoetekouw, V. Sofia, M. Zappia, JIMD Rep. 15 (2015) 39–45, https://doi.org/10.1007/8904_2014_295.
[13] W.L. Hwu, Y.H. Chien, N.C. Lee, M.H. Li, JIMD Rep. (2017), https://doi.org/10.1007/8904_2017_54.
[14] Y.H. Chien, P.W. Chen, N.C. Lee, W.S. Hsieh, P.C. Chiu, W.L. Hwu, F.J. Tsai, S.P. Lin, S.Y. Chu, Y.J. Jong, M.C. Chao, Mol. Genet. Metab. 118 (2016) 259–263, https://doi.org/10.1016/j.ymgme.2016.05.011 S1096-7192(16)30086-5 [pii].
[15] N. Himmelreich, R. Montioli, M. Bertoldi, C. Carducci, V. Leuzzi, C. Gemperle, T. Berner, K. Hyland, B. Thony, G.F. Hoffmann, C.B. Voltattorni, N. Blau, Mol. Genet. Metab. (2019), https://doi.org/10.1016/j.ymgme.2019.03.009 S1096-7192(18)30786-30788 [pii].
[16] W.L. Hwu, S. Muramatsu, S.H. Tseng, K.Y. Tzen, N.C. Lee, Y.H. Chien, R.O. Snyder, B.J. Byrne, C.H. Tai, R.M. Wu, Sci. Transl. Med. 4 (2012), https://doi.org/10.1126/scitranslmed.3003640 134ra161 4/134/134ra61 [pii].
[17] Y.H. Chien, N.C. Lee, S.H. Tseng, C.H. Tai, S.I. Muramatsu, B.J. Byrne, W.L. Hwu, Lancet Child Adolesc. Health 1 (2017) 265–273, https://doi.org/10.1016/S2352-4642(17)30125-6 S2352-4642(17)30125-6 [pii].
[18] N.C. Lee, Y.H. Chien, W.L. Hwu, Am. J. Med. Genet. (2019), https://doi.org/10.1002/ajmg.c.31670.
[19] C.H. Tseng, Y.H. Chien, N.C. Lee, Y.C. Hsu, S.F. Peng, W.I. Tseng, W.L. Hwu, Ann. Neurol. 85 (2019) 644–652, https://doi.org/10.1002/ana.25467.
[20] K. Kojima, T. Nakajima, N. Taga, A. Miyauchi, M. Kato, A. Matsumoto, T. Ikeda, K. Nakamura, T. Kubota, H. Mizukami, S. Ono, Y. Onuki, T. Sato, H. Osaka, S.I. Muramatsu, T. Yamagata, Brain 142 (2019) 322–333, https://doi.org/10.1093/brain/awy331 5296575 [pii].
[21] C. Caine, M. Shohat, J.K. Kim, K. Nakanishi, S. Homma, E.V. Mosharov, U.R. Monani, Hum. Mol. Genet. 26 (2017) 4406–4415, https://doi.org/10.1093/hmg/ddx326 4090955 [pii].
[22] N.C. Lee, Y.D. Shieh, Y.H. Chien, K.Y. Tzen, I.S. Yu, P.W. Chen, M.H. Hu, M.K. Hu, S. Muramatsu, H. Ichinose, W.L. Hwu, Neurobiol. Dis. 52 (2013) 177–190, https://doi.org/10.1016/j.nbd.2012.12.005 S0969-9961(12)00388-9 [pii].
[23] M.Z. Zhang, B. Yao, S. Wang, X. Fan, G. Wu, H. Yang, H. Yin, S. Yang, R.C. Harris, J. Clin. Investig. 121 (2011) 2845–2854, https://doi.org/10.1172/JCI57324 57324 [pii].
[24] S.Y. Ho, Y.H. Chien, L.K. Tsai, S.I. Muramatsu, W.L. Hwu, H.H. Liou, N.C. Lee, Front. Cell. Neurosci. 13 (9) (2019), https://doi.org/10.3389/fncel.2019.00009.
[25] R. Montioli, M. Dindo, A. Giorgetti, S. Piccoli, B. Cellini, C.B. Voltattorni, Hum. Mol. Genet. 23 (2014) 5429–5440, https://doi.org/10.1093/hmg/ddu266 ddu266 [pii].
[26] P. Burkhard, P. Dominici, C. Borri-Voltattorni, J.N. Jansonius, V.N. Malashkevich, Nat. Struct. Biol. 8 (2001) 963–967, https://doi.org/10.1038/nsb1101-963 nsb1101-963 [pii].
[27] G. Giardina, R. Montioli, S. Gianni, B. Cellini, A. Paiardini, C.B. Voltattorni, F. Cutruzzola, Proc. Natl. Acad. Sci. U. S. A. 108 (2011) 20514–20519, https://doi.org/10.1073/pnas.1111456108 1111456108 [pii].
[28] E.A. Peterson, H.A. Sober, J. Am. Chem. Soc. 76 (1954) 7.
[29] A.F. Sherald, J.C. Sparrow, T.R. Wright, Anal. Biochem. 56 (1973) 300–305 0003-2697(73)90194-2 [pii].
[30] A. Charteris, R. John, Anal. Biochem. 66 (1975) 365–371 0003-2697(75)90604-1 [pii].
[31] R. Montioli, A. Paiardini, M.A. Kurian, M. Dindo, G. Rossignoli, S.J.R. Heales, S. Pope, C.B. Voltattorni, M. Bertoldi, Biochim. Biophys. Acta 1864 (2016) 676–682, https://doi.org/10.1016/j.bbapap.2016.03.011 S1570-9639(16)30053-X [pii].
[32] M. Bertoldi, C. Borri Voltattorni, Biochem. J. (2000) 533–538 352 Pt 2.
[33] M. Bertoldi, P. Frigeri, M. Paci, C.B. Voltattorni, J. Biol. Chem. 274 (1999) 5514–5521.
[34] E. Krissinel, K. Henrick, J. Mol. Biol. 372 (2007) 774–797, https://doi.org/10.1016/j.jmb.2007.05.022 S0022-2836(07)00642-0 [pii].
[35] R. Montioli, B. Cellini, C. Borri Voltattorni, J. Inherit. Metab. Dis. 34 (2011) 1213–1224, https://doi.org/10.1007/s10545-011-9340-6.
[36] R. Montioli, G. Janson, A. Paiardini, M. Bertoldi, C. Borri Voltattorni, IUBMB Life 70 (2018) 215–223, https://doi.org/10.1002/iub.1718.
[37] R. Montioli, R. Battini, A. Paiardini, M. Tolve, M. Bertoldi, C. Carducci, V. Leuzzi, C. Borri Voltattorni, Mol. Genet. Metab. 127 (2019) 132–137, https://doi.org/10.1016/j.ymgme.2019.05.004 S1096-7192(19)30245-8 [pii].
[38] R. Montioli, R. Battini, A. Paiardini, M. Tolve, M. Bertoldi, C. Carducci, V. Leuzzi, C. Borri Voltattorni, Mol. Genet. Metab. (2019), https://doi.org/10.1016/j.ymgme.2019.05.004 S1096-7192(19)30245-8 [pii].
[39] M. Bertoldi, M. Gonsalvi, R. Contestabile, C.B. Voltattorni, J. Biol. Chem. 277 (2002) 36357–36362 10.1074/jbc.M204867200 M204867200 [pii].
[40] R. Montioli, E. Oppici, B. Cellini, A. Roncador, M. Dindo, C.B. Voltattorni, Hum. Mol. Genet. 22 (2013) 1615–1624, https://doi.org/10.1093/hmg/ddt011 ddt011 [pii].
[41] M. Mastrangelo, F. Manti, L. Patane, S. Ferrari, C. Carducci, G. Mangili, V. Leuzzi, Mov. Disord. Clin. Pract. 5 (2018) 446–447 10.1002/mdc3.12622 MDC312622 [pii].
[42] G. Helman, M.B. Pappa, P.L. Pearl, JIMD Rep. 17 (2014) 23–27, https://doi.org/10.1007/8904_2014_327.
[43] C. Graziano, A. Wischmeijer, T. Pippucci, C. Fusco, C. Diquigiovanni, M. Noukas, M. Sauk, A. Kurg, F. Rivieri, N. Blau, G.F. Hoffmann, A. Chaubey, C.E. Schwartz, G. Romeo, E. Bonora, L. Garavelli, M. Seri, Gene 559 (2015) 144–148, https://doi.org/10.1016/j.gene.2015.01.026 S0378-1119(15)00042-6 [pii].
[44] S. Ide, M. Sasaki, M. Kato, T. Shiihara, S. Kinoshita, J.Y. Takahashi, Y. Goto, Brain Dev. 32 (2010) 506–510, https://doi.org/10.1016/j.braindev.2009.05.004 S0387-7604(09)00165-X [pii].
[45] K. Gucuyener, C.S. Kasapkara, L. Tumer, M.M. Verbeek, Ann. Indian Acad. Neurol. 17 (2014) 234–236 10.4103/0972-2327.132652 AIAN-17-234 [pii].
[46] T. Wassenberg, M.A. Willemsen, P.B. Geurtz, M. Lammens, K. Verrijp, M. Wilmer, W.T. Lee, R.A. Wevers, M.M. Verbeek, Mol. Genet. Metab. 101 (2010) 349–356, https://doi.org/10.1016/j.ymgme.2010.08.003 S1096-7192(10)00299-4 [pii].

Aromatic L-amino acid decarboxylase deficiency: a patient-derived neuronal model for precision therapies

Giada Rossignoli,[1,2] Karolin Krämer,[1] Eleonora Lugarà,[3] Haya Alrashidi,[4] Simon Pope,[5] Carmen De La Fuente Barrigon,[4] Katy Barwick,[1] Giovanni Bisello,[2] Joanne Ng,[1,6] John Counsell,[1] Gabriele Lignani,[3] Simon J. R. Heales,[5,7] Mariarita Bertoldi,[2] Serena Barral[1] and Manju A. Kurian[1,8]

Abstract

Aromatic L-amino acid decarboxylase (AADC) deficiency is a complex inherited neurological disorder of monoamine synthesis which results in dopamine and serotonin deficiency. The majority of affected individuals have variable, though often severe cognitive and motor delay, with a complex movement disorder and high risk of premature mortality. For most, standard pharmacological treatment provides only limited clinical benefit. Promising gene therapy approaches are emerging, though may not be either suitable or easily accessible for all patients. In order to better characterize the underlying disease pathophysiology and guide precision therapies, we generated a patient-derived midbrain dopaminergic (mDA) neuronal model of AADC deficiency from induced pluripotent stem cells (iPSCs). The neuronal model recapitulates key disease features, including absent AADC enzyme activity and dysregulated dopamine metabolism. We observed developmental defects affecting synaptic maturation and neuronal electrical properties, which were improved by lentiviral gene therapy. Bioinformatic and biochemical analyses on recombinant AADC predicted that the activity of one variant could be improved by L-3,4-dihydroxyphenylalanine (L-DOPA) administration; this hypothesis was corroborated in the patient-derived neuronal model, where L-DOPA treatment leads to amelioration of dopamine metabolites. Our study has shown that patient-derived disease modelling provides further insight into the neurodevelopmental sequelae of AADC deficiency, as well as a robust platform to investigate and develop personalised therapeutic approaches.

Author affiliations:

1 Developmental Neurosciences, GOS Institute of Child Health, University College London, London, UK

2 Biological Chemistry, NBM Department, University of Verona, Verona, Italy

3 Clinical and Experimental Epilepsy, Queen Square Institute of Neurology, University College London, London, UK

4 Genetics and Genomic Medicine, GOS Institute of Child Health, University College London, London, UK

5 Neurometabolic Unit, National Hospital for Neurology and Neurosurgery, Queen Square, London, UK

6 Gene Transfer Technology Group, EGA-Institute for Women's Health, University College London, UK

7 Centre for Inborn Errors of Metabolism, GOS Institute of Child Health, University College London, London, UK

8 Department of Neurology, Great Ormond Street Hospital, London, UK

Correspondence to: Prof. Manju Kurian

Zayed Centre for Research, UCL – GOS Institute of Child Health, 20 Guilford St, WC1N 1DZ, London, UK

E-mail: manju.kurian@ucl.ac.uk

Correspondence may also be addressed to: Prof. Mariarita Bertoldi

Room 1.24, Biological Chemistry Section, Dep. of Neuroscience, Biomedicine and Movement Sciences, Strada le Grazie 8, 37134, Verona, Italia

E-mail: mita.bertoldi@univr.it

Running title: Neuronal models for precision therapies

Keywords: induced pluripotent stem cells; dopaminergic neurons; aromatic L-amino acid decarboxylase deficiency; neurodevelopment; personalized medicine

Abbreviations

3-OMD	3-O-methyldopa
AADC	Aromatic L-amino acid decarboxylase
AP	action potential
DEGs	differentially expressed genes
DOPAC	3,4-Dihydroxyphenylacetic acid
HPLC	High Performance Liquid Chromatography
HVA	homovanillic acid
iPSCs	induced pluripotent stem cells
L-DOPA	L-3,4-dihydroxyphenylalanine
mDA	midbrain dopaminergic
PLP	pyridoxal 5'-phosphate
sEPSCs	spontaneous excitatory postsynaptic currents

Introduction

Neurodevelopmental processes are commonly disrupted in the vast majority of inborn errors of metabolism, resulting in a wide repertoire of clinical manifestations from severe cognitive, neuropsychiatric, and motor problems to more subtle learning difficulties.[1] Aromatic L-amino acid decarboxylase (AADC) deficiency is a rare inborn error of neurotransmitter metabolism due to bi-allelic mutations in *DDC,* which encodes the enzyme that catalyzes the final step of serotonin and dopamine synthesis.[2] The resultant enzyme deficiency leads to combined serotonin and catecholamine (dopamine, norepinephrine, epinephrine) deficiency.[3] Although there is a wide phenotypic spectrum,[4,5] the majority of affected patients show many of the typical features seen in recessively inherited, early-onset neurotransmitter disorders[6], including severe global neurodevelopmental delay, oculogyric crises, a complex movement disorder (characterised by central and peripheral hypotonia with commonly features of dystonia/chorea) and symptoms of dysautonomia, as well as secondary gastrointestinal, respiratory and orthopedic complications.[7,8] As a result, the majority of patients have significant disability and

high risk of premature mortality. AADC deficiency is associated with a characteristic CSF monoamines profile, with reduced 5-hydroxyindoleacetic acid, homovanillic acid (HVA), and 3,4-dihydroxyphenylacetic acid (DOPAC), and a concomitant increase in 5-hydroxytryptophan, L-3,4-dihydroxyphenylalanine (L-DOPA), and 3-O-methyldopa (3-OMD). Definitive diagnosis is ideally achieved by confirming a decrease or absence of plasma AADC enzymatic activity, and *DDC* gene sequencing. To date, there are no clear correlations between patient genotype, CSF monoamine profile, AADC enzyme activity and phenotype.

A recently published consensus guideline outlines recommendations for the diagnosis and management of AADC deficiency.[8] Pharmacological therapy provides some, though often limited, clinical benefit and patients often show variable drug response. It has been postulated that the variability in disease severity and medication response may be partly attributed to genotype[9,10] and as a result, a number of studies have focused on characterising the underlying molecular defects caused by different pathogenic variants.[11–15] More recently, promising gene therapy approaches are emerging for AADC deficiency, with a number of clinical trials evaluating the safety and efficacy of targeted intraparenchymal delivery of AAV2-based vectors.[16–18] It is hoped that with time, these studies may clarify the effect of patient genotype, age at surgery, pre-treatment motor function and target delivery site on overall therapeutic efficacy. Although early clinical studies on AADC gene therapy are encouraging, it is likely that this therapeutic strategy may not be either viable, suitable or easily accessible for a proportion of patients. Moreover, with advances in diagnostic testing, the global incidence and prevalence of AADC deficiency continues to increase,[19] and the need for alternative precision therapies is increasingly apparent.

Recently, patient-derived cellular models of neurodevelopmental disorders have proven to be a valuable experimental system to unravel disease mechanisms and test novel therapeutic strategies with translational potential.[20] As such, we have developed a humanized neuronal model of AADC deficiency, by reprogramming patient fibroblasts into induced pluripotent stem cells (iPSCs) for differentiation into midbrain dopaminergic (mDA) neurons. This model system has allowed us to gain further insight into the neurodevelopmental consequences of AADC deficiency, with effects on synaptic maturation and neuronal function. Moreover, it has also provided a suitable platform to evaluate the effects of precision medicine approaches at a cellular level, demonstrating the potential for rational development of patient-specific strategies in such rare monogenic disorders.

Materials and methods

iPSCs generation and maintenance

Generation of iPSCs from patient dermal fibroblasts was approved by the Local Research Ethics Committee (Reference 13/LO/0171). Written informed consent was obtained from all patients. Age-matched healthy control fibroblasts were collected from the MRC Centre for Neuromuscular Disorders Biobank. Patient fibroblasts were isolated from skin biopsies and maintained in DMEM (Gibco), 10% fetal bovine serum (Gibco), 2 mM L-glutamine (Gibco), 1% MEM non-essential amino acids (Gibco), and 1% penicillin/streptomycin (P/S, Gibco), and tested for mycoplasma contamination. Reprogramming was performed using the commercially available CytoTune®-iPS 2.0 Sendai Reprogramming kit (Invitrogen), following manufacturer instructions. Fibroblast were transduced at 80% confluence (1-1.5x10^5 cells/well). After 6 days, infected cells were harvested with TrypLE™ (Invitrogen) and 8,000 cells/well were seeded onto gamma-irradiated mouse embryonic fibroblasts. After 24 hours, cells were cultured into KO-DMEM (Gibco), 20% serum replacement (Gibco), 2 Mm L-glutamine, 50 μM 2-mercaptoethanol, 1% MEM non-essential amino acids, 1% P/S, and 10 ng/ml basic fibroblast growth factor (Gibco). 13 days post-transfection, cells were cultured in gamma-irradiated mouse embryonic fibroblasts-conditioned medium. Around day 30 post-transduction, 8-10 independent colonies with iPSCs-like morphology were collected and expanded using ReLeSR (Stemcell™ technologies). Between passage 15 and 20, 3 colonies were converted to mTeSR1 medium (Stemcell™ technologies) on Matrigel® (Corning®) coated plates. Derived iPSC lines were maintained in mTeSR1/matrigel system, regularly passaged with ethylenediaminetetraacetic acid, 0.02% solution (Sigma-Aldrich) and again tested for mycoplasma infection, as previously. Two iPSC lines for each patient (Patient 1-04, Patient 1-10; Patient 2-01, Patient 2-06) and the age-matched healthy control (Control-05, Control-03) were characterized at the iPSCs stage and further differentiated into mDA neurons to exclude clonal variability. Given the relative homogeneity reported in clonal lines with respect to transcriptome, growth, and capability of germ layer formation,[21,22] one clone per patient (Patient 1-04; Patient 2-01) and age-matched healthy control (Control-05) were then used for downstream experiments.

Differentiation of iPSCs into mDA neurons

iPSCs were differentiated into mDA dopaminergic neurons as previously described.[23] Briefly, iPSCs were harvested using TrypLE™ (Invitrogen), and plated onto non-adherent bacterial

dishes in a concentration of $1.5x10^5$ per cm^2 in DMEM/F12:Neurobasal (1:1), N2 (1:100) and B27 minus vitamin A (1:50) supplements (Invitrogen), 2 mM L-glutamine and ROCK-inhibitor for the first two days. EBs were plated at day 4 onto polyornithine (PO; 15 µg/ml; Sigma), fibronectin (FN; 5 µg/ml Gibco) and laminin (LN; 5 µg/ml; Sigma) coated dishes in DMEM/F12:Neurobasal (1:1), N2 (1:200), B27 minus vitamin A (1:100), 2 mM L-glutamine. From day 0 to day 9, medium was supplemented with: 10 µM SB431542 (Tocris Bioscience), 100 nM LDN193189 (Stemgent Inc.), 0.8 µM CHIR99021 (Tocris Biosceince) and 100 ng/ml hSHH-C24-II (R&D Systems). On day 2, 0.5 µM purmorphamine (Cambridge Bioscience) was added. SB431542 was withdrawn on day 6. On day 11, cells were either processed for mDA precursors analysis or harvested with Accumax and re-plated on PO/FN/LN coated dishes in droplets of 1-1.5 $x10^4$ cells/µl in Neurobasal/B27 minus vitamin A (1:50), 2 mM L-glutamine, 0.2 mM ascorbic acid (AA) and 20ng/ml BDNF (Miltenyi Biotech). On day 14 of differentiation, 0.5 mM dibutyryl c-AMP (Sigma-Aldrich) and 20ng/ml GDNF (Miltenyi Biotech) were added. On day 30 of differentiation, cells were re-plated as describe above onto PO/FN/LN coated dishes or Labteck slides (Nunc™), and γ-secretase inhibitor DAPT (10 µM, Tocris) was added until final differentiation at day 65. Cells were then harvested or processed for further analysis.

AADC activity assay

AADC enzyme assay was performed using the refined method developed in [24], from [25]. Neuronal cultures at day 65 in phenol red free medium were harvested and lysed by snap freezing twice in liquid nitrogen in 100 µl of 10 mM Tris pH 7.4 (Sigma-Aldrich), 1 mM ethylenediaminetetraacetic acid, 320 mM sucrose (Sigma-Aldrich) and protease inhibitor cocktail (Roche). 50 µl of cell lysate was incubated with 70 µM pyridoxal 5'-phosphate (PLP, Sigma-Aldrich) in assay buffer composed by 500 mM sodium phosphate pH 7.0, 0.167 mM ethylenediaminetetraacetic acid, and 39 mM dithiothreitol (Sigma-Aldrich) for 120 min at 37°C, and subsequently 2 mM final concentration of L-DOPA (Sigma-Aldrich) was added and incubated for 20 min at 37°C. The reaction was stopped with 250 µl of 0.8 M perchloric acid (final concentration 0.4 M) for 10 min at room temperature and centrifuged at 12.000×*g* for 5 min at 4°C. A substrate blank with no L-DOPA and a sample blank without cell lysate were performed for each sample. Dopamine in the supernatant was then quantified by High Performance Liquid Chromatography (HPLC, see below).

HPLC for quantification of activity assay and metabolic profile

Dopamine produced in the activity assay was separated by reverse-phase HPLC using a HiQSil C18 column 250x4.6mm (Kya technologies) and detected by coulometric electrochemical detection using a Coulochem III detector (ESA) with 5010 analytical cell (ESA) setting the detector electrode at 350 mV and the screening electrode at 20 mV. The mobile phase consisted of 50 mM sodium phosphate pH 3.6, 5 mM octaensulfonic acid, 67 µM ethylenediaminetetraacetic acid, 43 mM orthophosphoric acid and 230 ml/l methanol diluted in 18.2 Ω HPLC grade water, at a flow rate of 1.2 ml/min at 25 °C. Dopamine was quantified with Azur software package using a 1000 nM external standard and enzymatic activity was expressed as pmol/min/mg protein.

HPLC analysis of metabolic profile in derived mature cultures was performed on the phenol red-free medium incubated for 48h on day 65 mDA neurons. 1:1 medium was mixed with perchloric acid to a final concentration of 0.4 M, incubated 10 min at 4°C in the dark, centrifuged at 12000×*g* for 5 min at 4°C, and supernatant was collected for analysis by HPLC [26]. Metabolites were separated by reverse-phase HPLC using a C:18HS column 250 mm×4.5 mm (Kromatek) and detected by coulometric electrochemical detection using a Coulochem II detector (ESA) with 5010A analytical cell (Thermo Fisher Scientific) setting the detector electrode at 450 mV and the screening electrode at 20 mV. Mobile phase consisted of 20 mM sodium acetate trihydrate pH 3.45, 12.5 mM citric acid monohydrate, 100 µM ethylenediaminetetraacetic acid, 3.35 mM octaensulfonic acid and 16% methanol diluted in 18.2 Ω HPLC grade water, at a flow rate of 1.5 ml/min at 27 °C. Metabolites were quantified with EZChrom Elite™ chromatography software (JASCO) using a 500 nM external standard mixture, and expressed as pmol/mg protein.

Bulk RNA-Seq analysis

Total RNA was isolated using the RNeasy mini kit (Qiagen) following manufacturer's instructions. RNA libraries were prepared from 100 ng of total RNA using KAPA mRNA HyperPrep kit (Roche) according to manufacturer's protocol and sequenced with Illumina NextSeq 500 Mid Output 75bp paired-end (~22M reads/sample). FASTQ obtained files were uploaded to Galaxy web platform, and the public server at usegalaxy.org was used for downstream analyses.[27] FASTQ-files were filtered with Trimmomatic (v.0.38), with SLIDINGWINDOW trimming and low quality (phread score <20) reads filter.[28] Obtained reads were mapped to human reference genome (GRCh38) with HISAT2 (v.2.1.0).[29] Fragments counts for genes were extracted with featureCounts (v.1.6.4) excluding duplicates, multimapping reads and chimeric fragments.[30] Differential gene expression was analysed using

edgeR (v.3.24.1), filtering low counts with 0.35 minimum CPM in at least 3 samples,[31] and comparing disease status (patients vs control) and disease-specific genotype (patient 2 vs patient 1). DEGs with a p-value<0.05 and absolute fold change>2 were considered as statistically significant. Heatmaps were generated from the row-scaled z-score of DEGs normalised counts obtained by EdgeR with complete-linkage Euclidean hierarchical clustering. GO enrichment analyses were performed using ShinyGO v0.61[32] for biological process, and ClueGO v.2.5.7[33] for cellular component and molecular function enrichments and groupings, with Benjamini-Hochberg p-value correction of FDR<0.05 for statistical significance. Results from the expression analysis along with the raw sequence data were deposited in GEO (Gene Expression Omnibus), under accession GSE153990.

Electrophysiology

Current-clamp recordings were performed on neurons at day 65 of differentiation. The internal solution contained 135 mM K-gluconate, 4 mM KCl, 10 mM Hepes, 4 mM Mg-ATP, 0.3 mM Na-GTP, and 10 mM of Na_2-phosphocreatine, at pH 7.3 and mOsm 291-295. The recording extracellular solution contained 125 mM NaCl, 2.5 mM KCl, 2 mM $MgCl_2$, 1.25 mM KH_2PO_4, 2 mM $CaCl_2$, 30 mM glucose, and 25 mM of HEPES at pH 7.4. Experiments were performed at room temperature (22-24°C). Neurons with unstable resting potential (or >-50mV), bridge-balance >20MΩ and/or holding current >200pA were discarded. Bridge balance compensation was applied in current clamp and the resting membrane potential was held at -70mV. Current steps protocol was used to evoke APs injecting 250ms long depolarizing current steps of increasing amplitude (Δ10pA). APs were triggered holding the neurons around -60mV/-55mV. Neurons with repetitive spontaneous APs and repetitive evoked APs were considered to be functional mature mDA neurons. Recordings were acquired using a Multiclamp 700A amplifier (Axon Instruments, Molecular Devices) at 10kHz and filtered at 2kHz (Bessel) using WinEDR (John Dempster, University of Strathclyde). Recording were not corrected for liquid junction potentials. The approximate cell capacitance was computed as $capacitance=tau/R_i$, whereby the time constant tau was found by fitting a single exponential function to the time points where the membrane voltage was between 10% and 95% of the initial charging decay slope of a negative hyperpolarizing current step. Input resistance was calculated fitting $\Delta V/\Delta I$ at two hyperpolarising steps (-20 and -10pA) and a positive one (+10pA). APs were identified when the voltage signal crossed 0V. sEPSCs were recorded in voltage clamp and automatically detected with a template-based algorithm using Clampfit (Molecular Device).

Treatment with L-DOPA and cytotoxicity assay

Neuronal cultures at day 65 of differentiation were treated with 80 μM L-DOPA in phenol red-free medium for 24 h. The medium was subsequently removed and analysed by HPLC, as described above. Dead-cell proteases release measurement was quantified using CytoTox-Glo™ Cytotoxicity Assay (Promega) according to manufacturer instructions.

Statistical Analysis

Two-tailed Student's *t*-test for single comparisons and statistical one-way ANOVA followed by Tukey's multiple comparisons test were performed using GraphPad Prism. Results are reported as mean SEM from at least three independent biological replicates, the exact number of which is stated for each experiment in each figure legend. Significance levels were determined by p-value, and shown on graphs with asterisks. One asterisk (*) represents p-values between 0.05 and 0.01, two asterisks (**) represent p-values between 0.01 and 0.001, and three asterisks (***) represent p-values of less than 0.001.

Data availability

Data supporting the findings of this study are available from the corresponding authors, upon reasonable request.

Results

Patient-derived mDA neurons show disease-specific loss of AADC enzymatic activity and dysregulated dopamine synthesis.

Dermal fibroblasts were obtained from two patients with AADC deficiency (Table 1). Patient 1 (homozygous missense variant c.1039C>G, p.R347G) presented with classical infantile onset disease, with early hypotonia, oculogyric crises and neurodevelopmental delay.[15] He is currently 6½ years of age, and although he continues to make neurodevelopmental progress, remains non-ambulant and non-verbal. Patient 2 (compound heterozygous variants c.19C>T, p.Arg7*; c.299G>C, p.C100S) had a classical infantile-onset presentation of disease with severe global developmental delay, oculogyric crises and hypoglycaemia, but over time showed a positive response to therapy and had an overall milder disease course. Once AADC deficiency was diagnosed at 3½ years of age, the instigation of dopaminergic medication and other specific AADC deficiency treatments was associated with neurodevelopmental progress; independent ambulation was achieved by 4½ years and spoken language by 5½ years. From 10-18 years, adjunct therapies were needed to combat side effects from long-term use of the

original treatments to maintain basic motor and verbal function. Now aged 22 years, he has ongoing learning difficulties, mild motor impairments, behavioral issues, autistic traits and neuropsychiatric symptoms of anxiety and intermittent low mood. iPSC lines were generated from dermal fibroblasts of both patients and from an age-matched healthy individual (Control). Sequencing of genomic DNA confirmed that patient iPSC lines retained their specific *DDC* mutation (Supplementary Fig. 1A). All iPSCs lines showed clearance of viral transgenes, genomic integrity (Supplementary Fig. 1B-C), and true pluripotency (Supplementary Fig. 2A-D).

iPSCs were then differentiated into mDA neurons, and both patient and control iPSC lines showed similar differentiation efficiency. After 11 days of differentiation, all lines showed high levels of mDA progenitors and typical midbrain precursors gene expression profile (Supplementary Fig. 3A-C). By 65 days of differentiation, both control and patient lines comparably matured into neurons, in particular with dopaminergic identity (Supplementary Fig. 4A-B). Both control and patient-derived neuronal cultures showed upregulation of midbrain-related genes (Supplementary Fig. 4C). Whole-cell patch clamp electrophysiology confirmed that iPSC-derived mDA neurons were functional and exhibited continuous and rhythmic pacemaker-like activity (Supplementary Fig. 4D). Derived neuronal cultures were almost devoid of serotonergic neurons, restricting all further analyses specifically to the mDA neuronal subtype (Supplementary Fig. 5A).

We first investigated the effect of patient mutations on AADC enzyme activity and protein expression. Measurement of AADC activity showed significantly lower enzymatic function in patients when compared to control-derived neurons (Fig. 1A). HPLC analysis of extracellular metabolites showed a disease-specific absence of dopamine and HVA with significantly reduced levels of DOPAC. In contrast, 3-OMD, a downstream metabolite of the AADC substrate L-DOPA, was significantly increased in patient-derived neurons (Fig. 1B). Analysis of AADC protein levels showed an increase in Patient 1 neuronal cultures when compared to the Control; in contrast, a significant reduction of AADC protein was detected in Patient 2 neuronal cultures (Fig. 1C-D and Supplementary Fig. 5B), in line with the second heterozygous early stop codon variant predicted to result in nonsense mediated mRNA decay.

We then explored whether the aberrant AADC protein levels in patients could be linked to a difference in intrinsic protein stability. Recombinant AADC proteins were produced for the homozygous R347G variant (Patient 1) and C100S variant (Patient 2). Circular dichroism and

dynamic light scattering analyses showed comparable values for both mutant and wild-type AADC protein, inferring similar intrinsic protein stability (Supplementary Table 1).

To investigate whether aberrant AADC protein levels related to *DDC* gene expression, qRT-PCR studies were undertaken. In line with protein expression data, we observed a statistically significant increase in *DDC* expression in Patient 1 when compared to the Control (Supplementary Figure 5C). For Patient 2, we observed comparable levels of *DDC* expression to the Control (Supplementary Figure 5C), despite the predicted nonsense-mediated decay of a proportion of transcripts. We also observed an increase in tyrosine hydroxylase (TH) gene and protein expression in both patient lines when compared to the control (Supplementary Figure 5D-E).

AADC deficiency has mutation-specific effects on neuronal synaptic maturation and connectivity.

We then sought to investigate the neurodevelopmental consequences of AADC deficiency in our *in vitro* model. Immunofluorescence analysis of the mature neuronal marker NeuN showed comparable levels in Patient 1 and Control mDA neurons, while Patient 2 cultures showed a significant decrease in NeuN positivity when compared to both Control and Patient 1 lines (Fig. 2A-B). Moreover, analysis of the vesicular protein synaptophysin revealed a significant decrease in protein levels for both Patient 1 and 2 when compared to control-derived neuronal cultures (Fig. 2C-D).

In order to further investigate the neurodevelopmental effects of AADC deficiency, we undertook bulk RNA sequencing for analysis of differentially expressed genes (DEGs) between patient and control-derived neurons, with a particular focus on protein-coding genes. In a combined analysis of Patient 1 and Patient 2-derived neuronal cultures, we identified 750 DEGs (75% underexpressed and 25% overexpressed) when compared to the Control (Fig. 3A). Gene Ontology (GO) analysis of underexpressed DEGs revealed a strong enrichment in synaptic transmission-related biological processes and nervous system development, whilst overexpressed DEGs mainly enriched protein transcription and general organ developmental processes (Fig. 3B). Furthermore, underexpressed DEGs were associated with membranous cellular compartments (in particular the cell periphery and synaptic region), and enriched in gated channels and regulators of membrane transport (Fig. 3C). In contrast, overexpressed DEGs were associated with non-membrane-bounded cell compartments (nucleus), with enrichment in transcriptional regulator proteins (Fig. 3D).

Considering the previously detected differences between the two patient lines (Fig. 2), single-comparison RNA sequencing analysis was also performed. We identified 842 protein-coding DEGs for Patient 1 compared to the Control (Supplementary Fig. 6A) and 871 protein-coding DEGs for Patient 2 compared to the Control (Supplementary Fig. 7A). For both analyses, underexpressed genes showed common enrichment for synaptic transmission (Supplementary Fig. 6B and 7B) - reflected in the significant P-values observed in the combined analysis (Fig. 3B) - representing genes encoding proteins mainly localized at the cell periphery or synapses, and associated with ion channel function (Patient 1 and Patient 2) and gated channel function (for Patient 2 in particular) (Supplementary Fig. 6C and 7C). Differences in separate single Patient 1 and Patient 2 comparisons with the Control were mainly detected for upregulated genes with regard to biological processes and significance (Supplementary Fig. 6B and 7B): for Patient 1, overexpressed DEGs were enriched for developmental and cell projection assembly genes (Supplementary Fig. 6B and 6D), whilst for Patient 2 overexpressed DEGs were enriched for genes encoding endoplasmic reticulum and membrane-targeting processes and function (Supplementary Fig. 7B and 7D). Despite these inter-patient differences, the combined analysis reflects a common, disease-specific overexpression of developmental and transcriptional/translational processes from both single comparisons (Fig. 3B).

We then explored DEGs between the two different patient-derived neuronal cultures. We identified a total of 763 protein-coding DEGs for Patient 2 when compared to Patient 1 (Fig. 4A). The underexpressed DEGs showed enrichment in cell adhesion and membrane transport-related processes, while overexpressed DEGs enriched endoplasmic reticulum and membrane-targeting processes categories (Fig. 4B). Underexpressed DEGs corresponded to proteins localized both in cell periphery/membrane regions and nuclear compartment, with enrichment for genes regulating transcription and transmembrane transport (Fig. 4C). Overexpressed DEGs showed enrichment in both cytosolic transcriptional and extracellular compartments, with molecular functions mainly linked to structural/binding molecules, and transcriptional/activity regulators (Fig. 4D), resembling the result from the single comparison between Patient 2 and Control (Supplementary Fig. 7B and 7D).

Whole-cell patch clamp electrophysiology studies were undertaken to determine whether the observed differences in gene expression were associated with functional differences in neuronal activity. The parameters analysed are similar to other studies using iPSC-derived dopaminergic neurons, with comparable findings for firing pattern, pacemaker and synaptic activity in controls.[34–37] Recordings with increasing current amplitude (Fig. 5A) showed that

the current threshold to elicit an action potential (AP) for Patient 2 was significantly lower than for the Control (Fig. 5B-C) and failed to follow current injection up to 100pA (Fig. 5D). On investigation of passive neuronal properties, both patients displayed lower capacitance compared to control neurons without affecting input resistance (Fig. 5C), in accordance with a decreased average number of primary neurite branches (Fig. 5E). For both control and patient-derived neurons showing spontaneous excitatory postsynaptic currents (sEPSC), we observed no differences in either the percentage of functionally connected neurons or current amplitude, although the inter-event interval was significantly higher in Patient 2-derived neurons (Fig. 5F).

DDC lentiviral gene-transfer significantly improves neurodevelopmental defects in patient-derived neurons.

Given that gene therapy is an emerging new treatment for AADC deficiency,[16–18] we sought to investigate the cellular effects of human *DDC* (h*DDC*) transgene delivery in our model; in particular we wished to evaluate whether this therapeutic approach could improve the neurodevelopment sequelae of AADC deficiency, independent of genetic background. We generated a lentiviral construct for the delivery of h*DDC* under the control of the neuronal-specific promoter human synapsin (hSyn1) (Supplementary Fig. 8). Patient-derived mDA precursors were transduced at day 24 of differentiation and analysed at day 65. For both patient lines, lentiviral gene transfer resulted in an increase in AADC protein levels (Supplementary Fig. 9A-B), and rescued enzymatic activity to levels comparable to those observed in Control neurons (Supplementary Fig. 9C). Furthermore, Patient 2 transduced neurons showed a significant increase in the NeuN-positive neuronal population, and in particular mDA neurons, to levels comparable to Patient 1 (Fig. 6A-B and Supplementary Fig. 10A). h*DDC* lentiviral delivery also resulted in a significant increase in synaptophysin protein levels in both patients-derived neuronal cultures (Fig. 6C) and more specifically in the mDA neuronal subpopulation (Fig. 6D and Supplementary Fig. 10B), with a significant increase in primary branching (Fig. 6E).

In silico and recombinant biochemical analyses predict mutation-specific L-DOPA response for Patient 2.

The different mutations harbored by Patient 1 and 2 were further investigated to determine whether they had differential effects on enzymatic function. For Patient 1, despite supraphysiological levels of protein expression (Fig. 1C), the homozygous missense

substitution R347G significantly impairs catalytic function of AADC leading to undetectable enzyme activity (Fig. 1A) without impacting the protein structure by a molecular mechanism extensively investigated in [15]. In contrast, despite significantly low levels of AADC protein in Patient 2-derived neuronal cultures (Fig. 1C), residual enzymatic activity was still detected, albeit at a fraction of that evident in Control line (Fig. 1A). It is likely that this residual AADC enzyme activity can be attributed to the p.C100S variant, since the second heterozygous mutation leads to an early stop codon at Arg7, predicted to result in nonsense mediated mRNA decay and absent protein production. The missense mutation C100S results in an amino acid substitution at the beginning of an essential loop (loop 2, residues 100 to 110) that contains key hydrophobic active site residues involved in substrate binding, in particular Ile101 and Phe103.[38] The cysteine-to-serine amino acid substitution has the potential to alter the conformation of loop 2 and consequently the substrate-binding cleft, thereby affecting substrate affinity (Fig. 7A). AADCC100S was produced *in vitro* in recombinant form to further characterize the effects of this mutation through spectroscopic, circular dichroism and fluorescence analyses, and calculation of kinetic parameters. A minor perturbation of PLP cofactor microenvironment (in particular for the enolimine tautomer) was observed (Supplementary Fig. 11A-B). However, PLP binding affinity (Supplementary Table 1) was not particularly affected, with a $K_{D(PLP)}$ consistently lower than previously reported values for AADC variants with cofactor binding impairment.[13] Calculation of kinetic parameters (Supplementary Table 1) revealed that AADCC100S retains more residual enzyme activity than that reported for other AADC variants.[12,13] The catalytic activity (k_{cat}) of AADCC100S was indeed similar to that observed for wild-type, with the actual decrease in overall AADCC100S catalytic efficiency (k_{cat}/K_M) attributed to a slight decrease in L-DOPA affinity (K_M) (Supplementary Table 1). As such, we postulated that dopamine production by AADCC100S could be enhanced with L-DOPA administration, as demonstrated for other AADC variants.[39]

Patient 2-derived mDA neurons specifically respond to L-DOPA administration.

To determine whether the C100S mutation resulted in L-DOPA responsivity, we sought to investigate the effect of L-DOPA treatment in Patient 2-derived mDA neurons. After 65 days of differentiation, both patients and control-derived neuronal cultures were incubated with 80 μM L-DOPA for 24 hours, a dose just below that considered to be toxic in neuronal and other cellular systems.[40,41] Subsequent HPLC analysis of extracellular metabolites was then undertaken. As expected in a system with catalytically competent AADC, HVA levels were

significantly higher in treated Control compared to untreated Control neurons (Fig. 7B). Furthermore, as predicted, there was no detectable HVA in Patient 1-derived neuronal cultures both pre- and post- L-DOPA treatment. However, for Patient 2, we observed a significant increase of HVA levels in L-DOPA treated cultures when compared to untreated cultures (Fig. 7B). In order to evaluate any potential toxicity related to L-DOPA administration[40] or dopamine production,[42] we measured dead-cell protease release and found no increase in membrane permeability for both Patient and Control-derived neuronal cultures treated with 80 μM L-DOPA for 24 hours (Fig. 7C). Moreover, analysis of JNK protein phosphorylation, which increases in response to toxic levels of dopamine,[43] showed a significant increase in the phosphorylated form of this kinase in treated Control neurons only, while no significant increase was detected in both treated Patient 1 and 2 cultures (Supplementary Fig. 11C).

Discussion

AADC deficiency is a complex and often pharmacoresistant neurological disorder, with a broad phenotypic spectrum, variable drug response, substantial burden of disease and significant risk of premature mortality.[7] Improved understanding of the underlying pathogenic mechanisms and the development of better targeted treatments, such as gene therapy and other personalised medicine approaches, will be key in modifying disease and long-term outcome. In this study, we have developed a new humanized model of AADC deficiency. Our *in vitro* patient-derived mDA neuronal model of AADC deficiency has provided further insight into mechanisms governing disease, as well as an ideal system to evaluate the impact of approaches such as gene therapy at cellular level and a unique research platform to evaluate mutation-specific precision medicine approaches.

Importantly, our patient-derived mDA model recapitulates key features of the human phenotype with near-absent AADC enzyme activity and impaired dopamine metabolism. In our dopaminergic model, we observed a greater degree of residual AADC enzyme activity in Patient 2, which may relate to the more advanced motor gains observed in this patient. We also observed patient-specific altered levels of AADC protein. The reasons for this are not entirely clear, given that little is known about factors that govern AADC enzyme regulation. Our biochemical investigations did not show a differential intrinsic protein stability between mutant and wild-type protein. We did however observe a clear patient-specific increase in *DDC* gene expression for Patient 1 and higher than expected levels of *DDC* expression for Patient 2, given

the predicted nonsense-mediated decay of a proportion of Patient 2 transcripts. Furthermore for both patients there was an increase in TH gene and protein expression; interestingly, TH gene and protein expression has previously been shown to increase in Parkinson's disease, as a likely compensatory response to a state of dopamine deficiency in the context of striatonigral degeneration.[44,45] As such, it is plausible that the similar state of dopamine deficiency in AADC-deficient patient lines drives a positive feedback mechanism to modulate neuronal levels of key enzymes driving dopamine synthesis.

Moreover, our study suggests that AADC dysfunction may have widespread effects on gene expression that may impact neuronal development and functional maturation. As well as its pivotal role in monoamine neurotransmission, dopamine is postulated to have important functions in modulating neuronal structure and connectivity.[46] The early production of dopamine in midbrain development suggests that it may have neurodevelopmental influence,[47] a notion that is further corroborated by *DDC* knock-in mice and knockout zebrafish which show abnormal development.[48,49] Interestingly, our patient-derived cell model also shows that defective AADC enzymatic activity and dysregulated dopamine metabolism affects neuronal maturity, with altered expression of genes involved in neurodevelopment and synaptic formation, as well as disruption of electrophysiological properties and functional activity. Considering that iPSC-derived neurons resemble fetal neurons,[50] it is possible that the neuronal maturation defects observed in our *in vitro* model correlate with prenatal disease onset in humans. This is not surprising, given that many affected patients present with their first clinically discernible symptoms in early infancy. Our results are particularly relevant in the current climate of emerging gene therapy approaches,[18] where neuronal plasticity is considered to be an important requisite for clinical benefit.[51] It is likely that gene therapy within this 'therapeutic window' of brain plasticity may predict a more favorable long-term neurodevelopmental outcome.

In our system, we identified around the same number of differentially expressed genes between patients (when combined) and control and between the two patients; the latter observation likely reflects both the biological and clinical differences between patients affected by a disease with a broad phenotypic continuum. Patient 2-derived cultures showed indeed a greater degree of neuronal immaturity. Notably, Patient 2 had a number of behavioural issues, significant autistic traits and prominent neuropsychiatric symptoms, features that were less evident in Patient 1. Our data may indicate that the greater degree of neuronal immaturity evident in Patient 2 lines as seen on maturation marker analysis, transcriptome profiling and

electrophysiology may contribute to the aforementioned neurodevelopmental symptoms. Importantly, lentiviral treatment of patient-derived neurons restored AADC protein levels and enzymatic activity with significant improvement in neuronal maturity. Whether AADC protein has additional functions in governing neurodevelopment processes, that are independent of its catalytic activity in dopamine production, remains yet to be determined. Further studies with a greater number of patient lines and age-matched/isogenic controls, or analysis of multiple clones from each line, will help confirm and further delineate the complex neurodevelopmental biological phenotypes identified in this study. Additional genetic, epigenetic and environmental factors may also play a role in such phenotypic variability seen in the cell model and human phenotype; over time, advances in next generation sequencing technologies may also help further elucidate some of the underlying contributory genetic factors.

Our patient-derived model of AADC deficiency has proven to be a useful tool for evaluating therapeutic approaches. We have shown recovery of AADC enzyme activity and specific neuronal maturation defects using a gene therapy approach in patient-derived neurons. In tandem with other models, such therapeutic testing in iPSC-based systems may in the future guide and influence clinical trial design. Our model has also demonstrated the potential utility of L-DOPA treatment for some patients with AADC deficiency. Although L-DOPA is not traditionally used in the majority of patients,[8] it has been previously empirically used in patients suspected to have L-DOPA responsive AADC deficiency.[39] Our study confirms that it may indeed have a role for patients with specific *DDC* mutations associated with residual enzymatic activity due to altered substrate affinity. A planned therapeutic trial will further inform whether the positive effects of L-DOPA observed *in vitro* are recapitulated *in vivo*. More generally, our study shows that better definition of the physiochemical properties of specific mutations with subsequent validation in patient-relevant models has great potential in guiding personalised pharmacological strategies for rare disorders.

In conclusion, as new therapeutic avenues emerge for patients with AADC deficiency, our study shows the clear utility of an iPSC-based modelling system to elucidate disease mechanisms and evaluate therapeutic strategies.

Acknowledgments

We sincerely thank the AADC Research Trust for inspiring us to undertake this study, and our patients and their families for participating in this study. We also thank the MRC Centre for Neuromuscular Disorders Biobank for providing age-matched control fibroblasts.

Funding

GR, KK, MB and MAK received funding from the AADC Research Trust. EL and GL have been supported by European Union's Horizon 2020 research and innovation program under Marie Skłodowska-Curie grant agreement 642881 and an Epilepsy Research UK Fellowship (GL: ERUK F1701). HA received funding from Kuwait University. J.N. received funding from MRC MR/K02342X/1 and MR/R015325/1. J.C. has been supported by Wellcome Innovator Award (210774/2/18/Z). MB was supported by University of Verona Grant FUR2019. SB and MAK have received funding support from the Wellcome Trust (MAK: Wellcome Intermediate Clinical Fellowship WT098524MA) and is from the Rosetrees Trust. MAK is funded by an NIHR Research Professorship (NIHR-RP-2016-07-019) and the Sir Jules Thorn Award for Biomedical Research.

This research was supported by the NIHR Great Ormond Street Hospital Biomedical Research Centre. The views expressed are those of the author(s) and not necessarily those of the NHS, the NIHR or the Department of Health.

Competing interests

The authors report no competing financial interests.

Supplementary material

- Supplementary Figures
- Supplementary Material and Methods
- Supplementary full-length Blots

References

1. Saudubray JM, Garcia-Cazorla A. An overview of inborn errors of metabolism affecting the brain: From neurodevelopment to neurodegenerative disorders. *Dialogues Clin Neurosci*. 2018;20(4):301-325. doi:10.31887/dcns.2018.20.4/jmsaudubray
2. Ng J, Papandreou A, Heales SJ, Kurian MA. Monoamine neurotransmitter disorders - Clinical advances and future perspectives. *Nat Rev Neurol*. 2015;11(10):567-584. doi:10.1038/nrneurol.2015.172
3. Hyland K, Clayton PT. Aromatic amino acid decarboxylase deficiency in twins. *J Inherit Metab Dis*. 1990;13(3):301-304. doi:10.1007/BF01799380
4. Dai W, Lu D, Gu X, Yu Y. Aromatic L-amino acid decarboxylase deficiency in 17 Mainland China patients: Clinical phenotype, molecular spectrum, and therapy overview. *Mol Genet Genomic Med*. 2020;8(3). doi:10.1002/mgg3.1143
5. Helman G, Pappa MB, Pearl PL. Widening phenotypic spectrum of aadc deficiency, a disorder of dopamine and serotonin synthesis. In: *JIMD Reports*. Vol 17. Springer; 2014:23-27. doi:10.1007/8904_2014_327
6. Kurian MA, Gissen P, Smith M, Heales SJR, Clayton PT. The monoamine neurotransmitter disorders: An expanding range of neurological syndromes. *Lancet Neurol*. 2011;10(8):721-733. doi:10.1016/S1474-4422(11)70141-7
7. Pearson TS, Gilbert L, Opladen T, et al. AADC deficiency from infancy to adulthood: Symptoms and developmental outcome in an international cohort of 63 patients. *J Inherit Metab Dis*. 2020;43(5):1121-1130. doi:10.1002/jimd.12247
8. Wassenberg T, Molero-Luis M, Jeltsch K, et al. Consensus guideline for the diagnosis and treatment of aromatic l-amino acid decarboxylase (AADC) deficiency. *Orphanet J Rare Dis*. 2017;12(1). doi:10.1186/s13023-016-0522-z
9. Cellini B. Biochemical and Computational Approaches to Improve the Clinical Treatment of Dopa Decarboxylase-Related Diseases: An Overview. *Open Biochem J*. 2012;6(1):131-138. doi:10.2174/1874091x01206010131
10. Himmelreich N, Montioli R, Bertoldi M, et al. Aromatic amino acid decarboxylase deficiency: Molecular and metabolic basis and therapeutic outlook. *Mol Genet Metab*. 2019;127(1):12-22. doi:10.1016/j.ymgme.2019.03.009
11. Montioli R, Battini R, Paiardini A, et al. A novel compound heterozygous genotype associated with aromatic amino acid decarboxylase deficiency: Clinical aspects and biochemical studies. *Mol Genet Metab*. 2019;127(2):132-137. doi:10.1016/j.ymgme.2019.05.004
12. Montioli R, Bisello G, Dindo M, Rossignoli G, Voltattorni CB, Bertoldi M. New variants of AADC deficiency expand the knowledge of enzymatic phenotypes. *Arch Biochem Biophys*. 2020;682. doi:10.1016/j.abb.2020.108263
13. Montioli R, Dindo M, Giorgetti A, Piccoli S, Cellini B, Voltattorni CB orr. A comprehensive picture of the mutations associated with aromatic amino acid decarboxylase deficiency: from molecular mechanisms to therapy implications. *Hum Mol Genet*. 2014;23(20):5429-5440. doi:10.1093/hmg/ddu266
14. Montioli R, Janson G, Paiardini A, Bertoldi M, Borri Voltattorni C. Heterozygosis in aromatic amino acid decarboxylase deficiency: Evidence for a positive interallelic

complementation between R347Q and R358H mutations. *IUBMB Life*. 2018;70(3):215-223. doi:10.1002/iub.1718

15. Montioli R, Paiardini A, Kurian MA, et al. The novel R347g pathogenic mutation of aromatic amino acid decarboxylase provides additional molecular insights into enzyme catalysis and deficiency. *Biochim Biophys Acta - Proteins Proteomics*. 2016;1864(6):676-682. doi:10.1016/j.bbapap.2016.03.011

16. Chien YH, Lee NC, Tseng SH, et al. Efficacy and safety of AAV2 gene therapy in children with aromatic L-amino acid decarboxylase deficiency: an open-label, phase 1/2 trial. *Lancet Child Adolesc Heal*. 2017;1(4):265-273. doi:10.1016/S2352-4642(17)30125-6

17. Hwu WL, Muramatsu SI, Tseng SH, et al. Gene therapy for aromatic L-amino acid decarboxylase deficiency. *Sci Transl Med*. 2012;4(134). doi:10.1126/scitranslmed.3003640

18. Kojima K, Nakajima T, Taga N, et al. Gene therapy improves motor and mental function of aromatic l-amino acid decarboxylase deficiency. *Brain*. 2019;142(2):322-333. doi:10.1093/brain/awy331

19. Hyland K, Reott M. Prevalence of Aromatic L-Amino Acid Decarboxylase Deficiency in At-Risk Populations. *Pediatr Neurol*. 2020;106:38-42. doi:10.1016/j.pediatrneurol.2019.11.022

20. Lee KM, Hawi ZH, Parkington HC, et al. The application of human pluripotent stem cells to model the neuronal and glial components of neurodevelopmental disorders. *Mol Psychiatry*. 2020;25(2):368-378. doi:10.1038/s41380-019-0495-0

21. Schuster J, Halvardson J, Pilar Lorenzo L, et al. Transcriptome profiling reveals degree of variability in induced pluripotent stem cell lines: Impact for human disease modeling. *Cell Reprogram*. 2015;17(5):327-337. doi:10.1089/cell.2015.0009

22. Matsa E, Burridge PW, Yu KH, et al. Transcriptome Profiling of Patient-Specific Human iPSC-Cardiomyocytes Predicts Individual Drug Safety and Efficacy Responses In Vitro. *Cell Stem Cell*. 2016;19(3):311-325. doi:10.1016/j.stem.2016.07.006

23. Lehnen D, Barral S, Cardoso T, et al. IAP-Based Cell Sorting Results in Homogeneous Transplantable Dopaminergic Precursor Cells Derived from Human Pluripotent Stem Cells. *Stem Cell Reports*. 2017;9(4):1207-1220. doi:10.1016/j.stemcr.2017.08.016

24. Allen GFG. The neurochemical consequences of aromatic L-amino acid decarboxylase deficiency. *Dr thesis, UCL (University Coll London)* . Published online April 28, 2011.

25. Hyland K, Clayton PT. Aromatic L-amino acid decarboxylase deficiency: Diagnostic methodology. *Clin Chem*. 1992;38(12):2405-2410. doi:10.1093/clinchem/38.12.2405

26. de la Fuente C, Burke DG, Eaton S, Heales SJR. Inhibition of neuronal mitochondrial complex I or lysosomal glucocerebrosidase is associated with increased dopamine and serotonin turnover. *Neurochem Int*. 2017;109:94-100. doi:10.1016/j.neuint.2017.02.013

27. Afgan E, Baker D, Batut B, et al. The Galaxy platform for accessible, reproducible and collaborative biomedical analyses: 2018 update. *Nucleic Acids Res*. 2018;46(W1):W537-W544. doi:10.1093/nar/gky379

28. Bolger AM, Lohse M, Usadel B. Trimmomatic: A flexible trimmer for Illumina sequence data. *Bioinformatics*. 2014;30(15):2114-2120. doi:10.1093/bioinformatics/btu170

29. Kim D, Langmead B, Salzberg SL. HISAT: A fast spliced aligner with low memory requirements. *Nat Methods*. 2015;12(4):357-360. doi:10.1038/nmeth.3317

30. Liao Y, Smyth GK, Shi W. FeatureCounts: An efficient general purpose program for assigning sequence reads to genomic features. *Bioinformatics*. 2014;30(7):923-930. doi:10.1093/bioinformatics/btt656

31. Liu R, Holik AZ, Su S, et al. Why weight? Modelling sample and observational level variability improves power in RNA-seq analyses. *Nucleic Acids Res*. 2015;43(15). doi:10.1093/nar/gkv412

32. Ge SX, Jung D, Jung D, Yao R. ShinyGO: A graphical gene-set enrichment tool for animals and plants. *Bioinformatics*. 2020;36(8):2628-2629. doi:10.1093/bioinformatics/btz931

33. Bindea G, Mlecnik B, Hackl H, et al. ClueGO: A Cytoscape plug-in to decipher functionally grouped gene ontology and pathway annotation networks. *Bioinformatics*. 2009;25(8):1091-1093. doi:10.1093/bioinformatics/btp101

34. Hartfield EM, Yamasaki-Mann M, Ribeiro Fernandes HJ, et al. Physiological characterisation of human iPS-derived dopaminergic neurons. *PLoS One*. 2014;9(2). doi:10.1371/journal.pone.0087388

35. Wakeman DR, Hiller BM, Marmion DJ, et al. Cryopreservation Maintains Functionality of Human iPSC Dopamine Neurons and Rescues Parkinsonian Phenotypes In Vivo. *Stem Cell Reports*. 2017;9(1):149-161. doi:10.1016/j.stemcr.2017.04.033

36. Xi J, Liu Y, Liu H, Chen H, Emborg ME, Zhang SC. Specification of midbrain dopamine neurons from primate pluripotent stem cells. *Stem Cells*. 2012;30(8):1655-1663. doi:10.1002/stem.1152

37. Doi D, Magotani H, Kikuchi T, et al. Pre-clinical study of induced pluripotent stem cell-derived dopaminergic progenitor cells for Parkinson's disease. *Nat Commun*. 2020;11(1). doi:10.1038/s41467-020-17165-w

38. Burkhard P, Dominici P, Borri-Voltattorni C, Jansonius JN, Malashkevich VN. Structural insight into Parkinson's disease treatment from drug-inhibited DOPA decarboxylase. *Nat Struct Biol*. 2001;8(11):963-967. doi:10.1038/nsb1101-963

39. Chang YT, Sharma R, Marsh JL, et al. Levodopa-Responsive Aromatic L-Amino Acid Decarboxylase Deficiency. *Ann Neurol*. 2004;55(3):435-438. doi:10.1002/ana.20055

40. Sabens Liedhegner EA, Steller KM, Mieyal JJ. Levodopa activates apoptosis signaling kinase 1 (ASK1) and promotes apoptosis in a neuronal model: Implications for the treatment of Parkinson's disease. *Chem Res Toxicol*. 2011;24(10):1644-1652. doi:10.1021/tx200082h

41. Park KH, Shin KS, Zhao TT, Park HJ, Lee KE, Lee MK. L-DOPA modulates cell viability through the ERK-c-Jun system in PC12 and dopaminergic neuronal cells. *Neuropharmacology*. 2016;101:87-97. doi:10.1016/j.neuropharm.2015.09.006

42. Blum D, Torch S, Lambeng N, et al. Molecular pathways involved in the neurotoxicity of 6-OHDA, dopamine and MPTP: Contribution to the apoptotic theory in Parkinson's disease. *Prog Neurobiol*. 2001;65(2):135-172. doi:10.1016/S0301-0082(01)00003-X

43. Jiang H, Ren Y, Zhao J, Feng J. Parkin protects human dopaminergic neuroblastoma cells against dopamine-induced apoptosis. *Hum Mol Genet*. 2004;13(16):1745-1754. doi:10.1093/hmg/ddh180

44. Zigmond MJ. Do compensatory processes underlie the preclinical phase of neurodegenerative disease? Insights from an animal model of Parkinsonism. *Neurobiol Dis*. 1997;4(3-4):247-253. doi:10.1006/nbdi.1997.0157

45. Tong ZY, Kingsbury AE, Foster OJF. Up-regulation of tyrosine hydroxylase mRNA in a sub-population of A10 dopamine neurons in Parkinson's disease. *Mol Brain Res*. 2000;79(1-2):45-54. doi:10.1016/S0169-328X(00)00089-9

46. Money KM, Stanwood GD. Developmental origins of brain disorders: Roles for dopamine. *Front Cell Neurosci*. 2013;7(DEC). doi:10.3389/fncel.2013.00260

47. Arenas E, Denham M, Villaescusa JC. How to make a midbrain dopaminergic neuron. *Dev*. 2015;142(11):1918-1936. doi:10.1242/dev.097394

48. Lee NC, Shieh YD, Chien YH, et al. Regulation of the dopaminergic system in a murine model of aromatic l-amino acid decarboxylase deficiency. *Neurobiol Dis*. 2013;52:177-190. doi:10.1016/j.nbd.2012.12.005

49. Shih DF, Hsiao C Der, Min MY, et al. Aromatic L-Amino Acid Decarboxylase (AADC) Is Crucial for Brain Development and Motor Functions. *PLoS One*. 2013;8(8). doi:10.1371/journal.pone.0071741

50. La Manno G, Gyllborg D, Codeluppi S, et al. Molecular Diversity of Midbrain Development in Mouse, Human, and Stem Cells. *Cell*. 2016;167(2):566-580.e19. doi:10.1016/j.cell.2016.09.027

51. Tseng CH, Chien YH, Lee NC, et al. Gene therapy improves brain white matter in aromatic l-amino acid decarboxylase deficiency. *Ann Neurol*. 2019;85(5):644-652. doi:10.1002/ana.25467

Figures:

Fig. 1: Patient-derived neurons show loss of AADC enzymatic activity and dysregulated dopamine synthesis.

(**A**) AADC activity assay relative to total protein (n=19, 9, and 6 for Control, Patient 1 and Patient 2, respectively). (**B**) HPLC detection of extracellular dopamine, HVA, DOPAC and 3-OMD in Control, Patient 1 and Patient 2-derived neuronal cultures. Values are relative to total protein (n=6, 3, 3; n=3, 3, 3; n=5, 3, 3; n=4, 3, 3 respectively). (**C**) Immunoblot analysis for AADC protein in Control, Patient 1 and Patient 2 derived neurons at day 65 of differentiation. Quantification relative to loading control (GAPDH) (n=6, 5, 7 respectively). (**D**) Representative images for AADC and TH immunofluorescence in derived neurons. Scale bar 100µm. Data are represented as mean ±SEM. **P* <0.05; ***P* <0.01; ****P* <0.001, one-way ANOVA followed by Tukey's multiple comparisons test.

Fig. 2: Patient-derived neurons show defects in developmental maturation.

(**A**) Representative immunofluorescence images for NeuN and TH in Control and Patient-derived neurons. Arrows indicate double positive cells. Scale bar 100µm. Inserts show higher magnification of NeuN-positive dopaminergic neurons. (**B**) Quantification of NeuN positive, TH positive and NeuN negative, and TH/NeuN double positive cells in derived neuronal cultures (n=3 for all). (**C**) Representative immunoblot for synaptophysin and loading control (β-ACT) and quantification of relative synaptophysin abundance in total neuronal cell lysates (n=5 for all). (**D**) Representative immunofluorescence for synaptophysin and TH in derived neurons. Scale bar 100µm. Inserts show higher magnification of synaptophysin-positive dopaminergic neurons. Data are represented as mean ±SEM. **P* <0.05; ***P* <0.01; ****P* <0.001, one-way ANOVA followed by Tukey's multiple comparisons test.

Fig. 3: Bulk RNA-Seq analysis shows an abnormal gene expression profile in AADC deficiency patients.

(**A**) Heat map showing hierarchical clustering of protein-coding DEGs in AADC deficiency patients compared to Control (n=3). (**B**) GO terms enrichment for biological process of underexpressed (blue) protein-coding and overexpressed (red) protein-coding DEGs. Top 5 categories are shown. (**C**-**D**) ClueGO analysis of GO terms enrichment of under- (**C**) and over-

(**D**) expressed protein-coding DEGs, showing network graph and pie chart for cellular component (CC), and pie chart for molecular function (MF). Network graph nodes represent GO terms (the most significant are named) and edges indicate shared genes between GO terms. Functional groups of GO terms are indicated by the same color. Pie charts show the percentages of each functional group representation, named with the most significant term. GO functional groups exhibiting higher statistically significant differences using Benjamini-Hochberg p-value correction (FDR<0.05) are shown.

Fig. 4: Bulk RNA-Seq analysis reveals differences in gene expression profiles between Patient 1 and 2 derived-neurons.

(**A**) Heat map showing hierarchical clustering of protein-coding DEGs in Patient 2, compared to Patient 1 (n=3). (**B**) GO terms enrichment for biological process of underexpressed (blue) protein-codifying and overexpressed (red) protein-codifying DEGs. Top 5 categories are shown. (**C**-**D**) ClueGO analysis of GO terms enrichment of under- (**C**) and over- (**D**) expressed protein-codifying DEGs, showing network graph and pie chart for cellular component (CC), and pie chart for molecular function (MF). Network graph nodes represent GO terms (the most significant are named) and edges indicate shared genes between GO terms. Functional groups of GO terms are indicated by the same color. Pie charts show the percentages of each functional group representation, named with the most significant term. GO functional groups exhibiting higher statistically significant differences using Benjamini-Hochberg p-value correction (FDR<0.05) are shown.

Fig. 5: Patient-derived neurons show altered neuronal electrophysiological properties and defects in primary neurite branching.

(**A**) Representative traces of action potentials (APs) elicited by injecting 40pA current in patients and control lines. (**B**) Input/output plot showing number of APs triggered by incremental current steps. (**C**) Active (current threshold and max current sustained) and passive (capacitance) properties of neurons in Control, Patient 1 and Patient 2 neurons (n=39, 34, 26, n=35, 34, 25, and n=41, 38, 32, respectively, from 4 biological replicates). (**D**) Percentage of neurons which sustain >100pA current injection. (**E**) Representative images for dopaminergic neurons branching (scale bar 10μm) and quantification of average primary neurite branching in Control, Patient 1 and Patient 2 mDA neurons (n=11, 7, 11 respectively). (**F**) Representative traces showing sEPSCs at -70mV and quantification of neurons with sEPSC, sEPSC amplitude

and inter-time intervals in Control, Patient 1 and Patient 2 neurons (n=5 for all, n=27, 28, 28, and n=24, 28, 18, respectively, from 4 biological replicates).
Data are represented as mean ±SEM. *P <0.05; **P <0.01; ***P <0.001, one-way ANOVA followed by Tukey's multiple comparisons test and chi-square test in (D).

Fig. 6: Gene therapy significantly improves maturation defects in patient-derived neurons.

(**A**) Representative immunofluorescence for NeuN and TH of patient-derived neurons transduced with LV GFP or LV DDC-GFP. Scale bar 100µm. Inserts show higher magnification of NeuN-positive dopaminergic neurons. (**B**) Quantification of NeuN positive, TH positive and NeuN negative, and TH/NeuN double positive cells in patient-derived neuronal cultures transduced with LV GFP and LV DDC-GFP (n=3 each). (**C**) Representative immunoblot for synaptophysin and loading control (GAPDH), and quantification of relative synaptophysin abundance from total cell lysates extracted from LV GFP and LV DDC-GFP transduced neurons. Results are normalized to the corresponding LV GFP for each patient (n=4, 4, 5, 5 respectively). (**D**) Representative immunofluorescence for synaptophysin and TH in patient-derived neurons transduced with LV GFP or LV DDC-GFP. Scale bar 100µm. Inserts show higher magnification of synaptophysin-positive dopaminergic neurons. (**E**) Representative images for dopaminergic neurons branching (scale bar 10µm) and quantification of average primary neurite branches in patient-derived neurons transduced with LV GFP or LV DDC-GFP (n=15, 18, 13, 18 respectively). Data are represented as mean ±SEM. *P <0.05; **P <0.01; ***P <0.001, two-tailed Student's t-test.

Fig. 7: L-DOPA treatment increases dopamine metabolite production in Patient 2 derived neuronal cultures, with no evidence of cellular toxicity.

(**A**) Localisation of Cys100 in AADC protein structure. The structure corresponds to sus scrofa holoenzyme (PDB code: 1JS3), solved in complex with PLP and carbidopa, and rendered using PyMol™ software. AADC is shown as a schematic, with the two monomers composing the native rearrangement of the enzyme (wheat and marine blue, respectively). PLP and carbidopa are represented as green and yellow sticks, respectively. The side chain of Cys100 is represented as a pink stick. Side chains of Ile101 and Phe103 are represented as orange sticks. (**B**) HPLC detection of extracellular HVA after 80 µM L-DOPA treatment of neuronal cultures for 24 h. Values are relative to total protein (n=3, 3, 5, 5, 4, 4 respectively). (**C**) Dead-cell

proteases release assay after treatment. Results are normalized to the corresponding non-treated condition (n=3 for all).

Data are represented as mean ±SEM. *P <0.05; **P <0.01; ***P <0.001, one-way ANOVA followed by Tukey's multiple comparisons test.

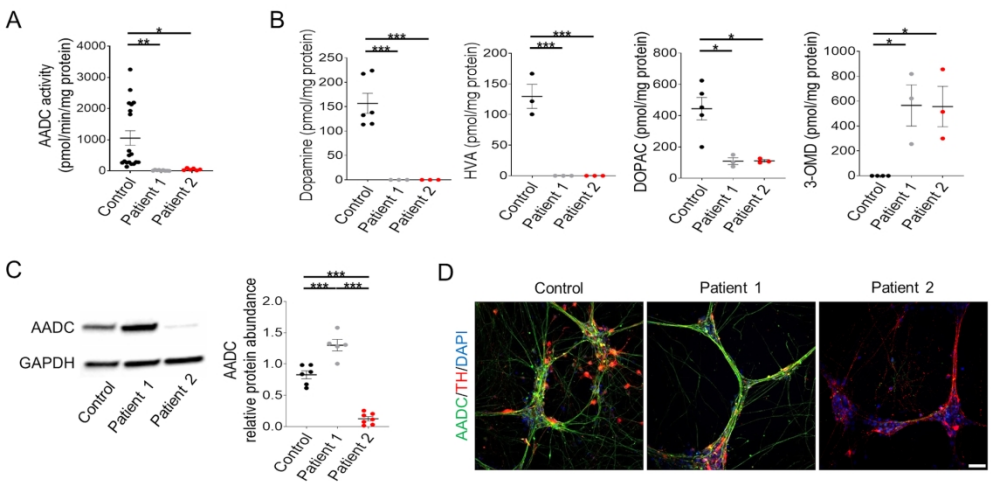

Fig. 1: Patient-derived neurons show loss of AADC enzymatic activity and dysregulated dopamine synthesis.

184x91mm (300 x 300 DPI)

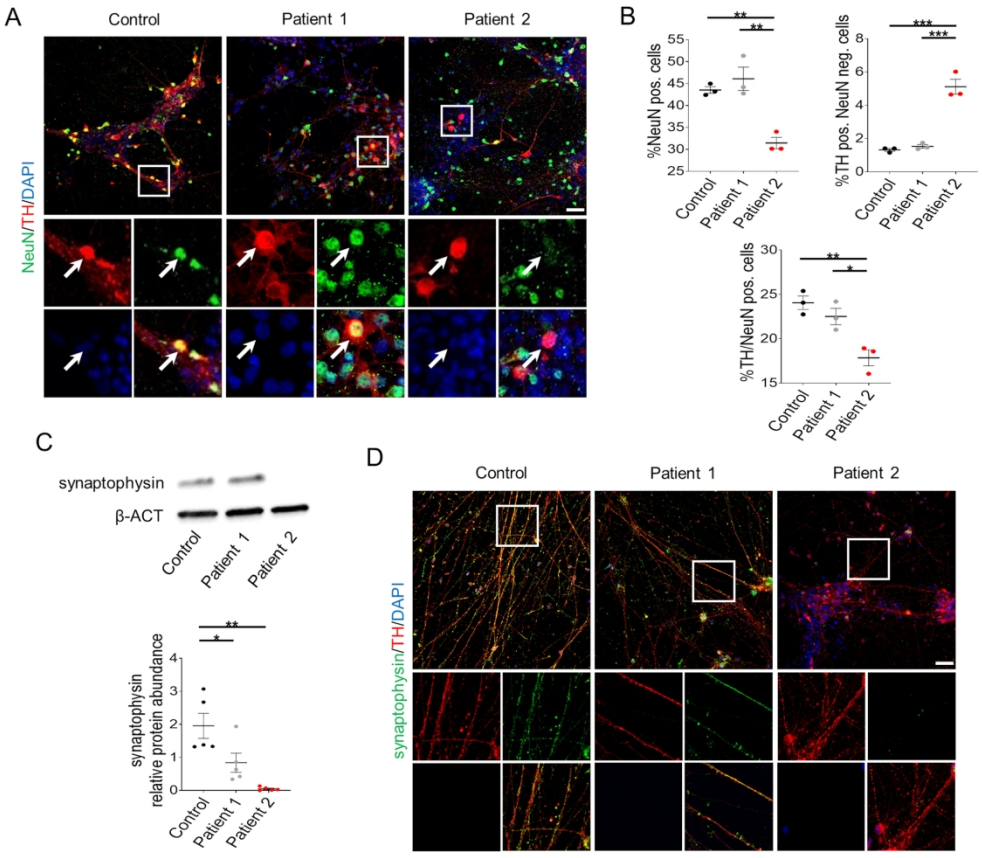

Fig. 2: Patient-derived neurons show defects in developmental maturation.

184x161mm (300 x 300 DPI)

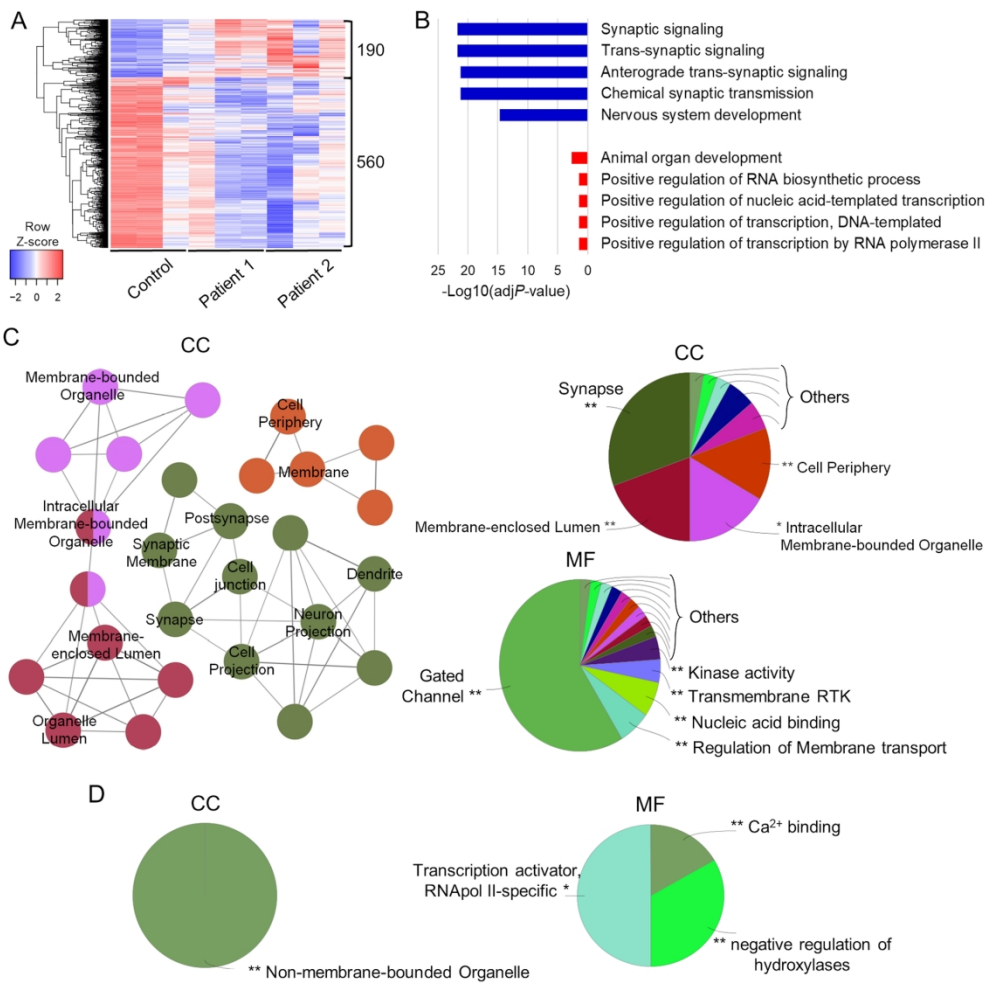

Fig. 3: Bulk RNA-Seq analysis shows an abnormal gene expression profile in AADC deficiency patients.

184x184mm (300 x 300 DPI)

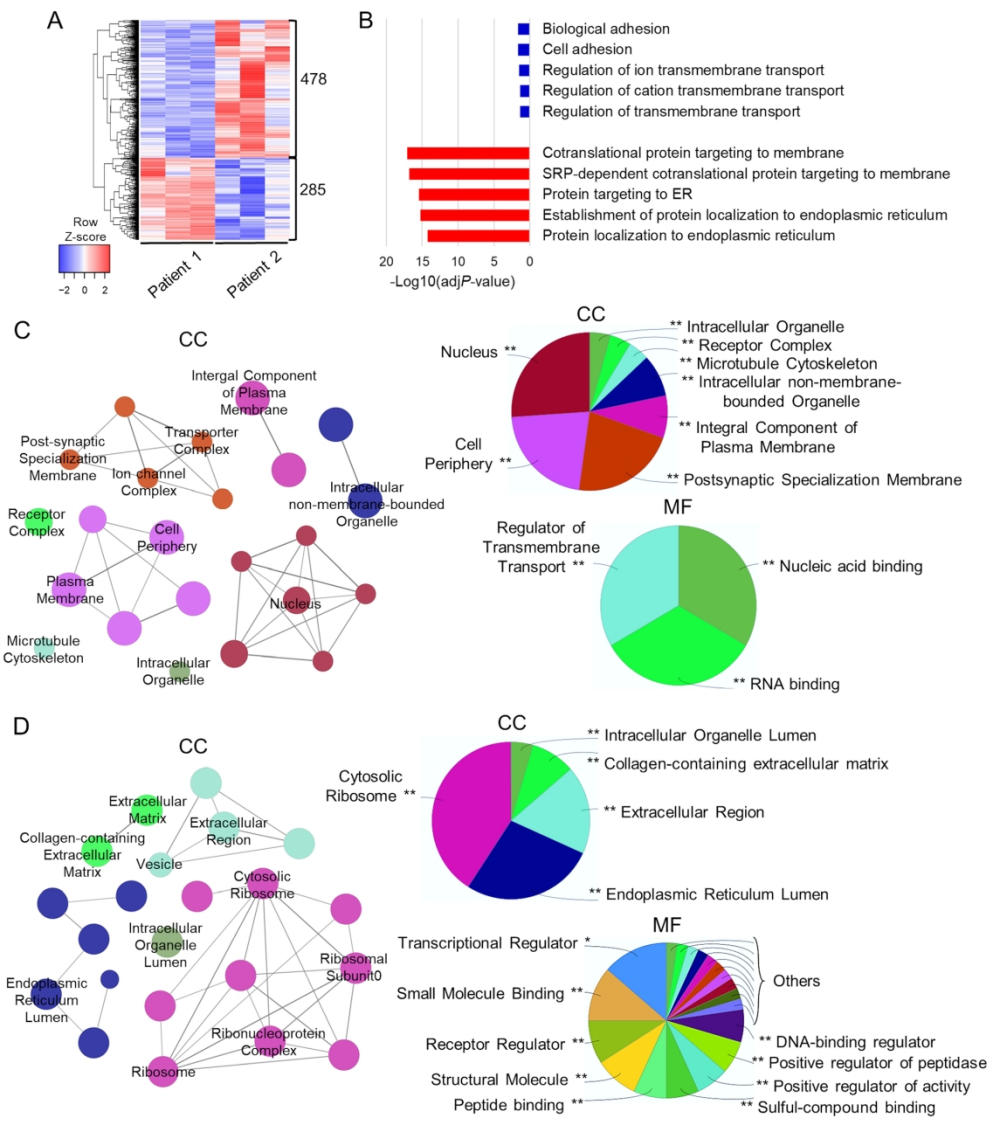

Fig. 4: Bulk RNA-Seq analysis reveals differences in gene expression profiles between Patient 1 and 2 derived-neurons.

184x208mm (300 x 300 DPI)

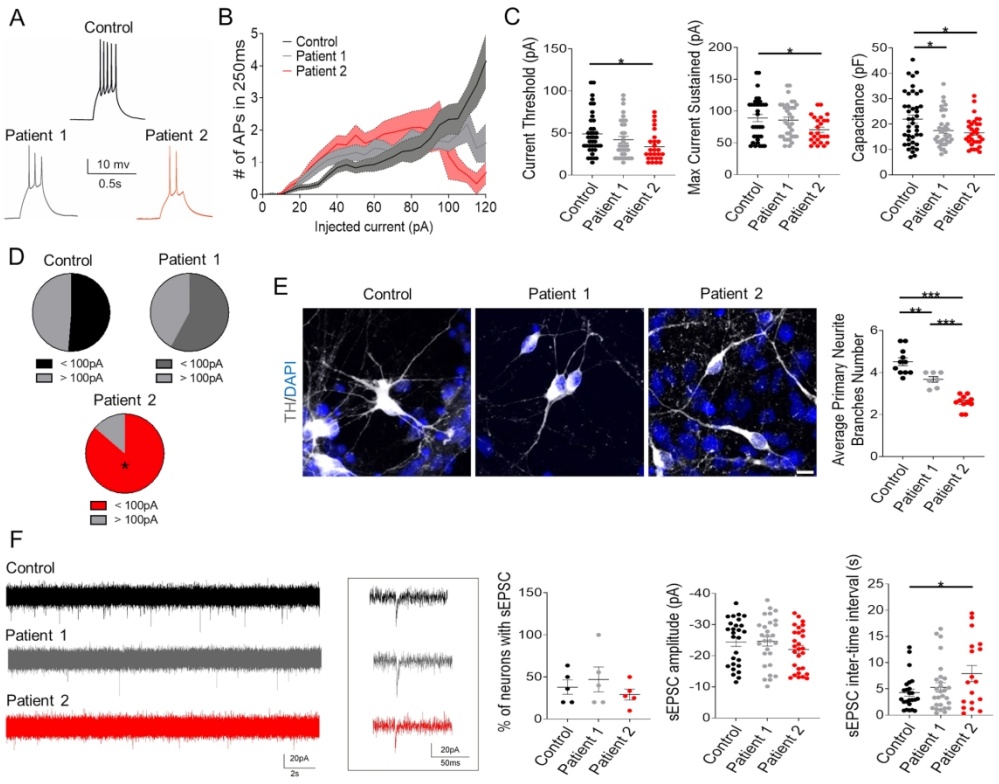

Fig. 5: Patient-derived neurons show altered neuronal electrophysiological properties and defects in primary neurite branching.

184x147mm (300 x 300 DPI)

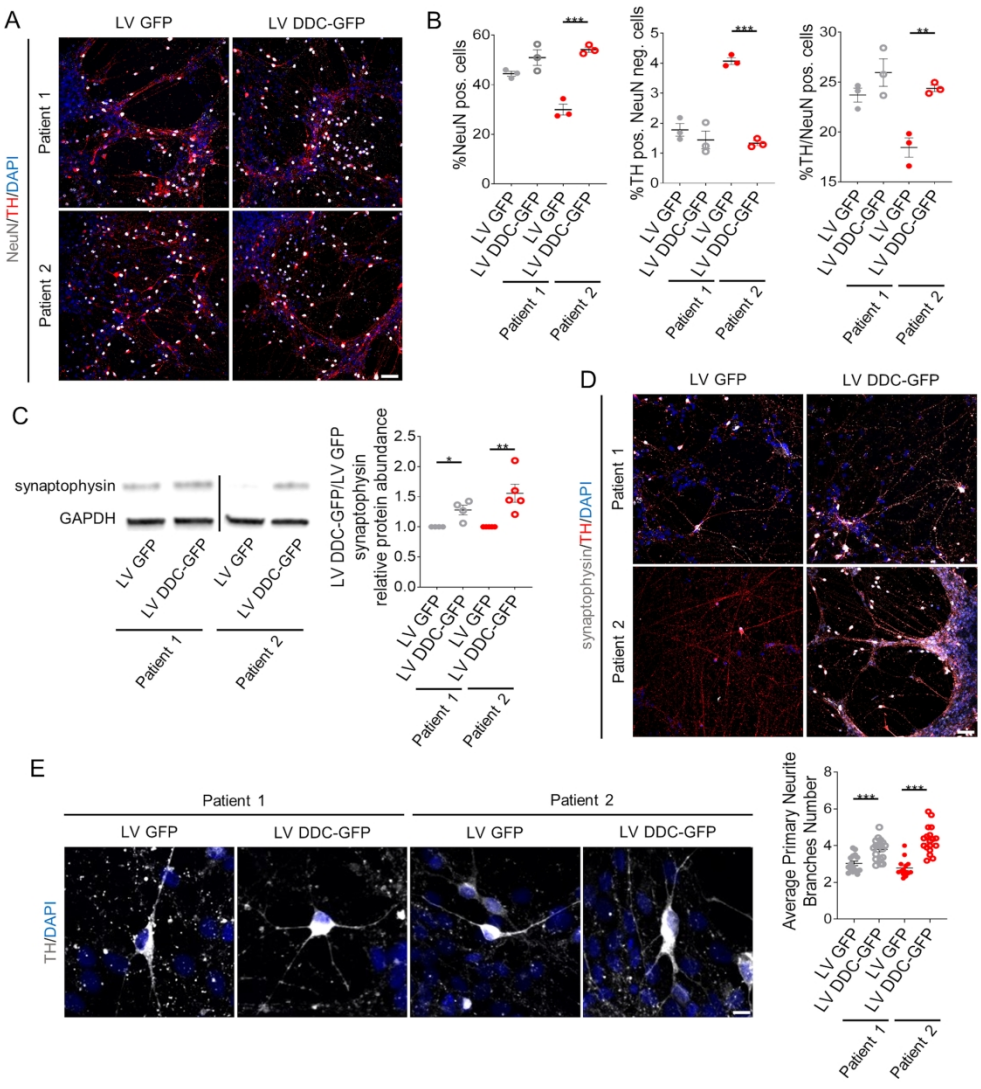

Fig. 6: Gene therapy significantly improves maturation defects in patient-derived neurons.

184x203mm (300 x 300 DPI)

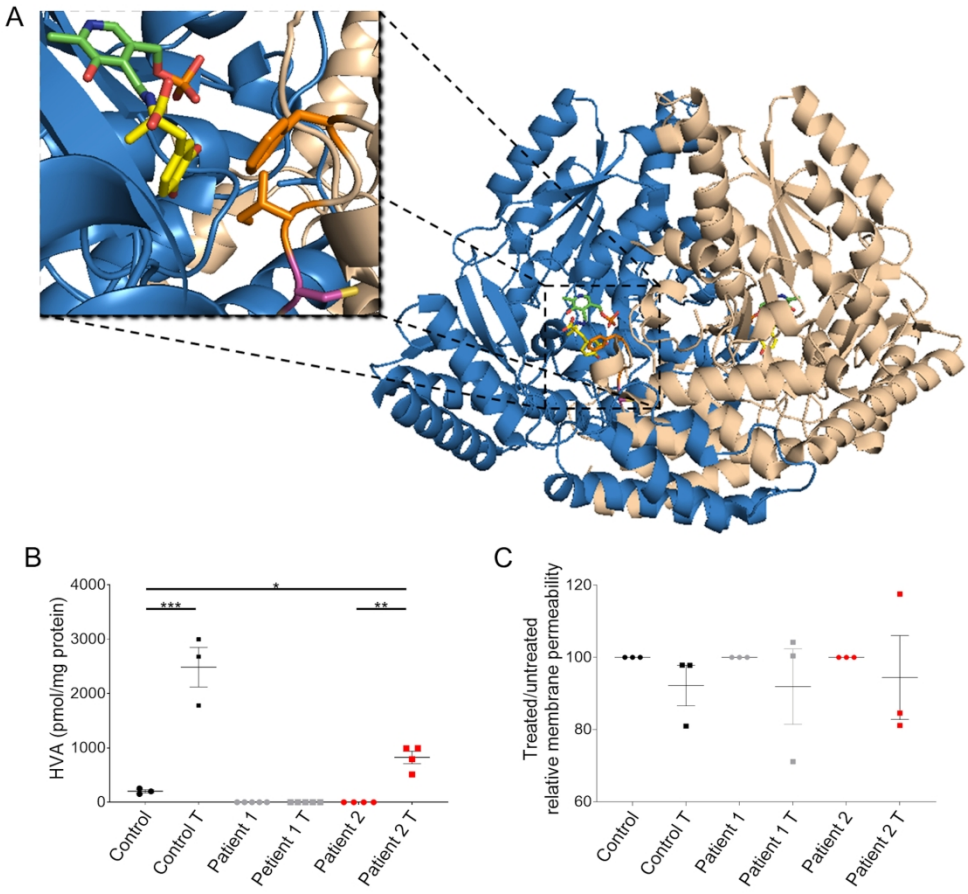

Fig. 7: L-DOPA treatment increases dopamine metabolite production in Patient 2 derived neuronal cultures, with no evidence of cellular toxicity.

184x169mm (300 x 300 DPI)

Table 1 Phenotype and genotype features of AADC deficiency patients

Patient number	Patient line	Clinical phenotype	Zygosity	Location of mutation	Type of mutation	Amino acid change
1	Patient 1-04 Patient 1-10	Oculogyric crises (frequent) Hypotonia Movement disorder Non-ambulant Autonomic features Neurodevelopmental delay Non-verbal	Homozygous	Exon 11	Missense	Arg347Gly
2	Patient 2-01 Patient 2-06	Oculogyric crises (infrequent) Mild motor disorder but achieved independent ambulation Neurodevelopmental delay Behavioural issues Autistic traits Psychiatric symptoms	Heterozygous	Exon 2	Nonsense	Arg7*
				Exon 3	Missense	Cys100Ser

Rossignoli *et al*. develop the first humanized neuronal model of AADC deficiency. They use this patient-derived neuronal system to elucidate disease mechanisms, and in particular to better define neurodevelopmental features, as well as to test precision therapy approaches.

Amino Acids
https://doi.org/10.1007/s00726-020-02885-6

INVITED REVIEW

Oxygen reactivity with pyridoxal 5′-phosphate enzymes: biochemical implications and functional relevance

Giovanni Bisello[1] · Carmen Longo[1] · Giada Rossignoli[1] · Robert S. Phillips[2,3] · Mariarita Bertoldi[1]

Received: 6 May 2020 / Accepted: 18 August 2020

Abstract

The versatility of reactions catalyzed by pyridoxal 5′-phosphate (PLP) enzymes is largely due to the chemistry of their extraordinary catalyst. PLP is necessary for many reactions involving amino acids. Reaction specificity is controlled by the orientation of the external aldimine intermediate that is formed upon addition of the amino acidic substrate to the coenzyme. The breakage of a specific bond of the external aldimine gives rise to a carbanionic intermediate. From this point, the different reaction pathways diverge leading to multiple activities: transamination, decarboxylation, racemization, elimination, and synthesis. A significant novelty appeared approximately 30 years ago when it was reported that some PLP-dependent decarboxylases are able to consume molecular oxygen transforming an amino acid into a carbonyl compound. These side paracatalytic reactions could be particularly relevant for human health, also considering that some of these enzymes are responsible for the synthesis of important neurotransmitters such as γ-aminobutyric acid, dopamine, and serotonin, whose dysregulation under oxidative conditions could have important implications in neurodegenerative states. However, the reactivity of PLP enzymes with dioxygen is not confined to mammals/animals. In fact, some plant PLP decarboxylases have been reported to catalyze oxidative reactions producing carbonyl compounds. Moreover, other recent reports revealed the existence of new oxidase activities catalyzed by new PLP enzymes, MppP, RohP, Ind4, CcbF, PvdN, Cap15, and CuaB. These PLP enzymes belong to the bacterial and fungal kingdoms and are present in organisms synthesizing bioactive compounds. These new PLP activities are not paracatalytic and could only scratch the surface on a wider and unexpected catalytic capability of PLP enzymes.

Keywords Pyridoxal 5′-phosphate-dependent enzymes · Decarboxylase · Oxidase activity · Oxidative stress · Aromatic aldehyde

Abbreviations

PLP	Pyridoxal 5′-phosphate
AADC or DDC	Aromatic amino acid or dopa decarboxylase
GAD	Glutamate decarboxylase
DHPAA or DOPAL	3,4-Dihydroxyphenylacetaldehyde
DHPAAS	3,4-Dihydroxyphenylacetaldehyde synthase
PAAS	Phenylacetaldehyde synthase
GABA	γ-Aminobutyric acid
ODC	Ornithine decarboxylase
LDC	L-Lysine decarboxylase
ROS	Reactive oxygen species
TH	Tyrosine hydroxylase

Handling Editor: J. D. Wade.

✉ Mariarita Bertoldi
mita.bertoldi@univr.it

[1] Department of Neuroscience, Biomedicine and Movement Sciences, Section of Biochemistry, University of Verona, Verona, Italy

[2] Department of Chemistry, University of Georgia, Athens, GA 30602, USA

[3] Department of Biochemistry and Molecular Biology, University of Georgia, Athens, GA 30602, USA

Pyridoxal 5′-phosphate (PLP)-dependent enzymes are able to react with oxygen

Approximately 30 years ago, it was reported (Abell and Schloss 1991) that some enzymes that do not bind metals/cofactors typical of redox reactions are able to consume oxygen. These enzymes belong to diverse families and catalyze different chemical reactions.

Published online: 25 August 2020

The paper of Abell and Schloss represented a milestone, since it was the first time, after the identification of the oxygenase reaction catalyzed by ribulose 1,5-bisphosphate carboxylase/oxygenase (RuBisCO) (Bowes et al. 1971), that other enzymes were reported to catalyze an oxygenase side reaction and raised the issue of how such activity could occur.

Actually, the question of the reactivity with oxygen for enzymes lacking a proper metal or redox cofactor is still puzzling. It is known that molecular oxygen could be present as an excited singlet and a ground triplet state, the former being highly reactive, the latter more stable, since its reaction with organic substrates is a spin-forbidden process. This latter biradical species must be activated by a series of one-electron stepwise transfer reactions leading sequentially to superoxide anion, hydrogen peroxide, hydroxyl radical, and, finally, water (Klinman 2007). A metal or a redox cofactor like flavin can readily accomplish these subsequent steps. Flavoproteins are often considered a prototype, since the flavin cofactor is able to catalyze single-electron transfers in the absence of a metal. The spin-forbidden paradox is overcome in this class of enzymes by a single-electron transfer of a reduced flavin to the triplet state of oxygen to generate superoxide and flavin semiquinone cage radical pair, leading to different reaction pathways spanning from the dissociation to produce oxygen radicals, to a second electron transfer to form hydrogen peroxide and oxidized flavin, to the formation of a covalent hydroperoxy-flavin leading to further dissociation to hydrogen peroxide or insertion of an oxygen atom into the substrate (Mattevi 2006; Chaiyen et al. 2012; Daithankar et al. 2012).

Schloss and others studied many enzymes that have unusual and non-canonical reactivity with O_2 (Abell and Schloss 1991; Hixon et al. 1996) and, based on the knowledge collected on RuBisCo that forms a oxygen-reactive enolate intermediate (Bowes et al. 1971), they suggested that any enzyme capable of forming carbanionic intermediates could have the propensity to react with molecular oxygen (Abell and Schloss 1991). The difference between the carbanion-forming enzymes consuming molecular oxygen and those exhibiting no susceptibility to it was proposed to lie in the accessibility of the carbanion intermediate and in the stabilization of a subsequent intermediate, a peroxide anion, occurring through protonation and/or metal coordination (Abell and Schloss 1991).

The oxygenase off-pathway activities of enzymes generating carbanionic intermediates have been designated as the so-called paracatalytic reactions with O_2 (Christen et al. 1976; Cogoli-Greuter et al. 1979; Christen and Gasser 1980). They have been proposed to play a role in the generation of reactive species important in signaling and also in contributing to the progression of neurodegenerative diseases (Bunik et al. 2007).

One of the enzymes able to catalyze an oxygenase side reaction (identified by Abell and Schloss) was the PLP-dependent *E. coli* glutamate decarboxylase (GAD). The authors reported that GAD was able to consume O_2 in the presence of L-glutamic acid, generating succinic semialdehyde at a rate of about 0.1% that of the main decarboxylation reaction generating γ-aminobutyric acid (GABA) (Abell and Schloss 1991). The peculiarity of this reaction is that dioxygen is not at all a substrate for PLP enzymes, whose usual substrates are amino acids, amines, and some few sugars.

It is known that the versatility of reactions catalyzed by PLP-dependent enzymes is largely due to the chemistry of their extraordinary catalyst. PLP is necessary for most reactions of amino acids, and it is invariably bound to the protein moiety of all PLP enzymes through a Schiff base linkage with a lysine residue forming an internal aldimine structure. In the presence of an incoming amino acid, the ε-amino group of the internal aldimine is exchanged with the α-amino group of the substrate generating the external aldimine intermediate. From this point, the different reaction pathways diverge leading to multiple non-electron transfer reactions: transamination, decarboxylation, racemization, elimination, and substitution (Fig. 1). This is accomplished by the breakage of a specific bond of the external aldimine. In 1966, Dunathan proposed (Dunathan 1966) that the scissile bond is oriented perpendicular to the plane of the imine–pyridine ring, since, in this conformation, the highest orbital overlap is achieved and, thus, the best transition state stabilization could be reached. Indeed, it is the protein scaffold that directs the positioning of the bond to be broken. This explains how reaction specificity of PLP-dependent enzymes is controlled. It follows that once the external aldimine is formed, the possibilities are that a carboxylate or a proton or a side chain will be removed. Thus, three possible different carbanionic intermediates, the quinonoid species Q1 or Q2 or Q3, are formed and, depending on the reaction that each of these quinonoids undergoes, several different pathways will be followed giving rise to the various PLP-dependent enzymatic activities (Fig. 1). This also explains the versatility of the PLP enzymes, which comprise up to 1.5% of enzymes in microbial genomes (Percudani and Peracchi 2003) and about 4% of all enzyme activities (Hoegl et al. 2018). However, the protein moiety is not able to completely abolish the intrinsic high reactivity of the cofactor, and this is the reason why PLP enzymes are promiscuous and able to catalyze, in addition to the main reaction, also side reactions with amino acids, albeit less efficiently (John 1995). Following this view, as an example, the prototype of all PLP enzymes, aspartate aminotransferase, can also perform a β-elimination and/or a racemization reaction (John and Fasella 1969; Kochhar and Christen 1988, 1992) in addition to the transaminase main reaction. This

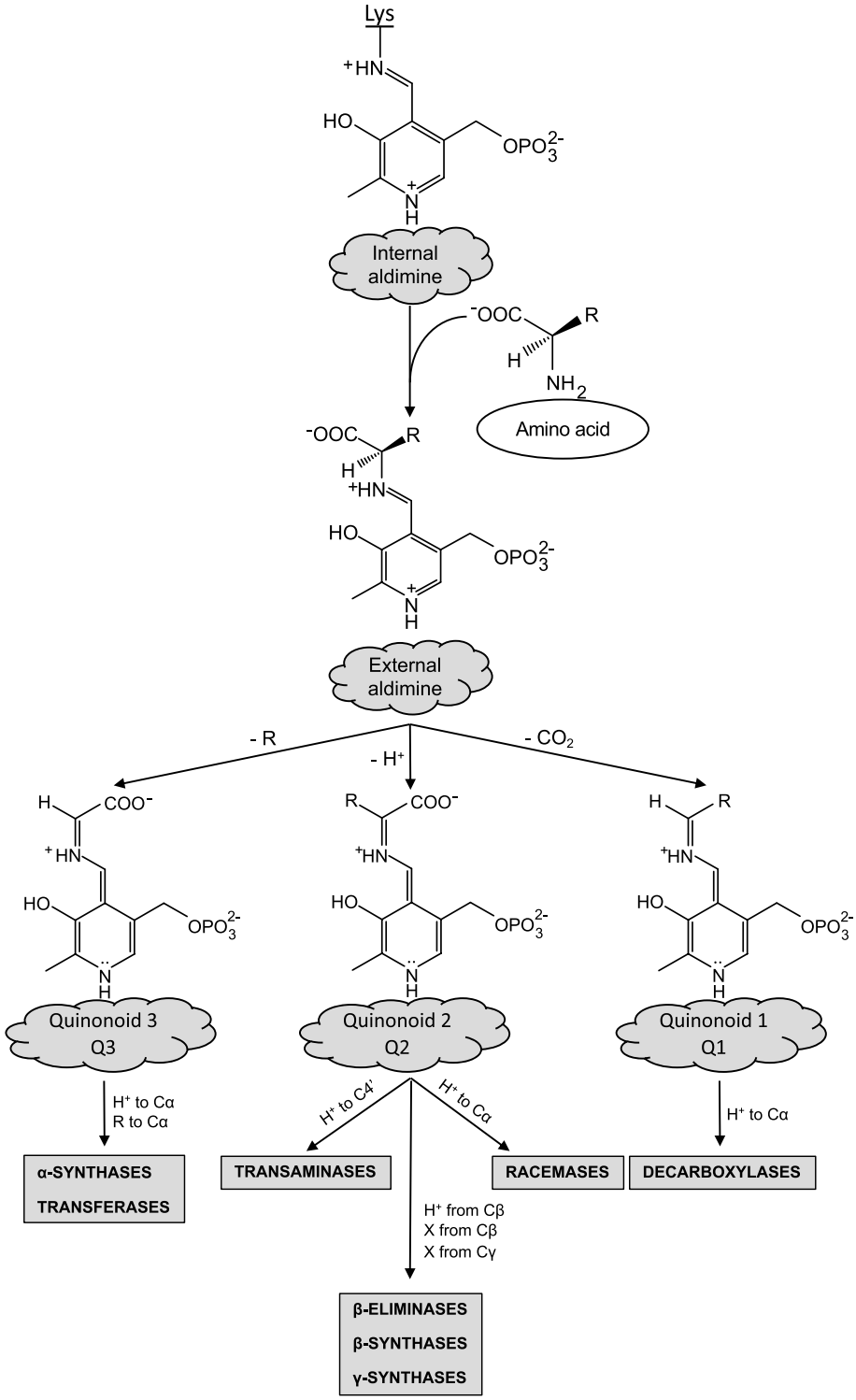

Fig. 1 Reaction pathways of PLP enzymes. The internal aldimine is converted into the external aldimine which, subsequently, undergoes a bond breakage. The fate of the generated carbanionic intermediate, the quinonoid Q1 or Q2 or Q3, depends on reprotonation to α-carbon or to C4′ leading to the different products and PLP-dependent enzyme activities

ability to catalyze one or more side reactions holds true for the majority of PLP enzymes; however, the substrates of these side reactions are always amino acids or amines. Nevertheless, given the common feature of generating carbanionic intermediates, PLP-dependent enzymes represent likely candidates also for oxygenase reactions (Fig. 1).

Since the identification of the reaction of GAD (Abell and Schloss 1991), reactivity towards O_2 has been determined for many other PLP enzymes, as reported in the recent reviews (Hoffarth et al. 2020; Bunik et al. 2011), highlighting that this propensity is more widespread than heretofore imagined and not only confined to paracatalytic reactions.

A recent detailed overview of all reactions catalyzed by PLP enzymes involving O_2 (Hoffarth et al. 2020) stimulates to provide more insight into the intricacy of these reaction mechanisms and to the physiological significance of this reactivity.

Looking into the literature, it is evident that reactions of PLP enzymes in aerobiosis and in anaerobiosis have been annotated in different ways: decarboxylation, oxidative deamination, decarboxylation-dependent transamination, decarboxylation-dependent oxidative deamination, oxidative decarboxylation, and decarboxylating oxygenation. While the first four reactions can be typical of PLP enzymes, oxidative decarboxylation is best used for ketoacid dehydrogenases, since the products of such reactions are not aldehydes/ketones nor ammonia. For the decarboxylating oxygenation, it is used as decarboxylation-dependent oxidative deamination; however, some attention should be payed (see below). To dispel some doubts, some terminology and activity to which it refers is given to contribute and improve clarity (Fig. 2).

The paradigmatic case of dopa decarboxylase (DDC)

DDC, also known as aromatic amino acid decarboxylase (AADC), has a broad substrate specificity being able to convert both L-dopa and L-5-hydroxytryptophan to dopamine and serotonin (Fig. 3a), respectively, in addition to other aromatic amino acids, producing the so-called trace amines (Bertoldi 2014). A scheme of all reactive substrates or products of DDC is reported in Fig. 4. A decarboxylation-dependent transamination was identified as a side reaction for DDC (O'Leary and Baughn 1977). This reaction consists of an off-pathway step following decarboxylation at Cα (Fig. 1) where protonation of Q1 occurs at C4′ instead of at Cα leading to equimolar amount of carbonyl compound

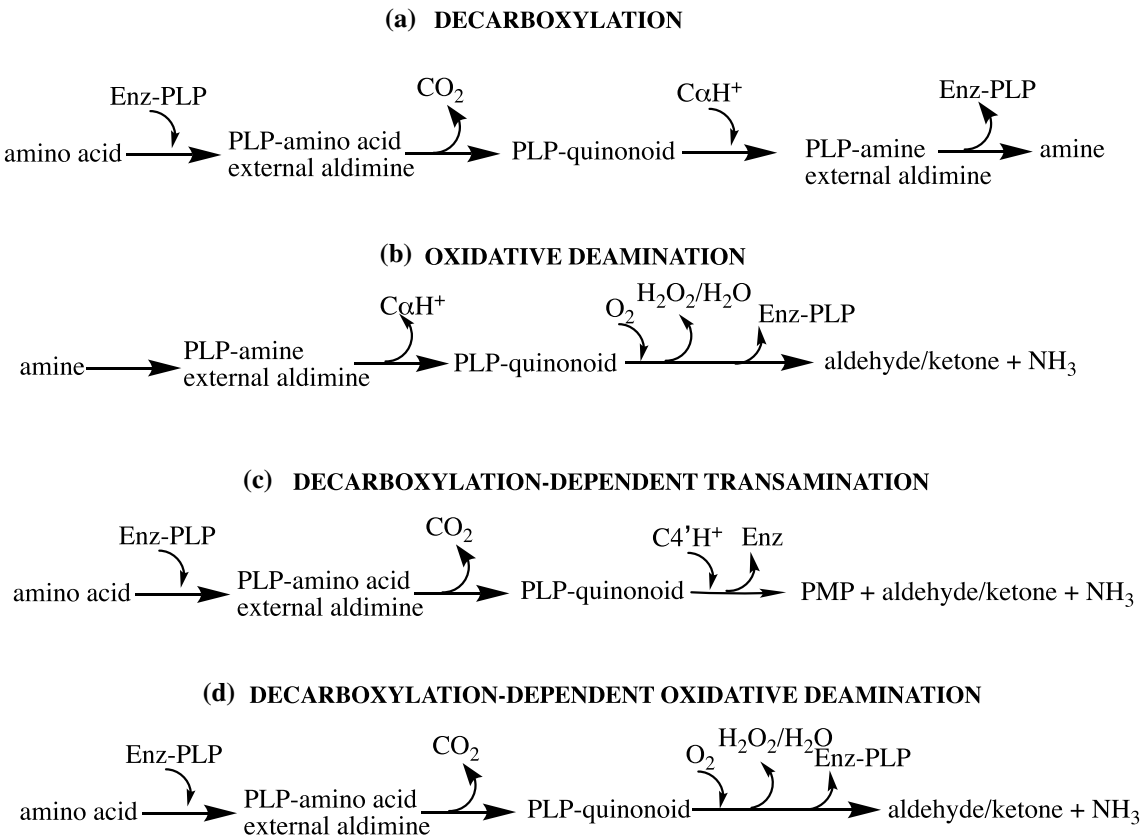

Fig. 2 Terminology of PLP reactions. **a** Decarboxylation of an amino acid to an amine catalyzed by a PLP decarboxylase; **b** oxidative deamination of an amine into the corresponding carbonyl compound and ammonia together with O_2 consumption; **c** decarboxylation-dependent transamination of an amino acid converted into the corresponding carbonyl compound and ammonia. Enz-PLP refers to the catalytic competent decarboxylase, Enz refers to a decarboxylase whose catalytically active coenzyme PLP has been transformed into PMP which is not a coenzyme for decarboxylation. Thus, once the PLP of the enzyme has been all transformed into PMP, the enzyme is inactivated. For this reason, the products are equimolar to PLP; **d** decarboxylation-dependent oxidative deamination of an amino acid first decarboxylated and then converted into the corresponding carbonyl compound and ammonia concomitantly with O_2 consumption

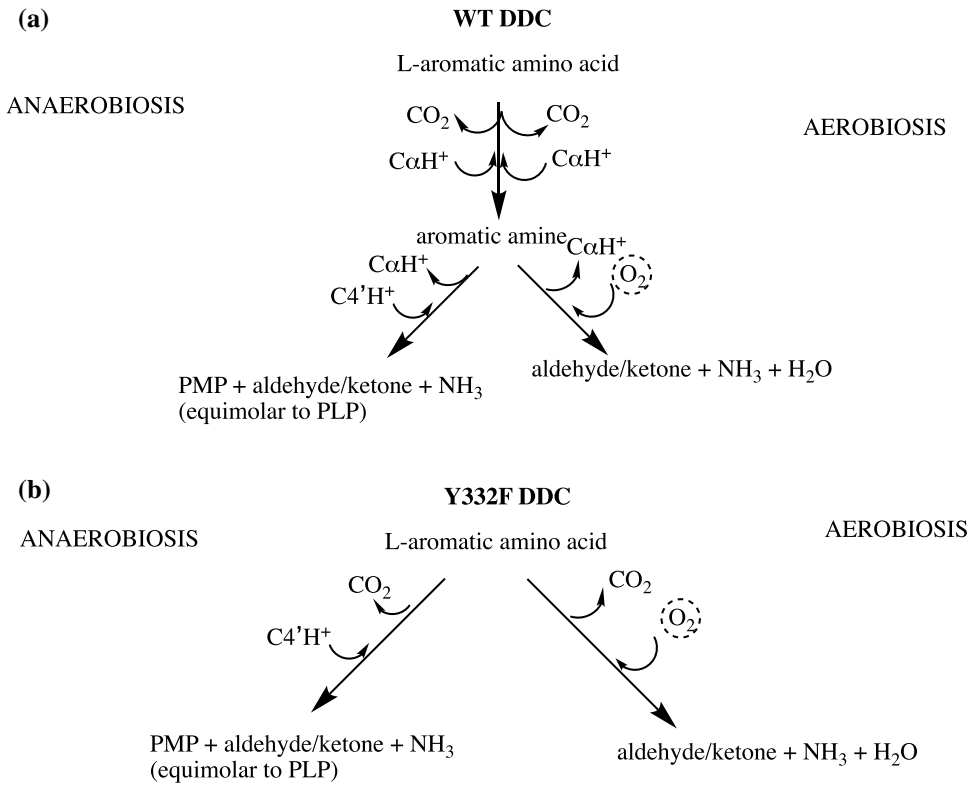

Fig. 3 Main and paracatalytic reactions of Dopa decarboxylase. **a** The reactions catalyzed by wild-type (WT) DDC under aerobic and anaerobic conditions; **b** the reactions catalyzed by Y332F DDC under aerobic and anaerobic conditions

and pyridoxamine 5′-phosphate (PMP), a coenzyme incapable of performing further decarboxylation and thus leading to enzyme inactivation. However, experimental data in the presence of α-methyldopa did not support this reaction mechanism, since the produced carbonyl compound far exceeded, on a molar basis, coenzyme content (Barboni et al. 1981). This behavior remained obscure until the end of last century, when our group has demonstrated that mammalian DDC catalyzes an oxidative deamination reaction with serotonin, dopamine, and α-methylDopa, following α-methyldopamine formation, concomitantly with oxygen consumption (Bertoldi et al. 1996, 1998, 1999b; Bertoldi and Borri Voltattorni 2003). These reactions are accompanied by enzyme inactivation through different pathways, mechanism-based (Bertoldi et al. 1996) or affinity labeling (Bertoldi et al. 1998) due to the covalent binding of the carbonyl product to the PLP coenzyme. This inactivation was interpreted as a possible regulation of DDC concurring in exacerbating oxidative stress conditions (see below). The proposed mechanism for oxidative deamination starts with PLP forming an external aldimine with the aromatic amine that is subsequently deprotonated, giving a quinonoid species accessible to oxygen, then forming the carbonyl compound, ammonia, and consuming oxygen. A small amount of PMP was produced, so the occurrence of the decarboxylation-dependent transamination (also called abortive transamination in some papers) was not excluded (Fig. 3a). It was also assessed that, in the absence of oxygen, aromatic amines undergo a half-transamination reaction (Bertoldi and Borri Voltattorni 2003), whereas α-methyldopa underwent the decarboxylation-dependent transamination (Bertoldi and Borri Voltattorni 2000), leading, in both cases, to the conversion of PLP into catalytically inactive PMP and a stoichiometric amount of the aldehyde/ketone. Thus, DDC has the ability to protonate the quinonoid intermediate at C4′ and not only at Cα (Fig. 3a).

It has also been demonstrated that the main decarboxylation reaction of DDC is somewhat sensitive to oxygen, since in its absence, both k_{cat} and K_m for L-Dopa and L-5HTP are decreased and PMP is formed, due to a decarboxylation-dependent transamination (Bertoldi and Borri Voltattorni 2000), reinforcing a possible regulation mechanism exerted by O_2. Until these findings, DDC was supposed to catalyze only paracatalytic reactions with oxygen.

In this complex picture, it was unexpected that mutation of Tyr-332, a conserved residue, to phenylalanine transforms DDC into a decarboxylation-dependent oxidative deaminase, that is an enzyme not able to catalyze amine formation, rather Y332F reacts with oxygen and forms 3,4-dihydroxyphenylacetaldehyde (DHPAA or DOPAL) and ammonia (Fig. 3b) pointing out a catalytic role for Tyr-332 in the main decarboxylation mechanism as the residue responsible for the Cα protonation (Bertoldi and Voltattorni 2001; Bertoldi et al. 2002). This residue belongs to a mobile loop of DDC presumed to play important roles in the activity of the enzyme, since it is

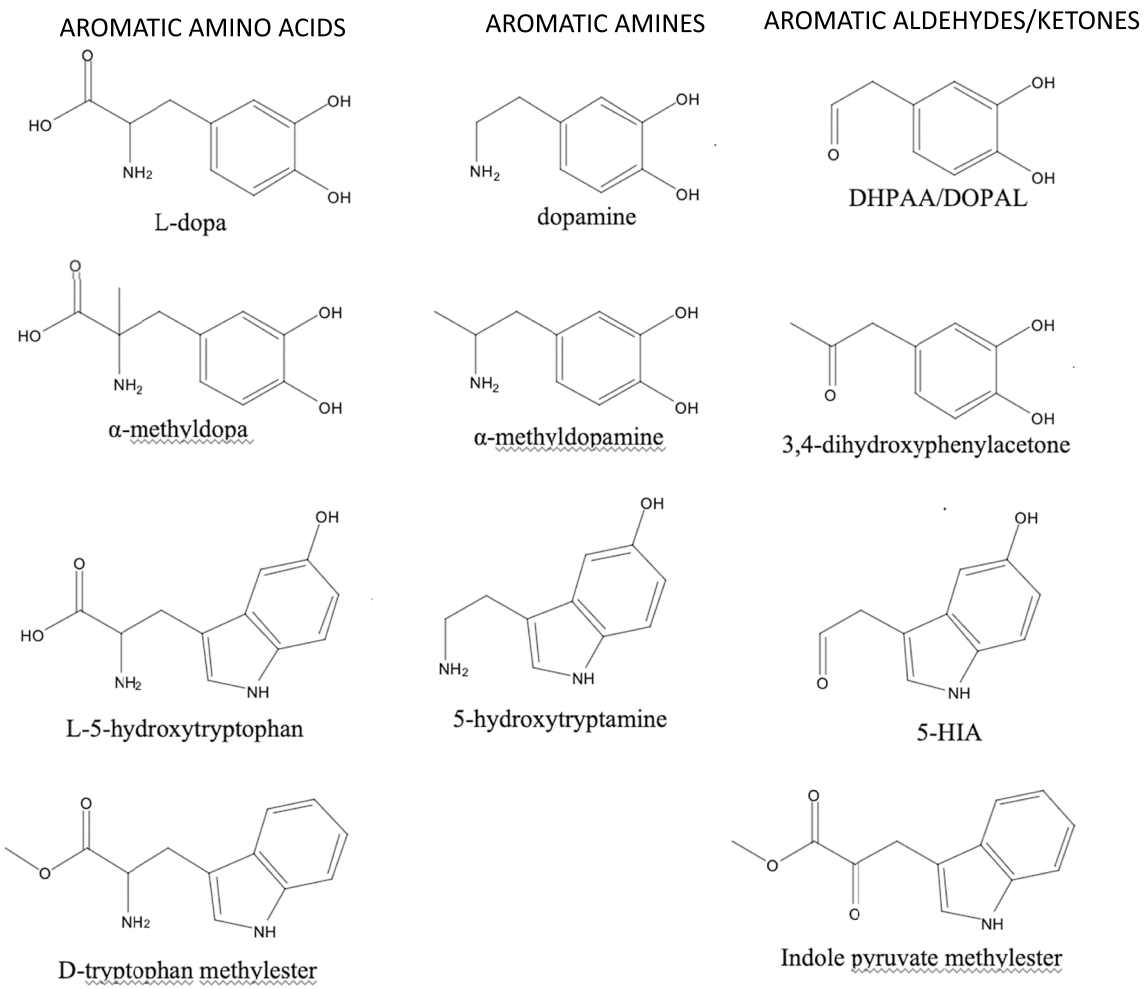

Fig. 4 Structures of substrates and products of DDC. Aromatic amino acid substrates of the decarboxylation reaction of DDC are on the left, aromatic amines products of decarboxylation and substrates of oxidative deamination are in the center, and aromatic aldehydes or ketones products of oxidative deamination are on the right. 5-HIA, 5-hydroxyindoleacetaldehyde

predicted to cover the active site as a lid positioning essential residues in a proper orientation and microenvironment useful for catalysis (Paiardini et al. 2017). Under anaerobic conditions, the reaction of the Y332F DDC with its substrates immediately converts PLP into PMP (Bertoldi et al. 2002). These observations pushed the investigation towards the identification of intermediates of the oxygen-consuming reaction catalyzed by DDC. A substrate analog, D-tryptophan methyl-ester, that mimics the position of the α-proton of the aromatic amines with its stereospecificity, allowed the identification and validation of a quinonoid species as an intermediate of the oxidative deamination reaction (Bertoldi et al. 2005), thus confirming what was hypothesized by Abell and Schloss about the reactivity of the carbanionic intermediate with oxygen. The step forward has been to elucidate what happens in the steps following oxygen binding to the quinonoid. An insight came from further investigations leading to the identification and characterization of other intermediates of the oxidase activity, so that a chemical mechanism could be advanced (Bertoldi et al. 2008), where it emerged how oxygen is able to control the equilibrium among reaction intermediates of DDC.

Overall, a reaction mechanism of DDC with O_2 has been finally accepted (Fig. 5) (Bertoldi et al. 2008). Once the external aldimine is formed, decarboxylation or deprotonation takes place leading to a quinonoid species in equilibrium with a ketimine species that forms upon reprotonation to C4′. The presence of oxygen controls this equilibrium in favor of the quinonoid species that is attacked by O_2 giving rise to a radical one-electron transfer and forming superoxide anion and semiquinone. Superoxide couples with semiquinone generating a hydroperoxide species. From this intermediate, the products of the reaction are then generated.

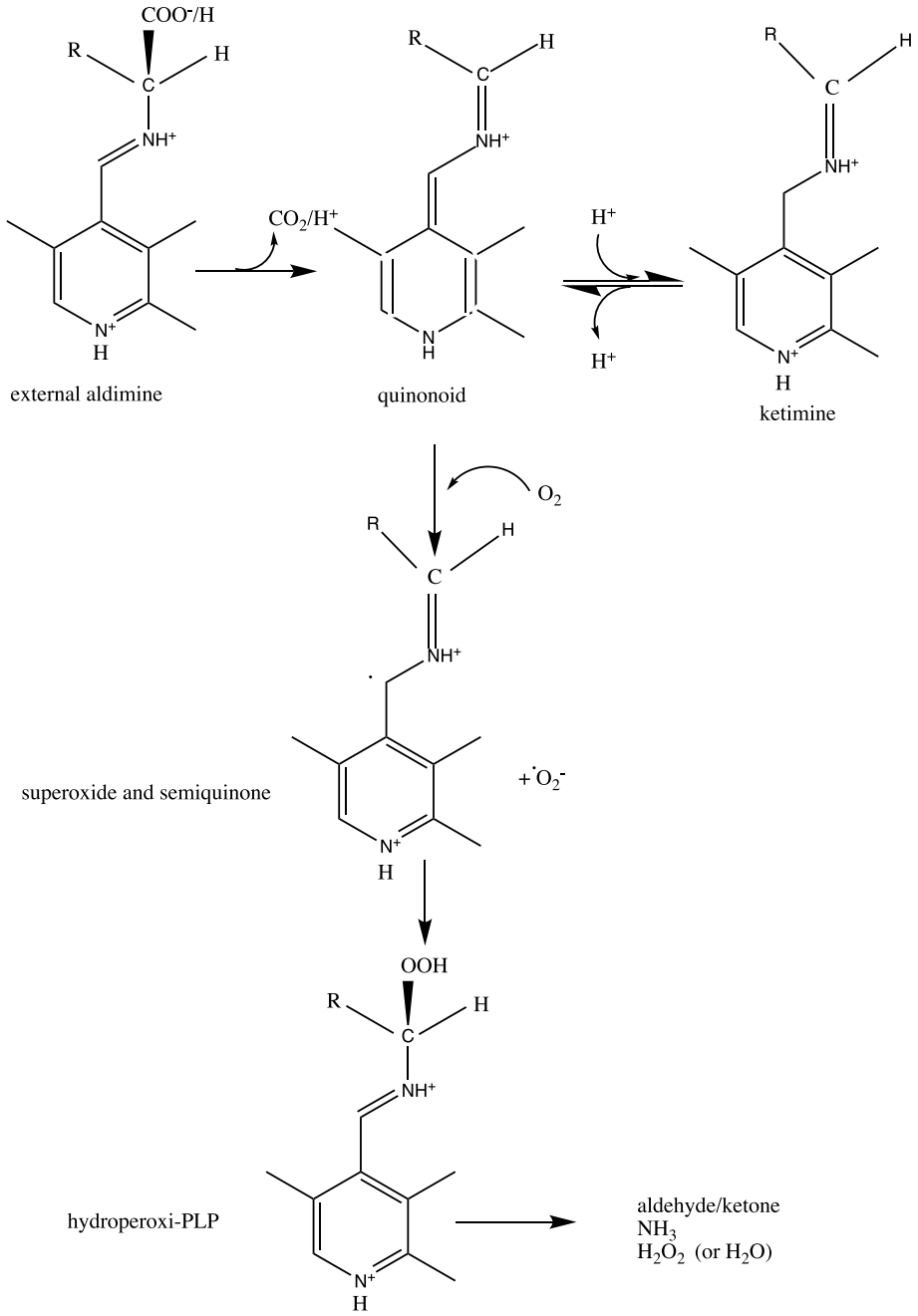

Fig. 5 Reaction mechanism of oxidative deamination catalyzed by DDC. The substrates of the reaction with oxygen (both aromatic amino acids or amines) at first form an external aldimine that is subsequently decarboxylated (from amino acids) or deprotonated (from amines) to give the quinonoid that partitions between C4′ protonation to give a ketimine that is in equilibrium with the quinonoid that could be attacked by oxygen generating a radical pair, semiquinone, and superoxide anion, that form a hydroperoxy-PLP intermediate responsible for the synthesis of the oxidative deamination products. R refers to the aromatic (cathecol or indole) moiety. (Adapted from (Bertoldi et al. 2008))

Other aromatic amino acid decarboxylases reactive towards oxygen: AADCs and aromatic aldehyde synthases (AAS)s

AADCs from other different sources (plants, mushrooms, and insects) are known, since these enzymes have evolved in many organisms yielding a number of paralogous enzymes with different substrate specificity and catalytic mechanisms (Facchini et al. 2000; Torrens-Spence et al. 2020).

The plant kingdom is particularly specialized, since plant AADCs, differently from those of mammals and insects, are characterized by a narrow substrate specificity, exhibiting a substrate preference for either phenol or indole amino acid, giving rise to L-tyrosine/L-dopa decarboxylases or to L-tryptophan decarboxylases (Noé et al. 1984; Facchini and De Luca 1994; Facchini et al. 2000). These enzymes, isolated from a variety of plant species (Facchini et al. 2000), produce aromatic monoamines acting as precursors for many important natural products useful to plant metabolism. No activity towards oxygen has been reported for these enzymes (Fig. 6).

In 2006, a paper reported the identification of a tomato PLP-L-phenylalanine decarboxylase able to remove CO_2 and produce phenethylamine, subsequently converted into

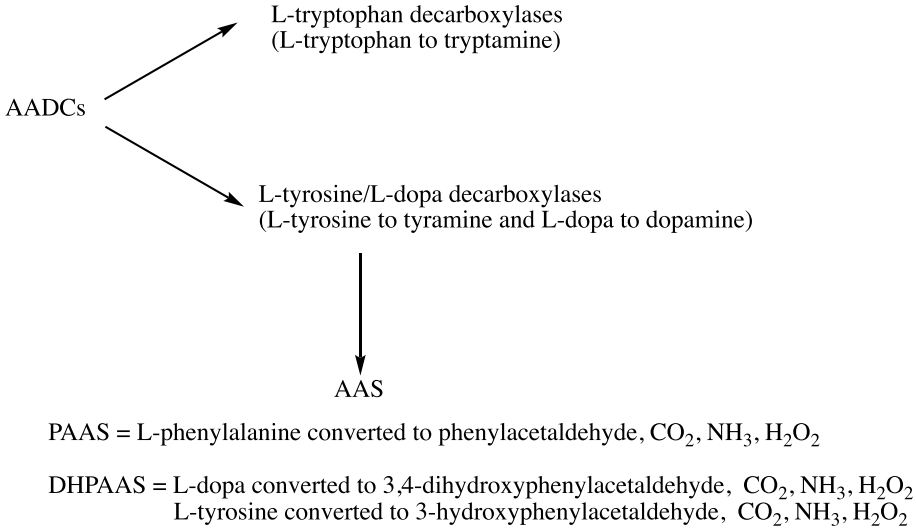

Fig. 6 Plant AADCs and AASs. Plant AADCs are specialized enzymes clustered in two groups: L-tryptophan decarboxylases producing tryptamine and L-tyrosine/L-dopa decarboxylase producing tyramine/dopamine. A different group probably originating from L-tyrosine/L-dopa decarboxylases identifies AASs such as PAAS and DHPAAS converting aromatic amino acids into the corresponding aromatic aldehydes, ammonia and hydrogen peroxide, and consuming oxygen

phenylacetaldehyde by an identified enzymatic activity in the pathway of 2-phenylethanol, a compound essential to contribute to tomato flavor (Tieman et al. 2006). In the same year, the identification of rose and petunia phenylacetaldehyde synthase (PAAS) has been reported. These PLP-dependent enzymes show high amino acid identity (about 65%) with plant L-tyrosine/L-dopa decarboxylases and L-tryptophan decarboxylases, and directly convert L-phenylalanine into phenylacetaldehyde by a decarboxylation followed by an oxidative deamination, consuming oxygen without accumulation of the amine (Kaminaga et al. 2006). Other aromatic aldehyde synthases (AAS) have been identified and characterized in the following years, even if it should be mentioned that, originally, these enzymes have been annotated as aromatic amino acid decarboxylases and not accurately investigated (Fig. 6). Then, it was assessed that PAAS enzymes represent a subgroup of L-tyrosine/L-dopa decarboxylases (Torrens-Spence et al. 2012), exhibiting high activity not only with L-phenylalanine but also with L-dopa and L-tyrosine: *Arabidopsis* PAAS seems to play a role in wounding/herbivory response and flower scent production (Gutensohn et al. 2011), while parsley PAAS synthesizes 4-hydroxyphenylacetaldehyde to enhance its stress/defense response (Torrens-Spence et al. 2012) (Fig. 6).

In an elegant paper, Torrens-Spence and coauthors have demonstrated by site-directed mutagenesis that a true AADC could be converted into AAS and vice versa by changing the chemical identity of a conserved residue (Torrens-Spence et al. 2013). A role as a signature residue has been proposed for a tyrosine of the mobile loop near the active site (which aligns with tyrosine-332 of mammalian DDC) that can be substituted by a phenylalanine in AADC in different plants. Interestingly, the presence of tyrosine gives rise to decarboxylases that produce aromatic amines, while that of phenylalanine gives decarboxylation-dependent oxidative deaminating enzymes (Torrens-Spence et al. 2013), reminiscent of the switch in activity displayed by the Y332F mammalian DDC (Bertoldi et al. 2002). The tyrosine residue has been suggested not to directly protonate the α-carbon to generate the amine product as it does for the mammalian DDC (Bertoldi et al. 2002); rather, it has been proposed that an active site histidine forms an hydrogen bond with the loop tyrosine that plays an indirect role in stabilizing the histidine side chain to the protonation of the α-carbon (Torrens-Spence et al. 2013). This is not the case for mammalian DDC, since mutation of the same histidine (His-192) to asparagine leads to a variant able to perform both decarboxylation with production of amine and decarboxylation-dependent oxidative deamination of aromatic amines (Bertoldi et al. 2001).

Insects use dopamine, in addition to its role as a neurotransmitter, in metabolic processes leading to cuticle sclerotization. In this context, AADC enzymes (Fig. 6) are known to play an important role. However, AADC from *Aedes aegypti*, with 70% sequence homology with the mammalian enzyme, has been demonstrated to catalyze the direct oxidation of L-dopa to 3,4-dihydroxyphenylacetaldehyde (DHPAA or DOPAL) bypassing dopamine formation, and is thus classified as DHPAA synthase (DHPAAS) (Vavricka et al. 2011). The role of aromatic aldehyde formation could be related to cross-linking complexes involved in cuticle hardening.

The mechanism of *Drosophila* DHPAAS has been extensively investigated and a catalytic role to the active site residue Asn-192 has been proposed, since its change to histidine leads to the partial conversion of DHPAAS to a classical decarboxylase (amine formation) rather to aldehyde synthase. On this basis, His-192 in AADCs of insects has been appointed as the residue responsible for quinonoid α-carbon protonation. However, since the mutational analysis did not give rise to enzymatic species completely devoid of one of

the two activities, the real effect of this residue (histidine or asparagine) appears difficult to be precisely defined (Liang et al. 2017).

In fungi, a few papers refer to AADC activity (Fig. 6), mainly related to the decarboxylation of L-tryptophan (Kalb et al. 2016). An in-depth investigation has been carried out in *Psilocybe cubensis*, a mushroom responsible for psychoactive alkaloid psilocybin synthesis, revealing the presence of both a DHPAAS with a phenylalanine instead of a tyrosine in the catalytic loop and an AADC-like protein (similar to plant L-tryptophan decarboxylases) (Torrens-Spence et al. 2018). Interestingly, in this AADC enzyme, a regulation by calcium ion was reported. (Torrens-Spence et al. 2018).

The reactivity of other fold-type I PLP decarboxylases with oxygen

In the same years, it was demonstrated that among PLP enzymes, the PLP-dependent decarboxylases are particularly able to perform oxidative reactions with O_2, in addition to their main reaction, maybe for their intrinsic possibility of exchanging CO_2 with O_2. It is not unprecedented that, just like RuBisCO, an enzyme able to exchange a gas like CO_2 could be prone to accept O_2, even this does not justify its reactivity.

By the way, fold-type I (or a-aspartate aminotransferase family) (Grishin et al. 1995) amino acid decarboxylases [that from an evolutionary point of view are clustered in Group II α-decarboxylases (Sandmeier et al. 1994)] are responsible for the synthesis of essential biomolecules, such as polyamines and hypotaurine, or neurotransmitters, such as dopamine, serotonin, and γ-aminobutyric acid (GABA) (Paiardini et al. 2017). They comprise aromatic amino acid, glutamate, and histidine decarboxylases from all sources together with the prokaryotic ornithine and lysine decarboxylases.

The main activities played by these enzymes together with the new oxidase reactions are reported in Fig. 7. *E. coli* glutamate decarboxylase (GAD), in addition to the decarboxylation of L-glutamic acid into GABA, transforms glutamate to succinic semialdehyde (Abell and Schloss 1991) and α-methylglutamate to levulinic acid (Bertoldi et al. 1999a) (Fig. 7a). There are some signs that corroborate the possibility for both human GAD65 and GAD67 to interact with oxygen; in fact, GAD65

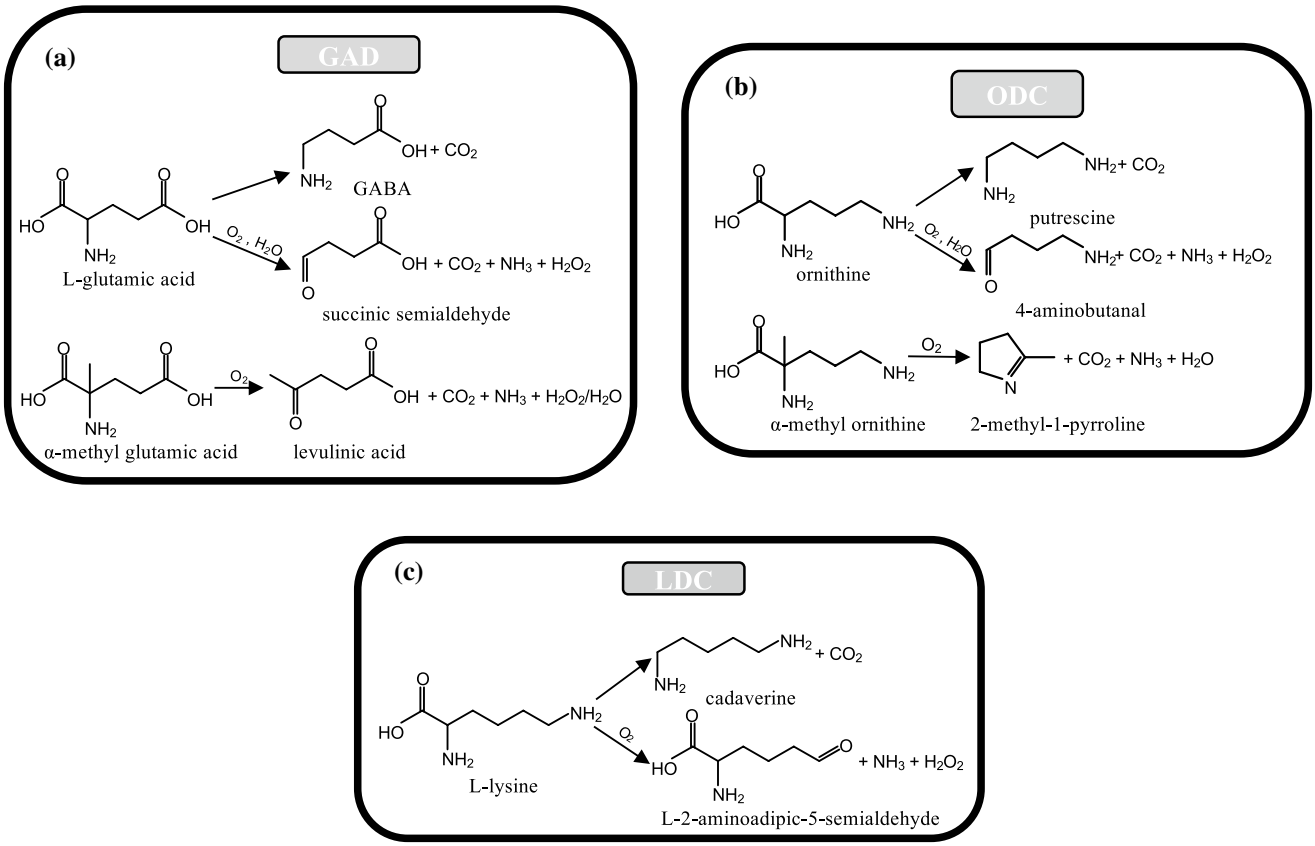

Fig. 7 Reactions of PLP α-decarboxylases. **a** GAD with L-glutamic acid and a-methylglutamate, **b** ODC with L-ornithine and α-methylornithine, and **c** LDC with L-lysine

produces succinic semialdehyde from glutamate, even if it was not demonstrated that oxygen is required (Choi and Churchich 1986; Bunik et al. 2011).

Ornithine decarboxylase (ODC) from different prokaryotic sources, such as *Lactobacillus 30a* or *Hafnia alvei*, has been demonstrated to catalyze, in addition to putrescine formation, a decarboxylation-dependent oxidative deamination (Bertoldi et al. 1999a; Sakai et al. 1997) of both ornithine and α-methylornithine, in a reaction directly converting the amino acid into the corresponding carbonyl compound and ammonia, without accumulation of the amine (Fig. 7b).

An L-lysine decarboxylase (LDC) from *Burkholderia* sp. AIU 395 has also been found to catalyze both α-decarboxylation, giving cadaverine, and an oxidative ε-deamination, giving L-2-aminoadipic 5-semialdehyde (Sugawara et al. 2014) (Fig. 7c).

Biological roles of oxidative side reactions of human PLP-dependent decarboxylases

The interpretation given for the O_2 interaction of PLP-dependent decarboxylases can be at least partially linked to pathological states or to a physiological regulation of the activities of some important brain enzymes (Fig. 8). It may be discussed if this catalytic activity could represent a mechanism of regulation of neurotransmitter synthesis or catabolism, and this fact could be of particular interest for diseases characterized by a dysregulation in neurotransmitters, such as Parkinson's Disease, AADC deficiency, pyridoxine oxidase-related epilepsy, and oxygen-induced seizures. The interplay of PLP decarboxylases with dioxygen may be involved in and regulate oxidative/metabolic stress in human brain diseases (Bunik et al. 2007). In addition, a survey regarding oxidative paracatalytic reactions catalyzed by enzymes able to form carbanionic intermediates,

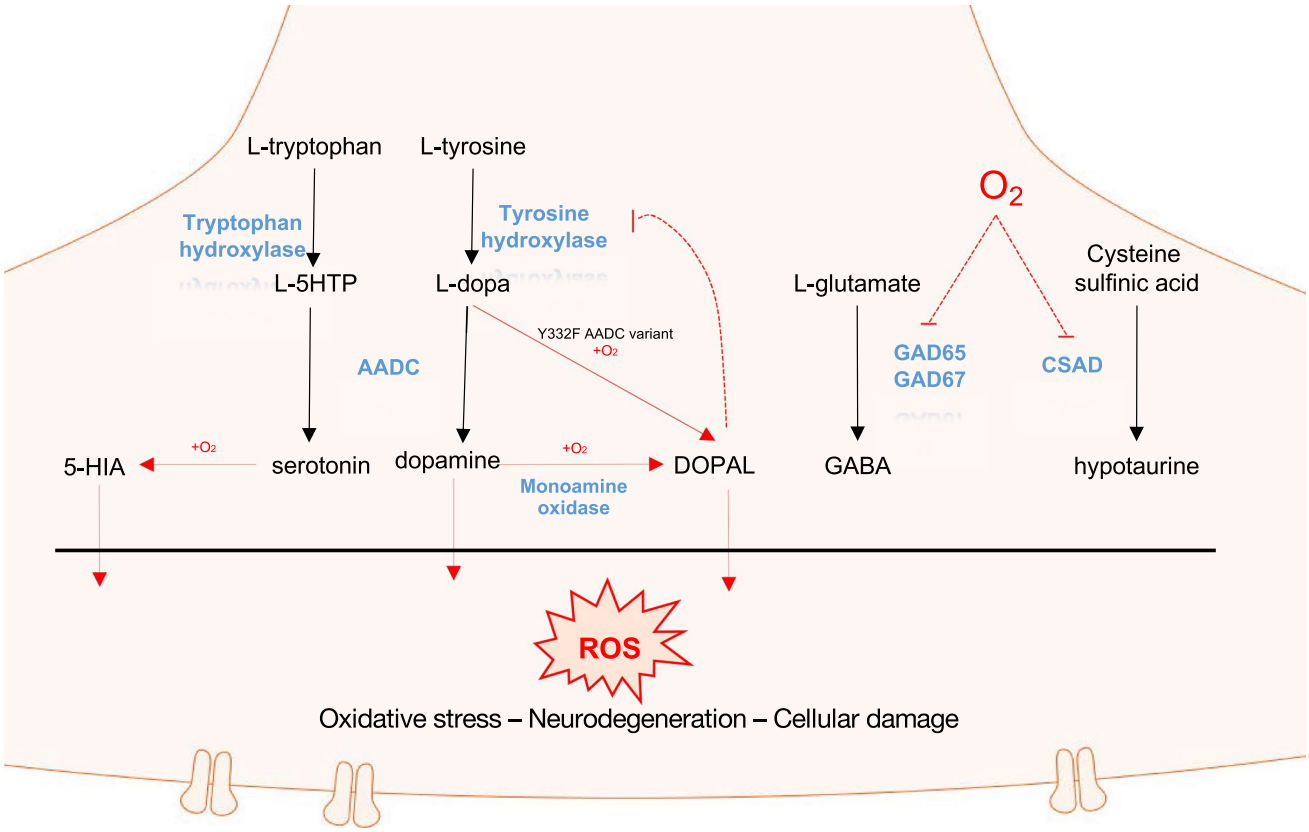

Fig. 8 Oxidative reactions played by mammalian PLP decarboxylases and their possible interplay. The metabolic pathways of aromatic amino acids and amine metabolism start with hydroxylation performed by tryptophan and tyrosine hydroxylase on the corresponding amino acids, and then, AADC decarboxylates L-5HTP and L-dopa to the corresponding amines serotonin and dopamine that in the presence of oxygen are oxidatively deaminated to the corresponding aromatic aldehydes, 5-HIA and DOPAL. Oxygen also influences mammalian GAD and CSAD activity by inhibiting these enzymes. Altogether, oxidative products (carbonyl compounds and ROS) could concur in exacerbating oxidative stress conditions and contributing to worsen neurodegeneration and cell damages. Monoamine oxidase is the known enzyme deputed to oxidase amine to aldehyde in an FAD-dependent manner. In black, amino acids amines and metabolic pathways, in red oxygen-related reactions, and in blue the name of the enzymes

including also some PLP-dependent enzymes, appeared in 2011 (Bunik et al. 2011). In this review, the authors pointed out the effects exerted by these side reactions involving oxygen especially in neurodegeneration and cancer. Regarding PLP enzymes, Bunik et al. highlighted that human AADC's ability to produce DHPAA/DOPAL, even possibly increased in altered forms of the enzyme, can result in pathology due to the known neurotoxicity of this compound, linked to Parkinson's disease neurodegeneration of the *substantia nigra* neurons (Burke et al. 2003). DOPAL neurotoxicity mechanisms, indeed, included DOPAL-α-synuclein cross-linked oligomerization (Follmer et al. 2015) as well as extensive DOPAL-induced protein-quinone adduct formation ("quinonization") and protein oligomerization, ubiquitination, and aggregation (Jinsmaa et al. 2018). Also 5-hydroxyindolacetaldehyde (5-HIA), produced by mammal AADC from serotonin ((Bertoldi et al. 1996), was demonstrated to promote α-synuclein oligomerization both in vitro and in a synuclein-overexpressing cell model, in a manner similar to DOPAL (Jinsmaa et al. 2015), possibly explaining the early degeneration of dorsal raphe nuclei serotonergic neurons in Parkinson's disease. Interestingly, among DOPAL-modified/inhibited targets, tyrosine hydroxylase (TH) shows a semi-reversible mechanism with consequent decrease in overall L-Dopa production, but a time- and concentration-dependent TH activity recovering was observed upon removal of DOPAL (Mexas et al. 2011). This DOPAL-dependent reversible inhibition of TH could provide a new perspective in AADC ability to perform oxidative deamination, linking this side reaction to a possible physiological feed-back mechanism by which a minor AADC product can regulate L-dopa production targeting the rate-limiting enzyme in the dopamine synthetic pathway.

Both human recombinant GAD65 and GAD67 were shown to be potently and reversibly inhibited by molecular oxygen. In particular, GAD65-O_2 dependent inhibition has been linked to the genesis of oxygen-induced seizures (Davis et al. 2001) by limiting GABA production and loading in vesicles (Hsu et al. 1999) and in the pathogenesis of type I diabetes mellitus (Trigwell et al. 2001). On the other side, the isoform GAD67 was shown to be related with convulsions induced by hyperbaric oxygen exposure both in vivo and in vitro (Li et al. 2008).

Like GAD65, also cysteine-sulfinic acid decarboxylase (CSAD) has been reported to be responsive to reversible inhibition by O_2 (Davis et al. 2001) (Fig. 8). Cysteine sulfinic acid decarboxylation product hypotaurine is then oxidized to taurine by an oxygenase, with the latter compound shown to be especially important in central nervous system, where it plays a wide range of different roles (Menzie et al. 2014) and is linked to early retinal degeneration (Preising et al. 2019). As such, inhibition of CSAD by O_2 could contribute to retinal damage pointed out in premature infants exposed to high O_2 levels at birth (Jewell et al. 2001). Noteworthy, these two decarboxylases are also inhibited by nitric oxide (Davis et al. 2001), another radical-containing compound as dioxygen, suggesting a possible radical mechanism in the inhibition. Reactions with species such as O_2 or NO could, in fact, proceed through a one-electron stepwise transfer eventually leading to radical intermediates, as mentioned before.

The interaction of PLP-dependent decarboxylases with molecular oxygen opens the way to the possibility that these enzymes could be strongly involved in oxidative damage, since the oxidase activity is linked to the concomitant production of hydrogen peroxide (Bunik et al. 2007). In this scenario, an enzyme producing ROS and carbonyl compounds could exacerbate oxidative stress conditions (Bunik et al. 2007). Moreover, it cannot be excluded that the proven sensitivity to or interaction with oxygen of these PLP-dependent decarboxylases could be extended to ROS compounds, underlying the possibility that these enzymes can be inactivated and/or form ROS-driven adducts with other proteins, and the consequent necessity of monitoring them as targets of ROS themselves. A broader effect of the oxidative reactions of PLP-dependent decarboxylases, responsible for neurotransmitters synthesis, could be the interplay between ROS and the important modulator nitric oxide which, in turn, leads to the production of nitrogen reactive species contributing to nitro-oxidative stress. Its synthesis and regulation involves a network of pathways that should be taken into consideration (Persichini et al. 2016).

The emerging question is how the propensity to react with oxygen is linked to inhibition exerted by the products of the oxidative paracatalytic reactions and their regulation in PLP decarboxylases. Although it is not easy to address such issue, an important review (Schloss 2002) interprets the oxygenase reaction of GAD as a consequence of a possible radical character also of the main decarboxylation reaction of the enzyme gaining assistance also in the main activity played by the enzyme.

New PLP enzymes of fold-type I are able to catalyze reactions involving O_2

In the last 5 years, a growth in papers reporting new oxygen-consuming PLP enzymes has occurred. Most of them belong to the bacterial or fungal kingdoms and can be grouped by the fact that dioxygen is a substrate of their main reaction.

An excellent recent review gives extensive details about the oxidative reaction catalyzed by each one of these new enzymes (Hoffarth et al. 2020). In the present review, we will briefly review the activity catalyzed and the functional role.

Three of these new PLP enzymes have the common feature of acting on L-arginine as substrate and could catalyze

the four-electron oxidation of L-arginine, with a mechanism involving either an oxidation or a hydroxylation, that are similar oxidative pathways undergoing through different fates of the carbonyl products.

Streptomyces wadayamensis MppP is a PLP enzyme that catalyzes the hydroxylation and deamination of L-arginine consuming molecular oxygen and producing the carbonyl compounds 2-ketoarginine and 2-keto-3,4-dehydroarginine in a 1:1.7 ratio (Fig. 9) (Han et al. 2015). The latter is an essential guanidino acid for the synthesis of bioactive peptides such as L-enduracididine (Han et al. 2015), which is a cyclic analog of arginine found in several antimicrobial peptides useful for treatment of drug-resistant pathogens. The structure of MppP reveals that it is a homodimer, belonging to the fold-type I of PLP enzymes, as the a-decarboxylases reported above, with the active sites present at the interface between the two subunits; however, unlike other aminotransferase family enzymes, in MppP, the contribution of the opposite chain to each active site is minimal (Han et al. 2015). An in-depth analysis of the catalytic activity of this enzyme was published subsequently (Han et al. 2018) and reported the exact stoichiometry of all products formed. A refined chemical mechanism of this PLP-driven oxidase activity together with a structural analysis was proposed, highlighting the role of the N-terminus switching from an ordered to a disordered state during binding/catalysis.

Another PLP enzyme, RohP, contributes to the biosynthesis pathway of azomycin (Hedges and Ryan 2019) and acts on L-arginine catalyzing an oxygen-consuming reaction leading to both hydroxylation and deamination (Fig. 9) (Hedges et al. 2018). RohP is from *Streptomyces cattleya* and presents a high sequence identity with both MppP and Ind4 (see below) (Hedges et al. 2018). From a functional point of view, RohP acts similarly to MppP, forming an identical product, i.e., a hydroxylated ketoacid.

Finally, *Streptomyces griseus* Ind4, a PLP enzyme of the indolmycin biosynthetic pathway catalyzing a reaction similar to those of MppP and RohP, thus converts L-arginine into an oxidized product (Du et al. 2016). The peculiarity of this reaction is that Ind4 forms a C=C bond rather than a carbonyl hydroxylated compound as do MppP and RohP (Fig. 8) even if 2-ketoarginine is produced.

Another PLP enzyme capable of consuming molecular oxygen is *E. coli* CcbF. It belongs to the metabolic pathway of lincosamide antibiotics, compounds that act on the large subunit of bacterial ribosomes blocking protein synthesis (Wilson 2014). In this process, CcbF catalyzes the transformation of a cysteine S-conjugate into an aldehyde with co-production of carbon dioxide, hydrogen peroxide, and ammonia in the presence of molecular oxygen which is concomitantly consumed (Fig. 10) (Wang et al. 2016). In this sense, the enzyme is more similar to a decarboxylation-dependent oxidative deaminase rather than to an enzyme that oxidizes an inactivated carbon–carbon bond (Wang et al. 2016).

The following three enzymes have been classified as catalyzing a decarboxylating oxygenation (Hoffarth et al. 2020); however, some differences should be pointed out. PvdN is a PLP enzyme of *Pseudomonas* involved in pyoverdine biosynthesis. From a structural point of view, it

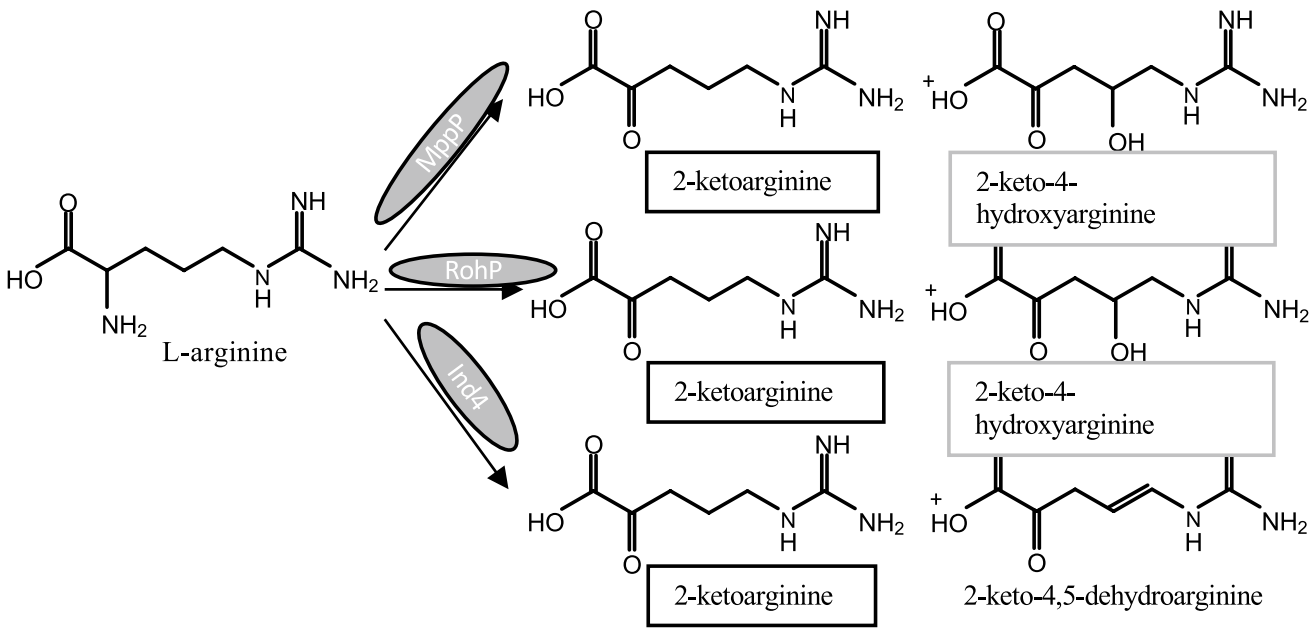

Fig. 9 Main reactions catalyzed by other PLP-dependent enzymes, MppP, RohP, and Ind4, in the presence of L-arginine

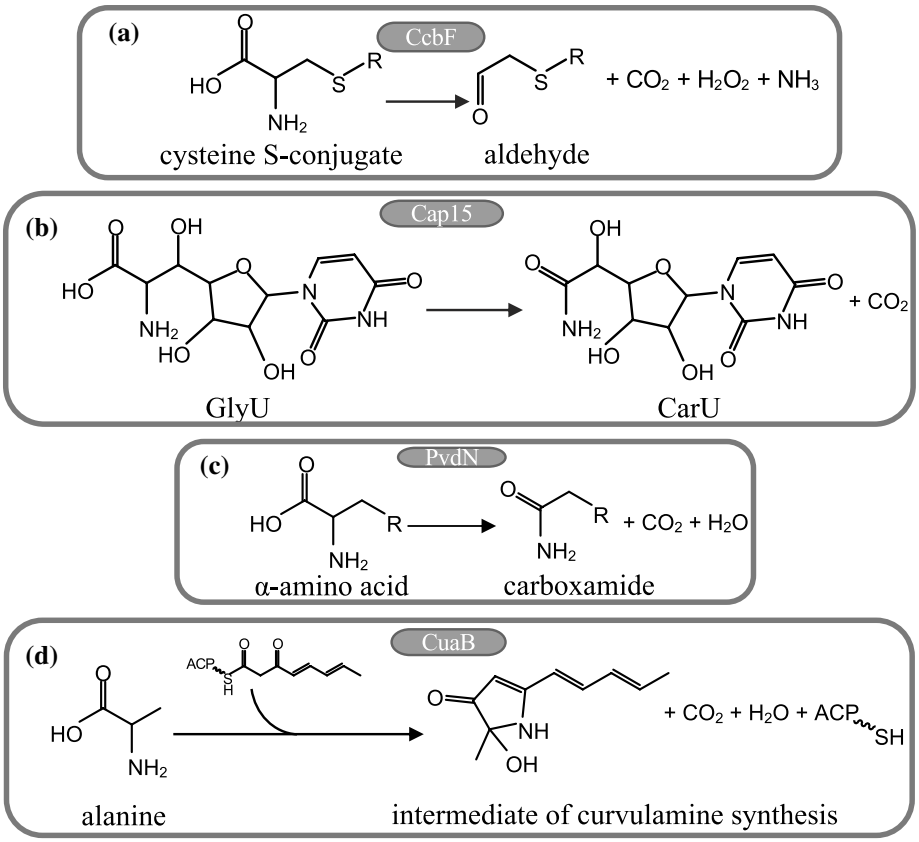

Fig. 10 Main reactions catalyzed by other PLP-dependent enzymes on bioactive compounds. **a** CcdF on a cysteine-S-conjugate, **b** Cap15 on GlyU, **c** PvdN, and **d** CuaB on more complex amino acidic substrates

belongs to the fold-type I of PLP enzymes (Drake and Gulick 2016). A recent investigation on its functional role suggests that it catalyzes the decarboxylation of its substrate generating a quinonoid intermediate that subsequently undergoes an oxygenase reaction leading to the products through a hydroperoxide species (Fig. 10) (Ringel, Dräger and Brüser 2016). The spatial structure shows two tunnels from each active site to the protein surface: a larger one accommodating the substrate and a narrower one for the possible exchange of CO_2 and O_2 (Drake and Gulick 2016). In no other structure of decarboxylases, catalyzing a decarboxylation and a successive oxygenation has such a channel been identified.

Cap15 is a *Streptomyces* PLP-dependent a-amino acid monooxygenase–decarboxylase acting in the biosynthetic pathway of capuramycins, a class of antimycobacterial antibiotics (Huang et al. 2018). The reaction catalyzed is the conversion of the unusual b-hydroxy-a-amino acid 5′-C-glycyluridine (GlyU) into the related carboxamide product CarU (Fig. 10). The novelty of such activity is that the catalytic mechanism proceeds by at first the deprotonation of the external aldimine intermediate, followed by oxygenation of the quinonoid species, generating a radical pair of hydroperoxy-PLP superoxide anion finally generating water and carbon dioxide (Huang et al. 2018), thus exclusively for this enzyme, decarboxylation occurs after oxygenation.

Recently, a new PLP enzyme, CuaB, has been identified in the gene cluster for the synthesis of an indolizidine alkaloid, curvulamine, in fungi (Dai et al. 2020), underlining the fact that the reactivity of PLP enzyme with oxygen is a widespread feature. CuaB is a bifunctional enzyme: it catalyzes the formation of C–C bonds through Claisen condensation, as other PLP enzymes are able to do, such as 8-amino-7-oxononanoate synthase and, unexpectedly, a hydroxylation using dioxygen (Fig. 10). A detailed enzyme mechanism has been proposed on the basis of the collected products (Dai et al. 2020). The external aldimine with the substrate is deprotonated to generate a quinonoid that follows the pathway of synthases (Fig. 1). Once the external aldimine with the product is formed, it is decarboxylated generating a second quinonoid reactive towards oxygen forming a hydroperoxide that is converted into a hydroxylated product and water. Interestingly, this sequential reaction with the product is reminiscent of the activities of DDC with serotonin, dopamine, and α-methyldopamine (Bertoldi et al. 1996, 1998, Bertoldi and Borri Voltattorni 2003).

The identification of these enzymes mainly in *Pseudomonas* and *Streptomyces* is perhaps related to investigations on bioactive compounds and it can be hypothesized that many other PLP enzymes are dispersed in the living kingdoms whose activities are still unrecognized. The ability to couple PLP and oxygen chemistry not only for

paracatalytic reactions but also in main enzymatic reactions broadens PLP-enzyme functional ability and paves the way for further studies.

A structural basis for oxygen reactivity of decarboxylases

This review points out that the reactivity with dioxygen, at first considered as a mere artifact of the carbanionic chemistry of some PLP decarboxylases, is more common than expected. From a structural point of view, it seems to be related not only to decarboxylases, but also to other fold-type I enzymes: however, it should be noticed that the majority of PLP enzymes consuming oxygen catalyze a decarboxylation reaction. While an oxidase activity could be related to a regulation role or alteration of the physiological state in mammalian or plant decarboxylases, it is not easy to envisage a role in other organisms such as bacteria or fungi. Literature on this topic is still lacking, maybe due to recent identification of such oxygen-consuming activities in PLP enzymes of these organisms.

The fact that this oxidase activity remains confined to enzymes of the aminotransferase family could be due, on one hand, to the fact that this family is the most abundant among PLP enzymes, on the other, to the fact that fold-type I enzymes could possess some structural element or active site conformation more prone to oxygen entrance.

There is as yet no evidence for oxygen-dependent reactions in the fold-type III decarboxylases, a large group containing eukaryotic lysine, eukaryotic ornithine, prokaryotic and eukaryotic arginine, and prokaryotic diaminopimelate decarboxylases (Grishin et al. 1995). Oxygen is not reported to react with PLP enzymes even belonging to other fold-types.

It could be interesting to compare the structural differences of the solved spatial arrangements of prokaryotic (Momany et al. 1995) and eukaryotic ODC (Kern et al. 1999) as prototypes of fold-type I and III decarboxylases, respectively. One of the main differences is the orientation of the reactive group on the external aldimine with respect to the buried or exposed face of the cofactor. In fold-type I enzymes, the lysine residue forming the internal aldimine is on the *si* face buried in the interior of the protein, while the opposite *re* face is exposed. When this intermediate is converted into the external aldimine, the carboxylate moiety protrudes on the buried *si* face and reaction then proceeds. Instead, in fold-type III enzymes, the coenzyme has a mirrored position and the lysine of the internal aldimine is buried on the *re* face of the cofactor, while the *si* face is exposed. The external aldimine thus presents the CO_2 on the exposed *si* face (Kern et al. 1999). This fact has been linked to stereospecificity of catalysis (Kern et al. 1999); however, it can be argued that dioxygen could bind and react better in a buried active site. A second structural feature is the dimer stability much higher in fold-type I ODC than in fold-type III ODC (Kern et al. 1999).

An elegant example of enzymes catalyzing the same reaction but belonging to different fold-types is also found in transaminases. The L-amino acid transaminases belong to fold-type I, while D-amino acid transaminase belong to fold-type IV (Grishin et al. 1995) and the differences are the PLP location in the active site and the dimer assembly (Humble et al. 2012).

From a functional point of view, there is evidence that diaminopimelate decarboxylase and D-ornithine/D-lysine decarboxylase have a concerted decarboxylation/protonation step, ruling out the quinonoid intermediate formation (Fogle and Toney 2011; Phillips et al. 2019). This could explain the lack of O_2 reactivity. However, the structural determinants responsible of this concerted step are presently still unknown. Whatever the structural difference could be, the identification in PvdN of the putative O_2 tunnel could foster re-evaluation of already deposited structures of decarboxylases for the presence of any potential channels.

Conclusions

The oxygen reactivity of PLP enzymes could be of great physiological interest, given the fact that it seems typical of enzymes producing important neurotransmitters or neuromodulators, whose effect could be greatly affected by redox conditions. Following this view, it would be interesting to further investigate the influence of oxygen on activity and inhibition of these enzymes.

The new biosynthetic pathways described in the last few years, mainly in bacteria and fungi, increase the evidence of the high catalytic versatility of PLP enzymes in nature. These activities have been generally identified by the following genome sequence-based survey. The approach of characterizing the potentially diverse activities arising from the ductile nature of PLP chemistry would allow access to unpredictable new biological processes.

Acknowledgements The contributions of the AADC Research Trust (UK) and of JP2017 and FUR2019 grants by the University of Verona (Italy) to MB are gratefully acknowledged.

Funding Open access funding provided by Università degli Studi di Verona within the CRUI-CARE Agreement.

Compliance with ethical standards

Conflict of interest The authors declare that they have no conflict of interest.

References

Abell LM, Schloss JV (1991) Oxygenase side reactions of acetolactate synthase and other carbanion-forming enzymes. Biochemistry 30:7883–7887

Barboni E, Voltattorni CB, D'Erme M, Fiori A, Minelli A, Rosei MA, Turano C (1981) An abnormal reaction occurring in the presence of L-aromatic aminoacid decarboxylase. Biochem Biophys Res Commun 99:576–583

Bertoldi M (2014) Mammalian dopa decarboxylase: structure, catalytic activity and inhibition. Arch Biochem Biophys 546:1–7

Bertoldi M, Borri Voltattorni C (2000) Reaction of dopa decarboxylase with L-aromatic amino acids under aerobic and anaerobic conditions. Biochem J 352(Pt 2):533–538

Bertoldi M, Borri Voltattorni C (2003) Reaction and substrate specificity of recombinant pig kidney dopa decarboxylase under aerobic and anaerobic conditions. Biochim Biophys Acta 1647:42–47

Bertoldi M, Voltattorni CB (2001) Dopa decarboxylase exhibits low pH half-transaminase and high pH oxidative deaminase activities toward serotonin (5-hydroxytryptamine). Protein Sci 10:1178–1186

Bertoldi M, Moore PS, Maras B, Dominici P, Voltattorni CB (1996) Mechanism-based inactivation of dopa decarboxylase by serotonin. J Biol Chem 271:23954–23959

Bertoldi M, Dominici P, Moore PS, Maras B, Voltattorni CB (1998) Reaction of dopa decarboxylase with alpha-methyldopa leads to an oxidative deamination producing 3,4-dihydroxyphenylacetone, an active site directed affinity label. Biochemistry 37:6552–6561

Bertoldi M, Carbone V, Borri Voltattorni C (1999a) Ornithine and glutamate decarboxylases catalyse an oxidative deamination of their alpha-methyl substrates. Biochem J 342(Pt 3):509–512

Bertoldi M, Frigeri P, Paci M, Voltattorni CB (1999b) Reaction specificity of native and nicked 3,4-dihydroxyphenylalanine decarboxylase. J Biol Chem 274:5514–5521

Bertoldi M, Castellani S, Bori Voltattorni C (2001) Mutation of residues in the coenzyme binding pocket of dopa decarboxylase. Effects on catalytic properties. Eur J Biochem 268:2975–2981

Bertoldi M, Gonsalvi M, Contestabile R, Voltattorni CB (2002) Mutation of tyrosine 332 to phenylalanine converts dopa decarboxylase into a decarboxylation-dependent oxidative deaminase. J Biol Chem 277:36357–36362

Bertoldi M, Cellini B, Maras B, Borri Voltattorni C (2005) A quinonoid is an intermediate of oxidative deamination reaction catalyzed by Dopa decarboxylase. FEBS Lett 579:5175–5180

Bertoldi M, Cellini B, Montioli R, Borri Voltattorni C (2008) Insights into the mechanism of oxidative deamination catalyzed by DOPA decarboxylase. Biochemistry 47:7187–7195

Bowes G, Ogren WL, Hageman RH (1971) Phosphoglycolate production catalyzed by ribulose diphosphate carboxylase. Biochem Biophys Res Commun 45:716–722

Bunik VI, Schloss JV, Pinto JT, Gibson GE, Cooper AJ (2007) Enzyme-catalyzed side reactions with molecular oxygen may contribute to cell signaling and neurodegenerative diseases. Neurochem Res 32:871–891

Bunik VI, Schloss JV, Pinto JT, Dudareva N, Cooper AJ (2011) A survey of oxidative paracatalytic reactions catalyzed by enzymes that generate carbanionic intermediates: implications for ROS production, cancer etiology, and neurodegenerative diseases. Adv Enzymol Relat Areas Mol Biol 77:307–360

Burke WJ, Li SW, Williams EA, Nonneman R, Zahm DS (2003) 3,4-Dihydroxyphenylacetaldehyde is the toxic dopamine metabolite in vivo: implications for Parkinson's disease pathogenesis. Brain Res 989:205–213

Chaiyen P, Fraaije MW, Mattevi A (2012) The enigmatic reaction of flavins with oxygen. Trends Biochem Sci 37:373–380

Choi SY, Churchich JE (1986) Glutamate decarboxylase side reactions catalyzed by the enzyme. Eur J Biochem 160:515–520

Christen P, Gasser A (1980) Production of glycolate by oxidation of the 1,2-dihydroxyethyl-thamin-diphosphate intermediate of transketolase with hexacyanoferrate(III) or H2O2. Eur J Biochem 107:73–77

Christen P, Cogoli-Greuter M, Healy MJ, Lubini D (1976) Specific irreversible inhibition of enzymes concomitant to the oxidation of carbanionic enzyme-substrate intermediates by hexacyanoferrate (III). Eur J Biochem 63:223–231

Cogoli-Greuter M, Hausner U, Christen P (1979) Irreversible inactivation of pyruvate decarboxylase in the presence of substrate and an oxidant. An example of paracatalytic enzyme inactivation. Eur J Biochem 100:295–300

Dai GZ, Han WB, Mei YN, Xu K, Jiao RH, Ge HM, Tan RX (2020) Pyridoxal-5′-phosphate-dependent bifunctional enzyme catalyzed biosynthesis of indolizidine alkaloids in fungi. Proc Natl Acad Sci USA 117:1174–1180

Daithankar VN, Wang W, Trujillo JR, Thorpe C (2012) Flavin-linked Erv-family sulfhydryl oxidases release superoxide anion during catalytic turnover. Biochemistry 51:265–272

Davis K, Foos T, Wu JY, Schloss JV (2001) Oxygen-induced seizures and inhibition of human glutamate decarboxylase and porcine cysteine sulfinic acid decarboxylase by oxygen and nitric oxide. J Biomed Sci 8:359–364

Drake EJ, Gulick AM (2016) 1.2 Å resolution crystal structure of the periplasmic aminotransferase PvdN from Pseudomonas aeruginosa. Acta Crystallogr F Struct Biol Commun 72:403–408

Du YL, Singh R, Alkhalaf LM, Kuatsjah E, He HY, Eltis LD, Ryan KS (2016) A pyridoxal phosphate-dependent enzyme that oxidizes an unactivated carbon-carbon bond. Nat Chem Biol 12:194–199

Dunathan HC (1966) Conformation and reaction specificity in pyridoxal phosphate enzymes. Proc Natl Acad Sci USA 55:712–716

Facchini PJ, De Luca V (1994) Differential and tissue-specific expression of a gene family for tyrosine/dopa decarboxylase in opium poppy. J Biol Chem 269:26684–26690

Facchini PJ, Huber-Allanach KL, Tari LW (2000) Plant aromatic L-amino acid decarboxylases: evolution, biochemistry, regulation, and metabolic engineering applications. Phytochemistry 54:121–138

Fogle EJ, Toney MD (2011) Analysis of catalytic determinants of diaminopimelate and ornithine decarboxylases using alternate substrates. Biochim Biophys Acta 1814:1113–1119

Follmer C, Coelho-Cerqueira E, Yatabe-Franco DY, Araujo GD, Pinheiro AS, Domont GB, Eliezer D (2015) Oligomerization and membrane-binding properties of covalent adducts formed by the interaction of α-synuclein with the toxic dopamine metabolite

3,4-dihydroxyphenylacetaldehyde (DOPAL). J Biol Chem 290:27660–27679
Grishin NV, Phillips MA, Goldsmith EJ (1995) Modeling of the spatial structure of eukaryotic ornithine decarboxylases. Protein Sci 4:1291–1304
Gutensohn M, Klempien A, Kaminaga Y, Nagegowda DA, Negre-Zakharov F, Huh JH, Luo H, Weizbauer R, Mengiste T, Tholl D, Dudareva N (2011) Role of aromatic aldehyde synthase in wounding/herbivory response and flower scent production in different Arabidopsis ecotypes. Plant J 66:591–602
Han L, Schwabacher AW, Moran GR, Silvaggi NR (2015) *Streptomyces wadayamensis* MppP is a pyridoxal 5′-phosphate-dependent L-arginine α-deaminase, γ-hydroxylase in the enduracididine biosynthetic pathway. Biochemistry 54:7029–7040
Han L, Vuksanovic N, Oehm SA, Fenske TG, Schwabacher AW, Silvaggi NR (2018) *Streptomyces wadayamensis* MppP is a PLP-dependent oxidase, not an oxygenase. Biochemistry 57:3252–3264
Hedges JB, Ryan KS (2019) In vitro reconstitution of the biosynthetic pathway to the nitroimidazole antibiotic azomycin. Angew Chem Int Ed Engl 58:11647–11651
Hedges JB, Kuatsjah E, Du YL, Eltis LD, Ryan KS (2018) Snapshots of the catalytic cycle of an O. ACS Chem Biol 13:965–974
Hixon M, Sinerius G, Schneider A, Walter C, Fessner WD, Schloss JV (1996) Quo vadis photorespiration: a tale of two aldolases. FEBS Lett 392:281–284
Hoegl A, Nodwell MB, Kirsch VC, Bach NC, Pfanzelt M, Stahl M, Schneider S, Sieber SA (2018) Mining the cellular inventory of pyridoxal phosphate-dependent enzymes with functionalized cofactor mimics. Nat Chem 10:1234–1245
Hoffarth ER, Rothchild KW, Ryan KS (2020) Emergence of oxygen- and pyridoxal phosphate-dependent reactions. FEBS J 287:1403–1428
Hsu CC, Thomas C, Chen W, Davis KM, Foos T, Chen JL, Wu E, Floor E, Schloss JV, Wu JY (1999) Role of synaptic vesicle proton gradient and protein phosphorylation on ATP-mediated activation of membrane-associated brain glutamate decarboxylase. J Biol Chem 274:24366–24371
Huang Y, Liu X, Cui Z, Wiegmann D, Niro G, Ducho C, Song Y, Yang Z, Van Lanen SG (2018) Pyridoxal-5′-phosphate as an oxygenase cofactor: discovery of a carboxamide-forming, α-amino acid monooxygenase-decarboxylase. Proc Natl Acad Sci U S A 115:974–979
Humble MS, Cassimjee KE, Håkansson M, Kimbung YR, Walse B, Abedi V, Federsel HJ, Berglund P, Logan DT (2012) Crystal structures of the *Chromobacterium violaceum* ω-transaminase reveal major structural rearrangements upon binding of coenzyme PLP. FEBS J 279:779–792
Jewell V, Northrop-Clewes C, Tubman R, Thurnham D (2001) Nutritional factors and visual function in premature infants. Proc Nutr Soc 60:8
Jinsmaa Y, Cooney A, Sullivan P, Sharabi Y, Goldstein DS (2015) The serotonin aldehyde, 5-HIAL, oligomerizes alpha-synuclein. Neurosci Lett 590:134–137
Jinsmaa Y, Sharabi Y, Sullivan P, Isonaka R, Goldstein DS (2018) 3,4-dihydroxyphenylacetaldehyde-induced protein modifications and their mitigation by. J Pharmacol Exp Ther 366:113–124
John RA (1995) Pyridoxal phosphate-dependent enzymes. Biochim Biophys Acta 1248:81–96
John RA, Fasella P (1969) The reaction of L-serine O-sulfate with aspartate aminotransferase. Biochemistry 8:4477–4482
Kalb D, Gressler J, Hoffmeister D (2016) Active-site engineering expands the substrate profile of the basidiomycete L-tryptophan decarboxylase CsTDC. ChemBioChem 17:132–136
Kaminaga Y, Schnepp J, Peel G, Kish CM, Ben-Nissan G, Weiss D, Orlova I, Lavie O, Rhodes D, Wood K, Porterfield DM, Cooper AJ, Schloss JV, Pichersky E, Vainstein A, Dudareva N (2006) Plant phenylacetaldehyde synthase is a bifunctional homotetrameric enzyme that catalyzes phenylalanine decarboxylation and oxidation. J Biol Chem 281:23357–23366
Kern AD, Oliveira MA, Coffino P, Hackert ML (1999) Structure of mammalian ornithine decarboxylase at 1.6 A resolution: stereochemical implications of PLP-dependent amino acid decarboxylases. Structure 7:567–581
Klinman JP (2007) How do enzymes activate oxygen without inactivating themselves? Acc Chem Res 40:325–333
Kochhar S, Christen P (1988) The enantiomeric error frequency of aspartate aminotransferase. Eur J Biochem 175:433–438
Kochhar S, Christen P (1992) Mechanism of racemization of amino acids by aspartate aminotransferase. Eur J Biochem 203:563–569
Li Q, Guo M, Xu X, Xiao X, Xu W, Sun X, Tao H, Li R (2008) Rapid decrease of GAD 67 content before the convulsion induced by hyperbaric oxygen exposure. Neurochem Res 33:185–193
Liang J, Han Q, Ding H, Li J (2017) Biochemical identification of residues that discriminate between 3,4-dihydroxyphenylalanine decarboxylase and 3,4-dihydroxyphenylacetaldehyde synthase-mediated reactions. Insect Biochem Mol Biol 91:34–43
Mattevi A (2006) To be or not to be an oxidase: challenging the oxygen reactivity of flavoenzymes. Trends Biochem Sci 31:276–283
Menzie J, Pan C, Prentice H, Wu JY (2014) Taurine and central nervous system disorders. Amino Acids 46:31–46
Mexas LM, Florang VR, Doorn JA (2011) Inhibition and covalent modification of tyrosine hydroxylase by 3,4-dihydroxyphenylacetaldehyde, a toxic dopamine metabolite. Neurotoxicology 32:471–477
Momany C, Ernst S, Ghosh R, Chang NL, Hackert ML (1995) Crystallographic structure of a PLP-dependent ornithine decarboxylase from Lactobacillus 30 a to 3.0 A resolution. J Mol Biol 252:643–655
Noé W, Mollenschott C, Berlin J (1984) Tryptophan decarboxylase from *Catharanthus roseus* cell suspension cultures: purification, molecular and kinetic data of the homogenous protein. Plant Mol Biol 3:281–288
O'Leary MH, Baughn RL (1977) Decarboxylation-dependent transamination catalyzed by mammalian 3,4-dihydroxyphenylalanine decarboxylase. J Biol Chem 252:7168–7173
Paiardini A, Giardina G, Rossignoli G, Voltattorni CB, Bertoldi M (2017) New insights emerging from recent investigations on human group II pyridoxal 5′-phosphate decarboxylases. Curr Med Chem 24:226–244
Percudani R, Peracchi A (2003) A genomic overview of pyridoxal-phosphate-dependent enzymes. EMBO Rep 4:850–854
Persichini T, Mariotto S, Suzuki H, Butturini E, Mastrantonio R, Cantoni O, Colasanti M (2016) Cross-talk between NO synthase isoforms in neuro-inflammation: possible Implications in HIV-associated neurocognitive disorders. Curr Med Chem 23:2706–2714
Phillips RS, Poteh P, Krajcovic D, Miller KA, Hoover TR (2019) Crystal structure of D-ornithine/D-lysine decarboxylase, a stereoinverting decarboxylase: implications for substrate specificity and stereospecificity of fold III decarboxylases. Biochemistry 58:1038–1042
Preising MN, Görg B, Friedburg C, Qvartskhava N, Budde BS, Bonus M, Toliat MR, Pfleger C, Altmüller J, Herebian D, Beyer M, Zöllner HJ, Wittsack HJ, Schaper J, Klee D, Zechner U, Nürnberg P, Schipper J, Schnitzler A, Gohlke H, Lorenz B, Häussinger D, Bolz HJ (2019) Biallelic mutation of human. FASEB J 33:11507–11527
Ringel MT, Dräger G, Brüser T (2016) PvdN enzyme catalyzes a periplasmic pyoverdine modification. J Biol Chem 291:23929–23938
Sakai K, Miyasako Y, Nagatomo H, Watanabe H, Wakayama M, Moriguchi M (1997) L-ornithine decarboxylase from Hafnia alvei has a novel L-ornithine oxidase activity. J Biochem 122:961–968

Sandmeier E, Hale TI, Christen P (1994) Multiple evolutionary origin of pyridoxal-5′-phosphate-dependent amino acid decarboxylases. Eur J Biochem 221:997–1002

Schloss JV (2002) Oxygen toxicity from plants to people. Planta 216:38–43

Sugawara A, Matsui D, Takahashi N, Yamada M, Asano Y, Isobe K (2014) Characterization of a pyridoxal-5′-phosphate-dependent L-lysine decarboxylase/oxidase from *Burkholderia* sp. AIU 395. J Biosci Bioeng 118:496–501

Tieman D, Taylor M, Schauer N, Fernie AR, Hanson AD, Klee HJ (2006) Tomato aromatic amino acid decarboxylases participate in synthesis of the flavor volatiles 2-phenylethanol and 2-phenylacetaldehyde. Proc Natl Acad Sci U S A 103:8287–8292

Torrens-Spence MP, Gillaspy G, Zhao B, Harich K, White RH, Li J (2012) Biochemical evaluation of a parsley tyrosine decarboxylase results in a novel 4-hydroxyphenylacetaldehyde synthase enzyme. Biochem Biophys Res Commun 418:211–216

Torrens-Spence MP, Liu P, Ding H, Harich K, Gillaspy G, Li J (2013) Biochemical evaluation of the decarboxylation and decarboxylation-deamination activities of plant aromatic amino acid decarboxylases. J Biol Chem 288:2376–2387

Torrens-Spence MP, Liu CT, Pluskal T, Chung YK, Weng JK (2018) Monoamine biosynthesis via a noncanonical calcium-activatable aromatic amino acid decarboxylase in psilocybin mushroom. ACS Chem Biol 13:3343–3353

Torrens-Spence MP, Chiang YC, Smith T, Vicent MA, Wang Y, Weng JK (2020) Structural basis for divergent and convergent evolution of catalytic machineries in plant aromatic amino acid decarboxylase proteins. Proc Natl Acad Sci USA 117:10806–10817

Trigwell SM, Radford PM, Page SR, Loweth AC, James RF, Morgan NG, Todd I (2001) Islet glutamic acid decarboxylase modified by reactive oxygen species is recognized by antibodies from patients with type 1 diabetes mellitus. Clin Exp Immunol 126:242–249

Vavricka C, Han Q, Huang Y, Erickson SM, Harich K, Christensen BM, Li J (2011) From L-dopa to dihydroxyphenylacetaldehyde: a toxic biochemical pathway plays a vital physiological function in insects. PLoS ONE 6:e16124

Wang M, Zhao Q, Zhang Q, Liu W (2016) Differences in PLP-dependent cysteinyl processing lead to diverse s-functionalization of lincosamide antibiotics. J Am Chem Soc 138:6348–6351

Wilson DN (2014) Ribosome-targeting antibiotics and mechanisms of bacterial resistance. Nat Rev Microbiol 12:35–48

Biochemistry

Article

Cite This: Biochemistry 2018, 57, 6336−6348

pubs.acs.org/biochemistry

Cysteine 180 Is a Redox Sensor Modulating the Activity of Human Pyridoxal 5′-Phosphate Histidine Decarboxylase

Giada Rossignoli,[†] Alessandro Grottesi,[‡] Giovanni Bisello,[†] Riccardo Montioli,[†] Carla Borri Voltattorni,[†] Alessandro Paiardini,[*,§] and Mariarita Bertoldi[*,†]

[†]Department of Neuroscience, Biomedicine and Movement, University of Verona, Strada Le Grazie, 8, 37134 Verona, Italy

[‡]Super Computing Applications and Innovation (CINECA), 00185 Rome, Italy

[§]Department of Biochemical Sciences "A. Rossi Fanelli", University "La Sapienza", Rome, P.zale A. Moro 5, 00185 Roma, Italy

Supporting Information

ABSTRACT: Histidine decarboxylase is a pyridoxal 5′-phosphate enzyme catalyzing the conversion of histidine to histamine, a bioactive molecule exerting its role in many modulatory processes. The human enzyme is involved in many physiological functions, such as neurotransmission, gastrointestinal track function, cell growth, and differentiation. Here, we studied the functional properties of the human enzyme and, in particular, the effects exerted at the protein level by two cysteine residues: Cys-180 and Cys-418. Surprisingly, the enzyme exists in an equilibrium between a reduced and an oxidized form whose extent depends on the redox state of Cys-180. Moreover, we determined that (i) the two enzymatic redox species exhibit modest structural changes in the coenzyme microenvironment and (ii) the oxidized form is slightly more active and stable than the reduced one. These data are consistent with the model proposed by bioinformatics analyses and molecular dynamics simulations in which the Cys-180 redox state could be responsible for a structural transition affecting the C-terminal domain reorientation leading to active site alterations. Furthermore, the biochemical properties of the purified C180S and C418S variants reveal that C180S behaves like the reduced form of the wild-type enzyme, while C418S is sensitive to reductants like the wild-type enzyme, thus allowing the identification of Cys-180 as the redox sensitive switch. On the other hand, Cys-418 appears to be a residue involved in aggregation propensity. A possible role for Cys-180 as a regulatory switch in response to different cellular redox conditions could be suggested.

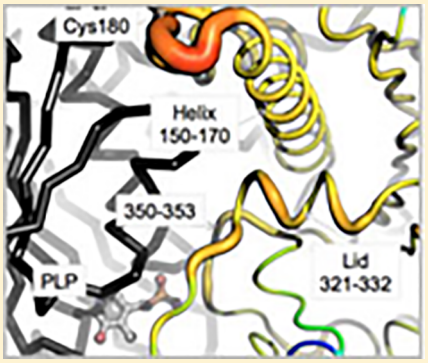

Histidine decarboxylase (HDC, EC 4.1.1.22) is a pyridoxal 5′-phosphate (PLP) enzyme that is responsible for the conversion of histidine to histamine. Histamine plays important roles in gastric acid secretion and immune responses and is also involved in cell growth, memory, appetite, and circadian rhythm regulation.[1] Impairment of histamine metabolism leads to multiple pathological states such as inflammatory responses, peptic ulcer, and several central nervous system disorders.[2,3]

From an evolutionary and structural point of view, HDC belongs to group II PLP-decarboxylases of fold type I. A recent review summarizes the spatial and functional correlations among the enzymes that belong to this group.[4] Although the prokaryotic HDC enzymes are mainly pyruvoyl-dependent (with the exception of a few Gram-negative bacteria such as *Morganella morganii* together with some *Enterobacter* and *Klebsiella* species), the eukaryotic, and thus the mammalian and human, enzymes are PLP-dependent. E. E. Snell and co-workers cloned, purified, and characterized the prokaryotic PLP HDCs.[5−11] Today, apart from a few mechanistic papers,[12] these prokaryotic decarboxylases are mainly studied for their role in contamination of food, especially fish, to find possible inhibitors that could prevent histamine accumulation.[13−15]

Mammalian HDC, which is different from the other homologous enzymes such as aromatic amino acid decarboxylase or glutamate decarboxylase,[4] has been poorly characterized until now, given its small quantities in the cell types where it is expressed: mast cells, a group of hypothalamic neurons, and enterochromaphin-like cells.[16,17] Indeed, its level is generally scarce also when it is cloned and expressed as a recombinant protein in bacterial systems. Moreover, the rat and mouse proteins, translated as 74 kDa inactive precursors, are very unstable and subjected to post-translational processing at the N- and C-termini.[18,19] The cleaved forms are active and range from 53 to 64 kDa, as seen in different cell types.[20−27] The minimum required for activity is 53 kDa,[28] which corresponds to the homologous domain of other PLP-decarboxylases. The mechanism of processing has been attributed to various systems such as calpains, proteasome, and caspase-9,[22,23,29−31] but it is far from being exhaustively elucidated.

Received: June 6, 2018
Revised: October 15, 2018
Published: October 22, 2018

DOI: 10.1021/acs.biochem.8b00625
Biochemistry 2018, 57, 6336−6348

Besides its role in histamine production, HDC is now attracting attention because of its involvement in the cell proliferation of many tumors and in Tourette syndrome. Among tumors, cholangiocarcinoma is difficult to diagnose and has limited treatments being chemoresistant.[32,33] Surgical resection, the treatment of choice in such a case, is not always feasible given frequent late diagnosis.[34] Recently, it has been demonstrated that HDC expression is enhanced in cholangiocarcinoma, and the increased level of histamine secretion is related to tumor growth.[35] Treatment with an inhibitor of HDC, namely α-methyl-D,L-histidine, decreases HDC activity and slows cancer progression.[35,36] A few inhibitors of HDC have been further explored,[4] such as α-fluoromethylhistidine,[37] histidine methylester,[37] epigallocatechin gallate,[38] and 4(5)-aminooxymethylimidazole,[39] however with no direct clinical results.

Tourette syndrome, a developmental neuropsychiatric disorder, has been linked to a mutation, present in heterozygosis, in the *Hdc* gene. This gives rise to a deleted protein (W317X) with no decarboxylase activity.[40] However, despite contradictory reports, it has been recently confirmed both in humans and in *Hdc* knockout (KO) mouse models that HDC deficiency represents a rare cause of Tourette syndrome and that histamine−dopamine interconnections in the basal ganglia are an important knot of pathology.[41] This monoamine interplay has recently been reviewed by Pittenger.[42]

KO mice, generated in 2001,[43] gave insights into previously unknown pathophysiological functions of histamine, expanding its roles from taking part in allergic and neurological responses to being involved in different fields such as cardiology, immunology, and infectious diseases.[2]

The three-dimensional structure of active human HDC (residues 2−477) in complex with the inhibitory substrate analogue histidine methylester was determined in 2012 using an enzymatic form bearing a double-amino acid substitution (C180S and C418S) to increase protein stability and prevent nonspecific aggregation.[44,45] In the functionally active dimeric arrangement, Cys-180 belongs to the large domain of each monomer that is responsible for dimeric interface formation and faces near to the corresponding Cys-180 of the other monomer, while Cys-418 is located at the surface of the C-terminal small domain far from the other subunit. It has been demonstrated that the catalytic efficiency of the doubly substituted enzyme is not altered compared to that of the wild-type (WT) enzyme[45] with measured k_{cat} values 10-fold higher than the k_{cat} values reported for most mammalian HDCs (<0.1 s^{-1}).[46] A possible role for a regulation played by the redox state and/or by calcium levels was advanced.[46]

Here, we show, for the first time, that human WT HDC exists as an equilibrium between a cysteine-reduced (redHDC) and cysteine-oxidized (oxHDC) form. These two species exhibit slight structural and functional differences. In addition, we show that Cys-180 is responsible for the intermolecular disulfide-bound dimer (oxHDC) and provide insight into its properties, while Cys-418, in agreement with ref 44, could be involved in the propensity of HDC to aggregate.

MATERIALS AND METHODS

Materials. Pyridoxal 5′-phosphate (PLP), L-histidine (L-His), 2,4,6-trinitrobenzene-1-sulfonic acid (TNB), isopropyl β-D-thiogalactopyranoside (IPTG), protease inhibitor cocktail EDTA-free tablets, phenylmethanesulfonyl fluoride (PMSF), 2,4,6-trinitrobenzenesulfonic acid (TNB), 1,8-anilinonaphthalenesulfonic acid (ANS), dithiothreitol (DTT), β-mercaptoethanol (β-MeSH), glutathione (GSH), and all the other chemicals and reagents were purchased from Sigma-Aldrich and were of the highest purity available. The gene encoding human HDC was purchased from ORIGENE.

Multiple-Sequence Alignment of HDCs. Amino acid sequences from various sources were taken from the NCBI Web site (https://www.ncbi.nlm.nih.gov/) and aligned using the Clustal Omega tool (http://www.ebi.ac.uk/Tools/msa/clustalo/) keeping all parameters at their default values.

Plasmid Constructs. The gene encoding human HDC, carried by mammalian expression vector pCMV6, was amplified to obtain the gene sequence corresponding to the amino acid sequence Met-2−Cys-479, followed by the thrombin protease cleavage site. In addition, the restriction sites for the enzymes NdeI and XhoI were inserted upstream and downstream, respectively, for subcloning the modified *HDC* gene sequence upstream of the six-His tag into bacterial expression plasmid pET28a. The designed and synthesized (Eurofins Genomics) primers were 5′-AGGGACCATGGGC-ATGGAGCCTGAGGAGTACAGA-3′ for the forward primer and 5′-ATTTACTCGAG**GGATCCACGCGGAACCAG**AC-AGTGCTGACTCAGGAT-3′ for the reverse primer (the NdeI and XhoI restriction sites are underlined in the forward and reverse primers, respectively, while the thrombin cleavage site is shown in bold).

The C180S and C418S variants were constructed starting from the cloned gene in the pET28a expression vector. Mutations were introduced by the QuickChange site-directed mutagenesis kit (Agilent Technologies) using the oligonucleotides 5′-GCTGATGAGTCCAGCCTAAATGCCCGA-3′ and its complement and 5′-GGGTCCTAATAGTCTCACAGAA-AATGTG-3′ and its complement for C180S and C418S, respectively (the mutated codons are underlined) (Eurofins Genomics). The correct nucleotide sequences of the constructs were confirmed by DNA sequencing (BMR Genomics).

Expression and Purification. *Escherichia coli* BL21 (DE3) chemically competent cells were transformed by heat shock at 42 °C with the appropriate construct and grown in 6 L of Luria-Bertani (LB) broth supplemented with 35 mg/mL kanamycin. The cultures were grown at 37 °C to an OD_{600} of 0.4−0.6, and expression was induced with 0.5 mM IPTG for 15 h at 30 °C. Cells were harvested and resuspended in 20 mM sodium phosphate buffer (pH 7.4) containing 0.5 M NaCl, 20 mM imidazole, 50 μM PLP, 0.5 mM PMSF, and protease inhibitor cocktail, with the addition of 10 mM β-MeSH. Lysozyme was then added to a concentration of 0.2 mg/mL, and the culture was incubated for 20 min at room temperature. After a freeze−thaw cycle, leupeptin (1 μg/mL) and pepstatin (1 μg/mL) were added, and the suspension was centrifuged at 30000*g* for 30 min. The cleared lysate was diluted to ∼30 mg/mL and loaded onto a HisPrep FF 16/10 column (GE Healthcare) equilibrated with 20 mM sodium phosphate buffer (pH 7.4) containing 0.5 M NaCl and 20 mM imidazole in the presence of 10 mM β-MeSH. A linear gradient was then inserted (0 to 100% in 200 mL) with the same buffer containing 350 mM imidazole. Soluble HDC elutes as a symmetrical peak and was incubated with 100 μM PLP. Imidazole and unbound coenzyme were removed by extensive washing with 0.1 M potassium phosphate buffer (pH 7.4) and 10 mM β-MeSH, and the protein solution (redHDC) was concentrated in the same buffer using Amicon Ultra 10 concentrators (Millipore). The enzyme concentration was

DOI: 10.1021/acs.biochem.8b00625
Biochemistry 2018, 57, 6336−6348

determined by using an ε_M of 1.57 × 10^5 M^{-1} cm^{-1} at 280 nm,[47] and the PLP content was determined by releasing the coenzyme in 0.1 M NaOH using an ε_M of 6600 M^{-1} cm^{-1} at 388 nm.[48] The purity of the protein was detected by a single band corresponding to a molecular weight of ∼56 kDa in a 12% reducing sodium dodecyl sulfate−polyacrylamide gel electrophoresis (SDS−PAGE) gel.

Semidenaturing and Native PAGE. Semidenaturing 10% SDS−PAGE used to evaluate the presence of the intermolecular disulfide bond of 5 μg of HDC incubated with increasing concentrations of β-MeSH, DTT, or GSH (the concentrations are listed in the Results and Discussion) for 1 h and loaded with the addition of 4× nonreducing sample buffer.

Native PAGE analysis was performed under the same conditions as semidenaturing SDS−PAGE, but samples were loaded with the addition of 2× native sample buffer.

Size-Exclusion Liquid Chromatography Analyses. Size-exclusion liquid chromatography was used to prepare the fully oxidized HDC (oxHDC) starting from the reduced form. RedHDC was loaded onto a Sephacryl H-200 (16/60) (GE Healtcare) column equilibrated with 0.1 M potassium phosphate buffer (pH 7.4) and 0.15 M NaCl on an Akta FPLC system (GE Healthcare). The run, using the same buffer, was performed at a flow rate of 0.5 mL/min with detection at 280 nm. The protein eluted as a single symmetrical peak and was incubated with 100 μM PLP. Unbound coenzyme was removed by extensive washing with 0.1 M potassium phosphate buffer (pH 7.4), and the protein solution was concentrated in the same buffer using Amicon Ultra 10 concentrators (Millipore). The redox state of the eluted protein was determined by loading it onto a nonreducing denaturing (semidenaturing, see above) SDS−PAGE gel.

Size-exclusion liquid chromatography was used to determine the molecular dimensions of the holoenzyme (300 μg) in both oxidized and reduced forms. The samples were loaded on a Sephacryl H-200 (16/60) (GE Healtcare) column equilibrated with 0.1 mM potassium phosphate buffer (pH 7.4) and 0.15 M NaCl with the addition of 10 mM β-MeSH for redHDC, on an Akta FPLC system (GE Healthcare). The injection volume was 500 μL at a flow rate of 0.5 mL/min with detection at 280 nm. Three chromatographic experiments were run per sample, and Unicorn version 5.01 (GE Healthcare) was used to calculate the elution volume of each peak. The apparent molecular dimension of the eluting species was calculated by comparing their elution volume to that of a set of molecular weight standards under the same experimental conditions.

Spectroscopic Measurements. Absorption measurements were performed using a Jasco V-550 spectrophotometer at a protein concentration of 1 mg/mL under conditions specified in the Results and Discussion for each case.

Circular dichroism measurements were taken with a Jasco J-710 spectropolarimeter at a protein concentration of 1 mg/mL for near-ultraviolet (near-UV) and visible spectra or 0.1 mg/mL for far-UV spectra. The thermostability was determined by monitoring the circular dichroic signal at 222 nm at a concentration of 0.1 mg/mL and a temperature increase from 25 to 90 °C at a rate of 1.5 °C/min.

Fluorescence spectra were recorded using a FP-750 Jasco spectrofluorimeter setting at 5 nm excitation and emission bandwidths, following excitation at different wavelengths, specified in the Results and Discussion for each case.

All the spectroscopic measurements were taken in 0.1 M potassium phosphate buffer (pH 7.4) at 25 °C, with the addition of 10 mM β-MeSH or 10 mM GSH for redHDC.

Coenzyme Binding Affinity Measurements. The apoenzyme was prepared by incubating 10 μM redHDC or oxHDC with 50 mM phenylhydrazine at 25 °C for 2 h in 0.5 M potassium phosphate buffer (pH 6.8), with the addition of 10 mM β-MeSH for redHDC. The solution was then loaded on a desalting 26/10 column (GE Healthcare) preequilibrated with the same buffer without phenylhydrazine. The eluted enzyme was then concentrated using Amicon Ultra 10 concentrators (Millipore) and washed with 0.1 M potassium phosphate buffer (pH 7.4), with the addition of 10 mM β-MeSH for apo-redHDC.

The equilibrium apparent dissociation constant for PLP, $K_{D(PLP)}$, was determined by measuring the quenching of the intrinsic fluorescence of the 0.03 μM HDC apoenzyme in the presence of PLP at concentrations ranging from 0.005 to 20 μM in 0.1 mM potassium phosphate buffer (pH 7.4), with the addition of 10 mM β-MeSH for redHDC.

The data were fitted to the following equation:

$$Y = Y_{max}\frac{[E]_t + [PLP]_t + K_{D(PLP)} - \sqrt{[[E]_t + [PLP]_t + K_{D(PLP)}]^2 - 4[E]_t[PLP]_t}}{2[E]_t}$$

where $[E]_t$ and $[PLP]_t$ represent the total concentrations of the enzyme and PLP, respectively, Y refers to the intrinsic quenching changes at a PLP concentration, and Y_{max} refers to the fluorescence changes when all enzyme molecules are complexed with coenzyme.

Curve fitting was performed using Origin 8 Pro (OriginLab).

Dynamic Light Scattering Analysis. The dynamic light scattering (DLS) analyses were performed using the Zetasizer Nano S (ZEN1600) instrument (Malvern Instruments) with a constant 90° scattering angle and a 633 nm wavelength laser at 25 °C. The sample volume used for analysis was 0.8 mL at an enzyme concentration of 2 μM in 0.1 M potassium phosphate buffer (pH 7.4), with the addition of 10 mM β-MeSH for redHDC. A total of 100 scans were obtained for each sample, after an equilibration time of 10 min, and all samples were analyzed in triplicate.

Enzyme Activity Assay. The decarboxylase activity was measured by a stopped spectrophotometric assay already used for DOPA decarboxylase and useful for quantifying aromatic amines.[49] HDC (WT or variants, 0.3 μM) was incubated for an appropriate incubation time (a time within which linear product formation is observed) with 1 mM L-His and 10 μM PLP in a final volume of 250 μL in 0.1 M potassium phosphate buffer (pH 7.4), with the addition 1 mM GSH for redHDC. The reaction was then stopped by heating the mixture at 100 °C for 2 min. TNB (1 mL of a 4.3 mM solution) and toluene (1.5 mL) were added, and the extraction of trinitrophenylhistamine was performed at 42 °C for 45 min with continuous shaking. The concentration of the trinitrophenyl derivative in the toluene layer was measured by using a prepared calibration curve of absorbance at 340 nm as a function of trinitrophenyl derivative concentration. The measured ε_M is 11300 M^{-1} cm^{-1}

DOI: 10.1021/acs.biochem.8b00625
Biochemistry 2018, 57, 6336−6348

at 340 nm. The kinetic parameters were determined by incubating the enzyme in the presence of different L-His concentrations (0.025−2 mM) at a saturating PLP concentration, and the obtained data were fitted to the Michaelis−Menten equation using Origin 8 Pro (OriginLab).

Atomic Coordinates and Modeling. Atomic coordinates of human HDC (entry 4E1O[45]) were taken from the Protein Data Bank (PDB)[50] and used as a starting point to model the disulfide bond between the Cys-180 residues of the polypeptide chain. Modeling was done using MODELER, version 9.17,[51] and PyMod.[52] Subsequently, local steepest descent energy minimization in vacuum was performed to relieve local structural strain using GROMACS version 4.0.7[53] in conjunction with the GROMOS53a6 force field. The structural stability of the obtained model was assessed by a number of structure analysis tools. Ramachandran plot calculations, computed with PROCHECK,[54] exhibited optimal stereochemical quality, with 95.3% of the residues in the most favored region and only 0.5% of the residues in the disallowed regions. The energy profile calculated by the Dope score of the model suggests that the obtained disulfide bond is energetically consistent and reliable. Normal mode (NM) analysis of the structure of HDC with reduced Cys-180 residues was performed using the elastic network model (ENM), a fast and simple way to compute the low-frequency normal modes of a macromolecule,[55] as implemented in the *PyANM* tool.[56] The lowest-frequency normal mode was kept and used for visual analysis.

Molecular Dynamics (MD). All simulations have been performed using Gromacs version 2018.2. The structures were centered in cubic boxes with minimum distance of 0.9 nm between each atom of the protein and the box to reduce. The SPC water model[57] was used to solvate the system. The ionic strength was adjusted to make sure all simulations were electrically neutral. MD simulations were performed with periodic boundary conditions in the isothermal−isochoric ensemble (*NVT*), using an integration step of 2 fs at a constant temperature (300 K) using the velocity rescaling algorithm.[58] The particle mesh Ewald method[59] was used to calculate the long-range contribution (reciprocal space) of the electrostatic interactions using a cutoff radius of 1.0 nm. The Gromos53a6 force field[60] was used. Before production runs, all systems were subject to a minimization cycle and thermalization procedure to bring the temperature gradually to 300 K. All runs consisted of at least 100 ns MD simulations in an *NVT* ensemble. MD analysis was performed using Gromacs and was based on the equilibrated part of all simulations, that is, beyond 20 ns. Root-mean-square fluctuations were calculated using the Cα atom deviation with respect to their average position. Trajectories were projected onto selected eigenvectors to show main dominant protein motions. PLP was included in all simulations, and the topology parameter of the Gromos53a6 force field was obtained using the PRODRG server.[61] Figures were generated using the Pymol 2.0 software (The PyMOL Molecular Graphics System, version 2.0, Schrödinger, LLC).

RESULTS AND DISCUSSION

HDC Cys-180 Is the Only Cysteine Residue Not Conserved among HDCs. A multiple-sequence alignment of HDCs from mammals and other sources such as *Gallus*, *Drosophila*, *Danio*, and prokaryotic organisms shows that only one cysteine residue is not conserved among the 11 cysteine residues present in each subunit of the functionally active dimeric human HDC, namely Cys-180 (Figure 1). A further comparison of the sequences of HDCs with those of decarboxylases of group II, in particular with that of human aromatic amino acid decarboxylase, points out that six of the 11 cysteine residues of human HDC are shared, while the remaining four are typical of HDCs. Cys-418, the other cysteine residue replaced with serine in the crystallization papers by Komori and co-workers,[44,45] belongs to the latter group. Interestingly, HDCs from primates (*Gorilla gorilla*, *Pongo abelii*, *Pan paniscus*, *Pan troglodytes*, and many species of the genera *Macaco*) are predicted to have Cys-180, thus dating at least to primates the substitution responsible for the presence of this cysteine residue in the human protein. The fact that Cys-180 is not conserved and, at the same time together with Cys-418, contributes to protein stability[45] raises questions about the role it could play.

Human Wild-Type HDC Exists in an Equilibrium between a Reduced (redHDC) and an Oxidized (oxHDC) Form Controlled by Cys-180. Human HDC has been cloned in pET28a, transformed in BL21 *E. coli*, expressed, and purified with an affinity column as reported in Materials and Methods. The yield is 2−5 mg/L, and the enzyme is pure as evidenced by a single band in an SDS−PAGE gel (Figure S1) and contains 2 mol of PLP per dimer. It has been immediately noted that, depending on the reducing agent concentration, HDC presents one or two bands on a semidenaturing SDS−PAGE gel. The molecular weight of the slow mobility band suggests that it is a dimer, while the fastest band, at ∼56 kDa, corresponds to the monomer (Figure 2A and Figure S2A,B). β-MeSH, DTT, or GSH has been used as a reducing agent, showing in every case the same results. To obtain a fully reduced species, the reductant:protein dimer ratio should be an at least 2000-fold molar excess. A native PAGE performed at increasing GSH concentrations confirms that HDC is present as a dimer (Figure S2C). The dimeric arrangement is also exhibited by size-exclusion chromatography analysis showing that the two species elute at nearly the same volume (62.6 ± 0.1 and 61.8 ± 0.2 mL for redHDC and oxHDC, respectively) (Figure S2D).

The C180S and C418S variant HDCs have been cloned, expressed, and purified to homogeneity as revealed by a single band on an SDS−PAGE gel (data not shown), and both of them bind 2 mol of PLP/dimer. A semidenaturing SDS−PAGE performed under the same conditions as the wild-type method shows that C180S appears as a monomer at any GSH concentration, while C418S exists as oxidized/reduced species in equilibrium depending on the absence or presence of a reducing agent, a behavior strongly ressembling that of the WT (Figure 2B,C).

From these data, it can be inferred that HDC exists in a reduced and oxidized state depending on the presence of a reductant and that Cys-180 appears as a good candidate for an intersubunit disulfide bond of one subunit with the same residue of the neighboring subunit. No other cysteine residue is in fact present within 10 Å of Cys-180. In this regard, it is of interest that a possible role for regulation by the redox state was advanced.[46]

We have then undertaken a spectroscopic characterization to highlight possible differences in physicochemical signals between redHDC and oxHDC.

The Spectroscopic Analyses Reveal That redHDC and oxHDC Display Slight Structural Changes. The absorbance spectra of redHDC (in the presence of 10 mM GSH) and

DOI: 10.1021/acs.biochem.8b00625
Biochemistry 2018, 57, 6336−6348

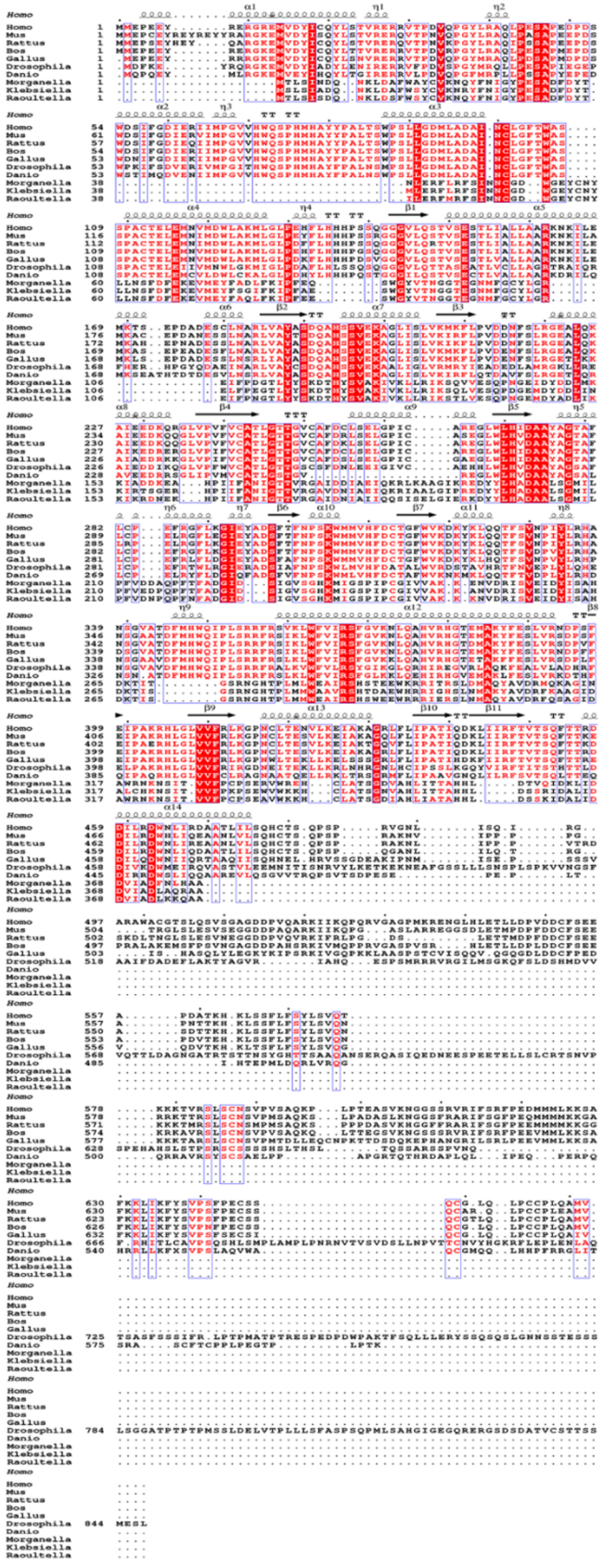

Figure 1. Multiple-sequence alignment of HDCs. Amino acid sequences from various sources were taken from the NCBI Web site (https://www.ncbi.nlm.nih.gov/) and are, in order, *Homo sapiens*, *Mus musculus*, *Rattus norvegicus*, *Bos taurus*, *Gallus gallus*, *Danio rerio*, *Drosophila melanogaster*, *Morganella morganii*, *Klebsiella aerogenes*, and *Raoultella planticola*. The one-letter amino acid code is used. Dashes represent insertions and deletions. Invariant positions are boxed in red. Similar residues are written in red characters. Homologous regions are boxed in light blue. The secondary structures of human HDC (PDB entry 4E1O) are reported in the first line of each block. α-Helices and β-strands are rendered as squiggles and arrows, respectively. ESPript (http://espript.ibcp.fr) was used to render this figure starting from a Clustal Omega alignment (http://www.ebi.ac.uk/Tools/msa/clustalo/).

Figure 1. continued

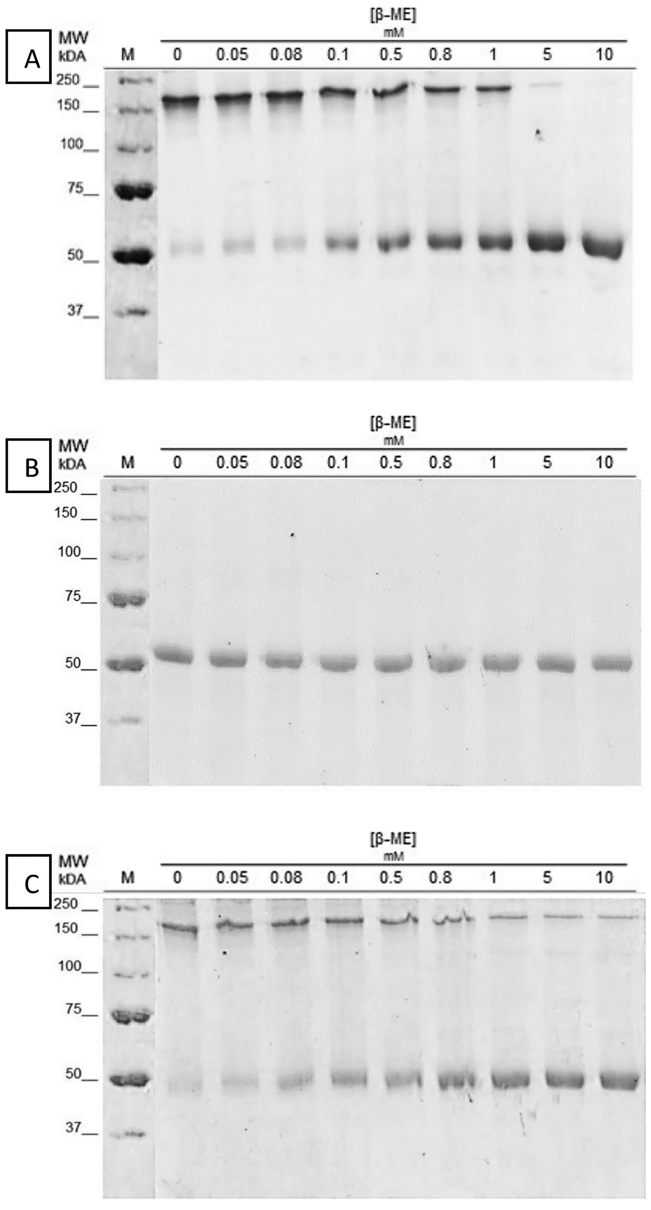

Figure 2. Semidenaturing 10% SDS–PAGE analysis of (A) WT, (B) C180S, and (C) C418S HDC with increasing β-MeSH concentrations. Five micrograms of (A) WT, (B) C180S, or (C) C418S HDC was incubated for 1 h at room temperature with the corresponding β-MeSH concentration in 0.1 M potassium phosphate buffer (pH 7.4). M, molecular weight marker.

DOI: 10.1021/acs.biochem.8b00625
Biochemistry 2018, 57, 6336–6348

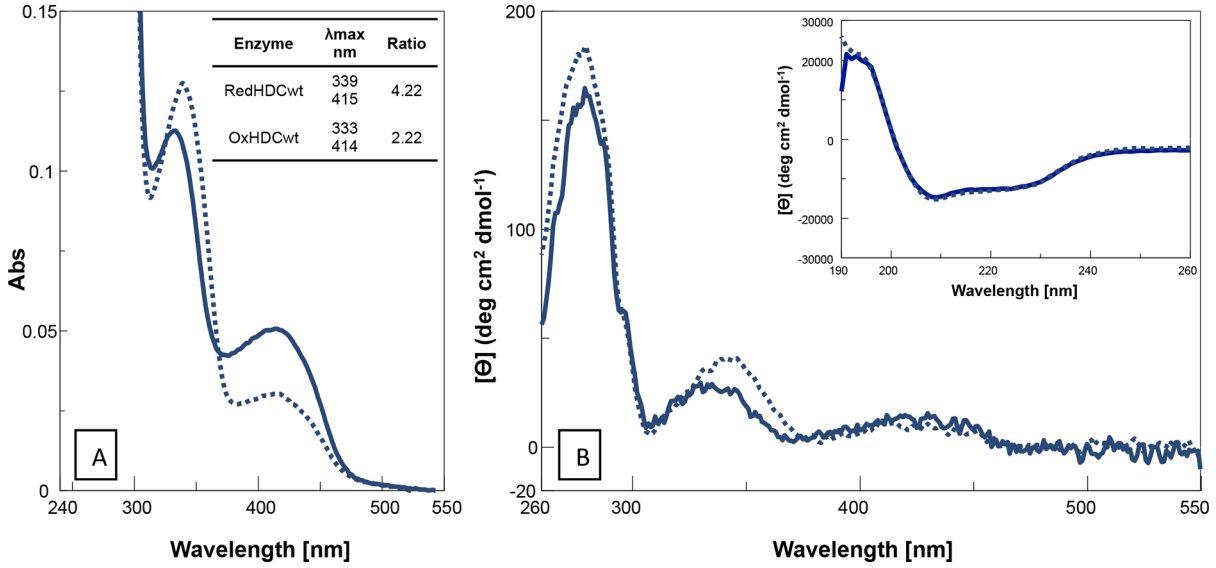

Figure 3. Spectroscopic characterization of WT HDC. (A) Absorbance and (B) near-UV and visible dichroic spectra of redHDC (dotted line) and oxHDC (straight line) were recorded at 1 mg/mL in 0.1 M potassium phosphate buffer (pH 7.4) without or with 20 mM GSH. The absorbance maximum wavelengths are reported in inset A. Inset B shows the far-UV spectra measured at 0.1 mg/mL in 0.1 M potassium phosphate buffer (pH 7.4) without or with 20 mM GSH.

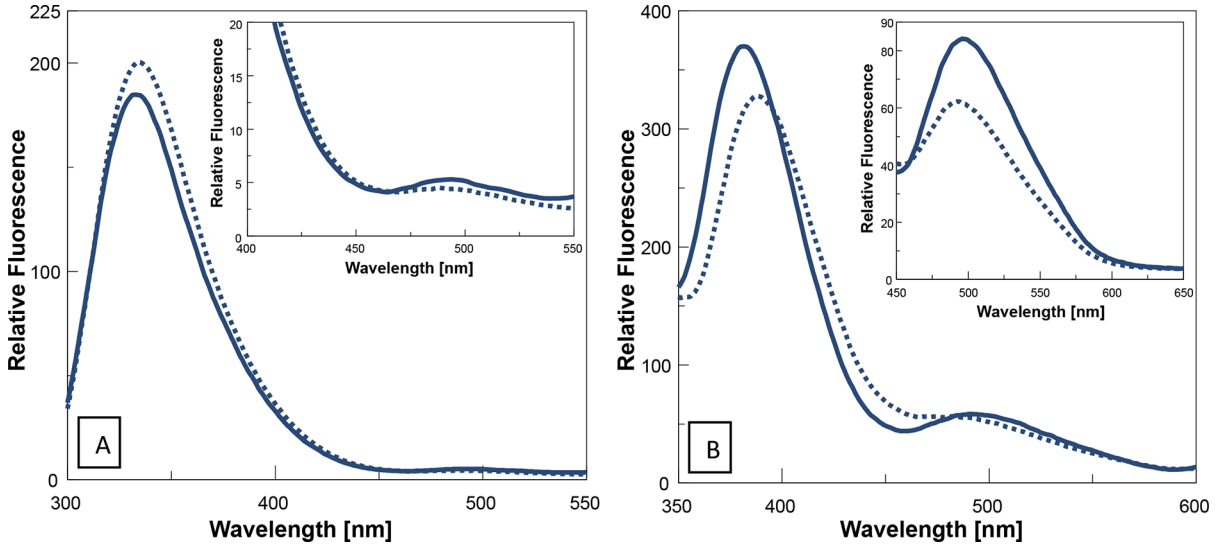

Figure 4. Emission fluorescence spectra of WT HDC. (A) Intrinsic fluorescence emission spectra of redHDC (dotted line) and oxHDC (straight line) after excitation at 280 nm. Spectra were recorded at 0.1 mg/mL in 0.1 M potassium phosphate buffer (pH 7.4) without or with 20 mM GSH. Inset A is a close-up of the fluorescence emission maximum in the 490 nm region. (B) Cofactor fluorescence emission spectra after excitation at 339 and 333 nm of redHDC (dotted line) and oxHDC (straight line), respectively, at 1 mg/mL in 0.1 M potassium phosphate buffer (pH 7.4) without or with 20 mM GSH. Inset B shows cofactor fluorescence emission spectra after excitation at 415 and 414 nm for redHDC and oxHDC, respectively.

oxHDC measured in 0.1 M potassium phosphate buffer (pH 7.4) show, in addition to the 280 nm band that can be attributed to the aromatic amino acids, the presence of two bands in the visible region with maxima at 339 and 415 nm for redHDC and at 333 and 414 nm for oxHDC. Besides the slight differences in wavelength maxima, the equilibrium between these two species is altered with 339 nm/415 nm and 333 nm/414 nm ratios of 4.22 and 2.22, respectively (Figure 3A). These species can be reasonably attributed to the enolimine and ketoenamine tautomers of the internal aldimine between PLP and Lys-304, and it can be thus suggested that the PLP microenvironment is altered in the two redox states of the enzyme.

The dichroic signals in the visible region reflect a similar coenzyme behavior displayed in absorbance, and in addition, the near-UV bands show a slight difference between redHDC and oxHDC (Figure 3B). The optical activities (millidegrees per absorbance unit at a fixed wavelength at the same protein concentration) for the enolimine and ketoenamine are 30.25 and 48.18 for redHDC and 24.53 and 20.12 for oxHDC, respectively, supporting the presence of an altered PLP microenvironment. Finally, the far-UV CD spectra are superimposable, indicative of a similar secondary structure content (inset Figure 3B).

Fluorescence data essentially provide the same information about the spectrophotometric and spectropolarimetric experi-

DOI: 10.1021/acs.biochem.8b00625
Biochemistry 2018, 57, 6336−6348

Table 1. Kinetic Parameters, Apparent Equilibrium Dissociation Constants for PLP, and Melting Temperatures of WT HDC and Its Variants[a]

enzyme	k_{cat} (s^{-1})	K_m (mM)	k_{cat}/K_m (s^{-1} mM^{-1})	$K_{D(PLP)}$ (nM)	T_m (°C)
redHDC WT	0.70 ± 0.02	0.064 ± 0.008	10.9 ± 1.4	32.8 ± 0.4	62.78 ± 0.06
oxHDC WT	1.10 ± 0.05	0.033 ± 0.006	33.3 ± 6.2	44.0 ± 0.3	65.97 ± 0.02
redHDC C180S	0.60 ± 0.02	0.057 ± 0.008	10.5 ± 1.5	–	–
oxHDC C180S	0.72 ± 0.02	0.062 ± 0.007	11.6 ± 1.3	30.5 ± 0.2	62.68 ± 0.04
redHDC C418S	0.74 ± 0.04	0.06 ± 0.01	12.3 ± 2.2	–	–
oxHDC C418S	1.05 ± 0.03	0.042 ± 0.007	25.0 ± 4.2	43.1 ± 0.2	65.49 ± 0.04

[a]From 0.05 to 2 mM L-His reacted with 0.075 nmol of each HDC species for 10 min in 250 μL of 0.1 M potassium phosphate buffer (pH 7.4) without or with 1 mM GSH. Dissociation constants for PLP were calculated from the measured enzyme intrinsic fluorescence quenching with an increasing concentration of the coenzyme as reported in Materials and Methods. Melting temperatures were calculated by dichroic changes at 222 nm as reported in Materials and Methods.

ments. Intrinsic fluorescence spectra recorded upon excitation at 280 nm show an emission band centered at 335 nm for redHDC and 333 nm for oxHDC with different relative intensities (207 vs 185). A red-shifted broad shoulder is present in oxHDC, emitting at 494 nm with a relative intensity of ∼5 for oxHDC suggesting an energy transfer and thus a different positioning of PLP with respect to aromatic amino acids. (Figure 4A). Cofactor emission fluorescence upon excitation of the enolimine tautomer at 339 and 333 nm for redHDC and oxHDC, respectively, shows emissions at 386 and 485 nm for redHDC and 381 and 491 nm for oxHDC. When the ketoenamine tautomer of the two species was excited at 415 nm (redHDC) and 414 nm (oxHDC), a band centered at 485 nm and at 496 nm was recorded (Figure 4B and inset). Altogether, these fluorescence results witnessed a modest change in the cofactor environment and in the interconnections among PLP and the surrounding residues in the two HDC forms.

These spectroscopic data suggest that redHDC and oxHDC present slight differences in all measured signals indicative of subtle structural changes. The optical activity values are also an expression of modest coenzyme-to-aromatic amino acid side chain microenvironment alterations. We thus investigated if these changes are related to the catalytic activity and to the stability of the enzyme.

OxHDC Is More Stable and More Active Than redHDC. The thermostability of the two enzymatic forms has been assessed by monitoring the dichroic signal at 222 nm with an increase in temperature from 25 to 90 °C at a rate of 1.5 °C/min. While the T_m of redHDC is 62.78 ± 0.06 °C, that of oxHDC is 65.97 ± 0.02 °C (Table 1), thus suggesting that the oxidized form of HDC is slightly more stable than the reduced form. DLS analyses show that the hydrodynamic diameter of redHDC is 9.90 ± 0.08 nm while that of oxHDC is 11.60 ± 0.04 nm. In addition, it should be pointed out that the theoretical diameter[62] is predicted to be 8 nm calculated on the basis of the determined structure of the double-mutant form (C180S/C418S)[45] that ressembles redHDC (see below).

Kinetic parameters of redHDC and oxHDC (Table 1) show that the catalytic efficiency of the oxidized form is 3-fold higher than that of the reduced form, and this is driven by the combination of both the 1.6-fold increase in k_{cat} and the 2-fold decrease in K_m. The apparent equilibrium dissociation constant for the coenzyme is quite similar, i.e., 33 nM for redHDC versus 44 nM for oxHDC.

Interestingly, the oxidized species is more active and more stable than the reduced form. Thus, we looked for a possible molecular cause as the basis for this different behavior.

The Cys-180 Redox State Is Responsible for a Structural Transition Affecting the C-Terminal Domain Reorientation and Could Be Responsible for Active Site Alterations. The availability of the recently determined crystal structure of human HDC (PDB entry 4E1O)[45] gave us the unprecedented opportunity to gain insights into the role of the intersubunit disulfide bridge of Cys-180 in controlling the structural rearrangement of human HDC and its catalysis. However, because Cys-180 was replaced with serine to prevent unwanted oligomerization,[45] we started our analysis by modeling the position of Cys-180 and the disulfide bridge in their reduced and oxidized forms, respectively (Figure 5). In

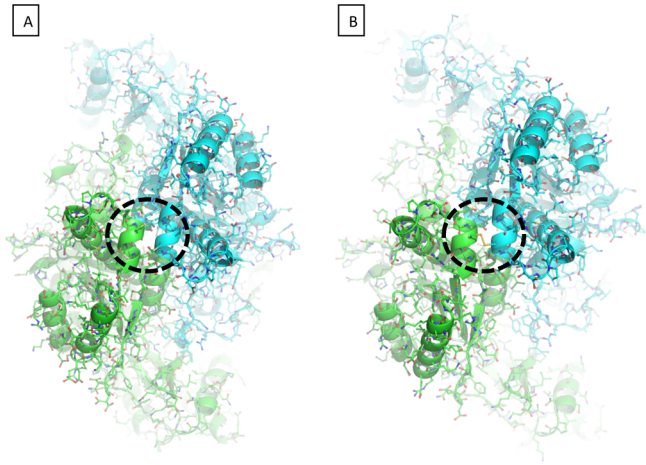

Figure 5. Modeling of WT HDC in its (A) reduced and (B) oxidized states. The two HDC subunits are represented as green and cyan cartoons and sticks, respectively. The dashed black circle indicates the position of the two Cys-180 residues.

their oxidized state, the two Cys-180 residues of each monomer are in a distance range (≈2.5 Å) that is compatible with the formation of an intersubunit disulfide bond. The latter, in turn, could be responsible for a "locking" of the two α-helices spanning residues 178−184 and comprising Cys-180, which face each other at the dimer interface. On the contrary, in the absence of the covalent bond between the two Cys residues, the two α-helices of redHDC are expected to freely move, because no other close contact is present. Indeed, an inspection of the physicochemical properties of the dimer interfaces of HDC and its close homologue aromatic amino acid decarboxylase (PDB entry 1JS3; root-mean-square deviation of ≈0.8 Å) in this region revealed that both enzymes (and other group II decarboxylases, e.g., glutamate decarbox-

DOI: 10.1021/acs.biochem.8b00625
Biochemistry 2018, 57, 6336−6348

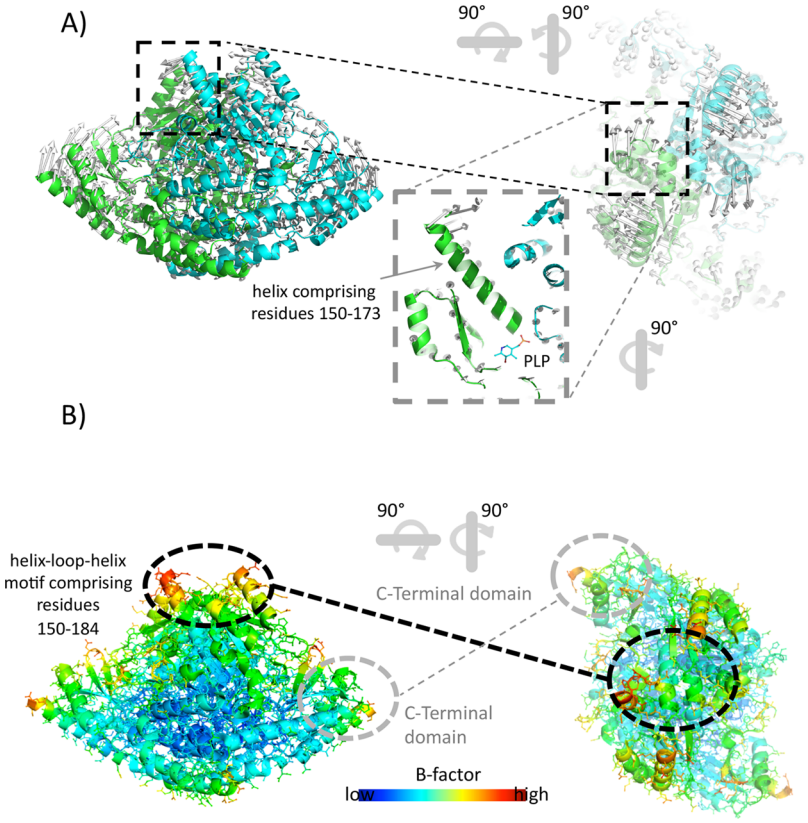

Figure 6. (A) NM analysis and (B) *B*-factors of WT HDC. (A) The two HDC subunits are represented as green and cyan cartoons. The gray arrows are trajectory vectors of the NM analysis. Each arrow's direction points in the direction where the residue will move, and each arrow's length indicates the moving scale for each residue. (B) Experimentally derived *B*-factor values, indicating local structural fluctuations, are in good agreement with NM analysis data.

ylase 65) share solvation properties that favor a partial opening.[4] Therefore, we reasoned that the presence or absence of a disulfide bridge between the Cys-180 residues of the HDC subunits[63] could lead to a subtle structural change, which in turn could be transmitted to the adjacent long α-helix of residues 150−173. The latter directly connects the α-helix of residues 178−184 to the active site of HDC. To test this hypothesis, we thus performed an all-Cα atom normal mode (NM) analysis of redHDC to investigate the conformational transitions of HDC. Indeed, it is well-known that NM analysis can probe large-amplitude motions that are often inaccessible to other atomistic simulations.[64] Moreover, NM analysis is insensitive to the presence of small molecules, such as PLP, in the context of large protein systems.

The NM symmetric rigid-body motions of the PLP binding and C-terminal domains of HDC, described by the lowest-frequency NM, are shown in Figure 6. According to NM analysis of human HDC, the magnitude of the structural fluctuations was highest at the C-terminal domains (CTDs) and at the flexible α-helix of residues 150−173 connecting the position of the α-helix residues of 178−184 and PLP (Figure 6A). Notably, HDC displayed a symmetric profile of fluctuations at the CTDs, as already observed in the close homologue glutamate decarboxylase.[65]

The obtained results of the NM simulations of HDC therefore suggested a tight coupling between the helix−loop−helix motif comprising residues 150−184 and the C-terminal domain of HDC, which in turn could drive a structural rearrangement of the two domains and of the catalytic loop lying at the interface between the N- and C-terminal domains of HDC. Interestingly, the conformation of the 150−184 helix−loop−helix motif comprises both Cys-180 and residues of the PLP binding cleft, directly linking therefore the redox state of Cys-180 to the position and stabilization of PLP. Most notably, the NM data corroborate the findings from the analysis of the structural flexibility of human HDC inferred from crystallographic *B*-factors[45] (Figure 6B), which can be used to assess the local dynamics of protein structures.[66]

To further corroborate the results obtained with coarse-grained NM analysis, MD simulations were performed to investigate the atomistic fluctuations of the PLP binding site as a function of the redox state of Cys-180. All simulations were 100 ns long, and all the analyses have been performed on the equilibrated part of all trajectories, i.e., after simulation for 20 ns. Insertion of a disulfide bridge between the Cys-180 residues of the two HDC subunits causes a general decrease in protein flexibility as measured by the root-mean-square fluctuation (RMSF) (see Materials and Methods). Figure 7 shows a comparison between the RMSF of the oxidized and reduced HDC for each monomer. As the plot shows, the introduction of a constraint in the S−S interchain disulfide bridge of Cys-180 confers upon oxHDC a generally higher rigidity compared to that of redHDC. From a structural viewpoint, the main RMSF differences between the oxidized and reduced HDC were localized on the helix encompassing residues 150−170.

We have checked the effect of conformational dynamics of helix 150−170 and all residues facing the active site on PLP mobility. In particular, we compared the flexibility (RMSF) of PLP atoms in the two HDC simulations and found that the RMSF in oxHDC was systematically lower than the

DOI: 10.1021/acs.biochem.8b00625
Biochemistry 2018, 57, 6336−6348

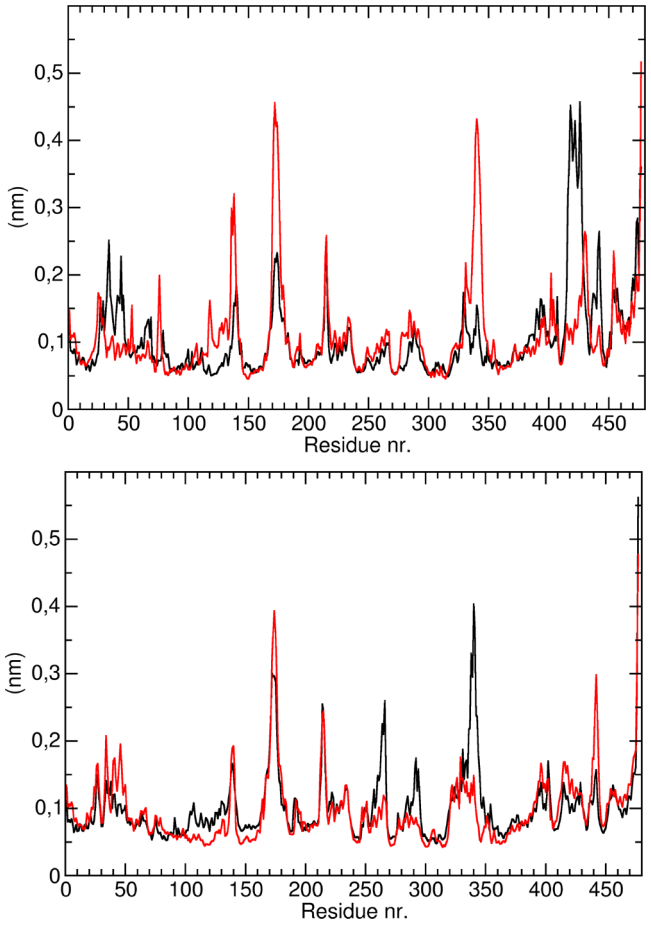

Figure 7. MD analysis of WT HDC in its reduced and oxidized states. Root-mean-square fluctuation of oxHDC (black) and redHDC (red) as a function of residue number for chain 1 (top) and chain 2 (bottom).

corresponding values for the PLP in the redHDC simulation (Figure 8), and this suggests that the disulfide bridge in Cys-180 affects the conformational mobility of the PLP moiety in its pocket by decreasing its conformational mobility

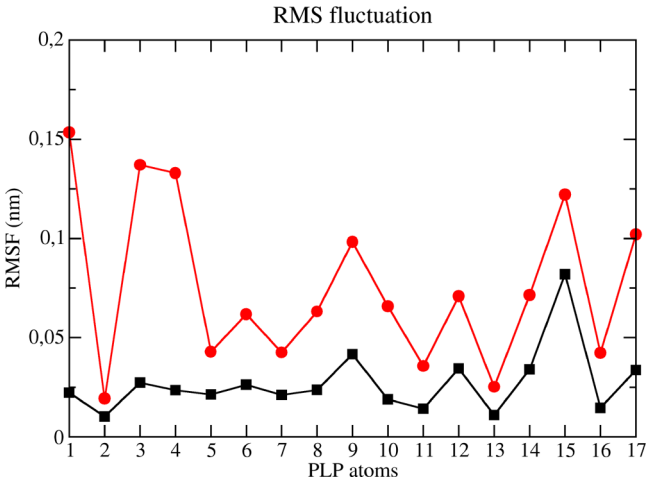

Figure 8. RMSF of PLP in oxNHD and redHDC. Root-mean-square fluctuation of PLP atoms with respect to their average position along the MD trajectories for the oxHDC simulation (black) and the redHDC simulation (red).

Further confirmation of this finding came from the essential dynamics analysis on the active site subset residues. This analysis showed that the overall fluctuation of the Cα atoms of active site residues (as calculated from the trace of the covariance matrix of positional atomic fluctuations of Cα atoms) was lower in oxHDC (0.32821 nm^2) than in redHDC (0.6821 nm^2). This confirms that the covalent bond in the Cys-Cys pair at position 180 confers a higher rigidity in the active site area.

In more detail, a ribbon representation of the HDC structure with a thickness and color scheme proportional to the difference between the RMSF of oxHDC and that of redHDC is reported in Figure 9 and a close-up inset. As shown, the N-

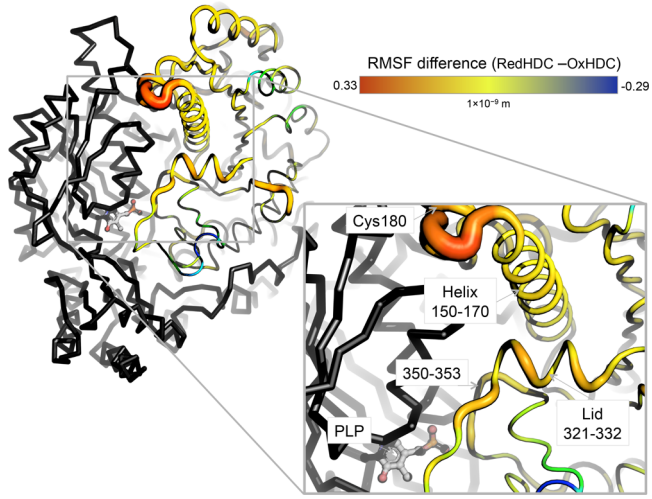

Figure 9. Difference between the RMSF of redHDC and that of oxHDC. Ribbon representation of the HDC structure with the difference between RMSF of redHDC and that of oxHDC mapped onto monomer A (rainbow scale going from 0.33 to −0.29 nm). Monomer B is colored gray. As shown in the inset, the N-terminal end of the redHDC is more flexible than its oxidized counterpart. This higher flexibility affects in turn the active site lid of HDC (residues 321−332) as well as the loop spanning residues 350−353.

terminal end of the redHDC is more flexible than its oxidized counterpart. This region is within the range of contact of either the active site lid of HDC (corresponding to residues 321−332) or the loop spanning residues 350−353 (comprising residues interacting with the phosphate moiety of PLP), which also show a higher flexibility in redHDC than in oxHDC. We suggest that this higher flexibility affects the pocket size hosting the PL, which in turn is more likely to have greater conformational freedom in redHDC than in oxHDC.

These bioinformatics data are in agreement with the slight differences evidenced by the spectroscopic analyses as well as by the kinetic features and by the protein thermal stability data between redHDC and oxHDC and suggest that oxidation could lead to a movement triggering subtle alterations at the active site. The stability could be due to the additional sulfur−sulfur covalent bond that causes a rearrangement of the overall protein structure determining an increase in the hydrodynamic diameter, as witnessed by DLS measurements. We then evaluated the functional properties of single variants C180S and C418S to gain insight into their specific contribution.

C180S Presents Features Similar to Those of redHDC, while C418S Is Sensitive to Reductants. The analyses of the absorbance, dichroic, and fluorescence properties of C180S

DOI: 10.1021/acs.biochem.8b00625
Biochemistry 2018, 57, 6336−6348

and C418S variants show that these species exhibit slight structural changes and no gross alterations in cofactor binding microenvironment (data not shown). We then focused our attention on the oxidized species of both variants because oxC180S should not form a disulfide-bound species and oxC418S should be less prone to aggregate. Interestingly, measurements of both the hydrodynamic diameter and of the thermostability show that oxC180S behaves like redHDC with a diameter of 10.56 ± 0.04 nm and a T_m value of 62.68 ± 0.04 °C, while oxC418S has a diameter of 11.6 ± 0.6 nm and a T_m of 65.49 ± 0.04 °C behaving like oxHDC. In addition, the functional features show that the catalytic efficiencies of both redC180S and oxC180S are almost identical to that of the redHDC while those of both redC418S and oxC418S are similar to those of redHDC and oxHDC, respectively (Table 1). No differences in PLP equilibrium binding constant are measured (Table 1).

Because it has been claimed that oxHDC tends to aggregate and for this reason the structure of the enzyme has been determined in the C180S/C418S double-mutant species,[45] we addressed this by concentrating 500 μL of 10 μM oxHDC, oxC180S, and oxC418S to 25 μL in an Amicon ultra device. The supernatants and the pellets (if present) were then run on an SDS gel under reducing and nonreducing conditions. We determined that a pellet was present in oxHDC and oxC180S solutions while no precipitation occurs with the oxC418S variant. Here, it follows that Cys-418 concurs in structural stability, although the molecular reason for the aggregation of oxHDC needs to be further investigated.

CONCLUSIONS

Even if human HDC belongs to the well-known group of the PLP-dependent α-decarboxylases, it is a poorly characterized protein, mainly because of its intrinsic instability. The only determined structure is that of the human protein engineered with two cysteine-for-serine substitutions (C180S and C418S) to increase its stability.[45] Here, for the first time, we provide evidence for the existence of an equilibrium between a reduced and an oxidized form of human HDC, the latter being slightly more active and stable than the former. We also identify Cys-180 as the residue that is responsible for this redox equilibrium. Bioinformatics analyses suggest a higher stability and active site alteration determined by the disulfide bridge in the oxHDC form. On this basis, human HDC may join the short list of PLP enzymes that present redox sensitive cysteine residues.[67−76] Interestingly, among PLP enzymes, the cysteine switch appears to be a peculiar and unique feature of human HDC. It has been documented that cysteine residues in proteins could play a role in the response to altered redox conditions in cancer.[77,78] At present, it is not easy to envisage a physiological role of this redox sensor in HDC. However, when the fact that the environment of a cell is highly reduced is taken into account, it is reasonable to suggest that HDC is mainly reduced under physiological conditions. However, in cancer cells, where redox conditions are altered, the highly oxidizing conditions could favor the more active and stable oxHDC. With this view in mind, it is worth mentioning that high histamine levels have been reported in cholangiocarcinoma, and the involvement of HDC in tumor progression was thus suggested.[35] Our results suggest that, under redox-altered conditions, the prevalence of oxHDC, which is more active and more stable because of the presence of an additional disulfide bridge involving Cys-180, could therefore lead to an increased level of production of histamine, which makes the pathological state worse. In this regard, the development of specific inhibitors directed toward oxHDC is highly desirable.

ASSOCIATED CONTENT

Supporting Information

The Supporting Information is available free of charge on the ACS Publications website at DOI: 10.1021/acs.biochem.8b00625.

SDS−PAGEs of the various steps of purification and the sensitivity to reducing agents (GSH, DTT, and β-MeSH) as well as size-exclusion chromatography analyses (PDF)

AUTHOR INFORMATION

Corresponding Authors

*Department of Neuroscience, Biomedicine and Movement, University of Verona, Strada Le Grazie, 8, 37134 Verona, Italy. Telephone: +39-0458027671. Fax: +39-0458027170. E-mail: mita.bertoldi@univr.it.

*Department of Biochemical Sciences "A. Rossi Fanelli", University "La Sapienza", Rome, P.zale A. Moro 5, Roma, Italy. Telephone: +39-0649917700. Fax: +39-0649917566. E-mail: alessandro.paiardini@uniroma1.it.

ORCID

Mariarita Bertoldi: 0000-0002-2337-9928

Funding

This work was supported by Grant FUR2017 (University of Verona) to M.B. and by AIRC Associazione Italiana Ricerca sul Cancro MFAG2017-Project Code 20447 and grants from Sapienza University of Rome, Italy (C26A149EC4), to A.P.

Notes

The authors declare no competing financial interest.

ACKNOWLEDGMENTS

The authors thank Dr. Alessandra Astegno (Department of Biotechnology, University of Verona) for the help with the native PAGE experiment.

ABBREVIATIONS

WT, wild-type; PLP, pyridoxal 5′-phosphate; HDC, histidine decarboxylase; oxHDC, oxidized HDC; redHDC, reduced HDC; DTT, dithiothreitol; β-MeSH, β-mercaptoethanol; GSH, glutathione; MD, molecular dynamics.

REFERENCES

(1) Medina, M. A., Quesada, A. R., Nunez de Castro, I., and Sanchez-Jimenez, F. (1999) Histamine, polyamines, and cancer. *Biochem. Pharmacol. 57*, 1341−1344.

(2) Ohtsu, H. (2010) Histamine synthesis and lessons learned from histidine decarboxylase deficient mice. *Adv. Exp. Med. Biol. 709*, 21−31.

(3) Panula, P., and Nuutinen, S. (2013) The histaminergic network in the brain: basic organization and role in disease. *Nat. Rev. Neurosci. 14*, 472−487.

(4) Paiardini, A., Giardina, G., Rossignoli, G., Voltattorni, C. B., and Bertoldi, M. (2017) New Insights Emerging from Recent Investigations on Human Group II Pyridoxal 5′-Phosphate Decarboxylases. *Curr. Med. Chem. 24*, 226−244.

(5) Guirard, B. M., Tanase, S., and Snell, E. E. (1984) Pyridoxal-P dependent bacterial histidine decarboxylase. *Prog. Clin. Biol. Res. 144A*, 235−244.

DOI: 10.1021/acs.biochem.8b00625
Biochemistry 2018, 57, 6336−6348

(6) Tanase, S., Guirard, B. M., and Snell, E. E. (1985) Purification and properties of a pyridoxal 5′-phosphate-dependent histidine decarboxylase from Morganella morganii AM-15. *J. Biol. Chem. 260*, 6738−6746.
(7) Hayashi, H., Tanase, S., and Snell, E. E. (1986) Pyridoxal 5′-phosphate-dependent histidine decarboxylase. Inactivation by alpha-fluoromethylhistidine and comparative sequences at the inhibitor- and coenzyme-binding sites. *J. Biol. Chem. 261*, 11003−11009.
(8) Snell, E. E., and Guirard, B. M. (1986) Pyridoxal phosphate-dependent histidine decarboxylase from Morganella AM-15. *Methods Enzymol. 122*, 139−143.
(9) Vaaler, G. L., Brasch, M. A., and Snell, E. E. (1986) Pyridoxal 5′-phosphate-dependent histidine decarboxylase. Nucleotide sequence of the hdc gene and the corresponding amino acid sequence. *J. Biol. Chem. 261*, 11010−11014.
(10) Vaaler, G. L., and Snell, E. E. (1989) Pyridoxal 5′-phosphate dependent histidine decarboxylase: overproduction, purification, biosynthesis of soluble site-directed mutant proteins, and replacement of conserved residues. *Biochemistry 28*, 7306−7313.
(11) Bhattacharjee, M. K., and Snell, E. E. (1990) Pyridoxal 5′-phosphate-dependent histidine decarboxylase. Mechanism of inactivation by alpha-fluoromethylhistidine. *J. Biol. Chem. 265*, 6664−6668.
(12) Tahanejad, F. S., and Naderi-Manesh, H. (2000) Quantum mechanical study of the intermediates formed following the reaction of the histidine decarboxylase's substrate and inhibitors with coenzyme. *Eur. J. Med. Chem. 35*, 283−289.
(13) Kim, D. H., Kim, K. B., Cho, J. Y., and Ahn, D. H. (2014) Inhibitory effects of brown algae extracts on histamine production in mackerel muscle via inhibition of growth and histidine decarboxylase activity of Morganella morganii. *J. Microbiol. Biotechnol. 24*, 465−474.
(14) Nitta, Y., Yasukata, F., Kitamoto, N., Ito, M., Sakaue, M., Kikuzaki, H., and Ueno, H. (2016) Inhibition of Morganella morganii Histidine Decarboxylase Activity and Histamine Accumulation in Mackerel Muscle Derived from Filipendula ulumaria Extracts. *J. Food Prot. 79*, 463−467.
(15) Wauters, G., Avesani, V., Charlier, J., Janssens, M., and Delmee, M. (2004) Histidine decarboxylase in Enterobacteriaceae revisited. *J. Clin Microbiol 42*, 5923−5924.
(16) Medina, M. A., Urdiales, J. L., Rodriguez-Caso, C., Ramirez, F. J., and Sanchez-Jimenez, F. (2003) Biogenic amines and polyamines: similar biochemistry for different physiological missions and biomedical applications. *Crit. Rev. Biochem. Mol. Biol. 38*, 23−59.
(17) Medina, M. A., Correa-Fiz, F., Rodriguez-Caso, C., and Sanchez-Jimenez, F. (2005) A comprehensive view of polyamine and histamine metabolism to the light of new technologies. *J. Cell. Mol. Med. 9*, 854−864.
(18) Joseph, D. R., Sullivan, P. M., Wang, Y. M., Kozak, C., Fenstermacher, D. A., Behrendsen, M. E., and Zahnow, C. A. (1990) Characterization and expression of the complementary DNA encoding rat histidine decarboxylase. *Proc. Natl. Acad. Sci. U. S. A. 87*, 733−737.
(19) Yamamoto, J., Yatsunami, K., Ohmori, E., Sugimoto, Y., Fukui, T., Katayama, T., and Ichikawa, A. (1990) cDNA-derived amino acid sequence of L-histidine decarboxylase from mouse mastocytoma P-815 cells. *FEBS Lett. 276*, 214−218.
(20) Taguchi, Y., Watanabe, T., Kubota, H., Hayashi, H., and Wada, H. (1984) Purification of histidine decarboxylase from the liver of fetal rats and its immunochemical and immunohistochemical characterization. *J. Biol. Chem. 259*, 5214−5221.
(21) Engel, N., Olmo, M. T., Coleman, C. S., Medina, M. A., Pegg, A. E., and Sanchez-Jimenez, F. (1996) Experimental evidence for structure-activity features in common between mammalian histidine decarboxylase and ornithine decarboxylase. *Biochem. J. 320* (2), 365−368.
(22) Viguera, E., Trelles, O., Urdiales, J. L., Mates, J. M., and Sanchez-Jimenez, F. (1994) Mammalian L-amino acid decarboxylases producing 1,4-diamines: analogies among differences. *Trends Biochem. Sci. 19*, 318−319.
(23) Olmo, M. T., Urdiales, J. L., Pegg, A. E., Medina, M. A., and Sanchez-Jimenez, F. (2000) In vitro study of proteolytic degradation of rat histidine decarboxylase. *Eur. J. Biochem. 267*, 1527−1531.
(24) Ohmori, E., Fukui, T., Imanishi, N., Yatsunami, K., and Ichikawa, A. (1990) Purification and characterization of l-histidine decarboxylase from mouse mastocytoma P-815 cells. *J. Biochem. 107*, 834−839.
(25) Dartsch, C., Chen, D., Hakanson, R., and Persson, L. (1999) Histidine decarboxylase in rat stomach ECL cells: relationship between enzyme activity and different molecular forms. *Regul. Pept. 81*, 41−48.
(26) Fleming, J. V., and Wang, T. C. (2000) Amino- and carboxy-terminal PEST domains mediate gastrin stabilization of rat L-histidine decarboxylase isoforms. *Mol. Cell. Biol. 20*, 4932−4947.
(27) Fajardo, I., Urdiales, J. L., Medina, M. A., and Sanchez-Jimenez, F. (2001) Effects of phorbol ester and dexamethasone treatment on histidine decarboxylase and ornithine decarboxylase in basophilic cells. *Biochem. Pharmacol. 61*, 1101−1106.
(28) Fleming, J. V., and Wang, T. C. (2003) The production of 53−55-kDa isoforms is not required for rat L-histidine decarboxylase activity. *J. Biol. Chem. 278*, 686−694.
(29) Olmo, M. T., Rodriguez-Agudo, D., Medina, M. A., and Sanchez-Jimenez, F. (1999) The pest regions containing C-termini of mammalian ornithine decarboxylase and histidine decarboxylase play different roles in protein degradation. *Biochem. Biophys. Res. Commun. 257*, 269−272.
(30) Rodriguez-Agudo, D., Olmo, M. T., Sanchez-Jimenez, F., and Medina, M. A. (2000) Rat histidine decarboxylase is a substrate for m-calpain in vitro. *Biochem. Biophys. Res. Commun. 271*, 777−781.
(31) Furuta, K., Nakayama, K., Sugimoto, Y., Ichikawa, A., and Tanaka, S. (2007) Activation of histidine decarboxylase through post-translational cleavage by caspase-9 in a mouse mastocytoma P-815. *J. Biol. Chem. 282*, 13438−13446.
(32) Gores, G. J. (2003) Cholangiocarcinoma: current concepts and insights. *Hepatology 37*, 961−969.
(33) Sirica, A. E. (2005) Cholangiocarcinoma: molecular targeting strategies for chemoprevention and therapy. *Hepatology 41*, 5−15.
(34) Aljiffry, M., Walsh, M. J., and Molinari, M. (2009) Advances in diagnosis, treatment and palliation of cholangiocarcinoma: 1990−2009. *World J. Gastroenterol 15*, 4240−4262.
(35) Francis, H., DeMorrow, S., Venter, J., Onori, P., White, M., Gaudio, E., Francis, T., Greene, J. F., Jr., Tran, S., Meininger, C. J., and Alpini, G. (2012) Inhibition of histidine decarboxylase ablates the autocrine tumorigenic effects of histamine in human cholangiocarcinoma. *Gut 61*, 753−764.
(36) Johnson, C., Huynh, V., Hargrove, L., Kennedy, L., Graf-Eaton, A., Owens, J., Trzeciakowski, J. P., Hodges, K., DeMorrow, S., Han, Y., Wong, L., Alpini, G., and Francis, H. (2016) Inhibition of Mast Cell-Derived Histamine Decreases Human Cholangiocarcinoma Growth and Differentiation via c-Kit/Stem Cell Factor-Dependent Signaling. *Am. J. Pathol. 186*, 123−133.
(37) Rodriguez-Caso, C., Rodriguez-Agudo, D., Moya-Garcia, A. A., Fajardo, I., Medina, M. A., Subramaniam, V., and Sanchez-Jimenez, F. (2003) Local changes in the catalytic site of mammalian histidine decarboxylase can affect its global conformation and stability. *Eur. J. Biochem. 270*, 4376−4387.
(38) Rodriguez-Caso, C., Rodriguez-Agudo, D., Sanchez-Jimenez, F., and Medina, M. A. (2003) Green tea epigallocatechin-3-gallate is an inhibitor of mammalian histidine decarboxylase. *Cell. Mol. Life Sci. 60*, 1760−1763.
(39) Castro-Oropeza, R., Pino-Angeles, A., Khomutov, M. A., Urdiales, J. L., Moya-Garcia, A. A., Vepsalainen, J., Persson, L., Sarabia, F., Khomutov, A., and Sanchez-Jimenez, F. (2014) Aminooxy analog of histamine is an efficient inhibitor of mammalian L-histidine decarboxylase: combined in silico and experimental evidence. *Amino Acids 46*, 621−631.
(40) Ercan-Sencicek, A. G., Stillman, A. A., Ghosh, A. K., Bilguvar, K., O'Roak, B. J., Mason, C. E., Abbott, T., Gupta, A., King, R. A., Pauls, D. L., Tischfield, J. A., Heiman, G. A., Singer, H. S., Gilbert, D.

DOI: 10.1021/acs.biochem.8b00625
Biochemistry 2018, 57, 6336−6348

L., Hoekstra, P. J., Morgan, T. M., Loring, E., Yasuno, K., Fernandez, T., Sanders, S., Louvi, A., Cho, J. H., Mane, S., Colangelo, C. M., Biederer, T., Lifton, R. P., Gunel, M., and State, M. W. (2010) L-histidine decarboxylase and Tourette's syndrome. *N. Engl. J. Med. 362*, 1901−1908.

(41) Castellan Baldan, L., Williams, K. A., Gallezot, J. D., Pogorelov, V., Rapanelli, M., Crowley, M., Anderson, G. M., Loring, E., Gorczyca, R., Billingslea, E., Wasylink, S., Panza, K. E., Ercan-Sencicek, A. G., Krusong, K., Leventhal, B. L., Ohtsu, H., Bloch, M. H., Hughes, Z. A., Krystal, J. H., Mayes, L., de Araujo, I., Ding, Y. S., State, M. W., and Pittenger, C. (2014) Histidine decarboxylase deficiency causes tourette syndrome: parallel findings in humans and mice. *Neuron 81*, 77−90.

(42) Pittenger, C. (2017) Histidine Decarboxylase Knockout Mice as a Model of the Pathophysiology of Tourette Syndrome and Related Conditions. *Handb. Exp. Pharmacol. 241*, 189−215.

(43) Ohtsu, H., Tanaka, S., Terui, T., Hori, Y., Makabe-Kobayashi, Y., Pejler, G., Tchougounova, E., Hellman, L., Gertsenstein, M., Hirasawa, N., Sakurai, E., Buzas, E., Kovacs, P., Csaba, G., Kittel, A., Okada, M., Hara, M., Mar, L., Numayama-Tsuruta, K., Ishigaki-Suzuki, S., Ohuchi, K., Ichikawa, A., Falus, A., Watanabe, T., and Nagy, A. (2001) Mice lacking histidine decarboxylase exhibit abnormal mast cells. *FEBS Lett. 502*, 53−56.

(44) Komori, H., Nitta, Y., Ueno, H., and Higuchi, Y. (2012) Purification, crystallization and preliminary X-ray analysis of human histidine decarboxylase. *Acta Crystallogr., Sect. F: Struct. Biol. Cryst. Commun. 68*, 675−677.

(45) Komori, H., Nitta, Y., Ueno, H., and Higuchi, Y. (2012) Structural study reveals that Ser-354 determines substrate specificity on human histidine decarboxylase. *J. Biol. Chem. 287*, 29175−29183.

(46) Sanchez-Jimenez, F., Pino-Angeles, A., Rodriguez-Lopez, R., Morales, M., and Urdiales, J. L. (2016) Structural and functional analogies and differences between histidine decarboxylase and aromatic l-amino acid decarboxylase molecular networks: Biomedical implications. *Pharmacol. Res. 114*, 90−102.

(47) Pace, C. N., Vajdos, F., Fee, L., Grimsley, G., and Gray, T. (1995) How to measure and predict the molar absorption coefficient of a protein. *Protein Sci. 4*, 2411−2423.

(48) Peterson, E. A., and Sober, H. A. (1954) Preparation of crystalline phosphorylated derivatives of vitamin B6. *J. Am. Chem. Soc. 76*, 169−175.

(49) Charteris, A., and John, R. (1975) An investigation of the assay of dopamine using trinitrobenzensulphonic acid. *Anal. Biochem. 66*, 365−371.

(50) Berman, H. M., Westbrook, J., Feng, Z., Gilliland, G., Bhat, T. N., Weissig, H., Shindyalov, I. N., and Bourne, P. E. (2000) The Protein Data Bank. *Nucleic Acids Res. 28*, 235−242.

(51) Webb, B., and Sali, A. (2014) Comparative Protein Structure Modeling Using MODELLER. *Curr. Protoc. Bioinf. 47*, 5.6.1−5.6.32.

(52) Bramucci, E., Paiardini, A., Bossa, F., and Pascarella, S. (2012) PyMod: sequence similarity searches, multiple sequence-structure alignments, and homology modeling within PyMOL. *BMC Bioinf. 13*, S2.

(53) Hess, B., Kutzner, C., van der Spoel, D., and Lindahl, E. (2008) GROMACS 4: Algorithms for Highly Efficient, Load-Balanced, and Scalable Molecular Simulation. *J. Chem. Theory Comput. 4*, 435−447.

(54) Laskowski, R. A., MacArthur, M. W., Moss, D. S., and Thornton, J. M. (1993) PROCHECK: a program to check the stereochemical quality of protein structures. *J. Appl. Crystallogr. 26*, 283.

(55) Tirion, M. M. (1996) Large Amplitude Elastic Motions in Proteins from a Single-Parameter, Atomic Analysis. *Phys. Rev. Lett. 77*, 1905−1908.

(56) Atilgan, A. R., Durell, S. R., Jernigan, R. L., Demirel, M. C., Keskin, O., and Bahar, I. (2001) Anisotropy of fluctuation dynamics of proteins with an elastic network model. *Biophys. J. 80*, 505−515.

(57) Berendsen, H. J. C., Postma, J. P. M., van Gunsteren, W. F., and Hermans, J. (1981) Interaction models for Water in Relation to Protein Hydration. In *Intermolecular forces. The Jerusalem symposia on quantum chemistry and biochemistry*, Vol. *14*, Springer, Dordrecht, The Netherlands.

(58) Bussi, G., Donadio, D., and Parrinello, M. (2007) Canonical sampling through velocity rescaling. *J. Chem. Phys. 126*, 014101.

(59) Darden, T., York, D., and Pedersen, L. (1993) Particle mesh Ewald: an N-log(N) method for Ewald sums in large systems. *J. Chem. Phys. 98*, 10089.

(60) Ponder, J. W., and Case, D. A. (2003) Force fields for protein simulations. *Adv. Protein Chem. 66*, 27−85.

(61) Schuttelkopf, A. W., and van Aalten, D. M. (2004) PRODRG: a tool for high-throughput crystallography of protein-ligand complexes. *Acta Crystallogr., Sect. D: Biol. Crystallogr. 60*, 1355−1363.

(62) Fleming, P. J., and Fleming, K. G. (2018) HullRad: Fast Calculations of Folded and Disordered Protein and Nucleic Acid Hydrodynamic Properties. *Biophys. J. 114*, 856−869.

(63) Giardina, G., Montioli, R., Gianni, S., Cellini, B., Paiardini, A., Voltattorni, C. B., and Cutruzzola, F. (2011) Open conformation of human DOPA decarboxylase reveals the mechanism of PLP addition to Group II decarboxylases. *Proc. Natl. Acad. Sci. U. S. A. 108*, 20514−20519.

(64) Batista, P. R., Robert, C. H., Marechal, J. D., Hamida-Rebai, M. B., Pascutti, P. G., Bisch, P. M., and Perahia, D. (2010) Consensus modes, a robust description of protein collective motions from multiple-minima normal mode analysis−application to the HIV-1 protease. *Phys. Chem. Chem. Phys. 12*, 2850−2859.

(65) Kass, I., Hoke, D. E., Costa, M. G., Reboul, C. F., Porebski, B. T., Cowieson, N. P., Leh, H., Pennacchietti, E., McCoey, J., Kleifeld, O., Borri Voltattorni, C., Langley, D., Roome, B., Mackay, I. R., Christ, D., Perahia, D., Buckle, M., Paiardini, A., De Biase, D., and Buckle, A. M. (2014) Cofactor-dependent conformational heterogeneity of GAD65 and its role in autoimmunity and neurotransmitter homeostasis. *Proc. Natl. Acad. Sci. U. S. A. 111*, E2524−2529.

(66) Schneider, B., Gelly, J. C., de Brevern, A. G., and Cerny, J. (2014) Local dynamics of proteins and DNA evaluated from crystallographic B factors. *Acta Crystallogr., Sect. D: Biol. Crystallogr. 70*, 2413−2419.

(67) Fleming, J. V., Sanchez-Jimenez, F., Moya-Garcia, A. A., Langlois, M. R., and Wang, T. C. (2004) Mapping of catalytically important residues in the rat L-histidine decarboxylase enzyme using bioinformatic and site-directed mutagenesis approaches. *Biochem. J. 379*, 253−261.

(68) Conway, M. E., Yennawar, N., Wallin, R., Poole, L. B., and Hutson, S. M. (2003) Human mitochondrial branched chain aminotransferase: structural basis for substrate specificity and role of redox active cysteines. *Biochim. Biophys. Acta, Proteins Proteomics 1647*, 61−65.

(69) Yennawar, N. H., Islam, M. M., Conway, M., Wallin, R., and Hutson, S. M. (2006) Human mitochondrial branched chain aminotransferase isozyme: structural role of the CXXC center in catalysis. *J. Biol. Chem. 281*, 39660−39671.

(70) Tremblay, L. W., and Blanchard, J. S. (2009) The 1.9 A structure of the branched-chain amino-acid transaminase (IlvE) from Mycobacterium tuberculosis. *Acta Crystallogr., Sect. F: Struct. Biol. Cryst. Commun. 65*, 1071−1077.

(71) Sagong, H. Y., and Kim, K. J. (2017) Lysine Decarboxylase with an Enhanced Affinity for Pyridoxal 5-Phosphate by Disulfide Bond-Mediated Spatial Reconstitution. *PLoS One 12*, e0170163.

(72) Matsui, D., and Oikawa, T. (2010) Detection and function of the intramolecular disulfide bond in arginine racemase: an enzyme with broad substrate specificity. *Chem. Biodiversity 7*, 1591−1602.

(73) Gavilanes, F., Peterson, D., Bullis, B., and Schirch, L. (1983) Structure and reactivity of cysteine residues in mitochondrial serine hydroxymethyltransferase. *J. Biol. Chem. 258*, 13155−13159.

(74) Chitnumsub, P., Ittarat, W., Jaruwat, A., Noytanom, K., Amornwatcharapong, W., Pornthanakasem, W., Chaiyen, P., Yuthavong, Y., and Leartsakulpanich, U. (2014) The structure of Plasmodium falciparum serine hydroxymethyltransferase reveals a novel redox switch that regulates its activities. *Acta Crystallogr., Sect. D: Biol. Crystallogr. 70*, 1517−1527.

DOI: 10.1021/acs.biochem.8b00625
Biochemistry 2018, 57, 6336−6348

(75) Coleman, C. S., Stanley, B. A., and Pegg, A. E. (1993) Effect of mutations at active site residues on the activity of ornithine decarboxylase and its inhibition by active site-directed irreversible inhibitors. *J. Biol. Chem. 268*, 24572−24579.
(76) Hasse, D., Andersson, E., Carlsson, G., Masloboy, A., Hagemann, M., Bauwe, H., and Andersson, I. (2013) Structure of the homodimeric glycine decarboxylase P-protein from Synechocystis sp. PCC 6803 suggests a mechanism for redox regulation. *J. Biol. Chem. 288*, 35333−35345.
(77) Schinagl, A., Kerschbaumer, R. J., Sabarth, N., Douillard, P., Scholz, P., Voelkel, D., Hollerweger, J. C., Goettig, P., Brandstetter, H., Scheiflinger, F., and Thiele, M. (2018) Role of the Cysteine 81 Residue of Macrophage Migration Inhibitory Factor as a Molecular Redox Switch. *Biochemistry 57*, 1523−1532.
(78) Xie, D., Wang, L., Xiao, Q., Wu, X., Zhang, L., Yang, Q., and Wang, L. (2018) New Insight into the Octamer of TYMS Stabilized by Intermolecular Cys43-Disulfide. *Int. J. Mol. Sci. 19*, 1393.

DOI: 10.1021/acs.biochem.8b00625
Biochemistry 2018, 57, 6336−6348

SCIENTIFIC REPORTS

OPEN

Oleuropein aglycone stabilizes the monomeric α-synuclein and favours the growth of non-toxic aggregates

Received: 15 March 2018
Accepted: 15 May 2018
Published online: 29 May 2018

Luana Palazzi[1], Elena Bruzzone[2], Giovanni Bisello[1], Manuela Leri[2,3], Massimo Stefani[2], Monica Bucciantini[2] & Patrizia Polverino de Laureto[1]

α-synuclein plays a key role in the pathogenesis of Parkinson's disease (PD); its deposits are found as amyloid fibrils in Lewy bodies and Lewy neurites, the histopathological hallmarks of PD. Amyloid fibrillation is a progressive polymerization path starting from peptide/protein misfolding and proceeding through the transient growth of oligomeric intermediates widely considered as the most toxic species. Consequently, a promising approach of intervention against PD might be preventing α-synuclein build-up, misfolding and aggregation. A possible strategy involves the use of small molecules able to slow down the aggregation process or to alter oligomer conformation favouring the growth of non-pathogenic species. Here, we show that oleuropein aglycone (OleA), the main olive oil polyphenol, exhibits anti-amyloidogenic power *in vitro* by interacting with, and stabilizing, α-synuclein monomers thus hampering the growth of on-pathway oligomers and favouring the growth of stable and harmless aggregates with no tendency to evolve into other cytotoxic amyloids. We investigated the molecular basis of such interference by both biophysical techniques and limited proteolysis; aggregate morphology was monitored by electron microscopy. We also found that OleA reduces the cytotoxicity of α-synuclein aggregates by hindering their binding to cell membrane components and preventing the resulting oxidative damage to cells.

Parkinson's disease (PD) is one of the most widely occurring neurodegenerative disorders whose symptoms are attributed to the progressive loss of dopaminergic neurons in the *substantia nigra*[1]. The cause of PD is still unknown; however, considerable evidence suggests a multifactorial aetiology involving genetic susceptibility and environmental factors. The main histopathological hallmark of PD is the presence, in the affected neurons, of intracellular inclusions known as Lewy bodies (LB) and Lewy neurites (LN), containing fibrillar aggregates of α-synuclein (Syn)[2]. Syn is implicated at different levels in the pathogenesis of PD and other neurodegenerative conditions, and its aging-related aggregation into amyloid fibrils is a key step in disease aetiology[3–5]. Autosomal dominant forms of PD, resulting from mutations in *SNCA*, the gene encoding Syn, as well as from its duplications and triplications are also known, whereas mutations in a number of different genes are considered risk factors for sporadic PD[6–10].

Syn is a predominantly presynaptic 140 residues natively unfolded protein[11,12] whose structure comprises three domains: an N-terminal domain (residues 1–60), a non-amyloid-β component of plaques (NAC) domain (residues 61–95), and a C-terminal domain (residues 96–140) (Fig. 1a, left). Approximately, the first 100 residues, containing 7 imperfect 11-residue repeats, constitute a lipid binding domain[13]. The hydrophobic region spanning residues 61–95 is responsible for the aggregation properties of the protein[14], that appear to be modulated by the acidic C-terminal tail, containing 15 Glu/Asp residues and many prolines[15].

Syn is intrinsically disordered in solution[11,12], but the protein can adopt different types of secondary structure in different environments, as in the presence of lipid micelles, vesicles and membranes, where it acquires α-helical

[1]Department of Pharmaceutical Sciences, CRIBI Biotechnology Centre, University of Padova, Padova, Italy. [2]Department of Biomedical, Experimental and Clinical Sciences, University of Firenze, Firenze, Italy. [3]Department of Neuroscience, Psychology, Drug Research and Child Health, University of Firenze, Firenze, Italy. Luana Palazzi and Elena Bruzzone contributed equally to this work. Correspondence and requests for materials should be addressed to M.B. (email: monica.bucciantini@unifi.it) or P.P.d.L. (email: patrizia.polverinodelaureto@unipd.it)

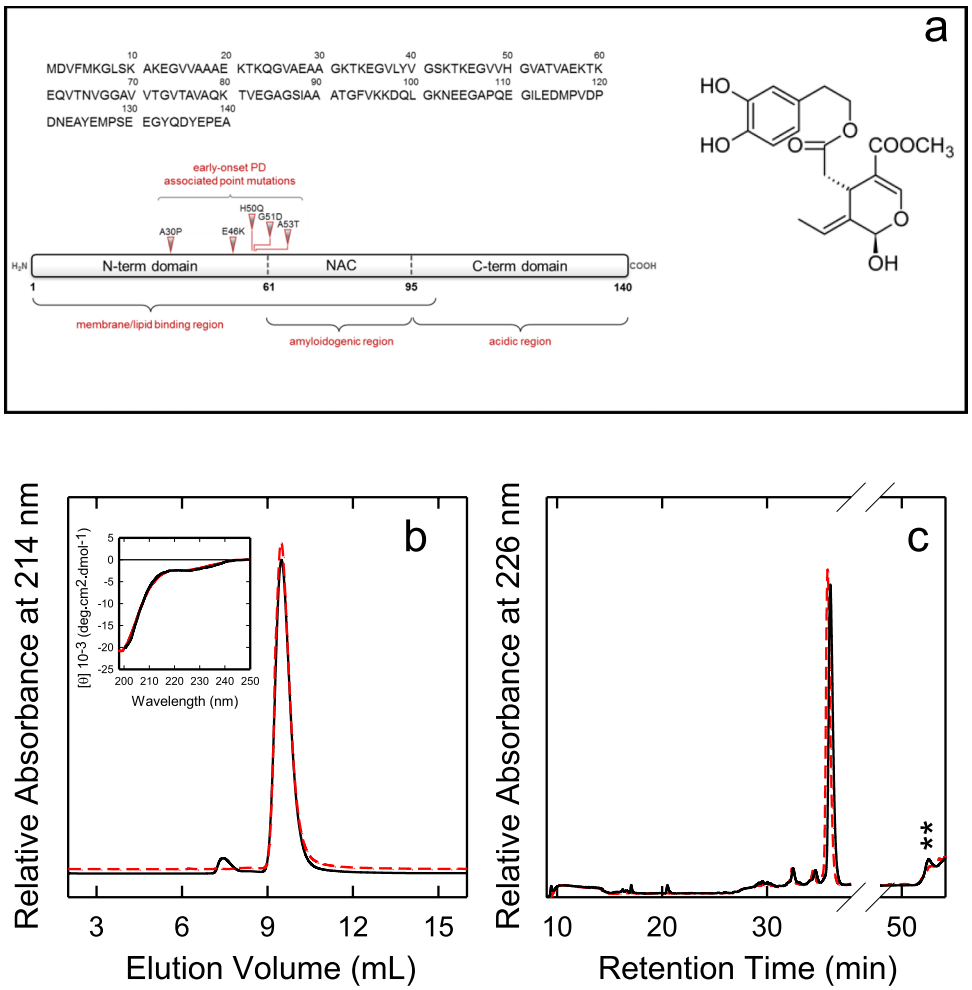

Figure 1. (**a**, left) Amino acid sequence of Syn and scheme of its three major domains: the N-terminal region involved in lipid and membrane binding, containing the mutations associated with familial forms of PD; the NAC domain (61–95) responsible for Syn aggregation properties; the acidic C-terminal region. (**a**, right) Chemical structure of OleA. Interaction between monomeric Syn and OleA. (**b**, inset) Far-UV CD spectra of Syn in the absence (red line) and in the presence of OleA (Syn/OleA 1:10) (black line). Spectra were taken at 25 °C in PBS (pH 7.4). (**b**) Gel filtration and (**c**) RP-HPLC chromatograms of Syn in the absence (red dashed line) and in the presence of 1:10 OleA (black line). In (**c**) the peak relative to RT 51.2 is highlighted with two stars.

secondary structure[16–19]. Syn interaction with membranes and lipids is considered functionally important[20]; in fact, although its physiological function is not yet fully understood, it has been suggested that Syn may modulate the presynaptic vesicular pool size, promote SNARE-complex assembly[21], and regulate dopaminergic neurotransmission[22]. The different biological functions of Syn could be a consequence of its conformational flexibility leading to suggest that *in vivo* the protein exists in dynamic equilibrium between different conformational states[23].

In the LB and LN, Syn is present as highly ordered insoluble polymeric fibrillar aggregates enriched in cross-β-sheet structure[24]. However, several studies have shown that soluble Syn oligomers are the toxic species responsible for disruption of cellular homeostasis and neuronal death through effects on various intracellular targets, including synaptic function[25–27]. Moreover, it is hypothesized a prion-like mechanism by which Syn oligomers can diffuse from one cell to the other, thus spreading the disease through the nervous system[5,26,28]. Increasing evidence indicates that, under pathological conditions, various types of oligomers with different morphologies and physicochemical features are present in tissue[26,27]. Accordingly, Syn oligomers have been generated *in vitro* at different conditions, but it is still unknown whether their structural features and size are similar to those displayed by the species grown *in vivo* or isolated from pathological tissue[28]. Defining the structure of the pathological oligomeric species would be of the utmost importance to understand, at the molecular level, their role in neurodegeneration and in Syn toxicity.

Since the loss of dopaminergic neurons is the primary neuropathological sign of PD, dopaminergic drugs (e.g. levodopa, dopamine agonists and monoamine oxidase, MAO-B, inhibitors) are the main therapeutic options to alleviate the motor symptoms of PD[29]. Levodopa is effective mainly in the early stage of the disease, less as disease progresses. Therefore, other therapeutic strategies, directly targeting Syn, have been proposed[22,30]. Promising approaches are based on the idea to prevent the intracellular and extracellular accumulation of Syn, thus disfavouring its aggregation *in vivo* by inhibiting Syn synthesis using SiRNA[31] or by increasing its autophagic

degradation[22]. It has also been proposed to interfere directly with the aggregation process of Syn by reducing fibrils formation or by stabilizing toxic oligomers confining them in an off-pathway non-toxic or inert form[22,30].

The use of natural or synthetic small molecules seems to be an attracting way to counteract amyloidogenesis. In particular, plant compounds, such as polyphenols and curcuminoids, have been reported to interfere with the amyloid aggregation of several proteins/peptides of neuropathological interest, including Syn, Aβ and tau[32]. For example, baicalein, curcumin and epigallocatechin 3-gallate (EGCG) have been reported to inhibit Syn fibrillation by stabilizing off-pathway oligomers or by increasing protein solubility and by disrupting long-range interactions that allow a faster reconfiguration rate reducing Syn tendency to aggregate[32–39]. Moreover, NMR studies have led to hypothesize that the production of these non-toxic oligomers is driven by EGCG binding to the Syn region responsible for long-range intramolecular interactions[36,37].

Oleuropein, the main polyphenol in olive leaves and drupes[40] is a glycosylated seco-iridoid, which appears mainly in the de-glycosylated (aglycone) form in olive oil (Fig. 1a, right). Oleuropein aglycone (OleA) displays several pharmacological activities including antioxidant, anti-inflammatory, anti-atherogenic, anti-diabetic, anti-cancer, antimicrobial, and antiviral properties[41] and is commercially available as food supplement or nutraceutical[41]. Recently, it has been reported that OleA interferes with the aggregation *in vitro* of several peptides/proteins associated with amyloid diseases including amylin[42], Aβ peptides[43], tau[44], transthyretin[45] and beta2-microglobulin (M. Leri *et al*., data not published). It has been proposed that OleA can be beneficial against several amyloid diseases, either systemic (type-2 diabetes)[46] or neurodegenerative[47]. However, no data are presently available on the interference of OleA with Syn aggregation and its possible protection against the toxicity of Syn aggregates.

In this study, we report that OleA interferes with the path of Syn aggregation and modifies the biophysical properties of preformed Syn assemblies. We also investigated the influence of OleA on the cytotoxicity of variously Syn aggregates and analysed the structural and biological features of the so-generated oligomeric species. Finally, we isolated and characterized an oligomeric species of Syn grown in the presence of OleA.

Experimental Procedures

Materials. Oleuropein glycoside was purchased from Extrasynthase and deglycosilated by treatment with almond β-glycosidase (EC 3.2.1.21, Fluka, Sigma-Aldrich) as previously described[42]. Briefly, a 10 mM solution of oleuropein glycoside in 310 µl of 0.1 M sodium phosphate buffer, pH 7.0, was incubated with 8.9 I.U. of β-glucosidase overnight at room temperature. The aglycone (OleA) was precipitated by centrifuging the reaction mixture at 13200 × g for 10 min. The precipitate was suspended in dimethylsulfoxide (DMSO) at 50 mM concentration and batched in aliquots kept frozen and protected from light. Oleuropein deglycosylation was confirmed by mass spectrometry analysis and by assaying the glucose released in the supernatant with the Glucose (HK) Assay kit (Sigma-Aldrich, Saint Louis, MO, USA). Each batch of OleA was used within 1 week once opened. All chemicals were of analytical reagent grade and were obtained from Sigma or Fluka (St. Louis, MO).

Expression and purification of recombinant human α-synuclein. Syn was expressed in *Escherichia coli* BL21(DE3) cell line transfected with the pET28b/α-syn plasmid. The recombinant protein was expressed and purified according to a previously described procedure[19] and further purified by RP-HPLC. The identity and purity of the eluted material were assessed by mass spectrometry.

Aggregation and disaggregation experiments. To induce Syn aggregation, 70 µM protein samples were filtered with a 0.22 µm pore-size filter (Millipore, Bedford, MA, USA) and incubated at 37 °C in PBS (8.0 mM Na_2HPO_4, 137 mM NaCl, 2.0 mM KH_2PO_4, 2.7 mM KCl, pH 7.4) for up to 7 days under shaking at 500 rpm with a thermo-mixer (Compact, Eppendorf, Hamburg, DE) in the absence or in the presence of OleA (210–700 µM, corresponding to a Syn:OleA molar ratio of 1:3 or 1:10, respectively). Protein aggregation in sample aliquots collected at the indicated incubation times was checked by Thioflavin T (ThT) binding assay, 1-anilinonaphtalene-8-sulfonate (ANS) fluorescence, transmission electron microscopy (TEM), limited proteolysis, gel filtration (GF) chromatography and reverse phase (RP)-HPLC. The interference of OleA in ThT and ANS analysis was assayed by performing controls experiments where the polyphenol was added in pre-made Syn aggregates (48 h and 168 h) either immediately before or after the addition of ThT or ANS solution. Oligomer-enriched or fibril-enriched sample were prepared by incubating Syn for 48 h or up to 168 h, respectively. For disaggregation experiments, 48 h-aged oligomers were incubated with OleA (1:10) at 37 °C under shaking at 500 rpm, for 24 h (Syn 48 h + OleA 24 h) or 5d (Syn 48 h + OleA 5d); 168 h-aged fibrils were incubated with OleA for 8 h (Syn 168 h + OleA 8 h) or for 5d (Syn 168 h + OleA 5d). All aggregate concentrations were expressed as monomer protein concentration.

Structural characterization. Protein concentrations were determined by absorption measurements at 280 nm using a double-beam Perkin Elmer (Norwalk, CT) Lambda-20 spectrophotometer. The molar absorptivity at 280 nm for Syn was 5960 cm^{-1} M^{-1}, as evaluated from its amino acid composition by the method of Gill and von Hippel[48]. Circular dichroism (CD) spectra were recorded by a Jasco (Tokyo, Japan) J-710 spectropolarimeter, using a 1.0-mm path-length quartz cell and a protein concentration of 7.0 µM. The mean residue ellipticity [θ] (degcm^2 $dmol^{-1}$) was calculated according to the formula $[\theta] = (\theta_{obs}/10)(MRW/lc)$, where θ_{obs} is the observed ellipticity in deg, MRW is the mean residue molecular weight of the protein, *l* is the optical path-length (as cm) and *c* is protein concentration (as mg/ml). The spectra were recorded in PBS, pH 7.4. Fluorescence measurements were performed using a Jasco (Tokyo, Japan) FP-6500 spectrofluorimeter and a 0.1-cm path length cuvette. The ThT binding assay was performed accordingly to LeVine[49] using a 25 µM ThT solution in 25 mM sodium phosphate buffer, pH 6.0. Aliquots (30 µl) of protein samples were collected at the indicated times and diluted into the ThT buffer. Fluorescence emission measurements were performed at 25 °C at an excitation wavelength of 440 nm

by recording the ThT fluorescence emission in the 455–600 nm interval. For ANS binding experiments, a 350 nm excitation wavelength was used and the emission spectra were scanned in the 380–600 nm interval[50]. All spectra were recorded at 25 °C using a 50 μM ANS solution and a 2.5 μM protein solution. ANS-binding experiments were carried out in 50 mM Tris-HCl buffer, pH 7.4. ANS concentration was determined using a molar absorption coefficient of 4950 M^{-1} cm^{-1} at 350 nm. To evaluate the possible interference of OleA with the ThT and ANS fluorescence assay, two different controls were performed by monitoring the emission fluorescence spectra intensity of Syn aggregates before and after OleA addition: i) OleA was added together to the probe or ii) OleA was added after the probe and the fluorescence spectra were re-acquired immediately.

TEM and DLS analysis. Size and morphology of Syn aggregates were investigated by transmission electron microscopy (TEM) and dynamic light scattering (DLS). Negative staining was obtained by placing a drop of the sample solution on a Butvar-coated copper grid (400-square mesh) (TAAB-Laboratories Equipment Ltd, Berks, UK). Then, the sample was dried and negatively stained with a drop of uranyl acetate solution (1.0%, w/v). TEM pictures were taken on a Tecnai G2 12 Twin instrument (FEI Company, Hillsboro, OR) at an excitation voltage of 100 kV. Size distribution of protein samples was calculated on the basis of 382 particles manually extracted from the micrographs using ImageJ software. Only clearly defined spherical and isolated particles were selected. Measurements were obtained with a standard deviation of 5.04. Size distributions were also evaluated by DLS experiments carried out in duplicate, at 25 °C in PBS, pH 7.4, using a Zetasizer Nano-ZS instrument (Malvern Instrument, UK). 12 runs were collected during each measurement.

Chemical characterization. Gel filtration (GF) chromatography was performed by a Superdex 75 10/300GL column (Amersham Biosciences, Uppsala, Sweden), using an ÄKTA FPLC system (Amersham Biosciences, Uppsala, Sweden). Sample aliquots (200 μL) were taken from the aggregation mixture, filtered (0.22 μm filters), loaded onto the column and eluted at 0.5 ml/min in 20 mM Tris-HCl, 0.15 M NaCl, pH 7.4. The effluent was monitored by recording the absorbance at 214 nm. Column calibration was performed using the following standards: blue dextran (void volume); albumin, 67 kDa; ovalbumin, 45 kDa; α-lactalbumin, 14.4 kDa and aprotinin, 6.5 kDa. The RP-HPLC analyses were carried out on an Agilent 1200 chromatographer (Santa Clara, CA) using a Jupiter C18 column (4.6 × 250 mm; Phenomenex, CA, USA), eluted with the following acetonitrile/0.085% TFA- water/0.1% TFA gradient: 5–25%, 5 min, 25–28%, 13 min, 28–39%, 3 min, 39–43%, 21 min. The effluent was monitored by recording the absorbance at 226 nm. The identity of the eluted material was assessed by mass spectrometry, carried out with an electrospray ionization (ESI) mass spectrometer equipped with a Q-Tof analyzer (Micro) (Waters, Manchester, UK) or a QTof Xevo G2S (Waters, Manchster, UK). Measurements were carried out at 1.5–1.8 kV capillary voltage and 30–40 V cone voltage.

Limited proteolysis. Limited proteolysis experiments of Syn and Syn/OleA (1:3, 1:10) samples were carried out in PBS, pH 7.4, at room temperature using proteinase K at E/S ratio of 1:1000 (by weight) at 70 μM Syn concentration. The reactions were quenched after 5 min by acidification with TFA in water (4.0%, v/v) and analysed by RP-HPLC, as described above.

Fingerprinting analysis of off-pathway oligomers. The Syn aggregated species were purified by harvesting the material eluted from RP-HPLC at RT 51.2 min at the conditions described above. The protein samples were dried in Savant and solubilised in 6.0 M guanidine(Gnd)-HCl/20 mM Tris-HCl, pH 8.5. Then, the samples were diluted 1:10 and trypsin was added to an 1:25 enzyme to substrate (E/S) ratio. After 15 h of incubation at 37 °C, the proteolysis mixture was analysed with RP-HPLC by the same column and gradient used for purification and the peptide species were identified by ESI-MS. For proteinase K proteolysis, the sample was further diluted reaching a final concentration of 1.0 M Gnd-HCl before adding the enzyme (E/S 1:1000). The reactions were carried out for 5- or 70-min at 37 °C.

Cell culture and cell viability assay. SH-SY5Y cells were cultured at 37 °C in complete medium (50% HAM, 50% DMEM, 10% foetal bovine serum, 3.0 mM glutamine, 100 units/ml penicillin and 100 μg/ml streptomycin), in a humidified, 5.0% CO_2 incubator. All materials used for cell culture were from Sigma. The samples containing aggregating Syn were administered to the cells at a 5.0 μM final concentration. The cytotoxicity of the variously aggregated Syn samples was assessed by the 3-(4,5-dimethylthiazol-2-yl)-2,5-diphenyltetrazolium bromide (MTT, Sigma-Aldrich) reduction inhibition assay based on the protocol described for the first time by Mosmann[51]. In all MTT-experiments, the cells were plated and incubated for 24 h at a density of 10000 cells/well on 96-well plates in 100 μl culture medium. Then, the cells were treated for 48 h with 5.0 μM Syn aggregates grown in the absence or in the presence of OleA (1:10). After exposure to the aggregates, the cells were incubated for 2 h with 100 μl DMEM without phenol red, containing 0.5 mg/ml MTT. Then, 100 μl of cell lysis buffer (20% SDS, 50% N,N-dimethylformamide, pH 4,7) was added to each well and the samples were incubated at 37 °C to allow complete cell lysis. The blue formazan absorbance was recorded at 595 nm with an automatic plate reader (Bio-Rad, Hercules, Cal). Final absorption values were calculated by averaging three independent measurements of each sample after subtraction of the average of the blank solution (100 μl of MTT solution and 100 μl of lysis buffer). All data were expressed as mean ± standard deviation.

Reactive oxygen species. The intracellular reactive oxygen species (ROS) were determined by monitoring the increase in fluorescence at 538 nm of the fluorescent probe 20,70–dichlorofluorescein diacetate, acetyl ester (CM-H_2 DCFDA; Sigma-Aldrich), a cell-permeant ROS indicator that becomes fluorescent on removal of the acetate groups by cellular esterases and subsequent oxidation. The SH-SY5Y cells were plated at a density of 10000 cells/well on 96-well plates. The cells were exposed for 48 h to 5.0 μM aggregates, then 10 mM DCFDA in

RT[a] (min)	Found mass[b] (Da)	Theoretical mass[c] (Da)	Protein species
35.5	14461.5 (±0.1) 14477.2 (±0.8) 14682.8 (±0.8)	14460.5 14476.5 14683.2	Syn Syn + 1ox Syn + 223
51.2	14462.1 (±1.5) 14478.5 (±1.8) 14665.2 (±0.5) 14683.2 (±0.1)	14460.5 14476.5 14665.2 14683.2	Syn Syn + 1ox Syn + 205 Syn + 223

Table 1. Chemical characterization of the main protein species in the mixture formed by Syn and OleA in the 1:10 ratio eluted from the RP-HPLC column (Fig. 1c). The term ox indicates an oxidized derivative (+16 Da). [a]Proteins are listed in order of retention time (RT). [b]Experimental molecular masses determined by ESI-QTOF-MS. [c]Molecular masses calculated from Syn amino acid sequence.

DMEM without phenol red was added. After 30 min, the fluorescence values were detected by Fluoroscan Ascent FL (Thermo-Fisher, Illkinch, France).

Confocal immunofluorescence. Subconfluent SH-SY5Y cells grown on glass coverslips were treated for 48 h with Syn aggregates at a 5.0 μM final concentration and then washed with PBS. Labelling at the cell surface monosialotetrahexosylganglioside (GM1) was obtained by incubating the cells with 10 ng/ml CTX-B Alexa488 in complete medium for 30 min at room temperature. Then, the cells were fixed in 2.0% buffered paraformaldehyde for 10 min, permeabilized by a cold 1:1 acetone/ethanol solution for 4 min at room temperature and blocked with PBS containing 0.5% BSA and 0.2% gelatine for 30 min. After blockage, the cells were incubated for 1 h at room temperature with a rabbit polyclonal anti-Syn antibody (Abcam, Cambridge UK) diluted 1:500 in blocking solution and then washed with PBS for 30 min under stirring. The immunoreaction was revealed by Alexa 568-conjugated anti-rabbit Abs (Molecular Probes, Eugene, Oregon, USA) diluted 1:100 in PBS. Finally, the cells were washed twice in PBS and once in water to remove non-specifically bound Abs. Cell fluorescence was imaged using a confocal TCS SP5 scanning microscope (Leica) equipped with a HeNe/Ar laser source for fluorescence measurements. Sample observations were performed by a Leica Plan Apo X63 oil immersion objective suited with optics for differential interference contrast acquisition. FRET analysis was carried out by the FRET sensitized emission method as previously reported[52].

Data analysis and statistics. Statistical analysis was performed using Student's t-test. The results were compared using Student's *t*-test between two groups, *$P < 0.05$; **$P < 0.01$; ***$P < 0.001$ versus untreated cells and °$P < 0.05$; °°$P < 0.01$; °°°$P < 0.001$ versus cells treated with aggregates grown in the absence of OleA.

Results

Interaction between OleA and monomeric Syn. The effect of OleA on the secondary structure of Syn was evaluated by far-UV CD spectroscopy (Fig. 1b, inset). We found that at neutral pH the protein displays a far-UV CD spectrum typical of a substantially unfolded polypeptide chain, with an intense minimum near 198 nm and the absence of characteristic bands in the 208–230 nm region (Fig. 1b, red dashed line). In the presence of OleA at two different Syn/OleA molar ratios (1:3 or 1:10), no changes in the shape or intensity of the spectra recorded just after sample preparation were detected, supporting the lack of any direct conformational modification. For simplicity, Fig. 1b, inset, reports only the spectrum relative to the 1:10 Syn/OleA ratio (black continuous line). To confirm this, we also analysed Syn in the absence and in the presence of OleA (1:10) by gel filtration (GF) (Fig. 1b) and RP-HPLC (Fig. 1c). To avoid technical problems, the samples for GF analysis were filtered (0.22 μm filters) before loading; to simplify the figure, the profiles obtained in the presence of 1:3 Syn/OleA ratio are not shown. The GF profiles of Syn in the absence or in the presence of OleA are similar and show a major species eluting at ~9.4 ml, corresponding to monomeric Syn. In the presence of OleA a minor high MW species (~1%) at shorter elution volume was also seen (Fig. 1b). No variation in the retention time (RT 35.5 min) of Syn when eluted in the presence of OleA was seen in RP-HPLC; however, we noticed the presence of a new peak at RT 51.2 min (Fig. 1c, highlighted with two stars), indicating increased hydrophobicity, likely due to some chemical modifications or change in the aggregation state of this species. These two main fractions were collected and analyzed in more detail. Mass spectrometry analysis indicated the presence of Syn species in both fractions (Table 1). Syn appeared chemically modified in very low percentage (~5.0%) by the presence of some covalent adducts resulting in mass increases of 205 and 223 Da. These adducts could result from the reaction of Syn with demethylated and dehydrated forms of the elenolic acid arising from OleA degradation[53]. The presence of these modifications in both monomeric and late-eluting Syn allows to exclude they are the cause of the RP-HPLC shift.

OleA interferes with Syn aggregation into amyloid fibrils. When incubated *in vitro* at 37 °C and pH 7.4 for 168 h, Syn aggregates into fibrils[12]. The kinetics of amyloid fibril formation were monitored by following the increase of ThT fluorescence emission at 485 nm during the aggregation process. According to previous data[54,55], we found an initial lag phase followed by an exponential growth phase and a final plateau, consistent with a nucleation-dependent mechanism (Fig. 2a). TEM imaging showed that the 48 h sample was populated with oligomers and pre-fibrillar aggregates (Fig. 2c), while fibrils with typical amyloid morphology became the major aggregated species after 168 h of incubation (Fig. 2f). Then, we investigated the effect of OleA on the kinetics of fibril formation by using a Syn/OleA ratio of 1:3. We found that the curve maintained a sigmoid trend, yet in the presence of OleA (Fig. 2a), and some amyloid fibrils were still detectable in the sample (Fig. 2d,g). When we used

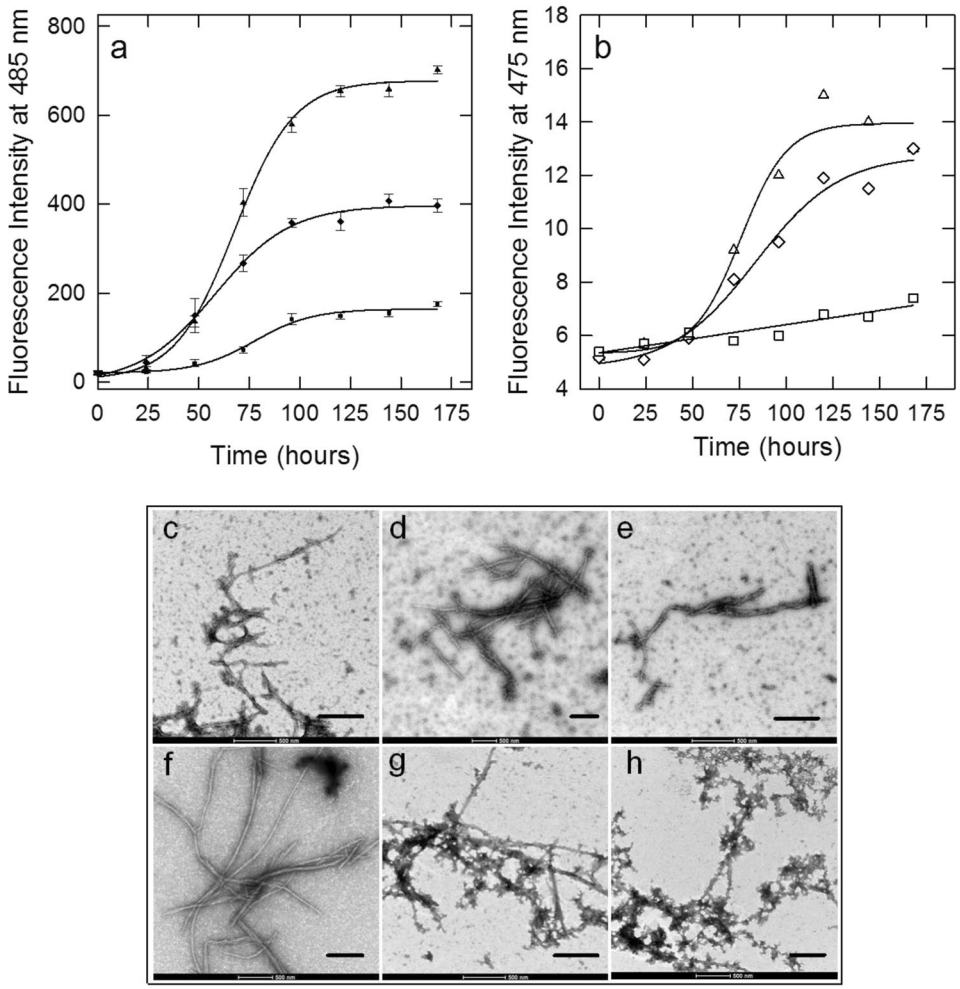

Figure 2. Effect of OleA on Syn aggregation probed by ThT (**a**), ANS (**b**) fluorescence spectroscopy and TEM (**c**–**h**). Syn aggregation kinetics (triangle), Syn aggregation in the presence of 1:3 (diamond) or 1:10 (square) OleA. For the ThT assay, aliquots (30 μl) of the protein solution, incubated for the indicated times, were added to a 25 μM solution (470 μl) of ThT in 25 mM phosphate buffer, pH 6.0. Excitation wavelength: 440 nm, fluorescence emission: 485 nm. For the ANS assay, excitation wavelength: 350 nm, fluorescence emission: 475 nm at 25 °C. TEM pictures taken from Syn aggregation mixture after 48 h and 168 h of incubation in the absence (**c**,**f**) or in the presence of a 1:3 (**d**,**g**) or 1:10 (**e**,**h**) Syn/OleA ratio. Scale bar in every picture corresponds to 500 nm.

a 1:10 Syn/OleA ratio, the ThT fluorescence intensity was scarcely increased (Fig. 2a) but other types of aggregates populated the sample, as seen by TEM imaging (Fig. 2e,h), suggesting some interference of the polyphenol with the aggregation process.

Syn aggregation was further characterized in terms of hydrophobic exposure, monitored as ANS binding, by recording the increase of fluorescence emission at 475 nm by ANS added to sample aliquots withdrawn from the aggregation mixture at different incubation times (Fig. 2b). The experimental data points fit an irregular sigmoidal curve recalling, in part, the trend observed in the ThT experiment. When the aggregation was carried out at Syn/OleA 1:10, we found a moderate increase of fluorescence intensity during the process. Overall, these data confirm that OleA interferes with the aggregation process of Syn.

Mapping α-synuclein conformation during aggregation in the presence of OleA by limited proteolysis. The propensity of Syn to be hydrolysed by proteinase K at different stages of amyloid aggregation was investigated by highlighting the sites of proteolysis in the absence or in the presence of OleA. Proteinase K was chosen because of its broad specificity[56]; accordingly, its cleavage sites are not expected to be dictated by the amino acid sequence, rather, they depend on the conformational and dynamical features of the polypeptide chain[57,58]. An E/S ratio of 1:1000 was used in the experiment and the proteolysis mixtures were analysed by RP-HPLC after 5 min incubation of Syn with the protease (Fig. 3). The sites of proteolysis were determined by mass spectrometry analysis of the isolated HPLC fractions (Table S1). As expected from its natively unfolded character, monomeric Syn was highly susceptible to the proteolytic attack and many fragments were seen in the chromatogram after 5 min-incubation (Fig. 3a). When Syn was kept for 48 h in aggregation buffer, a slightly reduced susceptibility to

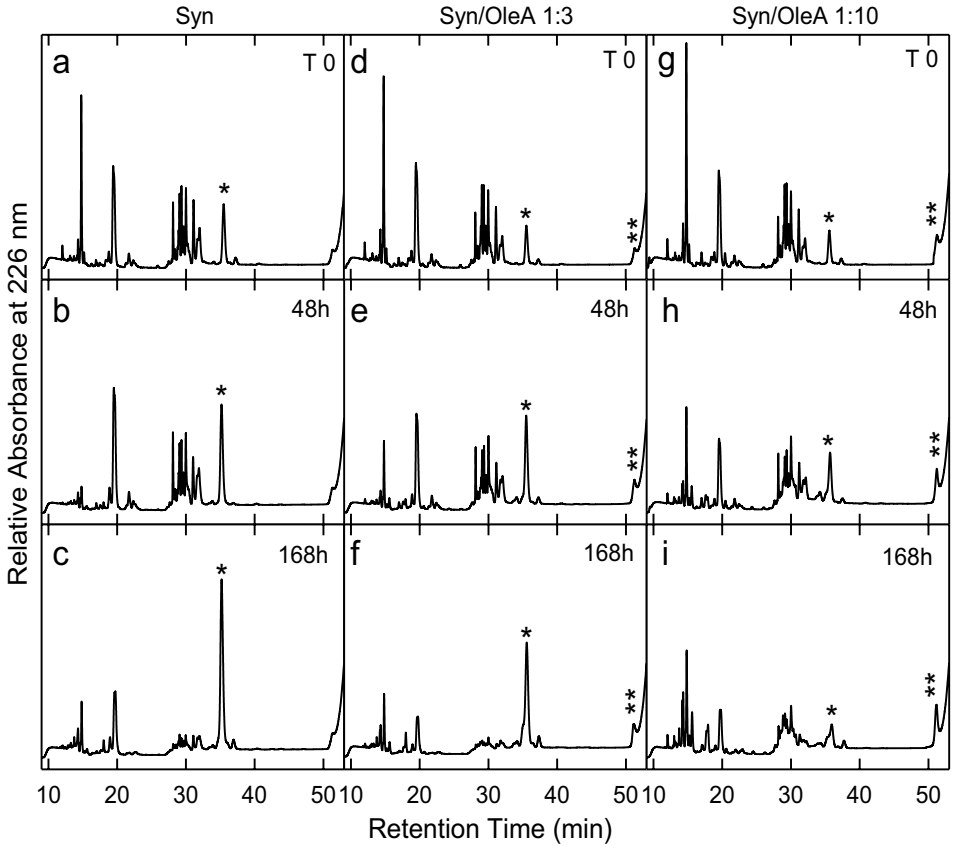

Figure 3. Syn aggregation in the absence or in the presence of OleA 1:3 and 1:10 ratio investigated by limited proteolysis. During aggregation, proteinase K was added at an E/S ratio of 1:1000 (by weight) to aliquots (40 µl) taken from the mixture at different time intervals (0, 48, 168 h). Proteolysis was allowed to take place at 22 °C for 5 min and then quenched by addition of 4.0% TFA in water. The proteolysis samples were analysed by RP-HPLC using a Jupiter C18 column (4.6 × 250 mm) and eluted with a gradient of acetonitrile/0.085% TFA vs water/0.1% TFA from 5.0% to 25% in 5 min, from 25% to 28% in 13 min, from 28% to 39% in 3 min, from 39% to 43% in 21 min. The peaks relative to intact Syn and to the oligomeric species are highlighted.

proteolysis was evident (Fig. 3b); moreover, at longer incubation times, Syn became progressively more resistant to proteolysis, in parallel with the increase of fibril content in the aggregation mixture, as previously observed for other proteins[58] (Fig. 3c). Then, the proteolysis experiment was carried out on the Syn/OleA 1:3 or 1:10 samples. We found that at time 0 all proteolytic mixtures showed a similar pattern (Fig. 3a,d,g). As the aggregation time increased, Syn appeared apparently less resistant to proteolysis (Fig. 3e,f,h,i); in fact, the peak relative to the intact protein (RT 35.5 min) was slightly less intense than that obtained in the absence of OleA (highlighted with a star in the figure). It is worth noting the presence of the peak at RT 51.2 min (highlighted with two stars in Fig. 3). This species increased as far as the aggregation time was prolonged (from T 0 to T 168 h,) and OleA concentration in the sample was increased (Fig. 3d–f,g–i).

Overall, the proteolysis data indicate that the presence of OleA in the aggregation mixture of Syn increases the monomeric Syn sensitivity to proteolysis. Moreover, OleA favours the growth of other types of aggregated species, that elute late in RP-HPLC and exhibit increased resistance to proteolysis. To better evaluate the relative amount of each population, the area of the peaks relative to the material obtained by PK digestion at different times of aggregation was calculated (Fig. S3) and commented in the Discussion.

Characterization of the off-pathway species arising during Syn aggregation in the presence of OleA. Next, we look at the fraction eluted at RT 51.2 min by RP-HPLC under aggregation conditions in the presence of OleA. This species was collected and concentrated for further characterization. Figure 4a reports the GF chromatogram relative to the Syn/OleA (1:10) mixture after 168 h of aggregation. Two main fractions (7.4 ml; 9.4 ml) were detected. The species eluting at 7.4 ml and increasing over time (cfr. Fig. 1b) was related to that eluting at 51.2 min in RP-HPLC, when an aliquot of the corresponding GF fraction was reloaded onto the RP-HPLC column (not shown). Its UV-vis spectrum (Fig. 4a, inset, continuous line) showed a profile characterized by two main signals at 340 nm and 280 nm, indicative of the presence of both OleA and Syn. The UV-Vis spectrum of OleA alone obtained just after sample preparation and after 168 h of incubation was shown in Fig. S1b, as a reference. The fraction at 9.4 ml, eluted as monomeric Syn, also contained OleA, whose absorbance bands were detectable in the UV-vis spectrum (Fig. 4a, inset, dashed line).

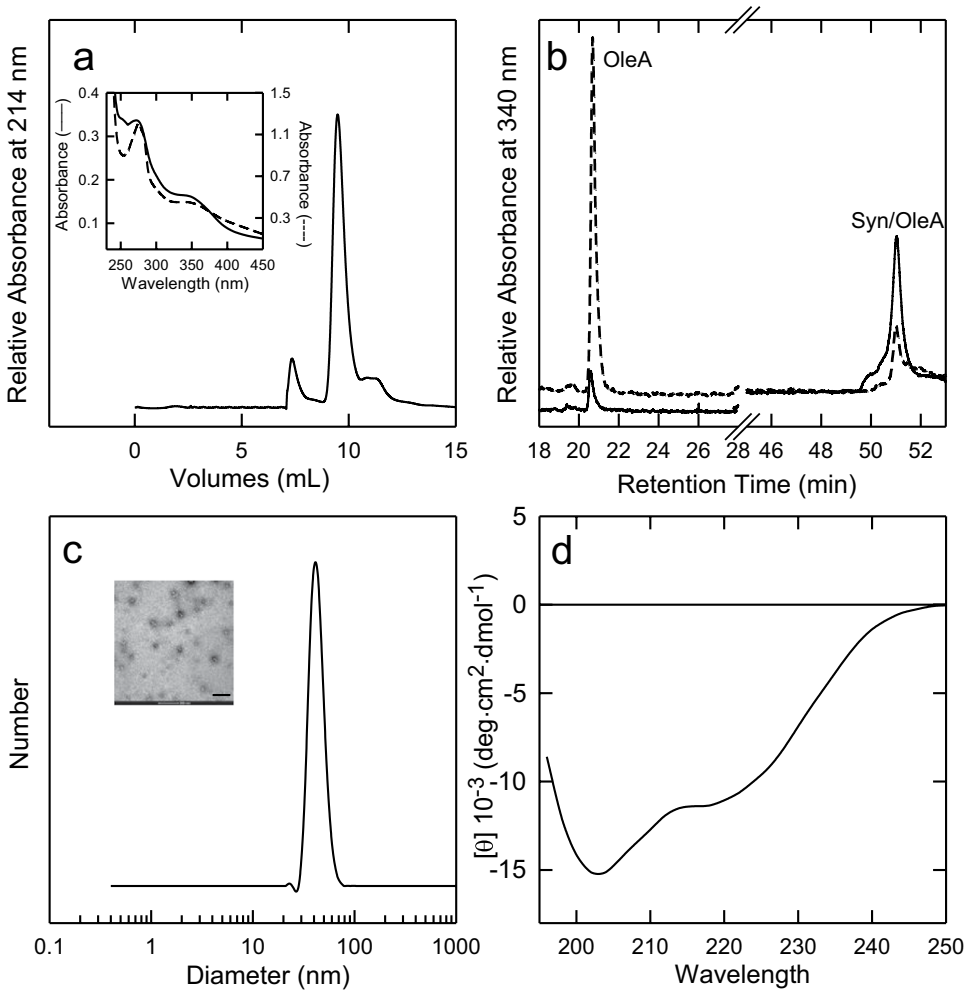

Figure 4. Characterization of Syn off-pathway oligomers (RT 51.2) grown in the presence of OleA. (**a**) Gel filtration chromatography of the Syn/OleA (1:10) mixture after 168 h of incubation Inset: UV-vis spectra of the fractions at 7.4 (—) and 9.4 (- - -) mL of elution volume in GF. (**b**) RP-HPLC chromatogram at 340 nm of the Syn/OleA (ratio 1:10) mixture at time 0 (dashed line) and 168 h (continuous line) of incubation. (**c**) DLS and TEM (inset) analysis of the purified oligomers. (**d**) Far-UV CD of the purified oligomers. The oligomers were purified by RP-HPLC and concentrated until organic solvent and TFA removal, but never dried to avoid morphological changes. Other experimental details are reported in the methods section. The scale bar in the TEM image correspond to 200 nm.

The same mixture (Syn/OleA, 1:10 ratio; 168 h) was also analysed by RP-HPLC by recording the effluent at 340 nm (Fig. 4b) to monitor OleA absorbance. The chromatogram relative to the analysis of the freshly prepared Syn/OleA mixture is also reported as a reference (dashed line). The chromatograms were characterized by two main peaks at RT 20.5 min and RT 51.2 min, respectively. These fractions were analysed by MS, confirming the presence of OleA in both and the absence of protein material in the peak at 20.5 min (not shown). The intensity of the peaks at 20.5 min and 51.2 min reciprocally changed during incubation. At the beginning, the signal relative to OleA was higher and decreased with time, probably due to the formation of the OleA-Syn complex eluting at 51.2 min. When imaged by negative stain TEM, the latter sample showed a morphology consistent with an oligomeric structure (Fig. 4c, inset). These oligomers appeared as not fully homogenous spheroidal particles with an average diameter of 22.5 nm (12.5 nm the smaller species, 42.3 nm the larger ones). The largest aggregates were not included in these measurements. By DLS analysis, the average hydrodynamic diameter was of ~43 nm (Fig. 4c).

The far-UV CD spectrum of the RT 51.2 sample is reported in Fig. 4d. The shape of the spectrum and the presence of two minima at ~203 and ~220 nm indicate that oligomer structure is not disordered, when compared to that resulting from the CD spectrum of monomeric Syn (Fig. 1c, inset). The spectra also showed that different conformers, partially folded and unfolded, did exist at equilibrium. Further characterization is required to better define the secondary structure content of these species.

Then, we mapped the overall structure of the oligomeric species at RT 51.2 min by finger printing analysis using trypsin after partial destabilization of the complex by Gnd-HCl (Fig. 5). Indeed, these oligomers were quite resistant to proteolysis, probably because of some protection by OleA or by OleA-induced conformational

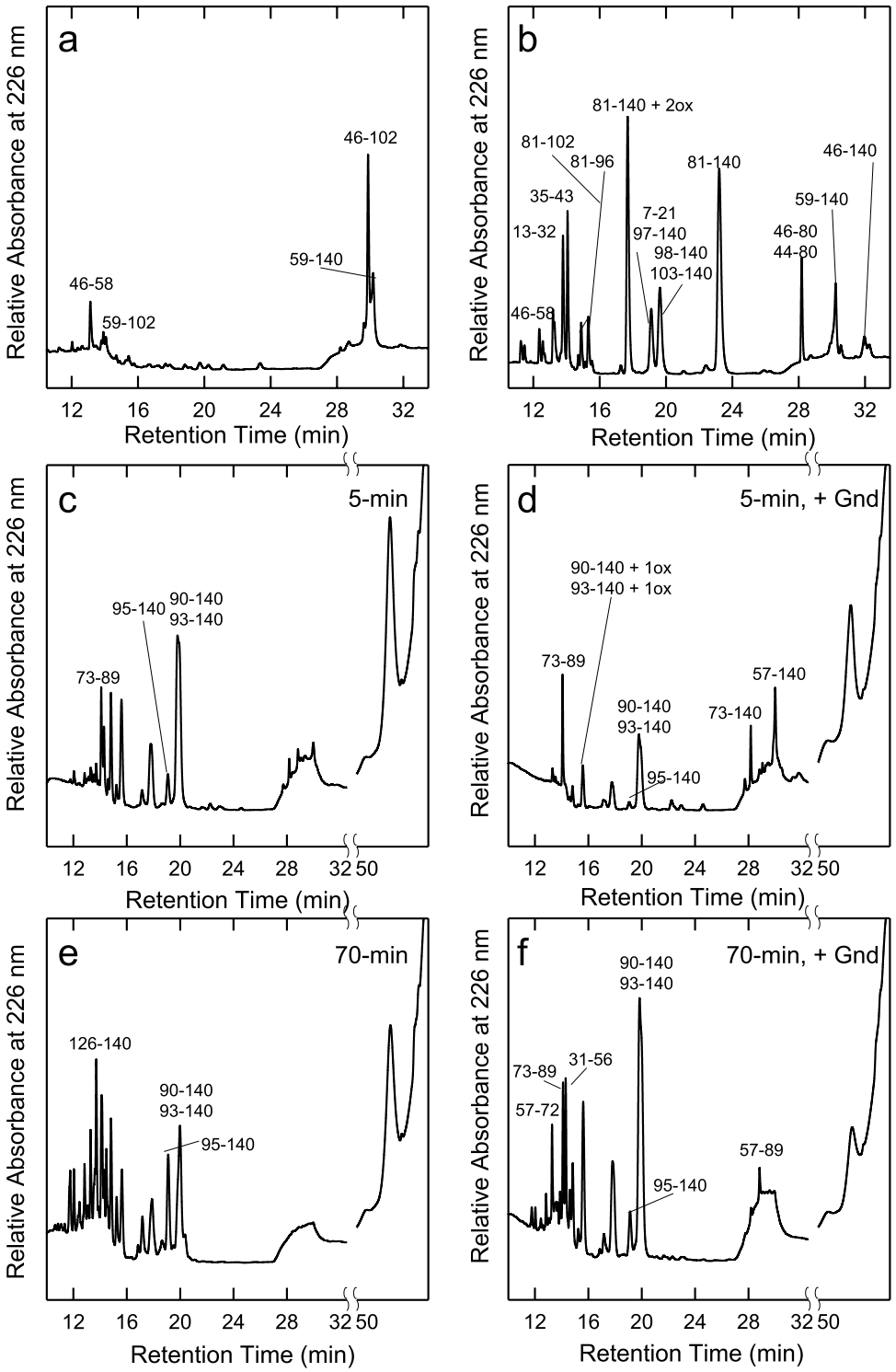

Figure 5. Mapping of (**a**) Syn off-pathway oligomers (RT 51.2) and (**b**) Syn monomers by trypsin proteolysis. The chromatograms refer to incubation with PK of the RT 51.2 sample for 5-min (**c**,**d**) or 70 min (**e**,**f**). In (**d**) and (**f**), the proteolysis was carried out on samples partially destabilized in Gnd-HCl. The numbers close to the peaks indicate the identified fragments. The term ox refers to the presence of oxidation in the peptides.

modifications (cfr. Fig. 3). By performing exhaustive fragmentation by trypsin (15 h), only a few peptide species were found in the proteolysis mixture of the RT 51.2 species (Fig. 5a), when compared with same analysis carried out with monomeric Syn (Fig. 5b); at variance, fragments encompassing the entire sequence were detected in the latter (Table S2). In particular, the large fragments corresponding to the sequences 59–140 and 46–102 remained undigested even after 15 h (Fig. 5a) of incubation in the proteolysis mixture, suggesting that these species are rigid, structured or protected. To explain the presence of these peptide species, a pattern of fragmentation can be

hypothesized and it is conceivable that RT 51.2 was cleaved, initially, at the level of the 45–46 peptide bond, thus generating the 1–45 and 46–140 fragments. The N-terminal species 1–45 was not visible, since it was further fragmented into smaller fragments. The C-terminal 46–140 was further cleaved at the level of the 102–103 peptide bond, producing the quite resistant 46–102 fragment and the 103–140 fragment, that was further degraded in smaller species. On the other hand, the 59–140 fragment was also seen in the chromatogram. This species could arise from the cleavage of the 58–59 peptide bond in the 46–140 fragment. Then, the 59–140 species underwent further fragmentation generating the 59–102 species. In conclusion, the 46–102, and in minor extent the 59–140, are the most resistant, upon prolonged trypsin treatment and after oligomer destabilization by Gnd-HCl.

A better structural characterization of the off-pathway oligomers (RT 51.2) was obtained by carrying out the mapping by PK with (Fig. 5d,f) or without (Fig. 5c,e) destabilization by Gnd-HCl. Indeed, the rationale of this approach was based on the general observation that, in the absence of the denaturant, the substrate of the protease is the most flexible species in equilibrium with a more structured one, not accessible by PK. Gnd-HCl addition destabilized the PK-resistant species, making it more susceptible to proteolysis. Moreover, in this case, the proteolysis reactions were carried out for 5- and 70-min, to identify the first proteolytic events (Fig. 5c,d) and those occurring subsequently on a perturbed substrate, in order to recognise the proteolysis resistant species accumulating in the mixture (Fig. 5e,f). In the absence of Gnd-HCl, the RT 51.2 species was only partially fragmented by the protease, as indicated by the fact that its peak was still visible even after 70 min of reaction (Fig. 5e) and that any peculiar fragment did not accumulate in the mixture. However, following partial destabilization of the complex, this species was almost exhaustively digested upon incubation up to 70 min (Fig. 5f). Moreover, in the presence of Gnd-HCl, after 5 min some species seemed to accumulate and two main cleavages did occur (Fig. 5d). The first, involving the 56–57peptide bond, generated the 1–56 and 57–140 fragments, whereas the other, involving the 72–73 peptide bond, produced the 1–72 and 73–140 fragments (Table S3). The two N-terminal fragments (1–56 and 1–72) were scarcely represented in comparison to the C-terminal ones (57–140 and 73–140) since the former were probably cleaved into smaller hydrophilic fragments. After longer incubation with the enzyme (Fig. 5f, 70 min), further cleavages took place on the C-terminal species, which generated mainly the 57–89, 73–89 and 90–140 fragments, that remained undigested even after 70 min of incubation with PK (Fig. 5f). These data confirm those obtained by trypsin and suggest the coexistence of two different population of off-pathway oligomers: one more susceptible to proteolysis, undergoing fragmentation in the absence of denaturant, and another, more resistant, that is cleaved only after denaturation. Moreover, from a comparison between the two proteolytic patterns, those encompassing residues 46–102, 57–89, 59–140 and 90–140 appear to be the more protected regions, belonging to the NAC and C-terminal regions of the Syn sequence.

Syn aggregates grown in the presence of OleA show reduced cytotoxicity. Once described at the molecular level the interference of OleA with Syn aggregation, we investigated whether OleA also affected aggregate cytotoxicity. A first experiment was designed to determine the cytotoxicity of Syn aggregates at different fibrillation times. To this purpose, we used human neuroblastoma, SH-SY5Y, cells exposed for 24 or 48 h to Syn solutions enriched of protein in different conformations: monomer, oligomers or fibrils, obtained by incubating the protein for 0, 48 or 168 h in aggregation conditions, respectively. Oligomers and fibrils were dose-dependently cytotoxic to cells exposed for 48 h, as shown by the MTT assay (Fig. 2S). Under these conditions, the solution enriched in Syn fibrils (Syn 168 h) was the most cytotoxic sample, followed by the solution enriched in oligomers (Syn 48 h); some cytotoxicity, not dose-dependent, was also seen in the case of the monomeric protein before aggregation started (Syn) (Fig. 2S). Based on these data, we decided to expose the cells for 48 h to the three different Syn solutions (5.0 μM) enriched in monomers, oligomers or fibrils, in the absence or in the presence of 1:10 Syn/OleA. The MTT assay showed a significant decrease of toxicity when the cells were treated with samples aggregated for 48 or 168 h in the presence of OleA (Syn 48 h/OleA, Syn 168 h/OleA) (Fig. 6a). Cell survival after exposure to the Syn 48 h/OleA was around 100% ± 10.6 while cell survival was around 80% ± 3.1 in the presence of the Syn 168 h/OleA indicating that OleA was only partially effective in protecting cells against fibril cytotoxicity. Furthermore, the evaluation, by MTT assay, of the toxic power of the species eluted in RP-HPLC at RT 51.2 min showed that this sample was completely harmless even when tested purified at the final concentration of 5.0 μM (Fig. 6a).

In consideration of the key role performed by oxidative stress in the pathogenesis of PD, we also sought to assess the redox status of the variously treated cells by using the ROS-sensitive fluorescent probe CM-H_2 DCFDA. We found that the different Syn aggregates stimulated some ROS production in SH-SY5Y cells that was particularly evident when the cells were exposed for 48 h to Syn fibrils (Syn 168 h) (Fig. 6b). However, cell exposure to the different aggregates of Syn grown in the presence of 1:10 Syn/OleA did not result in any statistically significant increase of ROS levels (Fig. 6b). These data led us to conclude that the presence of OleA during Syn aggregation decreases the ability of the resulting aggregates to raise ROS production thus making non-toxic the oligomers whereas the toxicity of the fibrillar sample was not completely abolished.

OleA effect on pre-formed Syn oligomers and fibrils. Once established that OleA interferes with Syn aggregation yielding substantially non-toxic aggregates, we analysed the effect of OleA on preformed Syn oligomers and fibrils to assess whether it favoured fibrils disassembly with leakage of toxic oligomers. OleA (1:10 ratio) was added to preformed solutions enriched in oligomeric species (48 h) or fibrils (168 h). The disaggregation activity by OleA was followed by fluorescence spectroscopy, limited proteolysis and MTT assay. The ThT spectra (Fig. 7a) were obtained from Syn oligomers (48 h) after further 24 h of incubation in the presence (48 h + OleA 24 h) or in the absence (72 h) of OleA in comparison with Syn oligomers (the starting point) (48 h). As expected, in the absence of OleA, the aggregation process proceeded towards fibrils formation with substantial increase of ThT intensity (as indicated by the arrow). The 48 h + OleA 24 h sample showed a decrease of ThT fluorescence, indicative of a stop or a slowdown of the formation of Syn aggregates. The same experimental scheme was followed with Syn fibrils samples (168 h). In this case, ThT fluorescence spectra were recorded after further 8 h

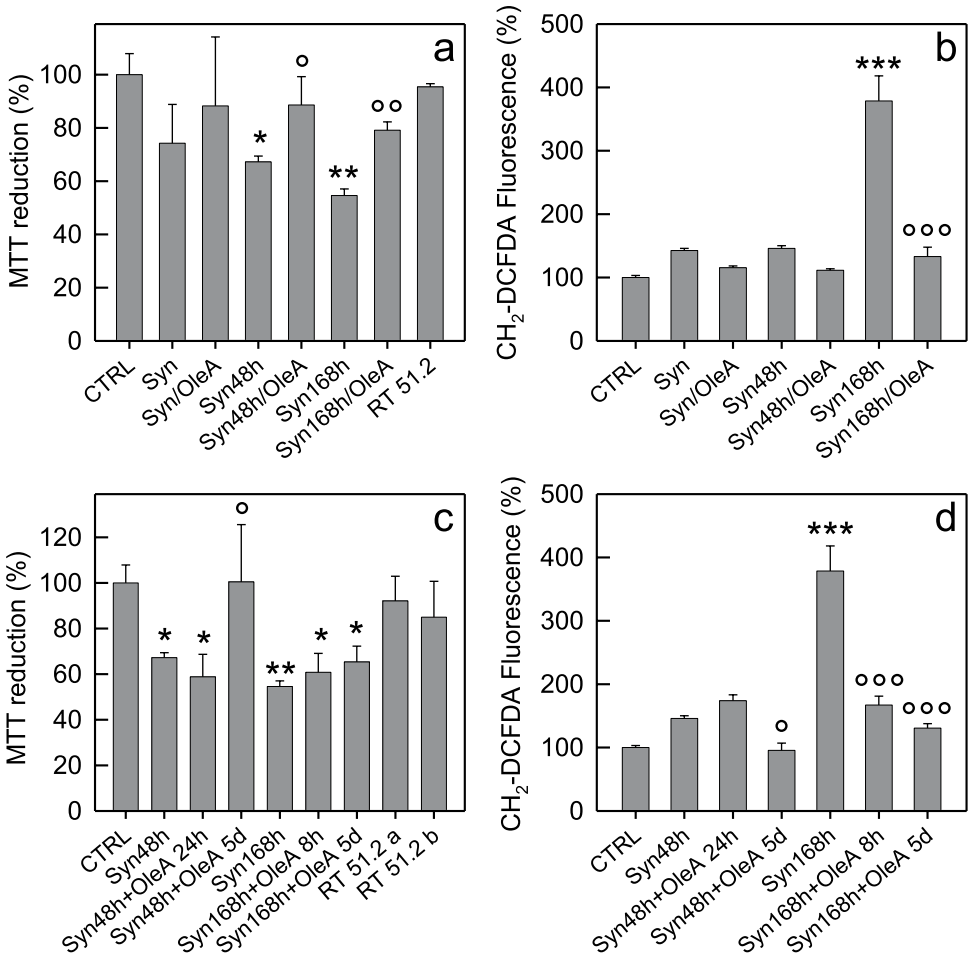

Figure 6. Cell viability and ROS levels. (**a**,**b**) SH-SY5Y cells treated for 48 h with a 5.0 μM Syn solution obtained at different times of aggregation (0, 48 and 168 h) enriched in monomeric (Syn), oligomeric (Syn 48 h) or fibrillar (Syn 168 h) species, respectively. Each sample was obtained in the absence or in the presence of OleA (Syn:OleA, 1:10). (**a**) Cell viability assessed by the MTT reduction assay and (b) by ROS production. For the MTT assay, the RT 51.2 species purified by RP-HPLC was also tested. (**c**,**d**) OleA modulates the toxicity of preformed Syn assemblies. (**c**) MTT assay and (**d**) ROS endogenous levels in SH-SY5Y cells exposed for 48 h to 5.0 μM Syn enriched in oligomers (Syn 48 h) or fibrils (Syn 168 h). The oligomeric samples were also analysed following addition of OleA after further incubation of 24 h or 5 d (Syn 48 h + OleA 24 h) and (Syn 48 h + OleA 5d). The fibrillar species were analysed after 8 h or 5 d of incubation in the presence of OleA (Syn 168 h + OleA 8 h) and (Syn 168 h + OleA 5d). The RT 51.2 samples purified by RP-HPLC from the mixture corresponding to (Syn 48 h + OleA 24 h) sample (RT 51.2a) and from that corresponding to (Syn 168 h + OleA 8 h) sample (RT 51.2b) were also tested by the MTT assay. Error bars indicate the standard deviation of independent experiments carried out in triplicate. Statistical analysis was performed using Student's t-test. The results were compared using Student's *t*-test between two groups, *P < 0.05; **P < 0.01; ***P < 0.001 versus untreated cells and °P < 0.05; °°P < 0.01; °°°P < 0.001 versus treated cells with Syn aggregates grown without OleA.

of incubation with (168 h + OleA 8 h) or without OleA (176 h). We did not find any remarkable reduction of ThT fluorescence in the (168 h + OleA 8 h) sample, which indicated a negligible effect of OleA on preformed fibrils.

The same samples were also subjected to limited proteolysis (Fig. 7c–h). As expected, the sample aged for 72 h in the absence of OleA (Fig. 7d) showed a slightly increased resistance to proteolysis in comparison to the sample aged for 48 h (Fig. 7c) and small fragments eluting at short RT appeared in the chromatogram. In the proteolytic pattern obtained from samples treated with OleA for 24 h (48 h + OleA 24 h), the low intensity of the peak relative to intact Syn (RT 35.5 min) suggested that the monomeric Syn still present in the mixture was fragmented and resulted, under these conditions, more susceptible to proteolysis (Fig. 7e). In the meantime, the species at RT 51.2 min, previously found to increase as far as the aggregation time was prolonged, appeared in the chromatogram. In synthesis, monomeric Syn underwent formation of a species more susceptible to proteolysis (the peak of intact Syn was decreased) and a protease-resistant one (RT 51.2).

The proteolytic patterns relative to the aggregation mixture at 168 h and 176 h, in the absence of OleA, are quite similar since no critical events occurred in this time (Fig. 7f,g). However, upon addition of OleA (Fig. 7h), the proteolytic pattern was completely different and the RT 51.2 species arose in higher percentage (Fig. S4). Also

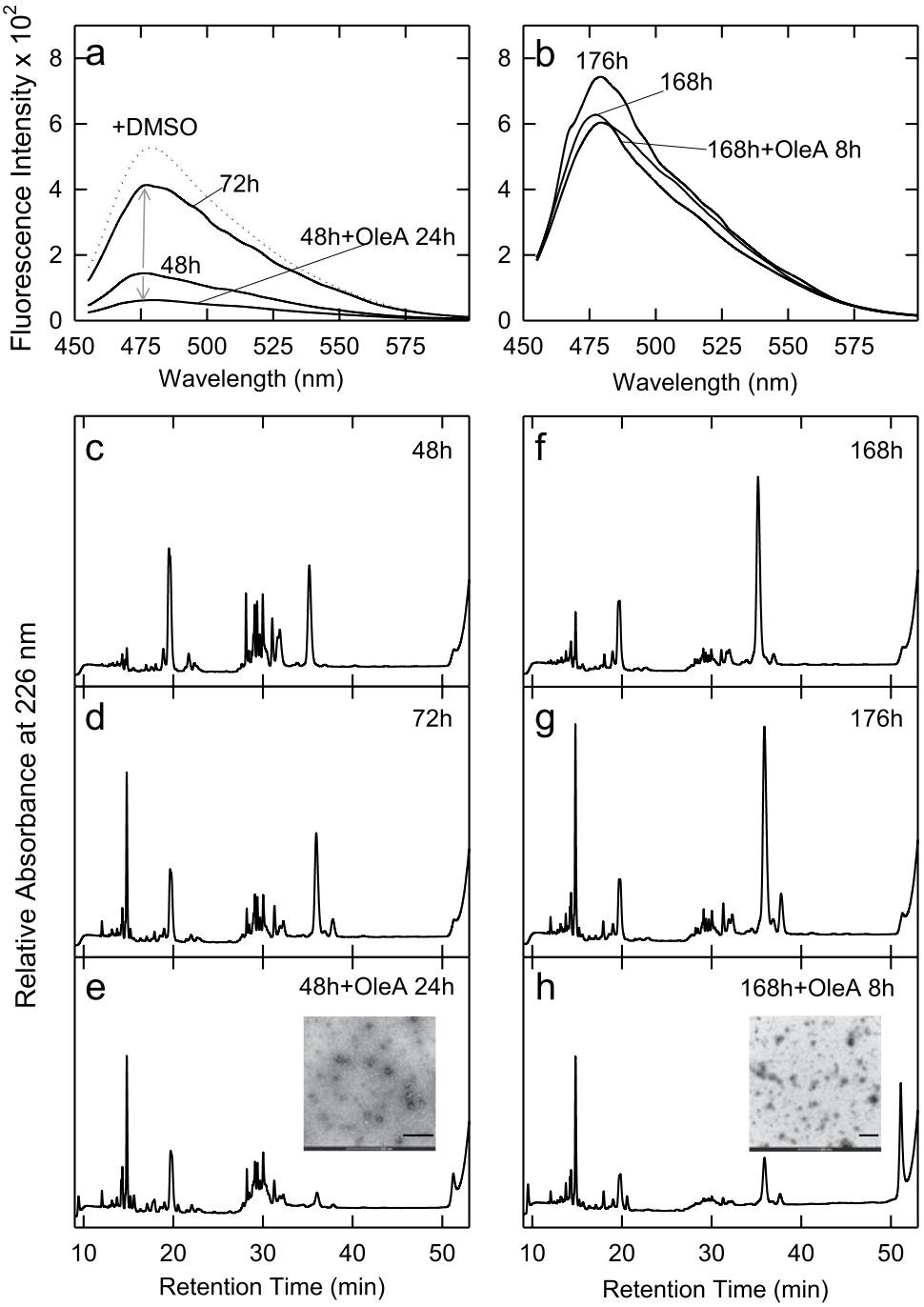

Figure 7. OleA-induced Syn disaggregation probed by (**a**,**b**) ThT fluorescence and (**c**–**h**) limited proteolysis. During aggregation, aliquots were collected from the mixture at 48 h and 168 h, then OleA was added to a 1:10 final Syn:OleA ratio. ThT spectra in (**a**) refer to Syn samples corresponding to 48 h of aggregation (48 h) and to further 24 h of incubation in the absence (72 h) or in the presence (48 h + OleA 24 h) of OleA. The ThT spectra in (**b**) were recorded at 168 h and after additional 8 h of incubation without (176 h) or with (168 h + OleA 8 h) OleA. (c-h) RP-HPLC analysis of the proteolysis mixture of Syn samples during aggregation (**c**) at 48 h, (**d**) after further 24 h of incubation in buffer without polyphenol (72 h), (**e**) in the presence of OleA. The same scheme was followed for Syn samples collected from the aggregation mixture at 168 h of incubation (**f**), after further 8 h of incubation in the absence (**g**) or in the presence (**h**) of OleA. (**e**,**h**, inset), TEM images taken from samples corresponding to the peaks eluting at RT 51.2 min; scale bar: 200 nm.

in this case, the proteolysis data can be explained with the co-existence, in the mixture, of species characterized by different susceptibility to proteolysis. The species eluting at RT 51.2 min, an aggregated and highly hydrophobic one induced by the presence of OleA either during aggregation or at the end of the latter, was accumulating in the mixture and represented a PK- resistant fraction.

We also investigated whether OleA modified the toxicity of Syn preformed oligomers and fibrils. To this aim, we compared the (Syn 48 h + OleA 24 h) and (Syn 168 h + OleA 8 h) cytotoxicity to SH-SY5Y cells with that displayed by the same samples without the polyphenol by using the MTT and ROS assay. In addition, Syn oligomers and fibrils were incubated in the presence of OleA for an extra time (5 days), to assess whether OleA had some effects under extreme experimental conditions. Figure 6c,d show that the (Syn 48 h + OleA 24 h) sample maintained its potential toxicity; however, a prolonged OleA treatment (Syn 48 h + OleA 5d) made it harmless to cells (Fig. 6c) that also displayed reduced endogenous ROS levels (Fig. 6d). As far as the effect of OleA on preformed fibrils is concerned, we observed a very slight decrease of fibril cytotoxicity in both samples (Syn 168 h + OleA 8 h) and (Syn 168 h + OleA 5d) (Fig. 6c). In spite of an evident cell sufferance, the fibrils treated with OleA for short and long incubation times, induced a significant decrease in ROS intracellular levels (Fig. 6d). We also evaluated the toxicity of the RT 51.2 samples after its purification by RP-HPLC from the mixture corresponding to the Syn 48 h + OleA 24 h sample (RT 51.2a) and from that corresponding to the Syn 168 h + OleA 8 h sample (RT 51.2b). The MTT assay confirmed that this sample was completely innocuous to SH-SY5Y cells (Fig. 6c).

OleA interferes with the interaction of Syn aggregates with the cell membrane. Finally, we investigated whether OleA interfered with the ability of Syn aggregates to interact with the cell membrane. In fact, recent data have widely reported that amyloid aggregates are able to bind to lipid bilayers and that aggregate interaction with the cell membranes is a crucial step of amyloid cytotoxicity[59,60]. In particular, it has been reported that exogenous oligomers and fibrils bind to the cell membrane and accumulate in lipid rafts, liquid-ordered membrane microdomains rich in functional proteins (receptors, carriers, signalling molecules), sphingosine, cholesterol and ganglioside GM1[61,62]. In this context, Syn oligomers have been reported to display membrane-disrupting power on anionic lipid bilayers and to alter the permeability and the integrity of the cell membrane[63].

To assess whether Syn amyloid species grown in the presence of OleA modified their propensity to interact with the cell membrane, we performed a sensitized FRET analysis between Alexa-488 GM1 fluorescence and Alexa-546 immunofluorescence on Syn aggregates. We found that both Syn oligomers and fibrils interacted with the cell membrane at the lipid raft level, as shown by the aggregate-GM1 co-localization (Fig. 8a,c) and by FRET efficiency (Fig. 8b,d). Such interaction was drastically reduced when the cells were treated with Syn aggregates grown in the presence of OleA (Fig. 8e,f,g,h). Then, SH-SY5Y cells were treated for 48 h with preformed Syn assemblies exposed for short (Syn 48 h + OleA 24 h, Syn 168 h + OleA 8 h) or long (Syn 48 h + OleA 5d, Syn 168 h + OleA 5d) time to OleA before supplementation to the cell medium. Confocal images and FRET analysis revealed that short treatment of the aggregates with the polyphenol did not alter significantly the ability of the Syn 48 h and Syn 168 h samples to interact with the membrane at the level of the GM1 component of lipid raft domains (Fig. 8i,l,m,n), whereas a prolonged exposure reduced significantly oligomers, but not fibrils, interaction with the cells (Fig. 8o,p,q,r), in agreement with the results of the toxicity experiments reported in the preceding section.

Discussion

In this study, we show that OleA interferes with Syn fibrillation in a dose-dependent manner, with the optimal 1:10 Syn/OleA ratio; the inhibition is due, apparently, to OleA interaction with Syn monomeric and oligomeric species, an effect similar to that reported for other polyphenols[64,65]. We also report that OleA reduces the toxicity of Syn amyloid aggregates, favouring the growth of harmless off-pathway oligomers. In fact, Syn aggregates grown in the absence or in the presence of OleA, displayed a very different ability to interact with the plasma membrane and to induce sufferance and oxidative stress in exposed cells. Recently, the ability of Syn to self-propagate and spread progressively between interconnected brain regions via a cell-to-cell transmission in PD model and patients has been repeatedly reported and is increasingly accepted as a central mechanism in the development of the disease[66,67]. In view of this notion, several new therapeutic strategies to combat PD are aimed at inhibiting not only Syn misfolding and aggregation, but also the prion-like interneuronal transport of aggregation seeds[22]. In this context, our findings showing a decreased interaction of the OleA/Syn complex with GM1-enriched sites at the cell membrane and the OleA interaction with preformed Syn aggregates (notably oligomers and prefibrillar assemblies), converting them into stable and inert species are of interest. Overall, these data suggest that the polyphenol, besides interfering with the aggregation path, also hinders the association of Syn and/or its aggregates with the cell membrane, presumably, by generating new species with different surface properties. Our findings are of importance in the evaluation of the potential use of OleA in PD treatment, suggesting that OleA could be beneficial not only by interfering with toxic aggregation of Syn and by favouring aggregate disassembly in non-toxic species, but also by hampering their self-propagation.

To better elucidate the mechanism of OleA effects at the molecular level, we investigated the modifications of the structure and cytotoxicity of Syn in different aggregated states arising in the presence of OleA. Syn-OleA interaction was probed by several biophysical and biochemical techniques. We found that OleA does not modify the secondary structure of monomeric Syn and its chromatographic behaviour (retention time in RP and elution volume in GF). On the other hand, the immediate appearance, in the protein/OleA mixture, of a late eluting species in RP (51.2 min), yet earlier than monomeric Syn in GF, clearly indicates that the polyphenol exerts an instantaneous effect on Syn, inducing the formation of a new species (see Figs 4 and 5, for its characterization). The abundance of this species appeared to be dependent on incubation time and OleA concentration, however it did not evolve into fibrils; overall, the structural features of this species allow to classify it as a population of off-pathway oligomers[28,68]. Interestingly, when OleA was added to the aggregation mixture during the elongation phase, the growing aggregates (oligomers and protofibrils) were apparently solubilised into species recalling the off-pathway oligomers formed when OleA was present since the beginning of aggregation. The harmless off-pathway oligomers appeared characterized by a heterogeneous morphology, even though mainly spheroidal. Their secondary structure was substantially random, yet in the presence of a minor content of beta-sheet. Of note,

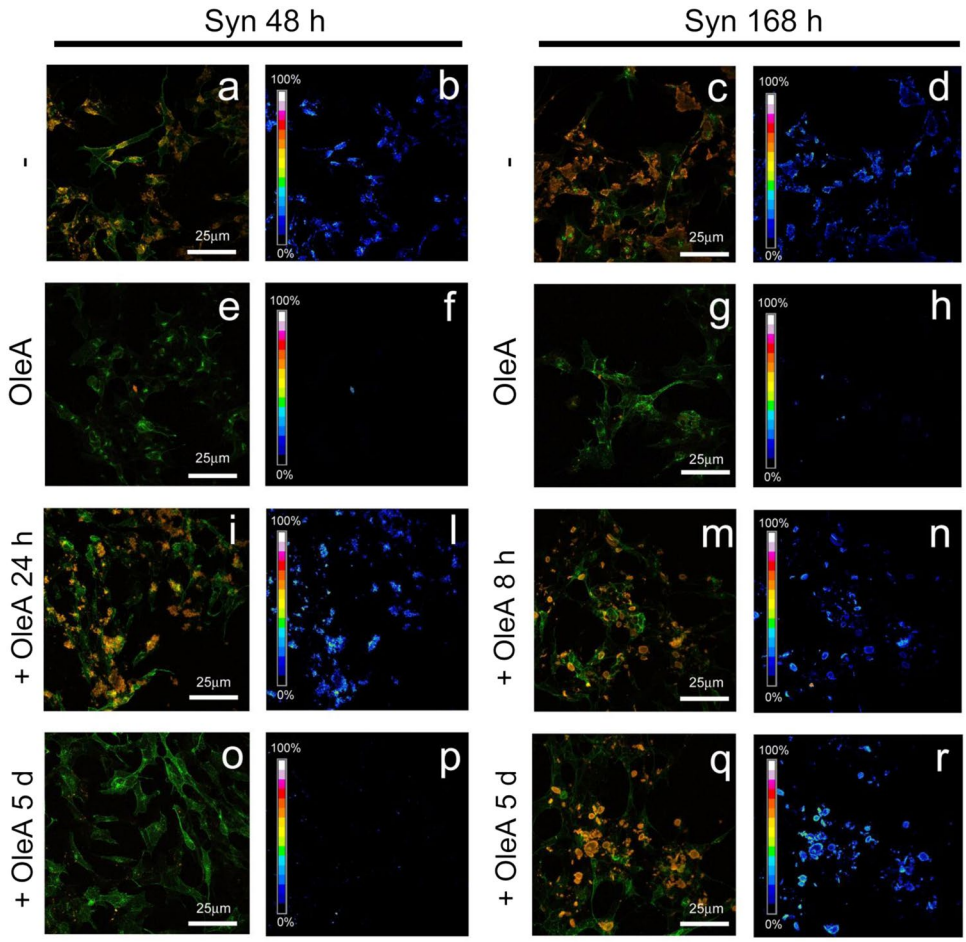

Figure 8. The complex OleA-Syn does not bind to the plasma membrane. (**a**,**e** and **c**,**g**) Z-projection of Syn samples grown in the presence (Syn 48/OleA, Syn 168/OleA) or in the absence of OleA (Syn 48 h, Syn 168 h) by immunostaining (red) and GM1 staining (green) on SHSY5Y cell membrane. (**b**,**f** and **d**,**h**) FRET analysis between GM1 staining and aggregate immunostaining. OleA affects preformed Syn assemblies and their membrane interaction. (**i**,**o**, and **m**,**q**) Z-projection of preformed Syn assemblies (oligomers and fibrils) treated with OleA for two different times (Syn 48 h + OleA 24 h and Syn 48 h + OleA 5d) and (Syn 168 h + OleA 8 h and Syn 168 h + OleA 5d) by immunostaining (red) and GM1 staining (green) on SH-SY5Y cell membrane. (**l**,**p**, and **n**,**r**) FRET analysis between GM1 staining and aggregate immunostaining.

the proteolysis mapping experiments on off-pathway oligomers showed that the NAC and C-terminal regions of Syn are most persistent in solution and suggested a high affinity of OleA for specific regions of Syn. In fact, OleA stabilized the NAC and C-terminal region and hindered the long-range interactions favouring amyloid aggregation.

The limited proteolysis data provided important information on Syn dynamics and structural rearrangement during the aggregation process in the presence or in the absence of OleA. Actually, Syn displayed increased resistance to proteolysis as far as the aggregation process proceeded; this is not surprising, when one considers that, as reported for other amyloid forming proteins, during aggregation the Syn polypeptide chain is progressively embedded into the highly ordered, compact fibrillar structure[58,69]. In the presence of OleA, Syn exhibited a reduced tendency to aggregate and a concomitant increased sensitivity to proteolysis, whereas, the off-pathway oligomeric species eluting at RT 51.2 min were proteolysis-resistant. To better describe this finding, the Syn species were classified as PK-sensitive, PK-resistant and PK-resistant off-pathway oligomers (Fig. S3). The first fraction contained the soluble components of the aggregation mixture; the PK-resistant Syn contained the pre-fibrillar and fibrillar species in equilibrium with the soluble ones; the PK-resistant off-pathway oligomers fraction contained the protease-resistant molecular species eluting at RT 51.2 min. At the beginning of the aggregation (Fig. S3a), the most populated fraction was the PK-sensitive one. As expected, as far as aggregation proceeds, the PK-resistant population increased, at the expense of the PK-sensitive fraction that decreased inversely (Fig. S3b,c). However, when Syn aggregation was carried out in the presence of OleA, the PK-sensitive fraction was stabilized, preventing the formation of the PK-resistant Syn species, while the PK-resistant off-pathway oligomers were increasingly produced over time. The same approach was used to understand (i) whether the same partitioning event between PK-sensitive and PK-resistant species resulted from aggregate disassembly by OleA added at the elongation and plateau phases and (ii) to define Syn conformers preference of OleA. For these

reasons, we carried out limited proteolysis on samples enriched either in on-pathway oligomers aged 48 h or on fibrils aged 168 h. ThT measurements clearly showed that OleA decreases fibril formation, when added to a solution enriched in oligomers. In this case, the PK-resistant fraction strongly decreased, while the PK-sensitive Syn increased and the PK-resistant off-pathway oligomers were grown (Fig. S4a). These data confirm that the oligomeric species in the mixture do interact with OleA, giving rise to off-pathway oligomers (PK-resistant RT 51.2) and to a stabilized form of monomeric Syn (PK-sensitive). Moreover, the species populating this sample showed a membrane activity and cytotoxicity that decreased as far as the incubation with the polyphenol was prolonged. In parallel, we observed a concomitant decrease in ROS levels, one of the events associated to amyloid toxicity, which, in this case, was assigned to OleA re-modelling of the growing assemblies, that, eventually, showed different surface properties. In the case of pre-formed fibrils, the ThT data showed a modest effect of OleA. However, the limited proteolysis experiments suggest that the polyphenol induces the formation of the PK-resistant species eluted at RT 51.2 with reduction of PK-resistant Syn, whereas monomeric PK-sensitive Syn was scarcely affected (Fig. S4b). Furthermore, the toxicity of pre-formed fibrils treated with the polyphenol was not significantly affected even after a prolonged treatment (5 days), yet in the presence of a significant reduction of oxidative stress. The reduced cellular levels of ROS could result from the radical scavenging properties of OleA in accordance with previous studies describing the role of the antioxidant properties of this polyphenol in the prevention of amyloid assembly cytotoxicity[70,71]. However, in this case, aggregate toxicity persisted because OleA failed to reduce the membrane activity of the pre-formed fibrils treated with the polyphenol.

In conclusion, our data support the existence of parallel mechanisms of action of OleA. We hypothesized that OleA interacts differently with the previously reported interconverting conformers of monomeric Syn in solution[72], stabilizing the best-fitting conformation. Moreover, OleA might select the most prone-to-aggregation conformation, confining it into a non-toxic off-pathway oligomer. This view can be supported by the faster conversion of the aggregation-prone monomeric Syn into off-pathway oligomers in the presence of OleA, during the early elongation phase; the latter normally is populated by aggregation-prone monomeric Syn and early on-pathway oligomers, that become solubilised and stabilized in the presence of OleA. At the plateau phase, the effect of OleA on pre-formed fibrils is different, since OleA did not solubilize the fibrils but converted them into smaller assemblies that eluted in RP-HPLC as the off-pathway oligomers grown from aggregation prone Syn. In addition, at molecular level, OleA stabilized the NAC and C-terminal regions of Syn, preventing the long-range and hydrophobic interactions that favour amyloid aggregation[72,73].

Taken together, our data support the potentiality of polyphenols and similar compounds as neuroprotective agents extending the beneficial properties of olive polyphenols or their molecular scaffolds as promising candidates for long-term nutraceutical treatment of PD. The latter could reduce and delay aging-associated neurodegeneration in sporadic PD limiting the need of the symptomatic pharmacological treatment, the only one presently available, in the expectation that new therapies, such as cell therapy, will improve their efficacy in large number of patients. Moreover, our analysis of the structural and biological features of the Syn oligomeric species grown at different aggregation conditions provides an useful contribution to better understand, at the molecular level, their neurotoxicity in neurodegeneration, as issue of particular relevance in PD pathogenesis.

References

1. Giasson, B. I. *et al.* A panel of epitope-specific antibodies detects protein domains distributed throughout human α-synuclein in Lewy bodies of Parkinson's disease. *J. Neurosci. Res.* **59**, 528–533 (2000).
2. Galvin, J. E., Uryu, K., Lee, V. M.-Y. & Trojanowski, J. Q. Axon pathology in Parkinson's disease and Lewy body dementia hippocampus contains α-, β-, and γ-synuclein. *Proc. Nat. Acad. Sci. USA* **96**, 13450–13455 (1999).
3. Lashuel, A. H. *et al.* α-Synuclein, especially the Parkinson's disease-associated mutants, forms pore-like annular and tubular protofibrils. *J. Mol. Biol.* **322**, 1089–1102 (2002).
4. Peelaerts, W. *et al.* α-Synuclein strains cause distinct synucleinopathies after local and systemic administration. *Nature* **522**, 340–344 (2015).
5. Chu, Y. & Kordower, J. H. The Prion hypothesis of Parkinson's disease. *Curr. Neurol. Neurosci. Rep.* **15**, 28 (2015).
6. Polymeropoulos, H. M. *et al.* Mutation in the α-synuclein gene identified in families with Parkinson's disease. *Science* **276**, 2045–2047 (1997).
7. Krüger, R., Riess, O. & Jakes, R. Genetic dissection of familial Parkinson's disease. *Mol. Med. Today* **4**, 438–444 (1998).
8. Singleton, A. B. *et al.* α-Synuclein locus triplication causes Parkinson. *Science* **302**, 841 (2003).
9. Proukakis, C., Houlden, H. & Schapira, A. H. Somatic Alpha-Synuclein Mutations in Parkinson's Disease: Hypothesis and Preliminary Data. *Mov. Disorders* **28**, 705–712 (2013).
10. Pasanen, P. *et al.* A novel α-synuclein mutation A53E associated with atypical multiple system atrophy and Parkinson's disease-type pathology. *Neurobiol. Aging* **35**, 2180–2185 (2014).
11. Weinreb, H. P., Zhen, W., Poon, W. A., Conway, A. K. & Lansbury, T. P. NACP, a protein implicated in Alzheimer's disease and learning, is natively unfolded. *Biochemistry* **35**, 13709–13715 (1996).
12. Uversky, V. N. Neuropathology, biochemistry and biophysics of α-synuclein aggregation. *J. Neurochem.* **103**, 17–37 (2007).
13. Dettmer, U., Newman, A. J., von Saucken, V. E., Bartels, T. & Selkoe, D. KTKEGV repeat motifs are key mediators of normal α-synuclein tetramerization: Their mutation causes excess monomers and neurotoxicity. *Proc. Natl. Acad. Sci. USA* **112**, 9596–9601 (2015).
14. Uéda, K. *et al.* Molecular cloning of cDNA encoding an unrecognized component of amyloid in Alzheimer disease. *Proc. Nat. Acad. Sci. USA* **90**, 11282–11286 (1993).
15. Fernández, C. O. *et al.* NMR of α-synuclein–polyamine complexes elucidates the mechanism and kinetics of induced aggregation. *EMBO J.* **23**, 2039–2046 (2004).
16. Segrest, J. P. *et al.* The amphipathic helix in the exchangeable apolipoproteins: a review of secondary structure and function. *J. Lipid Res.* **33**, 141–166 (1992).
17. Eliezer, D., Kutluay, E., Bussell, R. & Browne, G. Conformational properties of α-synuclein in its free and lipid-associated states. *J. Mol. Biol.* **307**, 1061–1073 (2001).
18. Chandra, S., Chen, X., Rizo, J., Jahn, R. & Südhof, T. C. A broken alpha -helix in folded alpha–synuclein. *J. Biol. Chem.* **278**, 15313–15318 (2003).
19. De Franceschi, G. *et al.* Molecular insights into the interaction between α-synuclein and docosahexaenoic acid. *J. Mol. Biol.* **394**, 94–107 (2009).

20. Snead, D. & Eliezer, D. Alpha-synuclein function and dysfunction on cellular membranes. *Exp. Neurobiol.* **23**, 292–313 (2014).
21. Burré, J. *et al.* α-Synuclein promotes SNARE-complex assembly *in vivo* and *in vitro*. *Science* **329**, 1663–1667 (2010).
22. Lashuel, H. A., Overk, C. R., Oueslati, A. & Masliah, E. The many faces of α-synuclein: from structure and toxicity to therapeutic target. *Nat. Rev. Neurosci.* **14**, 38–48 (2013).
23. Burré, J. *et al.* Properties of native brain α-synuclein. *Nature* **498**, E4–E7 (2013).
24. Spillantini, M. G. Parkinson's disease, dementia with Lewy bodies and multiple system atrophy are α-synucleinopathies. *Parkinsonism Rel. Dis.* **5**, 157–162 (1999).
25. Conway, A. K., Harper, D. J. & Lansbury, T. P. Fibrils formed *in vitro* from α-synuclein and two mutant forms linked to Parkinson's Disease are typical amyloid. *Biochemistry* **9**, 2552–2563 (2000).
26. Rockenstein, E. *et al.* Accumulation of oligomer-prone α-synuclein exacerbates synaptic and neuronal degeneration *in vivo*. *Brain* **137**, 1496–1513 (2014).
27. Cremades, N. *et al.* Direct Observation of the interconversion of normal and toxic forms of α-synuclein. *Cell* **149**, 1048–1059 (2012).
28. Breydo, L. & Uversky, V. N. Structural, morphological and functional diversity of amyloid oligomers. *FEBS Lett.* **589**, 2640–2648 (2015).
29. Schapira, A. H. Neurobiology and treatment of Parkinson's disease. *Trends Pharmacol. Sci.* **30**, 41–47 (2009).
30. Wong, Y. C. & Krainc, D. α-Synuclein toxicity in neurodegeneration: mechanism and therapeutic strategies. *Nat Med.* **23**, 1–13 (2017).
31. Lewis, J. *et al. In vivo* silencing of alpha-synuclein using naked siRNA. *Mol. Neurodegener.* **3**, 19 (2008).
32. Masuda, M. *et al.* Small molecule inhibitors of α-synuclein filament assembly. *Biochemistry* **45**, 6085–6094 (2006).
33. Hong, D. P., Fink, A. L. & Uversky, V. N. Structural characteristics of the α-synuclein oligomers stabilized by the flavonoid Baicalein. *J. Mol. Biol.* **383**, 214–223 (2008).
34. Basir, A. & Lapidus, J. L. Curcumin prevents aggregation in α-synuclein by increasing reconfiguration rate. *J. Biol. Chem.* **287**, 9193–9199 (2011).
35. Singh, P. K. *et al.* Curcumin modulates α-synuclein aggregation and toxicity. *ACS Chem. Neurosci.* **4**, 393–407 (2013).
36. Ehrnhoefer, E. D. *et al.* EGCG redirects amyloidogenic polypeptides into unstructured, off-pathway oligomers. *Nat. Struc. Mol. Biol.* **15**, 558–566 (2008).
37. Bieschke, J. *et al.* EGCG remodels mature α-synuclein and amyloid-β fibrils and reduces cellular toxicity. *Proc. Nat. Acad. Sci. USA* **107**, 7710–7715 (2009).
38. Zhu, M. *et al.* The Flavonoid Baicalein inhibits fibrillation of α-synuclein and disaggregates existing fibrils. *J. Biol. Chem.* **279**, 26846–26857 (2004).
39. Jiang, M. *et al.* Baicalein reduces E46K α-synuclein aggregation *in vitro* and protects cells against E46K α-synuclein toxicity in cell models of familiar Parkinsonism. *J. Neurochem.* **114**, 419–429 (2010).
40. Rodríguez-Morató, J. *et al.* Potential role of olive oil phenolic compounds in the prevention of neurodegenerative diseases. *Molecules* **20**, 4655–4680 (2015).
41. Omar, S. H. Oleuropein in olive and its pharmacological effects. *Scientia Pharm.* **78**, 133–154 (2010).
42. Rigacci, S. *et al.* Oleuropein aglycon prevents cytotoxic amyloid aggregation of human amylin. *J. Nutr. Biochem.* **21**, 726–735 (2010).
43. Rigacci, S. *et al.* Aβ(1-42) Aggregates into non-toxic amyloid assemblies in the presence of the natural polyphenol Oleuropein Aglycon. *Curr. Alzheimer Res.* **8**, 841–852 (2011).
44. Daccache, A. *et al.* Oleuropein and derivatives from olives as Tau aggregation inhibitors. *Neurochem. Intern.* **58**, 700–707 (2011).
45. Leri, M. *et al.* The polyphenol Oleuropein aglycone hinders the growth of toxic transthyretin amyloid assemblies. *J. Nutr. Biochem.* **30**, 153–166 (2016).
46. Rigacci, S. & Stefani, M. Nutraceutical properties of olive oil polyphenols. An itinerary from cultured cells through animal models to humans. *Intern. J. Mol. Sci.* **17**, 843 (2016).
47. Casamenti, F. & Stefani, M. Olive polyphenols: New promising agents to combat aging-associated neurodegeneration. *Ex. Rev. Neurother.* **17**, 345–358 (2017).
48. Gill, S. G. & von Hippel, P. H. Calculation of protein extinction coefficients from amino acid sequence data. *Anal. Biochem.* **182**, 319–326 (1989).
49. LeVine, H. Quantification of beta-sheet amyloid fibril structures with Thioflavin T. *Met. Enzymol.* **309**, 274–284 (1999).
50. Hawe, A., Sutter, M. & Jiskoot, W. Extrinsic fluorescent dyes as tools for protein characterization. *Pharm. Res.* **25**, 1487–1499 (2008).
51. Mosmann, T. Rapid colorimetric assay for cellular growth and survival: application to proliferation and cytotoxicity assays. *J. Immunol. Met.* **65**, 55–56 (1983).
52. Nosi, D. *et al.* A molecular imaging analysis of Cx43 association with Cdo during skeletal myoblast differentiation. *J. Biophotonics* **6**, 612–621 (2013).
53. Gutierrez-Rosales, F., Romero, P. M., Casanovas, M., Motilva, J. M. & Mínguez-Mosquera, I. M. Metabolites involved in Oleuropein accumulation and degradation in fruits of Olea europaea L. Hojiblanca and Arbequina Varieties. *J. Agric. Food Chem.* **58**, 12924–12933 (2010).
54. Spillantini, M. G., Crowther, R. A., Jakes, R., Hasegawa, M. & Goedert, M. Alpha-Synuclein in filamentous inclusions of Lewy bodies from Parkinson's disease and dementia with Lewy bodies. *Proc. Nat. Acad. Sci. USA* **95**, 6469–6473 (1998).
55. Uversky, V. N., Li, J. & Fink, A. L. Evidence for a partially folded intermediate in α-synuclein fibril formation. *J. Biol. Chem.* **276**, 10737–10744 (2001).
56. Ebeling, W. *et al.* Proteinase K from Tritirachium album Limber. *Eur. J. Biochem.* **47**, 91–97 (1974).
57. Fontana, A. *et al.* Probing protein structure by limited proteolysis. *Acta Biochim. Pol.* **51**, 299–321 (2004).
58. Polverino de Laureto, P. *et al.* Protein aggregation and amyloid fibril formation by an SH3 domain probed by limited proteolysis. *J. Mol. Biol.* **334**, 129–141 (2003).
59. Canale, C., Oropesa-Nunez, R., Diaspro, A. & Dante, S. Amyloid and membrane complexity: the toxic interplay revealed by AFM. *Semin. Cell Dev. Biol.* **73**, 82–94 (2018).
60. Walsh, P. *et al.* The mechanism of membrane disruption by cytotoxic amyloid oligomers formed by PrP(106–126) is dependent on bilayer composition. *J. Biol. Chem.* **289**, 10419–10430 (2014).
61. Wakabayashi, M. & Matsuzaki, K. Ganglioside-induced amyloid formation by human islet amyloid polypeptide in lipid rafts. *FEBS Lett.* **583**, 2854–2858 (2009).
62. Leri, M. *et al.* Molecular insights into cell toxicity of a novel familial amyloidogenic variant of β2-microglobulin. *J. Cell. Mol. Med.* **20**, 1443–1456 (2016).
63. Van Maarschalkerweerd, A., Vetri, V., Langkilde, A. E., Foderà, V. & Vestergaard, B. Protein/lipid coaggregates are formed during α-synuclein-induced disruption of lipid bilayers. *Biomacromol.* **15**, 3643–3654 (2014).
64. Hong, D. P., Fink, L. A. & Uversky, N. V. Structural characteristics of α-synuclein oligomers stabilized by the flavonoid baicalein. *J. Mol. Biol.* **383**, 214–223 (2008).
65. Lorenzen, N. *et al.* How Epigallocatechin Gallate can inhibit α–synuclein oligomer toxicity *in vitro*. *J. Biol. Chem.* **289**, 21299–21310 (2014).
66. Sano, K. *et al.* Prion-Like Seeding of Misfolded α-Synuclein in the Brains of Dementia with Lewy Body Patients in RT-QUIC. *Mol. Neurobiol.* https://doi.org/10.1007/s12035-017-0624-1 (2017).

67. Danzer, K. M., Krebs, S. K., Wolff, M., Birk, G. & Hengerer, B. Seeding induced by alpha-synuclein oligomers provides evidence for spreading of alpha-synuclein pathology. *J. Neurochem.* **111**, 192–203 (2009).
68. Bemporad, F. & Chiti, F. Protein misfolded oligomers: experimental approaches, mechanism of formation, and structure-toxicity relationships. *Chem Biol.* **19**, 315–327 (2012).
69. Frare, E. *et al*. Identification of the core structure of lysozyme amyloid fibrils by proteolysis. *J. Mol. Biol.* **361**, 551–561 (2006).
70. Nardi, M. *et al*. Synthesis and antioxidant evaluation of lipophilic oleuropein aglycone derivatives. *Food Funct.* **8**, 4684–4692 (2017).
71. Rizzoa, M. *et al*. Antioxidant activity of oleuropein and semisynthetic acetyl-derivatives determined by measuring malondialdehyde in rat brain. *J. Pharm. Pharmacol.* **69**, 1502–1512 (2017).
72. Esteban-Martin, S., Silvestre-Ryan, J., Bertoncini, W. C. & Salvatella, X. Identification of fibril-like tertiary contacts in soluble monomeric α–synuclein. *Biophys. J.* **105**, 1192–1198 (2013).
73. Dedmon, M. M., Lindorff-Larsen, K., Christodoulou, J., Vendruscolo, M. & Dobson, C. M. Mapping long-range interactions in alpha-synuclein using spin-label NMR and ensemble molecular dynamics simulations. *J. Am. Chem. Soc.* **127**, 476–477 (2005).

Acknowledgements

This project was supported by Ente Cassa di Risparmio di Firenze (N 2015.1002A2202.3931) and by Progetti di Ateneo-University of Padova 2017-N. C93C1800002600. M.L. was supported by grant from AIRAlzh Onlus financed by ANCC-COOP (Reg. no. 0043966. 30–10–2014). We thank Alessandra Carrer for help in the experiments and Dr. Marino Bellini for technical assistance.

Author Contributions

P.P.D.L. and M.B. conceived and supervised the project; L.P., E.B., G.B. and M.L. designed and performed the experiments; L.P., E.B., G.B., M.L., M.B. and P.P.D.L. analysed the data; M.B. and P.P.D.L. wrote the paper; M.S. critically revised the paper. All authors analysed the results and approved the final version of the manuscript.

Additional Information

Supplementary information accompanies this paper at https://doi.org/10.1038/s41598-018-26645-5.

Competing Interests: The authors declare no competing interests.

Publisher's note: Springer Nature remains neutral with regard to jurisdictional claims in published maps and institutional affiliations.

PLOS ONE

RESEARCH ARTICLE

The influence of N-terminal acetylation on micelle-induced conformational changes and aggregation of α-Synuclein

David Ruzafa[1], Yuriko S. Hernandez-Gomez[1], Giovanni Bisello[1], Kerensa Broersen[2], Bertrand Morel[1], Francisco Conejero-Lara[1]*

1 Departamento de Química Física e Instituto de Biotecnología, Facultad de Ciencias, Universidad de Granada, Granada, Spain, **2** Nanobiophysics Group, MIRA Institute for Biomedical Technology and Technical Medicine, Faculty of Science and Technology, Universiteit Twente, Enschede, The Netherlands

* conejero@ugr.es

Citation: Ruzafa D, Hernandez-Gomez YS, Bisello G, Broersen K, Morel B, Conejero-Lara F (2017) The influence of N-terminal acetylation on micelle-induced conformational changes and aggregation of α-Synuclein. PLoS ONE 12(5): e0178576. https://doi.org/10.1371/journal.pone.0178576

Editor: Stephan N. Witt, Louisiana State University Health Sciences Center, UNITED STATES

Received: February 25, 2017

Accepted: May 15, 2017

Published: May 31, 2017

Data Availability Statement: All relevant data are within the paper and its Supporting Information files.

Funding: This research was funded by Grants BIO2009-07317 and BIO2013-40697-R from the Spanish Ministry of Economy and Competitivity (http://www.mineco.gob.es), Grant FQM-02838 from the Andalusian Government (http://www.juntadeandalucia.es), Grant PP2012-PI06 from the Research Program of the University of Granada (http://investigacion.ugr.es) and by the European

Abstract

The biological function of α-Synuclein has been related to binding to lipids and membranes but these interactions can also mediate α-Synuclein aggregation, which is associated to Parkinson's disease and other neuropathologies. In brain tissue α-Synuclein is constitutively N-acetylated, a modification that plays an important role in its conformational propensity, lipid and membrane binding, and aggregation propensity. We studied the interactions of the lipid-mimetic SDS with N-acetylated and non-acetylated α-Synuclein, as well as their early-onset Parkinson's disease variants A30P, E46K and A53T. At low SDS/protein ratios α-Synuclein forms oligomeric complexes with SDS micelles with relatively low α-helical structure. These micellar oligomers can efficiently nucleate aggregation of monomeric α-Synuclein, with successive formation of oligomers, protofibrils, curly fibrils and mature amyloid fibrils. N-acetylation reduces considerably the rate of aggregation of WT α-Synuclein. However, in presence of any of the early-onset Parkinson's disease mutations the protective effect of N-acetylation against micelle-induced aggregation becomes impaired. At higher SDS/protein ratios, N-acetylation favors another conformational transition, in which a second type of α-helix-rich, non-aggregating oligomers become stabilized. Once again, the Parkinson's disease mutations disconnect the influence of N-acetylation in promoting this transition. These results suggest a cooperative link between the N-terminus and the region of the mutations that may be important for α-Synuclein function.

Introduction

Parkinson's disease (PD) is the most common neuronal motor system disorder affecting more than 1% of the population aged over 65 [1]. PD is characterized by the loss of dopaminergic neurons in the "*substantia nigra*" and the appearance of intraneuronal inclusions known as Lewy bodies, which are composed principally by fibrillar amyloid aggregates of proteins. α-Synuclein (aS) is the major component in these aggregates [2]. A genetic link between PD and

Regional Development Fund of the European Union.

Competing interests: The authors have declared that no competing interests exist.

aS was also established with the discovery of several missense mutations, corresponding to A30P, E46K and A53T substitutions, in the gene SNCA encoding for aS in kindreds with autosomal-dominantly inherited, early-onset PD [3–5]. Other pathogenic mutations have also been reported more recently [6,7]. A variety of environmental and physiological factors can induce aS self-assembly into oligomers and aggregates, some of which are highly neurotoxic, leading to PD and other neurodegenerative disorders [8,9].

aS is a 140-residue protein widely expressed in brain cells and particularly abundant at the presynaptic terminals of neurons [10]. Its sequence comprises a N-terminal domain, which contains seven imperfect 11-residue lipid-binding repeats, and a C-terminal highly acidic tail. Accumulating evidence relates aS function to a variety of interactions with lipids and membranes. This protein seems to modulate presynaptic vesicle pool size and vesicle recycling and participates in the regulation of synaptic plasticity and dopamine neurotransmission [11]. It also participates in the transport and regulation of polyunsaturated fatty acids (PUFAs) in dopaminergic neurons [12,13], sequestration of arachidonic acid in exocytosis regulation [14], and induction of curvature and remodeling of membranes [15–17].

Although native soluble aS has been considered for many years to be an intrinsically disordered protein [18,19], it acquires α-helical structure upon binding to membranes [20], micelles [21,22] or PUFAs [23,24]. This suggests an important role for this helical structure in aS function. Diverse studies with model micelles and membranes have described that, depending on the surface curvature, aS can adopt different α-helical conformations in its membrane bound state, including an extended helix [20,25], a curved helix [26], or a helix-turn-helix hairpin conformation [21,27]. On the other hand, the influence of lipid interaction on aS aggregation is complex and whether lipids and membranes favor or inhibit formation of toxic oligomers and amyloid fibrils depends on the aS/lipid proportion and the environmental context [28–30].

The anionic surfactant sodium dodecyl sulfate (SDS) has been widely used in biophysical studies to mimic lipid interactions with proteins and to study its effects on protein aggregation [31–33]. Previous studies have shown that SDS can strongly enhance aS fibrillation at relatively low SDS/aS ratios, whereas formation of α-helical structure and interaction with bulk SDS micelles protects from fibrillation [34–36].

The N-terminal region of aS has been described to play a crucial role in the interaction of aS with lipid membranes [37,38]. N-terminal acetylation increases helical propensity of the N-terminal region of aS in its free monomeric state [39]. It also enhances helical structure of aS in the bound state to SDS micelles or negatively charged lipid micelles, as well as affinity for physiological membranes [40,41]. In addition, it has been observed that N-acetylation reduces the aS fibrillation rate by *in vitro* incubation in buffer under shaking conditions [39,42], as well as in the presence of lipid vesicles containing GM1 ganglioside [40]. Despite the evidence that N-acetylated aS (Ac-aS) is universally present *in vivo*, in both the soluble and insoluble fractions of brain tissues of PD patients [43], most *in vitro* biophysical studies of aS aggregation and micelle and membrane interaction have been made with recombinant non-acetylated aS. It is therefore important to increase our understanding of how aS modifications such as N-acetylation and early-onset PD mutations affect the interplay between aS conformational changes, lipid interactions oligomerization and aggregation propensity.

Here we used a variety of biophysical methods to analyze the effects of the interactions with SDS on the structure, oligomerization and amyloid aggregation of aS and Ac-aS. We show that both aS and Ac-aS variants bind and stabilize diverse micellar SDS-aS complexes. In this process, the proteins acquire several interconverting conformational/oligomerization states at different SDS/protein ratios. N-acetylation and early-onset PD mutations alter significantly the equilibrium between these states in different ways, changing the propensity of aS to

oligomerize and aggregate. The results suggest the existence of a cooperative link between the N-terminus and the regions of PD mutations than may play an important role for aS function.

Materials and methods

Protein production and purification

The different aS variants were produced by overexpression in *E.Coli* modified with the plasmid containing the respective sequences. To obtain the respective N-acetylated form, the N-terminal acetyl-transferase B (NatB) plasmid was added to the cells together with 5 μg/mL chloramphenicol to the culture media [44]. The cells were cultured in LB media in the presence of 100 μg/mL of ampicillin at 37˚C with shaking until an optical density at 600 nm of 0.6–0.8. Protein expression was induced by adding isopropyl 1-thio-β-D-galactopyranoside to a final concentration of 50 μg/mL (0.2 mM) for 4 h. The cells were harvested by centrifugation at 2200 g for 10 min at 4˚C. The pellets were resuspended in buffer (25 mM Tris, 1 mM EDTA, 0.1 mM DTT, pH 7.4, 1 x protease inhibitor mixture (Roche, Penzberg, Germany) and lysed by ultrasonication. The lysate was ultracentrifuged at 105000 g for 45 min at 4˚C. The supernatant was filtered (0.45 μm) and applied onto a HiTrap QFF anion-exchange column (GE Healthcare, Chicago, Illinois) previously equilibrated in buffer (50 mM Tris, 0.1 mM DTT, pH 7.4). The protein was eluted using a NaCl gradient of (0–500 mM). After analysis by SDS-PAGE, the pooled protein fractions were precipitated with ammonium sulfate at 47.5% of saturation and the suspension was ultracentrifuged at 105000 g for 30 min at 4˚C. The precipitate was resuspended (50 mM Tris, 50 mM NaCl, 0.1 mM DTT, pH 8.3, containing 8M urea) and injected onto a HiLoad 26/60 Superdex 200 column (GE Healthcare, Chicago, Illinois). Subsequently, the protein fractions were pooled and dialyzed extensively against the same buffer in the absence of urea. Then, the protein was concentrated (Amicon ultracentrifugal filter units MWCO 3.000, Millipore, Billerica, Massachusetts) and injected onto a HiLoad 26/60 Superdex 75 column (GE Healthcare, Chicago, Illinois). Pure pooled fractions were dialyzed against 20 mM HEPES, 0.05% NaN_3, pH 7.2, lyophilized and kept frozen at −20˚C. The purified proteins were >95% pure according to SDS-PAGE. The identity of each protein was assessed by electrospray mass spectrometry.

Circular dichroism

Far-UV CD measurements were performed at 25˚C with a Jasco J-715 spectropolarimeter (Tokyo, Japan) equipped with a thermostatic cell holder in a 0.2 mm path length cuvette. The protein concentration was 100 μM and SDS was added from a stock solution of 100 mM to a final concentration ranging between zero and 10 mM. The CD spectra were the average of 5 scans using a bandwidth of 1 nm and a scan speed of 100 nm/min. Baseline spectra were measured with buffer containing each SDS concentration and subtracted from the sample spectra. Data were normalized as mean residue ellipticity and the α-helix content was obtained using its value at 222 nm as described previously [45].

Dynamic light scattering

DLS measurements were performed at 25˚C using a DynaPro MS-X instrument (Wyatt Technology Corporation, Santa Barbara, CA, USA) in a thermostated 30 μL quartz cuvette. The protein solutions and the buffer were filtered through 0.02 μm Anotop 10 filters (Whatman plc, Brentford, Middlesex, UK) before the measurements. Sets of DLS data were acquired every 5 s until at least 20 sets of data were obtained. The measurements were performed in triplicate. Dynamics V6 software (Wyatt Technology Corporation, Santa Barbara, CA, USA) was used in data collection and processing. The experimental autocorrelation curves were analyzed to obtain the particle size distributions using the implemented regularization fit.

Size-exclusion chromatography

SEC experiments were carried out at room temperature on a Superdex 200 10/300 GL column (GE Healthcare, Chicago, Illinois) at a flow rate of 0.5 mL/min, equilibrated in 20 mM HEPES, 0.05% NaN_3, pH 7.2, including the appropriate SDS concentration. The column was first calibrated with protein standards of different molecular weight. The aS and Ac-aS samples were freshly prepared in the same buffer, containing the desired SDS concentration at a protein concentration of 100 μM and filtered through 0.02 μm Anotop 10 filters (Whatman plc, Brentford, Middlesex, UK).

Measurement of aggregation rates by thioflavin T fluorescence

Amyloid aggregation was monitored at 37˚C by thioflavin T (ThT) fluorescence using a Varian Cary Eclipse spectrofluorimeter (Agilent Technologies, Santa Clara, CA, USA) equipped with a Peltier-controlled thermostatic cell holder. Protein samples at a final concentration of 100 μM were freshly prepared in 20 mM HEPES, 0.05% NaN_3, pH 7.2, containing 10 μM ThT and the appropriate SDS concentration. To avoid evaporation during the experiments, the cuvette was sealed using a specific stopper.

NMR spectroscopy

NMR experiments were performed on a Varian Direct Drive 600 MHz spectrometer (California, USA) at 25˚C. For each experiment samples were freshly prepared in deuterium oxide at a protein concentration of 100 μM in 5 mM sodium phosphate buffer, 0.05% sodium azide, pH 7.2, containing the desired SDS concentration. Diffusion-ordered spectroscopy (DOSY) spectra were obtained using a gradient length of 3 ms and a diffusion delay of 250 ms. Gradient strength was previously calibrated using the HDO signal in a doped D_2O standard. The DOSY data sets were composed by 30 gradient strengths with 128 scans every increment. The DOSY data were processed using MestreNova 10.0 (Mestrelab Research S.L, Spain). Diffusion coefficients were obtained by fitting the intensity decays versus the gradient strength as described elsewhere [46]. The hydrodynamic radii were calculated with the Stokes-Einstein equation, $R_h = k_BT/6\pi\eta D$, where k_B is the Boltzmann constant, T is the absolute temperature, D is the diffusion coefficient and η is the viscosity of D_2O at 298 K.

Transmission electron microscopy

The morphology of aS aggregates was studied using a Carl Zeiss LEO 906E transmission electron microscope (Zeiss, Oberkochen, Germany). Freshly prepared protein samples were previously incubated at 37˚C for different time periods in the presence of several SDS concentrations. 10 μL of the incubated protein solution were left to adsorb on a Formvar 300-mesh copper grid (ANAME, Madrid, Spain) for 1 minute. Then, the sample was negatively stained with 10 μL of 1% (w/v) uranyl acetate solution for 1 minute without previous washing steps. Excess stain was removed with a tissue paper and the grids were air dried before visualization. The samples were observed at a magnification between 60000× and 100000×.

Results

Conformational transitions of aS induced by SDS

The structural changes of 100 μM wild-type (WT) aS and Ac-aS induced by SDS were observed by CD spectroscopy at 25˚C varying the SDS concentration from zero to 10 mM. Under the conditions of this study (20 mM HEPES, pH 7.2, 25˚C), the critical micellar concentration (CMC) of SDS was determined by scattering measurements to be 6.4 ± 0.6 mM (S1 Fig),

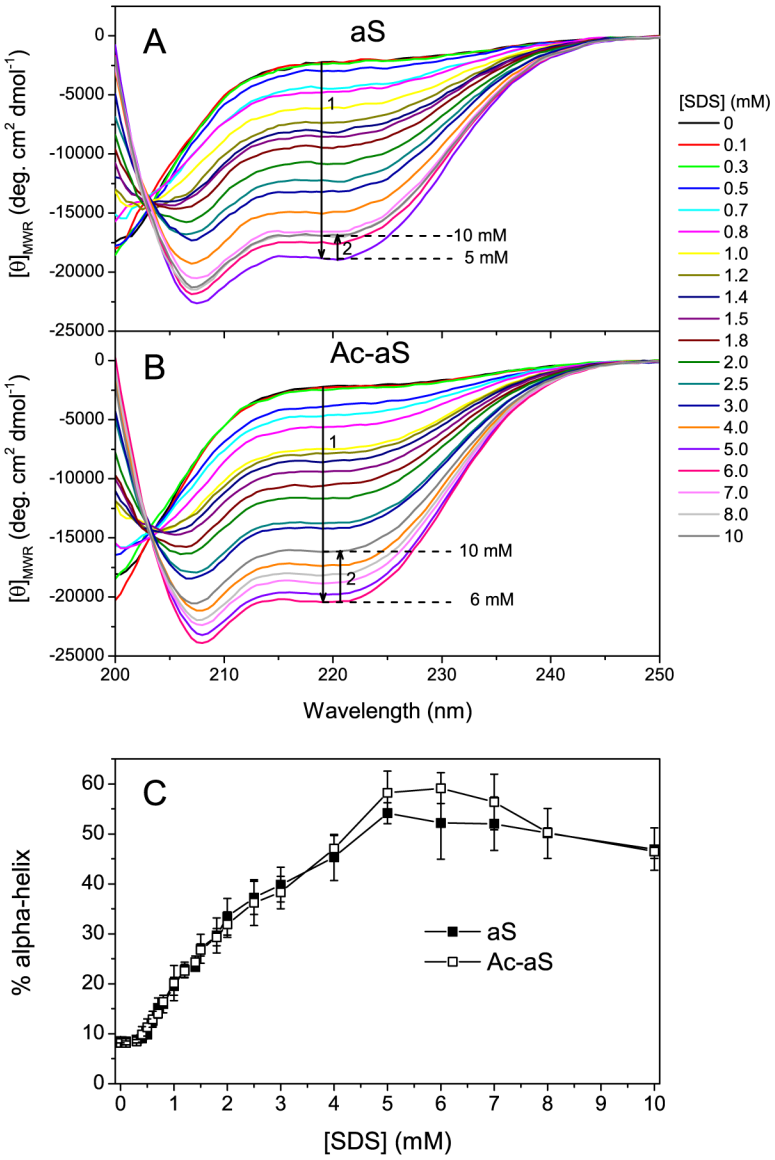

Fig 1. Effect of SDS on the secondary structure of aS and Ac-aS. (A and B) Far-UV CD spectra were recorded at 25˚C in 20 mM HEPES buffer pH 7.2, in presence of increasing SDS concentrations for aS (A) and Ac-aS (B). The protein concentration was 100 μM in all measurements. The spectra were normalized to mean residue molar ellipticity. (C) Percentage of α-helix structure of 100 μM aS (filled symbols) and Ac-aS (open symbols) at different SDS concentrations. The values have been calculated from the mean residue ellipticity at 222 nm measured in the far-UV CD spectra [45]. The error bars correspond to at least two independent measurements.

https://doi.org/10.1371/journal.pone.0178576.g001

analogous to the value of 7.5 mM reported elsewhere under similar conditions but pH 7.0 [34]. We chose this low ionic strength buffer in order to attain a relatively wide sub-CMC SDS concentration range, since previous studies have shown that binding of helical aS to bulk SDS micelles protects it from aggregation [36]. Below 0.3 mM SDS the two aS variants are mostly unstructured as previously observed, with an estimated 8% α-helix, indicating some α-helical propensity (Fig 1). Above 0.4–0.5 mM SDS there is a gradual formation of α-helical structure produced by SDS. The data suggest three structural transitions. First, between 0.4 mM and

about 3 mM SDS the α-helix percent increases gradually to about 40%. In this SDS concentration range the changes are very similar for aS and Ac-aS. Second, between 3 and 5 mM SDS the α-helicity increases slightly more steeply and reaches a maximum. This maximum appears slightly more pronounced for N-acetylated aS although the difference is not statistically significant. Third, between 7 mM and 10 mM SDS the α-helical structure decreases again to about 45%. Similar conformational transitions were observed in a previous study for aS [36].

Formation of SDS-aS oligomeric complexes

To investigate the changes in molecular size of aS and Ac-aS as a result of their interaction with SDS, we analyzed the mixtures by dynamic light scattering (DLS) (Fig 2). In the absence of SDS, both aS and Ac-aS show identical hydrodynamic radius (R_h) of 2.6 ± 0.1 nm, in agreement with compact disordered aS [47]. Between zero and 0.3 mM SDS the apparent R_h does not change significantly for most of the protein mass and only trace amounts of oligomers and large aggregates could be detected. Between 0.4 mM and 0.8 mM SDS, a significant and increasing fraction of the proteins form particles with apparent R_h ranging between 5 and 9 nm, which may be attributed to SDS-associated aS oligomers. These oligomers could be discerned from the aS monomers only in some of the DLS measurements, whereas in others the two different sizes could not be resolved, resulting in an averaged R_h. This may be due to a limited resolving power of DLS for these size differences but is also possible that the time scale of DLS (μs to ms) may be close to that of this oligomerization equilibrium. The fraction of protein mass that forms oligomers increases rapidly for both variants with a rise in SDS concentration, with concomitant reduction in the monomer fraction. From 1 mM to 3 mM SDS, a single average R_h value could only be measured for both proteins, reaching about 4.5 nm between 0.8 mM and 1.5 mM SDS and then decreasing gradually to about 3 nm at ∼3 mM SDS for Ac-aS and at ∼4 mM for aS. This suggests a reduction in the number of aS molecules in each SDS-aS complex but it could also indicate a more compact conformation of aS in the bound state, as a result of a higher α-helical content, as observed by CD. In fact, the average α-helix content of both Ac-aS and aS increases up to about 40% at these SDS concentrations.

More prominent differences between the two protein variants were found in the 4–10 mM SDS concentration interval. A second increase in the apparent R_h takes place between 3 and 6 mM SDS for Ac-aS. This is again a result of exchange between two types of particles of different sizes that could be resolved in some DLS measurements. A maximum average R_h of 4 nm is observed for Ac-aS between 5 and 6 mM SDS, coincidently with the maximum α-helical percentage, and is followed by a further R_h decrease to about 2.5 nm at the highest SDS concentration investigated (10 mM). These results indicate that self-association of protein-SDS complexes to form larger particles involves an additional α-helical conformational change in Ac-aS. This second oligomerization process is considerably less pronounced for non-acetylated aS.

Free SDS and aS are in rapid exchange with SDS-aS oligomeric complexes

The protein-SDS mixtures were also analyzed by size-exclusion chromatography (SEC) at different SDS concentrations (Fig 3). Unfortunately, the SDS concentration could be increased only up to 3 mM because SDS interacted with the column matrix at higher concentrations. In the absence of SDS, both monomeric aS and Ac-aS elute at volumes corresponding to a 36 kDa globular protein, in good agreement with the apparent hydrodynamic radii measured by DLS corresponding to a compact disordered protein. At 0.4 mM SDS a considerable peak broadening could be observed, suggesting exchange between the free monomer and SDS-

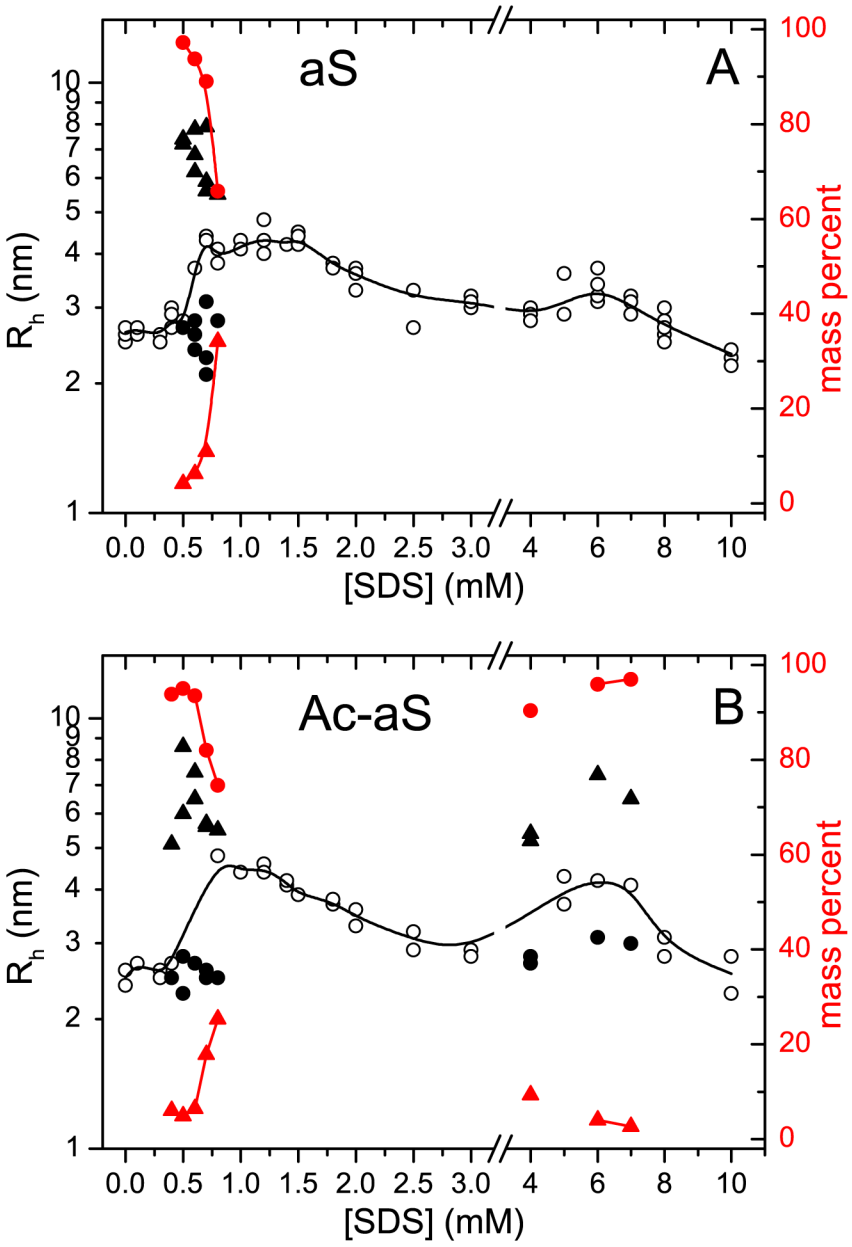

Fig 2. Changes in molecular size of aS (A) and Ac-aS (B) as a result of interactions with SDS. The apparent hydrodynamic radius (R_h) of 100 μM protein in presence of different SDS concentrations was measured by DLS at 25˚C. The black symbols represent the R_h of particles (left scale) corresponding to more than 2% of the protein mass and more than 10% of the scattered intensity. Measurements reporting two different particle sizes (circles and triangles) are represented with filled symbols. The black solid line corresponds to the intensity-averaged R_h at each SDS concentration. The red symbols represent the mass percent of each type of particle (right scale).

https://doi.org/10.1371/journal.pone.0178576.g002

bound protein oligomers. At higher SDS concentrations the proteins eluted at lower elution volumes and always as single peaks indicating fast exchange between aS monomers and aS-SDS oligomers. When aS was preincubated with SDS and then analyzed in pure buffer the protein eluted as monomer (not shown), which confirms that the SDS-protein interaction is rapidly reversible. No evidence of large aggregates eluting in the exclusion volume was

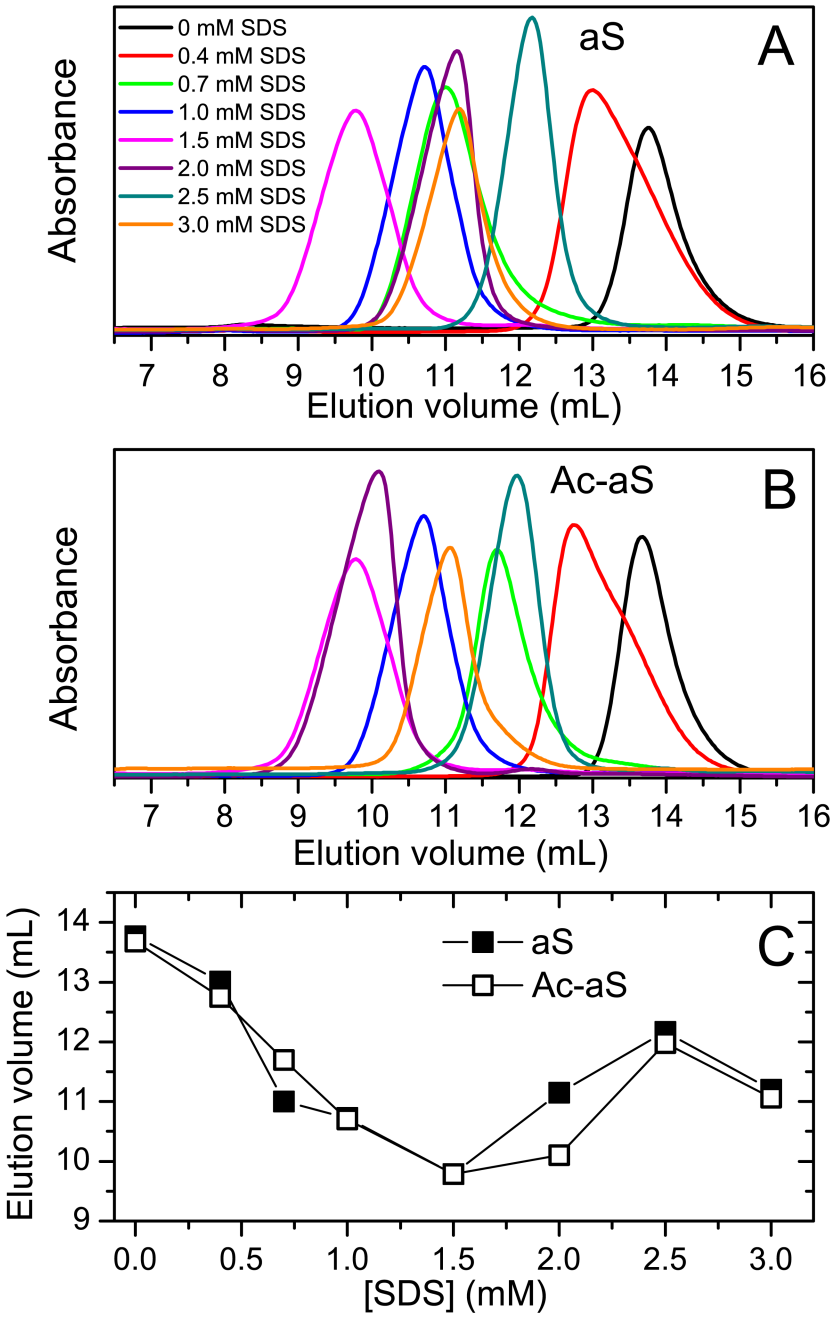

Fig 3. Hydrodynamic properties of aS and Ac-aS. Size-exclusion chromatography analysis aS (A) and Ac-aS (B) in presence of different SDS concentrations, as indicated in different colors. (C) Elution volumes of each peak maximum at each SDS concentration.

https://doi.org/10.1371/journal.pone.0178576.g003

observed under these conditions. The elution volumes changed in parallel for both proteins with the SDS concentration. The lowest elution volume was observed at 1.5 mM SDS corresponding to that of a globular protein of about 220 kDa.

1D ^{1}H-NMR spectra of the two aS variants were recorded at 25˚C at different SDS concentrations. To avoid interference from the intense resonances from the HEPES buffer, we used 5

mM sodium phosphate buffer pH 7.2 in 100% D_2O for these experiments. The ionic strength of this buffer (about 0.014 M) is similar to that of the HEPES buffer used in the rest of the experiments. Many protein resonances become broadened at SDS concentrations between 0.25 mM and 3.5 mM and sharpened again above 5 mM SDS (Fig 4). Particularly evident is the behavior of the well-resolved $H_{\varepsilon 1}$ resonance of the His50 side chain, which is considerably broadened and gradually downfield shifted between 7.7 and 8.5 ppm, as a result of the interactions with SDS. This is consistent with a moderately rapid exchange in the NMR time scale between the free protein and SDS-aS oligomeric complexes. The conformational change sensed by His50 is complete above 5 mM SDS. Another interesting observation is that below 2 mM there are no visible sharp resonances attributable to free monomeric SDS, as a result of strong line broadening. Above 3.5 mM the free SDS resonances start to emerge in the spectra, although still broadened, and their intensities increase linearly with the total SDS concentration. Signal integration around the position of the free SDS signals shows two separate trends with a sharp break around 4.5 mM (Fig 4C). These results indicate a maximum binding stoichiometry of about 40–50 SDS molecules per aS molecule, similar to that reported elsewhere [36]. At higher concentrations, SDS is in rapid exchange between SDS monomers, free SDS micelles and SDS-aS micellar complexes.

Diffusion-ordered spectroscopy (DOSY) ^{1}H-NMR measurements were carried out for each aS variant at 100 μM protein concentration in the presence of SDS from zero to 10 mM. The CMC of free SDS under these conditions was determined as 3.7 ± 0.3 mM by scattering measurements (S1 Fig) and 3.8 mM from DOSY measurements (Fig 5A). The diffusion coefficient of monomeric SDS is $(4.6 \pm 0.2) \times 10^{-10}$ m^2 s^{-1}, in good consistency with values ranging from 4.7 to 4.9×10^{-10} m^2 s^{-1}, as published elsewhere [48]. Above the CMC, monomeric SDS is in rapid exchange with micelles and its diffusion coefficient decreased progressively with an increase in concentration.

Translational diffusion coefficients were measured for aS and Ac-aS by fitting the decay of the intensity of the protein resonances with the gradient strength, using the integrals of spectral regions devoid of the influence of SDS signals, *i.e.*, the region between 6.5 and 7.5 ppm, corresponding to the aromatic protons, and the region between 1.7 and 3.2, in the aliphatic region. The diffusion coefficients of both proteins are represented in Fig 5A. The apparent hydrodynamic radii derived from these data are plotted in Fig 5B. In the absence of SDS the apparent R_h of the two proteins is consistent with their monomeric state. Above 0.5 mM SDS the R_h of the two proteins increases to about 5.5 nm at 1.25–1.5 mM SDS and then decreases to about 3 nm at 3.5 mM SDS, consistently with the observations by DLS. However, in contrast to DLS, monomeric and oligomeric particles could not be resolved in the DOSY experiments. The size increase starts at slightly lower SDS concentration for Ac-aS than for aS. At higher SDS concentrations there is another size increase for Ac-aS that is much less pronounced for aS, as it was observed by DLS. This confirms that Ac-aS shows a higher propensity than aS to form oligomeric complexes with SDS in the high SDS concentration range.

To estimate the diffusion coefficient of SDS in the mixtures we used the decays of the integrals of two spectral regions around the SDS signals, *i.e.*, the region between 4.5 and 3.2 ppm and the region between 1.6 and 0.4 ppm. Since these regions include both SDS and protein resonances, the signal decays were fitted using a double exponential function, fixing the diffusion coefficient of the protein to the values previously obtained from the spectral regions devoid of SDS resonances (S2 Fig). The diffusion coefficient of SDS (Fig 5A) decreases sharply between zero and 1 mM SDS and then fluctuates around $1.5–2.0 \times 10^{-10}$ m^2 s^{-1} for the rest of the SDS concentration range. These diffusion coefficients tend to converge with those measured for free SDS above its CMC. These data suggest that above 1 mM a major fraction of SDS becomes incorporated in aS-SDS micellar complexes.

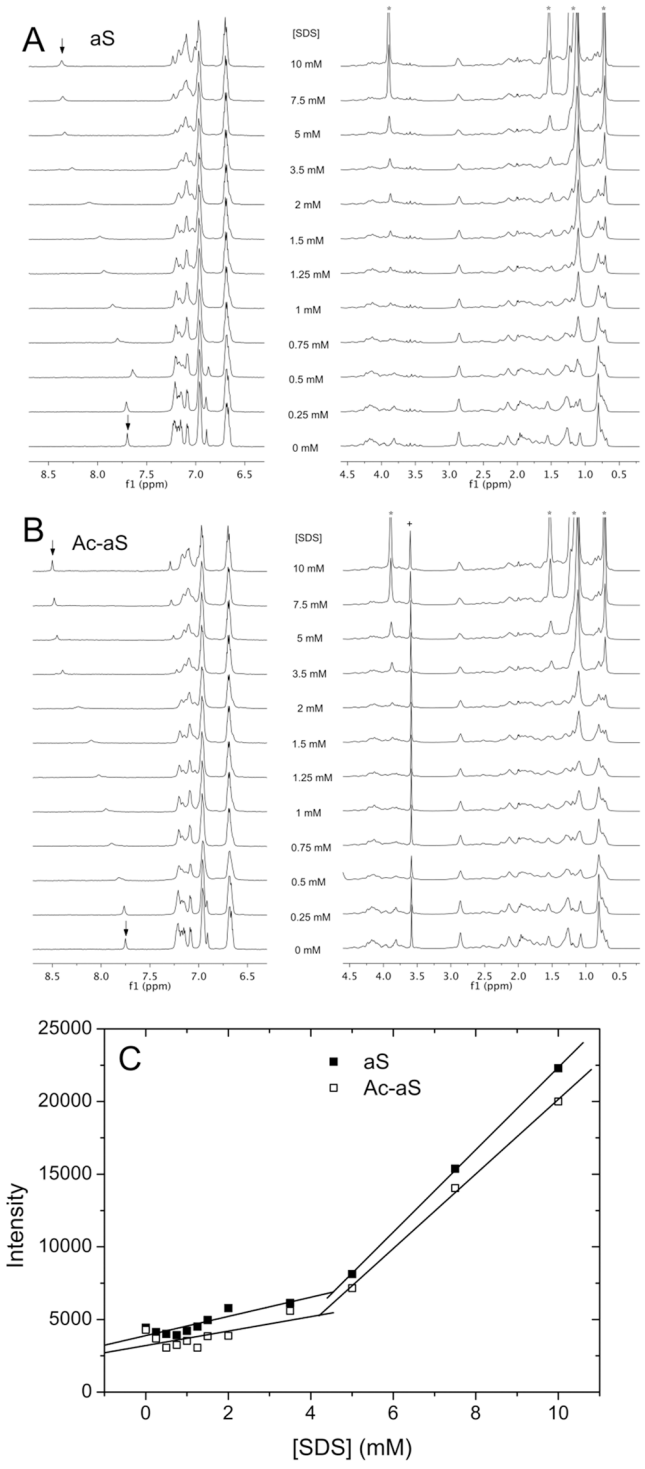

Fig 4. Effect of SDS on the NMR spectra of aS and Ac-aS. Aromatic and aliphatic regions of the 1D ^{1}H NMR spectra of aS (A) and Ac-aS (B) in 100% D_2O, 5 mM sodium phosphate buffer pH 7.2, in the presence of different SDS concentrations. Spectra were acquired at 25˚C at 100 μM protein concentration. The intensities of each spectral region have been adapted for proper visualization. The $H_{\varepsilon 1}$ resonance of the His50 is identified with arrows at 0 and 10 mM SDS. The signal marked with a cross corresponds to an impurity. The positions of the free SDS resonances have been marked with asterisks. (C) Signal intensity at the position of the resonance of α-methylene protons of free SDS at different SDS concentrations in presence of 100 μM aS and Ac-aS. The intensity values correspond to the integral of the spectra between 3.80 and 3.95 ppm.

https://doi.org/10.1371/journal.pone.0178576.g004

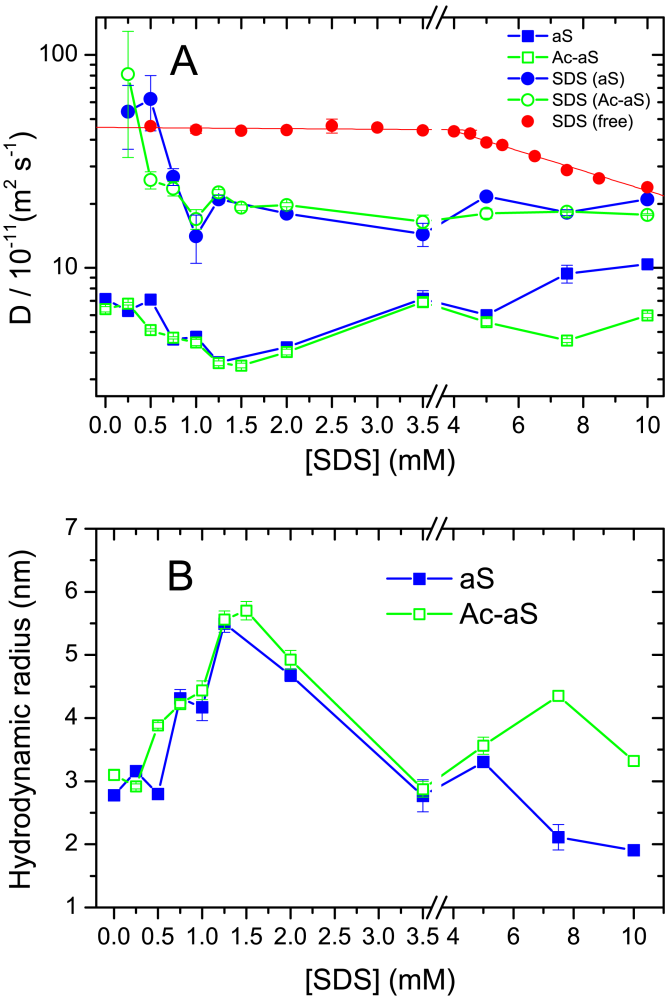

Fig 5. Hydrodynamic properties of SDS, aS and Ac-aS measured by DOSY NMR. (A) Diffusion coefficients of SDS, aS and Ac-aS in free SDS solutions and protein-SDS mixtures at different SDS concentrations. DOSY experiments were carried out at 25˚C in 100% D_2O, 5 mM sodium phosphate buffer pH 7.2. Protein concentration in the mixtures was 100 μM. Errors correspond to 95% confidence intervals of the fittings of the DOSY intensity decays. The CMC of SDS (3.8 mM) was estimated from the intercept of the two observed linear tendencies. (B) Apparent hydrodynamic radius of aS and Ac-aS in presence of different SDS concentrations calculated from the diffusion coefficients shown in (A).

https://doi.org/10.1371/journal.pone.0178576.g005

Rapid formation of amyloid oligomers and fibrils induced by SDS

To investigate how the N-terminal acetylation influences the aggregation of aS induced by SDS, we monitored the aggregation of both acetylated and non-acetylated aS variants in the presence of different SDS concentrations by thioflavin T (ThT) fluorescence. Aggregation kinetics were measured at 37˚C in 20 mM HEPES buffer pH 7.2 at a protein concentration of 0.1 mM under quiescent conditions (Fig 6). In the absence of SDS, neither of aS nor Ac-aS aggregated significantly for several weeks under our experimental conditions. However, low SDS concentrations ranging between 0.2 mM and 1.5 mM induced rapid aS aggregation (Fig 6A–6B). The initial slopes in the kinetics are representative of a rapid nucleation of amyloid structure [49]. The measured initial rates (Fig 6D) show however considerable variability in different sample preparations with identical SDS concentrations, resulting in large uncertainties. Nevertheless, aggregation of non-acetylated aS is significant above 0.3 mM SDS.

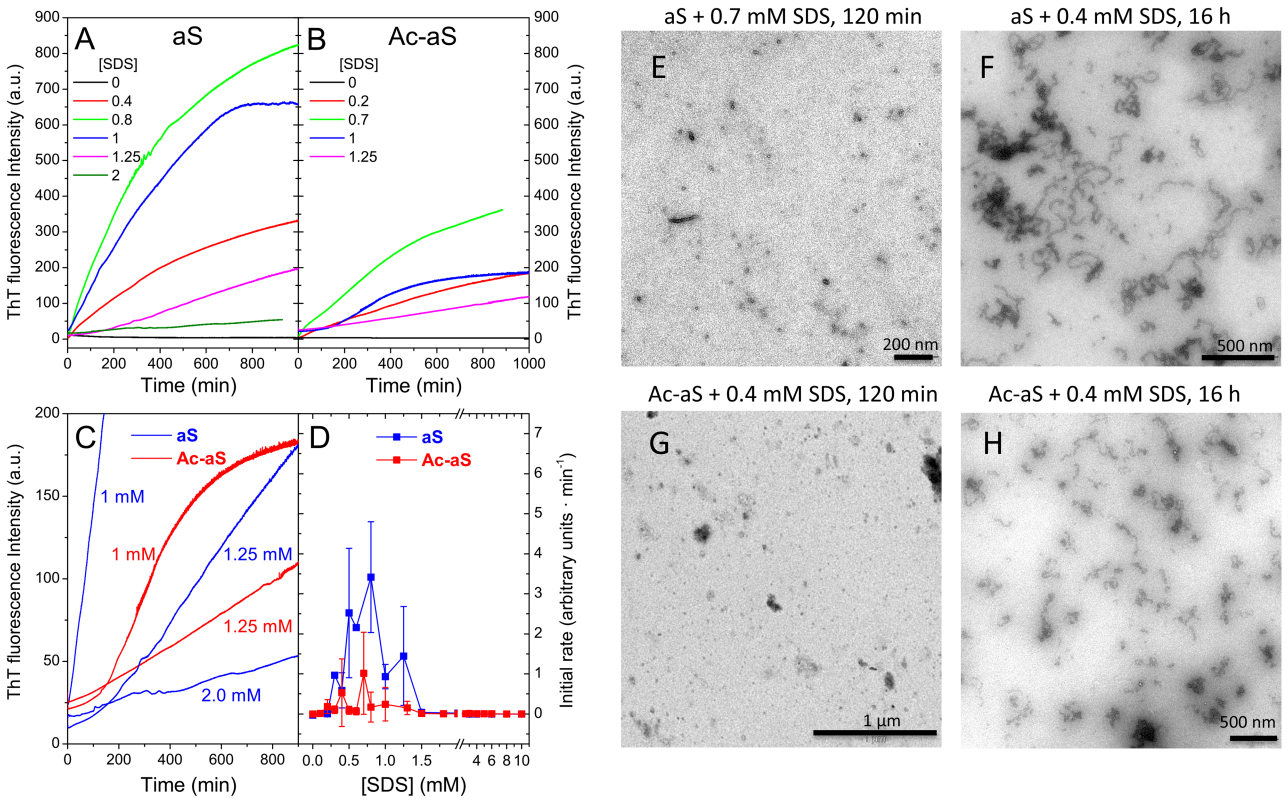

Fig 6. Amyloid aggregation induced by SDS. (A and B) Representative aggregation kinetics of aS (left panel) and Ac-aS (right panel) at 37˚C followed by ThT fluorescence in presence of different SDS concentrations. (C) Scale expansion of some of the kinetics showing incipient lag phases. Numbers alongside each trace indicate the SDS concentration for aS (blue) and Ac-aS (red). (D) Initial aggregation rates at 37˚C of WT aS and Ac-aS in presence of different SDS concentrations. The rates have been determined from the initial slopes of the ThT fluorescence kinetics. Error bars correspond to standard deviations from several independent measurements. (E-H) Transmission electron microscopy images of SDS-induced aggregates of aS (E and F) and Ac-aS (G and H). Samples at 100 μM concentration were incubated at 37˚C in presence of SDS during the times lengths and at the SDS concentrations indicated on top of each image.

https://doi.org/10.1371/journal.pone.0178576.g006

Maximum aggregation rates occur between 0.5–0.8 mM SDS and then decrease. At 1.25 mM SDS, an incipient lag phase becomes noticeable in the kinetics (Fig 6C). Above 2.5 mM SDS the aggregation rate is negligible. A similar tendency was observed for Ac-aS but the aggregation rates are considerably reduced compared to aS and some lag is perceptible at lower SDS concentrations (Fig 6C). For both protein variants, the maximum aggregation rates occur at SDS concentrations where monomeric aS coexists with large SDS-aS oligomeric complexes, suggesting that both states may contribute to productive formation of amyloid nuclei.

The morphology of the aS aggregates induced by SDS was analyzed by transmission electron microscopy (TEM) (Fig 6E–6H and S3–S5 Figs). At early time points during the aggregation kinetics, only small globular aggregates or clusters of them and few small protofibrils were observed for both proteins. Formation of these aggregates produced a rapid growth of ThT fluorescence, which indicates that they have amyloid structure. After 16 hours of incubation, more protofibrils and curly fibrils appear to develop by association of the globular aggregates. Longer and straighter fibrils grow after several weeks of incubation for both protein variants (S5 Fig). No clear differences in the morphology of the aggregates could be observed between aS and Ac-aS, although the progress of the fibril assembly under each condition seemed to be slower for the acetylated protein, in agreement with the ThT fluorescence experiments.

Effects of N-acetylation in early-onset PD variants

We also explored the influence of the early-onset PD mutations A30P, E46K and A53T, on the conformational changes and interactions of aS and Ac-aS induced by SDS by CD and DLS measurements. In the absence of SDS, all variants have a similar disordered structure and practically identical hydrodynamic radii. None of the mutations affects noticeably the growth of α-helical structure in the low SDS concentration range. The structural differences in the high SDS concentration range are however more remarkable. Both the acetylated and non-acetylated A53T variants acquire higher α-helix content between 4 mM and 10 mM SDS than the two WT variants (Fig 7). In contrast, the A30P variants show a more steady growth in α-helix structure than the WT forms and do not display a clear maximum in α-helix between 4 and 10 mM SDS. The E46K variants show a conformational behavior more analogous to the WT proteins.

According to our DLS analysis, all the PD variants form SDS-aS oligomers similar to the WT proteins between 0.4 mM and 4 mM SDS (Fig 8). The overall evolution of the averaged R_h with the SDS concentration is roughly similar for all the aS variants in this SDS concentration range, with only subtle differences. Similarly to the WT variants, at low SDS/aS concentration ratios two different particle sizes could be resolved in some DLS measurements, indicating coexistence of monomeric protein with large oligomeric SDS-protein complexes. This is particularly evident for the non-acetylated A53T aS variant. In contrast, the formation of α-helix-rich oligomers at high SDS concentrations is affected considerably by the mutations. The A53T mutation clearly promotes the formation of this type of oligomeric complexes to a similar extent as the WT Ac-aS, as evidenced by the transient increase in R_h, coincidently with the high content in α-helix observed for this variant in this concentration range. In contrast, none of the A30P variants showed a size increase in the 4–10 mM SDS concentration range, in agreement with the absence of transient α-helical increase. This indicates that the A30P mutation inhibits this transition irrespective of the presence or absence of N-acetylation. The E46K aS variant shows an intermediate behavior similar to the WT non-acetylated aS but in contrast to the WT protein the N-acetylation of this variant appears to reduce the oligomerization

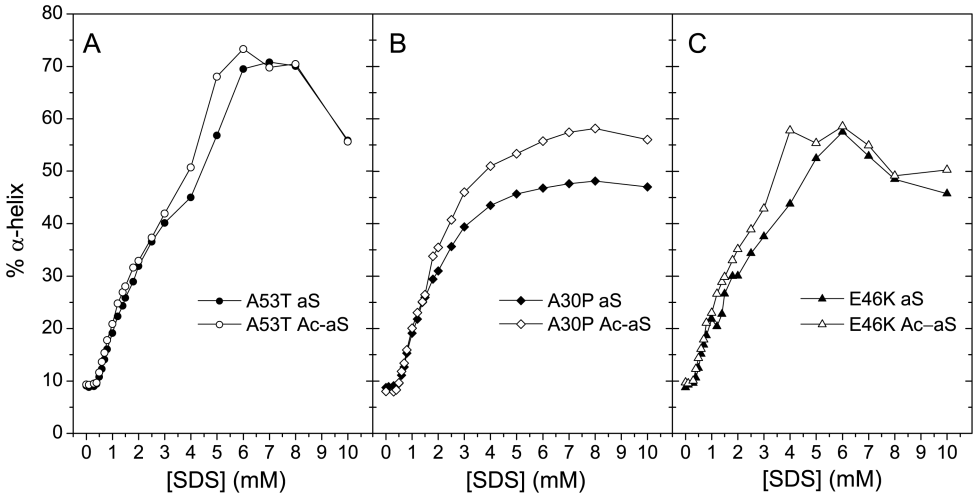

Fig 7. Changes in secondary structure in early-onset PD variants. Percentage of α-helix structure of early-onset PD variants of aS (filled symbols) and Ac-aS (open symbols) at different SDS concentrations. The values have been calculated from the mean residue ellipticity at 222 nm measured in the far-UV CD spectra [45].

https://doi.org/10.1371/journal.pone.0178576.g007

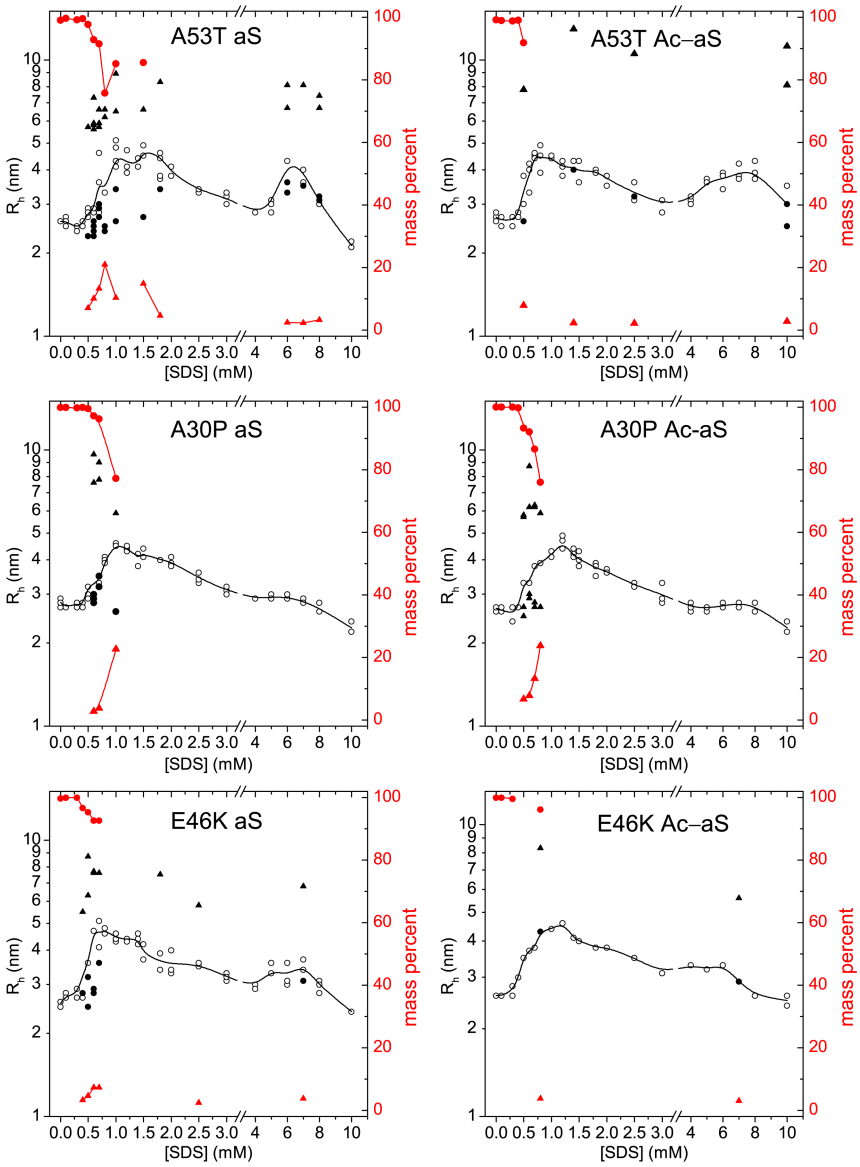

Fig 8. Changes in molecular size of early-onset PD variants. The apparent hydrodynamic radius (R_h) of 100 μM aS variants (left panels) or Ac-aS variants (right panels) in presence of different SDS concentrations was measured by DLS at 25˚C. The open symbols represent the R_h of particles (left scale) corresponding to more than 2% of the protein mass and more than 10% the scattered intensity. Measurements reporting two different particle sizes (circles and triangles) are represented in red. The black solid line corresponds to the intensity-averaged R_h at each SDS concentration. Closed symbols represent the mass percent of each type of particle (right scale).

https://doi.org/10.1371/journal.pone.0178576.g008

process. This suggests an antagonistic effect between the E46K mutation and the N-acetylation with regards to this oligomerization transition.

The aggregation rates of the early-onset PD variants in the presence of SDS were also measured by ThT fluorescence (Fig 9 and S6 Fig). Similar to the WT variants, most the aggregation kinetics show no lag phases but the initial aggregation rates varied considerably in measurements with carefully prepared identical experiments. Nevertheless, overall effects of the mutations could be observed. The maximum aggregation rates measured did not change

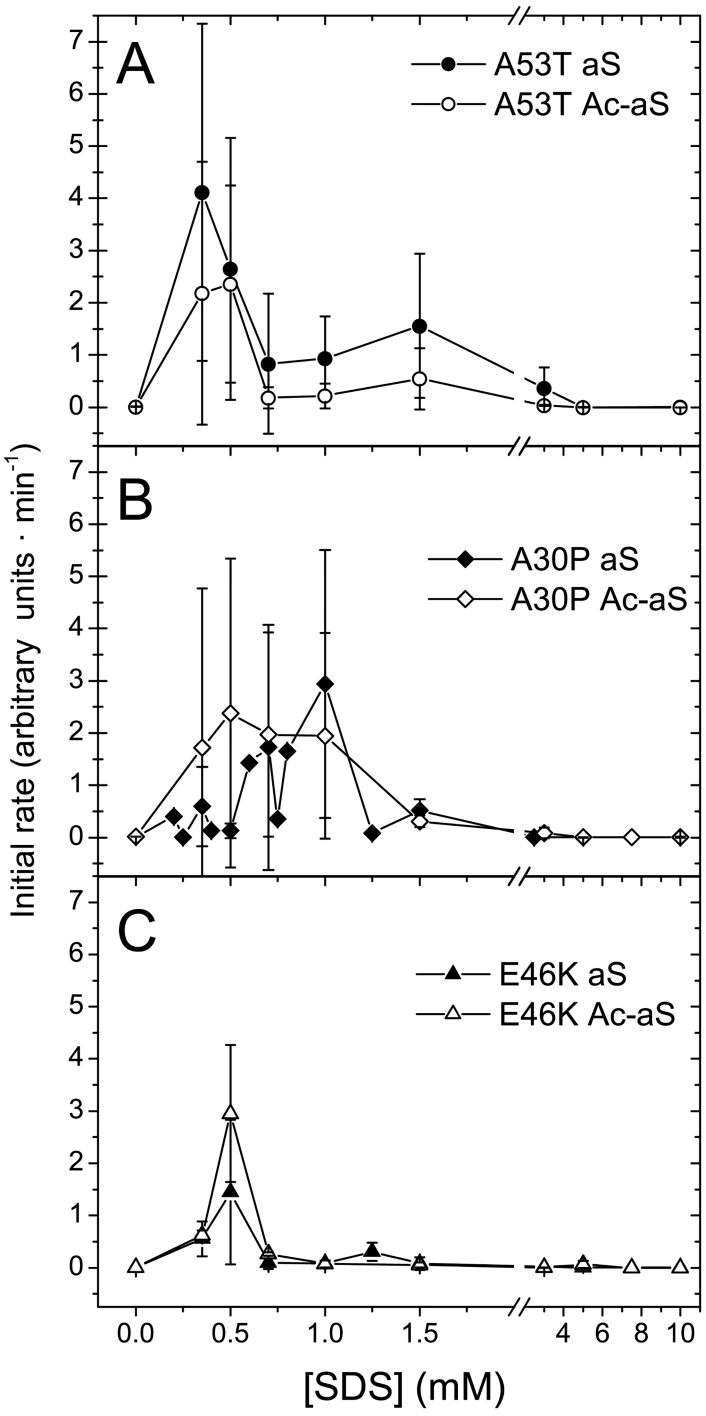

Fig 9. Amyloid aggregation rates of early-onset PD variants. Initial aggregation rates at 37˚C of aS and Ac-aS PD variants in presence of different SDS concentrations were measured by ThT fluorescence. The rates were determined from the initial slopes of the ThT fluorescence kinetics. Error bars correspond to standard deviations from several independent measurements.

https://doi.org/10.1371/journal.pone.0178576.g009

dramatically between the different variants but the SDS concentration range where significant aggregation occurs was markedly different. The fastest aggregation of the A53T aS variant occurred around 0.3–0.5 mM SDS, a concentration where a majority of the protein is monomeric. However, this variant aggregates over a broad range of SDS concentrations and significant aggregation remains even up to 3 mM SDS. This may be related to the coexistence of large oligomers and aS monomers over a relatively broad SDS concentration range as detected by DLS for the non-acetylated A53T variant (Fig 8). N-acetylation of the A53T variant appears to reduce only moderately the aggregation rates in the high SDS concentration range. The A30P variants aggregate in an intermediate range of SDS concentrations, whereas the two E46K variants only aggregate around 0.5 mM in a much narrower SDS concentration range than the other variants. No significant changes in aggregation propensity due to N-acetylation could be measured for these two variants. These results suggest that the protective effect of N-acetylation against micelle-induced aggregation observed for the WT proteins is considerably impaired for the PD variants.

Discussion

In this study we examined in detail the interactions between SDS and aS, both in its N-acetylated and non-acetylated forms. Many observations made in previous studies for WT non-acetylated aS [34,36,50,51] were confirmed here but we provided new evidence highlighting an essential role of oligomerization in a variety of interactions between aS and SDS, as well as in the SDS-mediated aS aggregation. Fig 10 shows a schematic cartoon illustrating the proposed conformational-oligomerization equilibria of aS and SDS at different SDS concentrations and explaining how the interactions with SDS micelles may induce or inhibit aS aggregation depending on the SDS/aS ratio.

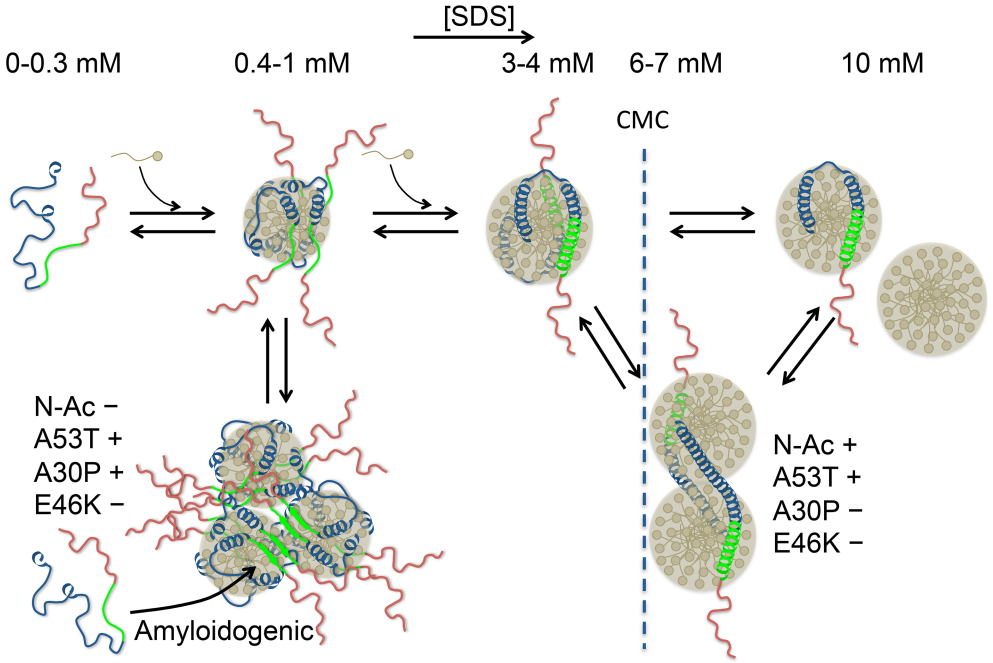

Fig 10. Schematic illustration of the proposed conformational-oligomerization equilibria of aS in the presence of different concentrations of SDS. The N-terminal lipid-binding region of aS is colored in blue, the NAC region in green and the acidic C-terminal tail in red. Spherical SDS micelles have been depicted for simplicity. The effect of N-acetylation and PD mutations on the amyloid aggregation rate and on the stability of α-helix-rich oligomers is indicated with + or − symbols.

https://doi.org/10.1371/journal.pone.0178576.g010

Under an SDS concentration threshold α-Synuclein remains as a compact disordered monomer irrespective of N-acetylation

In a low SDS concentration range (0–0.3 mM) all the aS variants studied are mainly unstructured and monomeric. Our DLS and DOSY data did not detect any size change in either aS or Ac-aS in this SDS concentration range. Moreover, the apparent diffusion coefficient of SDS was not significantly reduced in presence of the proteins at 0.25 mM SDS. Therefore, although monomeric aS may interact with SDS in this concentration range, this interaction is likely weak and unspecific and does not induce a detectable conformational change. In the absence of SDS, N-acetylation has been shown previously to increase the α-helical propensity at the first nine residues in WT aS and produce long-range perturbations at regions 28–31, 43–46 and 50–66 of the sequence [39]. These effects did not produce however any detectable changes in the size or overall conformation when comparing N-acetylated and non-acetylated aS variants. Nevertheless, these long-range links between conformational propensities of the N-terminus and the regions of the early-onset PD mutations have been proposed to be important in the fibrillation propensity of aS in the absence of SDS [52]. This is of interest because we observed high SDS-induced aggregation rates under conditions where a large fraction of aS is still monomeric, suggesting a key role of the monomer as substrate for aggregate growth. The importance of the ratio of monomeric to aggregated forms for productive amyloid fibril growth and neuronal toxicity has also been highlighted for β-amyloid peptide [53].

Mixed SDS-aS oligomeric amyloidogenic complexes form at low SDS/aS ratios

Above 0.4–0.5 mM and up to 0.8–1 mM SDS, depending on the aS variant, there was a rapid increase in the fraction of aS that becomes associated to SDS. This process resulted in an increase in the average molecular size and in the overall α-helix structure. Our results show that the maximum rate of formation of amyloid aggregates occurs when monomeric disordered aS is in exchange with a significant population of large oligomeric SDS-aS complexes where aS acquires partial α-helical structure. This supports the notion that aS clustering within these complexes may favor the conformational conversion necessary to nucleate the amyloid structure, which further grows by monomer incorporation. Supporting this view there is a recent study showing that rapid aS fibrillation is nucleated on the surface of negatively charged lipid vesicles [54]. This nucleation mechanism becomes enhanced by several orders of magnitude relative to other nucleation mechanisms likely due to a local concentration effect. However, productive aggregation appears to depend also on the availability of aS monomers, as inferred by the decrease in the rates of aggregation at SDS concentrations where monomeric aS is depleted favoring the SDS-aS complexes.

Given the key role of the SDS-aS oligomeric complexes in aggregation it is important to discuss about their nature. Even assuming that a large fraction of SDS is bound to aS under these conditions, a relatively low SDS/aS stoichiometry is conceivable in the oligomers formed between 0.5 and 1 mM SDS. Also, aS still has a low level of α-helix structure (<20%) in this SDS concentration range, which implies a relatively disordered protein in these micellar complexes. Ahmad et al. [34] also reported the formation of fibrillogenic SDS-aS ensembles below 2 mM SDS under conditions very similar to this study. In these complexes aS was described as partially structured and exposing significant hydrophobic surface according to the observed binding of bis-ANS. Giehm et al. [36] also described maximum aS fibrillation around 0.4–0.6 mM SDS. These authors proposed a model in which fibrillogenic complexes are formed by an average of 4 aS molecules associated to a micelle of 40–50 SDS molecules.

On the surface of such small micelles, 4 aS molecules are likely too crowded to acquire considerable α-helix structure and therefore remain relatively unstructured. The size of such a micellar complex would be however relatively small compared to the oligomers detected here by DLS. This suggests a self-association of SDS/aS micelles, likely mediated by hydrophobic collapse between unstructured aS regions and possibly involving the non-amyloid component (NAC) region. These clusters would provide a template facilitating intermolecular interactions leading to nucleation of amyloid structure by incorporation of existing aS monomers (Fig 10).

N-acetylation reduces the rate of amyloid nucleation but PD mutations impair this protective effect against aggregation

In our study N-acetylation did not appear to alter dramatically the conformational- oligomerization transitions in WT aS at low SDS concentrations. We could not detect significant changes in the onset of the formation SDS/aS complexes or in the growth of α-helical structure. However, we observed a clear reduction in the rate of amyloid aggregation induced by SDS as a result of N-acetylation. It is likely that subtle changes produced by N-acetylation on the conformational propensity and dynamics of the aS monomer could make it a poorer substrate for amyloid nucleation, as discussed above. Another possibility is that an increase in alpha-helical propensity at the N-terminal region produced by acetylation may become propagated through the aS chain to the NAC region, enhanced by the interaction with the micelle surface, as observed for small vesicles [55]. A higher affinity for SDS and an enhanced α-helical structure in the SDS-bound state induced by N-acetylation, as reported elsewhere [41], may increase the kinetic barrier of the conformational changes necessary to nucleate amyloid structure within the micellar complexes.

Similarly to the WT variants, the PD variants aggregate mostly under conditions where monomeric aS coexists with a population of the large SDS-aS oligomer complexes. Each PD mutation appears however to favor or disfavor this situation differently, altering the range of SDS concentrations where aggregation occurs. The A53T variants and to a lesser extent the A30P variants aggregate in a broader SDS concentration range than the WT forms. In contrast, the E46K variants aggregate only in a narrow SDS concentration range. The effects of PD mutations in the non-acetylated aS are similar to those observed for aS aggregation catalyzed by surface of small unilamelar vesicles [56]. These effects do not correlate, however, with the overall affinity of each variant for membrane surfaces. The A30P mutation has been reported to decrease aS affinity for anionic phospholipids, whereas the E46K mutation enhances it and the A53T variant shows a similar affinity to the WT form [57]. It is possible that the mutations alter differently the structure and dynamics of the micelle-bound state, as it has been observed for aS interactions with phospholipid vesicles [58], allowing diverse propensities to intermolecular interactions. Nevertheless, N-acetylation does not appear to protect the variants against SDS-induced aggregation as it does for WT aS. This suggests that a long-range cooperative connection between the N-terminal region and the region mediating aggregation may be impaired by the early-onset PD mutations.

Charge removal by N-acetylation in the context of the different PD mutations may also play a role in changing the aggregation propensity but these effects are difficult to envisage in the absence of more precise information about the amyloidogenic aS-SDS micelle clusters. Also, the interactions with the negatively charged SDS head groups may play a determinant role. Different charge-charge interactions might contribute to modify the oligomeric arrangement of aS molecules within these complexes favoring or disfavoring the correct intermolecular contacts for the nucleation process.

An increase in SDS/aS ratio enhances SDS-aS interactions and reduces aS aggregation

A subsequent rise in SDS concentration above 1.2–1.5 mM produced a gradual decrease in molecular size of the SDS-aS complexes and involves additional growth in the α-helix structure. A higher availability of SDS would probably allow a reduction in the number of aS molecules per micelle [36] allowing and a higher degree of α-helical folding of aS on a larger micelle surface. In the absence of any additional transition, the progressive size decrease would continue up to 10 mM SDS and higher to reach the expected size of a SDS micelle decorated with a single aS molecule, which should be slightly higher than the R_h of a SDS micelle (about 2.1 nm). Such behavior is actually observed for the A30P aS variants. In these compact and structured micellar complexes aS becomes protected against aggregation, as observed in all aS variants.

N-acetylation stabilizes aS-SDS oligomeric complexes with extended α-helical structure

In another transition between approximately 4 and 7 mM SDS, a transient maximum in α-helix structure could also be associated to different oligomerization process, as observed by DLS and DOSY experiments. Contrary to the first one, this transition is considerably enhanced by N-acetylation in the WT protein. Giehm et al. [36] also observed a transient maximum in α-helix, which was attributed to non-fibrillogenic clusters of highly α-helical aS-decorated SDS micelles. Another comprehensive study by CD of the aS-SDS interactions under a variety of pH values and temperatures described a multistate conformational behavior of aS under the effect of SDS binding [50]. In addition to the disordered structure, two partially folded conformations with different α-helical content were proposed, *i.e.*, a broken-helix horseshoe bent structure, similar to that observed in micelle-bound aS [21], and an elongated helical conformation, such as that observed for aS bound to small unilamellar vesicles [26]. This extended conformation was also described using pulsed dipolar ESR measurements with doubly spin-labeled aS variants [59]. Single-molecule FRET studies using dye-labeled aS confirmed the existence of the micelle-bound bent and extended helical structures occurring at different SDS concentrations [51,60].

Collectively, all this previous evidence in combination with our results indicate that aS can transiently acquire an extended α-helical conformation at SDS concentrations near the CMC of SDS, resulting in micelle crosslinking or micelle remodeling, giving rise to α-helix-rich oligomeric SDS-aS particles (Fig 10). We show here that this transition is enhanced by N-acetylation in WT aS. Assuming that the bent-to-extended conformational transition must involve α-helical folding of the 37–45 segment in the N-terminal domain, there must be some type of long-range connection between this region and the aS N-terminus. This sort of cooperativity appears to be encoded in the aS sequence [39] and would also operate in the initiation and enhancement of membrane binding [37,55].

Many studies have suggested that the actual native functional form of aS is an aggregation-resistant helical multimer [61–63], favored by N-acetylation [40,64] and a yet-to-know additional component, likely of lipid nature [65]. In addition, the equilibrium between aS monomers and aggregation-resistant helical multimers *in vivo* has been associated to a vesicle clustering function of aS [63,66]. These observations may have fundamental consequences to define the role of aS in PD because they suggest that dissociation and unfolding of the helical tetramer could be an obligatory step in the formation of the pathological aggregates [63].

PD mutations strongly affect the propensity of aS to undergo a bent-to-extended conformational-oligomerization transition

While N-acetylation of WT aS enhances the formation of extended helical oligomers, this effect appears to be disconnected in the PD variants. The two A53T variants could form highly alpha-helical oligomers at high SDS concentrations, independently of N-acetylation. In contrast, none of the A30P variants could undergo this oligomerization transition. The behavior of both E46K aS variants was similar to that of the non-acetylated WT protein but no enhancement of the transition was observed as a result of N-acetylation. These observations are fully consistent with those observed by Ferreon et al. for the non-acetylated PD variants [67]. Our results support the view that the PD mutations may impair the cooperative connection between the N-terminal acetylation and the ability to undergo this conformational-oligomerization transition.

It has been proposed that the switch between the bent and the extended conformation of aS may have a key role for aS function *in vivo* by allowing the protein to bridge between different membranes, thereby regulating synaptic vesicle fusion [59]. aS can induce membrane curvature, budding and tubulation [68] and has been shown to remodel phospholipid vesicles into cylindrical micelles, in which bound aS acquires an extended helical conformation [69]. aS has been also shown to form membrane-bound multimers that promote SNARE complex assembly during vesicle fusion [70] and aS multimerization have been proposed to be implied in the clustering synaptic vesicles, regulating neurotransmitter release [66]. On the other hand, oligomers of aS in a broken helix structure form around small lipid nanoparticles, when incubated at low lipid/protein ratios [71]. This lipoprotein-like function has been related to intracellular transport and metabolism of lipids. All this variety of lipid and membrane interactions are likely to be very finely regulated *in vivo* and involve the concerted action of other proteins. Therefore, besides its importance in initiating and enhancing aS membrane interactions, N-acetylation may have an important role in finely tuning the conformational switch that allows aS to adapt to diverse lipid and membrane contexts related to its function. In this regard, early-onset PD variants may act by deteriorating this connection resulting in diverse deleterious effects under a variety of physiological contexts.

Supporting information

S1 Fig. Determination of the CMC of SDS by light scattering.
(TIF)

S2 Fig. DOSY determination of the diffusion coefficient of SDS in SDS-aS mixtures.
(TIF)

S3 Fig. TEM images of SDS-induced oligomers and protofibrils of aS.
(TIF)

S4 Fig. TEM images of SDS-induced oligomers and protofibrils of Ac-aS.
(TIF)

S5 Fig. TEM images of SDS-induced amyloid fibrils of aS and Ac-aS.
(TIF)

S6 Fig. ThT fluorescence kinetics of aggregation of PD variants in presence of SDS.
(TIF)

Acknowledgments

We gratefully thank Prof. D.P. Mulvihill from the University of Kent, UK, for providing the NatB plasmid, and Prof. Michel Goedert from the University of Cambridge for providing the WT and PD-mutant expression vectors of aS.

Author Contributions

Conceptualization: DR BM FC-L.

Data curation: DR YSH-G GB FC-L.

Formal analysis: DR YSH-G GB FC-L.

Funding acquisition: FC-L.

Investigation: DR YSH-G GB BM FC-L.

Methodology: DR BM FC-L.

Project administration: BM FC-L.

Resources: DR YSH-G GB KB BM FC-L.

Supervision: BM FC-L.

Validation: BM FC-L.

Visualization: DR YSH-G GB FC-L.

Writing – original draft: DR FC-L.

Writing – review & editing: DR BM KB FC-L.

References

1. Moore DJ, West AB, Dawson VL, Dawson TM (2005) Molecular pathophysiology of Parkinson's disease. Annu Rev Neurosci 28: 57–87. https://doi.org/10.1146/annurev.neuro.28.061604.135718 PMID: 16022590
2. Spillantini MG, Schmidt ML, Lee VMY, Trojanowski JQ, Jakes R, Goedert M (1997) alpha-synuclein in Lewy bodies. Nature 388: 839–840. https://doi.org/10.1038/42166 PMID: 9278044
3. Polymeropoulos MH, Lavedan C, Leroy E, Ide SE, Dehejia A, Dutra A, et al. (1997) Mutation in the alpha-synuclein gene identified in families with Parkinson's disease. Science 276: 2045–2047. PMID: 9197268
4. Kruger R, Kuhn W, Muller T, Woitalla D, Graeber M, Kosel S, et al. (1998) Ala30Pro mutation in the gene encoding alpha-synuclein in Parkinson's disease. Nat Genet 18: 106–108. https://doi.org/10.1038/ng0298-106 PMID: 9462735
5. Zarranz JJ, Alegre J, Gomez-Esteban JC, Lezcano E, Ros R, Ampuero I, et al. (2004) The new mutation, E46K, of alpha-synuclein causes Parkinson and Lewy body dementia. Ann Neurol 55: 164–173. https://doi.org/10.1002/ana.10795 PMID: 14755719
6. Appel-Cresswell S, Vilarino-Guell C, Encarnacion M, Sherman H, Yu I, Shah B, et al. (2013) Alpha-synuclein p.H50Q, a novel pathogenic mutation for Parkinson's disease. Movement Disord 28: 811–813. https://doi.org/10.1002/mds.25421 PMID: 23457019
7. Kiely AP, Asi YT, Kara E, Limousin P, Ling H, Lewis P, et al. (2013) alpha-Synucleinopathy associated with G51D SNCA mutation: a link between Parkinson's disease and multiple system atrophy? Acta Neuropathol 125: 753–769. https://doi.org/10.1007/s00401-013-1096-7 PMID: 23404372
8. Chiti F, Dobson CM (2006) Protein misfolding, functional amyloid, and human disease. Annu Rev Biochem 75: 333–366. https://doi.org/10.1146/annurev.biochem.75.101304.123901 PMID: 16756495
9. Uversky VN (2007) Neuropathology, biochemistry, and biophysics of alpha-synuclein aggregation. J Neurochem 103: 17–37. https://doi.org/10.1111/j.1471-4159.2007.04764.x PMID: 17623039

10. Maroteaux L, Campanelli JT, Scheller RH (1988) Synuclein—a Neuron-Specific Protein Localized to the Nucleus and Presynaptic Nerve-Terminal. J Neurosci 8: 2804–2815. PMID: 3411354
11. Cheng FR, Vivacqua G, Yu S (2011) The role of alpha-synuclein in neurotransmission and synaptic plasticity. J Chem Neuroanat 42: 242–248. https://doi.org/10.1016/j.jchemneu.2010.12.001 PMID: 21167933
12. Sharon R, Bar-Joseph I, Mirick GE, Serhan CN, Selkoe DJ (2003) Altered fatty acid composition of dopaminergic neurons expressing alpha-synuclein and human brains with alpha-synucleinopathies. J Biol Chem 278: 49874–49881. https://doi.org/10.1074/jbc.M309127200 PMID: 14507911
13. Golovko MY, Rosenberger TA, Faergeman NJ, Feddersen S, Cole NB, Pribill I, et al. (2006) Acyl-CoA synthetase activity links wild-type but not mutant alpha-synuclein to brain arachidonate metabolism. Biochemistry 45: 6956–6966. https://doi.org/10.1021/bi0600289 PMID: 16734431
14. Darios F, Ruiperez V, Lopez I, Villanueva J, Gutierrez LM, Davletov B (2010) alpha-Synuclein sequesters arachidonic acid to modulate SNARE-mediated exocytosis. Embo Rep 11: 528–533. https://doi.org/10.1038/embor.2010.66 PMID: 20489724
15. Perlmutter JD, Braun AR, Sachs JN (2009) Curvature Dynamics of alpha-Synuclein Familial Parkinson Disease Mutants. Molecular simulations of the micelle- and bilayer-bound forms. J Biol Chem 284: 7177–7189. https://doi.org/10.1074/jbc.M808895200 PMID: 19126542
16. Rao JN, Kim YE, Park LS, Ulmer TS (2009) Effect of Pseudorepeat Rearrangement on alpha-Synuclein Misfolding, Vesicle Binding, and Micelle Binding. J Mol Biol 390: 516–529. https://doi.org/10.1016/j.jmb.2009.05.058 PMID: 19481090
17. Ouberai MM, Wang J, Swann MJ, Galvagnion C, Guilliams T, Dobson CM, et al. (2013) alpha-Synuclein Senses Lipid Packing Defects and Induces Lateral Expansion of Lipids Leading to Membrane Remodeling. J Biol Chem 288: 20883–20895. https://doi.org/10.1074/jbc.M113.478297 PMID: 23740253
18. Weinreb PH, Zhen WG, Poon AW, Conway KA, Lansbury PT (1996) NACP, a protein implicated in Alzheimer's disease and learning, is natively unfolded. Biochemistry 35: 13709–13715. https://doi.org/10.1021/bi961799n PMID: 8901511
19. Kim HY, Cho MK, Kumar A, Maier E, Siebenhaar C, Becker S, et al. (2009) Structural Properties of Pore-Forming Oligomers of alpha-Synuclein. J Am Chem Soc 131: 17482–17489. https://doi.org/10.1021/ja9077599 PMID: 19888725
20. Trexler AJ, Rhoades E (2009) alpha-Synuclein Binds Large Unilamellar Vesicles as an Extended Helix. Biochemistry 48: 2304–2306. https://doi.org/10.1021/bi900114z PMID: 19220042
21. Ulmer TS, Bax A, Cole NB, Nussbaum RL (2005) Structure and dynamics of micelle-bound human alpha-synuclein. J Biol Chem 280: 9595–9603. https://doi.org/10.1074/jbc.M411805200 PMID: 15615727
22. Bisaglia M, Tessari I, Pinato L, Bellanda M, Giraudo S, Fasano M, et al. (2005) A topological model of the interaction between alpha-synuclein and sodium dodecyl sulfate micelles. Biochemistry 44: 329–339. https://doi.org/10.1021/bi048448q PMID: 15628875
23. Broersen K, van den Brink D, Fraser G, Goedert M, Davletov B (2006) alpha-synuclein adopts an alpha-helical conformation in the presence of polyunsaturated fatty acids to hinder micelle formation. Biochemistry 45: 15610–15616. https://doi.org/10.1021/bi061743l PMID: 17176082
24. De Franceschi G, Frare E, Bubacco L, Mammi S, Fontana A, de Laureto PP (2009) Molecular Insights into the Interaction between alpha-Synuclein and Docosahexaenoic Acid. J Mol Biol 394: 94–107. https://doi.org/10.1016/j.jmb.2009.09.008 PMID: 19747490
25. Georgieva ER, Ramlall TF, Borbat PP, Freed JH, Eliezer D (2008) Membrane-bound alpha-synuclein forms an extended helix: Long-distance pulsed ESR measurements using vesicles, bicelles, and rodlike micelles. J Am Chem Soc 130: 12856–12857. https://doi.org/10.1021/ja804517m PMID: 18774805
26. Jao CC, Hegde BG, Chen J, Haworth IS, Langen R (2008) Structure of membrane-bound alpha-synuclein from site-directed spin labeling and computational refinement. Proc Natl Acad Sci U S A 105: 19666–19671. https://doi.org/10.1073/pnas.0807826105 PMID: 19066219
27. Chandra S, Chen X, Rizo J, Jahn R, Sudhof TC (2003) A broken alpha -helix in folded alpha -Synuclein. J Biol Chem 278: 15313–15318. https://doi.org/10.1074/jbc.M213128200 PMID: 12586824
28. Zhu M, Fink AL (2003) Lipid binding inhibits alpha-synuclein fibril formation. J Biol Chem 278: 16873–16877. https://doi.org/10.1074/jbc.M210136200 PMID: 12621030
29. Martinez Z, Zhu M, Han SB, Fink AL (2007) GM1 specifically interacts with alpha-synuclein and inhibits fibrillation. Biochemistry 46: 1868–1877. https://doi.org/10.1021/bi061749a PMID: 17253773
30. Butterfield SM, Lashuel HA (2010) Amyloidogenic Protein Membrane Interactions: Mechanistic Insight from Model Systems. Angew Chem Int Edit 49: 5628–5654.
31. Rivers RC, Kumita JR, Tartaglia GG, Dedmon MM, Pawar A, Vendruscolo M, et al. (2008) Molecular determinants of the aggregation behavior of alpha- and beta-synuclein. Protein Sci 17: 887–898. https://doi.org/10.1110/ps.073181508 PMID: 18436957

32. Serra-Batiste M, Ninot-Pedrosa M, Bayoumi M, Gairi M, Maglia G, Carulla N (2016) A beta 42 assembles into specific beta-barrel pore-forming oligomers in membrane-mimicking environments. Proc Natl Acad Sci U S A 113: 10866–10871. https://doi.org/10.1073/pnas.1605104113 PMID: 27621459

33. Otzen DE (2010) Amyloid Formation in Surfactants and Alcohols: Membrane Mimetics or Structural Switchers? Curr Protein Pept Sc 11: 355–371.

34. Ahmad MF, Ramakrishna T, Raman B, Rao Ch M (2006) Fibrillogenic and non-fibrillogenic ensembles of SDS-bound human alpha-synuclein. J Mol Biol 364: 1061–1072. https://doi.org/10.1016/j.jmb.2006.09.085 PMID: 17054982

35. Necula M, Chirita CN, Kuret J (2003) Rapid anionic micelle-mediated alpha-synuclein fibrillization in vitro. J Biol Chem 278: 46674–46680. https://doi.org/10.1074/jbc.M308231200 PMID: 14506232

36. Giehm L, Oliveira CL, Christiansen G, Pedersen JS, Otzen DE (2010) SDS-induced fibrillation of alpha-synuclein: an alternative fibrillation pathway. J Mol Biol 401: 115–133. https://doi.org/10.1016/j.jmb.2010.05.060 PMID: 20540950

37. Lorenzen N, Lemminger L, Pedersen JN, Nielsen SB, Otzen DE (2014) The N-terminus of alpha-synuclein is essential for both monomeric and oligomeric interactions with membranes. FEBS Lett 588: 497–502. https://doi.org/10.1016/j.febslet.2013.12.015 PMID: 24374342

38. Maltsev AS, Chen J, Levine RL, Bax A (2013) Site-Specific Interaction between alpha-Synuclein and Membranes Probed by NMR-Observed Methionine Oxidation Rates. J Am Chem Soc 135: 2943–2946. https://doi.org/10.1021/ja312415q PMID: 23398174

39. Kang L, Moriarty GM, Woods LA, Ashcroft AE, Radford SE, Baum J (2012) N-terminal acetylation of alpha-synuclein induces increased transient helical propensity and decreased aggregation rates in the intrinsically disordered monomer. Protein Sci 21: 911–917. https://doi.org/10.1002/pro.2088 PMID: 22573613

40. Bartels T, Kim NC, Luth ES, Selkoe DJ (2014) N-Alpha-Acetylation of alpha-Synuclein Increases Its Helical Folding Propensity, GM1 Binding Specificity and Resistance to Aggregation. Plos One 9: e103727. https://doi.org/10.1371/journal.pone.0103727 PMID: 25075858

41. Dikiy I, Eliezer D (2014) N-terminal acetylation stabilizes N-terminal helicity in lipid- and micelle-bound alpha-synuclein and increases its affinity for physiological membranes. J Biol Chem 289: 3652–3665. https://doi.org/10.1074/jbc.M113.512459 PMID: 24338013

42. Iyer A, Roeters SJ, Schilderink N, Hommersom B, Heeren RM, Woutersen S, et al. (2016) The Impact of N-terminal Acetylation of alpha-Synuclein on Phospholipid Membrane Binding and Fibril Structure. J Biol Chem 291: 21110–21122. https://doi.org/10.1074/jbc.M116.726612 PMID: 27531743

43. Anderson JP, Walker DE, Goldstein JM, de Laat R, Banducci K, Caccavello RJ, et al. (2006) Phosphorylation of Ser-129 is the dominant pathological modification of alpha-synuclein in familial and sporadic Lewy body disease. J Biol Chem 281: 29739–29752. https://doi.org/10.1074/jbc.M600933200 PMID: 16847063

44. Johnson M, Coulton AT, Geeves MA, Mulvihill DP (2010) Targeted amino-terminal acetylation of recombinant proteins in E. coli. PLoS One 5: e15801. https://doi.org/10.1371/journal.pone.0015801 PMID: 21203426

45. Luo P, Baldwin RL (1997) Mechanism of helix induction by trifluoroethanol: a framework for extrapolating the helix-forming properties of peptides from trifluoroethanol/water mixtures back to water. Biochemistry 36: 8413–8421. https://doi.org/10.1021/bi9707133 PMID: 9204889

46. Price WS (1997) Pulsed-field gradient nuclear magnetic resonance as a tool for studying translational diffusion. 1. Basic theory. Concept Magnetic Res 9: 299–336.

47. Lendel C, Bertoncini CW, Cremades N, Waudby CA, Vendruscolo M, Dobson CM, et al. (2009) On the mechanism of nonspecific inhibitors of protein aggregation: dissecting the interactions of alpha-synuclein with Congo red and lacmoid. Biochemistry 48: 8322–8334. https://doi.org/10.1021/bi901285x PMID: 19645507

48. Barhoum S, Booth V, Yethiraj A (2013) Diffusion NMR study of complex formation in membrane-associated peptides. Eur Biophys J Biophys Lett 42: 405–414.

49. Ruzafa D, Morel B, Varela L, Azuaga AI, Conejero-Lara F (2012) Characterization of Oligomers of Heterogeneous Size as Precursors of Amyloid Fibril Nucleation of an SH3 Domain: An Experimental Kinetics Study. Plos One 7: e49690. https://doi.org/10.1371/journal.pone.0049690 PMID: 23209591

50. Ferreon AC, Deniz AA (2007) Alpha-synuclein multistate folding thermodynamics: implications for protein misfolding and aggregation. Biochemistry 46: 4499–4509. https://doi.org/10.1021/bi602461y PMID: 17378587

51. Ferreon AC, Gambin Y, Lemke EA, Deniz AA (2009) Interplay of alpha-synuclein binding and conformational switching probed by single-molecule fluorescence. Proc Natl Acad Sci U S A 106: 5645–5650. https://doi.org/10.1073/pnas.0809232106 PMID: 19293380

52. Kang L, Janowska MK, Moriarty GM, Baum J (2013) Mechanistic Insight into the Relationship between N-Terminal Acetylation of alpha-Synuclein and Fibril Formation Rates by NMR and Fluorescence. Plos One 8: UNSP e75018. https://doi.org/10.1371/journal.pone.0075018 PMID: 24058647

53. Jan A, Gokce O, Luthi-Carter R, Lashuel HA (2008) The ratio of monomeric to aggregated forms of Abeta40 and Abeta42 is an important determinant of amyloid-beta aggregation, fibrillogenesis, and toxicity. J Biol Chem 283: 28176–28189. https://doi.org/10.1074/jbc.M803159200 PMID: 18694930

54. Galvagnion C, Buell AK, Meisl G, Michaels TCT, Vendruscolo M, Knowles TPJ, et al. (2015) Lipid vesicles trigger alpha-synuclein aggregation by stimulating primary nucleation. Nat Chem Biol 11: 229–U101. https://doi.org/10.1038/nchembio.1750 PMID: 25643172

55. Maltsev AS, Ying J, Bax A (2012) Impact of N-terminal acetylation of alpha-synuclein on its random coil and lipid binding properties. Biochemistry 51: 5004–5013. https://doi.org/10.1021/bi300642h PMID: 22694188

56. Flagmeier P, Meisl G, Vendruscolo M, Knowles TPJ, Dobson CM, Buell AK, et al. (2016) Mutations associated with familial Parkinson's disease alter the initiation and amplification steps of alpha-synuclein aggregation. Proc Natl Acad Sci U S A 113: 10328–10333. https://doi.org/10.1073/pnas.1604645113 PMID: 27573854

57. Stockl M, Fischer P, Wanker E, Herrmann A (2008) alpha-Synuclein selectively binds to anionic phospholipids embedded in liquid-disordered domains. J Mol Biol 375: 1394–1404. https://doi.org/10.1016/j.jmb.2007.11.051 PMID: 18082181

58. Bodner CR, Maltsev AS, Dobson CM, Bax A (2010) Differential Phospholipid Binding of alpha-Synuclein Variants Implicated in Parkinson's Disease Revealed by Solution NMR Spectroscopy. Biochemistry 49: 862–871. https://doi.org/10.1021/bi901723p PMID: 20041693

59. Georgieva ER, Ramlall TF, Borbat PP, Freed JH, Eliezer D (2010) The lipid-binding domain of wild type and mutant alpha-synuclein: compactness and interconversion between the broken and extended helix forms. J Biol Chem 285: 28261–28274. https://doi.org/10.1074/jbc.M110.157214 PMID: 20592036

60. Veldhuis G, Segers-Nolten I, Ferlemann E, Subramaniam V (2009) Single-molecule FRET reveals structural heterogeneity of SDS-bound alpha-synuclein. Chembiochem 10: 436–439. https://doi.org/10.1002/cbic.200800644 PMID: 19107759

61. Bartels T, Choi JG, Selkoe DJ (2011) alpha-Synuclein occurs physiologically as a helically folded tetramer that resists aggregation. Nature 477: 107–U123. https://doi.org/10.1038/nature10324 PMID: 21841800

62. Wang W, Perovic I, Chittuluru J, Kaganovich A, Nguyen LT, Liao J, et al. (2011) A soluble alpha-synuclein construct forms a dynamic tetramer. Proc Natl Acad Sci U S A 108: 17797–17802. https://doi.org/10.1073/pnas.1113260108 PMID: 22006323

63. Dettmer U, Selkoe D, Bartels T (2016) New insights into cellular α-synuclein homeostasis in health and disease. Curr Opin Neurobiol 36: 15–22. https://doi.org/10.1016/j.conb.2015.07.007 PMID: 26282834

64. Trexler AJ, Rhoades E (2012) N-terminal acetylation is critical for forming a-helical oligomer of a-synuclein. Protein Sci 21: 601–605. https://doi.org/10.1002/pro.2056 PMID: 22407793

65. Iljina M, Tosatto L, Choi ML, Sang JC, Ye Y, Hughes CD, et al. (2016) Arachidonic acid mediates the formation of abundant alpha-helical multimers of alpha-synuclein. Sci Rep 6.

66. Wang LN, Das U, Scott DA, Tang Y, McLean PJ, Roy S (2014) alpha-Synuclein Multimers Cluster Synaptic Vesicles and Attenuate Recycling. Curr Biol 24: 2319–2326. https://doi.org/10.1016/j.cub.2014.08.027 PMID: 25264250

67. Ferreon AC, Moran CR, Ferreon JC, Deniz AA (2010) Alteration of the alpha-synuclein folding landscape by a mutation related to Parkinson's disease. Angew Chem Int Ed Engl 49: 3469–3472. https://doi.org/10.1002/anie.201000378 PMID: 20544898

68. Varkey J, Isas JM, Mizuno N, Jensen MB, Bhatia VK, Jao CC, et al. (2010) Membrane Curvature Induction and Tubulation Are Common Features of Synucleins and Apolipoproteins. J Biol Chem 285: 32486–32493. https://doi.org/10.1074/jbc.M110.139576 PMID: 20693280

69. Mizuno N, Varkey J, Kegulian NC, Hegde BG, Cheng NQ, Langen R, et al. (2012) Remodeling of Lipid Vesicles into Cylindrical Micelles by alpha-Synuclein in an Extended alpha-Helical Conformation. J Biol Chem 287: 29301–29311. https://doi.org/10.1074/jbc.M112.365817 PMID: 22767608

70. Burre J, Sharma M, Sudhof TC (2014) alpha-Synuclein assembles into higher-order multimers upon membrane binding to promote SNARE complex formation. Proc Natl Acad Sci U S A 111: E4274–E4283. https://doi.org/10.1073/pnas.1416598111 PMID: 25246573

71. Varkey J, Mizuno N, Hegde BG, Cheng NQ, Steven AC, Langen R (2013) alpha-Synuclein Oligomers with Broken Helical Conformation Form Lipoprotein Nanoparticles. J Biol Chem 288: 17620–17630. https://doi.org/10.1074/jbc.M113.476697 PMID: 23609437

antioxidants

MDPI

Article

Tyrosine Phosphorylation Modulates Peroxiredoxin-2 Activity in Normal and Diseased Red Cells

Alessandro Mattè [1,†], Enrica Federti [1,†], Elena Tibaldi [2,†], Maria Luisa Di Paolo [2], Giovanni Bisello [3], Mariarita Bertoldi [3,*], Andrea Carpentieri [4], Pietro Pucci [4,5], Iana Iatchencko [1], Anand B. Wilson [1], Veronica Riccardi [1], Angela Siciliano [1], Francesco Turrini [6], Dae Won Kim [7], Soo Young Choi [7], Anna Maria Brunati [2] and Lucia De Franceschi [1,*]

1 Department of Medicine, University of Verona and AOUI Verona, 37134 Verona, Italy; alessandro.matte@univr.it (A.M.); enrica.federti@univr.it (E.F.); ianaiatcenko@gmail.com (I.I.); anand.wilson16@gmail.com (A.B.W.); veronica.riccardi@univr.it (V.R.); angela.siciliano@univr.it (A.S.)
2 Department of Molecular Medicine, University of Padua, 35128 Padua, Italy; elena.tibaldi@unipd.it (E.T.); marialuisa.dipaolo@unipd.it (M.L.D.P.); Annamaria.brunati@unipd.it (A.M.B.)
3 Department of Neuroscience, Biomedicine and Movement Sciences, Section of Biological Chemistry, University of Verona, 37134 Verona, Italy; giovanni.bisello@univr.it
4 Department of Chemical Sciences, University Federico II of Napoli, 80126 Napoli, Italy; andrea.carpentieri@unina.it (A.C.); pucci@unina.it (P.P.)
5 CEINGE Biotecnologie Avanzate, 80145 Napoli, Italy
6 Department of Oncology, University of Torino, 10124 Torino, Italy; francesco.turrini@unito.it
7 Department of Biomedical Sciences and Institute of Bioscience and Biotechnology, Hallym University, Chuncheon 24252, Korea; dwkim@hallym.ac.kr (D.W.K.); sychoi@hallym.ac.kr (S.Y.C.)
* Correspondence: mita.bertoldi@univr.it (M.B.); lucia.defranceschi@univr.it (L.D.F.); Tel.: +39-045-8027671 (M.B.); +39-045-8124401 (L.D.F.)
† These authors have equally contributed.

check for updates

Citation: Mattè, A.; Federti, E.; Tibaldi, E.; Di Paolo, M.L.; Bisello, G.; Bertoldi, M.; Carpentieri, A.; Pucci, P.; Iatchencko, I.; Wilson, A.B.; et al. Tyrosine Phosphorylation Modulates Peroxiredoxin-2 Activity in Normal and Diseased Red Cells. *Antioxidants* **2021**, *10*, 206. https://doi.org/10.3390/antiox10020206

Academic Editor: Ho Hee Jang
Received: 29 November 2020
Accepted: 21 January 2021
Published: 1 February 2021

Publisher's Note: MDPI stays neutral with regard to jurisdictional claims in published maps and institutional affiliations.

Abstract: Peroxiredoxin-2 (Prx2) is the third most abundant cytoplasmic protein in red blood cells. Prx2 belongs to a well-known family of antioxidants, the peroxiredoxins (Prxs), that are widely expressed in mammalian cells. Prx2 is a typical, homodimeric, 2-Cys Prx that uses two cysteine residues to accomplish the task of detoxifying a vast range of organic peroxides, H_2O_2, and peroxynitrite. Although progress has been made on functional characterization of Prx2, much still remains to be investigated on Prx2 post-translational changes. Here, we first show that Prx2 is Tyrosine (Tyr) phosphorylated by Syk in red cells exposed to oxidation induced by diamide. We identified Tyr-193 in both recombinant Prx2 and native Prx2 from red cells as a specific target of Syk. Bioinformatic analysis suggests that phosphorylation of Tyr-193 allows Prx2 conformational change that is more favorable for its peroxidase activity. Indeed, Syk-induced Tyr phosphorylation of Prx2 enhances in vitro Prx2 activity, but also contributes to Prx2 translocation to the membrane of red cells exposed to diamide. The biologic importance of Tyr-193 phospho-Prx2 is further supported by data on red cells from a mouse model of humanized sickle cell disease (SCD). SCD is globally distributed, hereditary red cell disorder, characterized by severe red cell oxidation due to the pathologic sickle hemoglobin. SCD red cells show Tyr-phosphorylated Prx2 bound to the membrane and increased Prx2 activity when compared to healthy erythrocytes. Collectively, our data highlight the novel link between redox related signaling and Prx2 function in normal and diseased red cells.

Keywords: peroxiredoxin-2; tyrosine phosphorylation; Syk; sickle cell disease; oxidation

1. Introduction

Peroxiredoxin-2 (Prx2) is the third most abundant cytoplasmic protein in red blood cells. Prx2 belongs to a well-known family of antioxidant proteins, the peroxiredoxins (Prxs), widely expressed in mammalian cells [1–7]. Prx2 is a member of the typical, homodimeric, 2-Cys Prxs, a wider group that uses two cysteine residues to accomplish

the task of detoxifying a vast range of organic peroxides, H_2O_2, and peroxynitrite. The catalytic mechanism is characterized by a sequence of events, starting from one cysteine sulfhydryl of the first subunit that is oxidized by the substrate, to sulfenic acid (the so-called peroxidatic cysteine, Cys-S_PH). This is then resolved by the action of a second cysteine sulfhydryl of the cognate subunit (the so-called resolving cysteine, Cys-S_RH) through the formation of a disulfide subsequently re-reduced by the action of thioredoxin or glutathione and glutathione reductase [2,8].

In addition to the enzymatic function, Prxs have been shown to acquire a chaperone function under oxidative stress conditions, and are able to interact with multiple proteins [2,9]. Accordingly, a crucial role is played by the possibility of switching the oligomeric structure from a homodimer to a homodecamer in the reduced state, while sulfur oxidation of the two essential cysteine residues leads to decamer dissociation into disulfide-linked dimers. Hyperoxidation of the peroxidatic cysteine (Cys-S_PO_2H) leads to the formation of catalytically inactive, high-molecular-weight oligomers with chaperone function [2]. Since redox conditions are so crucial for cell viability, it is not strange that Prxs could be highly regulated by several modifications, such as phosphorylation, acetylation, glutathionylation, and nitrosylation. Prx1 and Prx2 exhibit particular sensitivity to post-translational changes [8,10,11].

Focusing on phosphorylation, Prx1 has been reported to be phosphorylated both on tyrosine (Tyr) and on threonine/serine residues. Although several phosphorylation sites of Prx1 have been identified, limited data are available on their impact on Prx1 function [10,12]. Concerning Prx2, several threonine/serine residues and only one Tyr residue (Tyr-193) have been identified as being phosphorylated [12]. We carried out a revision of the literature and found Tyr-193 to be the most frequently tyrosine residue identified as phosphorylated in Prx2, suggesting a possible biologic importance of this post-translation modification for Prx2 function (Figure 1).

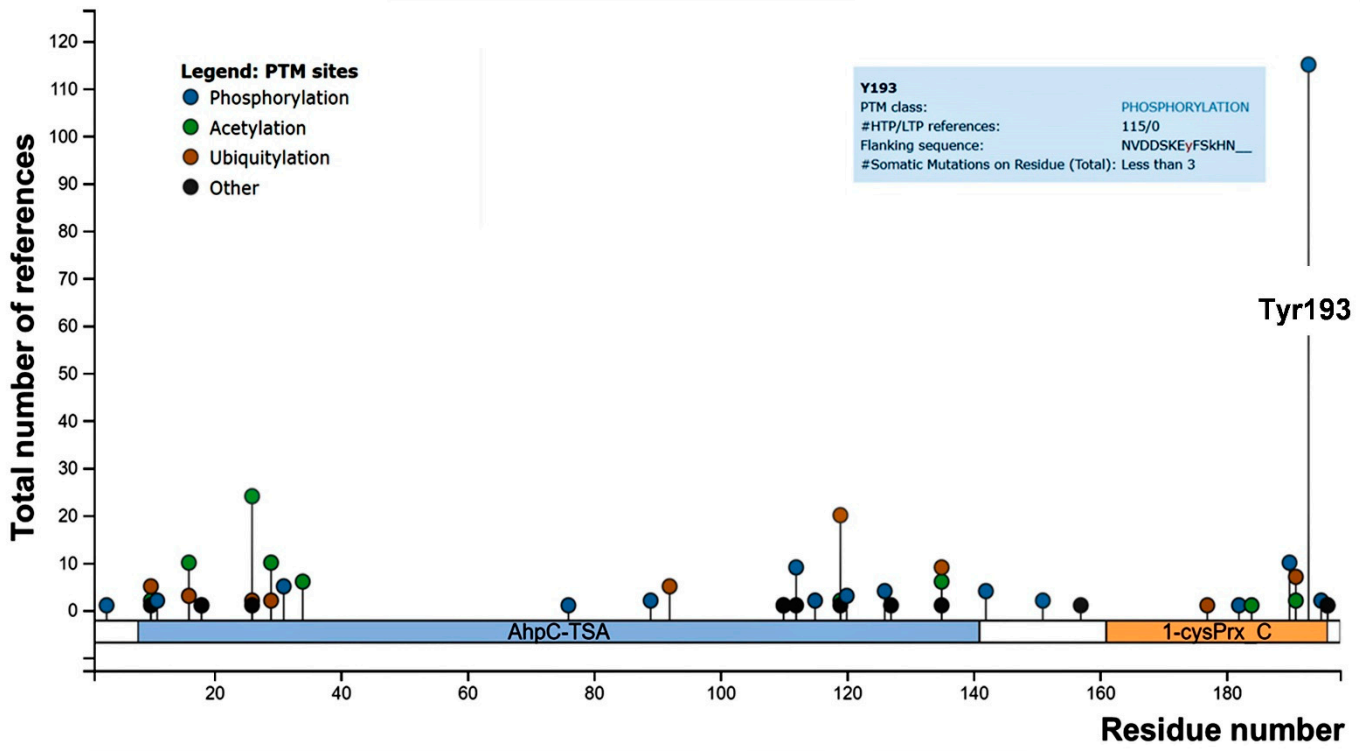

Figure 1. PhosphoSitePlus lollipop plot of mouse peroxiredoxin-2 (Prx2), showing the number of references for the post-translational modified sites throughout the Prx2 aminoacidic sequence. Both high (HTP) and low (LTP) throughput papers were included in the report. Tyrosine (Tyr)-193 is highlighted, and details are shown in the blue square.

Previous studies have shown that changes in the phosphorylation of Prxs might affect not only their activity, but also their molecular size, by shifting the dimer–decamer protein equilibrium to an inactive, high-molecular-weight decamer species with a chaperone function [12]. This suggests a possible link between oligomerization, peroxidase activity, chaperone activity, and post-translational modifications.

Red cells are an exceptional model to study Prx2 function and post-translational modifications, due to their highly oxidative physiologic environment. Recently, we have shown that Prx2 is important in both red cells and erythropoiesis to ensure cell survival, growth, and differentiation against physiologic and pathologic oxidation [13–16]. In addition, we found that Prx2 might act as a chaperone-like protein targeting key membrane proteins, such as band 3, against oxidation [17–19]. Indeed, mice genetically lacking Prx2 display accelerated red cell senescence. This is associated with an overactivated Syk kinase-dependent intracellular signaling pathway, ending with the release of erythroid microparticles to clear damaged proteins [17–20]. In red cells, the biologic importance of redox-related signaling pathways is supported by studies in red cells from both animal models and human subjects with hemoglobinopathies or glucose 6-phosphate dehydrogenase G6PD deficiency [13–15,17,21,22]. In response to oxidation, Syk translocates to the membrane and favors band 3 clusterization, resulting in erythroid vesiculation followed by red cell membrane rearrangement [17–19]. This mechanism is important in pathologic red cells, such as in β-thalassemia, or in sickle cell disease (SCD) [14,17,20]. Both conditions are characterized by severe membrane oxidation and activation of the intracellular Syk signaling pathway [14,17,20]. In red cells from a mouse model of SCD, we previously reported a membrane translocation of Prx2 in response to oxidation related to hypoxia/reoxygenation stress, mimicking sickle cell-related vaso-occlusive crisis [22,23]. This suggests a possible connection between the redox-related signaling pathway and Prx2 in both normal red cells exposed to exogenous oxidation and pathologic erythrocytes, such as in SCD.

Here, we first found that Prx2 is Tyr-phosphorylated in response to oxidation and translocates to the membrane. We identified Tyr-193 on Prx2 as specific target of Syk kinase, resulting in increased Prx2 activity. The bioinformatic analysis revealed that Tyr-193 is involved in the conformational changes that Prx2 undergoes during catalysis. The biologic importance of phosphorylated, active Prx2 is further supported by the observation of phospho-Prx2 bound to the membrane that is associated with increased Prx2 activity in sickle red cells. Taken together, our data show that Tyr-phosphorylation of Prx2 contributes to activating Prx2, and to partitioning Prx2 between the cytoplasm and membrane, thus participating in redox-related signaling machinery linking the Syk pathway to Prx2 post-translational changes in normal and diseased red cells.

2. Materials and Methods

2.1. Mouse Strains and Design of the Study

The Institutional Animal Experimental Committee of University of Verona (CIRSAL) and the Italian Ministry of Health approved the experimental protocols (prot. 56DC9.21). Three-month old C57B6/2J wild-type (WT) mice and SCD (*Hba*$^{tm1(HBA)Tow}$ *Hbb*$^{tm2(HBG1,HBB*)Tow}$) mice were studied [24–26]. Whenever indicated, red cells underwent to in vitro treatments with oxidative agents or specific inhibitors [17,27,28]; details are reported in the Supplementary Materials.

2.2. Two-Dimensional Electrophoresis, Phosphoprotein Enrichement, Western-Blot Analysis, and Immunoprecipitation Assay

Red cell membrane (ghost) and cytosol fractions were obtained as previously reported [13,15,26,29,30] (Figure S1).

2.2.1. Two-Dimensional Electrophoresis (2D) Analysis

Red cell membrane proteins underwent two-dimensional electrophoresis (2D) analysis and separated, in the first dimension, onto a 3.0–5.6 immobilized pH gradient IPG strip, and in the second dimension, by SDS-PAGE [31]. Details are in the Supplementary Materials.

2.2.2. Phosphoprotein-Enriched Samples

Phosphoprotein-enriched samples were generated from red cell membrane protein extracts using a TALON PMAC Phosphoprotein Enrichment Kit (ClonTech, CA, USA) according to the manufacturer's instructions [32,33].

2.2.3. Western-Blot Analysis and Immunoprecipitation Assay

Red cell membrane (ghost) and cytosol fractions were analyzed by SDS-PAGE [13,15,26,29,30]. Gels were transferred to nitrocellulose membranes for immunoblot analysis with specific antibodies. Details are in the Supplementary Materials. Immunoprecipitations of anti-phospho-Tyr proteins from red cells were carried out using Protein A Agarose (Thermo Fisher Scientific, Waltham, Massachusetts, United States), as well as a mix of the anti phospho-Tyrosine monoclonal antibodies PY99 (Santa Cruz Biotechnology, Dallas, TX, USA) and 4G10 (Merck Group, Darmstadt, Germany) as previously reported [17].

2.3. Generation of Recombinant Prx2 and In Vitro Prx2 Activity

Human WT Prx2 and mutated Prx2-Y193F and Prx2-Y115F were cloned in a pET15b vector to produce the recombinant enzymes. Details are reported in the Supplementary Materials. Prx2 activity of recombinant enzyme (both of the control and the phosphorylated enzyme) was performed according to the basic protocol IV reported in Nelson and Parsonage [34], with minor modifications (see Figure S2 and Supplementary Materials).

2.4. Mass Spectrometry

Proteins were either analyzed by a Tofspec SE (Micromass, Manchester, United Kingdom) and a LTQ Orbitrap XL Hybrid Ion Trap-Orbitrap Mass Spectrometer (Thermo Fisher Scientific, Bremen, Germany). Details are reported in the Supplementary Materials.

2.5. Bioinformatic Analysis

Structural analysis of the Prx2 active site in its hyperoxidized (PDB = 1qmv) and oxidized disulfide form (PDB = 5ijt) was carried out using Pymol 2.0 (PyMOL Molecular Graphics System, Version 2.0 Schrödinger Inc, New York, NY, United States). In order to simplify the representation, only a dimer for each decamer is shown.

2.6. Prx2 Activity on Mouse Red Cells

Enzymatic activity of Prx2 on red cells from wild-type and humanized sickle cell [24,25] mice was assayed, as previously reported [15] in the presence of the coupled assay thioredoxin, thioredoxin reductase, and NADPH. The relative activity was determined by measuring the $\Delta A/\text{min}$ at 340 nm of 10 µL of samples for both WT and SCD, considering as a reference the activity of WT as 100% of peroxidase activity.

2.7. Statistical Analysis

Data were analyzed using either a *t*-test or one-way ANOVA for longitudinal studies, or one-way ANOVA for multiple comparisons. A difference with $p < 0.05$ was considered significant.

3. Results

3.1. Prx2 Is Tyrosine-Phosphorylated in Response to Oxidation and Associates to the Membrane

To address the question of whether post-translational modification might affect Prx2 in response to oxidation, we exposed wild-type mouse erythrocytes to diamide, an oxidant known to promote red cell membrane damage, requiring Prx2 membrane translocation [13,17]. We performed 2DE analysis of the membrane fraction (ghost) from mouse red cells treated with either vehicle or diamide (2 mM) [13,14]. Prx2 was identified by mass-spectrometric analysis in both vehicle- and diamide-treated red cells (AC #Q61171, Prdx2_mouse; the vehicle matched 5 peptides, with coverage of 24%, while the Prx2 di-

amide matched 4 peptides, with coverage of 22%) (Figure 2a). The immunoblot analysis carried out in twin-gels revealed the presence of trains of Prx2, which were left shifted in red cells treated with diamide when compared to vehicle-treated erythrocytes, suggesting a possible post-translational Prx2 modification, such as phosphorylation (Figure 2a). This intrigued us, since previous studies on Tyr-phospho-maps of red cells from both healthy mice and human subjects did not find phospho-Tyr–Prx2 associated with the membrane [14,31]. We then carried out phospho-peptide enrichment using a phospho-specific metal ion affinity resin (TALON PMAC Phosphoprotein Enrichment Kit) of mouse red cells exposed to diamide [32,33]. Prx2 was identified by MALDI-TOF analysis and further confirmed by LC-MS/MS analysis (Figure 2b).

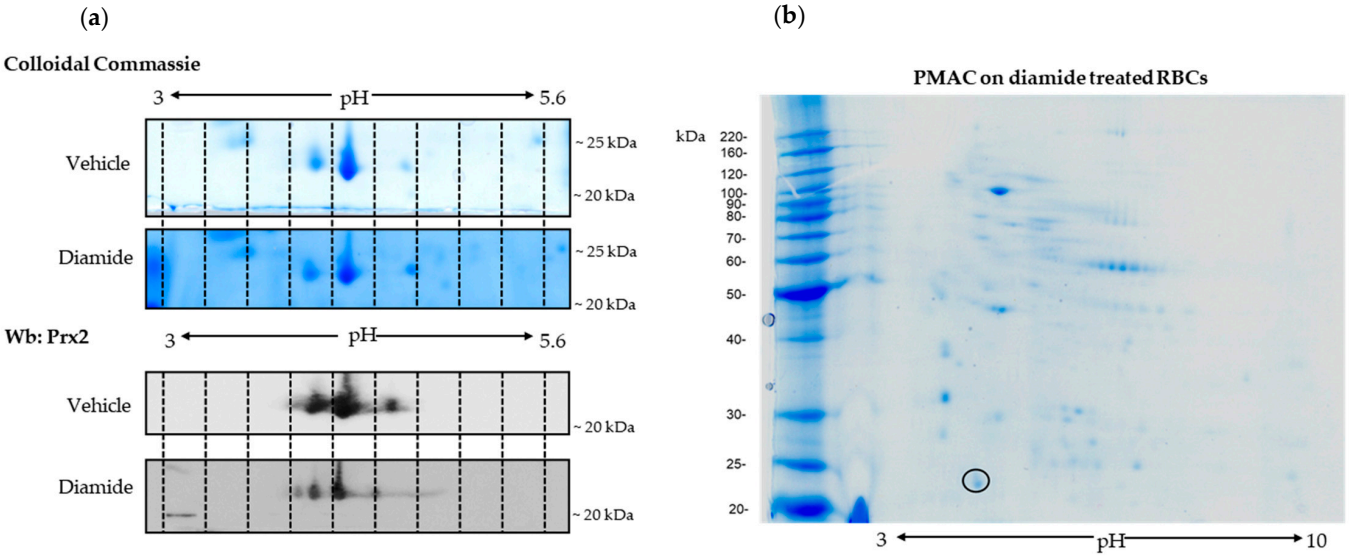

Figure 2. Prx2 is phosphorylated in response to oxidative stress. (**a**) Two-dimensional electrophoresis (2D) analysis of ghosts from wild-type (WT) red cells treated with vehicle or 2 mM diamide. Gradient strips of 3.0–5.6 immobilized pH were used. One representative experiment of three performed with similar results is shown. We ran twin gels, one stained with colloidal Coomassie and the other one blotted with a specific anti-Prx2 antibody. (**b**) Phospho-enriched proteins from diamide (2 mM)-treated, wild-type red cell membrane proteins were obtained by a PMAC metal affinity column and analyzed by bi-dimensional electrophoresis (2D) in a 3–10 immobilized pH gradient (right panel). Shown is a representative experiment of three performed with similar results. Gels were stained with colloidal Coomassie. The black circle indicates the spot identified as Prx2 by MALDI-TOF analysis and further confirmed by LC-MS/MS analysis. Prx2 was identified with the following peptides: RGLFIIDAKG; KNDEGIAYRG; KSLSQNYGVLKN; RQITVNDLPVGRS; K.SAPDFTATAVVDGAFKE.

Since Syk is the key kinase in red cell signaling networks in response to oxidation, we have explored the Syk pathway in diamide-treated erythrocyte with respect to Prx2 [17–19,31,35]. As shown in Figure 3a, Syk was activated in diamide-treated red cells, compared to vehicle-treated erythrocytes. The amount of active phospho-Syk was further increased in the presence of $NaVO_4$, blocking families of phosphatases (Figure 3a). No major change was observed in Syk activity in H_2O_2-treated erythrocytes (Figure 3a) [13,17,28]. Thus, we focused on diamide-treated red cells. As shown in Figure 3b, we found increased membrane association of both Tyr-phosphorylated Prx2, corresponding to almost 47% of total membrane-bound Prx2, and Syk in response to oxidation when compared to vehicle-treated erythrocytes. This was paralleled with increased Tyr phosphorylation of Prx2, also in the cytoplasmatic compartment of diamide-treated red cells (corresponding to 3% of total cytoplasmic Prx2; Figure 3b, see also Figure S3a).

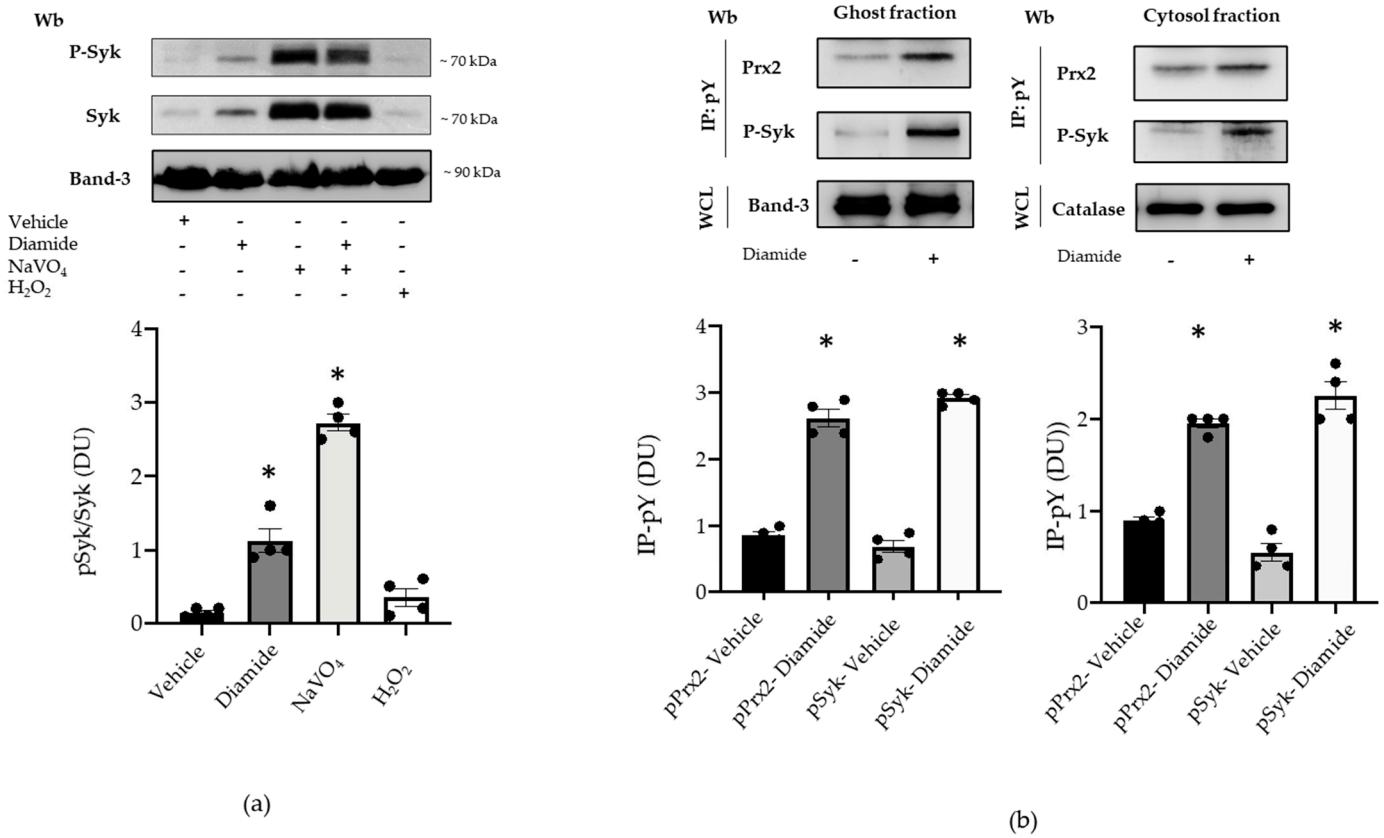

Figure 3. Prx2 is Tyr-phosphorylated in diamide-treated red cells, characterized by activation of the Syk canonical pathway. (**a**) Upper panel: Western blot (Wb) analysis with specific antibodies against P-Syk and Syk of the cytosolic fraction from red cells of WT mice treated with vehicle or diamide, $NAVO_4$, and/or H_2O_2. Band 3 is used as loading control. One representative gel from other four with similar results is presented. Lower panel: densitometric analysis is presented as means ± standard error of the mean (SEM) (n = 4); * $p < 0.05$ compared to vehicle-treated red cells. (**b**) Upper panel: ghost and cytosol fractions from red cells of wild-type (WT) mice treated with either vehicle or diamide underwent immunoprecipitation with specific anti-phospho-tyrosine antibodies (IP: pY), and were then revealed with specific anti-Prx2 or anti-P-Syk antibodies. Band 3 and catalase, as well as colloidal Coomassie-stained gels (see Figure S3a) in whole-cell lysate (WCL), were used as loading controls. One representative gel from the other four with similar results is presented (see also Figure S3a). Lower panel: densitometric analysis is presented as means ± SEM (n = 4); * $p < 0.05$ compared to vehicle treated red cells.

To explore whether the membrane translocation of phospho-Prx2 was dependent on Syk activation, we used specific inhibitors for either Syk or Src family kinases, such as PP1 and PP2. As shown in Figure 4a, Syk inhibitors I–II fully blocked Prx2 phosphorylation and Prx2 membrane translocation. However, PP1 and PP2 did not modify the amount of Tyr-phosphorylated Prx2 associated with the membrane of diamide-treated red cells (Figure 4a). The oxidative dependent compartmentalization of Prx2 was further supported by the observation that dithiotretol (DTT), a known thiol group donor, prevented the membrane association of Tyr-phosphorylated Prx2 (Figure 4b) [15,21]. Noteworthily, Prx2 was associated with the membrane as both a monomer and dimer in diamide-treated red cells, and DTT again prevented Prx2 dimer formation, as previously reported by us [13,36] (Figure S3b). Taken together, our data suggest that Prx2 is Tyr-phosphorylated by Syk in response to oxidation, binding to the membrane of diamide-treated red cells.

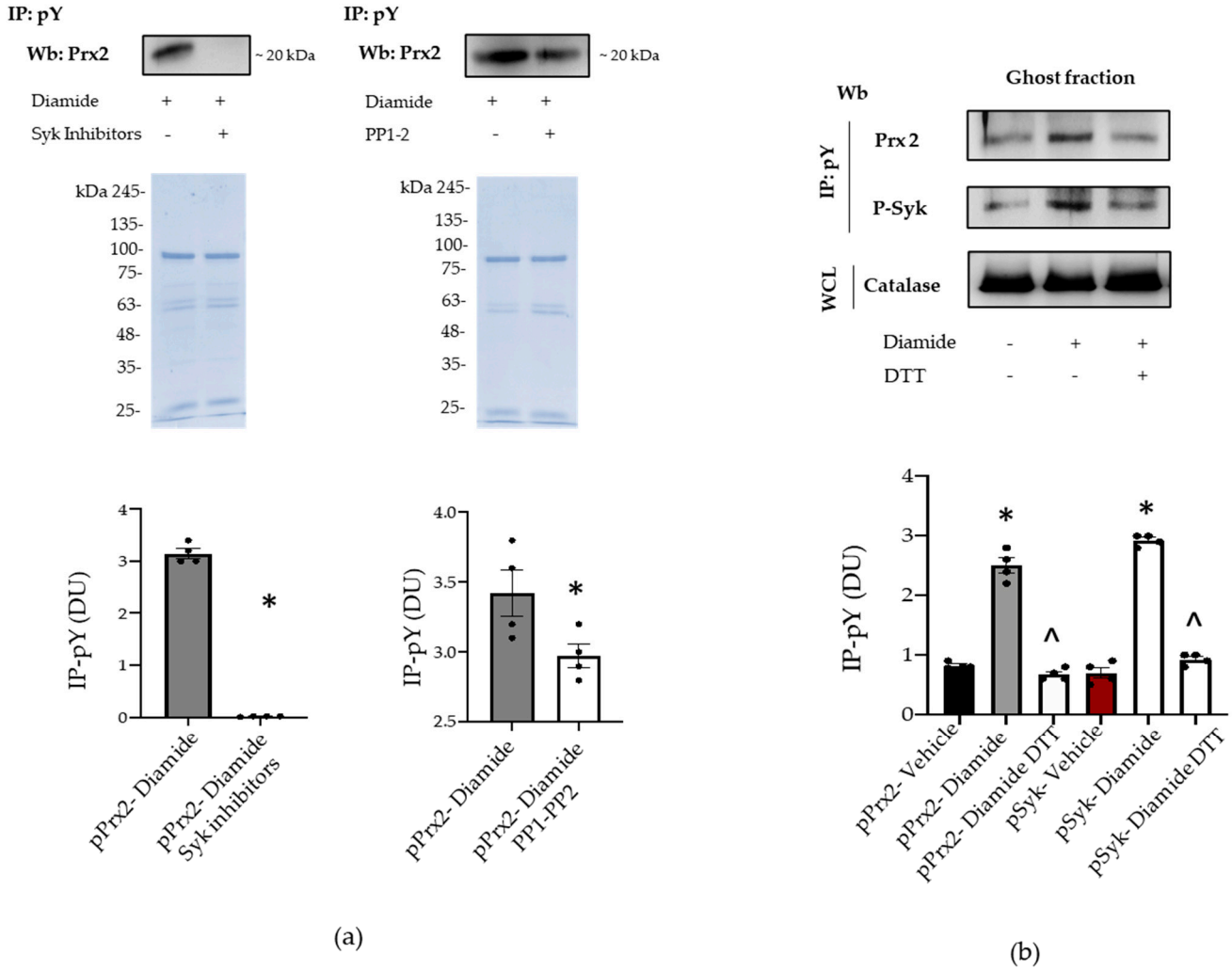

Figure 4. Syk inhibitors and dithiothreitol (DTT) prevents the phosphorylation of Prx2. (**a**) Ghost fraction from the red cells of wild-type (WT) mice treated with diamide and/or Syk inhibitors (I–II) and PP1–2 underwent immunoprecipitation with specific anti-phospho-tyrosine antibodies (IP: pY), and then were used for Western blot (Wb) analysis with anti-Prx2 antibodies. Colloidal Coomassie-stained gels in whole-cell lysate (WCL) were used as loading controls. One representative gel from three with similar results is presented. Densitometric analysis is presented means ± SEM (n = 4); * $p < 0.05$ compared to vehicle-treated red cells. (**b**) Ghost fraction from red cells of wild-type (WT) mice treated with vehicle or diamide and/or DTT underwent immunoprecipitation with specific anti-phospho-tyrosine antibodies (IP: PY), and then were used for Western blot (Wb) analysis with either anti-Prx2 or anti-P-Syk antibodies. Band 3, as well as colloidal Coomassie-stained gels (see Figure S3c) in whole-cell lysate (WCL), was used as a loading control. One representative gel from three with similar results is presented. Densitometric analysis is presented as means ± SEM (n = 4); * $p < 0.05$ compared to vehicle-treated red cells; ^ $p < 0.05$ compared to diamide-treated red cells.

3.2. Syk Phosphorylates Prx2, Resulting in an Increase in Prx2 Activity

To define the contribution of Syk in the phosphorylation of Prx2, recombinant Prx2 underwent in vitro phosphorylation assays in the presence of equal units of Syk or some of members of the Src family (Src family kinases, or SFKs), which are known to be sensitive to PP1/PP2s, such as Lyn, Fyn, or Fgr [37,38] (see Materials and Methods for experimental details and the source of the enzymes). The mixture was then resolved by SDS-PAGE and visualized by autoradiography. As shown in Figure 5a, Syk was able to abundantly phosphorylate Prx2 (lane 1), whereas out of the SFKs added to the kinase mixture, Fyn only phosphorylated Prx2 to a comparable extent (lane 5). On the other hand, the Prx2 phosphorylation by Lyn and Fgr was negligible (lanes 3 and 5). These results support

the notion that the substrate specificity of SFKs can widely vary, as further highlighted recently [36–38]. That the incorporation of ^{32}P labels had occurred on tyrosine residues was further confirmed by Western blot analysis of Prx2 with anti-phospho-tyrosine antibodies (Figure 5b). Afterwards, to determine the level of incorporation of phosphate onto Prx2, time-course phosphorylation in the presence of either enzyme was performed for one hour, with single aliquots being drawn at discrete time points to be analyzed by autoradiography after SDS-PAGE (data not shown). The bands corresponding to Prx2 were excised, and the ^{32}P radioactivity was determined by Cerenkov counting (Figure 5c, upper panel), the molar ratio of phosphate bound to Prx2 being found to be approximately 0.88:1.00. In addition, to assess the role of phosphorylation on Prx2 by Syk, the peroxidase activity was determined on Prx2 previously subjected to nearly exhaustive phosphorylation under the conditions described above. Results shown in Figure 5c clearly highlight that the phosphorylation of Prx2 increases its enzyme activity 2.3-fold, compared to the non-phosphorylated form of the enzyme. Noteworthily, the Prx2-specific activity here reported is comparable to that described for other Prx preparations with the same assay method, using DTT as a reducing agent [39]. Whereas we used the Trx–TrxR reducing system in red cell preparation (see Figure below). This method usually obtains more highly specific activities compared to the DTT system [39]. Independent of the method, the main result to consider is the increase of Prx2 activity, due to the phosphorylation of the enzyme compared to the non-phosphorylated form.

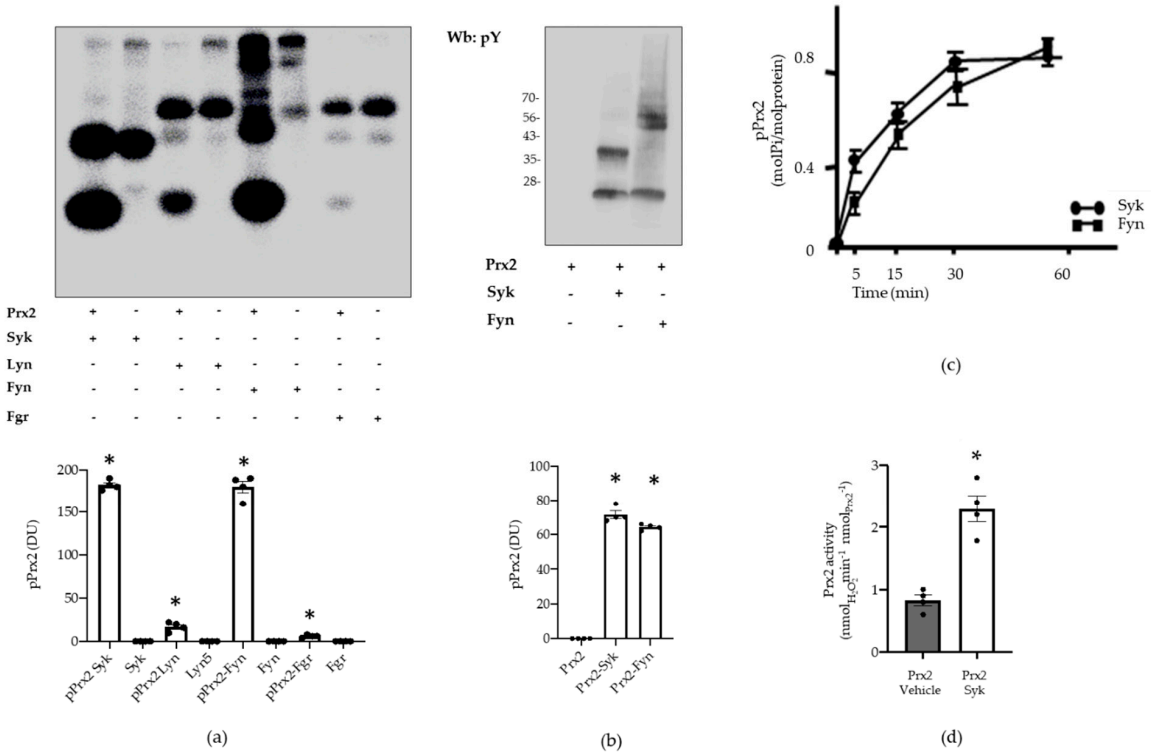

Figure 5. Prx2 activity is affected by Syk-mediated phosphorylation. (**a**) Upper panel: Prx2 (0.4 µg) was phosphorylated in the presence or absence of either Syk (lanes 1–2), Lyn (lanes 3–4), Fyn (lanes 5–6), or Fgr (lanes 7–8) (see Materials and Methods for further details) for 10 min, resolved by SDS-PAGE, and visualized by autoradiography. Lower panel: densitometric analysis is presented as means ± SEM (n = 3); * $p < 0.05$ compared to vehicle-treated red cells. (**b**) Upper panel: tyrosine phosphorylation of Prx2 and autophosphorylation of Syk or Fyn was assessed by Western blot analysis with anti-phosphotyrosine antibody after separation on SDS-PAGE, transfer onto nitrocellulose, and reveal by ECL peroxidase assay. Lower panel: densitometric analysis is presented as means ± SEM (n = 3); * $p < 0.05$ compared to vehicle-treated red cells. (**c**) Time course of Prx2 phosphorylation by Syk and Fyn. Values are the mean ± SEM of four determinations performed at each time point. (**d**) Enzymatic activity of Prx2 before (vehicle) and after phosphorylation by Syk. Values are the mean ± SEM (n = 4; * $p < 0.01$ compared to control Prx2 by Student's t-test).

3.3. Syk Specifically Targets Tyr-193 Residues on Prx2

We then carried out phospho-proteomic analysis of recombinant Prx2 in vitro, phosphorylated by either Syk or Fyn, a Tyr-kinase of the Src family. Following Syk incubation, Prx2 was digested with trypsin and AspN, and the resulting peptide mixture was directly analyzed by LC-MS/MS. Mass spectral data showed the occurrence of a triply charged mass signal at m/z 655.96, corresponding to the peptide DTIKPNVDDSKEYFSK, with a mass increase of 80 Da, thus suggesting the presence of a phosphate group. Figure 6 shows the partial MS/MS spectrum of the triply charged ion at m/z 655.96, showing the occurrence of both the y and b ion series that confirmed the peptide sequence. As highlighted in the figure, the 243 Da mass difference between the y ions at m/z 624.25 (y_4) and 381.20 (y_3) unambiguously located the phospho-Tyr residue at position 193. Noteworthily, Tyr-193 was also identified in immune-enriched Prx2 from diamide-treated red cells, supporting the biologic importance of Tyr 193 in Prx2 function against oxidation.

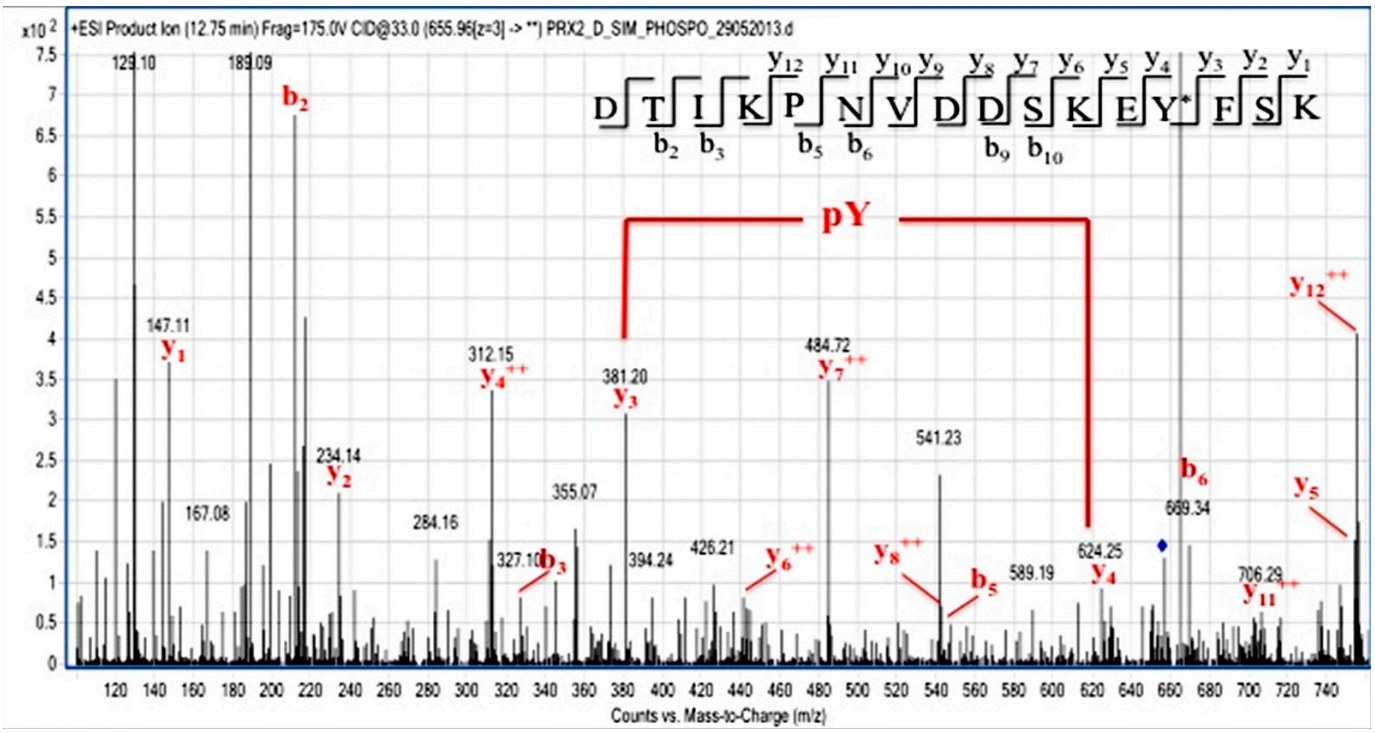

Figure 6. Identification of Tyr-193 on Syk-phosphorylated recombinant Prx2. Partial MS/MS spectrum of the triply charged ion at m/z 655.96 from the tryptic and AspN double digest of Prx2 following Syk incubation. Manual inspection of the y and b fragment ion series confirmed the peptide sequence. The mass difference between the y_4 and y_3 ions unambiguously indicate the occurrence of a phosphoTyr residue at position 193.

Similarly, the LC-MS/MS analysis of the tryptic peptides from Prx2 incubated with Fyn revealed the occurrence of a mass signal at m/z 630.31 that was assigned to the doubly charged phosphorylated peptide RLSEDYGVLK bearing a phosphate group. The corresponding MS/MS spectrum reported in Figure S4 showed the occurrence of a phosphoTyr residue at position 115, as demonstrated by the mass difference of 243 Da between the y ions at m/z 844.32 and 601.30.

3.4. Tyr-193 Is Positioned in Proximity to the Active Site of Prx2

A structural inspection of Prx2 in its hyperoxidized (mimicking the reduced) state shows that Tyr-193 is part of an extensive hydrogen bond network in place concurrent with both the resolving Cys-172 (Figure 7a) and the buried catalytic Cys-51 (present in this structure as hyperoxidated C-S_PO_2H)) (Figure 7b). In detail, Tyr-193 belongs to the

important structural YF motif on the C-terminal helix interacting with Phe-194, and is base-stacked to His-197 and on the same helix. His-197, in turn, stabilizes a loop containing Trp-176 by subsequential interactions with Asp-181 and Ser-180. In this conformation, Cys-51 and Cys-172 are ~13.4 Å distant, as visible in Figure 7b. Sulfinic Cys-51-S_P-O_2H (mimicking Cys-S_PH-51) is buried into the active site and stabilized by a network of interactions with Arg-127, and with a water molecule that is coordinated also by Thr-48, Phe-49, and Val-50. The formation of the inter-subunit disulfide bond (Cys-51–S_P–S_R–Cys-172) leads to a local unfolding of the C-terminal region: the Trp-176 of one monomer moves ~18 Å apart and is packed in proximity of the GGLG motif of the second monomer, as shown in Figure 7c. The rearrangement of the C-terminal coil causes a disruption of the Tyr-193 interactions, and the YF motif completely loses its helical structure and electron density. Arg-127 is displaced, and Phe-49 is shifted 5.4 Å.

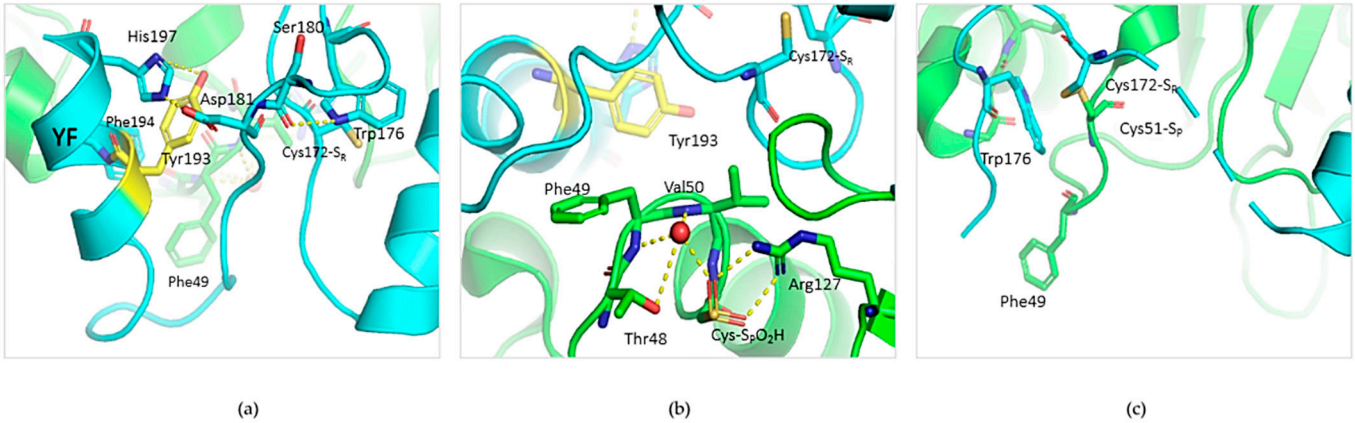

Figure 7. Structural environment of Tyr-193 in reduced and oxidized Prx2. (**a**) Structural features of the active site of reduced Prx2 evidencing one monomer (in cyan) and highlighting (in yellow) Tyr-193 in the hydrogen bond network stabilized with the resolving Cys-172. (**b**) Insight into the network existing from Tyr-193 to the peroxidatic Cys51, here in its sulfinic form (from PDB 1qmv). The green color refers to the neighboring subunit. (**c**) Active site rearrangement in the oxidized form of Prx2 (from PDB: 5ijt).

Based on our experimental data and the bioinformatic analysis, we argue that negative charges introduced on the hydroxyl moiety of Tyr-193 upon phosphorylation would on one side preserve the polar environment, and on the other impair the extensive network of interactions of the C-terminal domain. It follows that phosphorylated Try-193 could positively concur with the fully folded-to-locally unfolded conversion.

3.5. Red Cells from a Humanized Mouse Model of Sickle Cell Disease Display Tyr-Phosphorylated Prx2 Associated with the Membrane

To understand the biologic importance of Prx2 Tyr-phosphorylation in pathologic red cells, we studied erythrocytes from a humanized mouse model of SCD [24,25].

SCD is a globally distributed hereditary red cell disorder. SCD is characterized by presence of the pathologic hemoglobin S (HbS), which polymerizes when deoxygenated [24,25,40–42]. This promotes a severe red cell membrane oxidative damage, resulting in activation of Syk, aggregation of band 3, and membrane translocation of Prx2 [14,22]. In red cells from humanized SCD mice, we observed increased membrane translocation of Prx2 when compared to healthy mice (Figure 8a). Prx2 was present as both a monomer and dimer only in sickle red cells when compared to healthy erythrocytes. Noteworthily, we observed high molecular polymers of band 3 again in SCD red cells when compared to healthy erythrocytes, in agreement with previous reports on membrane oxidation of SCD red cells [22] (Figure 8a). Indeed, we found sulfonate Prx in both the cytosol and membrane compartments in SCD red cells, but not in healthy erythrocytes (Figure S5a). We then evaluated the amount of phospho-Prx2 in both healthy and SCD

erythrocytes. As shown in Figure 8b, we observed membrane translocation of both active Syk and Tyr-phosphorylated Prx2 only in SCD red cells. The enzymatic activity of Prx2 was increased by a factor of 3.6-fold in SCD red cells with respect to healthy erythrocytes, underlining the contribution of overactivation of Prx2 as phosphoPrx2 to face severe oxidation in SCD red cells.

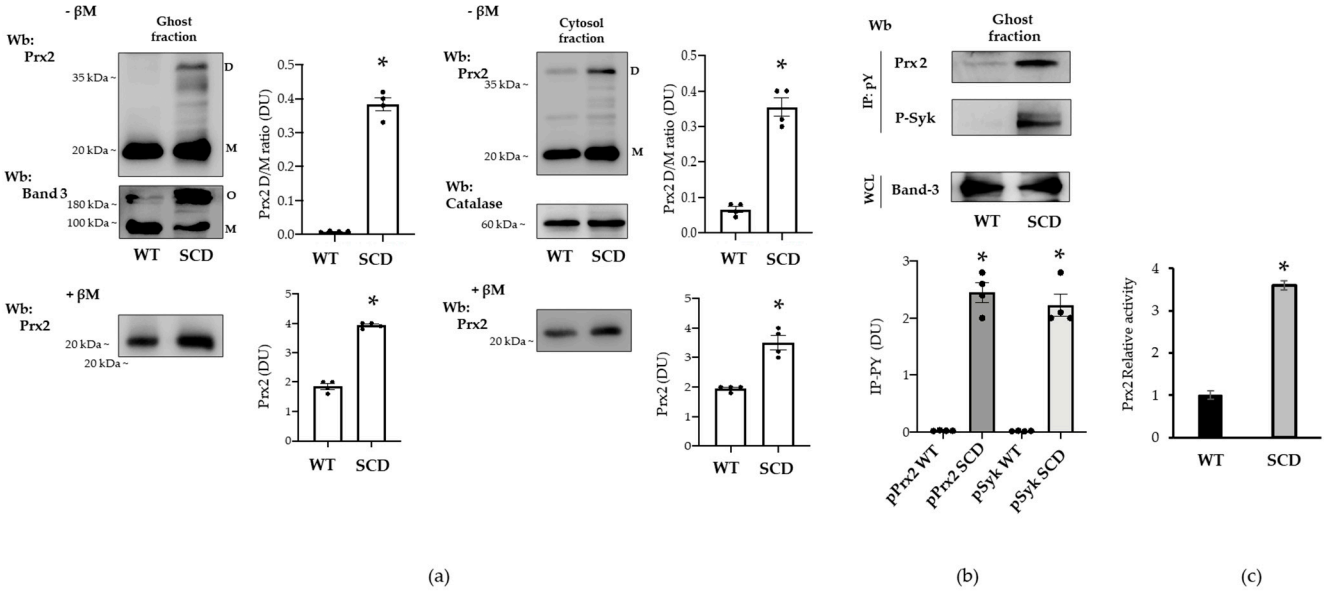

Figure 8. Prx2 is Tyr-phosphorylated in red cells from humanized mouse model for sickle cell disease. (**a**) Western blot (Wb) analysis with specific antibodies against Prx2 of ghost and cytosolic fractions from red cells of WT and SCD mice with or without β-mercaptoethanol (βM). Band 3 and catalase were used as loading controls. M: monomers, D: dimers, O: oligomers. One representative gel from three with similar results is presented. Densitometric analysis is presented as means ± SEM (n = 4); * $p < 0.05$ compared to vehicle-treated red cells. (**b**) Ghost fraction from red cells of WT and SCD mice underwent immunoprecipitation with specific anti-phospho-tyrosine antibodies (IP: PY), and then were used for Western blot (Wb) analysis with anti-Prx2 and P-Syk antibodies. Band 3, as well as colloidal Coomassie-stained gel (see Figure S5b) in whole-cell lysate (WCL) were used as loading controls. One representative gel from three with similar results is presented. Densitometric analysis is presented as means ± SEM (n = 4); * $p < 0.05$ compared to vehicle-treated red cells. (**c**) Prx2 activity of WT and SCD mouse cell ghosts measured as described under Materials and Methods section. Activity of WT was considered as 100%. Results were repeated three times with a standard error less than 5%.

4. Discussion

Here, we show for the first time that Prx2 is Tyr-phosphorylated in red cells in response to either exogenous oxidation by diamide or endogenous oxidation, such as in sickle red cells. We found that Syk specifically phosphorylates Prx2 at Tyr-193, resulting in increased Prx2 activity. This is extremely interesting, since Prx2 is the third most abundant protein in red cells, playing a key role in the antioxidant system and as an atypical chaperone in normal and diseased erythrocytes [17,36,40].

To date, Prx2 function has been mainly related to the redox state of the essential cysteine residues that are directly involved in the peroxidase activity of Prx2 in response to oxidation. Our in vitro studies with recombinant Prx2 have allowed us to identify Syk and Fyn as candidate kinases capable of phosphorylating Prx2. Indeed, we found Syk to phosphorylate Tyr-193 and Fyn to phosphorylate Tyr-115 residues on Prx2. Our attention was captured by Syk, since the amount of Prx2 phosphorylated by this Tyr kinase in vitro was larger than that phosphorylated by Fyn (Figure 5). In addition, Tyr-115 seems less important in relation to Prx2 function, since this residue is located in a hydrophobic cleft remote from the active site, its position remaining unchanged both in the reduced and oxidized form of Prx2 (Figure S6). On the other hand, Tyr-193 is

situated in a key region, both for the catalytic activity and for the control of the oligomeric structure. Indeed, Syk-mediated Tyr-phosphorylation of Prx2 enhances Prx2 activity, as observed using recombinant Prx2 and confirmed by testing the activity of Prx2 from red cells exposed to oxidation (diamide). Tyr-193 is highly mobile, shifting from the ordered, fully folded, reduced state to the locally unfolded, disulfide-oxidized form, as shown by the bioinformatic analyses; it is able to re-order at the end of the catalytic cycle. If the sulfenic cysteine undergoes hyper-oxidation, Tyr-193 is responsible for an extensive network of H bonds, which help to stabilize the decameric assembly, thus the chaperone activity. It is possible that Tyr-193, when phosphorylated, contributes less to the rigid, fully folded form, thus allowing catalysis to occur in a favorite manner. In this sense, its post-translational, modified state helps to keep red cells more protected in highly oxidative conditions, preventing hyper-oxidation by increasing the partition ratio towards peroxidase rather than chaperone activity. In this sense, the oligomer-to-dimer equilibrium is more easily achieved at each catalytic cycle, and high molecular weight aggregates are unfavorably generated.

The biologic importance of Tyr-193, and of its neighboring residues Lys-196 or Phe-194, located in the C-terminus of Prx2, has been also suggested by studies, both in the recombinant form and in different cell lines. Although functional studies are limited, Randall et al. have reported that Prx2 nitration on Tyr-193 results in increased Prx2 activity, associated with increased resistance of Prx2 to overoxidation [12,43]. In our model, the effects of the phosphorylation of Tyr-193 on Prx2 activity are presented using both native and recombinant Prx2. Interestingly, there is an increase in activity following the phosphorylation of Tyr-193, analogous to nitration of the same residue [43], thus suggesting that the modification of this residue, due to the addition of a negative moiety and the related structural effect, could play a key role in strengthening the peroxidase activity.

Since red cells should survive 120 days in the peripheral circulation, an efficient antioxidant and chaperone machinery is required. The functional link between Syk and Prx2 ends in empowering Prx2 activity and contributes to ensure the survival of red cells against exogenous or endogenous oxidation, respectively induced by oxidative agents, such as diamide, or pathologic hemoglobin, such as in SCD.

In erythrocytes, Syk plays a crucial role in transduction cell signaling against oxidation. We have previously shown that Syk overactivation favors band 3 clusterization, allowing the release of erythroid microparticles and red cell membrane rearrangement. In addition, oxidation might also affect band 3 function as an anion exchanger [27,44,45]. Exogenous antioxidants, such as curcumin or melatonin, as well as the potentiation of endogenous cytoprotectors like PEP-Prx2, might prevent or limit band 3 oxidative damage, preserving band 3 structure and function [17,44,45]. Here, we observe that diamide strongly activates Syk, whereas H_2O_2 slightly changes the amount of active Syk. Noteworthily, diamide targets proteins thiol groups promoting S-thiolation, whereas H_2O_2 irreversibly oxidizes sulfhydryl groups to sulfinic or sulfonic acid, leading to a peroxidase-incompetent Prx2. Indeed, diamide promotes diamide cross-linking of band 3 with generation of oligomeric structures that are Tyr-phophorylated by Syk [18,19]. This requires that phospho-Prx2, the more active form of Prx2, is located at the red cell membrane. Indeed, our observations suggest that Tyr-phosphorylated Prx2 translocates to the membrane. However, we cannot exclude Tyr phosphorylation of the small amount of Prx2 already bound to the membrane, as the method employed is not sensitive enough to dissect these events. The membrane localization of more active Prx2 might represent a back-up mechanism to locally minimize oxidative damage of membrane proteins, such as band 3. In agreement, band 3 was found mainly in oligomeric state, as clusterized band 3, in sickle red cell membrane, which showed increased phospho-Prx2 bound to the membrane (Figure 9).

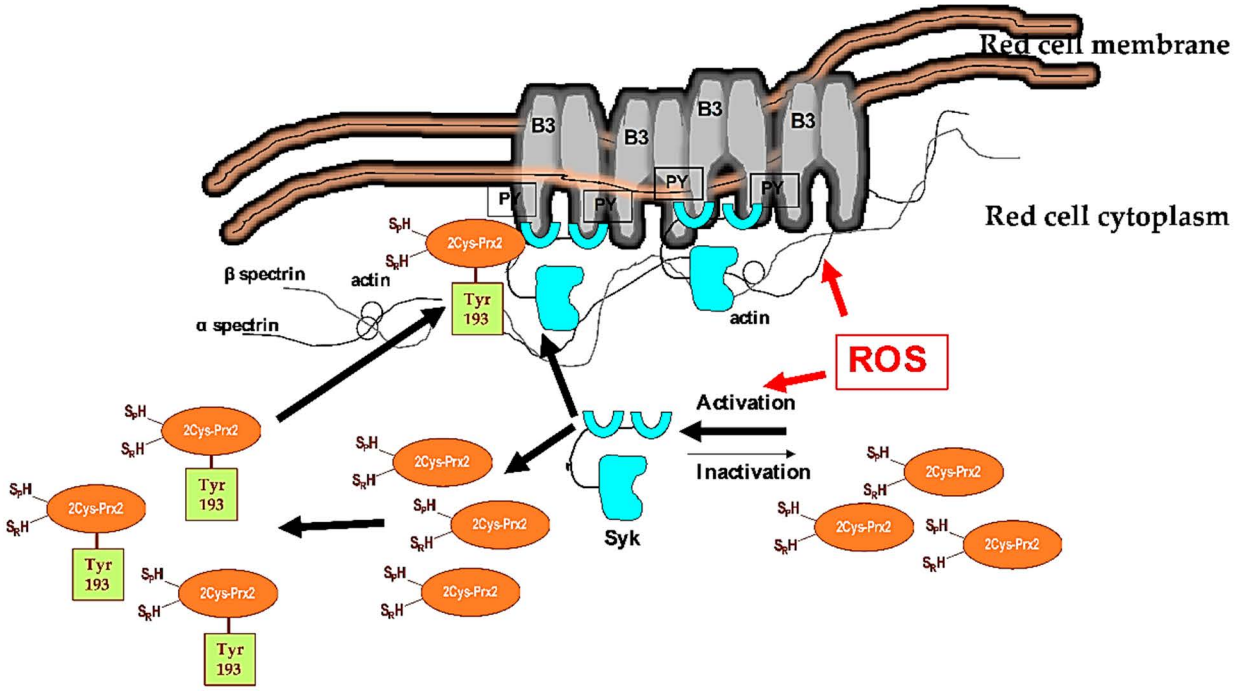

Figure 9. Schematic diagram of the functional model linking Syk activation in response to oxidation and Prx2 in red cells. Under steady-state conditions, Syk is inactive. Cellular stress, such as exogenous oxidation (ROS: reactive oxygen species) triggers Syk activation, resulting in increased tyrosine (Tyr) band 3 (B3) phosphorylation (PY). This modulates B3 interaction with neighboring proteins, such as band 4.1, band 4.2, adducin, or ankyrin. These multiprotein complexes bridging the membrane to the cytoskeleton contribute to the membrane's mechanical instability. Diseased red cells, such as in sickle cell disease (SCD), are characterized by severe oxidation. This results in membrane damage and the overactivation of Syk. The damaged, over-Tyr-phosphorylated B3 forms clusters, which favor erythroid vesicle release and the fast removal of the damaged red cells by splenic macrophages. Under oxidative stress, Syk targets also Prx2. This affects both the compartmentalization of Prx2 to the red cell membrane and Prx2 activity, representing a back-up mechanism to locally minimize oxidative damage of the membrane proteins, such as band 3.

Our data are also important in the unique biologic context of malaria, when *Plasmodium* imposes a strong oxidative stress on the host red cells [19,35,46]. To counteract this burden, the infected erythrocytes over-activate Syk that promotes band 3 clusterization with the release of erythroid microparticles. The erythrocyte ability to face oxidation is also vital for parasite blood stage. Noteworthy, *Plasmodium* has been reported to recruit Prx2 from red cells, most likely to potentiate its own defense [47,48]. The importance of Prx2 for *Plasmodium* is further supported by the observation that parasite growth is prevented in red cells with inhibited Prx2 [47,48]. Recently, we reported that pharmacologic Syk inhibitors, such as imatinib, might represent a novel and interesting new therapeutic option for the design of host-directed intervention strategies. Imatinib potentiates the action of standard malaria treatment with artemisinin, allowing more rapid parasite clearance [19,35,46]. Our novel data on Syk-dependent Tyr phosphorylation of Prx2 add a new piece of knowledge to the molecular mechanisms of malaria infestation, emphasizing at least two functional targets of therapeutic Syk inhibition in malaria parasite red cells, namely band 3 and Prx2.

Due to the ever-increasing knowledge regarding this complex family of biological sensors, the Prxs, endowed with both catalytical and regulation activities, this study might offer new important information on Prx2 function and regulation, as well as its crosstalk with red cell membranes in normal and diseased red cells, such as with SCD. However, some other points in the progression of this investigation could be addressed, such as the absence of mutagenesis experiments and the development of an anti-phspho-Tyr-193 Prx2 antibody to be used in different experimental conditions, in order to further functionally characterize the role of Tyr-193 Prx2 in different pathologic red cells. In addition, it is

possible that phosphorylated Prx2 is a small fraction of the total pool, and the site of phosphorylation (cytosol or membrane) of Prx2 has not been identified. These points are worth addressing in future investigations.

In fact, further studies are required to fully characterize phospho-Prx2 in both normal and diseased red cells. In addition, the potentiation of endogenous antioxidant systems by the modulation of intracellular signaling might represent an interesting new frontier of investigation.

Supplementary Materials: The following are available online at https://www.mdpi.com/2076-3921/10/2/206/s1, Figure S1. Colloidal Coomassie stained gels of ghost and cytosol fraction from red cells of wild-type (WT) mice treated with vehicle or diamide, Figure S2. Prx2 activity on hydrogen peroxide concentration. Dependence of the rate of reaction of the recombinant Prx2 (5 μM) at various hydrogen peroxide concentration, using DTT (200 μM) as reducing agent, Figure S3. (a) Western-blot (Wb) analysis with specific antibody against Prx2 of supernatant from immuno-precipitation assays, Figure S4. Identification of Tyr115 on Fyn phosphorylated recombinant Prx2, Figure S5. Western-blot (Wb) analysis with specific antibodies against Prx SO3, Figure S6. Localization of Tyr115 in the hyperoxidized (mimicking the reduced state) and oxidized Prx2, Methods.

Author Contributions: A.M., E.F., and A.S. generated the experimental data; E.T. and M.L.D.P. generated the functional data on in vitro recombinant Prx2 phosphorylation and activity; A.C. and F.T. generated the mass spectrometric data; L.D.F., A.M.B., M.B., F.T., P.P., E.T., A.M., and E.F. completed the writing—review and editing; L.D.F. and A.M.B. supervised. I.I., V.R., A.B.W., and A.S. contributed to data analysis. D.W.K. and S.Y.C. generated recombinant Prx2. G.B. contributed to bioinformatic analyses and carried out in vitro Prx2 activity in mouse red cells. All authors have read and agreed to the published version of the manuscript.

Funding: This paper was supported by FUR-Department of Medicine, University of Verona (LDF) and by FUR-Department of Neuroscience, Biomedicine and Movement Sciences, University of Verona (MB).

Institutional Review Board Statement: The Institutional Animal Experimental Committee of University of Verona (CIRSAL, Verona, Italy) and the Italian Ministry of Health approved the experimental protocol number (56DC9.12), following European directive 2010/63/EU and the Federation for Laboratory Animal Science Associations guidelines and recommendations.

Informed Consent Statement: Not applicable.

Data Availability Statement: Data is contained within the article or Supplementary Material.

Conflicts of Interest: Authors declare no conflict of interest.

References

1. Wood, Z.A.; Schroder, E.; Robin Harris, J.; Poole, L.B. Structure, mechanism and regulation of peroxiredoxins. *Trends Biochem. Sci.* **2003**, *28*, 32–40. [CrossRef]
2. Wood, Z.A.; Poole, L.B.; Hantgan, R.R.; Karplus, P.A. Dimers to doughnuts: Redox-sensitive oligomerization of 2-cysteine peroxiredoxins. *Biochemistry* **2002**, *41*, 5493–5504. [CrossRef] [PubMed]
3. Low, F.M.; Hampton, M.B.; Winterbourn, C.C. Peroxiredoxin 2 and peroxide metabolism in the erythrocyte. *Antioxid. Redox Signal.* **2008**, *10*, 1621–1630. [CrossRef]
4. Manta, B.; Hugo, M.; Ortiz, C.; Ferrer-Sueta, G.; Trujillo, M.; Denicola, A. The peroxidase and peroxynitrite reductase activity of human erythrocyte peroxiredoxin 2. *Arch. Biochem. Biophys.* **2009**, *484*, 146–154. [CrossRef] [PubMed]
5. Rhee, S.G. Overview on Peroxiredoxin. *Mol Cells* **2016**, *39*, 1–5.
6. Rhee, S.G.; Kang, S.W.; Chang, T.S.; Jeong, W.; Kim, K. Peroxiredoxin, a novel family of peroxidases. *IUBMB Life* **2001**, *52*, 35–41. [CrossRef]
7. Chae, H.Z.; Uhm, T.B.; Rhee, S.G. Dimerization of thiol-specific antioxidant and the essential role of cysteine 47. *Proc. Natl. Acad. Sci. USA* **1994**, *91*, 7022–7026. [CrossRef]
8. Hall, A.; Nelson, K.; Poole, L.B.; Karplus, P.A. Structure-based insights into the catalytic power and conformational dexterity of peroxiredoxins. *Antioxid. Redox Signal.* **2011**, *15*, 795–815. [CrossRef]
9. Bertoldi, M. Human Peroxiredoxins 1 and 2 and Their Interacting Protein Partners; Through Structure Toward Functions of Biological Complexes. *Protein Pept. Lett.* **2016**, *23*, 69–77. [CrossRef]
10. Rhee, S.G.; Woo, H.A. Multiple functions of 2-Cys peroxiredoxins, I and II, and their regulations via post-translational modifications. *Free Radic. Biol. Med.* **2020**, *152*, 107–115. [CrossRef]

11. Romero-Puertas, M.C.; Laxa, M.; Matte, A.; Zaninotto, F.; Finkemeier, I.; Jones, A.M.; Perazzolli, M.; Vandelle, E.; Dietz, K.J.; Delledonne, M. S-nitrosylation of peroxiredoxin II E promotes peroxynitrite-mediated tyrosine nitration. *Plant Cell* **2007**, *19*, 4120–4130. [CrossRef] [PubMed]
12. Skoko, J.J.; Attaran, S.; Neumann, C.A. Signals Getting Crossed in the Entanglement of Redox and Phosphorylation Pathways: Phosphorylation of Peroxiredoxin Proteins Sparks Cell Signaling. *Antioxidants* **2019**, *8*, 29. [CrossRef]
13. Matte, A.; Low, P.S.; Turrini, F.; Bertoldi, M.; Campanella, M.E.; Spano, D.; Pantaleo, A.; Siciliano, A.; De Franceschi, L. Peroxiredoxin-2 expression is increased in beta-thalassemic mouse red cells but is displaced from the membrane as a marker of oxidative stress. *Free Radic. Biol. Med.* **2010**, *49*, 457–466. [CrossRef]
14. Siciliano, A.; Turrini, F.; Bertoldi, M.; Matte, A.; Pantaleo, A.; Olivieri, O.; De Franceschi, L. Deoxygenation affects tyrosine phosphoproteome of red cell membrane from patients with sickle cell disease. *Blood Cells Mol. Dis.* **2010**, *44*, 233–242. [PubMed]
15. Matte, A.; Bertoldi, M.; Mohandas, N.; An, X.; Bugatti, A.; Brunati, A.M.; Rusnati, M.; Tibaldi, E.; Siciliano, A.; Turrini, F.; et al. Membrane association of peroxiredoxin-2 in red cells is mediated by the N-terminal cytoplasmic domain of band 3. *Free Radic. Biol. Med.* **2013**, *55*, 27–35. [CrossRef] [PubMed]
16. De Franceschi, L.; Bertoldi, M.; De Falco, L.; Santos Franco, S.; Ronzoni, L.; Turrini, F.; Colancecco, A.; Camaschella, C.; Cappellini, M.D.; Iolascon, A. Oxidative stress modulates heme synthesis and induces peroxiredoxin-2 as a novel cytoprotective response in beta-thalassemic erythropoiesis. *Haematologica* **2011**, *96*, 1595–1604. [CrossRef]
17. Matte, A.; Pantaleo, A.; Ferru, E.; Turrini, F.; Bertoldi, M.; Lupo, F.; Siciliano, A.; Ho Zoon, C.; De Franceschi, L. The novel role of peroxiredoxin-2 in red cell membrane protein homeostasis and senescence. *Free Radic. Biol. Med.* **2014**, *76*, 80–88. [CrossRef]
18. Pantaleo, A.; Ferru, E.; Giribaldi, G.; Mannu, F.; Carta, F.; Matte, A.; de Franceschi, L.; Turrini, F. Oxidized and poorly glycosylated band 3 is selectively phosphorylated by Syk kinase to form large membrane clusters in normal and G6PD-deficient red blood cells. *Biochem. J.* **2009**, *418*, 359–367.
19. Pantaleo, A.; Ferru, E.; Pau, M.C.; Khadjavi, A.; Mandili, G.; Matte, A.; Spano, A.; De Franceschi, L.; Pippia, P.; Turrini, F. Band 3 Erythrocyte Membrane Protein Acts as Redox Stress Sensor Leading to Its Phosphorylation by p (72) Syk. *Oxid. Med. Cell Longev.* **2016**, *2016*, 6051093. [CrossRef]
20. Ferru, E.; Pantaleo, A.; Carta, F.; Mannu, F.; Khadjavi, A.; Gallo, V.; Ronzoni, L.; Graziadei, G.; Cappellini, M.D.; Turrini, F. Thalassemic erythrocytes release microparticles loaded with hemichromes by redox activation of p72Syk kinase. *Haematologica* **2014**, *99*, 570–578. [CrossRef]
21. Tibaldi, E.; Federti, E.; Matte, A.; Iatcenko, I.; Wilson, A.B.; Riccardi, V.; Pagano, M.A.; De Franceschi, L. Oxidation Impacts the Intracellular Signaling Machinery in Hematological Disorders. *Antioxidants* **2020**, *9*, 353. [CrossRef] [PubMed]
22. Biondani, A.; Turrini, F.; Carta, F.; Matte, A.; Filippini, A.; Siciliano, A.; Beuzard, Y.; De Franceschi, L. Heat-shock protein-27, -70 and peroxiredoxin-II show molecular chaperone function in sickle red cells: Evidence from transgenic sickle cell mouse model. *Proteom. Clin. Appl.* **2008**, *2*, 706–719. [CrossRef] [PubMed]
23. De Franceschi, L.; Villa-Moruzzi, E.; Biondani, A.; Siciliano, A.; Brugnara, C.; Alper, S.L.; Lowell, C.A.; Berton, G. Regulation of K-Cl cotransport by protein phosphatase 1alpha in mouse erythrocytes. *Pflug. Arch.* **2006**, *451*, 760–768. [CrossRef] [PubMed]
24. Park, S.Y.; Matte, A.; Jung, Y.; Ryu, J.; Anand, W.B.; Han, E.Y.; Liu, M.; Carbone, C.; Melisi, D.; Nagasawa, T.; et al. Pathologic angiogenesis in the bone marrow of humanized sickle cell mice is reversed by blood transfusion. *Blood* **2020**, *135*, 2071–2084.
25. Matte, A.; Recchiuti, A.; Federti, E.; Koehl, B.; Mintz, T.; El Nemer, W.; Tharaux, P.L.; Brousse, V.; Andolfo, I.; Lamolinara, A.; et al. Resolution of sickle cell disease-associated inflammation and tissue damage with 17R-resolvin D1. *Blood* **2019**, *133*, 252–265. [CrossRef]
26. De Franceschi, L.; Turrini, F.; Honczarenko, M.; Ayi, K.; Rivera, A.; Fleming, M.D.; Law, T.; Mannu, F.; Kuypers, F.A.; Bast, A.; et al. In vivo reduction of erythrocyte oxidant stress in a murine model of beta-thalassemia. *Haematologica* **2004**, *89*, 1287–1298.
27. De Franceschi, L.; Olivieri, O.; Miraglia del Giudice, E.; Perrotta, S.; Sabato, V.; Corrocher, R.; Iolascon, A. Membrane cation and anion transport activities in erythrocytes of hereditary spherocytosis: Effects of different membrane protein defects. *Am. J. Hematol.* **1997**, *55*, 121–128.
28. Brugnara, C.; de Franceschi, L. Effect of cell age and phenylhydrazine on the cation transport properties of rabbit erythrocytes. *J. Cell Physiol.* **1993**, *154*, 271–280. [CrossRef]
29. Franco, S.S.; De Falco, L.; Ghaffari, S.; Brugnara, C.; Sinclair, D.A.; Matte, A.; Iolascon, A.; Mohandas, N.; Bertoldi, M.; An, X.; et al. Resveratrol accelerates erythroid maturation by activation of FoxO3 and ameliorates anemia in beta-thalassemic mice. *Haematologica* **2014**, *99*, 267–275. [CrossRef]
30. Dodge, J.T.; Mitchell, C.; Hanahan, D.J. The preparation and chemical characteristics of hemoglobin-free ghosts of human erythrocytes. *Arch. Biochem. Biophys.* **1963**, *100*, 119–130. [CrossRef]
31. De Franceschi, L.; Tomelleri, C.; Matte, A.; Brunati, A.M.; Bovee-Geurts, P.H.; Bertoldi, M.; Lasonder, E.; Tibaldi, E.; Danek, A.; Walker, R.H.; et al. Erythrocyte membrane changes of chorea-acanthocytosis are the result of altered Lyn kinase activity. *Blood* **2011**, *118*, 5652–5663. [CrossRef] [PubMed]
32. Ura, B.; Monasta, L.; Arrigoni, G.; Licastro, D.; Di Lorenzo, G.; Romano, F.; Gaita, B.; Scrimin, F.; Ricci, G. Leiomyoma phosphoproteins involved in inhibition of oxidative stress and synthesis of reactive oxygen species. *Int. J. Mol. Med.* **2019**, *44*, 2329–2335. [CrossRef] [PubMed]
33. Thingholm, T.E.; Larsen, M.R. Sequential Elution from IMAC (SIMAC): An Efficient Method for Enrichment and Separation of Mono- and Multi-phosphorylated Peptides. *Methods Mol. Biol.* **2016**, *1355*, 147–160. [PubMed]

34. Nelson, K.J.; Parsonage, D. Measurement of peroxiredoxin activity. *Curr. Protoc. Toxicol.* **2011**, *49*, 7–10. [CrossRef] [PubMed]
35. Pantaleo, A.; Ferru, E.; Carta, F.; Mannu, F.; Giribaldi, G.; Vono, R.; Lepedda, A.J.; Pippia, P.; Turrini, F. Analysis of changes in tyrosine and serine phosphorylation of red cell membrane proteins induced by P. falciparum growth. *Proteomics* **2010**, *10*, 3469–3479. [CrossRef] [PubMed]
36. Matte, A.; Lupo, F.; Tibaldi, E.; Di Paolo, M.L.; Federti, E.; Carpentieri, A.; Pucci, P.; Brunati, A.M.; Cesaro, L.; Turrini, F.; et al. Fyn specifically regulates the activity of red cell glucose-6-phosphate-dehydrogenase. *Redox Biol.* **2020**, *36*, 101639–101651.
37. Zonta, F.; Pagano, M.A.; Trentin, L.; Tibaldi, E.; Frezzato, F.; Gattazzo, C.; Martini, V.; Trimarco, V.; Mazzorana, M.; Bordin, L.; et al. Lyn-mediated procaspase 8 dimerization blocks apoptotic signaling in B-cell chronic lymphocytic leukemia. *Blood* **2014**, *123*, 875–883. [CrossRef]
38. Tibaldi, E.; Brunati, A.M.; Zonta, F.; Frezzato, F.; Gattazzo, C.; Zambello, R.; Gringeri, E.; Semenzato, G.; Pagano, M.A.; Trentin, L. Lyn-mediated SHP-1 recruitment to CD5 contributes to resistance to apoptosis of B-cell chronic lymphocytic leukemia cells. *Leukemia* **2011**, *25*, 1768–1781. [CrossRef]
39. Horta, B.B.; de Oliveira, M.A.; Discola, K.F.; Cussiol, J.R.; Netto, L.E. Structural and biochemical characterization of peroxiredoxin Qbeta from Xylella fastidiosa: Catalytic mechanism and high reactivity. *J. Biol. Chem.* **2010**, *285*, 16051–16065.
40. Lombardi, E.; Matte, A.; Risitano, A.M.; Ricklin, D.; Lambris, J.D.; De Zanet, D.; Jokiranta, S.T.; Martinelli, N.; Scambi, C.; Salvagno, G.; et al. Factor H interferes with the adhesion of sickle red cells to vascular endothelium: A novel disease-modulating molecule. *Haematologica* **2019**, *104*, 919–928. [CrossRef]
41. Matte, A.; Cappellini, M.D.; Iolascon, A.; Enrica, F.; De Franceschi, L. Emerging drugs in randomized controlled trials for sickle cell disease: Are we on the brink of a new era in research and treatment? *Expert Opin. Investig. Drugs* **2020**, *29*, 23–31. [CrossRef] [PubMed]
42. Matte, A.; Zorzi, F.; Mazzi, F.; Federti, E.; Olivieri, O.; De Franceschi, L. New Therapeutic Options for the Treatment of Sickle Cell Disease. *Mediterr. J. Hematol. Infect. Dis.* **2019**, *11*, e2019002. [CrossRef] [PubMed]
43. Randall, L.M.; Manta, B.; Hugo, M.; Gil, M.; Batthyany, C.; Trujillo, M.; Poole, L.B.; Denicola, A. Nitration transforms a sensitive peroxiredoxin 2 into a more active and robust peroxidase. *J. Biol. Chem.* **2014**, *289*, 15536–15543. [CrossRef] [PubMed]
44. Morabito, R.; Remigante, A.; Marino, A. Melatonin Protects Band 3 Protein in Human Erythrocytes against H_2O_2-Induced Oxidative Stress. *Molecules* **2019**, *24*, 2741. [CrossRef] [PubMed]
45. Remigante, A.; Morabito, R.; Marino, A. Natural Antioxidants Beneficial Effects on Anion Exchange through Band 3 Protein in Human Erythrocytes. *Antioxidants* **2019**, *9*, 25. [CrossRef]
46. Pantaleo, A.; Kesely, K.R.; Pau, M.C.; Tsamesidis, I.; Schwarzer, E.; Skorokhod, O.A.; Chien, H.D.; Ponzi, M.; Bertuccini, L.; Low, P.S.; et al. Syk inhibitors interfere with erythrocyte membrane modification during P falciparum growth and suppress parasite egress. *Blood* **2017**, *130*, 1031–1040.
47. Koncarevic, S.; Rohrbach, P.; Deponte, M.; Krohne, G.; Prieto, J.H.; Yates, J., 3rd; Rahlfs, S.; Becker, K. The malarial parasite Plasmodium falciparum imports the human protein peroxiredoxin 2 for peroxide detoxification. *Proc. Natl. Acad. Sci. USA* **2009**, *106*, 13323–13328. [CrossRef]
48. Brizuela, M.; Huang, H.M.; Smith, C.; Burgio, G.; Foote, S.J.; McMorran, B.J. Treatment of erythrocytes with the 2-cys peroxiredoxin inhibitor, Conoidin A, prevents the growth of Plasmodium falciparum and enhances parasite sensitivity to chloroquine. *PLoS ONE* **2014**, *9*, e92411.